Lecture Notes in Electrical Engineering 202

Qilian Liang · Wei Wang
Jiasong Mu · Jing Liang
Baoju Zhang · Yiming Pi
Chenglin Zhao *Editors*

Communications, Signal Processing, and Systems

The 2012 Proceedings of the International Conference on Communications, Signal Processing, and Systems

Springer

Lecture Notes in Electrical Engineering

For further volumes:
http://www.springer.com/series/7818

Qilian Liang • Wei Wang • Jiasong Mu
Jing Liang • Baoju Zhang • Yiming Pi
Chenglin Zhao
Editors

Communications, Signal Processing, and Systems

The 2012 Proceedings of the International Conference on Communications, Signal Processing, and Systems

Springer

Editors
Qilian Liang
University of Texas at Arlington
Arlington, Texas
USA

Jiasong Mu
College of Physical and Electronic Information
Tianjin Normal University
Tianjin, China

Baoju Zhang
College of Physical and Electronic Information
Tianjin Normal University
Tianjin, China

Chenglin Zhao
School of Information and Communication Engineering
Beijing University of Posts and Telecommunications
Bejing, China

Wei Wang
College of Physical and Electronic Information
Tianjin Normal University
Tianjin, China

Jing Liang
School of Electronic Engineering
University of Electronic Science and Technology
Chengdu, Sichuan
China

Yiming Pi
School of Electronic Engineering
University of Electronic Science and Technology of China
Chengdu, China

ISSN 1876-1100 ISSN 1876-1119 (electronic)
ISBN 978-1-4614-5802-9 ISBN 978-1-4614-5803-6 (eBook)
DOI 10.1007/978-1-4614-5803-6
Springer New York Heidelberg Dordrecht London

Library of Congress Control Number: 2012951651

Printed on acid-free paper

Springer is part of Springer Science+Business Media (www.springer.com)

Preface

The International Conference on Communications, Signal Processing, and Systems (CSPS) has been hold in Beijing during October 16–18, 2012. Beijing is universally acknowledged for its rich history and cultural development. It is also recognized as a modern international metropolis full of energy and vitality. CSPS 2012 brings together Chinese and international researchers and practitioners in communications, signal processing, and systems.

The accepted papers for CSPS 2012 are taken from various regions around the world to be presented in 13 different technical sessions: Synthetic Aperture Radar Imaging, Smart Grids, Wireless Sensor Networks, Cognitive Radio Systems, Image Processing, Design and Implementation of Signal Processing Systems, Information Theory and Coding, Millimeter Wave Communications, Radar Signal Processing, Communications Theory, Wireless Networks, Localization and Target Detection, and Biological Signal Processing.

The technical program team did an excellent job in soliciting submissions, coordinating the review process, and promoting the technical program. We would like to thank each one of them for playing leading roles in organizing the various aspects of the technical program.

Also we would like to express our thanks to all members of the organizing committee and all the volunteer reviewers who have been working hard day and night for this conference. We would like also to express our gratitude to the all the sponsors of this conference: IEEE Fort Worth Section, University of Texas at Arlington, Beijing University of Posts and Telecommunications, Tianjin Normal University, and University of Electronic Science and Technology of China

(UESTC). Finally, financial support from the Program of Introducing Talents of Discipline to Universities in UESTC, the National Natural Science Foundation of China (NSFC), and publication support from Springer is deeply appreciated.

Arlington, Texas — Qilian Liang
Tianjin, China — Wei Wang
Tianjin, China — Jiasong Mu
Chengdu, China — Jing Liang
Tianjin, China — Baoju Zhang
Chengdu, China — Yiming Pi
Bejing, China — Chenglin Zhao

Welcome Message from the General Chairs

It is our great honor and pleasure to welcome you to Beijing for the International Conference on Communications, Signal Processing, and Systems (CSPS) held during October 16–18, 2012. During this conference, scholars and practitioners from all over the world in communications, signal processing, and electronic systems will get together in Beijing.

Beijing is the capital city of the People's Republic of China. It is also the nation's political and cultural hub. Additionally, it is the focal point of the country's development in travel and transport, science and technology, education, and communications. Beijing is world famous for its trove of historical sites and enchanting natural beauty, making it a compelling tourist destination. It is a remarkable city offering an abundance of ancient and modern architecture, temples, gardens, and museums and a variety of colorful local flavors and customs.

CSPS 2012 is organized by an international team. The conference features 13 technical sessions and 2 keynote sessions. We invite you to join us in attending the technical and social events held in CSPS 2012.

On behalf of the organizing committee, the technical program committee, and all the volunteers that have been working hard for this conference, we warmly welcome you to CSPS 2012 and hope that you will enjoy the conference, and the beautiful city in which it takes place.

Tariq S. Durrani, Rabinder N. Madan,
Yiming Pi, Chenglin Zhao
General Cochairs, CSPS 2012

Organization

The International Conference on Communications, Signal Processing, and Systems (CSPS) is organized by University of Texas at Arlington, Beijing University of Posts and Telecommunications, Tianjin Normal University, and University of Electronic Science and Technology, China;

General Co-Chairs:
Tariq S. Durrani, University of Strathclyde, UK
Rabinder N. Madan, Office of Naval Research, USA
Yiming Pi, University of Electronic Science and Technology, China
Chenglin Zhao, Beijing University of Posts and Telecommunications, China

TPC Co-Chairs:
P. P. Vaidyanathan, California Institute of Technology, USA
Qilian Liang, University of Texas at Arlington, USA
Jing Liang, University of Electronic Science and Technology, China
Baoju Zhang, Tianjin Normal University, China

International Advisory Committee:
Leon Chua, University of California at Berkeley, USA
Gene Frantz, Texas Instruments, USA
Er Meng Hwa, Nanyang Technological University, Singapore
Sanjit Mitra, University of Southern California, USA
Zhisheng Niu, Tsinghua University, China
Wan-Chi Siu, Hong Kong Polytechnic University, Hong Kong
Tieniu Tan, Chinese Academy of Science, China
Xiaorong Wu, Tianjin Normal University, China
Zheng Zhou, Beijing University of Posts and Telecommunications, China

Publicity Chair:
Xiuzhen Cheng, George Washington University, USA
Haijiang Wang, Chengdu University of Information Technology, China
Zhiqin Zhao, University of Electronic Science and Technology, China

Financial and Local Arrangement Chair:
Luhong Fan, University of Electronic Science and Technology, China

Tutorial Co-Chairs:
Jun-Hong Cui, University of Connecticut, USA
Jingfu Bao, University of Electronic Science and Technology, China
Bin Tang, University of Electronic Science and Technology, China

Special Session Co-Chairs:
Jian Ren, Michigan State University, USA
Zinan Wang, University of Electronic Science and Technology, China
Dechang Chen, Uniformed Services University of the Health Sciences, USA

Publication Chair:
Wei Wang, Tianjin Normal University, China
Jiasong Mu, Tianjin Normal University, China
Zongjie Cao, University of Electronic Science and Technology, China
Zengshan Tian, Chongqing University of Posts and Telecommunications, China

Registration Chair:
Songbai He, University of Electronic Science and Technology, China
Huiyong Li, University of Electronic Science and Technology, China

TPC Members:
Jingfu Bao, University of Electronic Science and Technology, China
Zongjie Cao, University of Electronic Science and Technology, China
Dechang Chen, Uniformed Services University of Health Sciences, USA,
Jin Chen, Tianjin Normal University, China
Junjie Chen, University of Texas at Arlington, USA
Xiao Chen, Texas State University, USA
Ting Cheng, University of Electronic Science and Technology, China
Xiuzhen Cheng, George Washington University, USA
Junhong Cui, University of Connecticut, USA
Luhong Fan, University of Electronic Science and Technology, China
Qian He, University of Electronic Science and Technology, China
Songbai He, University of Electronic Science and Technology, China
Jiyan Huang, University of Electronic Science and Technology, China
Ting Jiang, Beijing University of Posts and Telecommunications, China
Huiyong Li, University of Electronic Science and Technology, China
Liying Li, University of Electronic Science and Technology, China
Shenghong Li, Shanghai JiaoTong University, China
Shuangtian Li, Institute of Acoustics Academia Sinica, China
Tongtong Li, Michigan State University, USA
Zhuo Li, University of Texas at Arlington, USA
Kuo Liao, University of Electronic Science and Technology, China
Ruian Liu, Tianjin Normal University, China
Ishrat Maherin, University of Texas at Arlington, USA

Jiasong Mu, Tianjin Normal University, USA
Yiming Pi, University of Electronic Science and Technology, China
Jian Ren, Michigan State University, USA
Qingchun Ren, Mircosoft, USA
Songlin Sun, Beijing University of Posts and Telecommunications, China
Bin Tang, University of Electronic Science and Technology, China
Haijiang Wang, University of Electronic Science and Technology, China
Lingming Wang, Coherent Logix, USA
Wenbo Wang, Beijing University of Posts and Telecommunications, China
Wei Wang, Tianjin Normal University, China
Xin Wang, University of Texas at Arlington, USA
Ji Wu, University of Texas at Arlington, USA
Zhengyu Wu, University of Electronic Science and Technology, China
Xinsheng Xia, AT&T, USA
Lei Xu, Broadcom, USA
Xin Yin, Tianjin Normal University, China
Feng Zhao, GuiLin University of Electronic Technology, China
Zhiqin Zhao, University of Electronic Science and Technology, China
Ying Zhang, University of Electronic Science and Technology, China
Daiying Zhou, University of Electronic Science and Technology, China
Xin Zhou, Tianjin Normal University, China
Zheng Zhou, Beijing University of Posts and Telecommunications, China
Hongbo Zhu,Nanjing University of Posts and Telecommunications, China

Web Chair:
Ji Wu, University of Texas at Arlington, USA

Sponsoring Institutions:
IEEE Fort Worth Section, USA
University of Texas at Arlington
Beijing University of Posts and Telecommunications
Tianjin Normal University
University of Electronic Science and Technology, China

Contents

Part I
Synthetic Aperture Radar Imaging

Chapter 1
A Hierarchy System for Automatic Target Recognition in SAR Images

Zongyong Cui, Zongjie Cao, Jianyu Yang, Jian Cheng, Yulin Huang, and Liyuan Xu

Abstract A novel SAR image automatic target hierarchy recognition (ATHR) system based on SVM and D-S evidence theory is proposed in this chapter. This system has three hierarchies corresponding to three features. PCA, LDA and NMF features are extracted from images without preprocessing, and are fed to SVM classifier. However, not all features are used in each recognition process. At each recognition process, a threshold is used to determine the used features and hierarchy depth. Experiments on MSTAR public data set demonstrate that the proposed system outperforms the system combining the outputs of three features directly.

Keywords SAR ATR • Hierarchy recognition • SVM • D-S evidence theory

1.1 Introduction

Synthetic aperture radar automatic target recognition (SAR ATR) is essential in SAR image interpretation and analysis. It plays an important role both in national defense and civil applications. A lot of researches attempt to represent the targets effectively and then classify them with high recognition rate. SAR ATR approaches can be roughly divided into three types: template-based [1, 2], model-based [3, 4] and pattern-based [5, 6]. Most current researches belong to the pattern-based framework.

In order to pursue high recognition performance, multiple features or multiple classifiers recognition with machine learning has become a research hotspot and has been extensively applied in many areas. An ensemble system which is composed of

Z. Cui (✉) • Z. Cao • J. Yang • J. Cheng • Y. Huang • L. Xu
School of Electronic Engineering, University of Electronic Science and Technology of China, Chengdu 611731, Sichuan, People's Republic of China
e-mail: cuizongyong@163.com; zjcao@uestc.edu.cn

Q. Liang et al. (eds.), *Communications, Signal Processing, and Systems*, Lecture Notes in Electrical Engineering 202, DOI 10.1007/978-1-4614-5803-6_1,

several independent base-level models is described in [7]. Reference [8] proposes a multiple classifier system, which uses three different feature sets and three different leaning algorithms to train three classifiers. Reference [9] introduces a three fusion strategies, including multi-view decision fusion strategy, multi-feature decision fusion strategy and multi-classifier decision fusion strategy. It proves that the multi-feature or multi-classifier recognition systems usually outperform the system that only depends on one feature and one classifier.

But the methods above mainly focus on recognition rate, ignoring the limit of time. Efficiency is more important in some applications. How to improve the efficiency of the recognition system but not 'win through the quantity superiority' is the research point in this chapter. Based on the consideration, a novel SAR ATR hierarchy system is proposed. This system has three hierarchies corresponding to three features: PCA, LDA and NMF, respectively. These three features are extracted from original image data without any preprocessing step, and are fed to SVM classifier. Then D-S evidence theory is used to fuse the result of the first two or all three hierarchies. The purpose of the hierarchy framework is to select the appropriate features to meet the need, rather than to use all features. If using one feature can get good result, there is no need to use other features. Compared to fusion methods which use all features in every recognition process, this system can save the recognition time. By settings of different thresholds in each hierarchy, this system can also have high recognition rate. Experiments on MSTAR data set demonstrate that the designed recognition system is very effective.

The rest of the chapter is organized as follows: Sect. 1.2 gives a detail description of our designed system. Then Sect. 1.3 presents experimental results. Finally in Sect. 1.4 the conclusion and future work are stated.

1.2 Hierarchy Recognition System

Just like most of recognition systems, the designed system in this chapter includes two parts: the offline part for training and the online part for testing and recognizing unknown objects.

1.2.1 Offline Part

Three features, F1, F2 and F3, are extracted from training samples without any preprocessing step, and then they are fed into SVM classifier. In this step, three models of SVM are got which will be further used in test processes.

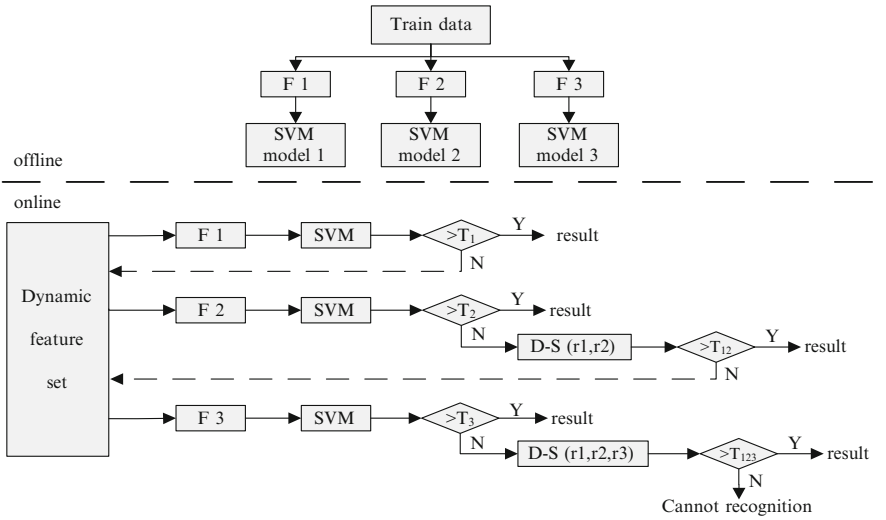

Fig. 1.1 Framework of three hierarchies and five levels recognition system

1.2.2 Online Part

There are five steps to recognize unknown targets in online part:

1. Extracting feature F1 of sample, and feeding F1 to SVM. If the SVM result r1 and threshold T_1 satisfy: $\max(r1) \geq T_1$, output the predicted class of sample; if $\max(r1) < T_1$, go to (2);
2. Extracting feature F2, and feeding F2 to SVM. If the SVM result r2 and threshold T2 satisfy: $\max(r2) \geq T2$, output the predicted class of sample; else go to (3);
3. Combining r1 and r2 by D-S theory. If the fusion result is equal or greater than threshold T_{12}, output the predicted class of sample; else goto (4);
4. Extracting feature F3,and feeding it to SVM. If the result $\max(r3) \geq T_3$, output the predicted class; else goto (5);
5. Combining r1,r2 and r3 by D-S theory. If the fusion result is equal or greater than threshold T_{123}, output the predicted class of sample; else output 'cannot recognition'.

The system framework is shown in Fig. 1.1.

To make it more clear, the time for feature invocation is defined as hierarchy and the time for decision is named as level. As a result, the system proposed in this chapter has three hierarchies and five levels.

1.3 System Composition

From Fig. 1.1, it can be seen that the online part includes three important parts: feature extracting, SVM classifier, and D-S evidence theory.

1.3.1 Feature Extraction

In our current research, three projection features are used. They are principal component analysis (PCA), linear discriminant analysis (LDA), and non-negative matrix factor (NMF).

1.3.1.1 PCA

Principal Component Analysis (PCA) is a common feature extraction method in pattern recognition, and has been widely used for target classification in SAR images. Through the Karhunen-Loève transformation, the principal component of one image is extracted. The detailed information about PCA is introduced in [6] and [10].

1.3.1.2 LDA

Supposing N sampled images be denoted as $\mathrm{X} = \{\mathrm{x}_1, x_2, \ldots \ldots \mathrm{x}_\mathrm{N}\}$, the *within-class* scatter matrix [10, 11] is defined as:

$$S_w = \sum_{j=1}^{c} \sum_{i=1}^{N_j} (x_i^j - \mu_j)(x_i^j - \mu_j)^T \tag{1.1}$$

Where x_i^j is the *i*thsample of class *j*, μ_j is the mean of class *j*, *c* is the number of classes, and N_j is the number of samples in class *j*.

The *between-class* scatter matrix is defined as:

$$S_b = \sum_{j=1}^{c} (\mu_j - \mu)(\mu_j - \mu)^T \tag{1.2}$$

where μ represents the mean of all classes.

The goal is to maximize the between-class measure while minimizing the within-class measure. One way to do it is to maximize the ratio $\frac{\det|S_b|}{\det|S_w|}$. If S_w is a nonsingular matrix, when the column vectors of the projection matrix $W = PCA(S_w^{-1}S_b)$, the ratio is maximized. It should be noted that the number of eigenvectors of $W$is at most $c - 1$.

1.3.1.3 NMF

Matrix $D \in \mathrm{R}^{n\times m}$ is decomposed into two matrices $W \in \mathrm{R}^{n\times r}$ and $H \in \mathrm{R}^{r\times m}$, so that [12]:

$$\mathrm{D} \approx \mathrm{WH} \qquad \mathrm{D_{i,j}}, \mathrm{W_{i,\mu}}, \mathrm{H_{\mu,j}} \geq 0 \tag{1.3}$$

with $0 \leq i<n-1, 0 \leq j<m-1$ and $0 \leq \mu<r-1$.

Define Cost Function by Square Euclidian Distance:

$$\arg\min_{W,H} \|D - WH\|^2 = \sum_{0\leq i<n, 0\leq j<m} \left(D_{i,j} - (WH)_{i,j}\right)^2 \tag{1.4}$$

The Square Eculidian Distance measure in (1.4) is non-increasing under the following iterative update rules:

$$H_{a\mu} \leftarrow H_{a\mu} \frac{(W^T D)_{a\mu}}{(W^T WH)_{a\mu}} \tag{1.5}$$

$$W_{ia} \leftarrow W_{ia} \frac{(DH^T)_{ia}}{(WHH^T)_{ia}} \tag{1.6}$$

for $0 \leq a<r, 0 \leq \mu<m$ and $0 \leq i<n$. Appropriate W, H can be found by iteration.

Comparing the equations of these three features, it can be shown that the computational complexity of PCA is the smallest, and the computational complexity of NMF is the largest. This can be proved when recognition depends on single feature. The first hierarchy of this system should use the feature which is computed fastest. So the F1, F2 and F3 in Fig. 1.1 correspond with PCA, LDA and NMF, respectively.

1.3.2 SVM Classifier

SVM classification method has extraordinary potential capacity, thus SVM is acted as classifier of SAR image target recognition in this chapter. Basic SVM is aimed at classification problem of two sorts. To realize the recognition of N sorts and provide probabilistic outputs, SVM is needed to be extended [13].

Give a test image, the outputs of SVM is in the following form:

$$result = \{p_1, p_2, \ldots p_j, \ldots p_c\} \tag{1.7}$$

where $0<j \leq c$, c is the number of class. And p_j is the probability value of recognizing the test image to class j.

1.3.3 D-S Evidence Theory

Dempster-Shafer Evidence Theory has been widely used in information fusion and classifier fusion [8, 9, 14, 15]. Assuming Θ is a mutually exclusive and exhaustive finite set, which is called *frame of discernment*. The mapping $m : 2^{\Theta} \rightarrow [0,1]$called Basic Probability Assignment Function (BPAF) is defined as:

$$\begin{cases} m(\Theta) = 0 \\ \sum\limits_{A \in \Theta} m(A) = 1 \end{cases} \tag{1.8}$$

If $A \subseteq \Theta$ and $m(A)>0$, A is called Focal Element.

If Θ has n Focal Elements: $A = \{A_1, A_2, \ldots A_i, \ldots A_n\}$, Dempster's rule of combination is described as follows:

$$\begin{cases} m(\Theta) = 0 \\ m(A) = \dfrac{\sum\limits_{\cap A_i = A} \prod\limits_{i=1}^{n} m_i(A_i)}{1 - \sum\limits_{\cap A_i = \Theta} \prod\limits_{i=1}^{n} m_i(A_i)} = \dfrac{\sum\limits_{\cap A_i = A} \prod\limits_{i=1}^{n} m_i(A_i)}{1-k} \end{cases} \tag{1.9}$$

And k is a measure of conflict between n evidences.

In the second and third hierarchies of online part, the n in (1.9) are 2 and 3, respectively.

1.4 Experimental Results

1.4.1 Training and Testing Data

The SAR images used in our experiments are taken from MSTAR public release database. The database consists of X-band SAR images with 1 ft. x ft. resolution. Three classes of objects of the data base: BMP2, BTR70, and T72 are used (Fig. 1.2).

Different from other methods, a novel data grouping mode is used. In order to test the designed system's ability of processing different condition data, the MSTAR database is divided into one training set and three testing sets. The images of BMP2-c21, BTR70-c71, and T72-132 in depression angles of 17° are employed as an training set: set1. And the other images are used for testing sets. The detail of the data sets is shown in Table 1.1.

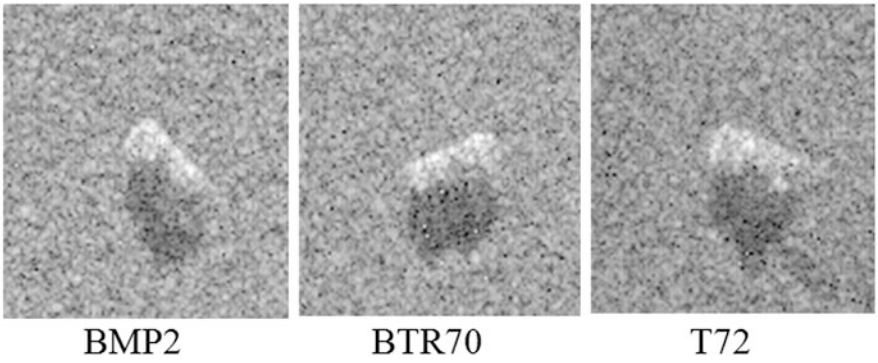

Fig. 1.2 Original SAR images in MSTAR

Table 1.1 Train and test data sets from MSTAR

	Set serial	Type	Depression angle	Size
Training set	Set 1	BMP2-c21	17°	233
		BTR70-c71	17°	233
		T72-132	17°	232
Testing set	Set 2	BMP2-c21	15°	196
		BTR70-c71	15°	196
		T72-132	15°	196
	Set 3	BMP2-9563	17°	233
		BMP2-9566	17°	232
		T72-812	17°	232
	set 4	BMP2-9563	15°	195
		BMP2-9566	15°	196
		T72-812	15°	195

Set2 versus set1: same target but different depression angles
Set3 versus set1: different targets but same depression angle
Set4 versus set1: different targets and different depression angles

1.4.2 Experimental Setup

In order to conform human's recognition rules, the value of threshold T is no less than 0.5. After testing, the values of T_1, T_2, T_{12}, T_3, and T_{123} are set to 0.6, 0.7, 0.5, 0.5, 0.5, respectively.

Radial Basis Function (RBF) is used for SVM, and penalty C and kernel parameter γ are set to 2^5 and 2^{-5}, respectively.

Table 1.2 Recognition results

Methods	Set2 (%)	Set3 (%)	Set4 (%)	Average (%)
PCA	94.22	79.02	73.72	82.14
LDA	92.52	80.03	77.47	83.16
NMF	97.79	88.07	82.76	89.47
Fusion [8]	98.30	86.49	84.47	89.57
Proposed method	99.32	90.52	87.54	92.35

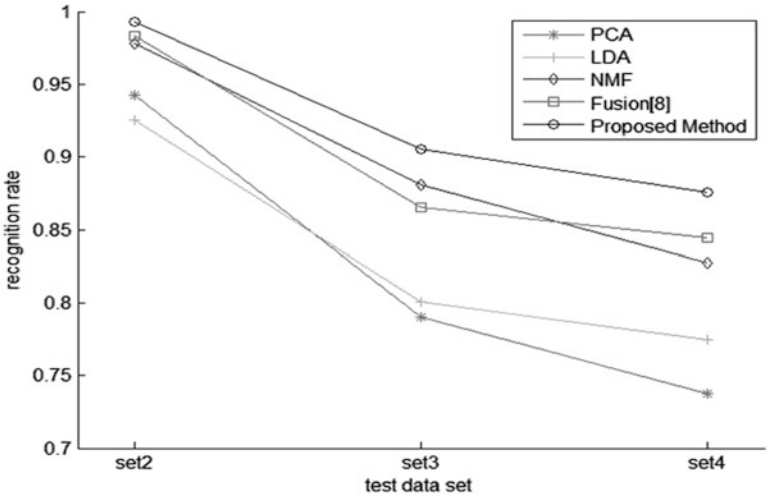

Fig. 1.3 The recognition results on different test sets

Table 1.3 The hierarchy depth of three testing sets

Hierarchy depth	Set2 (588)	Set3 (696)	Set4 (586)
First	522	357	288
Second	21	90	91
Third	44	244	201
Cannot recognition	1	5	6

1.4.3 Recognition Results

Table 1.2 and Fig. 1.3 present the recognition results of five methods on set2 ~ set4. Set4 has the lowest recognition rate, which means both target type and depression angle can have effect on recognition processing. However, the recognition rate of set2 is higher than set3, which means the target type has more effect on recognition than depression angle.

Meanwhile, Table 1.2 and Fig. 1.3 also show that the Fusion Method [8] indeed outperforms the method used single feature, but the proposed hierarchy framework in this chapter has the best results.

Table 1.4 Comparison with Fusion [8] on average RR and used time

Methods	Average RR (%)	Time
Fusion [8]	89.57	5.02 s
Proposed method	92.35	3.9 s

The hierarchy depth of three testing sets is presented in Table 1.3. For most samples of set 2, only the first hierarchy is used for recognition. Just a few recognition processes can reach the third hierarchy. However, the number of recognition processes which use all three hierarchies has obvious growth when recognizing the samples of set 3 and set 4. Therefore our system can choose different hierarchy depth according to the complexity of recognition processes.

The comparison on average recognition rate and used time with Fusion [8] when testing set2 ~ set4 is shown in Table 1.4. Obviously, the proposed method outperforms Fusion [8] both on recognition rate and time.

1.5 Conclusion

This chapter proposes a novel three hierarchies and five levels recognition system for ATR. Using PCA, LDA and NMF features, three models for SVM are got in the offline part. When testing, PCA feature of test image is extracted firstly. Whether to go to the next hierarchy depends on the comparison between probabilistic output and threshold T. The simple test may use the first hierarchy, and some complicated tests will go through all three hierarchies. This system can save the recognition time and use features and classifiers efficiently on the basis of high recognition rate. Experiments on MSTAR public data set demonstrate that the proposed system outperforms single classifier and ensemble classifiers.

The next step in our research work will consist in selecting the threshold T adaptively and using more features and more classifiers to build a recognition framework based on human cognition theory.

Acknowledgments This work is supported by Fundamental Research Funds for the Central Universities under Projects ZYGX2009Z005.

References

1. Novak LM, Owirka GJ, Weaver AL (1999) Automatic target recognition using enhanced resolution SAR data. IEEE Trans AES 35(1):157–175
2. Kaplan ML (2001) Analysis of multiplicative apeckle models for template- based SAR ATR. IEEE Trans AES 31(4):1424–1432
3. O'Sullivan JA, Devore MD (2001) SAR ATR performance using a conditionally Gaussian model. IEEE Trans AES 37(1):91–108

4. Bhanu B, Yingqiang Lin (2000) Recognition of occluded targets using stochastic models. In: Proceedings of IEEE workshop on computer vision beyond the visible spectrum: method and applications, Singapore, pp 73–82
5. Gong Cheng, Wei Zhao, Jinping Zhang (2006) A practical kernel criterion for feature extraction and recognition of MSTAR SAR images. In: Proceedings of ICIP, Singapore, vol 4
6. Changzhen Qiu, Hao Ren, Huanxin Zou (2009) Performance comparison of target classification in SAR images based on PCA and 2D-PCA features. In: Proceedings of 2nd APSAR, Singapore, pp 868–871
7. Rokach L (2010) Ensemble-based classifiers. Artif Intell Rev 33(1–2):1–39
8. Xin Yu, Yukuan Li, LC Jiao (2011) SAR target recognition based on classifiers fusion. In: Proceedings of M2RSM, Singapore, pp 1–5
9. Huan R, Pan Y (2011) Decision fusion strategies for SAR image target recognition. IET Radar Son Nav 5, lss. 7:747–755
10. Martinez AM, Kak AC (2001) PCA versus LDA. IEEE Trans PAMI 23(2):228–233
11. Belhumeur PN, Hespanha JP, Lriegman DJ (1997) Eigenfaces vs. fisherfaces: recognition using class specific linear projection. IEEE Trans PAMI 19(7):734–756
12. Lee DD, Seung HS (1999) Learning the parts of objects by non-negative matrix factorization. Nature 401:788–791
13. Cortes C, Vapnik V (1995) Support vector networks. Mach Learn 20(2):273–297
14. Kuncheva LI (2004) Combining pattern classifiers: methods and algorithms. Wiley, Hoboken
15. Huynh V-N, Nguyen TT, Le CA (2009) Adaptively entroy-based weighting classifiers in combination using Dempster-Shafer theory for word sending disambiguation. Comput Speech Lang 24(3):461–473

Chapter 2
Building Extraction of SAR Images Using Morphological Attribute Profiles

Lingzi Xue, Xiaqing Yang, and Zongjie Cao

Abstract A building extraction method is proposed in this chapter used to deal with the special situation of SAR images processing. Morphological attribute profiles (APs) are the generalization of the recently proposed method morphological profiles (MPs). APs extract a multilevel characterization of an image by sequential application of morphological attribute filters. According to the type of the attributes considered in the morphological attribute transformation, different parametric features can be modeled. Here, the method proposed above is used for building extraction of SAR images. SVMs (Support vector machines) are used for classifications at last. The experimental analysis proved the usefulness of Aps in modeling the spatial information present in the image.

Keywords Building extraction • SAR • Morphological attribute profiles • SVM • Features extraction

2.1 Introduction

Remote sensing technology is a rising and promising subject which was developed in 1960s. The first notable thing is SAR (Synthetic Aperture Radar) [1] which is very useful for the military high-altitude reconnaissance and is stepping into the civilian remote sensing areas. Facing the growing data collection capabilities of SAR image which is accomplished by the improvement of the SAR system and getting of plenty of high-resolution SAR image, the scientists around the world are working on the analysis and interpretation of the SAR image.

L. Xue • X. Yang • Z. Cao (✉)
School of Electronic Engineering, University of Electronic Science and Technology of China, Chengdu, China
e-mail: zjcao@uestc.edu.cn

Q. Liang et al. (eds.), *Communications, Signal Processing, and Systems*, Lecture Notes in Electrical Engineering 202, DOI 10.1007/978-1-4614-5803-6_2,

It is known that the building extraction is one of the most important subjects of urban remote sensing image interpretation which is of significant theoretical and applied value in some aspects such as remote sensing image registration, map update, density surveys of the building area, road network planning, urban monitoring and disaster assessment. In the field of optical remote sensing image processing, building extraction is a classic subject which has been researched for almost 20 years and lots of methods and practical systems have been proposed so far. In the contrast, the research on building extraction oriented SAR image is in the starting stage. Due to the restriction of sensor system, SAR images are low-resolution and it is difficult to distinguish the buildings of the scene. In the high-resolution optical image, the roof, side wall and some other structures of the building is clear, while in the SAR image, there are some geometric distortion because of the imaging mechanism and vogue ground subject. So we use morphological methods to deal with building extraction of SAR image.

Mathematical morphology [2, 3] is a very useful tool for the image processing which has become the main research subject of image analysis and processing. Now morphology is a new image processing method and theory which is a foundation for processing the image which contains lots of information. Pesaresi and Benediktsson [4–9] proposed building the differential morphological profiles (DMPs) in [4] and [5] and morphological profiles (MPs) in [5] to represent the differences in the values of the morphological profiles at different scales. After that, MPs have been used in the features extraction of remote sensing classification. Morphological attribute profiles (APs) in [8] and [9] are proposed as extended methods recently. Aps provide multilevel image features which are built by a series of morphological attribute filter operators which can be used to build different types of structures information models. According to the type of the attribute chose in the operators, different types of features can be built.

In this chapter, we use the APs for building extraction of high-solution SAR image. The results of the experiment show this method performed well as a feature extraction method which reflected the distribution of building area and got good results in building extraction.

2.2 Mps and Dmps

Firstly we consider an opening by reconstruction,$\gamma_R^{\mathrm{i}}(f)$ which is used in an image f with an SE of size i. The opening by reconstruction can be seen as a sequence of erosion with the SE followed by a reconstruction by dilation. By duality, a closing by reconstruction, $\phi_R^i(f)$, is defined as the dilation of the original image with SE of size i, followed by a geodesic reconstruction by erosion.

When opening by reconstruction is computed on the image with an SE of increasing size, we can obtain a morphological opening profile which can be formalized as

$$\Pi_{\gamma_R}(f) = \left\{\Pi_{\gamma_\lambda} : \Pi_{\gamma_\lambda} = \gamma_R^\lambda(f), \forall\lambda \in [0, \ldots, n]\right\} \tag{2.1}$$

This leads to perform a multiscale analysis of the image.

According to its definition, morphological opening profile which is a granulometry built by openings by reconstruction and fulfills the absorption property is defined as a idempotent, anti-extensive and increasing transformation in the mathematical morphology framework. Analogously, a morphological closing profile is defined as

$$\Pi_{\phi_R}(f) = \left\{\Pi_{\phi_\lambda} : \Pi_{\phi_\lambda} = \phi_R^\lambda(f), \forall\lambda \in [0, \ldots, n]\right\} \tag{2.2}$$

The closing profile is an anti-granulometry generated by closings by reconstruction. When the size, λ, of the SE is zero, $\Pi_{\gamma^0}(f) = \Pi_{\phi^0}(f)$, corresponding to the original image. A morphological profile is composed by the morphological opening profile and morphological closing profile which is defined as

$$\Pi(f) = \left\{\Pi_i : \left\langle \begin{array}{lll} \Pi_i = \Pi_{\phi_\lambda}, \ with & \lambda = (n-i+1), & \forall i \in [1,n] \\ \Pi_i = \Pi_{\gamma_\lambda}, \ with & \lambda = (i-n-1), & \forall i \in [n+1, 2n+1] \end{array} \right\}\right. \tag{2.3}$$

By computing the derivative of a MP, a differential morphological profile is generated as

$$\Delta(f) = \left\{\Delta_i : \left\langle \begin{array}{lll} \Delta_i = \Delta_{\phi_\lambda}, \ with & \lambda = (n-i+1), \forall i \in [1,n] \\ \Delta_i = \Delta_{\gamma_\lambda}, \ with & \lambda = (i-n), \forall i \in [n+1, 2n] \end{array} \right\}\right. \tag{2.4}$$

Above the differential opening profile, Δ_γ, and the differential closing profile, Δ_ϕ, are respectively defined as

$$\Delta_{\gamma_R}(f) = \left\{\Delta_{\gamma_\lambda} : \Delta_{\gamma_\lambda} = \Pi_{\gamma_{(\lambda-1)}} - \Pi_{\gamma_\lambda}, \forall\lambda \in [1,n]\right\} \tag{2.5}$$

$$\Delta_{\phi_R}(f) = \left\{\Delta_{\phi_\lambda} : \Delta_{\phi_\lambda} = \Pi_{\phi_\lambda} - \Pi_{\phi_{(\lambda-1)}}, \forall\lambda \in [1,n]\right\} \tag{2.6}$$

As we can see from (2.4), DMP contains the residuals of the subsequent increasing transformations applied in the image. Because in the DMP, corresponding to the MP, the residuals are more obvious which are more useful in the multiscale analysis.

2.3 Morphological Attribute Filters

2.3.1 Binary Attribute Operators

Binary connected opening, Γ_x, is a transformation for a binary image which is given a pixel x. It can keep the component which contains the x, leaving the rest unaffected. Binary trivial opening, Γ_T, operates on a given connected component

X according to an increasing criterion$T$. If the criterion is satisfied, the connected component is kept, or it is removed according to

$$\Gamma_T(X) = \begin{cases} X, & \text{if } T(X)=true \\ 0, & \text{if } T(X)=false \end{cases} \tag{2.7}$$

In general, the features which are used in the filter operators are compared to a given threshold defined by the rule. The increasing criteria are used to compare with the regions such as the area, the volume, the size of the bounding box, etc. It can be proved that the attribute values computed on a region is greater or equal to the values computed on the enclosed regions.

Binary attribute opening, Γ^T, given an increasing criterion T, is defined as binary trivial opening which is applied on every connected component of F. It can be formally represented as

$$\Gamma^T(F) = \bigcup_{x \in F} \Gamma_T[\Gamma_x(F)] \tag{2.8}$$

The definition above can be extended to binary attribute closing Φ^T:

$$\Phi^T(F) = \bigcup_{x \in F} \Phi_T[\Phi_x(F)] \tag{2.9}$$

It is based on binary trivial closing Φ_T and binary connected closing Φ_X.

2.3.2 Grayscale Attribute Operators

Binary attribute opening can be extended to grayscale images using the threshold decomposition principle. A grayscale image can be represented by a stack of binary images obtained by threshold the original image. Then, the binary attribute opening can be used in every binary image. This can be formally represented as

$$\gamma(f)(x) = \max\{k \ : \ x \in \Gamma^T[Th_k(f)]\} \tag{2.10}$$

$Th_k(f)$ is the binary image obtained by thresholding f at graylevel k.

Attribute openings represent series of operators including openings by reconstruction. If we consider a binary image with a connected component X and the increasing criteria the "size of the largest square enclosed by X must be greater than λ", the result of the operators is the same as applying an opening by reconstruction with a squared SE of size λ. The situation can be extended to grayscale cases.

The definition above can be directly extended to attribute closing:

$$\Phi^T(f)(x) = \min\{k \ : \ x \in \Phi^T[Th_k(f)]\} \tag{2.11}$$

2.4 Morphological Attribute Profiles

The definition of attribute opening profile is a type of granulometry transformation with a family of increasing criteria $T = \{T_\lambda : \lambda = 0, \ldots, n\}$. Thus, attribute opening profiles can be mathematically defined as

$$\Pi_{\gamma^T}(f) = \left\{\Pi_{\gamma^{T_\lambda}} : \Pi_{\gamma^{T_\lambda}} = \gamma^{T_\lambda}(f), \forall\lambda \in [0, \ldots, n]\right\} \tag{2.12}$$

As for MPs, it can be proved that when $\lambda = 0$, $\Pi_{\gamma^{T_0}}(f) = \gamma^{T_0} = f$. Both for MPs and Aps, the transformations are the multiscale analysis of the image with increasing scalar SE/T.

By duality, the attribute closing profiles can be defined as

$$\Pi_{\phi^U}(f) = \left\{\Pi_{\phi^{U_\lambda}} : \Pi_{\phi^{U_\lambda}} = \phi^{U_\lambda}(\mathrm{f}), \forall\lambda \in [0, \ldots, n]\right\} \tag{2.13}$$

Analogously to (2.3), we can define the attribute profile as

$$\Pi(f) = \left\{\Pi_i : \begin{cases} \Pi_i = \Pi_{\phi^{U_\lambda}}, & \text{with } \lambda = (\mathrm{n}-\mathrm{i}+1), \quad \forall \mathrm{i} \in [1,\mathrm{n}] \\ \Pi_i = \Pi_{\gamma^{U_\lambda}}, & \text{with } \lambda = (\mathrm{i}-\mathrm{n}-1), \quad \forall \mathrm{i} \in [\mathrm{n}+1, 2\mathrm{n}+1] \end{cases}\right\} \tag{2.14}$$

Similarly to MPs, we can also deduce the definition of differential attribute profiles as

$$\Delta(f) = \left\{\Delta_i : \begin{cases} \Delta_i = \Delta_{\phi^{U_\lambda}}, & \textit{with } \lambda = (n-i+1), \quad \forall i \in [1,\mathrm{n}] \\ \Delta_i = \Delta_{\gamma^{U_\lambda}}, & \textit{with } \lambda = (i-n), \quad \forall i \in [n+1, 2\mathrm{n}] \end{cases}\right\} \tag{2.15}$$

Here, $\Delta_{\phi^{U_\lambda}}$ and $\Delta_{\gamma^{U_\lambda}}$ represent differential opening and closing profiles.

2.5 Experimental Analysis

The experimental analysis is based on a 306 × 350 SAR image and a 93 × 121 SAR image which contains three main types of ground objects (buildings, lands and roads) intercepted from a high-resolution SAR image of Washington. The images are shown as Figs. 2.1 and 2.2. The process of the building extraction based on morphological attribute profiles and SVM is including two main phases: (1) feature extraction; (2) classification. These phases are presented in detail below

1. *Feature Extraction*
   In this phase, morphological attribute profiles are used in this step. The attribute specifically used in the method which we chose at first is area attribute to model the ground scene. Those criterion values were arbitrarily chosen and they are

Fig. 2.1 Data set 1—SAR image of 306 × 350 pixels. (**a**) original optical image of Washington and (**b**) the first applied SAR image obtained from the original image and its comparative optical image

Fig. 2.2 Data set 2—SAR image of 93 × 121 pixels. (**a**) original optical image of Washington and (**b**) the second SAR applied image obtained from the original image and its comparative optical image

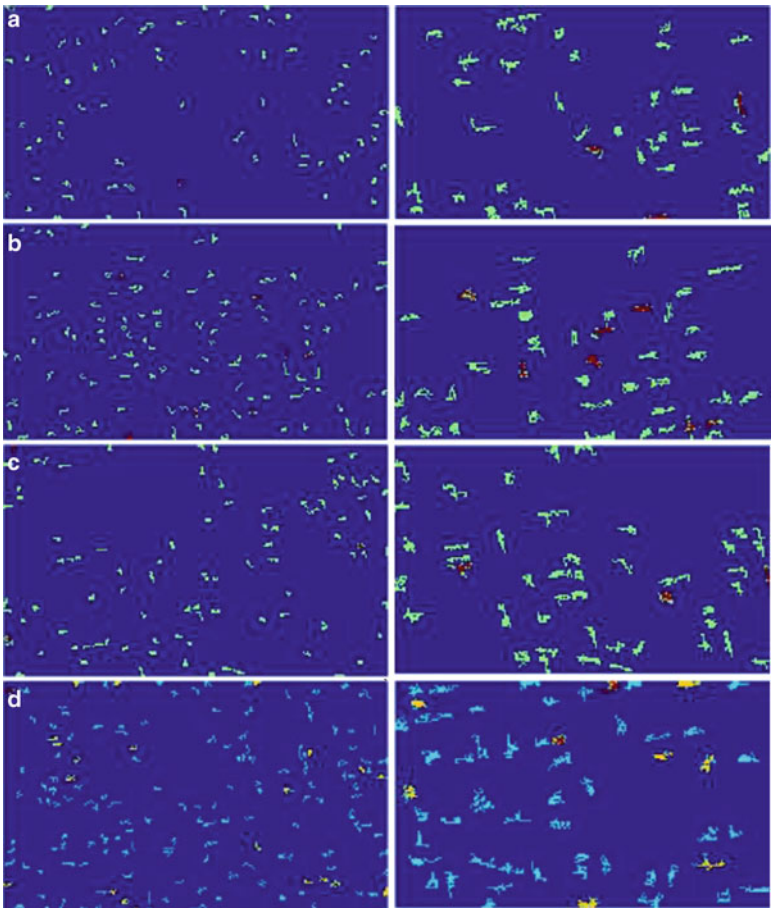

Fig. 2.3 Extracts of differential attribute profiles of area attribute. (**a**) the attribute opening profiles, (**b**) the attribute closing profiles on the second level and the forth level of data set 1, (**c**) the attribute opening profiles with (**d**) the attribute closing profiles on the second level and the forth level of data set 2

able to model the size of the objects in the scene. All the filter operators are applied on the max-tree data representation.

2. *Classification*
   In this phase, SVMs are used in this classification step. Firstly, we take the train data into SVM to get the model. Then the SAR image is used in the model to get the result of the building extraction.

In the experimental steps, the criterions are 5-time increasing areas and 10-D morphological profiles are formed. To compare the difference between the different profiles, we can use DMPs to describe them which are more straightforward and shown as Fig. 2.3.

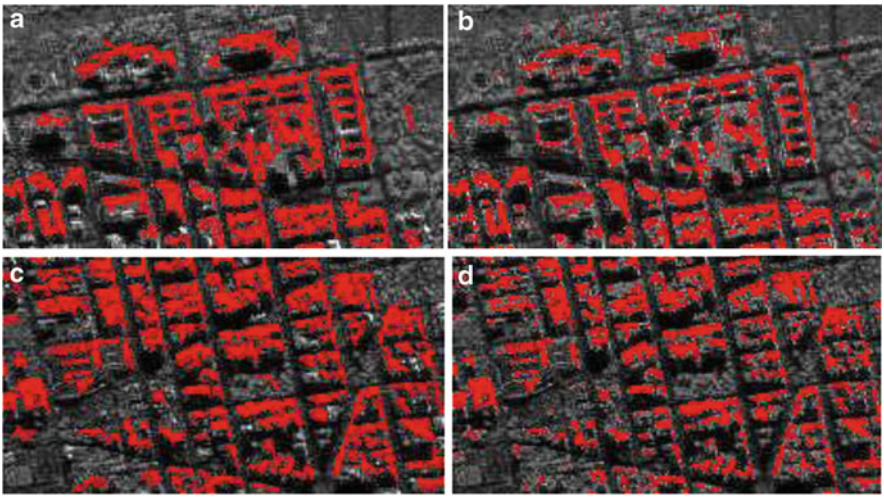

Fig. 2.4 Final building extraction results and the comparative result using basic morphological operators and SVMs. (**a**) the result of data set 1, (**c**) the result of data set 2 and (**b**), (**d**) the comparative results using basic morphological operators with SVMs

The final building extraction results and their comparative optical images are as Fig. 2.4. We can see the effective building extraction results of this method. To compare the effectiveness, the results got from building extraction using basic morphological operators (opening and closing operators) and SVMs are showed in Fig. 2.4. As we can see, we can get a good result using this method to get the building area of a SAR image. But in some details, there are still some classification errors exist.

2.6 Conclusion

In this chapter, morphological features are applied on the building extraction of SAR images which have shown the potential of SAR image classification using morphological information. There are two morphological transformation used in the chapter: attribute opening and attribute closing. Those two operators can keep the others goals unaffected while the targets are been processed. In this chapter, it is proved that APs and SVMs together can get a good result of building extraction of SAR images.

Acknowledgments This work is supported by the National Natural Science Foundation of China under Projects 60802065 and the Fundamental Research Funds for the Central Universities under Projects ZYGX2009Z005.

References

1. YiMing Pi (2007) Synthetic aperture radar imaging principle.University of Electronic Science and Technology Press, Chengdu
2. Gonzalez RC, Woods RE (2007) Digital image processing, 2nd ed. Publishing House of Electronic Industry, Beijing
3. Soille P (2003) Morphological image analysis, principles and applications, 2nd edn. Springer, Berlin
4. Pesaresi M, Benediktsson JA (2001) A new approach for the morphological segmentation of high-resolution satellite imagery. IEEE Trans Geosci Remote Sens 39(2):309–320
5. Benediktsson JA, Pesaresi M, Arnason K (2003) Classification and feature extraction for remote sensing images from urban areas based on morphological transformations. IEEE Trans Geosci Remote Sens 41(9):1940–1949
6. Benediktsson JA, Palmason JA, Sveinsson JR (2005) Classification of hyperspectral data from urban areas based on extended morphological profiles. IEEE Trans Geosci Remote Sens 43 (3):480–491
7. Soille P, Pesaresi M (2002) Advances in mathematical morphology applied to geoscience and remote sensing. IEEE Trans Geosci Remote Sens 40(9):2042–2055
8. Dalla Mura M, Benediktsson JA, Waske B, Bruzzone L (2009) Morphological atribute filters for the analysis of very high resolution images. In: Proceedings of IEEE IGARSS, vol. III. Cape Town, 12–19 Jul 2009, pp 97–100
9. Dalla Mura M, Benediktsson JA, Waske B, Bruzzone L (2010) Morphological attribute profiles for the analysis of very high resolution images. IEEE Trans Geosci Remote Sens 48 (10):3747–3762

Chapter 3
Variational Segmentation of Polarimetric SAR Image By Using a Continous Potts Model and Automatic Initialization

Ying Tan, Zongjie Cao, Jilan Feng, and Zongyong Cui

Abstract In this chapter, a polarimetric synthetic aperture radar (PolSAR) image segmentation approach is proposed in the variational framework. A novel continuous Potts model which takes advantage of the complex Wishart distribution is built for PolSAR image segmentation. Moreover, an automatic initialization technique is adopted to initialize the segmentation process. The automatic initialization approach can determine the number of clusters by PolSAR data itself. Compared with previous variational PolSAR segmentation approaches, the proposed approach makes use of the scattering characteristic and statistical characteristic together to segment PolSAR images in a completely unsupervised way. Experimental results demonstrate the effectiveness of the proposed approach. Without any artificial supervision, the proposed approach can produce superior segmentation results than the traditional level set method and $Wishart - H - \alpha$ classification approach.

Keywords Variational • PolSAR image segmentation • Level set • Automatic initialization

3.1 Introduction

Segmentation is an important step for SAR image processing and interpretation. Although many methods have been proposed for SAR image segmentation [1–3], it is still a challenge problem because of the complexity and low quality of SAR images. The proposition of variational framework [4, 5] provides another sort of methods for SAR image segmentation. I. B. Ayed [6] had set up energy functional about SAR images with regard to Gamma distribution. Then the level set method

Y. Tan (✉) • Z. Cao • J. Feng • Z. Cui
School of Electronic Engineering, University of Electronic Science and Technology of China, Chengdu, China
e-mail: Tanying1028@126.com

Q. Liang et al. (eds.), *Communications, Signal Processing, and Systems*, Lecture Notes in Electrical Engineering 202, DOI 10.1007/978-1-4614-5803-6_3,

is used to get the segmentation results. However, this method often depends on the initializing conditions. Different initializations may lead to different results. Therefore, it is important to define a good initialization.

Segmentation of PolSAR images is different from SAR images. The segmentation method mentioned above can not apply to PolSAR images directly. But the variational framework can also be put into PolSAR image segmentation. The energy functional based on the complex Wishart distribution of coherency matrix has been established [7]. However, proper initialization is still in need to get satisfying results. Cloude and Pottier proposed an unsupervised segmentation algorithm by using $H-\alpha$ decomposition theorem [8], where the scattering mechanisms, characterized by entropy H and angle α, are used for terrain type identification. The $H-\alpha$ plane is divided into eight zones, resulting in the partition of terrains with different physical scattering characteristics. But the segmentation result is very sensitive to noise as no spatial regularization is used in the variational approaches.

In this chapter, an automatic initialization variational method has been proposed to segment PolSAR images. A novel Potts model with regard to the complex Wishart distribution has been built. The minimum of the energy functional is obtained by using level set method. Besides, an automatic initialization program, which is based on $H-\alpha$ decomposition and complex Wishart distribution, is put forward. By using this initializing process, statistical characteristic and scattering characteristic have been combined for the PolSAR image segmentation. As the number of clusters is defined by the polarimetric data itself, the segmentation result could be better.

The outline of this chapter is as follows: In Sect. 3.2, a novel Potts model based on the complex Wishart distribution is stated. In Sect. 3.3, the basic formulation of $H-\alpha$ decomposition and the automatic initialization method are introduced. In Sect. 3.4, the experiments on AIRSAR data verify the excellent performance of our method. Finally, the chapter is concluded in Sect. 3.5.

3.2 A Novel Potts Model

This chapter builds an energy functional by combining the complex Wishart distribution with Potts model. The level set method is used to minimize the energy functional. The complex Wishart distribution of coherency matrix is introduced firstly [6, 7].

3.2.1 The Introduction of the Complex Wishart Distribution

The information of PolSAR data often stores in the scattering matrix or coherency matrix. Assuming that the scattering vector has a Gaussian distribution, the coherency matrix T has a complex Wishart distribution with n degrees of freedom, i.e.

$$P(T/C) = \frac{n^{qn}|T|^{n-q}\exp\left(-tr\left(nC^{-1}T\right)\right)}{K(n,q)|C|^{n}} \tag{3.1}$$

where $K(n,q) = \pi^{(1/2)q(q-1)}\Gamma(n)\cdots\Gamma(n-q+1)$, tr is the trace of a matrix, $q = 3$ for the reciprocal case, and C is the cluster center coherency matrix.

The following metric can be used to measure the distance between any coherency matrix T and a cluster with cluster center C:

$$d_m(T,C) = In(C) + tr\left(C^{-1}T\right) \tag{3.2}$$

3.2.2 Potts Model Based on the Complex Wishart Distribution

The proposition of Potts model makes it possible to use this model to segment images. The Potts model can partition the continuous domain into disjoint subdomains by the minimizing problem [9–11]:

$$\min_{\{\Omega_i\}_{i=1}^{m}} E = \sum_{i=1}^{m}\iint_{\Omega_i} f_i(x,y)dxdy + \lambda\sum_{i=1}^{m}|\partial\Omega_i| \tag{3.3}$$

where $f_i(x,y)$ is defined on Ω and expresses the characteristic of the i th subdomain, $|\partial\Omega_i|$ expresses the lengths of the boundaries of the disjoint subdomains. We let Heaviside functions $H(\phi_i)$ denote the characteristic functions of disjoint subdomains $\Omega_i,\ i = 1,\ldots,n$, define level set function vector as $\phi = (\phi_1,\ldots,\phi_m)$, and let:

$$f_i(x,y) = d_m(T,C_i) = In(C_i) + tr\left(C_i^{-1}T\right) \tag{3.4}$$

then the Potts model and the complex Wishart distribution are combined, and rewrite the Potts model as follows:

$$\min E(\phi) = \sum_{i=1}^{m}\iint_{\Omega} H(\phi_i)f_i(x,y)dxdy + \lambda\sum_{i=1}^{m}\iint_{\Omega}|\nabla H(\phi_i)|dxdy \tag{3.5}$$

Minimizing the energy functional (3.5), the segmentation results of images can be obtained. By introducing a time iteration parameter t into the level set method, the gradient descent equation for curve evolution is:

$$\frac{\partial\phi_i}{\partial t} = \delta(\phi_i)\left\{-f_i(x,y) + \lambda div\left(\frac{\nabla\phi_i}{|\nabla\phi_i|}\right)\right\} \tag{3.6}$$

If the initial values of $\phi_i, i = 1, \ldots, m$ are set, the segmentation results could be reached by iterative approach.

3.3 Automatic Initialization Process

Nowadays most segmentation methods about fully PolSAR data use a predefined number of clusters. But it may give rise to undesirable results. The number should be defined on the basis of the PolSAR data itself. In addition, the $H - \alpha$ decomposition [8], which can partition the data into 8 clusters, is taken as the initial segmentation. However the appropriate number is always less than 8, so the merging of the similar clusters is in need.

3.3.1 The Decision of the Number of Clusters

Due to the importance of the number, a novel method is adopted to get the appropriate number of clusters for PolSAR image segmentation [12]. By using the $H - \alpha$ decomposition, eight initial clusters are gotten. Now the optimal number of clusters needs to be determined. Giving a cluster φ_i, the probability density function of T can be obtained according to formula (3.1). For m clusters, the mixture probability density function is:

$$p(T/\Phi_m) = \sum_{i=1}^{m} p(i)p(T/\varphi_i) \tag{3.7}$$

where $p(i) = N_i/N, N_i$ is the number of data within cluster φ_i, N is the number of all data.

Let $X = \{T_1, \ldots, T_N\}$ be the whole sample coherency matrices. The m th data log-likelihood can be given by:

$$L_m(X) = In\left(\prod_{l=1}^{N} p(T_l/\Phi_m)\right) \tag{3.8}$$

By using the formula (3.7) and (3.8), and omitting the constant terms, the log-likelihood come down to

$$L_m(X) = \sum_{l=1}^{N} In\left(\sum_{i=1}^{m} p(i)\exp(-n \cdot d_m(T_l, C_i))\right) \tag{3.9}$$

The value of $L_m(X)$ depends on m only. Because $L_m(X)$ is a non-decreasing function about m, estimating the number of clusters by $L_m(X)$ is not practical. Another variable is defined to represent the change of the data log-likelihood:

$$D_m(X) = L_{m+1}(X) - L_m(X) \tag{3.10}$$

Now the optimal number of clusters can be decided by the following expression:

$$m_{opt} = \min(\{m|D_m(X) \leq \varepsilon) \quad m = 1, \ldots, M-1 \tag{3.11}$$

where ε is a small threshold. The appropriate number of clusters can be obtained by using formula (3.11).

3.3.2 Merging the Similar Clusters

When the appropriate number of clusters (less than 8) is gotten according to the subsection above, the merging of the similar clusters is necessary. The likelihood-ratio, which is based on the complex Wishart distribution, has been used to find out the minimum distance of two cluster center coherency matrices. Let the two hypothesis be

$$H_0 : C_i = C_j \ \ and \ \ H_1 : C_i \neq C_j \tag{3.12}$$

On the basis of formula (3.1), under H_0 hypothesis, assuming that $C_i = C_j = C$, the likelihood function is

$$L\left(C \Big/ \varphi_i \varphi_j\right) = \prod_{l=1}^{N_i} p(T_l/C) \prod_{l=1}^{N_j} p(T_l/C) \tag{3.13}$$

Under H_1 hypothesis, it is:

$$L(C_i/\varphi_i) L\left(C_j \Big/ \varphi_j\right) = \prod_{l=1}^{N_i} p(T_l/C_i) \prod_{l=1}^{N_j} p\left(T_l/C_j\right) \tag{3.14}$$

where C_i and C_j are the i th and j th cluster center coherency matrices, N_i and N_j are the number of data within i th and j th clusters respectively, and $i \neq j$. Let:

$$\hat{C}_i = \frac{1}{N_i} \sum_{l=1}^{N_i} T_l, \ \ \hat{C}_j = \frac{1}{N_j} \sum_{l=1}^{N_j} T_l, \ \ \hat{C} = \frac{1}{N_i + N_j} \sum_{l=1}^{N_i+N_j} T_l \tag{3.15}$$

then the likelihood-ratio can be expressed as:

$$\Lambda_{ij} = \frac{L\left(\hat{C}\middle/\varphi_i\varphi_j\right)}{L\left(\hat{C}_i/\varphi_i\right)L\left(\hat{C}_j\middle/\varphi_j\right)} \tag{3.16}$$

Taking the logarithm of formula (3.16), and ignoring the constant terms, the distance measure $d_m\left(C_i, C_j\right)$ between C_i and C_j at the m th iteration can be given by:

$$d_m\left(C_i, C_j\right) = -\frac{1}{n} In\Lambda_{ij} = \left(N_i + N_j\right) In\left|\hat{C}\right| - N_i In\left|\hat{C}_i\right| - N_j In\left|\hat{C}_j\right| \tag{3.17}$$

then the two clusters with the minimum distance $d_m\left(C_i, C_j\right)$ can be merged.

3.4 The Proposition of PolSAR Segmentation Algorithm

The level set method is used to minimize the energy functional (3.5). The $H - \alpha$ decomposition and complex Wishart distribution are been used to get the initialization. Thus the statistical characteristic and the scattering characteristic are used to segment the images. It can achieve better segmentation results than the other initialized conditions. The proposed algorithm can be described as follows: the Potts model with respect to the complex Wishart distribution is set up and the level set is used to get the optimum segmentation results of PolSAR images; meanwhile, the complex Wishart distribution and $H - \alpha$ decomposition are utilized to get the automatic initialization of level set method. The flow chart in Fig. 3.1 also explains it.

3.5 Experimental Results

The variational segmentation method has been applied to the PolSAR image segmentation. The AIRSAR data (Flevoland area) has been taked as an example. The threshold is set as $\varepsilon = 1e - 10$ and $D_m(X)$ is drawn in Fig. 3.2. The chart shows that the best number of clusters is 7 because $D_7(X)$ is not larger than ε. The without re-initialization level set method [13] is been used to partition the data into seven clusters.

Figure 3.3 presents the segmentation results of Flevoland area. The power image and the $Wishart - H - \alpha$ classification result are put in Fig. 3.3a and in Fig. 3.3b respectively, to make us compare conveniently. In Fig. 3.3c, one level set function is set as the background, such as the black cluster, and the other six level set functions are random circles with other six colors. The Fig. 3.3d is the

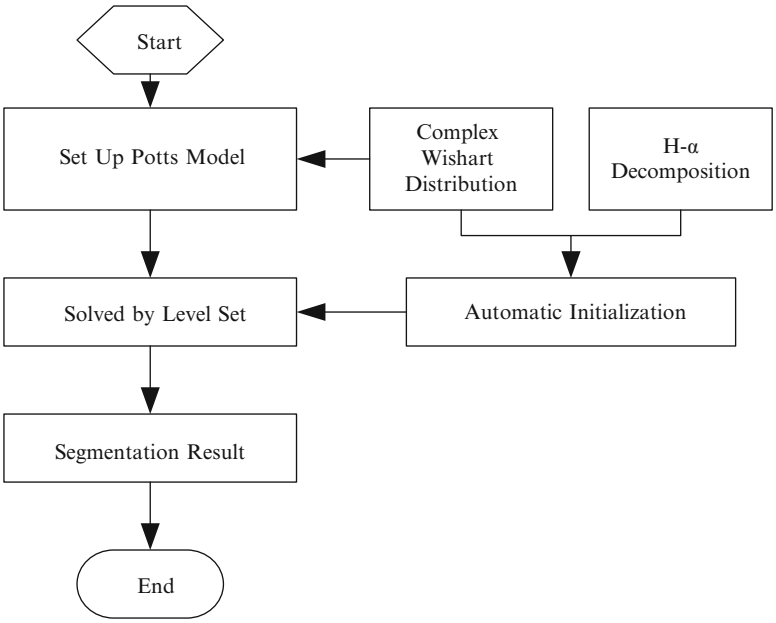

Fig. 3.1 The flow chart of the algorithm

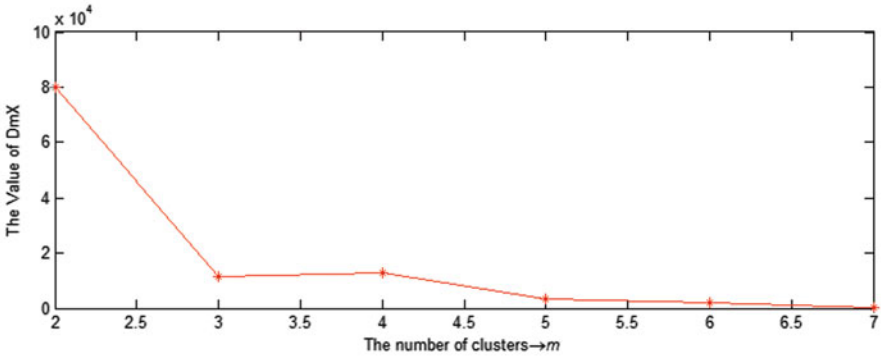

Fig. 3.2 $D_m(X)$ of AIRSAR data

corresponding segmentation result, which gets a rough segmentation. The seven colors have been utilized to analyze the segmentation result. In Fig. 3.3d, the orange cluster and green cluster occupy the most areas of the image, some other colors have embedded in the orange cluster and some areas have been mixed with several colors. Thus, the segmentation result in Fig. 3.3d shows that this initialized method could not get a reasonable result. In Fig. 3.3e, 6 level set functions are initialized by manual quadrangles and the seventh one is initialized to the black background, which give rise to the result in Fig. 3.3f. In Fig. 3.3f, the white cluster has some

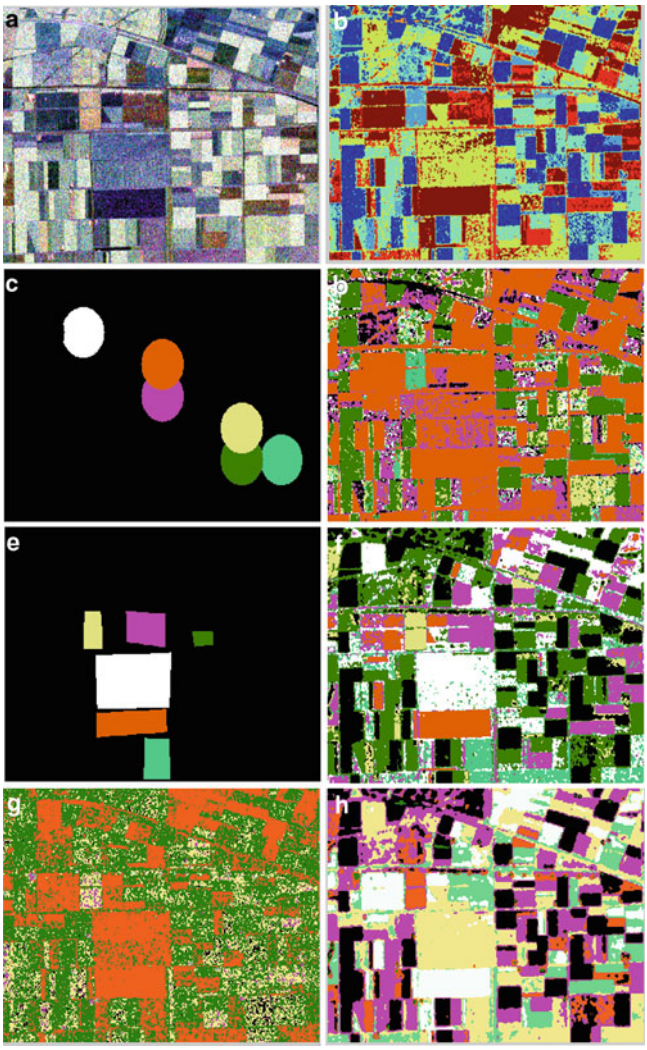

Fig. 3.3 (**a**) Is the power image of Flevoland area, (**b**) is the *Wishart* $-H-\alpha$ classification; (**c**) is the random initialization, the corresponding segmentation result is in (**d**); (**e**) is initialization by manual quadrangles, and (**f**) is the result correspond to (**e**); (**g**) is the automatic initialization, the relevant result is in (**h**)

pixels that are belong to the light green cluster, and some clusters do not have smoothed edges. Even though it's realizable to segment the PolSAR data into seven clusters in a general way, the manual quadrangles contain the artificial prior knowledge which is assumed by people. The expected automatic initialization based on the complex Wishart distribution and $H-\alpha$ decomposition is in Fig. 3.3g, and the Fig. 3.3h is the corresponding result. The automatic initialization unite scattering characteristic with statistical characteristic, resulting in a more

excellent segmentation result when there is no priori knowledge. We can compare it with the traditional level set method and $Wishart - H - \alpha$ classification. The result in Fig. 3.3d is awful, and the result in Fig. 3.3f is acceptable, but the initialization is manual quadrangles. For the result in Fig. 3.3b, the yellow cluster has been mixed with other colors more or less, but the corresponding cluster in Fig. 3.3h has little other colors. And the edges are more smoothed. These results show that the proposed approach is more convictive than the traditional level set method and $Wishart - H - \alpha$ classification approach.

3.6 Conclusion

This chapter proposes an automatic initialization approach for PolSAR image segmentation based on a novel Potts model with regard to complex Wishart distribution. The level set method is used to get the optimum value. The automatic initialization process makes use of the complex Wishart distribution and $H - \alpha$ decomposition, which combine scattering characteristic with statistical characteristic and lead to a better segmentation result. Experimental results show that our algorithm outperforms the traditional level set method and $Wishart - H - \alpha$ classification.

Acknowledgments This work is supported by the National Natural Science Foundation of China under Projects 60802065 and the Fundamental Research Funds for the Central Universities under Projects ZYGX2009Z005.

References

1. Fjortoft R, Lopes A, Marthon P, C-Castan E (1998) An optimal multiedge detector for SAR image segmentation. IEEE Trans Geosci Remote Sens 36(3):793–802
2. Deng H, Clausi DA (2005) Unsupervised segmentation of synthetic aperture radar sea ice imagery using a novel Markov random field model. IEEE Trans Geosci Remote Sens 43 (3):528–538
3. Xia GS, He C, Sun H (2007) A rapid and automatic MRF-based clustering method for SAR images. IEEE Geosci Remote Sens Lett 4(4):596–600
4. Kass M, Witkin A, D (1987) Snakes: active contour models. Int J Comput Vision:321–331
5. Osher S, Sethian J (1988) Fronts propagating with curvature dependent speed: algorithms based on the Hamilton-Jacbion formulation. JComput Phys 79(1):12–49
6. Ayed IB, Mitiche A, Belhadj Z (2006) Polarimetric image segmentation via maximum-likelihood approximation and efficient multiphase level-sets. IEEE Trans Pattern Anal Mach Intell 28(9):1493–1500
7. Lee JS, Grunes MR, Kwok R (1994) Classification of multi-lookpolarimetric SAR imagery based on complex Wishart distribution. Int J Remote Sens 15(11):2299–2311
8. Cloude SR, Pottier E (1996) A review of target decomposition theorems in radar polarimetry. IEEE Trans on Geosci Remote Sens 34:498–518

9. Potts RB (1952) Some generalized order–disorder transformations. Proc Camb Philos Soc 48:106–109
10. Bae E, Yuan J, Tai X-C (2011) Global minimization for continuous multiphase partitioning problems using dual approach. Int J Comput Vis 92:112–129
11. Chan T, Golub G, Mulet P (1999) A nonlinear primal-dual method for total variation-based image restoration. SIAM J Sci Comput 20(6):1964–1977
12. Fang Cao, Wen Hong, Yirong Wu, Pottier E (2007) An unsupervised segmentation with an adaptive number of clusters using the SPAN/H/α/A space and the complex wishart clustering for fully polarimetric SAR data analysis. IEEE Trans on Geosci Remote Sens 45 (11):3454–3467
13. Chunming Li, Chen yang Xu, Chang feng Gui, Fox MD (2005) Level set evolution without re-initialization: a new variational formulation. In: Proceedings of the 2005 I.E. computer society conference on computer vision and pattern recognition (CVPR'05), San Diego, CA, United States 1063–6919/05

Chapter 4
Mismatched Signal Jamming to Synthetic Aperture Radar

Xiaodong He and Bin Tang

Abstract Mismatched signal jamming to SAR is discussed in this chapter. According to the Range-Doppler algorithm, this chapter derived the output expression of jamming using a linear frequency modulation pulse compression SAR system, and analyzed the relationship between the modulation parameters and the location of the false target and suppressed jamming distance, and gave the 2-D compression processing output gain of mismatched signal.

Keywords Synthetic aperture radar • Mismatched signal • Pulse compression • Suppressed jamming

4.1 Introduction

Synthetic Aperture Radar (SAR) is a kind of two-dimensional (2-D) high-resolution microwave imaging radar. It could obtain high-resolution images of targets in all kinds of weather conditions, and has been widely used in many fields, especially in military scout, battlefield surveillance. It has attracted more and more attention in electronic counter measurements (ECM) field to against SAR [1].

The jamming technology of SAR is mainly divided into two kinds: non-coherent jamming and coherent jamming. Noise suppression jamming is a typical non-coherent jamming [2], and deceptive jamming is a typical coherent jamming. In this chapter, a new jamming style which called mismatched signal jamming based on the matched filter of SAR will be presented. The effect of mismatched signal jamming to SAR is between non-coherent and coherent jamming.

X. He (✉) • B. Tang
School of Electronic Engineering, University of Electronic Science and Technology of China, Chengdu 611731, People's Republic of China
e-mail: Winter_he@hotmail.com

Q. Liang et al. (eds.), *Communications, Signal Processing, and Systems*, Lecture Notes in Electrical Engineering 202, DOI 10.1007/978-1-4614-5803-6_4,

4.2 Generating Mismatched Jamming Signal

Assuming that SAR transmits linear frequency modulation (LFM) signal such as

$$s(t) = \mathrm{rect}\left(\frac{\mathrm{t}}{\mathrm{T}}\right)\exp\left(\mathrm{j}2\pi\left(\mathrm{f_c t} + \frac{1}{2}\mathrm{K_r t^2}\right)\right). \tag{4.1}$$

Where T is the pulse width, and $\mathrm{rect}\left(\frac{\mathrm{t}}{\mathrm{T}}\right) = \{1 \quad |\mathrm{t}| \le \mathrm{T}/20 \quad \text{others}$, f_c is the carrier frequency, K_r is the chirp rate, $B = KT$ is the bandwidth of mismatched jamming signal.

When jammer intercepts the LFM signal transmitted by SAR, it modulates a LFM signal $p(t)$ rapidly, then amplifies and retransmits the modulated LFM signal to SAR. The form of $p(t)$ is as follow,

$$p(t) = \mathrm{rect}\left(\frac{\mathrm{t}}{\mathrm{T_r}}\right)\exp\left(\mathrm{j}2\pi\left(\mathrm{f_j t} + \frac{1}{2}\mathrm{K_r^{'} t^2}\right)\right). \tag{4.2}$$

Where T_r is the pulse width, f_j is the center frequency, $\lambda = c/f$ is the carrier frequency wavelength, and $K_r^{'}$ is the chirp rate, $B_r^{'} = K_r^{'} T_r$ is the bandwidth.

Assumed that the modulated pulse width T_r is equal to T. Hence, SAR receives the mismatched jamming signal can be shown as the formula (4.3)

$$\begin{aligned} s_j(t, t_a) &= \mathrm{rect}\left(\frac{(\mathrm{t} - 2\mathrm{R(t_a)/c})}{\mathrm{T}}\right)\mathrm{rect}\left(\frac{\mathrm{t_a}}{\mathrm{T_L}}\right) \\ &\exp\left(\mathrm{j}2\pi\left(\left(\mathrm{f_c} + \mathrm{f_d} + \mathrm{f_j}\right)\left(\mathrm{t} - \frac{2\mathrm{R(t_a)}}{\mathrm{c}}\right) + \frac{1}{2}\mathrm{K}\left(\mathrm{t} - \frac{2\mathrm{R(t_a)}}{\mathrm{c}}\right)^2\right)\right). \end{aligned} \tag{4.3}$$

Where t is the fast time in range, t_a is the slow time in cross-range, T_L is the synthetic aperture time, $R(t_a) = \sqrt{(x_0 - Vt_a)^2 + y_0^2 + H^2}$ is the instantaneous distance from jammer to SAR, and the chirp rate of mismatched jamming signal K is equal to $K_r + K_r^{'}$ [3].

4.3 The Imaging Output of Mismatched Jamming Signal

The Range-Doppler algorithm is a classical and effective SAR imaging processing algorithm. In Fresnel approximation condition, its range and cross-range pulse compression processing can be fulfilled respectively, which is convenient to observe the range profile.

After the orthogonal channels and down-conversion, the mismatched jamming signal turns into two parts,

$$s_j(t,t_a) = s_r(t,t_a)s_a(t_a). \tag{4.4}$$

Here,

$$s_r(t,t_a) = \text{rect}\left(\frac{\left(\text{t}-\frac{2\text{R}(\text{t}_\text{a})}{\text{c}}\right)}{\text{T}}\right)\exp\left(\text{j}2\pi\left(\begin{array}{c}\left(\text{f}_\text{d}+\text{f}_\text{j}\right)\left(\text{t}-\dfrac{2\text{R}(\text{t}_\text{a})}{\text{c}}\right)\\ +\dfrac{1}{2}\text{K}\left(\text{t}-\dfrac{2\text{R}(\text{t}_\text{a})}{\text{c}}\right)^2\end{array}\right)\right), \tag{4.5}$$

which is related to the range direction signal.

And,

$$s_a(t_a) = \text{rect}\left(\frac{\text{t}_\text{a}}{\text{T}_\text{L}}\right)\exp\left(-\text{j}\frac{4\pi\text{R}(\text{t}_\text{a})}{\lambda}\right), \tag{4.6}$$

which is related to the cross-range direction signal.

According to the Principal of Stationary Phase (POSP), the spectrum of $s_r(t,t_a)$ is as below

$$\begin{aligned}S_r(f,t_a) = &\frac{1}{\sqrt{K}}\text{rect}\left(\frac{\text{f}-\left(\text{f}_\text{d}+\text{f}_\text{j}\right)}{\text{B}}\right)\\ &\times\exp\left(-\text{j}2\pi\left(\frac{\left(\text{f}-\left(\text{f}_\text{d}+\text{f}_\text{j}\right)\right)^2}{2\text{K}}+\text{f}\frac{2\text{R}(\text{t}_\text{a})}{\text{c}}\right)+\text{j}\frac{\pi}{4}\right).\end{aligned} \tag{4.7}$$

The reference function of the range pulse compression processing is given by

$$h_r(t) = \text{rect}\left(\frac{\text{t}}{\text{T}}\right)\exp\left(-\text{j}\frac{\text{K}_\text{r}}{2}\text{t}^\pi\right). \tag{4.8}$$

The spectrum of $h_r(t)$ is as below

$$H_r(f) = \frac{1}{\sqrt{K_r}}\text{rect}\left(\frac{\text{f}}{\text{B}_\text{r}}\right)\exp\left(\text{j}\frac{2\pi\text{f}^2}{2\text{K}_\text{r}}-\text{j}\frac{\pi}{4}\right), \tag{4.9}$$

where $B_r = K_rT$ is the bandwidth of SAR signal.

Therefore, the spectrum of the range pulse compression processing of SAR can be written as the following form

$$\begin{aligned}Y_r(f) = &\frac{1}{\sqrt{K_rK}}\text{rect}\left(\frac{\text{f}-\left(\text{f}_\text{d}+\text{f}_\text{j}\right)}{\text{B}}\right)\text{rect}\left(\frac{\text{f}}{\text{B}_\text{r}}\right)\\ &\times\exp\left(\text{j}2\pi\left(\frac{\text{f}^2}{2\text{K}_\text{r}}-\frac{\left(\text{f}-\left(\text{f}_\text{d}+\text{f}_\text{j}\right)\right)^2}{2\text{K}}-\text{f}\frac{2\text{R}(\text{t}_\text{a})}{\text{c}}\right)\right).\end{aligned} \tag{4.10}$$

Here, we assumed that $K_r^{'}$ is positive and smaller than K_r, and $|f_j + f_d| < \frac{TK_r^{'}}{2}$. Therefore [4],

$$Y_r(f) = \frac{1}{\sqrt{KK_r}} \mathrm{rect}\left(\frac{\mathrm{f}}{\mathrm{B_r}}\right) \times \exp\left(\mathrm{j}2\pi\left(\frac{\mathrm{f}^2}{2\mathrm{K_r}} - \frac{\left(\mathrm{f} - \left(\mathrm{f_d} + \mathrm{f_j}\right)\right)^2}{2\mathrm{K}} - \mathrm{f}\frac{2\mathrm{R}(\mathrm{t_a})}{\mathrm{c}}\right)\right). \tag{4.11}$$

Taking the inverse Fourier transformation to (4.11), we can get the time domain expression. Then, though the range migration correction (RMC) processing, the slow time varied in the same range resolution unit, which can be thought as a processing of turning $R(t_a)$ into a constant R_0, which is the slant range in zero Doppler plane. The output of range pulse compress processing turns into the following form

$$\begin{aligned} y_r(\tau_r, t_a) = &\sqrt{\frac{1}{2K_r^{'}}} \exp\left(-\mathrm{j}\frac{\pi \mathrm{K_r K}}{\mathrm{K_r^{'}}}\left(\tau_\mathrm{r} - \frac{2\mathrm{R_0}}{\mathrm{c}} + \frac{\mathrm{f_j} + \mathrm{f_d}}{\mathrm{K}}\right)^2\right) \\ &\times \exp\left(\mathrm{j}\left(\frac{\pi \mathrm{K_r}\left(\mathrm{f_j} + \mathrm{f_d}\right)^2}{\mathrm{KK_r^{'}}} - \frac{\pi\left(\mathrm{f_j} + \mathrm{f_d}\right)^2}{\mathrm{K_r^{'}}} - \frac{\pi}{4}\right)\right), \end{aligned} \tag{4.12}$$

where τ is the output domain of range pulse compression, which is described as

$$\frac{2R_0}{c} - \frac{2\left(f_j + f_d\right) + TK_r^{'}}{2\left(K_r + K_r^{'}\right)} \le \tau \le \frac{2R_0}{c} - \frac{2\left(f_j + f_d\right) - TK_r^{'}}{2\left(K_r + K_r^{'}\right)}. \tag{4.13}$$

The Maclaurin expansion of instantaneous distance from jammer to SAR can be described as

$$R(t_a) = \sqrt{(x_0 - Vt_a)^2 + y_0^2 + H^2} \approx R + \frac{-Vx_0}{R} t_a + \frac{V^2}{2R} t_a^2. \tag{4.14}$$

Where $R = \sqrt{x_0^2 + y_0^2 + H^2}$, V is the SAR platform velocity, H is the altitude, and (x_0, y_0) is the position of jammer. Therefore, the cross-range signal $s_a(t_a)$ turns into the following formula

$$s_a(t_a) = \mathrm{rect}\left(\frac{\mathrm{t_a}}{\mathrm{T_L}}\right) \exp\left(-\mathrm{j}\frac{4\pi}{\lambda}\left(\mathrm{R} + \frac{-\mathrm{Vx_0}}{\mathrm{R}}\mathrm{t_a} + \frac{\mathrm{V}^2}{2\mathrm{R}}\mathrm{t_a^2}\right)\right). \tag{4.15}$$

Assuming that the cross-range reference function of SAR is given by

$$h_a(t_a) = \mathrm{rect}\left(\frac{\mathrm{t_a}}{\mathrm{T_L}}\right)\exp\left(\mathrm{j}2\pi\frac{2\mathrm{V}^2}{\lambda\mathrm{R}}\mathrm{t_a^2}\right). \tag{4.16}$$

The output of cross-range pulse compression processing is shown by

$$\begin{aligned} y_a(\tau_a) &= s_a(t_a) \otimes h_a(t_a) \\ &= \sqrt{T_L\left(\frac{2V^2}{\lambda R}\right)^2}\frac{\sin\left(\pi\left(\frac{2V_{X_0}}{\lambda R}-\frac{2V^2}{\lambda R}\tau_a\right)T_L\right)}{\pi\left(\frac{2V_{X_0}}{\lambda R}-\frac{2V^2}{\lambda R}\tau_a\right)T_L}\exp\left(\mathrm{j}2\pi\left(\frac{2\mathrm{V}^2}{\lambda\mathrm{R}}\tau_\mathrm{a}^2\right)+\mathrm{j}\frac{\pi}{4}\right). \end{aligned} \tag{4.17}$$

Combine this with (4.12) to get the output of the 2-D pulse compress

$$y(\tau_r, \tau_a) = y_r(\tau_r, t_a)y_a(\tau_a). \tag{4.18}$$

4.4 The Effect of Mismatched Jamming Signal

According to the pulse compression theory of LFM signal, we can get the output position of the range pulse compression from (4.12) and (4.13),

$$\tau = \left(\frac{2R(t_a)}{c} - \frac{f_d + f_j}{K}\right) + \Delta\tau, \tag{4.19}$$

where $\frac{2R(t_a)}{c} - \frac{f_d+f_j}{K}$ is the center of range pulse compression output peak. And $\Delta\tau = \tau_{\max} - \tau_{\min} = \frac{TK_r'}{K}$ is the output width, caused by the mismatching of jamming signal with range pulse compression network, which could form linear suppressed jamming. According to the Range-Doppler coupling effect, jamming suppressed distance turns from range pulse compression output width is $R_j = \frac{c\Delta\tau}{2}$. Assume the distance of the protected target is known, we can get the chirp rate based on the pulse width [5].

In Fresnel approximation condition, the whole SAR signal processing gain is

$$G = DN = B_rTN, \tag{4.20}$$

where D is pulse compression ratio, B_rT is the range direction processing gain. And N is the cross-range direction processing gain, which is the sample numbers in T_L [6].

Assuming that modulated pulse width is equal to the SAR LFM signal, the pulse compression ratio of the mismatched jamming signal is

$$D^{'} = \frac{T}{\Delta\tau} = \frac{TK}{B_r^{'}} = \frac{T\left(K_r + K_r^{'}\right)}{B_r^{'}} = \frac{B_r + B_r^{'}}{B_r^{'}} = 1 + \frac{B_r}{B_r^{'}}. \tag{4.21}$$

In response mode, the jammer could maintain the coherence of cross-range. Then, the processing gain of mismatched signal is

$$G^{'} = D^{'}N = \left(1 + \frac{B_r}{B_r^{'}}\right)N. \tag{4.22}$$

From (4.22), we find that the mismatched signal could still obtain higher gain through SAR 2-D pulse compression processing.

4.5 Simulation Experiment

The parameters used in simulation experiments are shown in Table 4.1 to analyze the performance of mismatched signal jamming.

Assumed the jammer is located at (0, 10,000 m). The parameters modulated by the jammer to generate the mismatched jamming signal in simulation experiments are shown in Table 4.2.

The range profile of mismatched jamming signal through range pulse compression processing, and the image of SAR are show in Fig. 4.1.

Compared with Fig. 4.1a, b, and c, we find that, if the center frequency is not equal to 0 MHz, the output peak of range pulse compression deviated from the location of jammer. The deviation amount is related with the value of center frequency. Compared with Fig. 4.1a, b, and d, we find that, with the bandwidth of mismatched jamming signal increasing, the jamming signal is mismatched with range pulse compression network seriously. The output peak becomes wider, and the jamming distance becomes greater.

4.6 Conclusion

This chapter presented a mismatched signal jamming to SAR, analyzed the relationship between the mismatched signal modulation parameters and the location of the false target and suppressed jamming distance. Theoretical analysis and simulation results indicated that the mismatched signal jamming could obtain a higher 2-D compression processing gain, and produce point target deceptive jamming or line target suppress jamming.

Table 4.1 Parameters of Stripmap SAR

Pulse width	5 us	Bandwidth	50 MHz
Carrier frequency	8.5 GHz	Carrier velocity	100 m/s
Altitude	4,000 m	Synthetic aperture time	8 s
Range sampling frequency	63 MHz	Pulse repetition frequency	128 Hz

Table 4.2 Parameters of modulated signal

Label	Center frequency	Bandwidth	Pulse width
(A)	0 MHz	1 MHz	5 us
(B)	1 MHz	5 MHz	5 us
(C)	−1 MHz	5 MHz	5 us
(D)	1 MHz	10 MHz	5 us

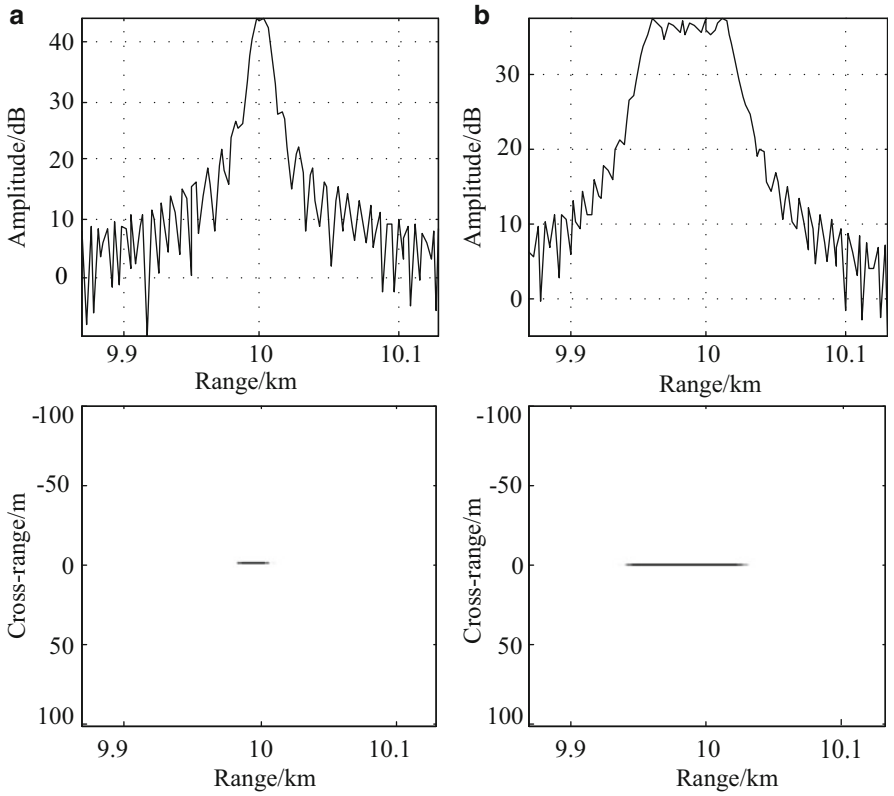

Fig. 4.1 The images of SAR

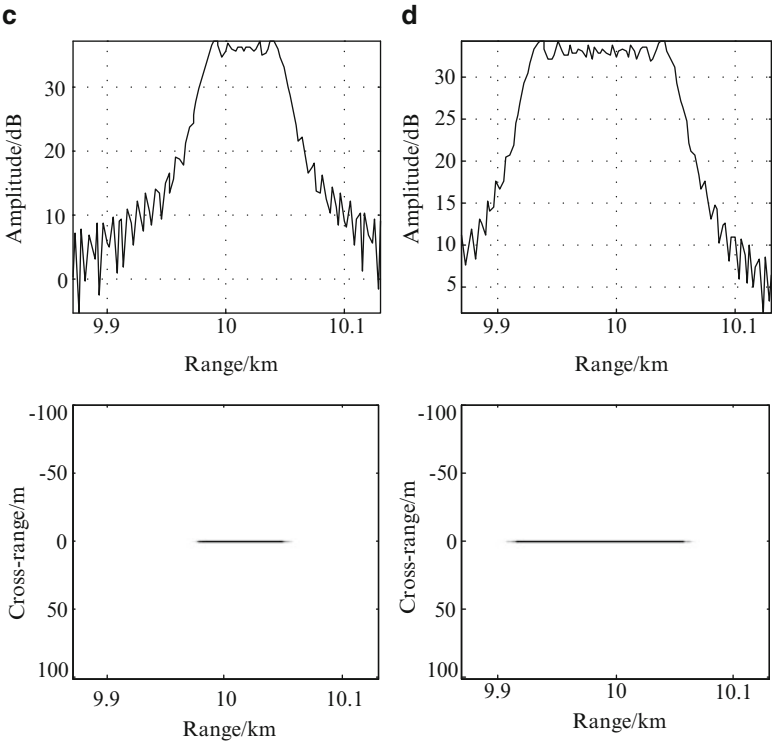

Fig. 4.1 (continued)

References

1. Goj WW (1993) Synthetic aperture radar and electronic warfare. Artech House, Boston
2. Dumper K, Cooper PS et al (1997) Spaceborne synthetic aperture Radar and noise jamming. In: IEEE Radar'97 conference, Edinburgh, pp 411–414
3. Cumming G, Wong FH (2005) Digital signal processing of synthetic aperture radar data: algorithms & implementation. Artech House, Norwood
4. Bo LV, Qi F, Naichang Y (2009) A study on frequency-shifting blanket jamming to LFM pulse-compression radar. Modem Radar 31(1):9–11
5. Chen Defeng, Gao Meiguo (2009) Effect of parameters detection error to SAR deception jamming. Trans Beijing Inst Technol 29(7):639–643
6. Doerry W (2006) Performance limits for synthetic aperture radar-second edition. Sandia National Laboratories, Techinal Report, 30, 32, 33, 34

Chapter 5
A CGRT-CLEAN Method for Circular SAR Three Dimensional Imaging*

Biao Zhang, Yiming Pi, and Rui Min

Abstract A three dimensional (3D) imaging method which is a complex-valued generalized Radon transform (CGRT)-CLEAN algorithm for circular synthetic aperture radar (CSAR) is proposed in this chapter. Based on the analysis of CSAR echo model, the echo of a scatterer in the range-azimuth domain can be modeled as a single cycle sinusoid. Inspired by the generalized Radon transform, this chapter utilizes the CGRT to estimate for scatterers' positions. Then, combining the CGRT with CLEAN technique, the parameters of a scatterer which include position information and reflection coefficient can be obtained. Thus, a 3D image of a target can also be reconstructed. The performances of the CGRT-CLEAN method have been verified by simulations, and the results confirm the effectiveness of the proposed algorithm for processing CSAR data.

Keywords Circular synthetic aperture radar (CSAR) • Complex-valued generalized radon transform (CGRT) • CGRT-CLEAN • 3D imaging

5.1 Introduction

Synthetic aperture radar (SAR) is widely investigated for both civilian and military applications, due to its high-resolution mapping in all time and all weather condition. Linear SAR systems operating along a straight line path at a certain altitude, measure target SAR signature only a limited aspect angle [1]. Comparing with

*This work is supported by the Fundamental Research Funds for the Central Universities under Projects ZYGX2009Z005.

B. Zhang (✉) • Y. Pi • R. Min
School of Electronic Engineering, University of Electronic Science and Technology of China, Chengdu, China
e-mail: zhangbiao_01@163.com

Q. Liang et al. (eds.), *Communications, Signal Processing, and Systems*, Lecture Notes in Electrical Engineering 202, DOI 10.1007/978-1-4614-5803-6_5,

linear SAR, circular SAR (CSAR) has many advantages, such as all-directional observation, high resolution, and three dimensional (3D) imaging [1–4]. Due to these attractive features, CSAR has raised the interests of many researchers.

Recently, for processing CSAR data, several approaches have been proposed. Confocal [5] or back-projection [6] algorithms can work easily with arbitrary geometries but have the disadvantage of computational inefficiency. An algorithm based on the wave-front reconstruction theory is presented by Soumekh [3]. The key step of this algorithm to convert the slant plane CSAR data to ground plane CSAR, which is achieved by taking pseudo-invert of the linear shift-varying system may cause instability.

In this chapter, a new 3D imaging algorithm for CSAR is proposed. Because the echo of a scatterer in the range-azimuth domain can be modeled as a single cycle sinusoid, which is equivalent to the Radon transform of its distribution function, we can perform the complex-valued generalized Radon transform to reconstruct the image [7]. Combining the CGRT with CLEAN technique, the 3D features of the target are extracted directly from the CSAR data in the range-azimuth domain. Each point in a 3D image achieved by the proposed algorithm corresponds with each scatterer and each scatterer's image does not have sidelobes. Therefore, the proposed algorithm can provide better resolution than other existing algorithms. The performances of the CGRT-CLEAN method in the condition of noise and scatterers' blockages are simulated, and the results show the feasibility and effectiveness of the CGRT-CLEAN method for processing CSAR data.

5.2 System Model

The CSAR imaging system geometry is shown in Fig. 5.1. The CSAR sensor moves along a circular trajectory with radius R_g on the plane $z = H$. Thus, the position of the sensor in spatial space is given by

$$\vec{r_s} = (X, Y, Z) = (R_g \cos\theta, R_g \sin\theta, H) \tag{5.1}$$

where $\theta \in [0, 2\pi)$ represents the slow time or aspect angle synthetic aperture domain. We define the slant range by

$$R_c = |\vec{r_s}| = \sqrt{{R_g}^2 + H^2} \tag{5.2}$$

and the incident angle via $\theta_i = \arctan(R_g/H)$.

As the sensor moves along the circular synthetic aperture, its beam is spotlighted on the scene of radius R_0 and height h and centered at the origin

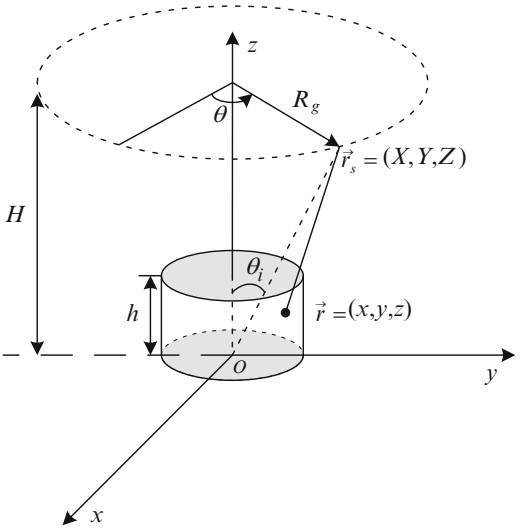

Fig. 5.1 CSAR imaging system geometry

of the spatial (x, y) domain. The distance from the sensor to a scatterer at location $\vec{r} = (x, y, z)$ is determined by

$$R(\theta) = |\vec{r}_s - \vec{r}| = \sqrt{(x - R_g \cos\theta)^2 + (y - R_g \sin\theta)^2 + (z - H)^2}. \tag{5.3}$$

Assume that there is a scatterer P located at $\vec{r}_p = (x_p, y_p, z_p)$ with reflectivity σ_p. For a chirp pulse radar system, the radar echo can be expressed as

$$S(\omega, \theta) = \sigma_p W(\omega, \theta) \exp[-j2kR_p(\theta)] \tag{5.4}$$

where $W(\omega, \theta)$ is the two dimensional window function, i.e.,

$$W(\omega, \theta) = rect\left(\frac{\omega - \omega_0}{2\pi B}\right) \bullet rect\left(\frac{\theta - (\theta_{\max} + \theta_{\min})/2}{\theta_{\max} - \theta_{\min}}\right) \tag{5.5}$$

$\theta_{\min}$ and $\theta_{\max}$ are the minimum and maximum aspect angles, ω_0 is the angular frequency of carrier wave, B is the bandwidth, $k = \omega/c$ is the wavenumber, c is the speed of light, $R_p(\theta)$ is the range to the scatterer, i.e.,

$$\begin{aligned} R_p(\theta) &= \sqrt{(x_p - X)^2 + (y_p - Y)^2 + (z_p - Z)^2} \\ &= R_c \sqrt{1 - 2Xx_p/{R_c}^2 - 2Yy_p/{R_c}^2 - 2Zz_p/{R_c}^2 + ({x_p}^2 + {y_p}^2 + {z_p}^2)/{R_c}^2}. \end{aligned} \tag{5.6}$$

When the sensor is in the far-field zone of the scatterer, i.e., $R_c \gg R_0, h$, (5.6) can be approximated into

$$\begin{aligned} R_p(\theta) &\approx R_c - x_p \cdot X/R_c - y_p \cdot Y/R_c - z_p \cdot Z/R_c \\ &= R_c - x_p \sin\theta_i \cos\theta - y_p \sin\theta_i \sin\theta - z_p \cos\theta_i. \end{aligned} \tag{5.7}$$

For simplicity, $x_p \sin\theta_i$, $y_p \sin\theta_i$, $z_p \cos\theta_i$ can be written as (x_p', y_p', z_p') of the scatterer in the spatial domain. Thus, (5.7) becomes

$$R_p(\theta) = R_c - x_p' \cos\theta - y_p' \sin\theta - z_p'. \tag{5.8}$$

By substituting (5.8) for (5.6), (5.4) can be expressed as

$$S(\omega, \theta) = \sigma_p W(\omega, \theta) \exp[-j2k(R_c - x_p' \cos\theta - y_p' \sin\theta - z_p')]. \tag{5.9}$$

After a reference function $H_1 = \exp(j2kR_c)$ is multiplied to (5.9), the signal becomes

$$S(\omega, \theta) = \sigma_p W(\omega, \theta) \exp[j2k(x_p' \cos\theta + y_p' \sin\theta + z_p')]. \tag{5.10}$$

Performing the inverse Fourier transform to (5.10) in the ω domain, the signal is expressed as

$$\begin{aligned} s(r, \theta) = \sigma_p B \cdot rect&\left(\frac{\theta - (\theta_{\max} + \theta_{\min})/2}{\theta_{\max} - \theta_{\min}}\right) \\ &\cdot \operatorname{sinc}\left[\frac{2\pi \mathrm{B}}{\mathrm{c}}(\mathrm{r} + \mathrm{x_p}' \cos\theta + \mathrm{y_p}' \sin\theta + \mathrm{z_p}')\right] \\ &\cdot \exp[j2k_0(r + x_p' \cos\theta + y_p' \sin\theta + z_p')]. \end{aligned} \tag{5.11}$$

where $k_0 = \omega_0/c$ is the wavenumber of carrier wave.

As indicated in (5.11), the variation of the echo of a scatterer in the azimuth domain causes the change of the corresponding peak in the range domain duo to the circular motion of the sensor. This change can be modeled by a sinusoid in the r-θ domain. Thus, if the information of this curve can be extracted, the 3D coordinate information and reflectivity of a scatterer can be obtained. According to this idea, the 3D images of the target can still be obtained.

5.3 CGRT-CLEAN Algorithm

The purpose of SAR imaging algorithm is to make sure position and reflectivity of scatterer in the scene from echo data. In this section, we will introduce methods which are to estimate scatterer position and reflection coefficient.

5.3.1 Scatterer Position Estimation

For a scatterer, the modulus and phase of its echo in the r-θ domain are sinusoids which can be expressed as

$$r = -x_p{}' \cos\theta - y_p{}' \sin\theta - z_p{}'. \tag{5.12}$$

This sinusoid is described by three parameters, $x_p{}'$, $y_p{}'$ and $z_p{}'$ which represent the position of a scatterer in spatial domain. Thus, by detecting the sinusoid in the r-θ domain, the position of a scatterer can be obtained. This is the same as the detection of a specific curve in a digital image.

The relation between image domain (r, θ) and parameter domain $(x_p{}', y_p{}', z_p{}')$ is similar to the Radon transform of its distribution function. Therefore, the generalized Radon transform can be used to estimate for position parameters of each scatterer and it is defined by the following expression

$$I(x, y, z) = \int_0^{2\pi} g(r, \theta) d\theta \tag{5.13}$$

where $I(x, y, z)$ denotes the generalized Radon transform of the image $g(r, \theta)$. Equation (5.13) indicates that the GRT is the integral of $g(r, \theta)$ along θ direction.

Because the target is composed of multiple scatterers, the echoes of the target are the sum of each echo. Several sinusoids may intersect with each other or have fractures in the r-θ domain. So the complex-valued generalized Radon transform method is proposed to estimate the positions of scatterers.

From (5.11), we can see that when the data in the r-θ domain is on the sinusoid, the phase term in (5.11) is equal to one and (5.11) can reach its maxima. This indicates that only the echo data of a scatterer can realize coherent superposition. Performing back-projection to (5.11) via CGRT method, the reconstructed image is achieved by

$$\hat{s}(x', y', z')_{CGRT} = \sigma_p \sum_{\theta_{\min}}^{\theta_{\max}} s(r, \theta) \tag{5.14}$$

Therefore, one scatterer which is related to one sinusoid in the r-θ domain generates one peak in the parameter domain. All scatterers' positions in the spatial domain can be estimated from peaks of $\hat{s}(x', y', z')$ by 3D parameter searching.

To understand the above method easily, some simulations have been performed. The incident angle is $\pi/3$, and the observation interval is 2π. The range-compression image of eight scatterers four of which are in the $z = 0$ plane and others are in the $z = 0.8$ plane is shown in Fig. 5.2. There are eight single cycle sinusoids which are related to eight scatterers in the spatial domain and interact with each other.

Figures 5.3, 5.4 and 5.5 show the CGRT results of Fig. 5.2 for $z = 0$, $z = 0.8\cos(\pi/3)$ and $z = 0.4\cos(\pi/3)$. In Fig. 5.3, four peaks are identified because of four

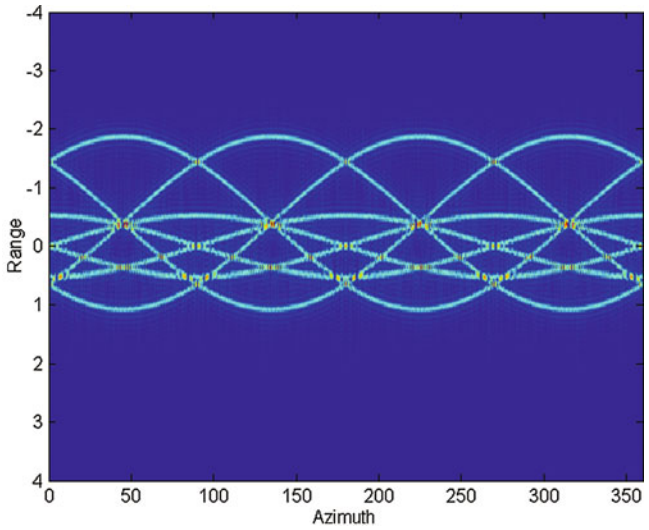

Fig. 5.2 The range-compression image of seven scatterers

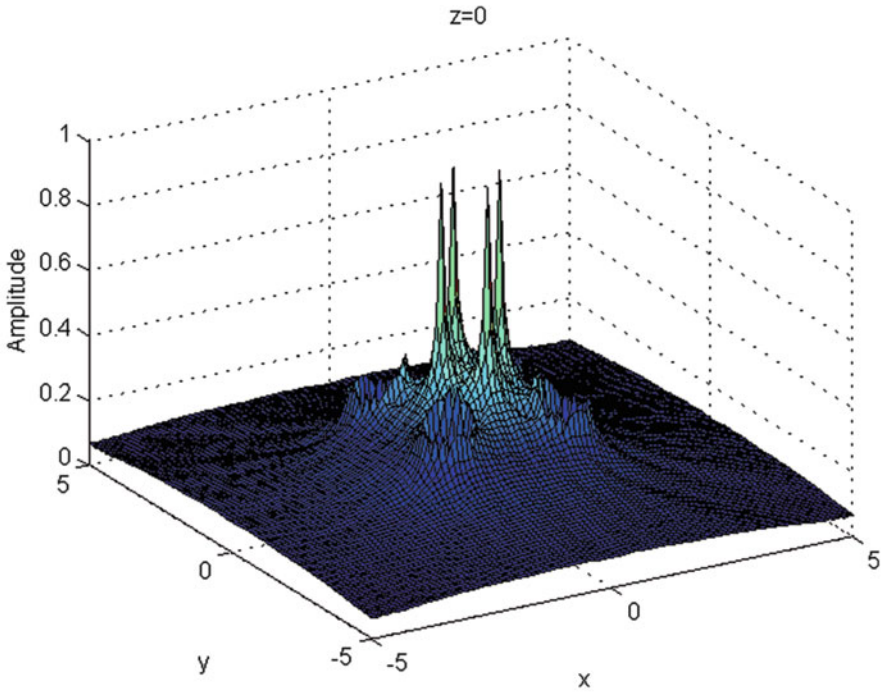

Fig. 5.3 The CGRT imaging result of Fig. 5.2 for $z = 0$

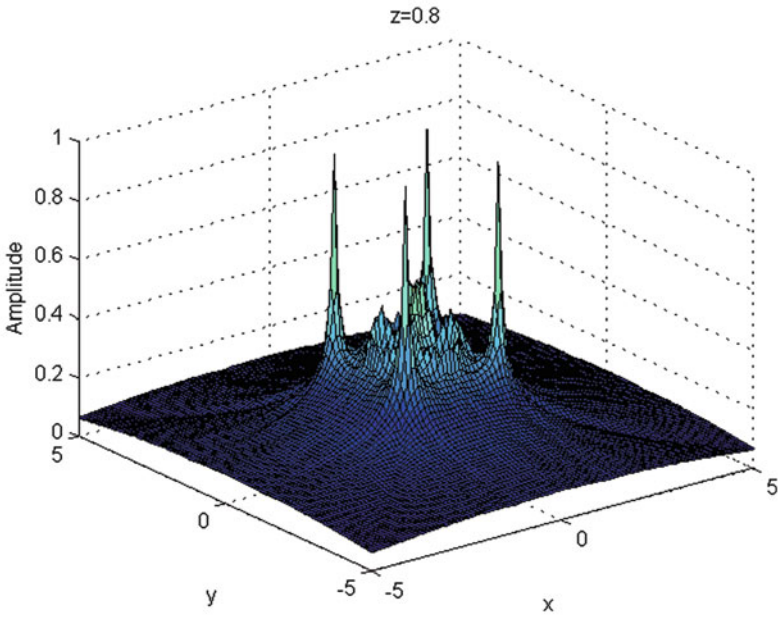

Fig. 5.4 The CGRT imaging result of Fig. 5.2 for $z = 0.8$

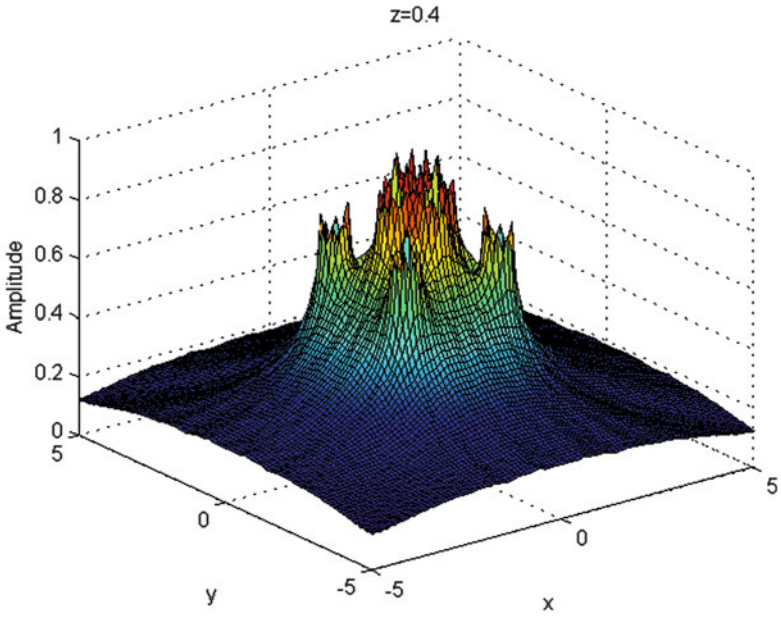

Fig. 5.5 The CGRT imaging result of Fig. 5.2 for $z = 0.4$

scatterers in the $z = 0$ plane. Four peaks are also found in Fig. 5.4 due to the four scatterers in the $z = 0.8$ plane. In Fig. 5.5, there are no obvious peaks, because no scatterers are in the $z = 0.4$ plane. Therefore, by carrying out the CGRT for the range-compression image, the peaks at different z in the parameter domain can be obtained. The estimation for all scatterers' positions in the spatial domain can be achieved by searching the peaks in the parameter domain.

5.3.2 Reflection Coefficient Estimation

Supposing that the position information of a scatterer P has been estimated using the CGRT method, then the point spread function can be expressed as

$$\begin{aligned} X_p(r,\theta) = B \cdot rect(&\frac{\theta - (\theta_{\max} + \theta_{\min})/2}{\theta_{\max} - \theta_{\min}}) \\ &\cdot \mathrm{sinc}[\frac{2\pi \mathrm{B}}{\mathrm{c}}(\mathrm{r} + \mathrm{x_p}' \cos\theta + \mathrm{y_p}' \sin\theta + \mathrm{z_p}')] \\ &\cdot \exp[j2k_0(r + x_p' \cos\theta + y_p' \sin\theta + z_p')]. \end{aligned} \tag{5.15}$$

The estimation of the reflection coefficient can be obtained through the following LSE method:

$$\hat{\sigma}_p = \arg \min_{\hat{\sigma}_p} I(\hat{\sigma}_p) = \arg \min_{\hat{\sigma}_p} \sum_{r,\theta} \left| s(r,\theta) - \hat{\sigma}_p X_p(r,\theta) \right|^2. \tag{5.16}$$

Letting the derivative $I(\hat{\sigma}_p)$ with respect to $\hat{\sigma}_p$ to zero, we can obtain the LSE value

$$\hat{\sigma}_p = \frac{\sum s(r,\theta) X_p{}^*(r,\theta)}{\sum \left| X_p(r,\theta) \right|^2} \tag{5.17}$$

where $X_p{}^*(r,\theta)$ is the conjugation of $X_p(r,\theta)$.

5.3.3 Processing Steps

Based on two parts presented above, the major processing steps of the proposed CGRT-CLEAN method to form 3D image are listed as follows.

Step 1 Perform the CGRT to (5.11) to extract the position (x_p', y_p', z_p') of a scatterer P by searching the peaks in the parameter domain.

Step 2 Use (x_p', y_p', z_p') to construct the point spread function $X_p(r, \theta)$ and estimate reflection coefficient $\hat{\sigma}_p$ through LSE method.

Step 3 Use the CLEAN technique to subtract the contribution of a scatterer P from echoes through the following expression

$$s_{new} = s - \hat{\sigma}_p X_p. \tag{5.18}$$

Step 4 Input s_{new} to Step (1) and repeat to Step (1)-Step (3) until the estimated energy $\hat{\sigma}X$ is smaller than the preset threshold.

5.4 Simulations

In order to validate the feasible of the proposed algorithm, several simulations have been performed. The main system parameters are: carrier frequency f_c is 9.6 GHz, bandwidth B is 1.2 GHz, incident angle θ_i is 60°, height H is 500 m, azimuth angle is [0 ~ 2π). Nine ideal simulation scatterers' coordinates are [0 0 0.6], [1.2 1.2 −0.6], [−1.2 −1.2 −0.6], [−1.2 1.2 −0.6], [1.2 −1.2 −0.6], [0.6 0 0], [−0.6 0 0], [0 0.6 0] and [0–0.6 0], and the reflection coefficients are 0.75, 0.7, 0.65, 0.65, 0.65, 0.7, 0.65, 0.65 and 0.65, respectively.

In this simulation, it is assumed that all scatterers are persistently illuminated by radar in the whole aperture. The range azimuth image is shown in Fig. 5.6. Via the CGRT-CLEAN algorithm, the reconstructed image is shown in Fig. 5.7. The color of points from red to blue represents the reflection intensity level of scatterers from high to low. From this figure, it can be seen that the coordinates of nine scatterers are estimated well and each reflection coefficient approximates to its theoretical value.

To verify the performance of the CGRT-CLEAN algorithm in the condition of both blockages and noise, white Gaussian noise is added into simulation data in Fig. 5.6 and the signal to noise ratio (SNR) is 14 dB. All scatterers' aperture length is 4π/3. Figure 5.8 shows the range azimuth image in this condition. As shown in this figure, some curves are discontinuous and blurry. The reconstructed image obtained by the proposed algorithm is shown in Fig. 5.9. Comparing with the imaging result in ideal condition, the reflection coefficient of each scatterer with theoretical coefficient 0.7 is greater than that of corresponding scatterer in Fig. 5.8. This phenomenon happens because of the effect of noise. But this does not influence the imaging result. Figure 5.9 demonstrates that the CGRT-CLEAN algorithm can also been used to process the echo suffering from blockages and noise.

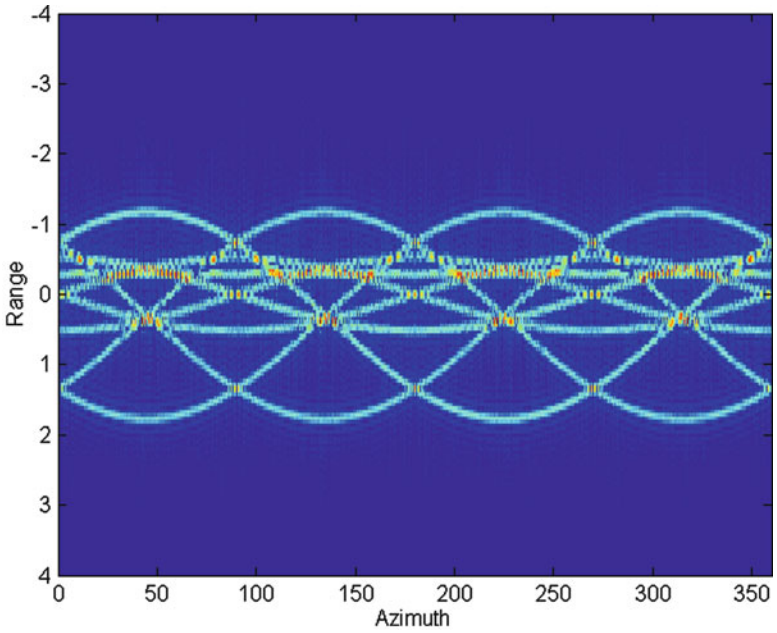

Fig. 5.6 The range azimuth image

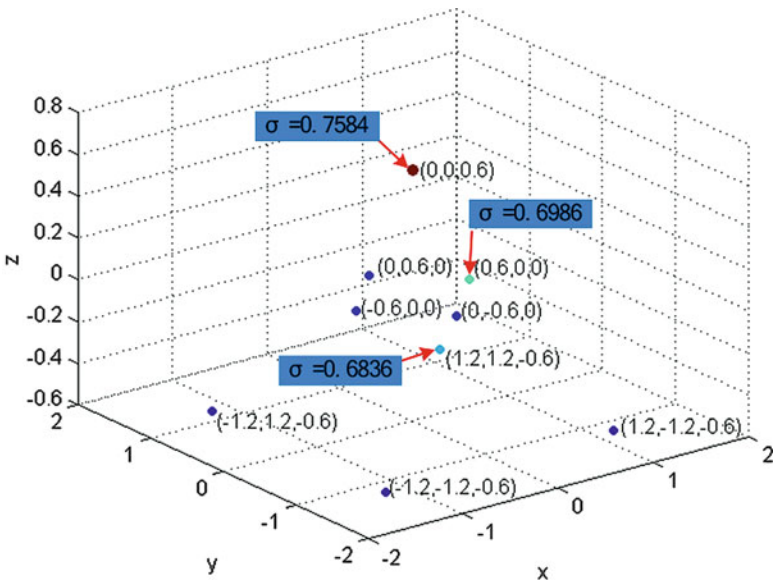

Fig. 5.7 The CGRT-CLEAN 3D image

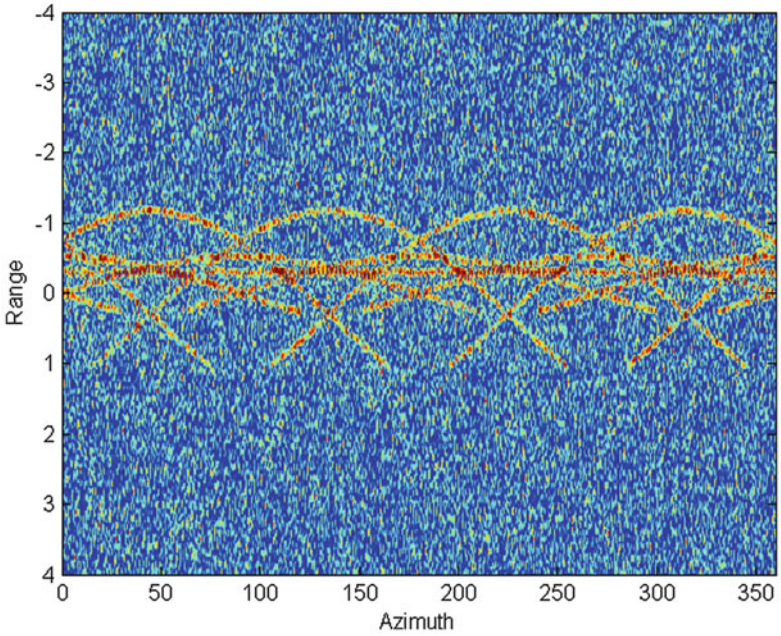

Fig. 5.8 The range azimuth image with noise and blockage

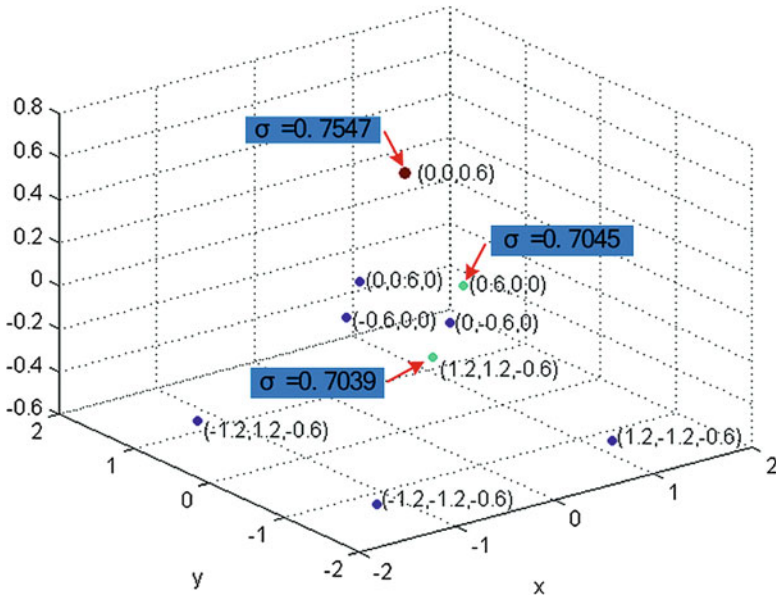

Fig. 5.9 CGRT-CLEAN 3D imaging result with noise and blockage

5.5 Conclusion

In this chapter, a 3D imaging algorithm adapted to circular synthetic aperture has been developed. Combining mathematical derivation of the echo of a scatterer, the CGRT method of estimation for scatterers' position and the estimation method for reflection coefficient which is based on LSE have been introduced in detail. To validate the performance of the CGRT-CLEAN method, some simulations have been performed. These results show the feasibility of CGRT-CLEAN and the robustness to noise and scatterers' blockages.

References

1. Soumekh M (1999) Synthetic aperture radar signal processing with Matlab algorithms. Wiley, New York
2. Soumekh M (1992) A system model and inversion for synthetic aperture radar imaging. IEEE Trans Image Process 1:64–76
3. Knaell KK (1994) Three-dimensional SAR from curvilinear aperture. Proc SPIE 2230:120–134
4. Soumekh M (1996) Reconnaissance with slant plane circular SAR imaging. IEEE Trans Image Process 5(8):1252–1265
5. Ishimaru A, Chan T, Kuga Y (1998) An imaging technique using confocal circular synthetic aperture radar. IEEE Trans Geosci Remote Sens 36(5):1524–1530
6. Cantalloube H, Koeniquer EC (2007) High resolution SAR imaging along circular trajectories. In: Proc IGARSS, Barcelona, Spain pp 2259–2262
7. Beylkin G (1985) Imaging of discontinuities in the inverse scattering problem by inversion of a causal generalized radon transform. J Math Phys 26:99–108

Part II
Smart Grid

Chapter 6
Outage Probability Analysis of HANs in Multiuser Downlink Scenario for Smart Grid Communications

Zhuo Li and Qilian Liang

Abstract Due to the importance of reliable communications in smart grid, this paper evaluates the outage probability of HANs in multiuser downlink scenario. The probability density function (PDF) of the signal to interference and noise ratio (SINR) for each user in the HAN is derived from the amplitude distribution property of the classic indoor Saleh-Valenzuela (S-V) channel. The numerical results are obtained by Monte-Carlo simulation and are furthermore compared with those of ordinary multiuser downlink without interference cancelation and WiFi Direct techniques. The comparisons indicate the by applying these two techniques, the outage performance is greatly improve, namely, the reliability of downlink communications in HANs for smart grid is enhanced.

Keywords Outage probability • Home Area Networks (HANs) • Saleh-Valenzuela (S-V) channel • Smart Grid Communicaitons

6.1 Introduction

Modernization of the electric power grid, which is considered as Smart Grid, is central to worldwide efforts to increase reliability and energy efficiency, transition to renewable sources of energy, reduce greenhouse gas emissions, and build a sustainable economy that ensures prosperity for future generations.

A typical smart grid communication system consists of an advanced metering infrastructure (AMI) which provides near real-time monitoring of power usage and create a two-way network between advanced meters and utility business systems, enabling collection and distribution of information to customers and other parties,

Z. Li (✉) • Q. Liang
Department of Electrical Engineering, University of Texas of Arlington,
416 Yates St., Arlington, TX 76019, USA
e-mail: zhuo.li@mavs.uta.edu; liang@uta.edu

Q. Liang et al. (eds.), *Communications, Signal Processing, and Systems*, Lecture Notes in Electrical Engineering 202, DOI 10.1007/978-1-4614-5803-6_6,

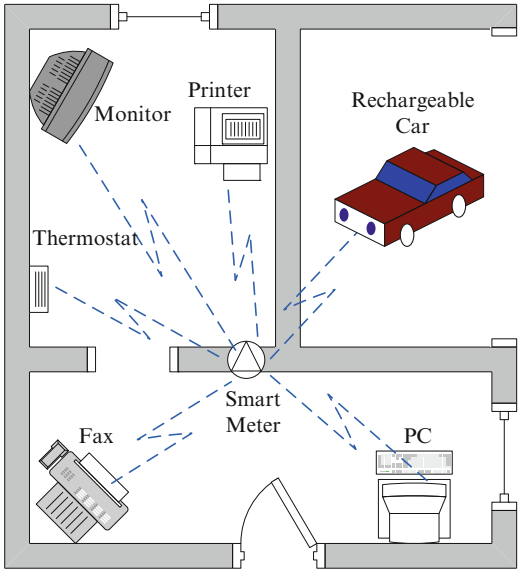

Fig. 6.1 Communications of a HAN in smart grid

such as the competitive retail supplier or the utility itself. These advanced metering networks are of a multi-tier communication infrastructure that includes: home area network (HAN), which is used to gather sensor information from a variety of devices within the home, and optionally send control information to these devices to better control energy consumption, and provides access to in-home appliances, as shown in Fig. 6.1; neighborhood area network (NAN) to connect the smart meters to the local access points; and a wide area network (WAN) to connect the grid to the core utility system [2, 11]. We can see from Fig. 6.1 that in a HAN of Smart Grid, the smart meter is in charge of gathering power usage data and status from the utilities within the home, and also distributing power information like prices and control signals to the utilities. The reliability of the communications in HAN of smart grid is of our interest. The performance analysis including outage probability and bit error rate (BER) of the multiuser uplink scenario in HAN of smart grid was presented in our previous work [4]. In this paper, we focus on the outage probability analysis of HANs in multiuser downlink scenario for Smart Grid communications. The probability density function (PDF) of the signal to interference and noise ratio (SINR) for each user in the HAN is derived according to the distribution property of channel gain. The outage probability of the downlink scenario is analyzed with the characteristics of interference cancelation technique [5], as well as WiFi Direct technique [9, 10], and is also compared with that without interference cancelation and WiFi Direct techniques.

The rest of this paper is organized as follows. Section 6.2 introduces the multiuser downlink model of the HAN in Smart Gird. The PDF of SINR for each user is derived in Sect. 6.3, followed by the statistics of outage probability. Numerical results and discussion are presented in Sect. 6.4. Finally, Sect. 6.5 draws the conclusion.

6.2 System Model

We consider a downlink scenario in the HAN with K active users as shown in Fig. 6.2. Assume that the independent signal matrix $\underline{\mathrm{X}} = [x_1, x_2, \ldots, x_k, \ldots, x_K]$ are transmitted, with transmitted power matrix $\underline{\mathrm{P}} = [P_1, P_2, \ldots, P_k, \ldots, P_K]$, where x_k is the signal transmitted from the smart meter to the k_{th} user, and P_k is correspondingly the power of x_k. The channel matrix is $\underline{\mathrm{H}} = [h_1, h_2, \ldots, h_k, \ldots, h_K]$, where h_k denotes the channel gain between the smart meter and the k_{th} user, and is independent S-V indoor channel. After normalization, $E\{{h_k}^2\} = 1, \ \forall k$.

By applying interference cancelation technique, the interference cancelation coefficient is added to each user, which is multiplied to the interference introduced by other users. The interference cancelation coefficient matrix is $\underline{\alpha} = [\underline{\alpha_1}, \underline{\alpha_2}, \ldots, \underline{\alpha_K}]$, where $\underline{\alpha_k} = [\alpha_{k1}, \alpha_{k2}, \ldots, \alpha_{kK}]^T$, and α_{ki} is the interference cancelation coefficient for the interference introduced by the i_{th} transmitted signal to the k_{th} user, which is a random variable ranges from 0 to 1, for $i = 1, 2, \ldots, K$. Specifically, $\alpha_{ki} = 0$ denotes that the interference is fully canceled, while $\alpha_{ki} = 1$ means that the interference is entirely present. It is easy to see that $\alpha_{kk} = 1$. Without interference cancelation, $\underline{\alpha}$ is a unit matrix since all the interferences are fully present.

6.3 Outage Probability Analysis

6.3.1 Statistics of SINR

In practical multiuser systems, each user would experience multiuser interference (MUI) from other users. Considering the effect of MUI, the SNIR that evaluates

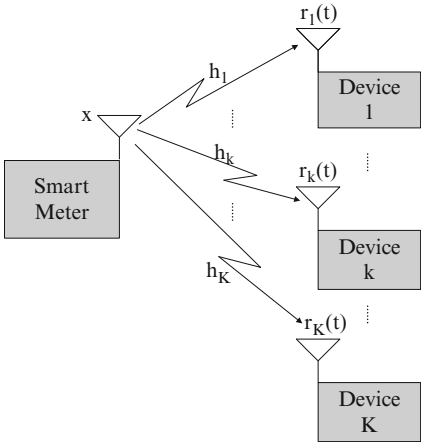

Fig. 6.2 Multiuser downlink model with K active users

the ratio between the desired signal power and the amount of noise and interference generated by all the other users, should be used in performance evaluation [5]. Thus the SINR γ_k at the k_{th} user is written as:

$$\gamma_k = \frac{|h_k|^2 P_k}{\sum_{j \neq k} \alpha_{kj} |h_k|^2 P_j + \sigma^2} \tag{6.1}$$

where σ^2 is the power of Addictive White Gaussian Noise (AWGN).

In the following, the PDF of γ_k is derived according to the distribution property of channel gain $|h_k|$.

$$\begin{aligned} \gamma_k &= \frac{|h_k|^2 P_k}{\sum_{j \neq k} \alpha_{kj} |h_k|^2 P_j + \sigma^2} \\ &= \frac{|h_k|^2 P_k}{\sum_{j=1}^{K} \alpha_{kj} |h_k|^2 P_j - \alpha_{kk} |h_k|^2 P_k + \sigma^2} \\ &= \frac{|h_k|^2 P_k}{|h_k|^2 \underline{\alpha_{\mathbf{k}} \mathbf{P}} - |h_k|^2 P_k + \sigma^2} \end{aligned} \tag{6.2}$$

$|h_k|^2$ can be represented by γ_k according to (6.2) as:

$$|h_k|^2 = \frac{\sigma^2}{\left(1 + \frac{1}{\gamma_k}\right) P_k - \underline{\alpha_{\mathbf{k}} \mathbf{P}}} \tag{6.3}$$

As to indoor S-V channel, since the amplitude of the channel gain follows Rayleigh Distribution [6], $|h_k|^2$ follows exponential distribution as [7]:

$$f_{|h_k|^2}(|h_k|^2) = \frac{1}{\overline{|h_k|}^2} \exp\left(- \frac{|h_k|^2}{\overline{|h_k|}^2} \right) \tag{6.4}$$

where $\overline{|h_k|}^2$ is the mean of $|h_k|^2$.
Thus, the pdf of γ_k is obtained based on (6.4):

$$f_{\gamma_k}(\gamma_k) = \frac{\sigma^2 P_k}{\overline{|h_k|}^2 \gamma_k^2 [(1 + \frac{1}{\gamma_k}) P_k - \underline{\alpha_{\mathbf{k}} \mathbf{P}}]^2} \exp\left(- \frac{\sigma^2}{\overline{|h_k|}^2 [(1 + \frac{1}{\gamma_k}) P_k - \underline{\alpha_{\mathbf{k}} \mathbf{P}}]} \right) \tag{6.5}$$

For tractable analysis, the pdf of γ_k with K active users in (6.5) is represented as $f_K(\gamma_k)$. After normalization of the channel, $\overline{|h_k|}^2 = 1$. Assume that the smart meter transmits signals to all the active users with equal power, that is, $P_1 = P_2 = \ldots = P_k = \ldots = P_K$. We can simplify (6.5) as:

$$f_K(\gamma_k) = \frac{\sigma^2}{\gamma_k^2[(1+\frac{1}{\gamma_k}) - \sum_{k=1}^{K}\alpha_k]^2 P_k} \exp\left(-\frac{\sigma^2}{[(1+\frac{1}{\gamma_k}) - \sum_{k=1}^{K}\alpha_k]P_k}\right) \tag{6.6}$$

Since $P_k/\sigma^2 = SNR$, (6.6) can be further simplified as:

$$f_K(\gamma_k) = \frac{1}{\gamma_k^2[(1+\frac{1}{\gamma_k}) - \sum_{k=1}^{K}\alpha_k]^2 SNR} \exp\left(-\frac{1}{[(1+\frac{1}{\gamma_k}) - \sum_{k=1}^{K}\alpha_k]SNR}\right) \tag{6.7}$$

6.3.2 Statistics of Outage Probability

Considering that each device with WiFi Direct technique in HANs of smart grid alternates between active state and doze state, the total number of active devices K is modeled as a Markov chain with the steady state probability P_K, $K = 1, 2, \ldots, M$ and traffic intensity ρ, where M is the total number of devices with WiFi-Direct technique of a HAN in Smart Grid [3]. The steady state probability $Pr(K)$ is expressed as below:

$$Pr(K) = \frac{\frac{1}{K!}\rho^K}{\sum_{i=0}^{M}\frac{1}{i!}\rho^i}, K = 0, 1, \ldots, M \tag{6.8}$$

Data transmission is considered successful if the transmission rate is below the the channel capacity. Otherwise, the link is said to be in *outage*. Thus the average outage probability with WiFi Direct technique of HANs in multiuser downlink scenario is expressed as [1, 8]:

$$\begin{aligned} P_{out} &= \sum_{k=1}^{M} Pr(K) Pr[\log_2(1+\gamma_k) \le R_{req}] \\ &= \sum_{k=1}^{M} Pr(K) Pr[\gamma_k \le 2^{R_{req}} - 1] \\ &= \sum_{k=1}^{M} Pr(K) \int_0^{2^{R_{req}}-1} f_K(\gamma_k) d\gamma_k \end{aligned} \tag{6.9}$$

On the other hand, without WiFi Direct technique, the outage probability is just written as:

$$P_{out}^{M} = Pr[\log_2(1+\gamma_k) \leq R_{req}] = \int_0^{2^{R_{req}}-1} f_M(\gamma_k) d\gamma_k \tag{6.10}$$

6.4 Simulation and Results

By taking (6.6) into (6.9) and (6.10), we can get the numerical results of the outage probability for each user using Monte-carlo Simulation. Figure 6.3 illustrates the comparison of outage probability between WiFi-Direct multiuser downlink scenario and ordinary multiuser downlink scenario when $\rho = 4$, $M = 5$ and 10. The solid lines are the outage probability without WiFi Direct technique, and the dash lines are the one with WiFi Direct. Figure 6.4 shows the comparison of downlink outage probability in a HAN with WiFi Direct technique when $\rho = 4$, $M = 5$ and 10. The solid lines are the outage probability without interference cancelation, and the dash lines are the one with interference cancelation.

From Figs. 6.3 and 6.4, we can see that: (1) with more users, the outage probability exhibits dramatically higher values due to a potentially worse SINR for each user. (2) The outage probability performance for downlink scenario in a HAN is greatly improved with WiFi Direct technique, especially at low SNR

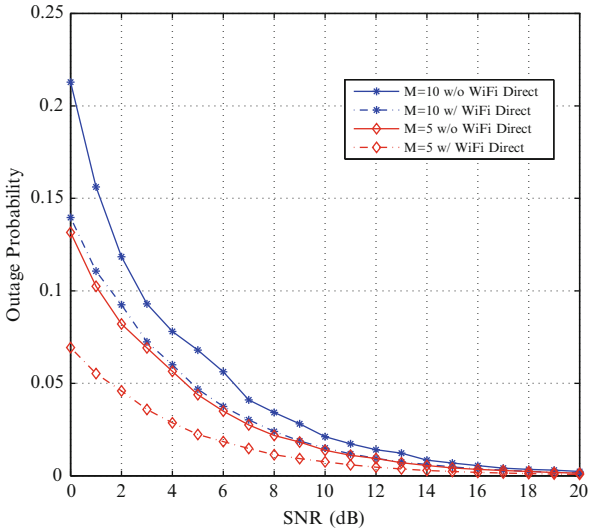

Fig. 6.3 Downlink outage probability with interference cancelation when $\rho = 4$

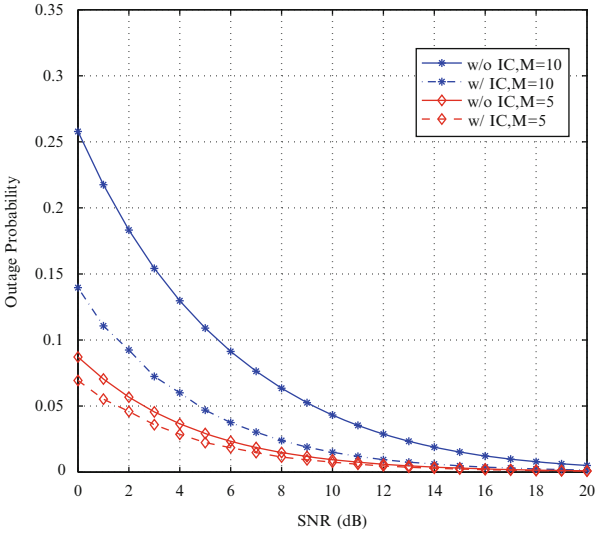

Fig. 6.4 Downlink outage probability with WiFi-direct when $\rho = 4$

region, which indicates that WiFi Direct technique not only improves the energy usage in Smart Grid, but also enhances the reliability of communications in Smart Grid. (3) The downlink HAN has better outage performance with interference cancelation, especially with large total number of WiFi-Direct users in the HAN.

6.5 Conclusion

In this paper, the outage probability of HANs in multiuser downlink scenario for smart grid communications is evaluated with interference cancelation and WiFi Direct techniques, and thus compared with ordinary multiuser downlink without interference cancelation and WiFi Direct techniques. The numerical results clearly show that by employing these two techniques in HANs for smart grid communications, the outage performance is dramatically improved.

Acknowledgements This work was supported by U.S. National Science Foundation under Grant CNS-1116749.

References

1. Cover MT, Thomas AJ(2006) Elements of information theory, 2nd edn. Wiley, Hoboken
2. Ghassemi A, Bavarian S, Lampe L (2010) Cognitive radio for smart grid communications. In: 2010 First IEEE international conference on smart grid communications, Gaithersburg, pp 297–302
3. Li Z, Liang Q WiFi direct networks in smart grid application: power consumption and outage performance evaluation. Submitted to IEEE Trans Smart Grid
4. Li Z, Liang Q Performance analysis of multiuser selection scheme in dynamic home area networks for smart grid communications. Submitted to Special Issue of IEEE Trans Smart Grid
5. Nam SS, Yang HC, Alouini MS, Kim DI (2012) Impact of interference on the performance of selection based parallel multiuser scheduling. IEEE Trans Wirel Commun 11(2):531–536
6. Saleh MA, Valenzuela AR (1987) A statistical model for indoor multipath propagation. IEEE J Sel Areas Commun SAC-5(2):128–137
7. Simon KM, Alouini M (2004) Digital communication over fading channels, 2nd edn. Wiley, Hoboken, pp 20–21
8. Tse D, Viswanath P (2004) Fundamentals of wireless communication. Cambridge University Press, Cambridge, New York, USA
9. Wi-Fi Alliance (2010) Wi-Fi for the smart grid. http://www.wi-fi.org/knowledge_center_overview.php?docid=4686
10. Yoon H, Kim J (2010) Collaborative streaming-based media content sharing in WiFi-enabled home networks. IEEE Trans Consum. Electron 54(4):2193–2200
11. Zhang Y, Wang L, Sun W, Green RC, Alan M (2011) Distributed intrusion detection system in a multi-layer network architecture of smart grids. IEEE Trans Smart Grid 2(4):796–808

Chapter 7
Bidirectional Energy Management for Plug-in Hybrid Electric Vehicles via Vehicle-to-Grid

Xin Wang and Qilian Liang

Abstract As a paradigm of the incoming smart grid, vehicle-to-grid (V2G) has been proposed as a solution to increase the adoption rate of plug-in hybrid electric vehicles (PHEVs). In this paper, we investigate the bidirectional energy management for PHEVs via V2G system. We formulate the energy management problem through dynamic programming, aiming at flattening the grid peak load and minimizing the daily energy cost. However, the "well-known" complexity in solving dynamic programming poses a computational challenge even for a small N. Therefore, we prove that a (s, S, s', S') feedback policy is optimal for PHEV battery charging/discharging based on inventory storage theory. Simulation results verified the validity of the proposed algorithm. The theoretical analysis and proofs are instrumental to the future large-scale PHEV adoption in smart grid.

Keywords Plug-in hybrid electric vehicles • Vehicle-to-grid • Battery charging • Dynamic programming • Stochastic inventory

7.1 Introduction

Driven by the desire to reduce emissions and achieve energy dependence, electric vehicles (EVs), especially plug-in hybrid electric vehicles (PHEVs) are poised to receive mass acceptance from the public. One million EVs and PHEVs are expected to be in use by individuals and fleets by 2015 [9].

However, mass adoption of PHEVs in the future is not without its challenge: unmanaged PHEV charging will add to the smart grid peak load and would require additional generation capacity [8]. One solution to mitigate the impact of

X. Wang (✉) • Q. Liang
Department of Electrical Engineering, University of Texas at Arlington,
416 Yates Street, Arlington, TX 76019, USA
e-mail: xin.wang51@mavs.uta.edu; liang@uta.edu

Q. Liang et al. (eds.), *Communications, Signal Processing, and Systems*, Lecture Notes in Electrical Engineering 202, DOI 10.1007/978-1-4614-5803-6_7,

PHEVs on smart grid is to optimize their charging profile, which are referred to as "smart charing". In other words, we need to keep the peak power demand as small as possible, taking into account the extra power consumption from the vehicle charging. Besides smart charging, another way to address this challenge is vehicle-to-grid (V2G), the provision of energy and ancillary services from a PHEV back to the grid [3].

In literature, [5] proposed a stochastic optimal control approach for PHEV power management via stochastic dynamic programming. An optimal store-carry-and-deliver energy management strategy for PHEV is proposed in [4], which also considers the TOU pricing. [8] investigated the optimal charging strategy for *unidirectional* V2G. In [7], the authors examines the economic issues of using PHEV battery packs to store grid electricity generated at off-peak hours for off-vehicle use during peak hours. However, to our best knowledge, it is still a open question considering the bidirectional energy flow, real-time electricity price and realistic PHEV battery models.

In this paper, aiming to minimize the daily energy cost, we design a (s, S, s', S') feedback policy for PHEV battery recharing/discharing based on inventory storage theory [1]. The household demand, realistic PHEV battery model and time-of-use (TOU) electricity pricing are integrated into our proposed bidirectional energy management model. The optimality of the (s, S, s', S') feedback policy is theoretically proved and simulation results verify the validity of our proposed algorithm.

7.2 System Model

Let random variable ξ_k denote the household energy demand in period k based on the smart meter readings, as shown in Fig. 7.1. Assume p_k is the total power drawn from the grid in slot k out of which r_k is used to recharge the battery, and d_k is the total power discharged from the battery in slot k. Within each time slot, the battery can be either recharged or discharged or do neither, but not both. This means for all time k, we have $r_k \cdot d_k = 0$. To eliminate the variable number, we use u_k to represent the recharging/discharging decision. The basic system model is

$$p_k = \xi_k + u_k, \tag{7.1}$$

where $u_k > 0$ and $u_k < 0$ means the battery is recharged or discharged, respectively. Note that, $u_k = 0$ stands for the battery's idle state.

Ideally, we would like to incorporate the following idiosyncrasies of battery operation into our model [10]. First, the battery lifetime is shorten with each recharging/discharging cycle. To model the effect of repeated recharging and discharging on battery's lifetime, we assume that within each recharge and discharge operation, a fixed cost (in dollars) of C_{rc} and C_{dc} is incurred, respectively [10]. Secondly, for each battery recharging and discharging, the batteries have

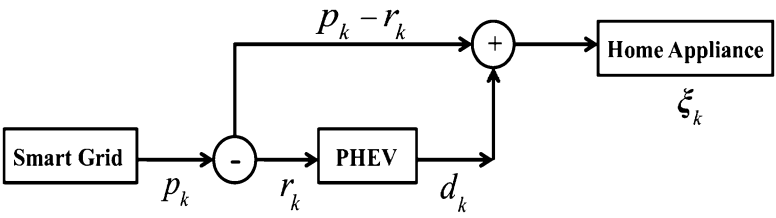

Fig. 7.1 System model

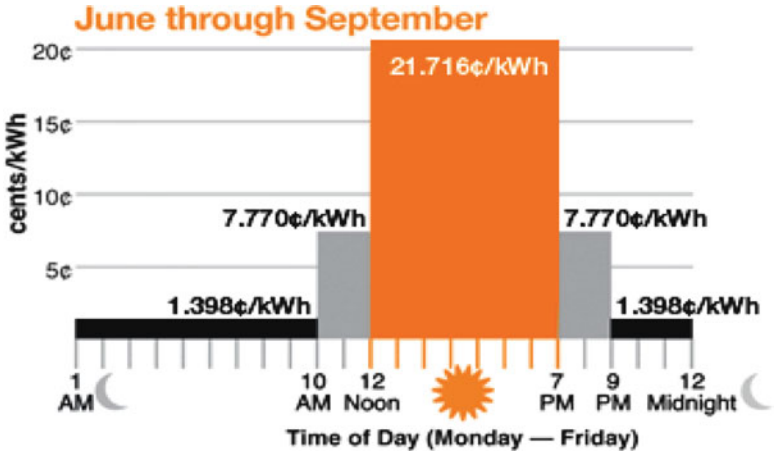

Fig. 7.2 O&R Electricity TOU Pricing [6]

conversion loss whereby a portion η of the energy stored is lost (e.g. about 10–15% for lead-acid batteries). Thirdly, to maximize the life of the battery pack, we limit the state of charging up to 90% of capacity (x_{max}) and never deplete the battery below 30% (x_{min}).

In this paper, we investigate the optimal energy management over TOU pricing. TOU pricing, whereby electricity prices are set for a specific time period on an advance or forward basis, will typically not change more often than twice a year. TOU rate from Orange and Rockland [6] is given by Fig. 7.2.

7.3 Optimal Energy Management Policy

Assume there exists $N + 1$ periods within the time span and the recharging/discharging decision variable is given by $U = (u_0, u_1, \cdots, u_N)$. Denoting the energy level at the beginning of period n as x_k and the energy level at the end of period n as y_k, the battery energy balance is then expressed as $y_k = x_k + u_k,\ k = 0, \cdots, N$.

Furthermore, we specify the energy cost at period k as

$$c_k(u_k, x_k) = (K + \frac{r_k}{\eta} \cdot u_k)\Pi_{u_k>0} + (K + r_k\eta \cdot u_k)\Pi_{u_k<0} + r_k \cdot \xi_k, \tag{7.2}$$

where r_k is the electricity real-time price and $K = \frac{C}{N}$ is the loss of the battery value for each charging or discharging, as we have discussed. Note that the indication function $\Pi_{u_k>0}$ equals 1 when $u_k > 0$ and equals 0 when $u_k < = 0$. Since the cost of the household demand $r_k \cdot \xi_k$ is irrelevant to the battery charging/discharging decision, we remove it from (7.2) in the following discussions.

We add the variable x_k to (7.2) due to the fact that the decision u_k depends on the current battery level, i.e.,

$$x_{min} \leq x_k + u_k \leq x_{max}, \tag{7.3}$$

$$-u_{max} \leq u_k \leq u_{max}. \tag{7.4}$$

In (7.4), the maximum recharging/discharging value $u_{max} = CR \cdot T$, where CR is the PHEV battery recharing/discharging *rate* and T is the per time slot duration.

Now the objective function to be minimized is the sum of all the costs incurred during the interval $< 0, N >$:

$$\inf_{U\in\Phi} J_0(x; U) = \inf_{U\in\Phi} \left\{ \sum_{k=0}^{N-1} c_k(u_k, x_k) + c_N(u_N, x_N) \right\} \tag{7.5}$$

where Φ denotes the class of all admissible recharging/discharging decisions. Of course, once the existence is established, the "*inf*" in (7.5) can be replaced by "*min*".

Note that, for period N, the PHEV battery should be fully recharged to support the daily use at the daytime. Therefore, the end-of-day cost function is given by

$$c_N(u_N, x_N) = K \cdot \Pi_{x_{max}>x_N} + \frac{r_N}{\eta}(x_{max} - x_N). \tag{7.6}$$

Employing the principle of optimality, we could develop the following *dynamic programming* equations satisfied by the value function:

$$v_n(x_n) = \inf_{u_n} \{c_n(u_n, x_n) + v_{n+1}(x_n + u_n)\}, \quad n \in [0, N-1]. \tag{7.7}$$

Theorem 2.1 in [1] has proved the existence of optimal battery management policy. However, the computational complexity for the optimal policy is prohibitive even for a small N [2]. In this section we will prove the optimality of a (s, S, s', S') feedback policy for PHEV battery charging/ discharging based on inventory storage theory. Before proceedings, let us give the following definitions.

Definition 1 A function g: $\mathbf{R} \rightarrow \mathbf{R}$ is said to be *K-convex*, $K \geq 0$, if it satisfies the property

$$K + g(y + a) \geq g(y) + a\frac{g(y) - g(y - b)}{b}, \quad for\ all\ a \geq 0, b{>}0. \tag{7.8}$$

Definition 2 Assume q: $\mathbf{R} \rightarrow \mathbf{R}$ be a *K-convex* function with the closed interval $[x_{min}, x_{max}]$. Let $q^* = \inf_{x_{min} \leq x \leq x_{max}} [q(x)]$ and the function $h' : [x_{min}, \infty) \rightarrow \mathbf{R}$

$$h'(x) = \inf_{y \leq x, x_{min} \leq y \leq x_{max}} \left[K \cdot \Pi_y + q(y)\right]. \tag{7.9}$$

We define the threshold S' and s', $S' \leq s'$ as follows:

$$S' = max\ \{x \in [x_{min}, x_{max}] | q(x) = q_*\}, \tag{7.10}$$

$$s' = max\ \{x \in [x_{min}, x_{max}] | q(x) \leq K + q(S')\}. \tag{7.11}$$

Because of space limitation, we omit the definitions of $h(x)$, p^*, s, S which are very similar to the definitions (C.3), (C.4), (C.5) in [1]. Given the above definitions of the thresholds s, S, s', S', the (s, S, s', S') policy could be expressed as

$$u_k = \begin{cases} u_{max}, & if\ x{<}s,\ x{<}S - u_{max} \\ S - x, & if\ S - u_{max} \leq x{<}s \\ 0, & if\ s \leq x \leq s' \\ S' - x, & if\ s'{<}x{<}S' + u_{max} \\ -u_{max}. & if\ x{>}s',\ x \geq S' + u_{max} \end{cases} \tag{7.12}$$

The principle of the proposed (s, S, s', S') policy is when the battery energy level is below s, the battery should be recharged to the energy level S; when the battery level is above s', the battery will be discharged to the energy level S'; otherwise, the battery is kept in the idle state.

Theorem 1 *Given the thresholds s, S, s', S', the proposed (s, S, s', S') feedback policy defined by (7.12) is optimal for PHEV battery recharging/discharging.*

Proof See the *Appendix*.

To implement proposed (s, S, s', S') battery recharging/discharging policy, we designed the following "$N \rightarrow 0$" backward iteration algorithm.

Algorithm 1 *"N →0"* backward iteration algorithm

1: Initialize *vN(xN)* according to (7.6);
2: for *k=N-1* to 0 do
3: Formulate the value function $v_k(x_k)$ as (7.7);
4: Calculate optimization value p^* and p^*;
5: Calculate the thresholds S_k , s_k , S'_k and s'_k;
6: Update $v_{k-1}(x_{k-1})$ according to (7.7);
7: end for

7.4 Simulation Results

We characterize the PHEV battery model as a typical lithium-ion battery (Table 7.1). Here we use an round trip efficiency (RTE) of 85% as our base case. The current PHEV battery price is approximately $450 per KWh. In terms of the battery recharging strategy, two charging levels, i.e., 120 V/16 A (Single phase) and 240 V/32 A (Split phase), are defined by SAE J1772, which is the North American standard for electrical connectors for electric vehicles.

In our paper, we mainly focus on the application of PHEV on local household load shaping at home. Therefore, the simulations are performed for the home charging between 5 P.M. and 8 A.M. For comparison, we consider two PHEV users whose PHEVs are equipped with the battery of 16 and 24 KW. Meanwhile, due to the different distance between home and their work place, there are 70 and 40% energy are left in the User A and User B' PHEV battery, respectively. The performance of our proposed (s, S, s', S') feedback policy on daily energy cost is shown in Fig. 7.3. The positive value means making profits while the negative value is the energy cost for recharging the PHEV. Without V2G system, the PHEV users could choose either to recharge the battery during the off-peak periods (smart charging) or to plug in to recharge the battery immediately they arrived home (normal charging). Compared to these two scenarios, the advantage of our proposed algorithm in reducing the daily energy cost is obvious. Employing our algorithm, user A could make even some profits (4.63 and 93.03 cents with respect to two charging types) with the PHEV fully recharged. Since user B's PHEV is equipped with a large battery, user B still need to pay for the battery charging even employing our algorithm. However, the situation could be improved if user B chooses fast charging (240 V/32 A). Note that, we have taken the battery price and battery life cycles into consideration. Hence, *fast* charging which deceases the recharging/discharging cycles will reduce the energy cost, as illustrated in Fig. 7.3.

Table 7.1 Battery Parameters

Parameters	Characteristics
Battery type	Lithium-ion
Round trip efficiency (RTE)	85%
Battery capacity	16 KW & 24 KW
Battery charging type-1 (single phase)	120 V/16 A
Battery charging type-2 (split phase)	240 V/32 A

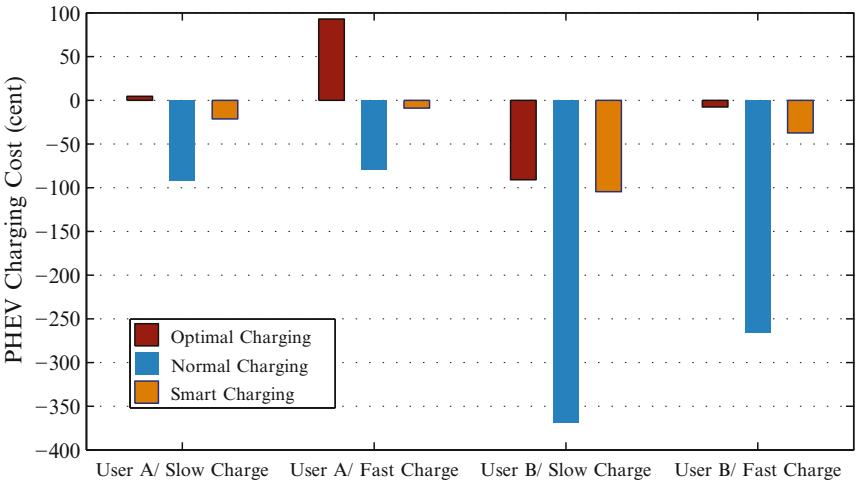

Fig. 7.3 PHEV recharging cost comparison

7.5 Conclusions

In this paper, we investigated the bidirectional energy management for PHEVs via V2G system. We first formulated the energy management problem of PHEV battery charging/discharging through dynamic programming. To avoid the computational complexity in solving dynamic programming, we proved that a (s, S, s', S') feedback policy based on inventory storage theory is optimal. A "$N \rightarrow 0$" backward iteration algorithm was then proposed to implement the (s, S, s', S') feedback policy. The simulation performances verified the validity of the proposed algorithm.

Acknowledgements This work was supported by U.S. National Science Foundation under Grant CNS-1116749.

Appendix

First of all, we need to prove $h_n(y)$ and $h'_n(y)$ are K-convex. This is could be done by induction. First, $v_N(x)$ is convex by definition (7.6) and, therefore, K-convex for any $K \geq 0$ [1]. Suppose for a given $n \leq (N-1)$,$v_{n+1}(x)$ is K-convex. According to [1], restriction of any K-convex function on any convex set is K-convex. Thus, $h_n(y)$ and $h'_n(y)$ are K-convex. Clearly, $v_n(x)$ is also K-convex, which completes the induction argument.

With the K-convexity of $h'_n(x)$, to prove the optimality of (s, S, s', S') feedback policy we only need to prove

$$h'(x) = \begin{cases} K + q(S'), & if\ x > s' \\ q(x). & if\ x_{min} \leq x \leq s' \end{cases} \tag{7.13}$$

The proof of $h(x)$ omitted here is similar to that of Theorem C.2.3 in [1]. Therefore, due to the space limitation, we only prove the function $h'(x)$. It is straightforward to see that $q(x) \geq q(S')$. Next, our main focus is to prove

$$q(x) \leq q(y) + K, \quad \forall\, x, y \quad with \quad x_{min} \leq x \leq y \leq s'. \tag{7.14}$$

Note that the inequality of (7.14) holds for $x = y$, $x = S'$, and $x = s'$, since $q(s') \leq q(S') + K \leq q(y) + K$. Then we mainly examine the following two cases: (1) $x_{min} \leq y < x \leq S'$ and (2) $x_{min} \leq y < x$, $S' \leq x < s'$.

- Case 1 ($x_{min} \leq y < x \leq S'$). According to the K-convexity of $q(x)$, we have

$$K + q(y) \geq q(x) + \frac{y - x}{x - z}[q(x) - q(z)]. \tag{7.15}$$

  Let $z = S'$, we could derive $q(x) < K + q(y)$ with $q(x) \geq q(S')$.
- Case 2 ($x_{min} \leq y < x$, $S' \leq x < s'$). With the definition of s', if $s' < x_{max}$ we obtain $q(s') = K + g(S')$.

  Together with the convexity of $q(x)$, it is concluded that

$$\begin{aligned} K + q(S') &\geq q(x) + \frac{S' - x}{x - s'}[q(x) - q(s')] \\ &\geq q(x) + \frac{S' - x}{x - s'}[q(x) - q(S') - K]. \end{aligned} \tag{7.16}$$

Transforming (7.16), we obtain

$$q(x) \leq K + q(S') \leq K + q(y). \tag{7.17}$$

We finished the proof of $h'(x)$ (7.13), and therefore the optimality of the (s, S, s', S') feedback policy.

References

1. Beyer D, Cheng F, Sethi S, Taksar M (2010) Markovian demand inventory models. Springer, New York
2. Bertsekas DP (2007) Dynamic programming and optimal control, Vol 1 and 2. Belmont, Athena Scientific
3. Kempton W, Tomic J (2005) Vehicle-to-grid power implementation: from stabilizing the grid to supporting large-scale renewable energy. J Power Sources 144(1):280–294
4. Liang H, Choi B, Zhuang W, Shen X (2012) Towards optimal energy store-carry-and-deliver for PHEVs via V2G system. Infocom 2012, Orlando, FL, March 2012, pp 1674–1682
5. Moura SJ, Fathy HK, Callaway DS, Stein JL (2011) A stochastic optimal control approach for power management in plug-in hybrid electric vehicles. IEEE Trans Comtrol Syst Technol 19 (3):545–555
6. Orange & Rockland Co. http://www.oru.com/index.html
7. Peterson SB, Whitacre JF, Apt J (2010) The economics of using plug-in hybrid electric vehicle battery packs for grid storage. J Power Sources 195(8):2377-2384
8. Sortomme E, El-Sharkawi MA (2011) Optimal charging strategies for unidirectional vehicle-to-grid. IEEE Trans Smart Grid 2(1):131–138
9. United States Department of Energy (2011) One Million Electric Vehicles By 2015, http://energy.gov/sites/prod/files/edg/news/documents/1 Million Electric Vehicle Report Final.pdf
10. Urgaonkar R, Urgaonkar B, Neely MJ, Sivasubramaniam A (2011) Optimal power cost management using stored energy in data centers. Proceedings of the ACM SIGMETRICS. ACM, New York

Chapter 8
Intelligent Power Management System Based Impedance Identification Technology for Safety of Power Utilization

Wei Song, Ning Xie, and Baoju Zhang

Abstract This chapter presents the design and implementation of the intelligent power management system, which consists of three part: the intelligent Electronic Power Meter (iEPM), the intelligent Electronic Management Concentrator (iEMC), and the intelligent Centralized Database Server (iCDS). The iEPM will be installed in every home of building; because it is based on the technology of impendence identification, iEPM can automatically distinguish which electronic appliance is connected in home. The iEPM is a high precision electronic power meter, so it can replace Electricity Meter currently and require no extra indoor wires. A certain amount of iEPM can be added to a group controlled by an iEMC which adopts the technology of WiFi-based WSN so that it can exchange the message with iCDS. The iCDS solves the key problem of system extension by using the multi-layered architecture; it can automatically send data to the iEPM or update the program of the iEPM. The intelligent power management system can make people use power with safety and efficiency. Using this system, the users or managers of the building can decide which electronic appliance can be used in which time up to their requirement. The system has been widely used in many universities of Tianjin in China, such as Tianjin Normal University, Tianjin Business University, Tianjin Medical University, and so on.

Keywords Impedance identification • Intelligent electronic power meter • Wireless sensor network

W. Song (✉) • N. Xie • B. Zhang
College of Physics and Electronic Information, Tianjin Normal University, Tianjin 300387, China
e-mail: wdxysw@mail.tjnu.edu.cn; xie.ning.1989@163.com; wdxyzbj@mail.tjnu.edu.cn

Q. Liang et al. (eds.), *Communications, Signal Processing, and Systems*, Lecture Notes in Electrical Engineering 202, DOI 10.1007/978-1-4614-5803-6_8,

8.1 Introduction

With growing concerns regarding not only the safety of power utilization but also efficient power management in recent years, how to help people use electronic appliances scientifically and reasonably has already been a significant study topic [1]. Some electronic appliances will do harm to our safety if inappropriate application is adopted. For example, the electrical heater (such as hair curler, temperature invariable cup, temperature invariable bottle, electrical hot board, dryer, hand warmer and so on) may cause dangerous fires. That is why the use of electrical heater is strictly prohibited in most of buildings especially student's apartment at school. In other situations, some electronic appliances are restricted to use for a specified period of time to safety and power savings. For these reasons, the Intelligent Power Management System with Middleware based Impedance Identification Technology for Safety of Power Utilization is proposed.

During recent years, even though a lot of research has been done in Power Manage System for home, the most of systems doesn't have the ability to automatically identify what limit these systems' application. In paper [2], the Home Power Management System is put forward early, and then papers [3–5] [1] have further to present an implementation of this intelligent system. These papers above are requested to install an additional new system in home. This will certainly cause the extra costs and home power consumption. At present, many countries have implemented their own "Smart Grid" plans, and the intelligent electronic power meter plays an important role. Papers [6–8] make a systematic elucidation of its structure and realizing methods. It is worth pointing out that paper [8] devise an algorithm electronic appliances identification and monitoring.

This chapter is organized as follows. In Sect. 8.2, we discuss impedance identification technology for identification of connected electronic appliances in home. In Sect. 8.3, we study the hardware implementation of *iEPM*. In Sect. 8.4, we give architecture of the Intelligent Power Management System. In Sect. 8.5 we summarize the implementation and conclude this chapter.

8.2 Impedance Identification

8.2.1 Active Power Increment

The first method developed to distinguish which electronic appliance is connected is based on the active power increment, while we assume that the voltage can be controlled within a permitted range. Figure 8.1 shows the feature of changing of active power when an electrical heater is connected into the system. In mathematical terms, if we define average value of instantaneous active power by $\overline{P_k}$, then we determine $\overline{P_k}$ such that

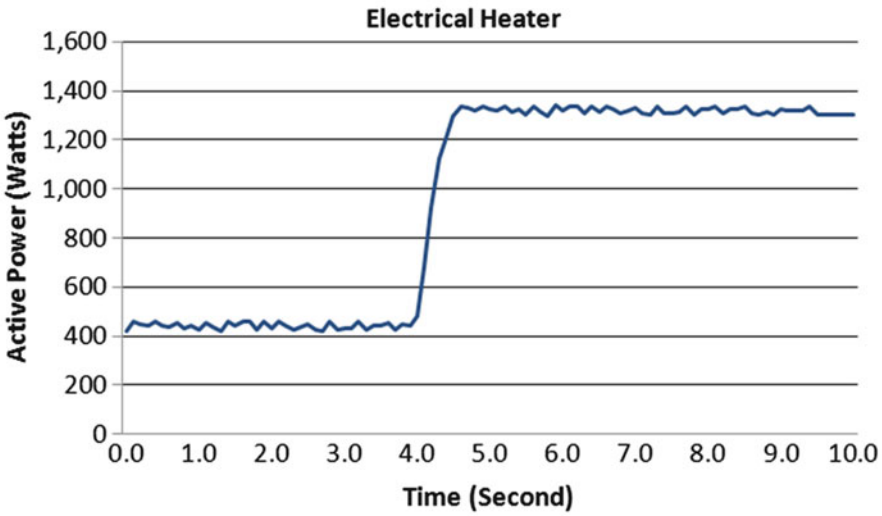

Fig. 8.1 Changing of active power's about electrical heater

$$\overline{P_k} = \overline{P_{current}} - \overline{P_{last}} \tag{8.1}$$

where $\overline{P_{current}}$ is defined as average value of instantaneous active power at the current stage, and $\overline{P_{last}}$ is defined as average value of instantaneous active power at the last stage. If $\overline{P_k} > 0$, we can conclude that a new electronic appliance is connected into the system. We can conclude that one of the electronic appliances has been removed from the system, if $\overline{P_k} < 0$. By making a comparison between $\overline{P_k}$ and the data that is stored to the local memory in advance, we can distinguish which electronic appliance is connected.

8.2.2 Impedance Identification

However, because of fluctuation of active power, we can't obtain an accurate value of every electronic appliance [9]. Because of the result that several electronic appliances in the system have the same $\overline{P_k}$, we need to add other parameters into distinguish algorithms. An electronic appliance is connected into the system, which mainly causes current changing. Furthermore, current changing contains two aspects: magnitudes and phases. The first method only pays attention to the magnitudes changing, and ignores phases changing, power factor.

If φ is the phase angle between the current and voltage, then the power factor is equal to the cosine of the angle, $|cos\varphi|$ and:

$$|P| = |S||cos\varphi| \tag{8.2}$$

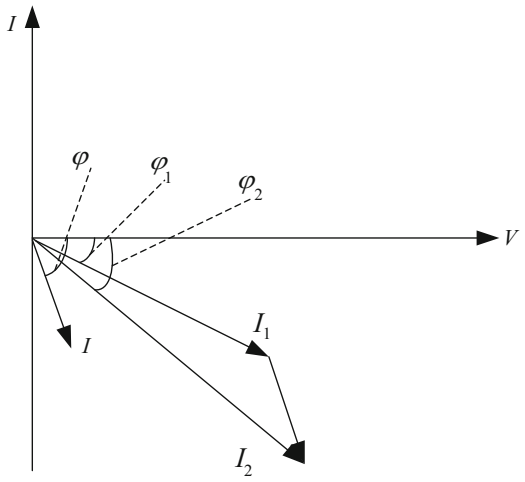

Fig. 8.2 Notation for *AC* current

where P is active power, and S is apparent power [10]. Figure 8.2 shows the notation for *AC* current by magnitudes and phases. In figure, there are 3 current vectors:

$$I_1 = |I_1|e^{j(\omega t+\varphi_1)} \tag{8.3}$$

$$I_2 = |I_2|e^{j(\omega t+\varphi_2)} \tag{8.4}$$

$$I = |I|e^{j(\omega t+\varphi)} \tag{8.5}$$

where I_1 is defined as current vectors at the last stage, I_2 is defined as current vectors at the current stage, and then I is the current vectors of the new connected electronic appliance.

Through calculating from I_1 and I_2, we obtain

$$|I| = \sqrt{(I_2\cos\varphi_2 - I_1\cos\varphi_1)^2 + (I_2\sin\varphi_2 - I_1\sin\varphi_1)^2} \tag{8.6}$$

$$\varphi = arctg\frac{I_2\sin\varphi_2 - I_1\sin\varphi_1}{I_2\cos\varphi_2 - I_1\cos\varphi_1} \tag{8.7}$$

Considering the voltage fluctuation, we present the concept of electronic impedance, which is defined as

$$|Z|e^{j\emptyset_z} = \frac{|V|e^{j(\omega t+\emptyset_V)}}{|I|e^{j(\omega t+\emptyset_I)}} \tag{8.8}$$

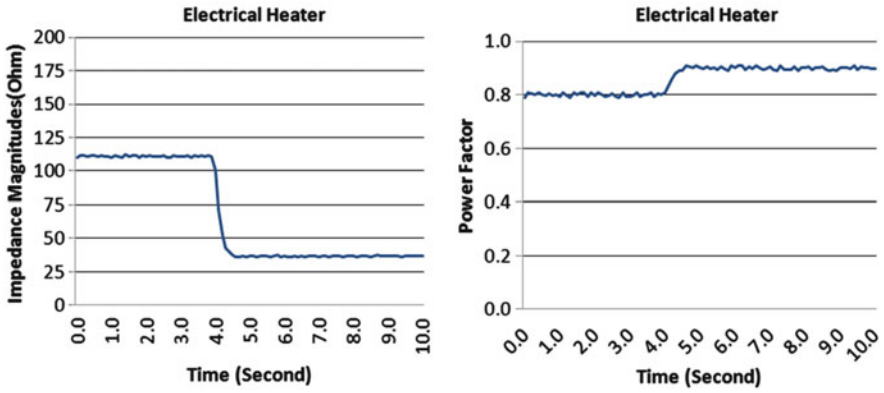

Fig. 8.3 Changing of impedance magnitudes and phase (power factor) about electrical heater

$$|Z| = \frac{|V|}{|I|} \tag{8.9}$$

$$\emptyset_z = 0 - \emptyset_I = -\emptyset_I \tag{8.10}$$

where we assume $\emptyset_V = 0$ in Fig. 8.2. We normally replace $\emptyset_z$ with power factor, $\cos(\emptyset_z)$.

In this way, we can use electronic impedance to identify which electronic appliance is connected; it represents three parameters, current magnitudes, current phase and voltage fluctuation, so the accuracy rate of identification is greatly improved.

8.2.3 Electrical Appliances Identification

In Fig. 8.1, power factor of electrical heater approximately equal to 1, and the increase of current changes smoothly. Considering the fluctuation of active power, we also using averages to describe each of parameters. Figure 8.3 shows the changing of impedance magnitudes and phase (power factor) about electrical heater.

Figure 8.4 shows the other electronic appliances, which have an impulse current. We also may calculate impedance of this appliance as Fig. 8.5 shown. These appliances general contain motor in their structure, such as air conditioner. Because the motor which be consisted of inductor maintains an unsteady state while connecting the power supply, it represents low impedance and high current rating. For these appliances, we may record impulse impedance, steady impedance, and impulse duration to identify.

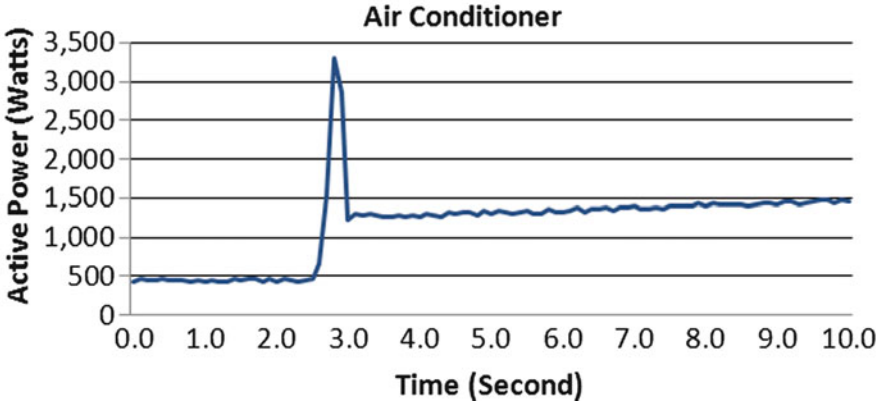

Fig. 8.4 Changing of active power's about air conditioner

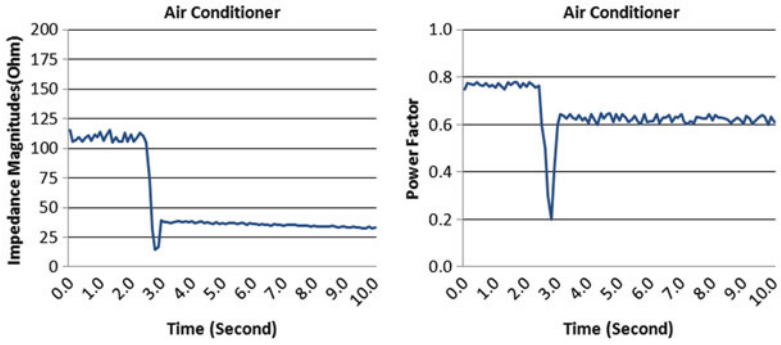

Fig. 8.5 Changing of impedance magnitudes and phase (power factor) about air conditioner

8.3 Hardware Implementation of iEPM

The above algorithm is designed as a real-time processing system, which means the result of the management system can also be seen in real time via the network. To accomplish this algorithm, the intelligent Electronic Power Meter (*iEPM*) must supply and store the following parameters in a given period of time:

- Instantaneous Voltage, Current and Power
- I_{RMS} and V_{RMS}, Active Power, Reactive Power, and Apparent Power

The *iEPM* use a CS5464 IC chip from Cirrus Logic for measuring electric power. The CS5464 is a CMOS monolithic power measurement device with a computation engine and an energy-to-frequency pulse output. The CS5464 combines two programmable gain amplifiers, three $\Delta\Sigma$ analog to digital converters, system calibration, and a computation engine on a single chip [11].

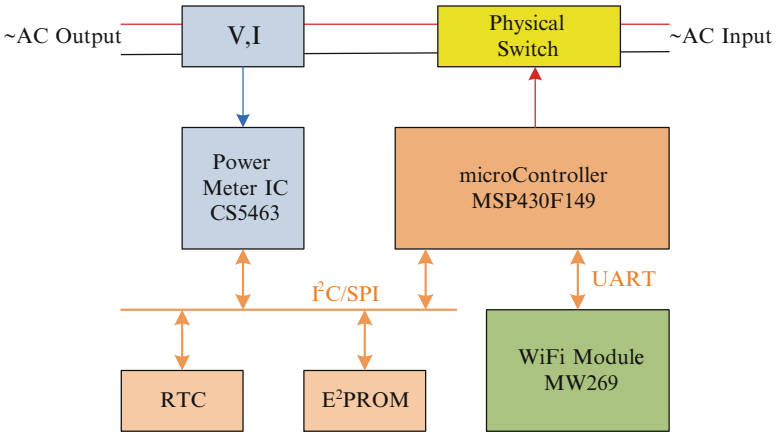

Fig. 8.6 Architecture of *iEPM*

The *iEPM* is illustrated in Fig. 8.6. It uses a local microcontroller, MSP430F149, for implementing data acquisition, processing and external communication functionalities. In comparison with other microcontrollers, the Texas Instruments MSP430F149 has two significant functions, ultra low power and hardware multiplier [12], so *iEPM* has the ability to achieve signal processing in real time and maintain an ultra low power state. The MPS430F149 may control the AC input of the entire home by the external relays, so the *iEPM* may cut off the electricity supply when exception is encountered. The SPI interface provides communication with the MSP430F149 and the power meter IC, CS5464, so *iEPM* has the advantages of speediness and double direction. The *iEPM* has also the other two modules, RTC for real time clock and the E^2PROM for data storage.

In the architecture, the WiFi module, MW269, is added to the *iEPM by the UART interface*, thus *iEPM* has the function of wireless network. Comparing with other Zigbee-based WSN (Wireless Sensor Network) technology, WiFi-based WSN has many advantages, such as high bandwidth, non-line transmission capacity, coverage range, comprehensive cost-effective, easy expansion, higher robustness and security. Through the WiFi-based WSN, the management system can exchange data with *iEPM* and update its program remotely, so the system has adaptive capacity for different environments.

8.4 Architecture of the Intelligent Power Management System

The architecture of intelligent power management system is shown in Fig. 8.7 and divided into three layers: *iEPM*, *iEMC*, and *iCDS*. In the first layer, the *iEPM* is responsible for acquiring the data of electronic power in each home, and process these data in real time; the *iEPM* calculates the impedance of electronic appliances which is connected into the system and compare the value with the stored data; the *iEPM* is

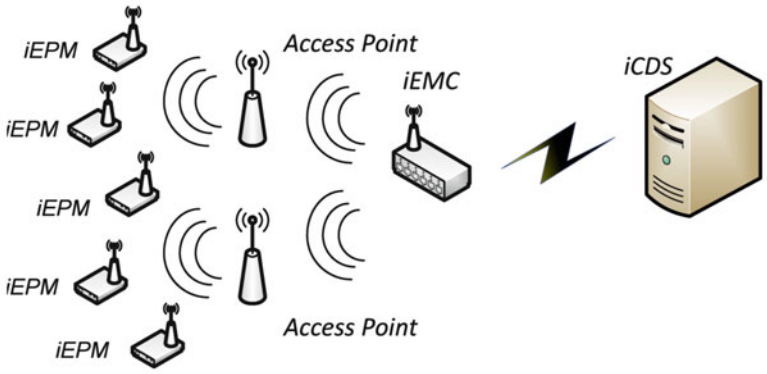

Fig. 8.7 Architecture of the intelligent power management system

also updated the program or the stored data by exchanging the message with the *iCDS*. The second layer of the network centers on *iEMC* which is the sink node of the *iEPM*; the topology of this layer maybe the star network, because the nodes are not too many and uniformly distributed in the building. The third layer network is *iCDS*, which is responsible for the remote data management and it has many optional communication mode, such as ADSL, VPN special network, GPRS, CDMA and so on.

8.5 Results of Implementation

Based the impedance identification technology, the system can closely monitor power use of specified electronic appliances, and gain some important parameters, such as voltage, current, power factor, active power, start time and stop time. We can fully understand the power use information of these specified electronic appliances base on above parameters, so the system can guide user to take proper technical measure to comprehensively save electricity and help user to develop a good electricity consumption habits. In some important situation, such as laboratory, we can use this system to monitor expensive equipments and record the real time data automatically, replacing the traditional method.

At school, many electronic appliances have already been extensively used, however certain kinds of mistreatment due to the adverse consequences. The system can help the school superintendent to resolve power security issues automatically and intelligently. Table 8.1 shows the detailed parameters of parts of electronic appliances which is not used in most cases at school collected from system, we can analyze some features of these electronic appliances:

- Shorter impulse duration, generally lower than 2 s;
- Impulse impedance and steady impedance has been basically similar;
- Power factor more close to 1, because most of these appliances are purely resistive.

Table 8.1 Detailed parameters of parts of electronic appliances

		Impulse impedance		Steady impedance	
Identification appliance	Impulse duration(S)	Magnitudes (Ω)	Power factor	Magnitudes (Ω)	Power factor
Electric kettle(AUX-12A15)	0.5	32.3	0.99	36.9	0.99
Steam iron(YP221B)	1.2	38.8	0.98	40.5	0.98
Electric cooker(CFXD-12XS)	0.9	187.5	0.97	196.7	0.98
Electric hand warmer(DR60-1)	0.5	97.2	0.99	97.7	0.99

The system can identify this kind of electronic appliances, based on above parameters. In some situation, a specified electronic appliance is allowed to use, although it has these above features in a home, this result from the impedance identification technology.

In summary, this system provides an achievable method with high accuracy for Identification of electronic appliances, which can be implemented by hardware in real time. This system can be widely used in many fields, especially in university, because it can display the effect in any kinds of building of the university, for example laboratory, office area, student apartment etc. In 2011, the system has been installed in many universities of Tianjin in China, such as Tianjin Normal University, Tianjin Business University, Tianjin Medical University, and so on, and make the better results.

References

1. Lee M, Uhm Y, Kim Y, Kim G, Park S (2009) Intelligent power management device with middleware based living pattern learning for power reduction. Consum Electron IEEE Trans 55:2081–2085
2. Inoue M, Higuma T, Ito Y, Kushiro N, Kubota H (2003) Network architecture for home energy management system. Consum Electron IEEE Trans 49:606–613
3. Jung Won K, Soon-heung J, Jae-Gon K, Jin-woo H (2007) Development of Qos-Aware ubiquitous content access (UCA) Testbed. Consum Electron IEEE Trans 53:197–203
4. Roth K, Brodrick J (2008) Home energy displays. ASHRAE J 50:136–138
5. Joon H, Choong Seon H, Seok Bong K, Sang Soo J (2008) Design and implement of control mechanism for standby power reduction. Consum Electron IEEE Trans 54:179–185
6. Qichang D, Ping D (2009) Network data transmission and information exchange of the wireless meter reading system. Tech Automat Appl 28:39–41
7. Das VV (2009) Wireless communication system for energy meter reading. Adv Recent Technol Commun Comput 2009:896–898
8. Wang Z, Zheng G (2012) Residential appliance identification and monitoring by a nonintrusive method. Smart Grid IEEE Trans 3:80–92
9. Alexander Charles, Sadiky Matthew (2006) Fundamentals of electric circuits. McGraw-Hill, Boston, pp 387–389. ISBN 9780073301150

10. IEEE Std (2000) 1459–2000 trial-use standard definitions for the measurement of electric power quantities under sinusoidal, nonsinusoidal, balanced, or unbalanced conditions, Institute of Electrical and Electronics Engineers Inc., 0-7381-1963-6
11. Single Phase, BI-directional Power/Energy IC. Cirrus Logic. http://www.cirrus.com/en/pubs/proDatasheet/CS5463_F3.pdf
12. MSP430x13x, MSP430x14x, MSP430x14x1 MIXED SIGNAL MICROCONTROLLER. Texas instruments. http://www.ti.com/lit/ds/symlink/msp430f149.pdf

Part III
Wireless Sensor Network

Chapter 9
Providing Destination-Location Privacy in Wireless Sensor Network Using Bubble Routing

Leron Lightfoot and Jian Ren

Abstract One of the most challenging problems for wireless sensor networks (WSNs) is in how to provide adequate location privacy. In this paper, we will address the concern to adequately provide routing-based destination-location privacy (DLP). The privacy of the location of the destination sensor node is critical and highly vulnerable by the usage of wireless communications. While message content privacy can be accomplished through message encryption, it is much more difficult to adequately address the location privacy. For WSNs, destination-location privacy service is further complex by the fact that sensors consist of low-cost and energy efficient radio devices. Therefore, using computationally intensive cryptographic algorithms (such as public-key cryptosystems) and large scale broadcasting-based protocols are not suitable for WSNs. We propose a unique routing technique that can provide strong destination-location privacy with low tradeoff in the energy overhead. In our proposed scheme, the source node randomly selects an intermediate node from pre-determined region located around the destination node, which we refer to as the bubble region. The bubble region would be large enough to make it infeasible for an adversary to monitor the entire area. Also, in this scheme, we will mix real messages with fake messages to add to the security strength in providing destination-location privacy. We compare our proposed scheme to other well known schemes.

Keywords Destination location privacy • Wireless sensor networks • Energy efficiency • Bubble region

L. Lightfoot • J. Ren (✉)
Department of Electrical and Computer Engineering, Michigan State University, East Lansing, MI 48864-1226, USA
e-mail: lightf13@egr.msu.edu; renjian@egr.msu.edu

Q. Liang et al. (eds.), *Communications, Signal Processing, and Systems*, Lecture Notes in Electrical Engineering 202, DOI 10.1007/978-1-4614-5803-6_9,

9.1 Introduction

Wireless sensor networks (WSNs) can provide the world with a technology for real-time event monitoring. It have been envisioned as a technology that has great potential to be widely used in both military and civilian applications. Privacy has been an extensively studied topic in wireless sensor networks. One of the major and unsettled issues in privacy of WSNs is in how to provide adequate routing-based destination-location privacy. Sensor networks rely on wireless communications, which is by nature a broadcast medium and is more vulnerable to security attacks than its wired counterpart due to lack of a physical boundary. When messages are transmitted wirelessly in the open air, any compatible destination within the transmission range of the sender is able to intercept the traffic. An adversary may be well-equipped with powerful transceivers to analyze the traffic patterns. They may be able to intercept traffic from one or multiple locations within the network environment. Without an adequate protection of the routing paths, an adversary may be able to determine the destination location by using radio frequency localization techniques to track the destination in a hop-by-hop approach. Therefore, even if a powerful encryption algorithm is used to protect the source identity, the adversary may still be able to determine the location of the destination by monitoring the traffic patterns and routing paths.

Privacy in a network consists of not only privacy of the message content but also the privacy of the source and destination locations. The focus of this paper is on destination-location privacy. The confidentiality of the message content can be protected by encryption but the source location can be exposed in routing patterns. To be more concise, there may be different types of information besides the message content that are linked with a message transmission.

In providing adequate destination-location privacy, the sensor devices present major limitations. Sensors in the network are meant to be low-cost and energy efficient devices. The sensors are designed to be deployed in environments where they can be damaged or destroyed; thus, the cost of these sensor nodes should be at a minimum. Clients can simply deploy many wireless sensor nodes into an environment and monitor the activities in the environment from one central location. Sensor nodes are also built to be placed in environments where they can be unattended for lengthy periods. These sensors may be deployed in areas where human attending and maintaining the sensors is impractical; thus, changing or recharging batteries in the sensor devices are infeasible. For the purpose of preserving battery life, using intensive cryptographic algorithms, such as public key cryptosystems, and the usage of powerful transmitters are not suitable for WSNs. Therefore, energy consumption along with location privacy are two very vital components for the successful deployment of wireless sensor networks.

In this paper, we propose a destination-location privacy scheme called *bubble routing*. We will analysis some security vulnerabilities of some existing DLP schemes. We propose a scheme that can provide both content confidentiality and DLP. In the routing scheme, the message source node randomly selects an

intermediate node within a pre-determined region located around the destination node. We will refer to this pre-determined region as the bubble region. The bubble region is large enough to make it unpractical for an adversary to monitor the entire region. In addition, as the real message is being routed to the destination node, fake messages will be injected in the network to increase the security protection of the destination-location. This routing technique can provide strong destination-location privacy with low tradeoff in the energy cost. Through security analysis, our scheme provides adequate destination-location privacy.

The remainder of this paper is organized as follows: In Sect. 9.2, the related work is reviewed. The system model and design goals are described in Sect. 9.3. Section 9.4 details the proposed destination-location privacy scheme. In Sect. 9.5, we provide security analysis of the proposed scheme and compare it to some well known schemes. We conclude in Sect. 9.6.

9.2 Related Work

In the past two decades, originated largely from Chaum's mixnet [1] and DC-net [2], a number of location privacy communication protocols have been proposed [3–18]. The mixnet family protocols use a set of mix servers that blend the received packets so that the communication source (including the sender and the recipient) becomes ambiguous. They rely on the statistical properties of background traffic, also referred to as cover traffic, to achieve the desired anonymity. However, these schemes all require public-key cryptosystems and are not suitable for WSNs.

The onion routing protocol, discussed in [7], provides anonymous communication in a network. As a message is passed in the network, onion routers repeatedly encrypts the message between routers. This technique provides privacy of the identity of the sender, destination and the message content. Onion routing prevents an adversary from eavesdropping on the message content and protect against traffic-analysis attacks by making the sender and destination anonymous. This protocol was designed to protect communication over the internet network and uses cryptosystems, which make it not suitable for WSNs.

Broadcasting-based schemes provide location privacy by mixing the real messages with fake messages so that they become indistinguishable to the adversaries. In [10], the DEEP (Differential Enforced Fractal Propagation) routing protocol is introduced. In this scheme, the source node send the real message to the destination using a random walk routing in the direction on the destination and nodes in the routing path injects fake messages into the network to create hot spots to help protect the destination location. The LPR (Location-Privacy Routing) with fake packet injection is proposed in [11]. This scheme is similar to the DEEP routing protocol but does not create hot spots and try to solve the vulnerability of the DEEP routing. The LPR protocol randomizes the routing paths so that the forwarding direction of the real message is not always towards the destination.

In Sect. 9.5, we will analysis the security vulnerability of these two schemes in providing destination-location protection.

Providing location privacy through dynamic routing is, in our opinion, one of the most feasible approaches in WSNs [14, 15]. The main idea is to prevent the adversaries from monitoring the traffic to the location of a source or destination node. A representative example of a routing-based protocol is the phantom routing protocol, which involves two phases: a random or direct walk phase and a subsequent flooding/single path routing phase. In the random walking phase, the message from the actual source will be routed to a phantom source along a random path or a designed directed path. The phantom source is expected to be far away from the actual source. With sector-based directed walk, the source node first randomly determines a direction that the message will be sent. Every forwarder on the direct walk path will forward this message to a random neighbor in the same direction to ensure that the phantom source will be away from the actual source. This scheme was design to protect the source node location and not the destination node location. The strength of this scheme is that the source node will first send the message to a phantom source that may or may not be in the direction of the destination node location. The weakness is when the phantom source route the message to the destination, the message will always be routed in the direction of the destination node.

9.3 Network Models and Design Goals

Destination location privacy is a vital security requirement for military and many civilian applications. WSNs can be deployed for military intelligence networks. On a battlefield, soldiers can be equipped with sensor devices, in which messages are routed to a destination that is located with a soldier within the battlefield. For the safety of the soldiers that are monitoring the destination devices, their location must remain unexposed as the message routed through the network. In military intelligence networks, both the destination-location and the message content must be protected from adversarial attacks. Before we describe our proposed DLP scheme in WSNs, we will provide the system model and adversarial model in this section to capture the relevant features of WSNs and potential adversaries in DLP applications.

9.3.1 The System Model

The following assumptions are made about the system:

– The network is divided into grids. The sensor nodes in each grid are fully connected. In each grid, there is one header node responsible for communicating with other nearby header nodes. The whole network is fully connected through multi-hop communications [19–22].

- Every node in the network can become a source node on a detection of an event. On detecting an event, a sensor source node will generate and send messages to the destination node through a multi-hop routing.
- Each message will include a unique node ID where the event was generated. The SINK node can only determine source node location based off the node ID.
- The sensor nodes are assumed to know their relative location and destination node location. We also assume that each sensor node has the knowledge of its adjacent neighboring nodes. The information about the relative location of the sensor domain may also be broadcasted through this network for routing information update [23, 24].
- The key management, including key generations, key distribution and key update, is beyond the scope of this paper. However, the interested readers are referred to references such as [25–28].

9.3.2 The Adversaries Model

In this paper, the adversary has the following characteristics:

- ***Well-equipped:*** The adversary does not need to worry about the energy consumption and has adequate computation capability. On detecting a transmitted message, the adversary could determine the receiver node by waiting to see which neighbor node retransmit the message. The adversary is able to move to this receivers location without much delay and has enough memory to store any useful information. If needed, the adversary could compromise some sensor nodes in the network.
- ***Passive:*** The adversaries carry out some passive attacks, which only involve eavesdropping work.
- ***Traffic-monitoring:*** The adversary is able to monitor the traffic in an area and receive all messages in this area. However, we assume that the adversary is unable to monitor the entire network.

9.3.3 Design Goals

Our design goals can be summarized as follows:

- The adversaries should not be able to get the destination-location information by analyzing the traffic pattern.
- The adversaries should not be able to get the destination-location information even if they are able to monitor a certain area of the sensor network and compromise a few network nodes.
- The length of each message should be as short as possible to save the previous sensor node power. This is because that on average, transmission of 1 bit consumes about as much power as executing 800–1,000 instructions [29].

9.4 Proposed Scheme

In this section, we will present our proposed secure destination-location privacy scheme for wireless sensor networks.

9.4.1 Bubble Routing Scheme

In this paper, we propose two phase routing scheme to protect the destination location. In the first phase, the source node randomly selects an intermediate node from a pre-determine sub-region, which we will refer to as the bubble region. We assume that the bubble region is large enough to make unfeasible for an adversary to monitor the entire region. In the second phase, the intermediate node will then route the message to the destination node.

For the source node to establish an intermediate node, it must do the following steps. The first step is to randomly select a location within a circular area of radius R around the destination node. We assume that each sensor node only has knowledge of its adjacent nodes relative location and the destination node relative location. Let (x_0, y_0) represent the relative location of the destination node. From these perimeters, (x_0, y_0); R, the source node is able to generate a random point within the pre-determine area. Since we assume that the destination node is located at the relative location (x_0, y_0), the source node selects the random location (x_c, y_c) according to the following procedures:

1. Randomly select d_c uniformly from $[0, R]$.
2. Randomly select θ_c uniformly from $[0, 2\pi]$.

In this way, we can calculate the coordinate of the random selected point as $(x_c, y_c) = (x_0 + d_c \cos(\theta_c), y_0 + d_c \sin(\theta_c))$.

After obtaining the random point (x_c, y_c), in second step, the source node will generate another random point located within a circular area of radius r around the random point (x_c, y_c). We will call the point (x_c, y_c) the center point for pre-determine sub-region. We will refer this pre-determine sub-region with radius r as the bubble region. Also, we assume that r is smaller than R.

Now with the new perimeters, (x_c, y_c); r, the source node can randomly generate a point (x_i, y_i) to determine an intermediate node. We can compute the random location (x_i, y_i) according to the following procedures:

1. Randomly select d_i uniformly from $[0, r]$.
2. Randomly select θ_i uniformly from $[0, 2\pi]$.
3. Calculate $(x_i, y_i) = (x_0 + d_i \cos(\theta_i), y_0 + d_i \sin(\theta_i))$.

After calculating the random selected point, (x_i, y_i), the source node will then route the message towards the grid that contains the location (x_i, y_i). Since each node knows its adjacent neighbor nodes's relative location, it can determine the

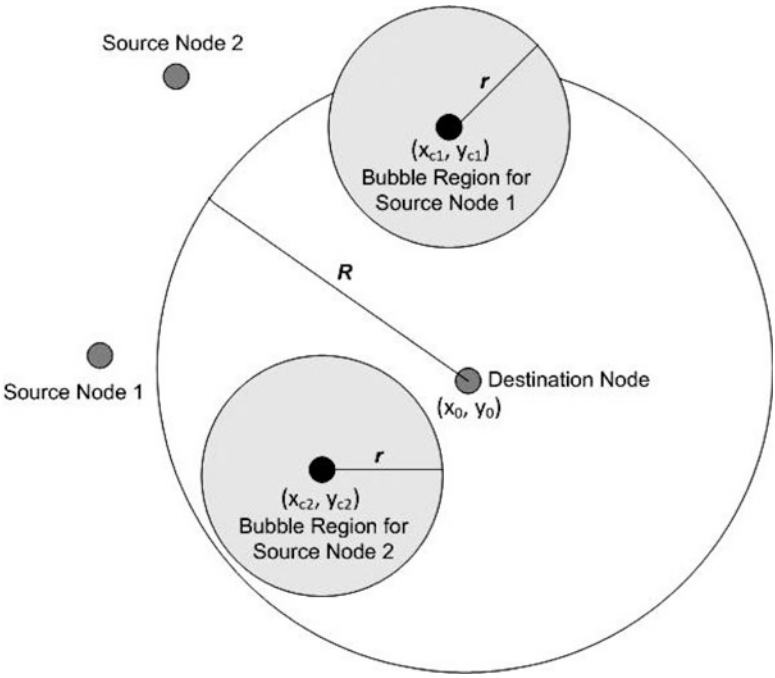

Fig. 9.1 Illustration of the bubble routing

direction that the message should be routed to. Once the message is within the desired grid of the random location, the message is routed to the header node of the grid. The header node then becomes the random intermediate node. If the desired grid does not contain any nodes, then the last node in the routing path would become the desired location and the header node in that grid would become the intermediate node. We assume that when node detects an event, it will send messages periodically. For every message that is created from a source node, the intermediate node location will be generated using the parameters (x_c, y_c); r and source node will calculated a new point for each message. In other words, the source node will send each message to a different intermediate node located in the same bubble area. Also, each source node in the network will determine its own bubble region by using the steps described above. Figure 9.1 illustrates the Bubble routing scheme. When source node 1 sends a message, it will forward the message to the bubble region 1 and source node 2 will forward messages to bubble region 2. As you can see, the message routes from the source node will not lead an adversary directly to the destination node. Once the intermediate node receives the message, then the message is forward to the destination node.

To increase the security on protecting the destination-location, we will inject fake messages into the network. As the real message is being routed in the network by a hop-by-hop approach, every node in the routing path will have the probability, p_{fake}, to generate a fake message. The real message and the fake messages will be

indistinguishable to the adversaries. By mixing real messages with fake messages will make it more difficult for an adversary to determine the direction of the routing path of the real message. A node that generates a fake message will randomly select a neighbor node to send the fake message to and also will forward the real message to the next node in the routing path. The fake message will have a pre-determined time-to-live (TTL_{fake}) parameter associated with it. As the fake message passes in the network, for each hop it takes the parameter TTL_{fake} decreases by 1. The node that receives the fake message with $TTL_{fake} = 0$ will discard the fake message. Also, when nodes receive fake messages, they can create another fake message with probability p_{fake}. The purpose of TTL_{fake} parameter is to limit to energy consumption used in injecting the network with fake messages. We refer to this routing scheme as the bubble routing scheme.

In bubble routing scheme, the security strength in protecting the destination-location rely on the parameters, r; R; p_{fake}; TTL_{fake}. To increase the security of this scheme you can simply increase any of the parameters r; R; p_{fake}; TTL_{fake}. Increasing any of these parameters will also increase the energy consumption. For any destination-location privacy schemes, there will be a tradeoff in security and energy cost. Our goal is to show that a small increase in the energy cost can cause a huge increase in security protection of the destination-location. In the next section, we will analysis the security of our proposed bubble routing scheme and other well known existing schemes.

9.5 Security Analysis

In this section, we will analyze that the proposed bubble routing scheme can provide destination-location privacy. Also, we will analysis other destination-location privacy schemes and determine its vulnerabilities for different adversary attacks.

DEEP routing [10] and LPR routing with fake packet injection [11] have similar adversary attack vulnerabilities. We assume that an adversary has full knowledge of the routing protocol that is being used in the WSNs. With the DEEP protocol, the vulnerability is that the real message is always forward towards the direction of the destination node. In other words, the real message will always be forward on a random shortest path to the destination. The traffic on these random shortest paths will be heavier than the fake messages routing paths. Also, the number nodes involved in forwarding the real messages, from source to destination, will be small due to the small number paths the real message can take. Figure 9.2 illustrates the DEEP scheme routing a real message to the destination node. From the figure, the shortest random path for the message to take from source to destination is 6 hops. As you can see, the real message can only take small number of random paths to reach the destination in 6 hops. The LPR protocol with fake packet injections attempts to solve the vulnerability of the DEEP routing. The LPR protocol randomizes the routing paths so that the forwarding direction of the real message

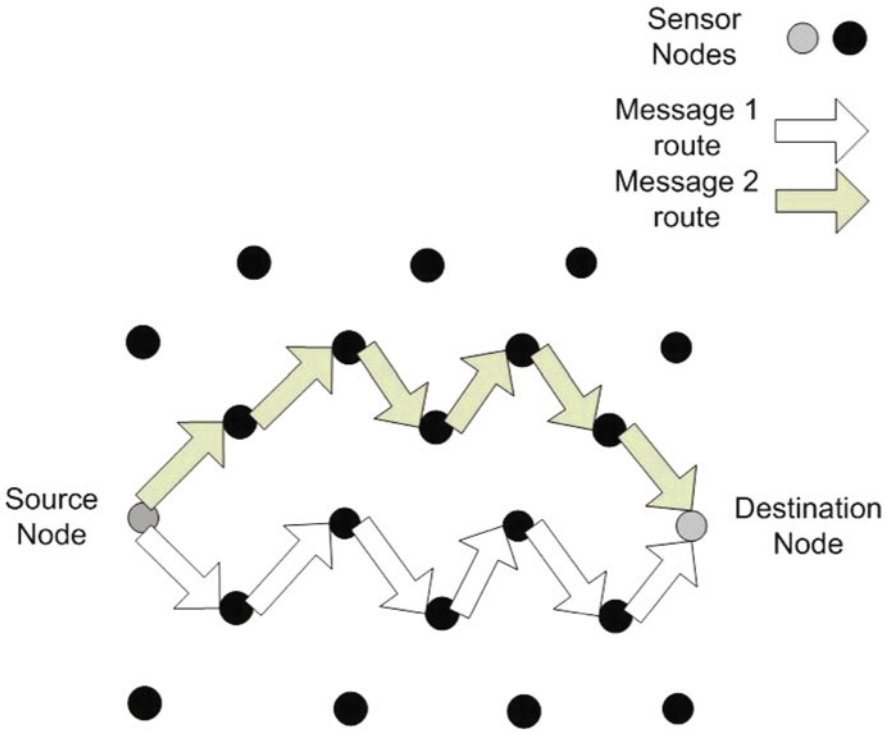

Fig. 9.2 Illustration of the routing for messages in the DEEP scheme

is not always towards the direction of the destination node. The vulnerability of the LPR scheme is that an adversary can use to its advantage the knowledge that more than 50% of the real packets will be forward towards the destination node and all of the fake packets will be forward away from the destination. Therefore, if two packets are forward in the similar direction from the same node, the adversary will know that destination node is not in that direction. The vulnerabilities of the DEEP and LPR schemes will be solved with our proposed scheme.

Our bubble routing scheme addresses the vulnerabilities of the DEEP and LPR routing schemes. In our scheme, random intermediate nodes are selected from a bubble region. We assume that the bubble region is large enough that it would be unpractical for an adversary to monitor entirely. From the probability point of view, for a large network, the chances that the messages will be routed using the same path and the same intermediate node are extremely low. The increase in the number routing paths to the intermediate nodes in the bubble region solves the vulnerabilities of the DEEP routing scheme. In addition to the increase of routing paths for the real messages, our scheme also injects fake messages into the network to make more difficult for an adversary to discover the destination-location. To solve the vulnerability of the LPR scheme, the fake messages are forward to any

random neighbor node. Therefore, based off transmission of fake messages, an adversary can not eliminate an area in the network of where the destination node may not be located. Also, if an adversary discovers an intermediate node, he will be located in the bubble region. For most cases, the bubble region will not contain the destination node. After discovering the bubble region, an adversary's work is only half way done. The security analysis shows that our proposed bubble routing scheme can provide much better security in protecting the destination-location privacy in comparison to the DEEP and LPR routing schemes.

9.6 Conclusions

For a successful deployment of wireless sensor networks, location privacy is vital. In this paper, we address the issue of destination-location privacy. We proposed a scheme called bubble routing, which we believe solves some of the security vulnerabilities of some existing schemes with little additional energy consumption. We believe this scheme is practical due to the simplicity of the design. In the future, we will provide some simulation and performance results to show the security strength in protecting the destination-location.

References

1. Chaum D (1981) Untraceable electronic mail, return addresses, and digital pseudonyms. Commun ACM 24:84–90
2. Chaum D (1988) The dinning cryptographer problem: unconditional sender and recipient untraceability. J Cryptol 1(1):65–75
3. von Ahn L, Bortz A, Hopper N (2003) *k*-anonymous message transmission. In: Proceedings of CCS, Washington DC, pp 122–130
4. Beimel A, Dolev S (2003) Buses for anonymous message delivery. J Cryptol 16:25–39
5. Golle P, Juels A (2004) Dining cryptographers revisited. In: Advances in cryptology – Eurocrypt 2004. Lecture notes in computer science, vol 3027. Springer, Berlin, pp 456–473
6. Goel S, Robson M, Polte M, Sirer E (2003) Herbivore: a scalable and efficient protocol for anonymous communication, Tech. Rep. 2003–1890, Cornell University, Ithaca
7. Reed M, Syverson P, Goldschlag D (1998) Anonymous connections and onion routing. IEEE J Sel Areas Commun 16(4):482–494
8. Reiter, M, Rubin A (1998) Crowds: anonymity for web transaction. ACM Trans Inf Syst Secur 1(1):66–92
9. Deng J, Han R, Mishra S (2004) Intrusion tolerance and anti-traffic analysis strategies for wireless sensor networks. In: DSN '04: proceedings of the 2004 international conference on dependable systems and networks, Washington, DC. IEEE Computer Society, p 637
10. Deng J, Han R, Mishra S (2005) Countermeasures against traffic analysis attacks in wireless sensor networks. In: First international conference on security and privacy for emerging areas in communications networks, 2005. SecureComm 2005, Athens, pp 113–126
11. Jian Y, Chen S, Zhang Z, Zhang L (2007) Protecting recieiver-location privacy in wireless sensor networks. In: INFOCOM 2007. Twenty-six annual joint conference of the IEEE computer and communications societies. IEEE, Piscataway, pp 1955–1963

12. Yang Y, Shao M, Zhu S, Urgaonkar B, Cao G (2008) Towards event source unobservability with minimum network traffic in sensor networks. In: WiSec '08: Proceedings of the first ACM conference on wireless network security. ACM, New York, pp 77–88
13. Shao M, Yang Y, Zhu S, Cao G (2008) Towards statistically strong source anonymity for sensor networks. In: INFOCOM 2008. The 27th conference on Computer Communications. IEEE. IEEE, Piscataway, pp 51–55
14. Kamat P, Zhang Y, Trappe W, Ozturk C (2005) Enhancing source-location privacy in sensor network routing. In: 25th IEEE international conference on distributed computing systems, 2005. ICDCS 2005. Proceedings, Columbus, pp 599–608
15. Ozturk C, Zhang Y, Trappe W (2004) Source-location privacy in energy-constrained sensor network routing. In: SASN '04: Proceedings of the 2nd ACM workshop on security of ad hoc and sensor networks. ACM, New York, pp 88–93
16. Xi Y, Schwiebert L, Shi W (2006) Preserving source location privacy in monitoring-based wireless sensor networks. In: IPDPS. IEEE, Piscataway
17. Gülcü C, Tsudik G (1996) Mixing email with babel. In: Proceedings of the symposium on network and distributed system security, San Diego
18. Möller U, Cottrell L, Palfrader P, Sassaman L (2003) Mixmaster protocol. Version 2
19. Ye M, Li C, Chen G, Wu J (2005) Eecs: an energy efficient clustering scheme in wireless sensor networks. In: Performance, computing, and communications conference, 2005. IPCCC 2005. 24th IEEE International, Phoenix, pp 535–540
20. Heinzelman WB (2000) Application-specific protocol architectures for wireless networks. Ph. D. thesis. Supervisor-Anantha P. Chandrakasan and Supervisor-Hari Balakrishnan
21. Neander J, Hansen E, Nolin M, Bjorkman M (2006) Asymmetric multihop communication in large sensor networks. In: 1st international symposium on wireless pervasive computing, 2006, Phuket, pp 7
22. Younis O, Fahmy S (2004) Heed: a hybrid, energy-efficient, distributed clustering approach for ad hoc sensor networks. IEEE Trans Mob Comput 3:366–379
23. Zhang Y, Liu W, Fang Y, Wu D (2006) Secure localization and authentication in ultra-wideband sensor networks. IEEE J Sel Areas in Commun 24:829–835
24. Cheng X, Thaeler A, Xue G, Chen D (2004) Tps: a time-based positioning scheme for outdoor wireless sensor networks. In: INFOCOM 2004. Twenty-third annual joint conference of the IEEE computer and communications societies, Hong Kong, vol 4, pp 2685–2696
25. Chan H, Perrig A (2005) Pike: peer intermediaries for key establishment in sensor networks. In: INFOCOM 2005. 24th annual joint conference of the IEEE computer and communications societies. Proceedings IEEE, Miami, vol 1, pp 524–535
26. Perrig A, Szewczyk R, Wen V, Culler D, Tygar J (2001) SPINS: security protocols for sensor networks. In: Seventh annual international conference on mobile computing and networks (MobiCOM 2001), Rome
27. Traynor P, Kumar R, Choi H, Cao G, Zhu S, La Porta T (2007) Efficient hybrid security mechanisms for heterogeneous sensor networks. IEEE Trans Mob Comput 6:663–677
28. Zhu S, Setia S, Jajodia S (2003) Leap: efficient security mechanisms for large-scale distributed sensor networks. In: CCS '03: proceedings of the 10th ACM conference on computer and communications security. ACM, New York, pp 62–72
29. Hill J, Szewczyk R, Woo SHA, Culler D, Pister K (2000) System architecture directions for networked sensors. In: Proceedings of ACM ASPLOS IX, Cambridge

Chapter 10
New Scalar Encoding Method to Accelerate Point Multiplication in Elliptic Curve Cryptography

Chalak Shakir Ahmed, Min Jia, and Xuemai Gu

Abstract The security of the wireless environment, especially for those which have limited resources like in the wireless sensor network, needs lightweight algorithms. Elliptic curve cryptography (ECC) is the unique algorithm which satisfies such property. It provides the high level of security with relatively small keys; therefore, it has been the core of many standards. The efficiency of ECC is depending mostly on the implementation of the scalar multiplication which is accomplished mainly by addition and doubling operations. In the add-double method, reducing the number of ones is considered the most likely way to diminish the total number of the entirety operations. In this chapter, we present the method for recoding this scalar such that decreasing the number of addition operations. We compared our method with the one's complement recoding method, and the simulation results showed that our proposed method produces mostly a better encoding.

Keywords Elliptic curve cryptography • Encoding • Scalar multiplication • Hamming weight • Wireless sensor network.

10.1 Introduction

Lately, wireless sensor networks (WSNs) have been widely used in pervading applications such as monitoring, detection and control applications. Security's issues are mandatory due to the unreliable behaviour in wireless communications, which almost make the packets to be downfallen [1, 2]. Symmetric key schemes generally require sophisticated key management, which leads to a large memory and communication overhead. In contrast, public key based schemes have

C.S. Ahmed (✉) • M. Jia • X. Gu (✉)
School of Electronics and Information Technology, Harbin Institute of Technology HIT, Heilongjiang, Harbin 150001, China
e-mail: ahmedchalak@hit.edu.cn; ahmed_nlp79@yahoo.com; jiamin@hit.edu.cn; guxuemai@hit.edu.cn

Q. Liang et al. (eds.), *Communications, Signal Processing, and Systems*, Lecture Notes in Electrical Engineering 202, DOI 10.1007/978-1-4614-5803-6_10,

straightforward key management, but more computation time is needed [3]. In this chapter, we concentrate on the fold of encoding method for scalar k in Scalar Multiplication (SM), kP, where k is the scalar (key) and P is the point in the EC, and delicately overwhelming the complexity of ECC. Our method is used to represent the scalar k into a new form in the binary system. It used to decrease the hamming weight (non-zero elements "number of ones in the binary form") of k , thereby, decreasing the number of addition operation, and as a result the calculations of SM is decreased. Nowadays, the direction of studies in the field of securing such miniature devices, as in wireless sensor networks, is focusing on the use of ECC with some considerations. Minimizing its computations is one of the most crucial attributes.

Katti [4] proposed a new method for accelerating SM by depending on the method of signed binary representation proposed by Reitwiesner [5]. Wang et al. [6] also proposed a method for representing scalar k and computing kP. They focused on eliminating the consecutive '1' in $\{a_i\}$. For a given integer of k, there is an equation such that ($k = 2^{d} - 1 - k_1$), where k_1 is the complement of A. If ($k_1 < k$) and there has consecutive '1' in sequence, then the transformation ($k = 2^{d} - 1 - k_1$) can be made. Mohamed et al. [7] improved the original ordinary binary method at the expense of some pre-computation operations, by reducing the number of addition operations and consequently the number of SM computations. Huang and Sharma [1] proposed a method that depends on the one's complement with the combination of complementary in order to minimise the hamming weight, but the checking process is achieved prior to the scalar multiplication and it is costly. Huang et al. [8] improved the window size algorithm in [9], which is achieved by using a fuzzy control system and provides a dynamic control to ensure the optimum window size that allows a trade-off between the available RAM and ROM of the sensor node, the pre-computations of this method are also costly.

Roadmap: in Sect. 10.2 the drawbacks of elliptic curve and cryptography are explained. In Sect. 10.3 the proposed method and its comparison with the one's complement recoding method are explored. The analysis of the experimental results is shown in Sect. 10.4. Finally, in Sect. 10.5 the conclusions are offered.

10.2 Difficulties of ECC

SM and modular reduction are the two main operations involved in ECC [10]. SM can be defined as the repeated addition of a point along the elliptic curve, and it is denoted as:

$$kP = \overbrace{P + P + P + P + \ldots.. + P}^{k \text{ times}}, \text{ repeatedly adding } P \text{ to itself } k \text{ times} \quad (10.1)$$

As specified in [11], 85% of execution time is spent by SM, this disadvantage makes the researchers which are fascinated in wireless security, especially in the sensor network to pay more attention to this problem in order to engender the best method appropriate for such tiny devices (motes) that have limited resources in terms of energy, processing, and storage. Hasting this main operation in ECC is the essence of this chapter.

10.3 Proposed Method

The encoding can be defined as is the process of converting a piece of information into another form of representation, not inevitably of the same type.

Finding the efficient encoding algorithm for the integer k in kP has the direct impact on the efficiency of SM which leads to accelerate the computations and thereby be suitable for use in WSN. This encoding affects the number of point doubling and point addition operations. The number of bits that represents the integer k (length of k) affects the doubling operation, whereas the number of ones in such representation affects the addition operation. In this chapter, we concentrated on the latter and minimized the hamming weight of k by encoding it using only '0' and '1' as in the binary system, but it differs from it so that using another algorithm for encoding not as in binary system. Algorithm1 depicts the idea:

Algorithm1: Encoding method of scalar k

Input:
$K = Integer$, base $A = \{a_1, a_2, \ldots\ldots, a_j\}$
Output:
$F(k) = (k_i\ldots., k_2^{(a2)}, k_1^{(a1)})$
$i = 0$
while $k > 0$ *do*
if $k \bmod a_1 = 0$ *or* $k \bmod a_2 = 0$ *or* .... *Or* $k \bmod a_j = 0$, *then* $k_i = 0$ *else*
$k_i = k \bmod a_1$
$k = k - k_i$
if $k \bmod a_1 = 0$, *then* $k = k/a_1$, $k_i = k_i^{(a1)}$
elseif $k \bmod a_2 = 0$, *then* $k = k/a_2$, $k_i = k_i^{(a2)}$
...
elseif $k \bmod a_j = 0$, *then* $k = k/a_j$, $k_i = k_i^{(aj)}$
$i = i + 1$
Return $(k_j^{(aj)}, \ldots\ldots, k_2^{(a2)}, k_1^{(a1)})$

To diminish the number of ones, more than one radix are taken. The proposed method is comprehended by the examples evident in Table 10.1. Let the remainder of the division and modulo be pointed by ‖ symbol. So, as depicted by the Table 10.1, number of ones is reduced from 8 to 4 for $(75337)_{10}$ which save four elliptic curve addition operations, as well as the length of the scalar is also reduced

Table 10.1 Hamming weight examples of scalar k by new representation

k (prime)	The base	Normal binary of k	Applying our method	Our encoding of k
$(75337)_{10}$	{3,5,7}	10010011001001001	(75337mod 2‖1)= ((75337–1)/3‖0)= (25112 mod 2‖0)= ((25112–1)mod 2‖1)= ((25111–1)/3‖0)= (8370/3‖0)= (2790/3‖0)= (930/3‖0)= (310/5‖0)= (62 mod 2 ‖0)= (61 mod 2‖1)= (60/3‖0)= (20/5‖0)= (4 mod 2‖0)= (3/3‖0)= (1 mod 2‖1)	1000010000001001
$(1237)_{10}$	{3,5,7}	10011010101	(1237 mod 2‖1)= ((1237–1)/3‖0) = (412 mod 2‖0) = ((412–1)/3‖0) = (137 mod 2‖1) = ((137–1)mod2‖0)= ((136–1)/3‖0)= (45/3‖0)= (15/3‖0)= (5/5‖0)= (1 mod 2‖1)	10000010001

in sometimes, in this instance it reduced from 17 to 16, which saves one elliptic curve doubling operation. Whereas for $(1237)_{10}$ the number of ones is reduced from 6 to 3, which saves three elliptic curve addition operations, but the length is unchanged in this case. For instance, we are using the binary representation of the scalar $(1237)_{10}$ shown in Table 10.1 before and after applying our method and multiply this scalar by the point (7,12) under the field of 23 such that a and b values of the equation are 1 and 0 respectively.

Computing kP by the double-add algorithm [12] before and after applying our method as shown in Tables 10.2 and 10.3 respectively.

By applying the one's complement method as in [12] to the same scalar 1237 the result will be as follows:

(01100101010), then the scalar can be represented as follows:

1237 = 10000000000-01100101010-1

1237 = 2048-512-256-32-8-2-1

Table 10.2 Computing kP using double—add method prior of applying the proposed method

					Addition	Doubling
#Iterations	Scalar	Binary representation	Bit-value	Evenlodd	R:=R + Q	Q = 2Q
1	$(1237)_{10}$	10011010101	1	Odd	(7,12)	(17,3)
2			0	even		(13,16)
3			1	Odd	(6,4)	(5,19)
4			0	even		(17,3)
5			1	Odd	(4,0)	(13,16)
6			0	Even		(5,19)
7			1	Odd	(7,12)	(17,3)
8			1	Odd	(12,4)	(13,16)
9			0	Even		(5,19)
10			0	Even		(17,3)
11			1	Odd	**(6,4)**	

Table 10.3 Computing kP using double—add method after applying the proposed method

					Addition	Doubling
#Iterations	Scalar	Our encoding representation	Bit-value	Evenlodd	R:=R + Q	Q = 2Q
1	—	10000010001	1	Odd	(7,12)	(17,3)
2			0	Even		(13,16)
3			0	Even		(5,19)
4			0	Even		(17,3)
5			1	Odd	(12,4)	(13,16)
6			0	Even		(5,19)
7			0	Even		(17,3)
8			0	Even		(13,16)
9			0	Even		(5,19)
10			0	Even		(17,3)
11			1	Odd	**(6,4)**	

In which the hamming weight of scalar is increased from 6 to 7, thereby increasing one more addition operation.

As shown below in Table 10.3, the number of addition operations is diminished from 6 to 3 which saves three addition operations.

10.4 Analysis of the Results

As mentioned earlier, SM has two main operations – addition and doubling. Where addition operation is affected by hamming weight of the scalar, while the doubling operation is affected by the length (e.g.; total number of bits) of the scalar. The hamming weight of such a scalar is reduced by our proposed method, and the results are compared with the one's complement method in [12], which always gives a low

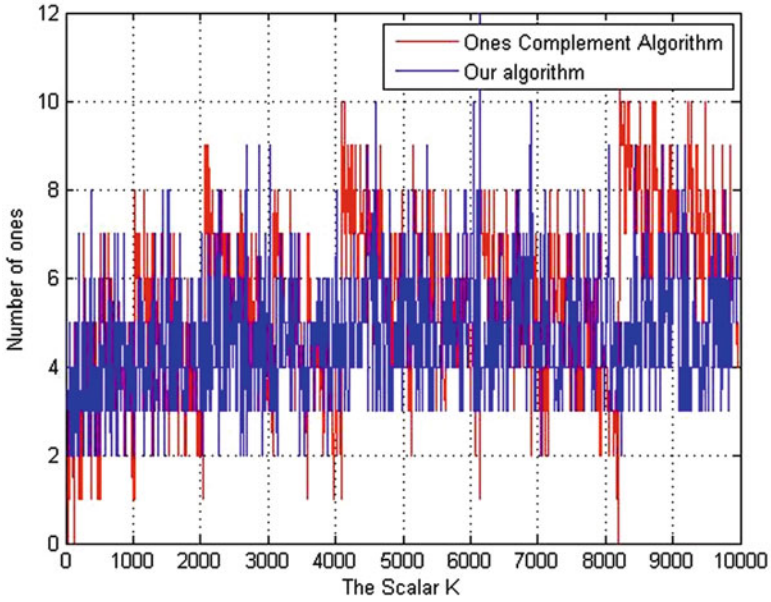

Fig. 10.1 Radix of A = {2, 3, 7}

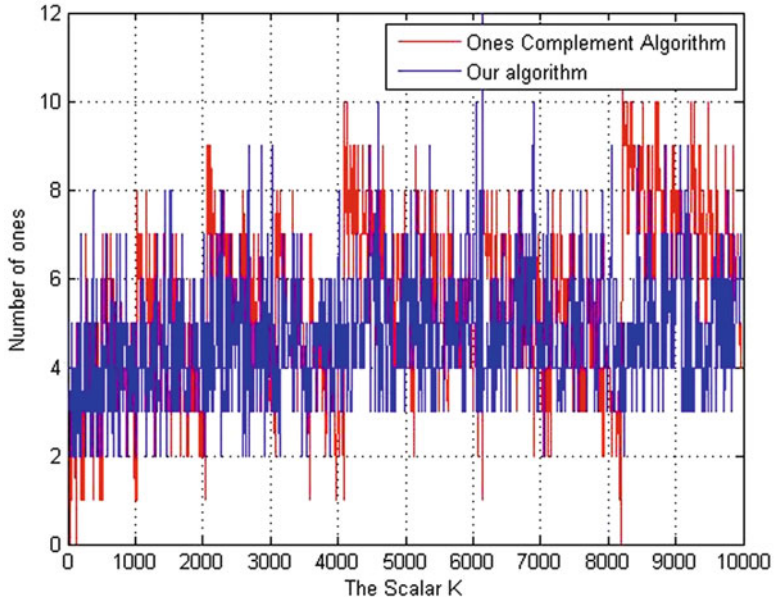

Fig. 10.2 Radix of A = {2, 5, 7}

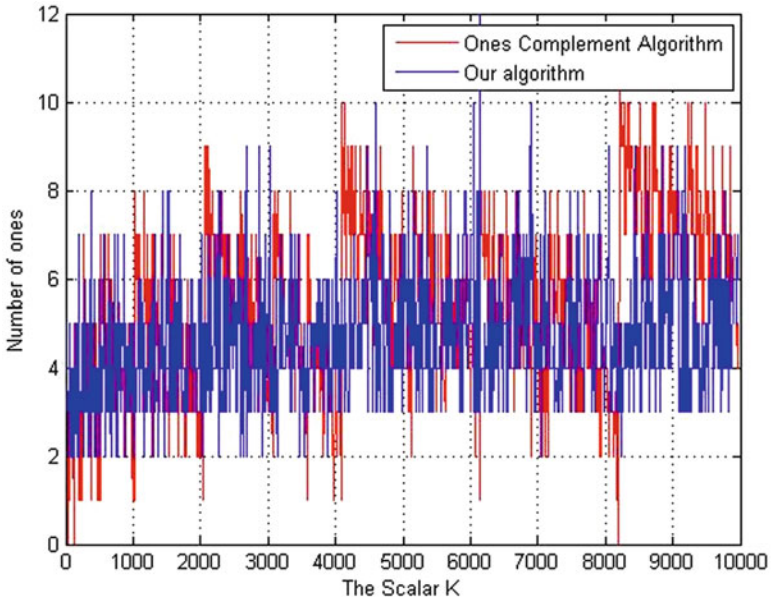

Fig. 10.3 Radix of A = {3, 5, 7}

Table 10.4 Comparisons between methods in terms of number of ratio of ones

Bases	Ratio of ones in one's comp.	Ratio of ones in proposed method	Ratio reduction of hamming weight by our method
2,5,7	0.4341	0.3518	0.0823
2,3,7	0.4341	0.3276	0.1065
3,5,7	**0.4341**	**0.2871**	**0.1471**

hamming weight among the methods we reviewed in Sect. 10.3. Lower hamming weight, and sometimes smaller number of bits that represents the scalar k are produced by our method, thereby, the number of doubling operation is also reduced. From 1 to 10,000 is the range of the prime numbers that are chosen for our test and simulation.

The comparisons between the one's complement and the proposed method using MATLAB, are referred in Figs. 10.1, 10.2, and 10.3. While the numerical results of comparisons are produced in Table 10.4. The proposed method takes the ratio of ones as a critical measurement to prove that it is better than the one's complement.

Four bases (2, 3, 5, and 7) are taken for the test on the prime numbers from 1 to 10,000. The simulation results showed that the bases {3,5,7} provide the best reduction ratio.

Figure 10.3 shows that the base {3,5,7} provides the best results in terms of reducing the hamming weight of the scalar.

10.5 Conclusions

Nowadays, ECC receives potential approval due to its characteristics and advantages over other methods, especially for use in the wireless devices like in the wireless sensor network. Therefore, it has been embedded in many standards (e.g. ANSI, IEEE, ISO, and NIST). Scalar Multiplication kP is the main operation in ECC, which requires complex and elaborate computations. By hastening this operation, ECC implementation will be more efficient and suitable for such tiny devices. In this chapter, the new method for diminishing the hamming weight of the scalar k is produced. Since the one's complement method represents the most important method used for such acceleration and decrease 50% of scalar's hamming weight, therefore, our comparisons were conducted with it. Experimental results showed that the proposed method has advantages over the one's complement method in terms of hamming weight reduction. Ultimately, this encoding increases the performance of the ECC due to the decreasing of entire operations. Hence, the implementation of ECC be more efficient.

Acknowledgments This work is supported by National Science and Technology Major Project of the Ministry of Science and Technology of China (2010ZX03006-002-02), the National Natural Science Foundation of China (Grant No. 61201143), the National Science Foundation for Post-doctoral Scientists of China (Grant No. 2012M510956), the Post-doctoral Funds of Heilongjiang Province (Grant No. LBHZ11128), and the Fundamental Research Funds for the Central Universities (Grant No. HIT. NSRIF. 2010091).

References

1. Huang X, Sharma D (2010) Fuzzy controller for a dynamic window in elliptic curve cryptography wireless networks for scalar multiplication. In: Proceedings of the 16th Asia-Pacific conference communications (APCC 2010), New Zealand, pp 509–514. ISBN: 978-1-4244-8127-9
2. Huang X, Sharma D, Aseeri M, Almorqi S (2011) Secure wireless sensor networks with dynamic window for elliptic curve cryptography. In: Proceedings of the electronics, communications and photonics conference (SIECPC), Saudi Arabia, pp 1–5
3. Wang H, Sheng B, Tan CC, Li Q (2008) Comparing symmetric-key and public-key based security schemes in sensor networks: a case study of user access control. In: Proceedings of the 28th international conference on distributed computing systems, Beijing, pp 11–18
4. Katti R (2002) Speeding up elliptic cryptosystems using a new signed binary representation for integers. In: Proceedings of the euromicro Symposium on digital system design (DSD'02), Dortmund, pp 380–384
5. Reitwiesner GW (1960) The determination of carry propagation length for binary addition. IRE Trans Electron Comput EC-9(1):35–38
6. Wang B, Zhang H, Wang Y (2007) An efficient elliptic curves scalar multiplication for wireless network. In: Proceedings of the IFIP international conference on network and parallel computing workshops, Dalian, pp 131–134
7. Mohamed MA, Md Said MR, Mohd Atan KA, Ahmad Zulkarnain Z (2010) An improved binary method for scalar multiplication in elliptic curve cryptography. J Math Stat 6(1):28–33. ISSN: 1549–3644

8. Huang X, Gajkumar Shah P, Sharma D (2010) Fast scalar multiplication for elliptic curve cryptography in sensor networks with hidden generator point. In: Proceedings of the international conference on cyber-enabled distributed computing and knowledge discovery, Huangshan, pp 243–249
9. Basu S (2011) A new parallel window-based implementation of the elliptic curve point multiplication in multi-core architectures. Int J Netw Secur 13(3):234–241
10. Certicom Research (2000) SEC 1: elliptic curve cryptography - standards for efficient cryptography. Certicom Corp. http://www.secg.org/collateral/sec1_final.pdf
11. Gura N, Pateland A, Wander A (2004) Comparing elliptic curve cryptography and RSA on 8-bit CPUs. In: Joye M, Quisquater JJ (eds) Proceedings of the 6th international workshop on cryptographic hardware and embedded systems (CHES), Lecture notes in computer science, Cambridge, MA, USA, 3156:119–132
12. Shah PG, Huang X, Sharma D (2010) Algorithm based on one's complement for fast scalar multiplication in ECC for wireless sensor network. In: Proceedings of the IEEE 24th international conference on advanced information networking and applications workshops, Australia, pp 571–576

Chapter 11
Model and Simulation of Data Aggregation Based on Voronoi Diagram in Hierarchical Sensor Network

Jianli Zhao and Qiuxia Sun

Abstract A hierarchical wireless sensor network is proposed which separates the sensing ability and routing ability at different layer respectively. It cannot only simplify the hardware design but also can reduce wireless node cost. Also, a mathematical model of data fusion based on hierarchical architecture and Voronoi diagram is given to make sure the connectivity of stochastic sensor nodes and can be more energy efficient. The simulation shows, network communication traffic are cut down sharply, which can reduce nodes energy cost and prolong the lifetime of the sensor network.

Keywords Wireless sensor network • Stochastic connectivity • Mathematical model • Data fusion

11.1 Introduction

With the development of micro-electro-mechanism system and communication technology, the tiny sensors can have the capability of sensing, wireless communication, memory and processing. Sensors cannot only sense the change of the objects, but also collect data from an appointed environment. These data can be processed and sent to the base station. Due to the trait of the sensor networks, it can be applied in two special fields:

J. Zhao (✉)
College of Information Science and Engineering Shandong University of Science and Technology, Qingdao, China
e-mail: zhaojianli@gmail.com

Q. Sun
School of Science, Shandong University of Science and Technology, Qingdao, China
e-mail: qiuxiasun@163.com

Q. Liang et al. (eds.), *Communications, Signal Processing, and Systems*, Lecture Notes in Electrical Engineering 202, DOI 10.1007/978-1-4614-5803-6_11,

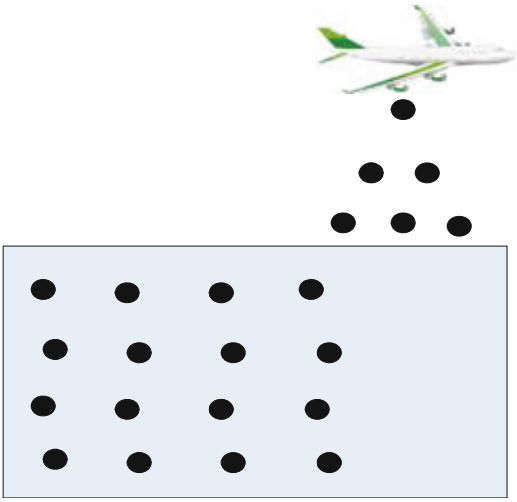

Fig. 11.1 Stochastic distribution of sensor nodes

Military affairs. Sensor network [1–4] will be an important part in C4ISRT system. C4ISRT system is to provide a battlefield chain of command integrated command, control, communication, computing, intelligence, surveillance, reconnaissance and targeting for future war using high-tech. Wireless sensor network can be used to find out the state of the war and the accomplished task. Soldiers and weapons can be equipped with sensors to corporate with each other in the war.

Emergency and temporary Environment. When fire, flood or earthquake happened, the fixed communication establishments are all destroyed or can't work well, and they can't be repaired in a short time. At that time, wireless network can be used because it is in a self-organizing way without relying on any established infrastructure and can be settled up soon. To some remote area, for example virgin forest, wireless network can be used to monitor the fire.

Due to the particularity of the two fields, for example in the battlefield and the worst-hit area, engineers can't set up the sensor network in workplace directly, the sensor nodes have to be spread by airplane or other tools just as Fig. 11.1. Because the spreading of the nodes is stochastic, so how to make sure the connectivity of the wireless sensor nodes is the first key problem. And the energy in the sensor nodes is limited and can't be recharged, so an efficient energy scheme of wireless sensor network is another key problem which can reduce the node energy cost and prolong the lifetime of the sensor network.

There some researches focuses on the connectivity and energy conservation of wireless sensor network now [5–8], but few is about stochastic distribution sensor networks. A Hierarchical Sensor network Based on Voronoi Graph is proposed in this chapter, which can make sure the connectivity of the stochastic distribution sensor network and reduce the traffic flow by data fusion.

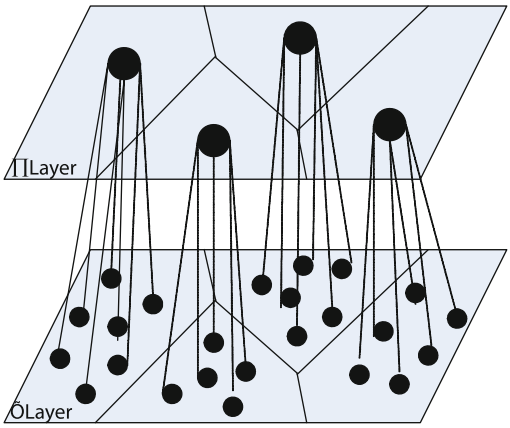

Fig. 11.2 The hierarchical architecture of sensor network

11.2 Hierarchical Wireless Sensor Network

Now the research of sensor network is limited to the isomorphic network, every node in the network is same, i.e. the nodes have the same sensor range, the same propagation power and the same battery, and the node integrated the capacity of sensing and routing into itself, which makes the function of sensor nodes too miscellaneous. So we proposed an isomeric sensor network. There are two kinds of nodes in this sensor network: type A and type B. The nodes of A type is the normal nodes in the network, they only have the capacity of sensing and propagation for little range and don't have the ability of routing. The nodes of B type can route and transfer but can't sense, they have a high propagation power and more battery storage to send data to the remote base station. To be robust, a high nodes density (it can be 20 nodes/m^3 [9]) is needed in sensor network, so the high nodes density will bring some redundant data that will burden to the limited bandwidth, the limited processing and communication capabilities of sensor network. Thus we should adopt some way to reduce the redundancy, and B type nodes in the sensor network proposed by us can do this work. The structure of A type nodes and B type nodes makes the function of nodes simpler and reduces the equipment cost.

B type nodes can be looked as the backbone of the sensor network. They should be connected to communicate with each other. B type nodes can transmit the data that A type nodes collected to the sink node. In this way, the sensor network can form two-layer architecture. In Fig. 11.2, layerIis the A type nodes that answer for collecting data from its monitoring area; layerIIis the backbone network (B type nodes) that makes sure the connectivity, reduces the redundancy, aggregates data and transfers the data to base station by one or more hop.

11.2.1 Formation of Layer IInetwork

LayerIInodes have high propagation power, more battery storage and a longer propagation range than layerInodes. LayerInodes can only collective data and can't route data, so layerIInodes must be connected to make the whole network can communicate and the data can be sent to the base station. To make the layerIInodes to be connected is not a difficult problem, [10] had proved that the connectivity of network can be assured by adjusting the propagation range: There are n nodes in a two-dimensional plane and the nodes distribute in Poisson distribution. If the sensing area of every node satisfies the expression $\pi r^2 = (\log n + c(n))/n$ (r is the sensing range), the network of n nodes will be connected with probability 1 if and only if $c(n) \to +\infty$. Feng Xue and Kumar [11] indicated to assured the network connectivity by adjusting the number of node's neighbors: n nodes distribute in a two-dimensional plane randomly, if the number of node's neighbors is less than 0.074 log n, the network will be disconnected with probability 1 when n increases, at that time, there are some isolated nodes in the network; if the number of node's neighbors is more than 5.1774 log n, the network will be connected with probability 1 when n increases. We can use the two ways to assure the connectivity of layerIInodes.

11.2.2 Partition Based on Voronoi Diagram

According to the hierarchical architecture of sensor network, layerInodes collective data from the monitored area, and send to the nodes of backbone network (layerInodes). This is related to the partition of layerInodes, i.e. an appointed node of layerIneeds to aggregate which area of nodes. To save the energy of layerInodes, the appointed node of layerIIshould be in the center of the monitored area. Voronoi Diagram can solve this problem well.

11.2.3 Voronoi Diagram

$V = \{v1, v2, \ldots, vi, \ldots vn\}$ is a node set in two-dimensional Euclidean plane. Voronoi Diagram is to distribute the n nodes into n area $\{p1, p2, \ldots, pi, \ldots pn\}$, and every area pi $(1 \leq i \leq n)$ only has one node vi. The distance between every point in area pi and vi is less than the distance between any other point in areapi and vi. So $pi = \{x : |vi - x| \leq |vj - x|, \ \forall j \neq i\}$, this can form a Voronoi Diagram.

We bring the Voronoi Diagram in the sensor network. LayerIInodes are partitioned based on Voronoi Diagram, every node of layerIIis in charge of collecting the data for layerInodes that are in the its Voronoi area, reducing the redundant data and aggregating data.

11.3 The Mathematics Model of Data Fusion for Hierarchical Sensor Network

11.3.1 The Ration of Data Fusion

In Fig. 11.3, there are N sensor nodes in a square area. C^1,C^2 and C^n are the sensing area of the sensor node 1, node 2 and node n respectively. When some of the sensor nodes have overlap area, the event is the overlap area can be sensed by the crossed nodes. So the transmitted data can be fusion to reduce the repetitive event by abandoning the overlapping area. The available sensing area of all n nodes in Fig. 11.3 is $\sum_{i=1}^{n} C^i - \sum_{i=1}^{n}\sum_{j=i+1}^{n}(C^i \cap C^j)$, $C^i \cap C^j$ is the overlapping area of node i and node j. So the data fusion ratio can be defined to $\left(\sum_{i=1}^{n} C^i - \sum_{i=1}^{n}\sum_{j=i+1}^{n}(C^i \cap C^j)\right) / \sum_{i=1}^{n} C^i$.

11.3.2 Mathematical Model of Data Fusion

To adapt to the hierarchical sensor network, we proposed simple mathematics model of data fusion. Assumption that layerInodes and layerIInodes are two independent Poisson distribution and in an square area, their intensity are λ_1 and λ_2. So every node of layerIIhas wireless links with λ_1/λ_2 nodes of layerIaveragely, i.e. in every Voronoi partition area there are λ_1/λ_2 nodes of layerIsending data to the node of layerII. If the range of node is r, we need nodes of layerIto cover the square area; we have known in 3.1 that if there are n nodes of layer I in the square, the data fusion ratio is $(n\pi r^2 - \sum_{i=1}^{n}\sum_{j=i+1}^{n}(C^i \cap C^j))/(n\pi r^2)$.

If a node of layer I send x data packages to a node of layerIIat one time, vi will receive $x\lambda_1/\lambda_2$ data packages averagely in its Voronoi partition area pi, so the number of data packages after data fusion is $x\lambda_1(n\pi r^2 - \sum_{i=1}^{n}\sum_{j=i+1}^{n}(C^i \cap C^j))/(\lambda_2 n\pi r^2)$.

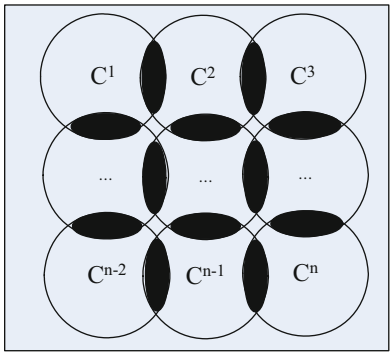

Fig. 11.3 The definition of data fusion ratio

So the nodes of layerIIcan distinguish some related data packages that the nodes of layerIhad send to them, and integrate these data packages into one package, which reduce the data bulk and relief the limited bandwidth and energy in sensor network.

11.4 Simulation

We complemented the hierarchical sensor network in NS2. The sensor nodes of two groups Poisson distribution that the intensities are λ_1 and λ_2 respectively are spread randomly in a square area (the length and width are both 100 m). In the center, there is a base station. The nodes that intensity is λ_1 are in layer I and the nodes that intensity is λ_2 are in layerII. The layerIInodes are partitioned based on Voronoi graph. The nodes all use omnidirectional antennas and MAC protocol is DCF of 802.11 wireless local area networks. In every Voronoi partition area, the layer nodes use CBR traffic flow that sends 4 traffic data packages per second, and every data package is 512 bit. We use $N = x\lambda_1(n\pi r^2 - \sum_{i=1}^{n}\sum_{j=i+1}^{n}(C^i \cap C^j))/(\lambda_2 n\pi r^2)$ to record the traffic data packages of layerII, and the traffic flow can be calculated by $512\lambda_1(n\pi r^2 - \sum_{i=1}^{n}\sum_{j=i+1}^{n}(C^i \cap C^j))/(\lambda_2 n\pi r^2)$. Calculating the traffic flow at $\lambda_1/\lambda_2 = 1, 2, \ldots, 10$ respectively.

As in Fig. 11.4, the traffic flow is obviously reduced after reducing redundancy and fusion data. And we find that the traffic flow has a big increment when the nodes of layerIIchanges from 1 to 10, but if more than 5, the traffic flow is always about 2,700 bit. It shows this Voronoi partition area can be covered by 5 nodes of layerII, if more than 5 nodes, the nodes of layerIIcan reduce the redundancy, then reduce the traffic flow. This coincides with the real condition and shows that our model is correct.

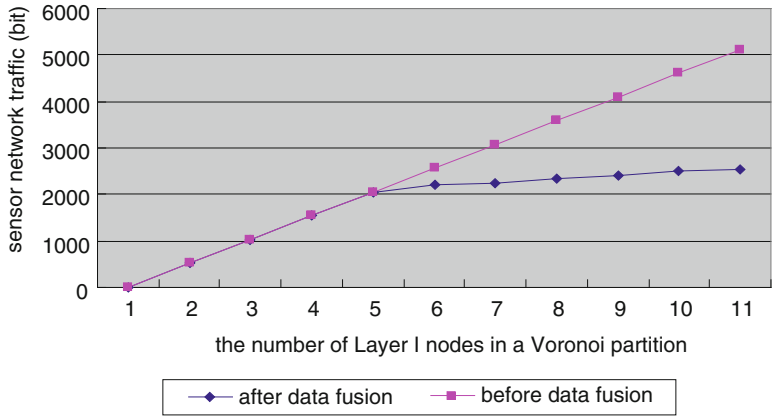

Fig. 11.4 Comparison of sensor network traffic

11.5 Conclusion

In this chapter, a hierarchical sensor network is proposed which place the sensing capacity and routing capacity at different layer nodes respectively. It cannot only simplify the hardware design but also reduce cost. Adopting Voronoi diagram to the partition of backbone network, a mathematical model of data fusion based on hierarchical architecture is given. The simulation shows, the number of transmission data packages is cut down sharply, which can reduce nodes energy cost and prolong the lifetime of the sensor network.

Acknowledgments This work is supported by science and technology plan of basic research projects of Qingdao under Grant No. 12-1-4-18-jch.

References

1. Akyildiz IF, Su W, Sankarsubramaniam Y, Cayirci E (2002) Wireless sensor networks: a survey. Comput Netw 38:393–422
2. Manjeshwar A, Agrawal DP (2001) TEEN: a routing protocol for enhanced efficiency in wireless sensor networks. In: Proceedings of the 15th parallel and distributed processing symposium. San Francisco: IEEE Computer Society, 2001, 2009–2015
3. Hester L et al (2002) neuRFon Netform: a self-organizing wireless sensor network. In: Proceedings of IEEE IC3N, pp 364–369
4. Cullar D, Estrin D, Strvastava M (2004) Overview of sensor network. Computer 37(8):41–49
5. Rezaei Z, Mobininejad S (2012) Energy saving in wireless sensor networks. Int J Comput Sci Eng Surv (IJCSES) 3(1):23–37
6. Jiang J-R, Sung T-M (2009) Energy-efficient coverage and connectivity maintenance for wireless sensor networks. J Netw 4(6):403–410
7. Dhivya M, Sundarambal M (2011) Energy efficient computation of data fusion in wireless sensor networks using cuckoo based particle approach (CBPA). Int J Commun Netw Syst Sci 4:249–255
8. Chamam A (2009) On the planning of wireless sensor networks: energy-efficient clustering under the joint routing and coverage constraint. IEEE Trans Mobile Comput 8:1077–1086
9. Shih E, Cho S, Ickes N, Min R, Sinha A, Wang A, Chandrakasan A (2001) Physical layer driven protocol and algorithm design for energy-efficient wireless sensor networks. In: Proceedings of the seventh annual international conference on Mobile computing and networking (MobiCom 01), Rome, pp 272–287
10. Gupta P, Kumar PR (1998) Critical power for asymptotic connectivity in wireless networks. In: McEneany WM, Yin G, Zhang Q (eds) Stochastic analysis, control, optimization and applications: a volume in honor of W.H. Fleming. Birkhauser, Boston, pp 547–566
11. Xue F, Kumar PR (2004) The number of neighbors needed for connectivity of wireless networks. Wirel Netw 10:169–181

Chapter 12
Lightweight Security for WSN Based on Network Coding

Xu Lu and Ting Jiang

Abstract The application of network coding has been improving the performance of Wireless Sensor Networks (WSN). Compared with previous, the security performance has been improved. But when faced with security attacks—especially eavesdroppers, the security of the WSN still needs to be improved. A Lightweight Permutation Encryption Coding (LPEC) is proposed in this chapter, which Combines with secure network coding and permutation encryption algorithm. Unlike end-to-end encryption, which encrypts the whole text, LPEC only encrypts the Local Encoding Vector (LEV), and hide it by permutation encryption. The mechanism effectively reduces the encryption complexity, and thwarts global eavesdroppers. At the same time, it improves the security performance for communication between WSN nodes.

Keywords WSN • Network coding • Security performance • LPEC

12.1 Introduction

Network coding is a kind of information exchange technology, which is a fusion of the routing and coding, its core idea is the linear or nonlinear processing of information received on each node and forwarding to the downstream node. The intermediate node plays the role of the encoder or signal processor. R Ahlswede pointed out that network coding can help in achieving the maximum flow of multicast routing transmission and improving the efficiency of information transmission, which lays the important position for network coding in modern network communications research [1].

X. Lu (✉) • T. Jiang
Key Laboratory of Universal Wireless Communication, Ministry of Education
Beijing University of Posts and Telecommunications, Beijing 100876,
People's Republic of China
e-mail: victorylu@163.com; tjiang@bupt.edu.cn

Q. Liang et al. (eds.), *Communications, Signal Processing, and Systems*, Lecture Notes in Electrical Engineering 202, DOI 10.1007/978-1-4614-5803-6_12,

Due to unreliable multi-hop transmission and random package reorganization, network coding systems are extremely vulnerable to different types of security threats such as eavesdroppers and link analysis attacks. Among them, eavesdroppers earn much attention on that the confidentiality of network coding systems are seriously affected by the eavesdroppers. Therefore, responding to the eavesdroppers, especially in RLNC system is a challenging problem needed to be solved. In this chapter, we will focus on lightweight security mechanisms for WSN based on network coding.

Currently, the security researches based on network coding are still in a theoretical stage. Chapter [2] proposed a secure linear network coding, which achieves better security to resist external eavesdroppers by limiting the number of links to access. Chapter [3] proposed the application of network coding, which resists against passive attacks by encrypt only part of the global encoding vector (GEV). Chapter [4] added the authentication information to the GEV by changing the structure of the coefficient matrix, which achieves a higher level of security with the same packet structure. Chapter [5] pointed out the problem that random linear network coding will encounter when faced with eavesdropper, and proposed a permutation encryption algorithm based on network coding. This method can effectively resist eavesdropper, and improved the robustness of the communication system.

In summary, the existing security mechanisms have some shortcomings in complexity and security performance. In this chapter, we propose a lightweight encryption algorithm—(LPEC), which Combines with secure network coding and permutation encryption algorithm. This method effectively improves the security performance of the WSN. The remainder of this article is structured as follows: Sect. 12.2 presents RLNC models. Section 12.3 describes LPEC in detail. We will analyze the performance of LPEC in Sect. 12.4. The last part gives the conclusions of this chapter.

12.2 System Model

Generally, a communication network can respected as an acyclic directed graph. $G = (V, E)$, in which V is the set of nodes, and E is the set of links. For each node v, define $\Gamma_I(v)$ as the set of links terminating at v, and $\Gamma_O(v)$ as the set of links originating from it. For each link e, let $y(e)$ be the packets carried on the link. Each packet is defined on the finite field F, which defined as a row vector $x_i = [x_{i,1}, \cdots, x_{i,l}]$ of length l. Consider a multicast system, the source node deliver a series of packets $x_1, \cdots, x_h$ to a series of receiver nodes, where h is the multicast capacity of the system.

For the sake of notation, we define $\Gamma_O(v)$ consists of h links $e_1, \cdots, e_h$, then $y(e_i) = x_i$. So, for each $e \in \Gamma_I(v), v \notin V, y(e)$ can be calculated by linear operations using the packets received by v:

$$y(e) = \sum\nolimits_{e' \in \Gamma_I(v)} \beta_{e'}(e) y(e') = \beta(e) Y(e') \tag{12.1}$$

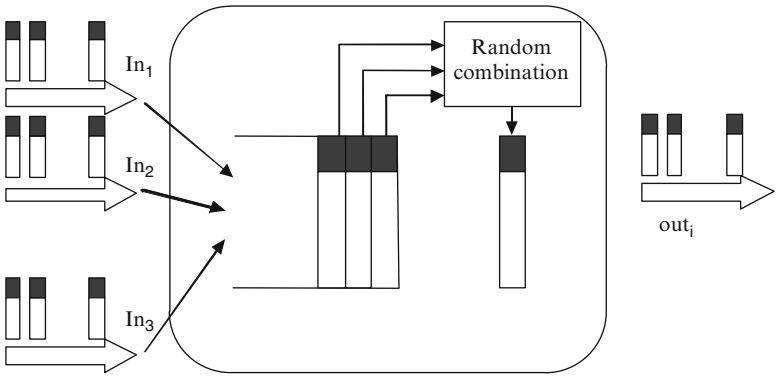

Fig. 12.1 RLNC at intermediate node

In (12.1), the coefficient $\beta_{e'}$ is randomly selected from the finite field F. The vector $\beta(e) = [\beta_{e'}(e)]$ termed as local encoding vector (LEV). By induction, $y(e)$ can be represented as a linear combination of $x_1, \cdots, x_h$:

$$y(e) = \sum_{i=1}^{h} g_i(e)x_i = g(e)X \tag{12.2}$$

In which, $g(e) = [g_1(e), \cdots, g_h(e)]$ is termed as global encoding vector (GEV). When the receive node has h packets $y(e_1), \cdots, y(e_h)$, we can induce (12.2) in the matrix form:

$$Y = [y(e_1), \cdots, y(e_h)]^T = [g(e_1), \cdots, g(e_h)]^T X = GX \tag{12.3}$$

In (12.3), G kwon as global encoding matrix (GEM). Then the receive node can reconstruct the source message X by $X = G^{-1}Y$.

Figure 12.1 shows the process of RLNC at intermediate nodes. Where, the shaded information is coding coefficient $\beta_{e'}$.

In this chapter, we assume without loss of generality, that the source and receivers are always trusted and can never be compromised by an adversary.

12.3 Lightweight Permutation Encryption Coding

In order to achieve the principle of confidentiality [6], traditional WSN systems are performing end-to-end encryption mechanism, such as RC5 [7], RC4, TEA, etc. However, considering the restrictions of node's resources, and along with the application of network coding, especially RLNC in WSN, reference [8] first

proposed the concept of lightweight encryption, named secure practical network coding (SPNC). SNPC is different from tradition end-to-end encryption method, which effectively reduces the length of data to be encrypted. Although this approach reduces the complexity of encryption, the security performance does not improve. A novel method combines SPNC with permutation encryption is proposed, which effectively increases the safety performance with the same level of encryption complexity. This is LPEC.

12.3.1 LPEC

The principle of transposition cipher is not to change the plaintext, but to change the order of characters to achieve encryption. This chapter proposes a lightweight encryption algorithm (LPEC), which bases on the basis of SPNC, and improves the transposition cipher algorithms.

The security of LPEC is based on twice encryption process, one is similar to the traditional encryption, and the other is permutation encryption. Different from the traditional cryptographic algorithms, they only encrypted the coefficient of RLNC. Due to this method, Attacker cannot get any useful information even if it comprises original encryption key.

Reference [7] describes the traditional RC5 encryption, so this section we focus on the contents of permutation encryption algorithm.

We term a sequence π of length n containing each element of set $\{1, 2, \cdots, n\}$. Let $\Pi(i)$ be the i^{th} element of the sequence, then the product operation $\Pi_1\Pi_2(i) = \Pi_1(\Pi_2(i))$. Let Π^{-1} be the inverse of Π with respect to product operation.

Definition 1 (Encryption Process) let m be a one-dimensional vector in F, define as $m = [m_1, m_2, \cdots, m_n]$, k be a permutation encryption key, then we denoted the Permutation Encryption Function (PEF) as follows:

$$E_k(m) = E_k([m_1, m_2, \cdots, m_n]) = [m_{k(1)}, m_{k(2)}, \cdots, m_{k(n)}] \tag{12.4}$$

Definition 2 (Decryption Process) let c be the information receive node receives; define as $c = [c_1, c_2, \cdots, c_n]$, k be the decryption key, then we denote the Permutation Decryption Function (PDF) as follows:

$$D_k(c) = D_k([c_1, c_2, \cdots, c_n]) = [c_{k^{-1}(1)}, c_{k^{-1}(2)}, \cdots, c_{k^{-1}(n)}] \tag{12.5}$$

The permutation encryption key is randomly selected, which is to hide the coefficient encrypted by RC5.

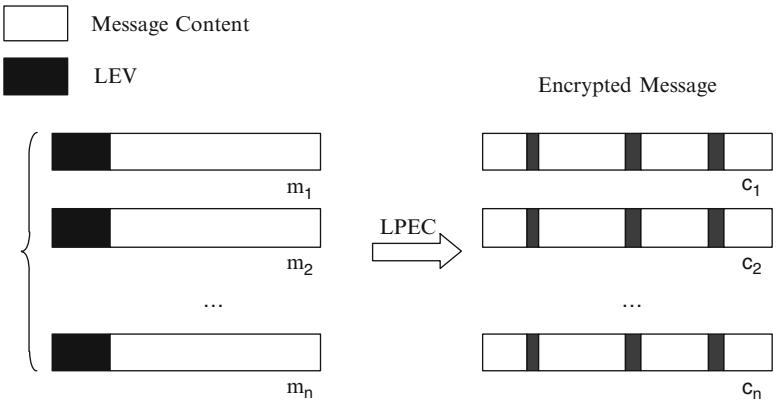

Fig. 12.2 Permutation encryption on coded messages

12.3.2 The LPEC Mechanism

The basic idea of the LPEC is to permute the coefficient after SPNC, so the adversary cannot obtain any useful information from the intercepted packets. LPEC can effectively thwart eavesdroppers, especially global eavesdroppers.

LPEC need to encrypt data twice, so it requires two keys. In this chapter, RC5 encrypt key is pre-assigned, defined as k, permutation encrypt key as PEK. In this mechanism, there is a key distribution center (KDC) responsible for symmetric key establishment, which makes the sending node and receiving node can get the permutation encryption key. LPEC can be divided into three stages: source node encryption, intermediate node encoding, receiving node decryption.

Source Node Encrypt: first, source node determines the multicast capacity h of the system [9], then divides the packet into h segments with equal length, say $x_1, x_2, \cdots, x_h, X$ as the original packet. Each segment is assigned with a unit vector. For the i^{th} segment $x_i (1 \le i \le h)$, the corresponding value λ_i is defined as follow: the i^{th} component of the vector is 1, and all the other components are 0. Then the source node randomly selects LEV $\beta(e_i)$ from the finite field F, and then gets the coding information $\beta(e_i)X$ after random linear coding, where $X = [x_1, x_2, \cdots, x_h]^T$. The message carried on the i^{th} link is: $y(e_i) = [\beta(e_i), \alpha, \beta(e_i)X]$, α is the link coefficient, which is responsible for the correlation judgment in the receiving node. According to LPEC, first encrypt the coefficient use RC5, then perform permutation encryption on it use formula (12.4), and get the cipher text $c[y(e_i)] = E_k[y(e_i)]$. See Fig. 12.2.

Intermediate Node Encoding: since the intermediate node does not know the PEK of the sending node, it does not decrypt. The only thing is to code the received packets future. Within the given time, intermediate node checks the received packets, and recodes the message to reduce the relevance of the packets. Then

$$c[y(e)] = c\left[\sum_{e' \in \Gamma_I(v)} \beta_{e'}(e).y(e')\right] \tag{12.6}$$

Obviously, even if the adversary comprises the intermediate node, as it does not know the PEK, it cannot obtain the original message. LPEC can effectively thwart adversaries, especially internal eavesdroppers.

Receiving Node Decryption: on receiving a packet, the receive node perform PDF to decrypt the message, as follows:

$$D_k\{c[y(e_i)]\} = E_{k^{-1}}\{E_k[y(e_i)]\} = y(e_i) \tag{12.7}$$

Then use k to decrypt the coefficient. After that, receive node has to judge the number k of decrypted packets: If $k \geq h$, then determine whether the coefficient vector matrix linearly independent. Once h linearly independent messages $y(e_1)$, $y(e_2), \cdots, y(e_h)$ are collected, receive node can reconstruct the original message use following matrix transformation:

$$Y = \begin{bmatrix} y(e_1) \\ \vdots \\ y(e_h) \end{bmatrix} = \begin{bmatrix} g(e_1), g(e_1)X \\ \vdots \\ g(e_h), g(e_h)X \end{bmatrix} = [G, GX] \tag{12.8}$$

Where G is a global encoding matrix. The source message could be recovered by applying Gaussian eliminations:

$$Y = [G, GX] \rightarrow [I, X] \tag{12.9}$$

Then receive node recovers the source message X.

12.4 Performance Evaluation

In the following discussion, we will analysis the performance of LPEC, and give the evaluation in two perspectives: encryption complexity and anti-attack capability. LPEC can reach the Shannon security.

12.4.1 Encryption Complexity

The tradition encryption is based on end-to-end encrypt, LPEC adopts two encryption processes. The first is RC5, the second is permutation encryption, but all the two encryptions are only to encrypt the coefficient. Figure 12.3 compares the volume of data to be encrypted according to the size of plaintext. We consider

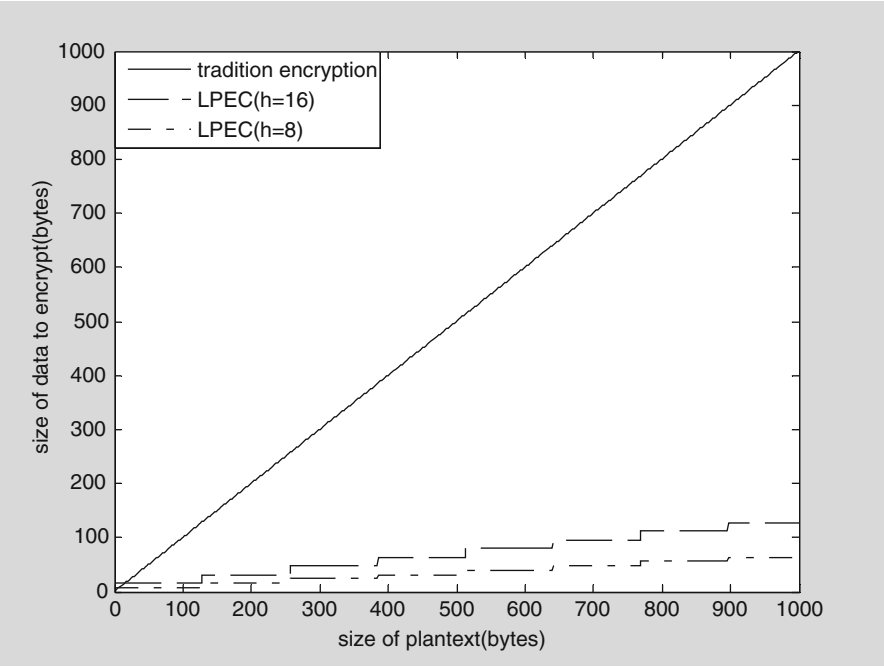

Fig. 12.3 The length of data to be encrypted

standard Zigbee packet of length128 bytes. It can be seen from the figure, in traditional encryption mechanism, which performs end-to-end encryption, the length of data to be encrypted increase linearly with the size of plaintext, while LPEC, which solely encrypts the coefficients, substantially reduces the size of information to be encrypted.

It can be seen from the figure, the length of the LPEC needs to encrypt increases in discrete steps, because only when the payload size exceeds the maximum length of Zigbee packet.

12.4.2 Anti-Attack Capability

Last section shows that LPEC significantly reduces the encryption complexity, meanwhile, it still guarantees strong confidentially of the payload. We will give the testimony in this section.

In this chapter, we assume that source node generates h packet of length l. According to the LEPC model, the length after LPEC is $n = a + h + l$ (α is the link coefficient as mentioned above). Set $m = a + h$, then $n = m + l$.

To the adversary, the PEK is randomly generated. So if the adversary wants to decrypt the packets, the probability it can get the same PEK meets:

$$P\left(\bigcap_{i=1}^{n}\{C(i)=x_{k(i)}\}|M=x\right)=\frac{1}{A_n^m},(\forall k,\forall x) \tag{12.10}$$

Proof:

$$P\left(\bigcap_{i=1}^{n}\{C(i)=x_{k(i)}\}|M=x\right)$$

$$=\frac{P\left(\bigcap_{i=1}^{n}\{K(k^{-1}(i))=i\}|M=x\right)}{P(M=x)}(|F|\to\infty)$$

$$=\frac{P\left(\bigcap_{i=1}^{n}\{K(k^{-1}(i))=i\}P(M=x\right)}{P(M=x)}=P(K=k)=\frac{1}{A_n^m}$$

From the above equation, the multitude to generate the same PEK as the original is A_n^m. Assume that the adversary has intercepted packets greater than h. Even if it has got the RC5 key, the multitude to recover the source message is $O(A_n^m.h^3), O(h^3)$ is the time using for Gaussian elimination. We consider standard Zigbee packet, $n=128, m=16$ and $h=5$ .we assume the adversary can guess 10^{20} possible plaintext per second, the average time to get the right message is:

$$T=\frac{A_{128}^{16}\times 5^3}{365\times 24\times 3600\times 10^{20}}=8.6\times 10^{10}(year) \tag{12.11}$$

From the above analysis we can see that LPEC effectively reduce the encryption complexity, and increase the ability to thwart eavesdroppers.

12.5 Conclusion

A lightweight encryption algorithm-LPEC is proposed in this chapter. This mechanism breaks the idea of traditional end-to-end encryption, which only to encrypt the coefficient. Result reveals that LPEC can effectively thwart eavesdroppers (external eavesdroppers and internal eavesdroppers). At the same time, it improves the security performance between WSN nodes.

Acknowledgments This work was supported by Important National Scenes & Technology Specific Projects (2010ZX03006-006), NSFC (61171176), Scientific Research Fund of Zhejiang Provincial Education Department under Grant No. Y201225956 and Natural Science Foundation of Ningbo under Grant No. 2012A610015.

References

1. LI SY-R, CAI N (2003) Linear network coding. IEEE Trans Inf Theory 49(2):371–381
2. Tan J, M´edard M (2006) Secure network coding with a cost criterion.In: Proceedings of 4th international symposium on modeling and optimization in mobile, ad hoc and wireless networks (WiOpt'06), Boston, April 2006
3. Fan Y, Jiang Y, Zhu H, Shen X (2009) An efficient privacy-preserving scheme against traffic analysis attacks in network coding. IEEE INFOCOM
4. Fathy A, ElBatt T (2011) SANC: source authentication using network oding. The first workshop on security in computers, networking and communication
5. Zhang P, Jiang P, Lin C, Fan Y, Shen X (2010) P-coding: secure network coding against eavesdropping attacks. IEEE INFOCOM
6. Bhattad K, Narayanan KR (2005) Weakly secure network coding. In: Proceedings of the first workshop on network coding, theory, & applications,
7. Yu Z, Wei Y, Ramkumar B, Guan Y (2008) An efficient signature-based scheme for securing network coding against pollution attacks. IEEE INFOCOM
8. Vilela JP, Lima L, Barros J (2008) Lightweight security for network coding. In: IEEE international conference on communications (ICC)

Part IV
Cognitive Radio System

Chapter 13
Improved Energy Detection Spectrum Sensing Method for OFDM-Based Cognitive Radio System

Min Jia, Hao Yang, and Xuemai Gu

Abstract The spectrum sensing scheme which is used for detecting primary users in a licensed spectrum are essential to utilize the spectrum effectively for cognitive radio communication systems. As a matter of fact, sensing accuracy is regarded as the most important factor for spectrum sensing with the intension of sufficient protection for the primary user. A novel spectrum sensing scheme which exploits the cyclic prefix of an orthogonal frequency-division multiplexing (OFDM) symbol as well as idle period containing no information symbols is proposed in this chapter. From the analysis and simulation results, it shows that the proposed scheme can improve sensing accuracy and increase system throughput compared with the conventional scheme which uses only idle period.

Keywords OFDM • Cognitive radio • Cyclic prefix • Energy detection

13.1 Introduction

The rapid growth of wireless services and devices tends to exhaust the available radio spectrum. Consequently, cognitive radio technology has been suggested with an effort to use the spectrum more efficiently [1]. A cognitive radio system that can learn from and adapt to the external radio environment potentially maximizes the spectrum utilization. Since the secondary user is required to return the occupied spectrum whenever the primary user appears, thus it is necessary that the secondary user can sense the availability of the licensed spectrum periodically.

OFDM is a newly appearing transmitting technique, by dividing the channel into several orthogonal sub-channels, the signal is transmitted in some of the sub-channels.

M. Jia (✉) • H. Yang • X. Gu (✉)
Communication Research Center, School of Electronics and Information Engineering
Harbin Institute of Technology, Harbin 150001, China
e-mail: jiamin@hit.edu.cn; sparrowyh@yahoo.com.cn; guxuemai@hit.edu.cn

Q. Liang et al. (eds.), *Communications, Signal Processing, and Systems*, Lecture Notes in Electrical Engineering 202, DOI 10.1007/978-1-4614-5803-6_13,

This transmitting method boasts lots of advantages like high efficiency of spectrum exploit, restrain of multi-path interference and easy to be realized in hardware layer. Nowadays, the OFDM is becoming the most prevalent technique in cognitive radio system. Applying the OFDM in cognitive radio will bring benefits in shaping the spectrum so as to make the secondary user be easy to access the available spectrum and enhance the efficiency of the whole system in spectrum usage.

There are plenty of schemes for spectrum sensing. And the performance of sensing scheme is mainly depended on the sensing time as well as the accurate. The traditional energy detection scheme does not require any information of the primary user and has a relatively short sensing period, making it one of the most popular spectrum sensing method in usage. In [2, 3], Zengyou Sun and Refik Fatih made some analysis on the performance of traditional energy sensing and the cyclic-stationary sensing. Anand Chandran proposed a method which used the eigenvalue to be the threshold in [4], in order to avoid using the Neyman-Person criterion and improve the performance of the system as a result. In an OFDM-based cognitive radio system [5, 6], the redundant information in the cyclic prefix can be used to improve the performance of energy detection scheme [7, 8].

In this chapter, a system model for the OFDM-base cognitive system is built up firstly, and then the sensing scheme which called the cyclic prefix energy detection (CP-ED) is proposed in the following section. The simulation and analysis is introduced in the third section. In the final part, the conclusion is given out.

13.2 System Model

13.2.1 OFDM-Based Cognitive Radio Transmitter

An OFDM system which has a prefix of N_G samples with N carriers is considered in this chapter. The complex-valued source symbols are modulated into parallel streams of N orthogonal subcarriers. To guarantee the continuity of the signal and orthogonality between subcarriers, the last N_G samples in the OFDM symbol are attached. Thus the cyclic prefix is formed. And then a complete OFDM symbol with $N + N_G$ samples can be expressed as follows

$$s = [s(0), s(1), \ldots, s(N + N_G - 1)]^T \tag{13.1}$$

Moreover, in order to guarantee the synchronization of OFDM symbols, a common method is to insert training sequence in front of every OFDM symbol, as shown in Fig. 13.1. During the idle period, no signal is transmitted. When the procedures above are done, the entire signal is transmitted over the wireless channel.

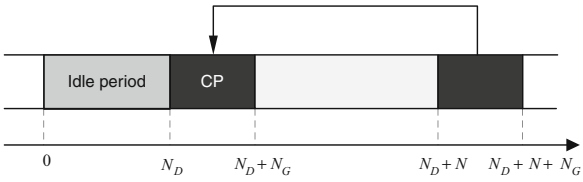

Fig. 13.1 OFDM symbol with cyclic prefix and idle period

13.2.2 OFDM-Based Cognitive Radio Receiver

In the receiver model, we assume that the time offset is compensated successfully; it can use a window with the width $N_D + N + N_G$ for observation. When both a primary user and a secondary user exist in the channel simultaneously, the received signal of the secondary user can be written as follows,

$$r(n) = \begin{cases} p(n) + w(n) & n = 0, 1, \ldots, N_D - 1 \\ p(n) + s(n) + w(n) & n = N_D, \ldots, N_D + N_G + N - 1 \end{cases} \tag{13.2}$$

where $p(n)$ is the primary user signal, $s(n)$ is the secondary user signal, and $w(n)$ is the noise. When there is no primary user in the channel, $p(n) = 0$. The primary user signal $p(n)$ is assumed to be a zero-mean, complex-valued, circularly symmetric, white Gaussian random process with a variance σ_p^2, which can be expressed as $p(n) \sim CN(0, \sigma_p^2)$. The complex-valued, circularly symmetric AWGN $w(n)$ with variance σ_w^2 can be expressed as $w(n) \sim CN(0, \sigma_w^2)$.

Therefore, the demonstration of an OFDM-based cognitive radio model can be given through the above discussion.

13.3 The Spectrum Sensing Scheme

Taking the customer service flows in a telecommunication operator as an example, the main problems exist in its customer service are illustrated in follows and a feasible solution is given.

In this section, this chapter proposed the refine energy sensing scheme which use both the idle period and the cyclic prefix. In contrast with the traditional energy sensing method that only utilize the N_D samples, our new scheme use not only the N_D samples but also the N_G samples as well. Since the sampling points for spectrum sensing are enlarged, we guess the performance will thus improve as well.

Before the actual detection procedure, we slightly modify the received signal. For convenience of usage, define the index sets as follows

$$\begin{aligned} I &= \{0, 1, \ldots, N_D - 1\} \\ J &= \{N_D, N_D + 1, \ldots, N_D + N_G - 1\} \\ K &= \{N_D + N_G, N_D + N_G + 1, \ldots, N_D + N_G + N - 1\} \end{aligned} \tag{13.3}$$

It is clear that the set I represents the indices of the idle period, the set J is the indices for the cyclic prefix period, the set K is the indices for the original samples from which the cyclic prefix copies. From the definition of cyclic prefix, we can easily know that the points in the set J and K are equal, namely

$$s(n) = s(n+N), \quad n = N_D, N_D+1, \ldots, N_D+N_G-1 \tag{13.4}$$

13.3.1 The Idle Period

In the idle period, the existence of the primary user signal is determined in the same way as the conventional scheme with-out cyclic prefix exploitation. We define a decision variable $d(n)$ for the set I.

$$d(n) = \sqrt{2}r(n), n \in I \tag{13.5}$$

The factor of $\sqrt{2}$ is chosen to normalize the variances of the signal in the idle period and the cyclic prefix period to be the same. Linear scaling to the received signal does not affect the detection result. For the idle period, the detection model is

$$\begin{aligned} H_0&: d(n) = \sqrt{2}w(n) \\ H_1&: d(n) = \sqrt{2}[p(n)+w(n)], n \in I \end{aligned} \tag{13.6}$$

13.3.2 The Cyclic Prefix

In the case of cyclic prefix, we first erase the duplicated signal in the set J and K, and then obtain the decision variable $d(n)$ as follow

$$d(n) = r(n) - r(n+N), n \in J \tag{13.7}$$

And thus the detection model can be obtained

$$\begin{aligned} H_0&: d(n) = w(n) - w(n+N) \\ H_1&: d(n) = [\ p(n) - p(n+N)] + [w(n) - w(n+N)\ ], n \in J \end{aligned} \tag{13.8}$$

13.3.3 The Detection Scheme

Because the received signals are Random Gauss signals, their characteristics maintain the same through the two linear processes above. Since the linear process

of Gaussian random process is still Gaussian random process, hence the test variable $d(n)$ is a Gaussian random signal. Thus we can model $d(n) \sim CN(0, 2\sigma_w^2)$ under situation H_0 and $d(n) \sim CN(0, 2(\sigma_w^2 + \sigma_p^2))$ under H_1 for $n = 0, 1, ..., N_D + N_G - 1$.

On purpose is to detect the existence of a random signal such as $p(n)$, we use an energy detection scheme to obtain this. As like the conventional method of the energy detection, the decision rule can be expressed as

$$T = \sum_{n=0}^{N_D+N_G-1} |d(n)|^2 \tag{13.9}$$

$$\begin{aligned} H_0&: T < \lambda \\ H_1&: T > \lambda \end{aligned} \tag{13.10}$$

where T is the test statistic and λ is the threshold. T is the sum of the squares of Gaussian random variables and equivalent to the chi-squared random variable with $2 \times (N_D + N_G)$ degrees of freedom. Thus the detection problems can be rewritten as

$$\begin{aligned} H_0&: \frac{T}{\sigma_w^2} \sim \chi^2_{2(N_D+N_G)} \\ H_1&: \frac{T}{\sigma_w^2 + \sigma_p^2} \sim \chi^2_{2(N_D+N_G)} \end{aligned} \tag{13.11}$$

where χ_m^2 denotes the chi-squared random variable with m degrees of freedom.

13.3.4 Performance Evaluation

Due to lack of information about the primary user, it is quite difficult to estimate a priori probabilities $P(H_0)$ and $P(H_1)$, hence we propose the Neyman-Pearson hypothesis test, which aim to maximize the detection probability under the given false-alarm probability. From (13.10) we get the false alarm probability

$$P_f = P_r(T > \lambda | H_0) = Q_{\chi^2_{2(N_D+N_G)}}\left(\frac{\lambda}{\sigma_w^2}\right) \tag{13.12}$$

where $Q_{\chi_n^2}(\cdot)$ is the right-tail probability for the chi-squared random variable with m degrees of freedom. Similarly the detection probability can be expressed as

$$P_D = P_r(T>\lambda|H_1) = Q_{\chi^2_{2(N_D+N_G)}}\left(\frac{\sigma_w^2}{\sigma_w^2+\sigma_p^2}Q^{-1}_{\chi^2_{2(N_D+N_G)}}(P_f)\right) \tag{13.13}$$

By the central limit theorem(CLT), we know that when N_G is sufficiently long, the chi-squared distribution approaches the Gaussian distribution. Using the CLT we can approximate the detection problem as

$$\begin{aligned} &H_0\text{: } T \sim N(2(N_D+N_G)\sigma_w^2, 4(N_D+N_G)\sigma_w^4) \\ &H_1\text{: } T \sim N(2(N_D+N_G)(\sigma_w^2+\sigma_p^2), 4(N_D+N_G)(\sigma_w^2+\sigma_p^2)^2) \end{aligned} \tag{13.14}$$

Thus we derive P_f and Pd as follows

$$\begin{aligned} P_f &= Q\left(\frac{\lambda}{\sqrt{4(N_D+N_G)\sigma_w^2}} - \sqrt{N_D+N_G}\right) \\ P_D &= Q\left(\frac{\sigma_w^2}{\sigma_w^2+\sigma_p^2}\left(Q^{-1}(P_f) - \frac{\sqrt{N_D+N_G}\sigma_p^2}{\sigma_w^2}\right)\right) \end{aligned} \tag{13.15}$$

where $Q(x) = erfc(x)$ is the right-tail probability for the Gaussian random variable.

As it can seen from the expression, the performance of Pd increase as $N_D + N_G$ grow, namely the sensing time is enlarged, which means that the performance is improved. Moreover, if we fixed the expected detection probability, thus by applying the CP-ED algorithm, the length of idle period can be reduce, and this lead to a shorter detecting time.

13.4 Simulation Results

An OFDM system with the carrier's frequency of 2 GHz is built up, and the bandwidth is 1 MHz, the carrier numbers are 64, separately. The traditional energy detection and the CP-ED algorithm is applied, respectively; the relationship of bit error with SNR is shown in Fig. 13.2.

It can be seen from Fig. 13.2 that the detecting probability of CP-ED is higher than the traditional energy detection method in the condition that the required false alarm probability is equal, which means that the performance of CP-ED is better in the receiver.

Moreover, notice that the CP-ED method utilizes the sample points of the cyclic prefix, which indicates that it has a relatively longer sensing time than the traditional energy detection, it makes us to assume that the CP-ED sensing scheme can use less sample points in the idle period when the detection probability is fixed. Thus we simulate the comparison of detecting time of the two methods in Fig. 13.3. From the simulation results we find that when the detection probability is equal, the detection samples of the CP-ED scheme are less than the traditional energy

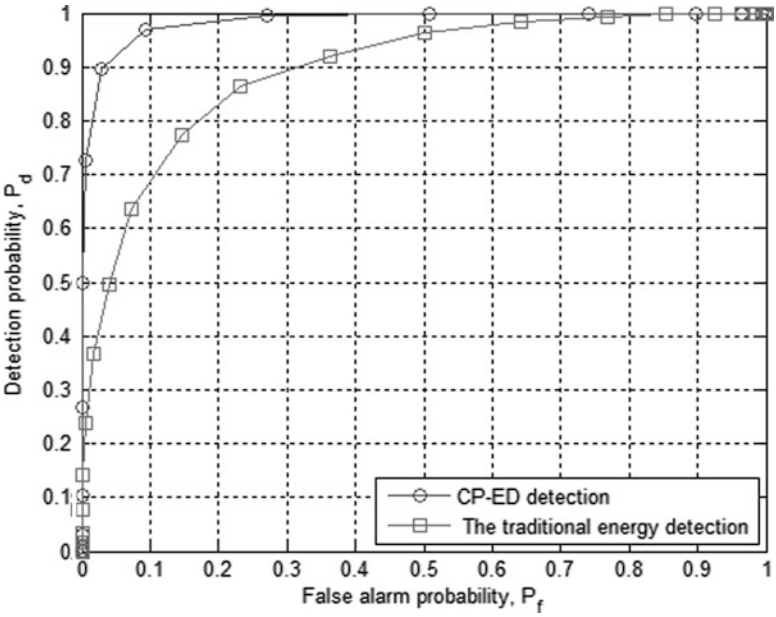

Fig. 13.2 The ROC comparison of the CP-ED scheme and the traditional energy detection

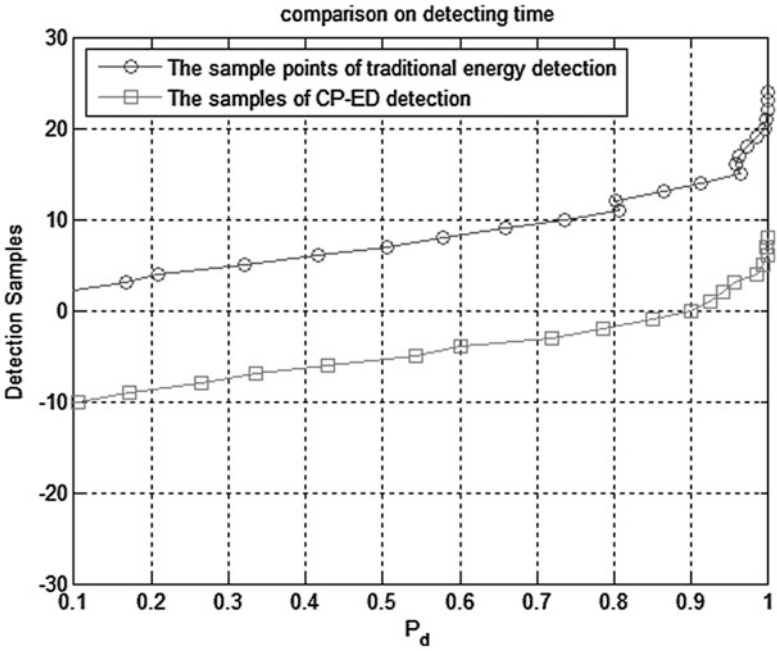

Fig. 13.3 The comparison of the two spectrum sensing scheme in sensing time

detection, which means that the required idle period can be shorten when applying the CP-ED sensing method. And this is coordinated with our expectation.

It can be seen that the performance of CP-ED algorithm is better than the traditional energy detection method from the above simulation results and theory analysis.

13.5 Conclusion

In this chapter, a spectrum detection algorithm for OFDM-based cognitive radio system is proposed, which utilize both the idle period as the conventional energy detection scheme and the cyclic prefix that is unique in the OFDM system. It can be seen that the detection probability can be increased under this scheme by analysis and simulation, and it indicates that the scheme is an appropriate sensing method in the OFDM-based cognitive system.

Acknowledgments This work is supported by the Fundamental Research Funds for the Central Universities (Grant No. HIT. NSRIF. 2010091), the National Natural Science Foundation of China (Grant No. 61201143), the National Science Foundation for Post-doctoral Scientists of China (Grant No. 2012 M510956), and the Post-doctoral Funds of Heilongjiang Province (Grant No. LBHZ11128).

References

1. Mitola J, Maguire GQ (1999) Cognitive radio: making software radios more personal. IEEE Pers Comm 6(4):13–18
2. Zengyou Sun, Qianchun Wang, Chenghua Che (2010) Study of cognitive radio spectrum detection in OFDM system. In: Proceedings of the 2010 Asia-Pacific conference on wearable computing systems, Shenzhen, pp 235–238
3. Refik Fatih USTOK (2010) Spectrum sensing techniques for cognitive radio systems with multiple aneennas. June 2010. http://library.iyte.edu.tr/tezler/master/elektrikveelektronikmuh/T000842.pdf
4. Anand Chandran, Anantha Karthik.R (2010) Evaluation of energy detector based spectrum sensing for OFDM based cognitive radio. In: Proceedings of the international conference on communication and computational intelligence—2010, Kongu Engineering College, Perundurai, Erode, 27–29 Dec 2010, pp 163–167
5. Jianping An (2010) Spectrum sensing for OFDM systems based on cyclostationary statistical test. In: Proceedings of the 2010 6th international conference on wireless communications networking and mobile computing (WiCOM), Chengdu, 23–25 Sept 2010, pp 1–4
6. Van Trees HL (2007) Detection, estimation, and linear modulation theory. Publishing House of Electronics Industry, Beijing, pp 187–286
7. Khambekar N, Dong L, Chaudhary V (2007) Utilizing OFDM guard interval for spectrum sensing. In: Proceedings of the IEEE wireless communications and networking conference, Hong Kong, Mar 2007, pp 38–42
8. Dong Chunli, Yang Zhen, Zhang Hui, Tian Feng (2010) Research of spectrum holes detection algorithms for cognitive radio. In proceedings of the 2010 12th IEEE international conference on communication technology (ICCT), Nanjing, 11–14 Nov 2010, pp 1449–1452

Chapter 14
Power Allocation in OFDM Based Cognitive Radio System

Ishrat Maherin and Qilian Liang

Abstract In this chapter, we investigate one suboptimal power allocation scheme for an OFDM based cognitive radio system. Optical power allocation for secondary user in OFDM subcarrier is complex since it has a power as well as an interference constraint. Mathematical analysis shows that interference between primary and secondary in OFDM based system depends on theirs spectral distance. In our suboptimal method we consider the spectral distance between the secondary and primary user and modify the traditional water-filling algorithm. By applying our suboptimal power allocation method, it is possible that we can get good performance comparable to the optimal scheme. We compare our method with traditional power allocations schemes like equal power allocation and water filling power allocation. Result shows that distance dependent modified water filling (DDMWF) scheme can achieve the highest data rate for the cognitive radio based Secondary user.

Keywords Cognitive radio • Water filling • OFDM • Power allocation

14.1 Introduction

Cognitive Radio solves the scarcity of spectrum for wireless communication by dynamically using the available spectrum. Most of the allocated spectrum is underutilized in today's world as shown by the Federal Communications Commission report [1]. A cognitive radio can sense the spectrum of the licensed user known as primary user (PU) and identify the underutilized spectrum known as white space or spectrum hole. This spectrum hole can be opportunistically used by the secondary user (SU) provided that the interference power introduced to the occupied spectrum is below a certain threshold known as interference temperature limit.

I. Maherin • Q. Liang (✉)
Department of Electrical Engineering, University of Texas at Arlington, Arlington, TX, USA
e-mail: liang@uta.edu

Q. Liang et al. (eds.), *Communications, Signal Processing, and Systems*, Lecture Notes in Electrical Engineering 202, DOI 10.1007/978-1-4614-5803-6_14,

The overall objective of this chapter is to increase the spectral efficiency by allocating the subcarrier power and increasing the SU's transmitted data rate and keeping the interference under limit. In order to achieve that goal we propose a CR network that is based on OFDM. Orthogonality of the OFDM system allows high spectral efficiency and guarantees less cross talk between the subcarriers. It simplifies the equalizer and it does not need guard interval between the carriers.

In literature, [2] proposes power control schemes for secondary femto cells and outage probability constraints are upper bounded by interference limits. It takes into account the Raleigh fading channel and also proposes an iterative power control schemes. In [3] besides the interference power constraints transmit power constraint for SU is also considered. As in [4], various combinations of peak and average power constraints are considered. Maximum capacity for MIMO-OFDM system is derived in [5]. Minimization of co-channel-interference in WLAN by cognitive radio based power adjustment techniques are studies in [6]. Interference aware radio resource allocation is studied in OFDM based cognitive radio network in [7]. Throughput optimization is studied in [8]. In [9] OFDM based CR power allocation schemes are proposed. Our work simplified that optimal scheme in [9] to reduce the processing complexity. Since optimal scheme, requires several steps, in our method we did consider the interference constraint and find the suboptimal power allocation that gave better result than the traditional equal power allocation schemes.

The rest of the chapter is organized as follows. In Sect. 14.2, we present the system model. In Sect. 14.3, we do the mathematical analysis. In Sect. 14.4, we propose the distance dependent modified water-filling algorithm (DDMWF). In Sect. 14.5, we present the simulation results. We conclude this chapter and propose some future research in Sect. 14.6.

14.2 System Model

In our chapter we follow collocated scenario where both the primary user's receiver and secondary user's receiver co-exist in same user's device in future generations laptops as shown in Fig. 14.1. One of these radios can be based on CR technology.

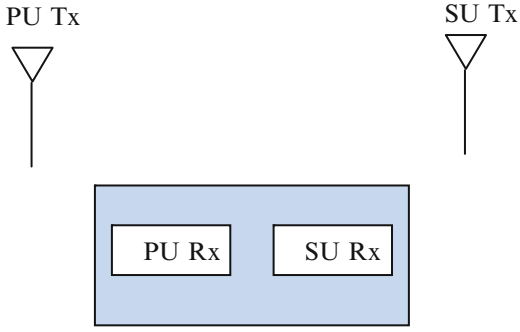

Fig. 14.1 Location of primary and secondary transmitter and receiver. Primary and secondary receivers are collocated

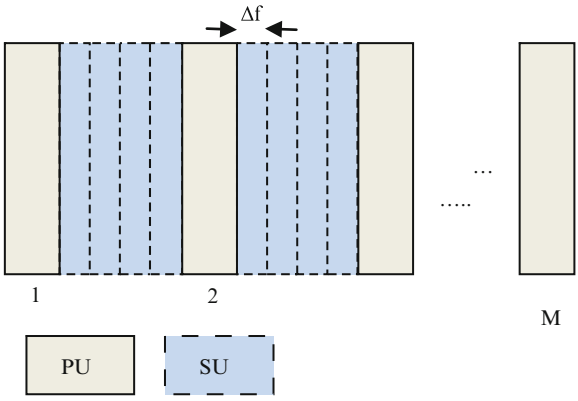

Fig. 14.2 Frequency domain distribution of primary and secondary user

In frequency domain we consider the unoccupied bands are located on each side of the PU band as shown in Fig. 14.2 [4]. Suppose we have M number of primary user band and available bandwidth for the SU is divided into N subcarrier of OFDM based systems. We assume there are three instantaneous fading gains that are known to the transmitter of the SU. The fading gain between SU transmitter and SU's receiver for the nth carrier is denoted as $h_n^{ss,}$ the gain between the SU's transmitter and the mth PU receiver is denoted as h_m^{sp} and the gain between the mth PU's transmitter and SU's receiver denoted as h_m^{ps}. It is assumed that each subcarrier transmits in Raleigh fading channel and the channels are estimated by channel estimation mechanism before the transmission. SU can measure h_n^{ss} and h_m^{ps}. Since both PU and SU are located in the same device the channel gain h_m^{sp} will be send to the transmitter of the SU. The bandwidth for each subcarrier is Δf. There are two types of the interference one is introduced by PUs and the other is introduced by SU's band.

14.3 Mathematical Analysis

It is already been shown in several chapters [9, 10] that the mutual interference played an important role in determining the power allocation scheme. Two kind of interferences are introduced in OFDM system, one is introduced by the SU to the PU and the other is between SUs. Both of them depend on the spectral distance and transmit power.

The power density spectrum assuming the nyquist pulse can be written as [9],

$$\Phi_n(f) = P_n T_s \left(\frac{sin\pi f T_s}{\pi f T_s} \right)^2 \tag{14.1}$$

where T_s is the symbol duration and P_n is the transmit power allocated to the nth subcarrier. The interference that will be introduced to the PU is the integration of the Power density spectrum across the PU band. This can be expressed as,

$$I_m{}^{(n)}(d_{nm}, P_n) = |h_n{}^{sp}|^2 P_n T_s \int_{d_{nm}-B_{M/2}}^{d_{nm}+B_{M/2}} \left(\frac{sin\pi f T_s}{\pi f T_s}\right)^2 df \tag{14.2}$$

where d_{nm} represents the distance in frequency between the nth subcarrier and mth PU band and B_M is the band width of the mth primary.

The interference introduced by the mth PU to the nth subcarrier is denoted as, $I_n{}^{(m)}(d_{nm},P_m)$ will be the integration of the power density spectrum of the PU signal across the nth subcarrier can be written as [9],

$$I_n{}^{(m)}(d_{nm}, P_m) = |h_n{}^{ps}|^2 \int_{d_{nm}-\Delta f/2}^{d_{nm}+\Delta f/2} E\{I_N(w)\} dw \tag{14.3}$$

where, $E\{I_N(w)\}$ can be written as,

$$E\{I_N(w)\} = \frac{1}{2\pi L} \int_{-\pi}^{\pi} \Phi PU(e^{jw}) \left(\frac{\sin(w-\Psi)L/2}{\sin(w-\Psi)L/2}\right)^2 d\Psi \tag{14.4}$$

is the power density spectrum of the PU after L FFT process. Here w represents the frequency normalized to the sampling frequency. To maximize the capacity formula we can use the Shannon's capacity formula under the power and interference constraints that can be expressed mathematically as,

$$C = \max_{P_n} \sum_{n=1}^{N} \Delta f \log_2 \left(1 + \frac{|h_n{}^{ss}|^2 P_n}{\sigma^2 + I_{PU}}\right) \tag{14.5}$$

subject to

$$\sum_{m=1}^{M} \sum_{n=1}^{N} I_m^{(n)}(d_{nm}, P_n) \leq I_{th} \tag{14.6}$$

and

$$P_n \geq 0, \quad \forall i = 1, 2, ...N\triangle \tag{14.7}$$

where I_{PU} can be expressed as,

$$I_{PU=}\sum_{m=1}^{M} I_{n}^{(m)}(d_{nm}, P_m) \tag{14.8}$$

where C denotes transmission capacity of the secondary user, N is the total numbers of the subcarriers, I_{th} denotes the interference temperature of the M, PU bands.

The capacity can be maximized by [9],

$$P_n{}^{*} = \max\left\{0, \frac{1}{\lambda \sum_{m=1}^{M} Q_n{}^{(m)}} - \frac{\sigma^2 + I_{PU}}{|h_n{}^{ss}|^2}\right\} \tag{14.9}$$

Where λ is the Lagrange multiplier for the inequality, where Q_{nm} can be expressed as,

$$Q_n{}^{(m)} = |h_m{}^{sp}|^2 T_s \int_{d_{nm}-B_{M/2}}^{d_{nm}+B_M/2} \left(\frac{\sin \pi f T_s}{\pi f T_s}\right)^2 df \tag{14.10}$$

From (14.10) and (14.6) we can say conclude

$$\sum_{m=1}^{M}\sum_{n=1}^{N} Q_n^{(m)} \times \max\left\{0, \frac{1}{\lambda \sum_{m=1}^{M} Q_n^{(m)}} - \frac{\sigma^2 + I_{PU}}{|h_n{}^{ss}|^2}\right\} \leq I_{th} \tag{14.11}$$

14.4 Distant Dependent Modified Water Filling

The objective of water filling is to achieve maximum data rate while exploiting the varying channel gain. The channel with better channel gain is allocated higher power so that better data rate is achieved. For the Cognitive radio the optimized power allocation is achieved by (14.9). Since the calculation of λ value is quiet complicated and required several steps, we try to avoid this optimal solution. If we ignore the second term in (14.9) the power is inversely proportional to the Q_n which depends on the spectral distance between primary and secondary. Then we can apply distant dependent modified water filling (DDMWF) where the initial water line is achieved by allocating the power in step method. We consider five subcarriers where the middle one will be given the highest power considering that it is furthest from the primary. Two of the subcarrier will be given the medium step

power and two of them will be given the lowest power as they are closest. The total power is still remain constant and depend on the given SNR. Then we repeat this allocation for three different blocks and total 15 subcarriers are considered on both sides of the PU. Let P_T denotes total power, sc is no of subcarrier per block and l is the no of block, for our particular case we divide the steps of the waterline, by the following:

1. If we have sc = 5 per block, then three strong subcarriers in three different block has initial power allocation as

$$P_i = \frac{P_T}{3 \times l} \tag{14.12}$$

2. If we have sc = 5, then six of the subcarriers can have the initial power as,

$$P_i = \frac{P_T}{6 \times l} \tag{14.13}$$

3. If we have sc = 5, six of the subcarriers can be given the initial power as,

$$P_i = \frac{P_T}{9 \times l} \tag{14.14}$$

After the initial power allocation the water line will be updated and sub-optimal solution will be found by the iterative process. Finally the capacity of the secondary user is measured. We made the assumption that since the sub-carrier that is spectrally far from the PU, has been given the highest power it will cause less interference and the interference threshold will not exceed the limit. However, we need to check the interference threshold time to time. If it exceeds the given threshold then the waterline has to be updated with a factor.

14.5 Result

In this chapter we consider the number of subcarriers N is 15 and no of primary user band, M is 2. Figure 14.3 shows the consecutive orthogonal subcarriers in Time domain. The capacity versus the SNR is plotted in Figs. 14.4, 14.5, and 14.6. SNR is varied from −15 to 30. The channel is considered as Raleigh fading channel.

In Fig. 14.4 we compare the traditional water-filling algorithm with equal power allocation without the interference constraint. This time no of subcarrier is taken as 4. It shows that water-filling algorithm performs much better than the equal power allocation.

In Fig. 14.5 we compare the traditional water-filling algorithm with equal power allocation without the interference constraint. This time no of subcarrier is taken as

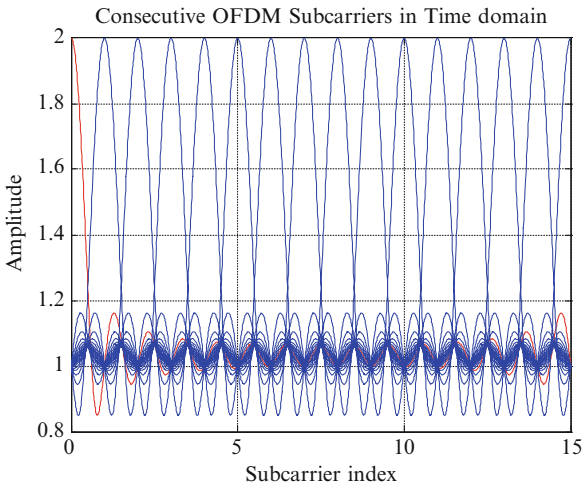

Fig. 14.3 Consecutive orthogonal subcarriers in time domain

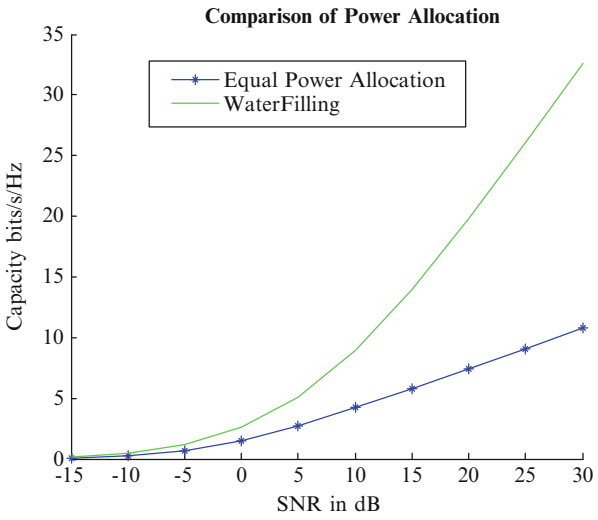

Fig. 14.4 Capacity versus SNR for traditional water-filling and equal power allocation with four different channels

16. Comparing the Figs. 14.4 and 14.5 it can be said that, when the no of subcarrier is increased, the capacity is higher.

In Fig. 14.6 DDMWF is compared with traditional water filling and equal power allocation scheme. This time no of subcarrier is taken as 15. The initial water line is set by the (14.12), (14.13), and (14.14). Clearly DDMWF out performs the traditional water-filling as well as the equal power allocation. Equal power allocation performed worst with interference and without interference case. This result proved

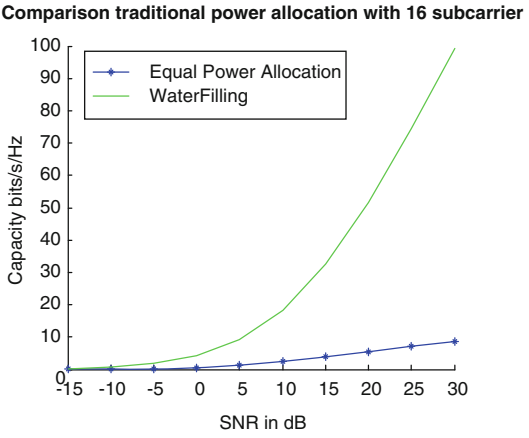

Fig. 14.5 Capacity versus SNR for traditional water-filling and equal power allocation with 16 different subcarriers

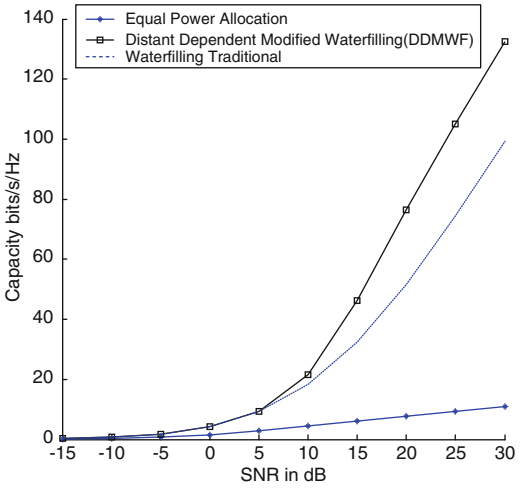

Fig. 14.6 Capacity versus SNR for three different power allocation schemes. OFDM based distant dependent modified water-filling (DDMWF) outperforms the traditional scheme

the suboptimal power allocation in CR based OFDM system is a good method to increase the data rate of the spectrum and the cognitive radio user as a whole. From Fig. 14.6 it is clear when the SNR is low all three methods have similar performance.

14.6 Conclusion

In this chapter, we investigate one suboptimal power namely distant dependent modified water filling (DDMWF). We consider the spectral distance of the Primary and secondary user and set the initial power allocation based on this. After this allocation water line is updated and suboptimal solution is found by the iterative

process. By applying our DDMWF suboptimal power allocation method, it is possible that we can get good performance comparable to the optimal scheme. We compare our method with traditional power allocations schemes like equal power allocation and water filling power allocation. Result shows that distance dependent modified water filling scheme can achieve the highest data rate for the cognitive radio based Secondary user. This method is applied to collocated future laptop system. In future we will change the scenario to wireless LAN and found the optimal and suboptimal power allocation schemes.

Acknowledgments This work was supported in part by National Science Foundation (NSF) under grant CNS-0964713, CNS-1050618 and office of Naval research (ONR) under grant N00014-11-1-0071 and N00014-11-1-0865.

References

1. Federal Communications Commission (2002) Spectrum Policy Task Force Trans Rep. ET Docket no. 02–135, Nov 2002
2. Kang X, Liang Y, Nallanathan A, Garg HK, Zhang R (2009) Optimal power allocation for fading channels in cognitive radio networks: ergodic capacity and outage capacity. IEEE Trans Wireless Commun 8(2):940–950
3. Chai CC, Che YH (2010) Power control for cognitive radios in Nakagami fading channels with outage probability requirement. In: IEEE Global telecommunication conference (GLOBECOM 2010), Miami, Florida, 6–10 Dec 2010, pp 1–5
4. Shahrokh H, Mohamed-pour K (2010) Sub-optimal power allocation in MIMO-OFDM based cognitive radio networks. In: 6th International conference wireless communication networking and mobile computing (WiCOM), Chengdu, China, 23–25 Sept 2010, pp 1–5
5. Hu Y, Kuo G (2007) Space-time-frequency domain water-filling in MIMO-OFDM fading system. In: IEEE conference on vehicular technology, Baltimore, MD, 22–25 Apr 2007, pp. 2475–2480
6. Tiwary PK, Maskey N, Khakurel S, Sachdeva G (2010) Effects of co-channel interference in WLAN and cognitive radio based approach to minimize it. In: International conference on advances in recent technologies in communication and computing (ARTCom), Kottayam, India, 2010, 16–17 Oct 2010, pp 158–160
7. Almalfouh SM, Stüber GL (2011) Interference-aware radio resource allocation in OFDMA-based cognitive radio networks. IEEE Trans Veh Technol 60(4):1699–1713
8. Babaei A, Jabbari B (2010) Throughput optimization in cognitive random wireless ad hoc networks. In: IEEE conference on global telecommunication (GLOBECOM 2010), Miami, Florida, 6–10 Dec 2010, pp 1–5
9. Bansal G, Hossain MJ, Bhargava VK (2008) Optimal and suboptimal power allocation schemes for OFDM-based cognitive radio systems. IEEE Trans Wireless Commun 7 (11):4710–4718
10. Jian W, Longxiang Y, Xu L (2011) Subcarrier and power allocation in OFDM based cognitive radio systems. In: International conference on intelligent computer technology and automation (ICICTA), Shenzhen, China, vol 2, 28–29 Mar 2011, pp 728–731

Part V
Image Processing

Chapter 15
The Infrared Image Enhancement Approach Based on Directionlet Transform*

Xin Zhou and Wei Wang

Abstract The chapter proposed a new multi-scale infrared image enhancement method based on directionlet transform, using directionlet transform to decompose the image's frequency domain, and the establishment of a multi-directional anisotropic filtration has enhanced the infrared image. The experiment has showed that the method has achieved better result in the aspects of visual effect and objective evaluation than the general transform domain enhancement method.

Keywords Infrared image • Image enhancement • Directionlet transform

15.1 Introduction

As the target in image and background of it have been influenced by the thermal balance, the infrared radiation of longer wavelength, and long transmission distance which leads to attenuation, the infrared image usually shows the strong correlation between poor textures, visual effects and fuzzy features in space. We need to enhance the important information in the infrared image, while weakening the redundant information in it.

The degree of change of the gray value of the infrared image which varies according to the spatial location can be expressed by the spatial frequency. For the larger points of the temperature gradient, the characteristics of the edges, curves, and noise have high spatial frequencies, that is to say: the pixel gray values in a narrow region changes faster. As far as the main structure of the tested structure which has larger surface area is concerned, the temperature distribution is more uniform and the

*Funded by Tianjin Normal University Doctoral Fund(52X09008)

X. Zhou (✉) • W. Wang
College of Physics and Electronic Information Science, Tianjin Normal University, Tianjin 300387, China
e-mail: zhouxintjnu@126.com; wangweivip@tju.edu.cn

Q. Liang et al. (eds.), *Communications, Signal Processing, and Systems*, Lecture Notes in Electrical Engineering 202, DOI 10.1007/978-1-4614-5803-6_15,

infrared temperature structure is stable, therefore, the gray value changes slowly, and thus the spatial frequency is low. The transformation domain enhancement methods first convert the image's pixel space gray variation into the frequency space in some way, and then process the image according to its frequency characteristics, and that is the component is suppressed within a certain frequency range and the other components enhanced or not affected, thereby the frequency distribution of the output image could be changed to achieve the purpose of image enhancement. The researchers such as Raghuveer M.R. and Sadjadi Firooz A. etc. have applied the wavelet transform in infrared image enhancement and de-noising works providing the better image for pattern recognition and classification processing [1, 2].

Although the wavelet transform has been applied in the field of image processing widely, however, the two-dimensional wavelet transform basis function is built up in horizontal and vertical directions, and it can only describe the singularity features in the infrared images, and cannot represent anisotropic boundary line characteristics. To express the singular characteristics of the two-dimensional images in the "Optimal" way, the multi-scale geometric analysis tool which has developed independently in the subject of mathematical analysis was introduced to the field of image processing, mainly including the, ridgelet, curvelet, beamlet, wedgelet, bandlet, and contourlet, and they make up for defects in expressing the image, therefore the image can be expressed more sparsely.

However, compared with the wavelet transform, the multi-scale tool has some shortcomings, for instance, the implementation of the transformation is in need of highly complex over-sampling and the filter cannot be separated, or transform correlation filter design is performed in the continuous domain (e.g., curvelet), therefore, it is difficult to directly apply to discrete two-dimensional image [3].

As far as the standard separable two-dimensional wavelet transform is concerned, it has the following two shortcomings in the analysis of images:

1. Using isotropic filter group, and isotropic wavelet basis cannot well described the highly anisotropic features in the image, and it cannot provide a sparse image in the edge of the image, resulting in many wavelet coefficient.
2. The isotropic filter group have only been established in the horizontal and vertical direction, therefore, the high-pass filter in transform has vanishing moments only in the two directions, and thus it is difficult to describe the multi-directional characteristics of the image.

For the second question, the researchers have proposed the basis function which can match anisotropic objects in the image, known as anisotropic wavelet transform (short for AWT). In the AWT, along the horizontal direction, the number of transformation is n_1; along the vertical direction, the number of transformation is n_2, denoted by $AWT(n_1, n_2)$, which are not necessarily equal, and the standard wavelet transform can be expressed as $AWT(1, 1)$. AWT can improve the approximation performance of the general image, but it is like the still standard wavelet transform which can only use horizontal and vertical changes of direction, and the high-pass filter in transformation only have vanishing moments in the two directions, and still could not descript the singular feature of the multi-direction of the image [4]. Therefore, we need to introduce a multi-directional anisotropy of transformation.

15.2 Directionlet Transform

The directionlet transform proposed by German researchers Vladan is the multi-directional anisotropy based upon the integer lattice [5–8]. It adopts multi-directional anisotropy basis functions, therefore, it has more advantages in expressing the image than the average wavelet transform. At the same time, it only uses the one-dimensional filter banks with separable filtering and critical structures, and can be reconstructed totally, thus, as far as the computational complexity is concerned, it has more advantage than other second generation wavelet transform. The directionlet transform is a new multi-scale analysis tools

When using one-dimensional filter banks to conduct multi-directional two-dimensional separable wavelet transform, we select any two rational slope $r_1 = b_1/a_1$ and $r_2 = b_2/a_2$'s digital line direction to filtering and down-sampling, however, When the critical sampling is enhanced, Two digital lines will have the issue of direction of mutual inductance, that is, along the slope r_1 and r_2, the concept of the digital line cannot provide a systematic rule for the down-sampling of the repeated filtering and repeat sampling.

Therefore, Vlada has proposed the multi-directional filtering and down-sampling which are based on lattice. First, chose any two reasonable slopes $r_1 = b_1/a_1$ $r_2 = b_2/a_2$'s directions in grid space z^2, expressed in matrix as:

$$\mathbf{M}_\Lambda = \begin{bmatrix} a_1 & b_1 \\ a_2 & b_2 \end{bmatrix} = \begin{bmatrix} d_1 \\ d_2 \end{bmatrix}, a_1, a_2, b_1, b_2 \in Z, n_1 \neq n_2 \tag{15.1}$$

The direction along the slope r_1 of the vector r_1 is called the change of direction; the direction along the slope r_2 of the vector d_2 is called the queue direction. Along the skewed collinear transform of the transformation of the lattice in the queue application, it has n_1 and $n_2 (n_1 \neq n_2)$ transformation in an iterative steps along the transform direction and queue direction. Marked as $\mathrm{S} - \mathrm{AWT}(\mathbf{M}_\Lambda, n_1, n_2)$. From $\mathbf{M}_\Lambda$, the integer lattice Λ can be ascertained. According to the case theory, z^2 has been divided into the $|\det \mathbf{M}_\Lambda|$'s co-set which is about the entire integer lattice Λ. The filtering and down-sampling has been conducted in every co-set, and then the remaining pixels belong to the lattice Λ' of integer lattice Λ, the matrix $\mathbf{M}'_\Lambda$ generated accordingly. Thereout, sparse representation of the anisotropic object on the direction of the image can be obtained. The principle is shown as in Fig. 15.1 (the change of direction in the figure is 45°).

The image which has gone through the above mentioned directionlet transform has a very sparse coefficient, and then can obtain more directional information, which can be better used to describe the edge contour of the infrared image.

15.3 The Infrared Image Enhancement

When adopting the directionlet transform in the infrared image enhancement of the high temperature components, firstly, the original image has been conducted by co-set decomposition according to a given generated matrix to acquired a series of sub-

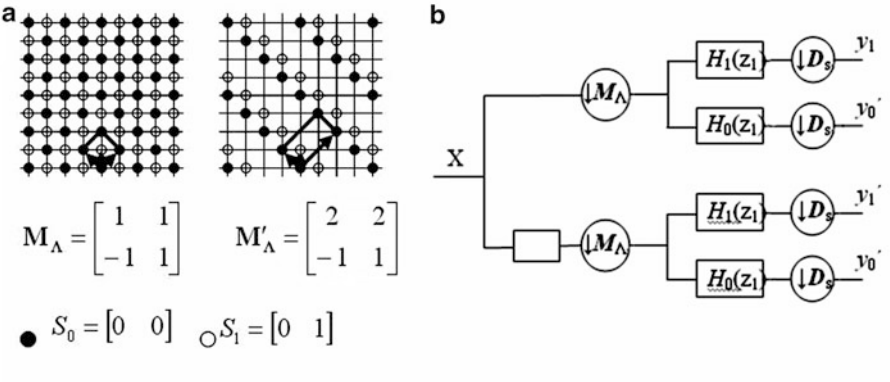

Fig. 15.1 Based on the integer lattice's filtering and down sampling. (**a**) Expressed with the generator matrix, (**b**) two-dimensional dual-channel filter

graph. Each of the two relative displacement between the two co-sets make their associated sub-graph correspond to a directional information. If the sub-graphs of a region in the image contain the edge and contour information, the sub-graph subtraction will be displayed in the region. And the direction perpendicular to the relative displacement vector is the main direction of the edge information. After the acquisition of the edge information, the enhanced image can be acquired after the inversed transform of the co-set decomposition. However, the calculation would also be more complex. The detailed process is: divide the $|\det \mathbf{M}_A|$'s co-set which can generate matrix, conducting one-dimensional filtering and the second sampling in the process of changing of direction, which is equivalent to generate the horizontal direction filtering, after the rotation of generating matrix. Therefore, the complexity of calculation is equivalent to calculating the $|\det \mathbf{M}_A|$'s wavelet transform. In the following parts, the main directions: 0°, 90°, ± 45° have been adopted as the transform direction.

15.4 Expriments

After the gray-scale transformation towards the high temperature components, the infrared image has been adapted the directionlet transform to enhance the quality of the image, and then compared with the histogram equalization, and the standard wavelet transform, as shown in chart 2. From the visual effect, the approach provided by this chapter is better than the Wiener filtering and wavelet transform as far as the performance of the intensity about the edge of the high temperature components is concerned, The directionlet transform approach has better performance in the image information maintenance and detail enhancement.

An objective evaluation method of image quality is the use of physical methods to measure the physical characteristics of the image, to arrive at the effect of the

Table 15.1 The comparison of the infrared image's transform domain of high-temperature object

	Original map	Histogram equalization	Wavelet	Directionlet
SNR	—	11.079	10.079	12.079
PSNR	—	12.117	11.117	14.117
Average gradient	14.145	12.145	13.145	17.145
SD	13.853	13.853	14.853	18.853

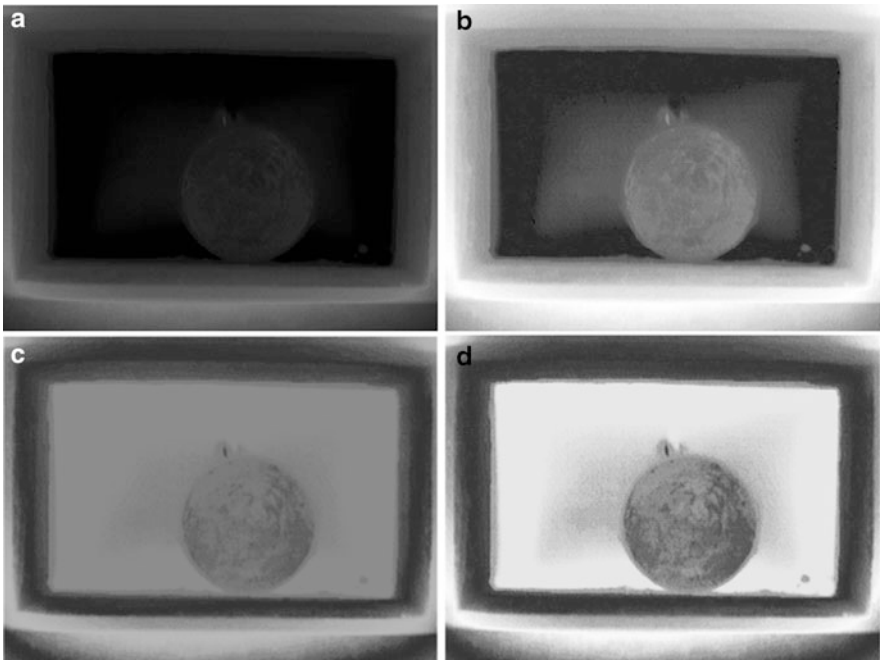

Fig. 15.2 The contrast of the enhanced infrared image of the high temperature components. (**a**) Component artwork, (**b**) histogram equalization enhancement, (**c**) wavelet transform enhancement, (**d**) directionlet transform enhancement

treatment. The objective evaluation method plays an important role in image processing applications, and can be adopted in the infrared image enhancement evaluation. The following objective evaluation is commonly used: signal to noise ratio (SNR), peak signal-to-noise ratio (PSNR), the average gradient, and the standard deviation. The objective evaluation to evaluating the above-mentioned enhancement method is shown in Table 15.1. From Table 15.1, the enhancement results based on directionlet transform enhancement is superior to other enhancement approaches.

Figure 15.3 is the second group of infrared image enhancement experiments. Compared with Figs. 15.2 and 15.3 contains more texture and detail information, such as building outline, windows and chimneys, etc.. In the process of enhancing and de-noising, these useful information should be retained and enhanced. From the

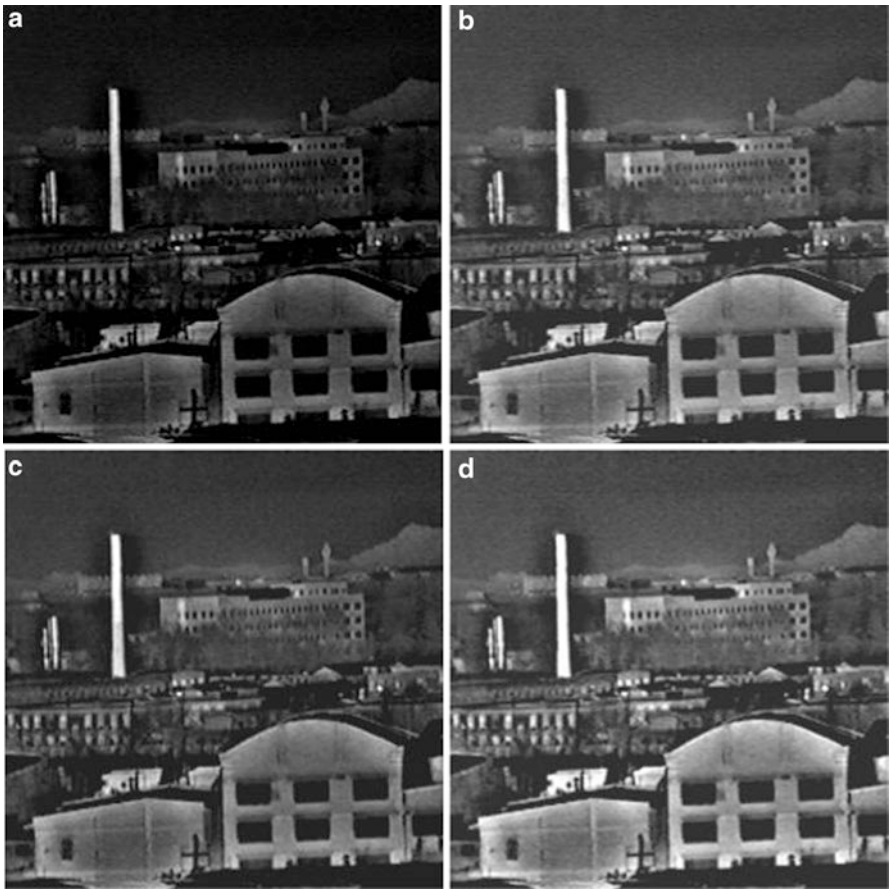

Fig. 15.3 Infrared image of buildings enhancement experiments. (**a**) Infrared image of buildings, (**b**) wavelet transform enhancement, (**c**) contourlet transform enhancement, (**d**) directionlet transform enhancement

Fig. 15.3b, c, and d is much clearer than the original image (a), and the visual effect is also much better than the original image. Some of the details in the images (b) and (c) are somewhat vague, this is caused by the wavelet transform not having the anisotropy and contourlet transform not having translational invariance. Relatively speaking, chart (d) is much better than (b) and (c) in the clarity of the details of the image. It can be seen from Table 15.2, and the values of the enhanced image's signal to noise ratio, the peak signal to noise ratio, the average gradient and standard deviation which are obtained with directionlet transform is higher than the other two methods. Therefore, the directionlet transform's approach can enhance the infrared image with more detailed information much better than the other two methods.

Table 15.2 The comparison of the enhanced infrared image transform domain of the building

	Original map	Histogram equalization	Contourlet	Directionlet
SNR	—	18.241	18.849	19.972
PSNR	—	23.473	23.981	24.210
Average gradient	23.954	26.003	26.915	27.411
SD	25.710	25.909	26.702	26.841

15.5 Conclusion

The infrared image enhancement method is based on directionlet transform using anisotropic filter group, and changes the shortcomings of the standard wavelet transform which cannot accurately describe the anisotropy of the image in the isotropic wavelet basis; at the same time, multi-directional filter banks are more in line with the multi-directional characteristics of the infrared image. The experiments show that this method can effectively highlight the edge of the profile of the measured target to improve the clarity of the infrared images.

References

1. Raghuveer MR (1997) Image enhancement and denoising by wavelet transform for concealed weapon detection. Proc SPIE Int Soc Opt Eng 2942:112–122
2. Sadjadi Firooz A (2004) Infrared target detection with probability density functions of wavelet transform subbands. Appl Opt 43(2):315–323
3. Liu Qi-hai, Lin Yu-chi, Feng Wei-chang (2010) Novel different-source image fusion algorithm using lifting Directionlet transform. Infrared Laser Eng 39(2):358–362
4. Velisavljevic V, Beferull-Lozano B, Vetterli M et al (2006) Directionlets: anisotropic multidirectional representation with separable filtering. Image ProcessIEEE Trans 15(7):1916–1933
5. Velisavljevic V (2009) Low-complexity Iris coding and recognition based on directionlets. Inform Forensics Secur IEEE Trans 4(3):410–417
6. Velisavljevic V, Beferull-Lozano B, Vetterli M (2007) Space-frequency quantization for image compression with directionlets. Image Process IEEE Trans 16(7):1761–1773
7. Velisavljevic V, Beferull-Lozano B, Vetterli M (2007) Efficient image compression using directionlets. In: Information, Communications & Signal Processing, 2007 6th International Conference on Digital Object Identifier, pp 1–5
8. BAI Jing, HOU Biao, WANG Shuang (2008) SAR image denoising based on lifting direction domain Gaussian scale mixtures model. Chinese J Comput 31(7):1234–1240

Chapter 16
Particle Filter Track-Before-Detect Implementation on GPU

Xu Tang, Jinzhou Su, Fangbin Zhao, Jian Zhou, and Ping Wei

Abstract Track-before-detect (TBD) based on the particle filter (PF) algorithm is known for its outstanding performance in detecting and tracking of weak targets. However, large amount of calculation leads to difficulty in real-time applications. To solve this problem, effective implementation of the PF-based TBD on graphics processing units (GPU) is proposed in this chapter. By recasting the particles propagation process and weights calculating process on the parallel structure of GPU, the running time of this algorithm can be greatly reduced. Simulation results in the infrared scenario are demonstrated to compare the implementation on two types of the graphic card with the CPU-only implementation.

Keywords Track-before-detect • Particle filter • GPU

16.1 Introduction

Classical targets detection and tracking is performed on the basis of pre-processed measurements, which are composed of the threshold output of the sensor. In this way, no effective integrations over time are taken place and much information is lost. To avoid this problem, the track-before-detect (TBD) directly uses un-threshold or low threshold measurements of sensors to utilize the raw information. The TBD-based procedures jointly process more consecutive measurements, thus can increase the signal to noise ratio (SNR), and realize the detection and tracking of weak targets simultaneously.

The scenarios faced by TBD are almost nonlinear and non-Gaussian, so the particle filter (PF) [1] is a reasonable solution. Salmond [2, 3] firstly introduced

X. Tang (✉) • J. Su • F. Zhao • J. Zhou • P. Wei
Department of EE, University of Electronic Science and Technology of China, Chengdu, People's Republic of China
e-mail: tangxu@uestc.edu.cn

Q. Liang et al. (eds.), *Communications, Signal Processing, and Systems*, Lecture Notes in Electrical Engineering 202, DOI 10.1007/978-1-4614-5803-6_16,

the PF implementation of track-before-detect (PFTBD) in infrared scenario. Then, Rutten [4–6] proposed several improved PFTBD algorithms. Boers and Driessen extended the work of PFTBD into radar targets detection and tracking application [7]. PFTBD algorithms have demonstrated the improved track accuracy and the ability to follow the low signal-to-noise ratio (SNR) targets but at the price of an extreme increase of the computational complexity.

In recent years, the graphic process unit (GPU) technology is rapidly developed. It is famous for its significant ability in parallel computing for both the graphic processing and the general-purpose computing. Moreover, NVIDIA puts forward the compute unified device architecture (CUDA) [8] to facilitate a hybrid utilization of GPU and CPU [9]. More specifically, the PF algorithm has been implemented on GPU [10], and achieves significant speedup ratio over the implementation on traditional central process unit (CPU).

From the best of our knowledge, there is no PFTBD algorithm implemented on GPU is given in the literature. Concerned with the new difficulty of PFTBD beyond the PF, we propose a novel implementation of PFTBD algorithm on GPU in this chapter. Different graphic cards are adopted in the simulations. Both of their results show the significant speedup over the implementation on the CPU.

This chapter is organized as follows. Section 16.2 reviews the theory about PFTBD. In Sect. 16.3, we introduce the parallel implementation of PFTBD on GPU and CUDA programming. The simulation results and discussions can be found in Sect. 16.4. Finally, we conclude in Sect. 16.5.

16.2 PFTBD Theory

Consider an infrared sensor that collects a sequence of two-dimensional images of the surveillance region, as in [5]. When the target presents, the state of the target is evolving as a constant velocity model.

16.2.1 Target Model and Measurement Model

The time evolution model of the target used here is a linear Gaussian process:

$$X_k = F \bullet X_{k-1} + \mathrm{Q} \bullet V_k \tag{16.1}$$

where $X_k = [x_k \ \bar{x}_k \ y_k \ \bar{y}_k \ I_k]^T$ is the state vector of the target. x_k, y_k is the position of the target and $\bar{x}_k$, $\bar{y}_k$ is the velocity of the target. I_k is the returned unknown intensity from the target. The process noise V_k is the standard white Gaussian noise. A constant-velocity (CV) process model is used, which is defined by the transition matrix and the process noise covariance matrix

$$F = \begin{bmatrix} F_s & 0 & 0 \\ 0 & F_s & 0 \\ 0 & 0 & 1 \end{bmatrix}, F_s = \begin{bmatrix} 1 & T \\ 0 & 1 \end{bmatrix}. \quad Q = \begin{bmatrix} Q_s & 0 & 0 \\ 0 & Q_s & 0 \\ 0 & 0 & q_2 T \end{bmatrix}, Q_s = q_1 \begin{bmatrix} T^3/3 & T^2/2 \\ T^2/2 & T \end{bmatrix}. \tag{16.2}$$

where T is the period of time between measurements, q_1 denotes q_2 denote the variance of the acceleration noise and the noise in target return intensity respectively.

The existence variable $E_k \in \{e, \bar{e}\}$ evolves according to the transitional probability matrix, $E_k = \prod_{ij}(E_{k-1})$, where $\prod_{ij} = \begin{pmatrix} 1-P_b & P_b \\ P_d & 1-P_d \end{pmatrix}$. P_b is the probability of target birth and P_d is the probability of target disappearance.

The measurement at each time is a two-dimensional image of the interested region consisting of the $n \times m$ resolution cells. The intensity $z_k^{(i,j)}$ of each cell with $i = 1, \ldots, n,\ j = 1, \ldots, m$ is as

$$z_k^{(i,j)} = \begin{cases} h^{(i,j)}(X_k) + W_k^{(i,j)}, & \text{target exists} \\ W_k^{(i,j)}, & \text{no target} \end{cases} \tag{16.3}$$

where $h^{(i,j)}(X_k)$ is the intensity of the target in the cell (i,j) $h^{(i,j)}(X_k)$ is the spread reflection form of target and is defined for each cell by

$$h^{(i,j)}(X_k) = \frac{\Delta_x \Delta_y I_k}{2\pi \sum^2} \exp\left(-\frac{(x_k - i\Delta_x)^2 + (y_k - i\Delta_y)^2}{2\sum^2} \right) \tag{16.4}$$

where Δ_x and Δ_y denote the size of a resolution cell in each dimension. The parameter $\sum$ represents the extent of blurring. Then the likelihood function during the presence and absence of the target in each cell can be written as

$$\begin{cases} p(z_k^{(i,j)} | X_k, E_k = 1) = \frac{1}{\sqrt{2\pi\sigma^2}} \exp\left(-\frac{\left[z_k^{(i,j)} - h^{(i,j)}(X_k)\right]^2}{2\sigma^2} \right) \\ p(z_k^{(i,j)} | X_k, E_k = 0) = \frac{1}{\sqrt{2\pi\sigma^2}} \exp\left(-\frac{\left[z_k^{(i,j)}\right]^2}{2\sigma^2} \right) \end{cases} \tag{16.5}$$

So, the likelihood ratio for cell (i,j) is giving as

$$\ell(z_k^{(i,j)} | X_k, E_k) = \begin{cases} \dfrac{p(z_k^{(i,j)} | X_k, E_k = 1)}{p(z_k^{(i,j)} | E_k = 0)}, & E_k = 1 \\ 1, & E_k = 0 \end{cases} \tag{16.6}$$

where $\ell(z_k|X_k, E_k = 1) \approx \prod_{i\in C_x(X_k)} \prod_{j\in C_y(X_k)} \exp\left(\frac{-h^{(i,j)}(X_k)[h^{(i,j)}(X_k) - 2z_k^{(i,j)}]}{2\sigma^2}\right)$ and $C_x(X_k)$, $C_y(X_k)$ are the index sets of cells that affected by the target in the x and y dimensions. The size of them is determined by the application parameter, such as the resolution of the observation area and the intensity of the target. The bigger of it the more latent information are utilized.

The measurement noise $W_k^{(i,j)}$ in each cell is assumed to be independent white Gaussian distribution with zero mean and variance σ^2. The SNR for the target is defined by $SNR = 10\log\left[(I_k\Delta_x\Delta_y/2\pi\Sigma^2)/\sigma\right]^2(dB)$.

16.2.2 Particle Filter Solution for TBD

The algorithm routine of PFTBD is given as follows:

Draw N_b of birth particles from proposal density $X_k^{(b)i} \sim q(X_k|E_k = 1, E_{k-1} = 0, z_k)$ and unnormalized weights of birth particle are calculated from the likelihood ratio:

$$\tilde{w}_k^{(b)i} = \frac{l(z_k|X_k^{(b)i}, E_k^{(b)i} = 1)p(X_k^{(b)i}|E_k^{(b)i} = 1, E_{k-1}^{(b)i} = 0)}{N_b q(X_k^{(b)i}|E_k^{(b)i} = 1, E_{k-1}^{(b)i} = 0, z_k)} \tag{16.7}$$

where $p(X_k^{(b)i}|E_k^{(b)i} = 1, E_{k-1}^{(b)i} = 0)$ is the prior density of the target.

Update N_c of continuing particles from the system dynamics and unnormalized weights are given as:

$$\tilde{w}_k^{(c)i} = \frac{1}{N_c} l(z_k|X_k^{(c)i}, E_k^{(b)i} = 1) \tag{16.8}$$

Calculate the probability of existence about the target according to the unnormalized weights of particles:

$$\hat{P}_k = \frac{\tilde{M}_b + \tilde{M}_c}{\tilde{M}_b + \tilde{M}_c + P_d\hat{P}_{k-1} + [1 - P_b][1 - \hat{P}_{k-1}]} \tag{16.9}$$

with $\tilde{M}_b = P_b[1 - \hat{P}_{k-1}]\sum_{i=1}^{N_b} \tilde{w}_k^{(b)i}, \tilde{M}_c = [1 - P_d]\hat{P}_{k-1}\sum_{i=1}^{N_c} \tilde{w}_k^{(c)i}$.

Normalize the weights of particles as $w_k^{(b)i} = \frac{P_b[1-\hat{P}_{k-1}]}{\tilde{M}_b+\tilde{M}_c}\tilde{w}_k^{(b)i}$, $w_k^{(c)i} = \frac{[1-P_b]\hat{P}_{k-1}}{\tilde{M}_b+\tilde{M}_c}\tilde{w}_k^{(c)i}$ and resample $M_b + M_c$ particles down to M_c particles.

The main difference of PFTBD from the general PF is that a product of cell's intensity in the observation area is needed in the calculation of particle weight, as in (16.7) and (16.8). Moreover, this operation is the main body that contributes the high time complexity of PFTBD. Suppose that the time complexity in weight process of PF is $O(m)$ with m particles. Then in PFTBD, the time complexity of weight process is $O(m \times n^2 \times n)$ for a sequential algorithm with $n \times n$ cells and m particles. Thus, some efficient parallel algorithms should be introduced to relief this overhead.

16.3 The Implementation of PFTBD on GPU

16.3.1 Parallel Processing on CUDA

In the modern GPUs, there are hundreds of processor cores, which are named as the stream multiprocessor (SM). Each SM contains many scalars stream processors (SP) and can perform the same instructions simultaneously. In CUDA programming, GPU can be responsible for the parallel computationally intensive parts and CPU accomplishes other parts. On GPU the kernel, as a task schedule unit, is performed in the block on the SM. Each thread in one block is performed on the SP [9]. Moreover, two thumb rules should be noted: (1) Overhead data transferring between GPU and CPU should be avoided. (2) Accessing data from the shared memory is much cheaper than from the global memory of GPU.

16.3.2 PFTBD on GPU

Obviously, in the implementation of PF and PFTBD, the particles propagation process and weights computing process have the high computational cost but with high concentration of parallelizability. Considering the implementation of PF on GPU, both processes above can be realized in one kernel because of the regular operations in individual threads. However, in PFTBD, different from the particles propagation process in PF, there are product operations among threads in the calculation of particle weight. Therefore, we schedule them with two CUDA kernels respectively onto GPU. Other operations, such as the resampling, which need interaction for all states of particles and their weights and can not be implemented in parallel, is arranged on CPU.

The first kernel is employed to obtain the state of particles in current time step. GPU blocks and threads are allocated according to the number of particles. The input data of first kernel, which are transferred from the CPU memory to the GPU global memory, is the state of continuing particles in the previous time step. These states are updated by the prior density of target. Meanwhile, the state of birth particles are sampling from the proposal density $q(\bullet)$ with uniform distribution

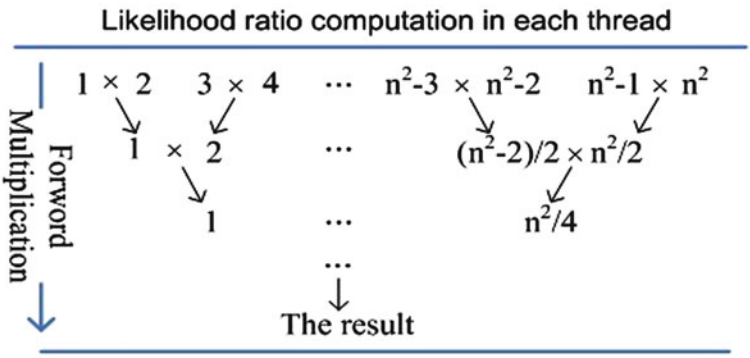

Fig. 16.1 Implementation of multiplication in shared memory

on GPU. As the outputs, the states of both parts of particles are transferred back to CPU to do resampling and estimate the state of the target.

The second kernel calculates the weight of the particles. Only the position dimension of the particle states and measurements are transferred to GPU. This kernel can be designed as various forms according to different size of $C_x(X_k)$ and $C_y(X_k)$ in (16.6). In our implementation, $C_x(X_k)$ and $C_y(X_k)$ include all the set of cell indices. The likelihood ratio function is a product over all the contributions of each cell. For a scale of n^2 array of cells with m particles are used, the computing of weight will entail m blocks and n^2 threads in each block. The value of n^2 should be smaller than the maximum number of threads limited by the hardware. Under this condition, the calculating of likelihood ratio in each cell can be parallelized in every thread, but the process of product cannot be parallelized.

In order to alleviate the time complexity caused by the product, the reduction algorithm is adopted in shared memory of each block to do the multiplication as illustrated in Fig. 16.1. In this way, running time of the multiplication can be reduced significantly. As a result, the time complexity of weight process in PFTBD could be $O(\log_2^n)$ comparing to $O(n)$ without using the shared memory.

16.4 Simulation Results

The simulation is based on the model in [5]. Length of observation time is 30 and target presents from frames 7–22. The observation area is divided into $n \times m = 20 \times 20$ cells and the cell size is $\Delta x = \Delta y = 1$. The probability of birth and death are set as $P_b = 0.05$ and $P_d = 0.05$. The initial state of the target is $X_7 = [4.2\ 0.45\ 7.2\ 0.25\ 20]^T$. The SNR is 3 dB. More information about the parameters can be seen in [5]. Various numbers of particles are adopted with each 100 Monte Carlo trials. To verify the effect of different implementation, simulations are performed on three systems, which are given in Table 16.1.

Table 16.1 Benchmark systems

	System 1	System 2	System 3
Software	Visual studio 2010 professional with CUDA 4.1 SDK		MATLAB 2010a
Hardware	Nvidia GeForce GT9500	Nvidia GeForce 240GT	Pentium(R) Dual-Core
	32 cores @ 550 MHz	96 cores @ 550 MHz	E5800 @ 3.20 GHz
	16.0 GB/s GDDR2	54.4 GB/s GDDR3	

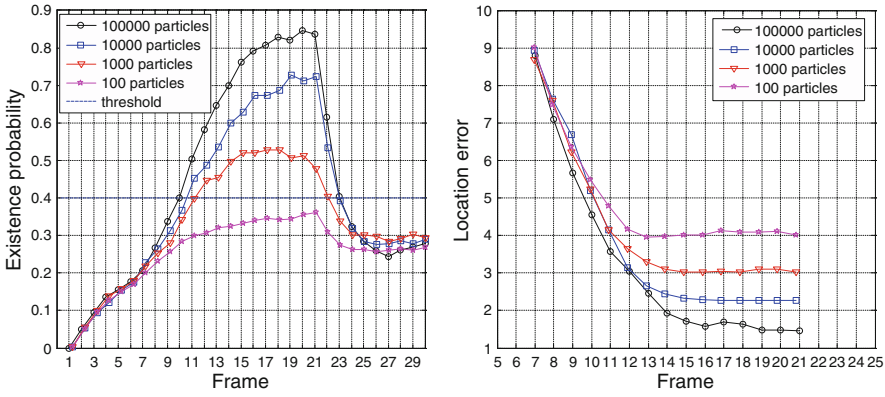

Fig. 16.2 The existence probability and location error with different number of particles

16.4.1 The Performances with Different Numbers of Particle

The performances of existence probability and location error on System 2 with different number of particles are compared in Fig. 16.2.

Figure 16.2 shows that with the increase in the number of particles, the probability of detection improves significantly. When the number of particle is 100, the existence probability is always below the detection threshold, so the target cannot be detected. However, with 100,000 particles, not only the target can be detected faster, but also the detection probability is increased rapidly. With the time accumulation, when the target appears, the detection probability can eventually reach more than 0.8. Therefore, the number of particles is one of the key factors of the detection performance in PFTBD. From the other side, Fig. 16.2 also shows that the location error decreases efficiently with the increase in the number of particles.

16.4.2 The Speedup Ratio of GPU to CPU

The run time on GT9500, 240GT and CPU, respectively, in different number of particles is given in Fig. 16.3.

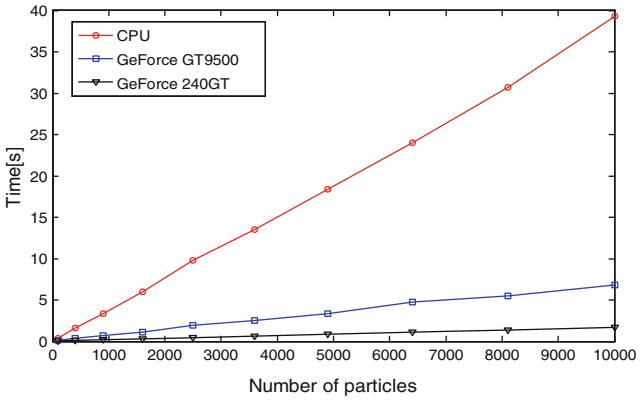

Fig. 16.3 Time comparison between CPU and GPU with different numbers of particles

From it, we can found that with the growing number of particles, the speedup ratio between GPUs and CPU improves significantly. Moreover, Fig. 16.3 shows that the speedup ratio of 240GT is quadruple than GT9500. It is consistent with the specifications, in Table 16.1, that 240GT has the number of CUDA cores triple than that in GT9500 and the memory interface width much larger than that in GT9500.

16.5 Conclusion

In this chapter, we propose an efficient implementation of PFTBD algorithm on GPU. Since the parallel part bears the main computation, by realizing it on GPU, the running time of algorithm is greatly reduced. Moreover, the efficiency of the algorithm can be significantly improved by employing much more particles than in CPU. Furthermore, from the comparison of different performance between GeForce GT9500 and GeForce 240GT, a conclusion is made that CUDA cores and memory interface width determines the efficiency of GPU in parallel computing.

In the future work, more optimization will be done on transferring of data between GPU and CPU. The strategy to apply our implementation in the application of larger scale will also be studied.

Acknowledgments The work is supported by the Fundamental Research Funds for the Central Universities of China (ZYGX2011J012).

References

1. Ristic B, Arulampalam S, Gordon N (2004) Beyond the Kalman filter: particle filters, for tracking applications. Artech House, Boston\London
2. Salmond DJ, Birch H (2001) A particle filter for track-before-detect. In: Proceedings of the American control conference, vol 5. Arlington. pp 3755–3760. doi:10.1109/ACC.2001.946220
3. Rollason M, Salmond D (2001) A particle filter for track-before-detect of a target with unknown amplitude. Target tracking: algorithms and applications, vol 1. Enschede: 14/1–4. doi:10.1049/ic:20010240
4. Rutten MG, Gordon NJ, Maskell S (2004) Efficient particle based track before detect in Rayleigh noise. In: Proceedings of Signal and Data Processing of Small Targets, International Society for Optical Engineering, Bellingham, pp 509–519
5. Rutten MG, Ristic B, Gredon NJ (2005) A comparison of particle filters for recursive track-before-detect. In: Proceedings of the 8th international conference on information fusion, vol 1. Piscataway, pp 169–175. doi:10.1109/ICIF.2005.1591851
6. Rutten MG, Gordon NJ, Maskell S (2005) Recursive track-before-detect with target amplitude fluctuations. IEE Proc Radar Son Nav 152:345–352. doi:10.1049/ip-rsn:20045041
7. Boers Y, Driessen JN (2004) Multitarget particle filter track before detect application. IEE Proc Radar Son Nav 151:351–357. doi:10.1049/ip-rsn:20040841
8. The resource for CUDA developers (2010) http://www.nvidia.com/object/cuda_home.html. Accessed Jan 2010
9. Shu Zhang, Yanli Chu (2009) GPU computing for high performance-CUDA. China Water & Power Press, Beijing
10. Peihua Li (2012) An efficient particle filter–based tracking method using Graphics Processing Unit (GPU). J Signal Process Syst 68:317–332

Chapter 17
An Improved Monopulse Forward-Looking Imaging Algorithm

Xiaomin Jiang, Yulin Huang, Jianyu Yang, and Wenchao Li

Abstract Forward-looking imaging plays a significant role in navigation, self-landing, etc. In this chapter, an improved monopulse forward-looking imaging algorithm is presented. Firstly, the angle of the target is estimated by monopulse angle measurement. Secondly, the radar return energy is placed to the azimuth bin indicated by the estimate angle. Then, upon completion of beam scan, a high-resolution image is gained. Finally, the mask technique is used to make the target's boundary clear. Simulation results validate the effectiveness of this algorithm.

Keywords Monopulse • Forward-looking imaging • Beam sharpening • Mask technique

17.1 Introduction

Forward-looking imaging is invaluable in many applications, such as terrain following and navigation. For the reason that the Doppler frequency changes slowly, SAR fails in imaging the forward-looking scenario [1–3]. Although the real beam radar is able to imaging the forward-looking scenario, the improvement in azimuth resolution in this system is achieved only by decreasing the antenna beam width [4].

Monopulse angle measurement technique is widely utilized in target tracking due to its angular accuracy [5–7]. Nevertheless, the Monopulse technique applied in the radar imaging is researched rarely.

X. Jiang (✉) • Y. Huang • J. Yang • W. Li
School of Electronic Engineering, University of Electronic Science and Technology of China (UESTC), Chengdu, Sichuan, China
e-mail: xmjiang980@163.com

Q. Liang et al. (eds.), *Communications, Signal Processing, and Systems*, Lecture Notes in Electrical Engineering 202, DOI 10.1007/978-1-4614-5803-6_17,

Based on monopulse angle measurement and the mask technique, an improved monopulse algorithm is proposed to image the forward-looking scenario in this chapter.

This chapter is organized as follows. In Sect. 17.2, the principle of monopulse angle measurement is given. The principle of monopulse improving azimuth resolution is presented in Sect. 17.3. Section 17.4 describes the improved monopulse forward-looking imaging algorithm in detail. In Sect. 17.5, the imaging performance of the proposed algorithm is discussed. Simulation results are shown in Sect. 17.6 and conclusion is given in Sect. 17.7.

17.2 Monopulse Angle Measurement

Monopuslse is a simultaneous lobing technique for determining the angular location of a source of radiation or "target" that reflects part of the energy incident upon it [8]. In an amplitude comparison monopulse radar system, a pulse of energy is transmitted, and the target echo is received with two beams that are squinted relative to boresight, as shown in Fig. 17.1. Then, two squinted beams are combined to form the sum S and difference D signals. The direction-of-angle (DOA) is estimated with the in-phase part (i.e., the real part) of the monopulse ratio, which is formed by dividing the difference of the two received signals by their sum. The DOA (η) can be expressed as follows:

$$\eta = \mathrm{Re}(D/S). \tag{17.1}$$

In a typical monopulse system, the DOA η and the target angle (θ) between the target and the direction of radar flight are related approximately as

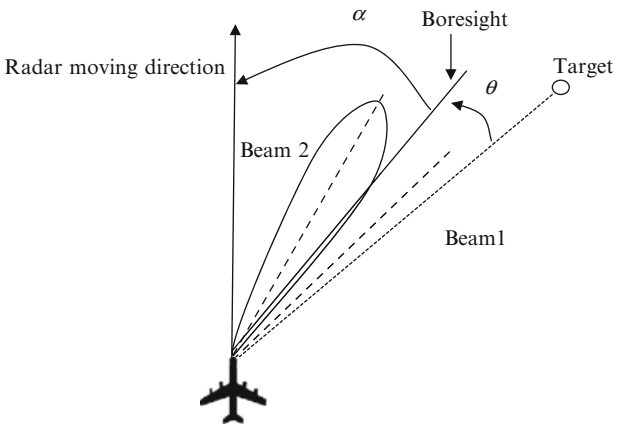

Fig. 17.1 Monopulse radar antenna model

$$\theta \approx \frac{F_{\Sigma}(0)}{F'_{\Delta}(0)}\eta + \alpha \tag{17.2}$$

where $F_{\Sigma}(0)$ and $F_{\Delta}(0)$ are the magnitude beam pattern(voltage gain), respectively, of the sum and difference channels for a target at angle 0 and α is the angle between the boresight and radar moving direction.

17.3 Monopulse Beam Sharpening Principle

Since monopulse technique can determine the angular location of a target accurately, it can be applied in radar imaging to improve the azimuth resolution.

Figure 17.2 illustrates the principle of monopulse improving azimuth resolution. In Fig. 17.2, the target is scanned by a radar beam from right to left during five successive radar "looks". The sum beam scan of the scanned space is divided into small angular bins, each bin being a fraction of the antenna beamwidth. As the beam first illuminates the target represented by "look" A, the radar return energy is indicated by intensity 1, which is added to the appropriate azimuth bin indicated by the target's angle θ, estimated by (17.2).

During the next "look" B, the radar return energy is indicated by a bigger intensity 2 because the beam is closer to the target. Then, the technique of monopulse angle measurement places the radar return energy at the same location in azimuth as it does for "look" A. Similarly, for each successive "look", the target's return energy is placed to the actual azimuth bin until the scanning beam no longer illuminates the target. As seen from Fig. 17.2, the radar return energy of each "look" is placed at the azimuth bin which the target is actually located in, and the gray value is strong at the actual location, while it is weak on either side of the actual location of the target, as illustrated by rectangle F.

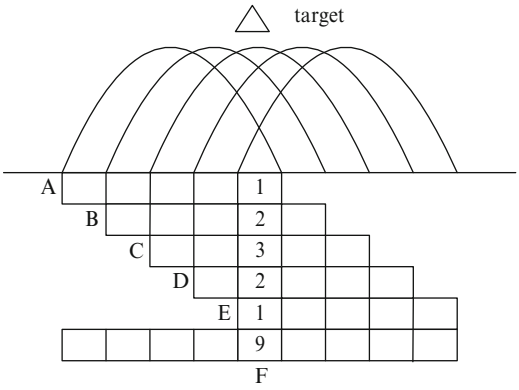

Fig. 17.2 Principle of monopulse improving azimuth resolution

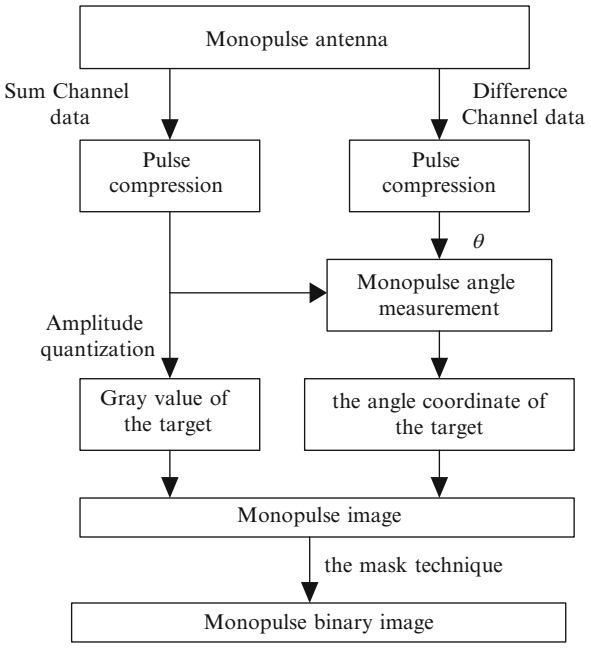

Fig. 17.3 Procedure of the monopulse imaging algorithm

17.4 Monopulse Forward-Looking Imaging Algorithm

As shown in Sect. 17.3, monopulse technique can achieve beam sharpening. In this section, the improved monopulse imaging algorithm will be described in detail.

Monopulse antenna scans over an area and transmit a plurality of radar pulses. The radar system can resolve targets in range direction by linear frequency-modulation pulse compression. Then, estimate the angle of target at each range gate and place the target's return energy to the azimuth bin indicated by the estimated angle. Upon completion of the scan, the monopulse radar gains a high-resolution radar image. Because false targets appear when the monopulse imaging algorithm resolves closely spaced targets, the mask technique is applied in the proposed algorithm to make the target's boundary clear. Firstly, the OSTU threshold method is used to image binarization. Secondly, we can get the clear image by multiplying the acquired binary image with the original monopulse image.

The procedure of the improved monopulse imaging algorithm is shown in Fig. 17.3.

Each step is described as follows.

Assuming that the angle between the target and the direction of radar flight is indicated by θ, as shown in Fig. 17.1, then it is estimated by

$$\theta = \frac{F_{\Sigma}(0)}{F'_{\Delta}(0)} \mathrm{Re}\left(\frac{D}{S}\right) + \alpha \tag{17.3}$$

where $F_{\Sigma}(0)$ and $F_{\Delta}(0)$ are the magnitude beam pattern(voltage gain), respectively, of the sum and difference channel for a target at angles 0, α is the angle between the boresight and the direction of the radar flight, and $D$and S are the return energy of target at the range r of the sum and difference channels respectively. Then, the angle coordinate of the target is determined. And the return energy of the sum channel is treated as the gray value of the radar imaging. Then, OSTU threshold method is used to search an optimal threshold for image binaryzation. Finally, multiply the acquired binary image with the original monopulse image.

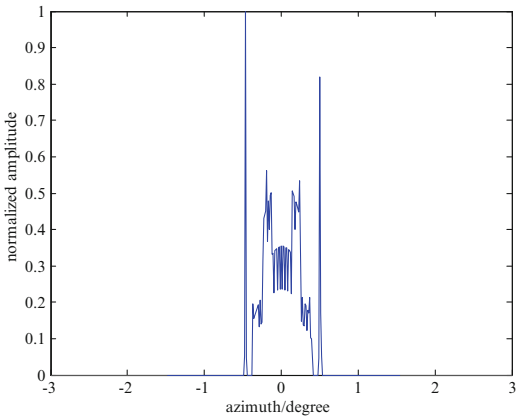

Fig. 17.4 Profile of the monopulse imaging with $\theta_1 = -0.5^{\circ}$, $\theta_2 = 0.5^{\circ}$ and $RCS_1 = RCS_2 = 1$

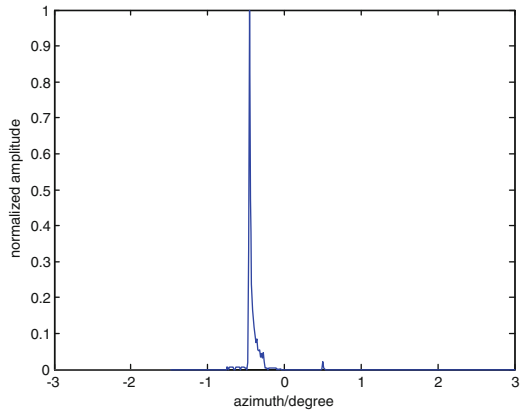

Fig. 17.5 Profile of the monopulse imaging with $\theta_1 = -0.5^{\circ}$, $\theta_2 = 0.5^{\circ}$ and $RCS_1 = 1, RCS_2 = 0.1$

Table 17.1 Simulation parameters

Parameter	Value
Sum beam width	3.6°
Scanning velocity(w)	30°/s
Scanning azimuth range	−10°–+ 10°
Aerocraft velocity(v)	100 m/s
Pulse repetition frequency(PRF)	2,000 Hz
The nearest range of the scene	8 Km
Chirp frequency(f_c)	10 GHz
Chirp bandwidth (B)	30 MHz

17.5 The Discussion of the Monopulse Imaging Performance

In principle, monopulse angle measurement provides excellent angular estimation by comparing energy returns from two beams that are squinted about boresight [9]. But the angle estimated by monopulse technique can wander far beyond the angular separation of the targets when the targets are closely in space.

This problem also exists in monopulse imaging. Figure 17.4 shows that false targets appear when imaging the two targets which are all strong scatters. But when one of the targets is strong and the other is weak, the monopulse imaging algorithm can image the strong target, as shown in Fig. 17.5. Hence, monopulse imaging algorithm is suited for imaging the scenario that consists of strong scatter in the clean background. For example, the algorithm can resolve the ships located in the sea.

17.6 Simulation Results

In this section, some simulations are performed to show the improvement in azimuth resolution with the improved monopulse imaging algorithm. The simulation parameters are listed in Table 17.1.

The original scene is a SAR image which consists of multiple ships, as shown in Fig. 17.6a. And Fig. 17.6b, c provide a comparison between real beam radar imaging and monopulse radar imaging. In the real beam radar imaging, the ships are indistinguishable, while they are resolved in the monopulse radar imaging. Through the comparison of Fig. 17.6c, d, we can see that the mask technique can make the targets boundary clear.

17.7 Conclusion

Based on monpulse angle measurement and the mask technique, the monopulse technique is studied to image the forward-looking scenario in this chapter. As the proposed algorithm has no requirements for Doppler frequency, it can be applied in

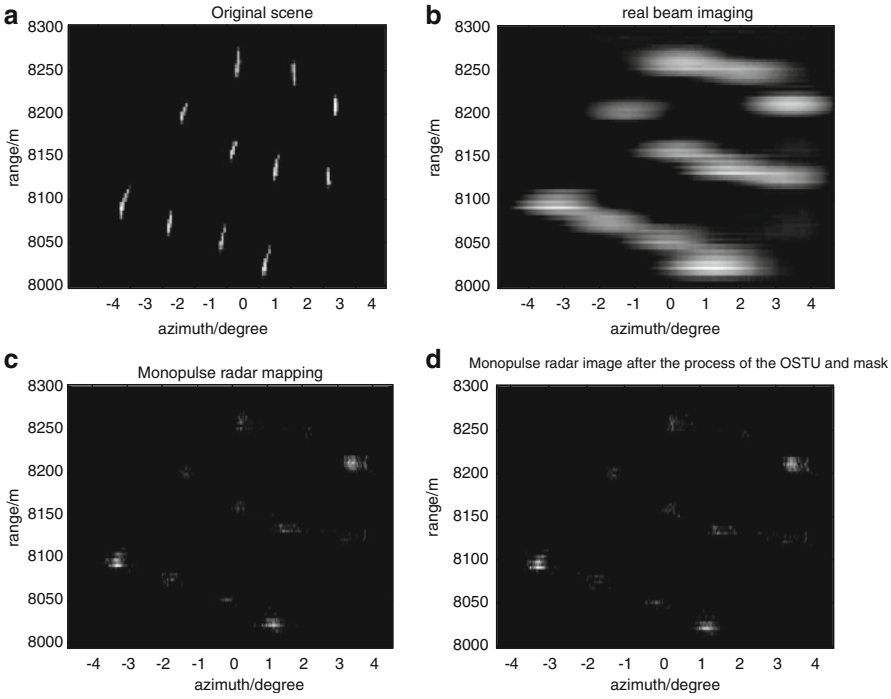

Fig. 17.6 Simulations results

forward-looking imaging. Because the algorithm has the special requirement of the scenario, it is suited to image the scenario which consists of strong scatters in the clean background.

Acknowledgments This work was supported by the Ph.D. Programs Foundation of Ministry of Education of China (No.A09010201100186110 13)

References

1. Curlander JC, Mcdonough RN (1991) Synthetic aperture radar: system and signal processing. Wiley, New York
2. Stimson GW (1998) Introduction to airborne radar. Scitech, New Jersey
3. Lohner AK (1998) Improved azimuth resolution o f forward looking SAR by sophisticated antenna illumination function design. IEE Proc-Radar Son Nav 145(2):128–134
4. Skolnik MI (2008) Radar handbook, 3rd edn. McGraw-Hill, New York
5. Blair WD, Brandt-Pearce M (2001) Monopulse DOA estimation of two unresolved Rayleigh targets. IEEE Trans Aero Elec Sys 37:452–469
6. Zhen W et al (2004) Angle estimation for two unresolved targets with monopulse radar. IEEE Trans Aero Elec Sys 40:998–1019

7. Isaac A et al (2008) Detecting and tracking separating objects using direct monopulse measurements. In: IEEE aerospace conference, Big Sky, MT, pp 1–11
8. Sherman SM (1984) Monopulse principles and techniques. Artech House, Boston
9. Levanon N (1988) Radar principles. Wiley, New York

Chapter 18
Compressed Sensing Based on the Contourlet Transform for Image Processing

Qing Lei, Bao-ju Zhang, and Wei Wang

Abstract In the compressed sensing, the sparse image is the prior condition. Contourlet transform is a non-adaptive multi-directional and multi-scale geometric analysis method, which could represent the image with contour and texture-rich more effective and has strong capability of nonlinear approximation. In this chapter, based on the advantages of Contourlet transform and the theory compressed sensing, an improved compressed sensing algorithm based on Contourlet transform was proposed. The improved compressed sensing algorithm only measured the high-pass Contourlet coefficients of the image but preserving the low-pass Contourlet coefficients. Then the image could be reconstructed by the inverse Contourlet transform. Compared with the traditional wavelet transformation in the compressed sensing image application, simulation results demonstrated that the proposed algorithm improved the quality of the recovered image significantly. For the same measurement number, the PSNR of the proposed algorithm was improved about 1.27–2.84 dB.

Keywords Contourlet transform • Compressed sensing • Image processing

18.1 Introduction

The sparse image representation plays an important role in the compressed sensing (CS), image denoising, image inpainting and super resolution and so on [1]. The wavelet transform is the optimal approximation in the representation of point singularity of piecewise smooth function. However, for the two-dimensional image information, the wavelet transform is inadequate in the areas of image multi-directional expression. Therefore, in order to seek more effective methods

Q. Lei • B.-j. Zhang • W. Wang (✉)
Department Physics and Electronic Information, Tianjin Normal University, Tianjin, China
e-mail: wangweivip@tju.edu.cn

Q. Liang et al. (eds.), *Communications, Signal Processing, and Systems*, Lecture Notes in Electrical Engineering 202, DOI 10.1007/978-1-4614-5803-6_18,

than wavelet transform sparse representation, the Do and the Vetterli proposed the Contourlet Transform algorithm, which expressed the edge and the texture of the image sparsely [2]. Compared to previous wavelet transform, the Contourlet transform can overcome the limitations of the wavelet transform. Contourlet transform has the better direction selectivity, and it can meet the nature of the image sparely. Therefore, this chapter uses Contourlet transform algorithm as the image sparse representation method. This method has the better restore original image by solving the inverse problems in the areas of compressed sensing.

In 2006, the Donoho and the Candes proposed a new sampling theory—the theory of compressed sensing [3, 4], which broke through the Nyquist sampling theorem. In recent years, compressed sensing has a great future. Such as: radar, imaging, image processing, data reconstruction and so on. And the image processing has the most rapid development in their applications. The theory of compressed sensing is a new method of image acquisition, which based on the development of sparse representation. The theory of compressed sensing main includes projection measurement methods, reconfigurable conditions and image reconstruction methods etc. [5]. In this chapter, we used the random Gaussian matrix to measure the image, and then using the orthogonal matching pursuit algorithm to reconstruct the image. Based on Contourlet transform and compressed sensing, the proposed algorithm can improve the quality of the recovered image.

18.2 The Basic Principle of Contourlet Transform

Contourlet transform palys an important part in multi-scale, multi-direction image processing. Contourlet transform uses the "rectangular" structure as its base of support range. And the "rectangular" structure varies with size the distribution in multi-scale [6]. However, the wavelet transform uses the "square" structure as its base of support range, and its multi-resolution was described by the different size squares. Compared with the traditional wavelet transformation, Contourlet transform offers a much richer sub-band set of different directions and shapes, so it can capture 2-D geometrical structure in natural images much more efficiently.

Contourlet transform makes the multi-resolution decomposition and multi-directional decomposition into two relatively independent processes. Its basic idea can be divided into two steps:

1. In the first stage, the Laplacian Pyramid (LP) is used to capture the edge points. LP decomposition at each step generates a sampled low-pass version of original image and a band-pass high-pass image.
2. In the second stage, the Directional filter bank (DFB) is used to link point discontinuities into linear structures. It is efficiently implemented using a l-level tree structured decomposition that lead to 2^l sub-bands with wedge-shaped frequency partition.

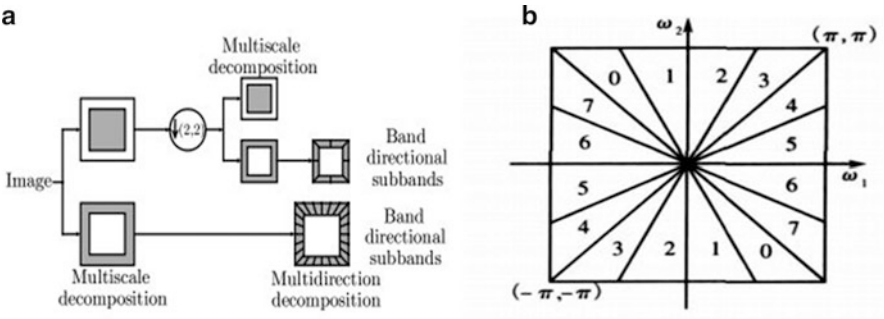

Fig. 18.1 Contourlet transform schematic diagram and DFB transform schematic diagram

Combining the advantage of LP and DFB, the Contoulet transform can effectively capture more edges and contours in natural images. The Contourlet transform schematic diagram show in Fig. 18.1a, and the DFB transform schematic diagram show in Fig. 18.1b.

18.3 Principle of Compressed Sensing

Compressed sensing is a novel framework that enables sampling below Nyquist rate, without sacrificing reconstruction quality by exploiting sparsity of the signal in some domain. Compressed sensing allows the highly efficient acquisition of many signals that could be difficult to capture or encode using conventional methods. Form a relatively small number of random measurements, a high-dimensional signal can be recovered if it has a sparse or near-sparse representation in a basis known to the decode [7]. The theory of compressed sensing mainly includes three aspects: the sparse representation of the signal, a projection measurement methods and reconstruction methods [8, 9].

The sparse image is the prior condition in the compressed sensing. Let $x = \{x[1], \ldots, x[N]\}$ be a set of N samples of real-valued, time-discrete random process. Let's be representation of x in the ψ domain, that is:

$$x = \psi y = \sum\nolimits_{k=1}^{N} \psi_k y_k \tag{18.1}$$

Where $y = \{y_{1,\ldots,} y_N\}$ is an N-vector of weighted coefficient, $y_k = \langle x, \psi_k \rangle$, and $\psi = \{\psi_{1,} \psi_{2,} \ldots . \psi_N\}$ is an N × N basic matrix with ψ_K being the k-th basic column vector.

We say that vector x is K-spare in the domain ψ, $K \ll N$, if only K out of N coefficients of y are non-zero. Sparsity of a signal is used for compression in conventional transform coding, where the whole signal is first acquired, then the N transform coefficients y are obtained via $y = \psi^T x$, and then N-K coefficients of y are discarded and the remaining are encoded.

Note that huge redundancy is present in the acquisition since large amount of data are discarded, because they carry negligible energy. The main idea of compressed sensing is to remove the "sampling redundancy" by requiring only M samples of the signal, where $K\langle M\langle\langle N$. Let s be a M-length measurement vector given by:

$$s = \Phi x \tag{18.2}$$

Where $\Phi = \{\phi_1, \phi_2, ...\phi_M\}$, Φ is an M × N measurement matrix. The above expression can be written in terms of y as:

$$s = \Phi\psi y = \Theta y \tag{18.3}$$

It has been shown that signal x can be recovered losslessly from $M \approx K$ or slightly more measurements (vector s in (18.3)) if the measurement matrix Φ is properly designed, so that Θ satisfies the so-called restricted isometry property (RIP) [10]. That means Θ satisfies the formula (18.4) as:

$$(1-\varepsilon)\|v\|_2 \leq \|\Theta v\|_2 \leq (1+\varepsilon)\|v\|_2 \tag{18.4}$$

Where $\varepsilon>0$. This will always be true if Φ and ψ are incoherent, that is the vectors of Φ cannot sparsely represented basic vectors and vice versa.

It was further shown that a Gaussian matrix Φ satisfies the above property for any ψ with high probability if $M \geq cK\log\left(\frac{N}{K}\right)$ for some small constant c. Thus, one can recover N measurements of x with high probability from only $M \approx cK\log\left(\frac{N}{K}\right) \ll N$ random Gaussian measurements s under the assumption that x is K-spare in some domain ψ. Note that it is not known in advance which y_K coefficients are zeros, or which $x[K]$ sample is not needed.

Unfortunately, reconstruction of $x = \{x[1], \ldots, x[N]\}$ (or equivalently, $y = \left\{y_{1,\ldots,}y_N\right\}$) form vector s of M samples is not trivial.

$$\min \|y\|_{l_0} s.t.\, s = \Phi\psi^H y \tag{18.5}$$

The solution of (18.5) is NP-hard and consists of finding the minimum l_0 norm (the number of non-zero elements). However, excellent approximation can be obtained via the l_1 norm minimization given by:

$$\min \|y\|_{l_1} s.t.\, s = \Phi\psi^H y \tag{18.6}$$

This convex optimization problem can be solved using a linear program algorithm of $o\left(N^3\right)$ complexity. In contrast to l_0 norm minimization, the l_1 norm

minimization usually requires more than $K + 1$ measurements. Due to complexity and low speed of linear programming algorithms, faster solutions were proposed at the expense of slightly more measurements, such as matching pursuit, tree matching pursuit, orthogonal matching pursuit and so on [11]. This chapter uses an orthogonal matching pursuit to reconstruct the image.

18.4 The Application of Contourlet Transform Based on CS

In this chapter, we proposed an improved compressed sensing algorithm based on the Contourlet transform. The proposed algorithm's specific steps as follows:

Step 1: We use three-layer Contourlet transform to deal with the N*N image. Then using DFB decomposed the high-frequency information in Ccontourlet transform coefficients of the image.

Step 2: We select the appropriate value of M to construct a Gaussian matrix. We use this matrix to measure the high-frequency coefficient and preserve the low-frequency coefficients.

Step 3: We use the OMP algorithm to recover the high-frequency coefficient matrix.

Step 4: For the highest layer high-frequency coefficient, it could be reconstructed by the inverse DFB. Then it combines with the low-frequency information as the input data for the next layer.

Step 5: Repeating the step 4 until we get the equivalent of the reconstructed image with the original image size.

18.5 Expreiments and Conclusion

Experiment makes use of Matlab software platform to simulate standard 512 * 512 Barbara.bmp image and standard 512 * 512 Lena.bmp image. When we selected nlevels [0,0,0] in the program, in fact, the decomposition of each layer is the wavelet transform decomposition. We can obtain the diagonal direction, vertical and horizontal direction directional information as well as low-pass sub-band information. When we selected nlevels [2,2,2] in the program, that means the high-frequency information in Contourlet transform coefficients were DFB decomposed in the two directions. We obtained respectively sub-band information of the four directions in the three-layer. For example: The standard test image Lena is tested and the image was decomposed by three-layers Contourlet transform and wavelet transform, the coefficient images of each layer decomposed shown in Fig. 18.2.

When the number of rows M = 100 in the measurement matrix Φ, we can get the decoded images. The decoded image (b) shown in Fig. 18.3, its method is

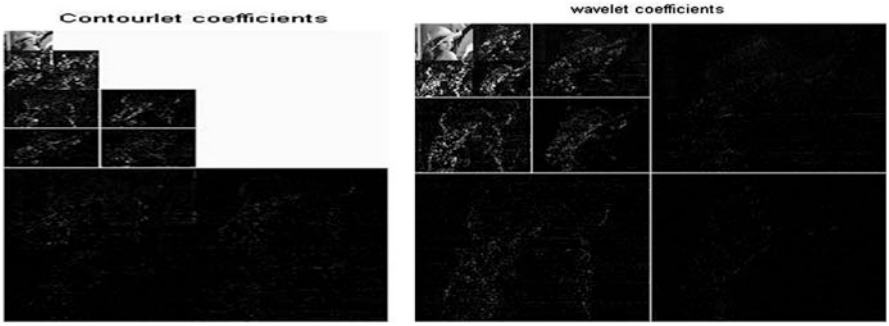

Fig. 18.2 The three-layers Contourlet transform and three-layers wavelet transform schematic diagram (Lena.bmp)

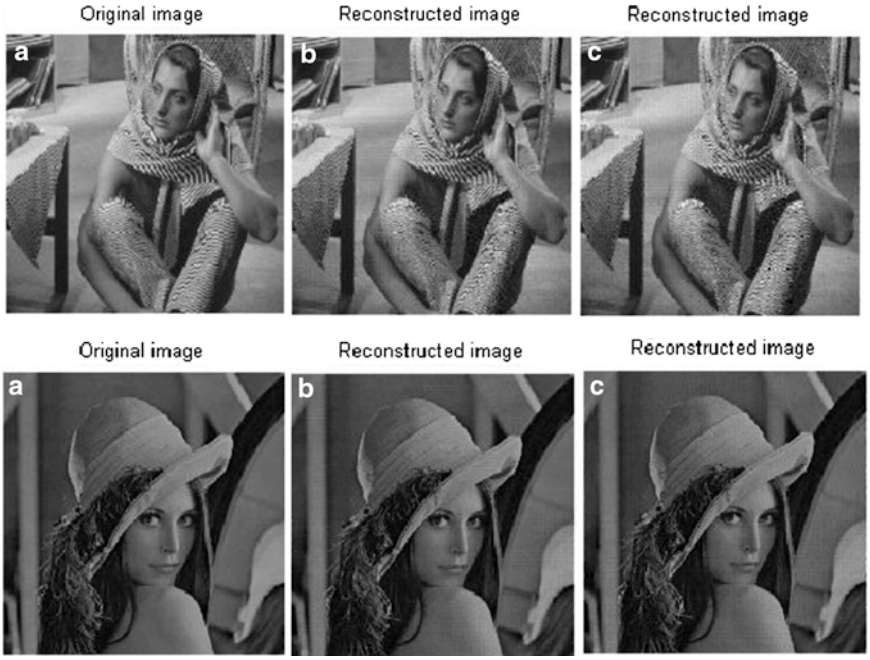

Fig. 18.3 The reconstructed images of the two algorithms (M = 100)

Table 18.1 The value of PSNR under the different the value of M (Barbara.bmp)

The value of M	40	50	60	70	80	90
PSNR(dB) CS based on contourlet transform	25.01	25.71	26.43	27.30	28.01	28.74
PSNR(dB) CS based on wavelet transform	22.35	23.04	23.71	24.46	25.31	26.60
The value of M	100	110	120	130	140	150
PSNR(dB) CS based on contourlet transform	29.48	30.27	31.03	31.83	32.59	33.33
PSNR(dB) CS based on wavelet transform	26.69	27.66	28.44	29.09	29.91	30.54

Table 18.2 The value of PSNR under the different the value of M (Lena.bmp)

The value of M	40	50	60	70	80	90
PSNR(dB) CS based on contourlet transform	30.30	31.35	32.54	33.47	34.43	35.27
PSNR(dB) CS based on wavelet transform	28.81	29.92	31.04	31.94	32.98	33.81
The value of M	100	110	120	130	140	150
PSNR(dB) CS based on contourlet transform	34.73	35.49	36.22	36.81	37.44	38.03
PSNR(dB) CS based on wavelet transform	26.69	27.66	28.44	29.09	29.91	30.54

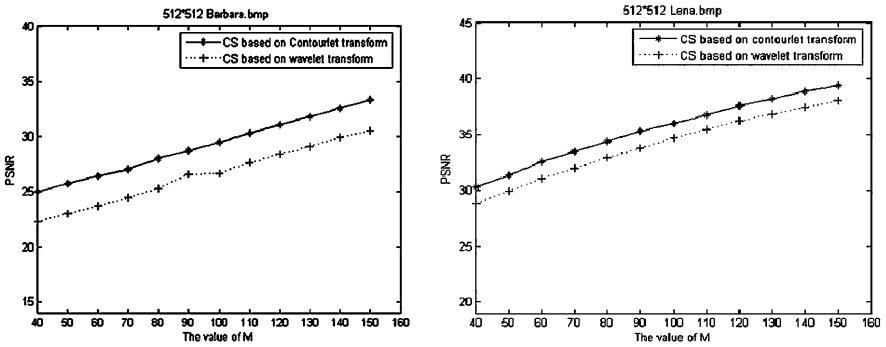

Fig. 18.4 The value of PSNR of the two algorithms

compressed sensing algorithm based on the Contourlet transform. The decoded image (c) shown in Fig. 18.3, its method is compressed sensing algorithm based on the wavelet transform.

According to the simulation results based on two algorithms,we can draw the value of PSNR, it based on different value of M, as shown in Tables 18.1 and 18.2. After a large number of experiments, we found that the PSNR of the reconstructed image will be a difference value about 0.2 dB in the same value of M. Therefore, we make the same program to run three times when we change the value of M. Then we take the average PSNR measurement results to record in Tables 18.1 and 18.2, it will reduce the errors.

In order to compare the two algorithms results of the reconstruction image more intuitive, we have simulation results in Tables 18.1 and 18.2 plotted as shown in Fig. 18.4. Among them, the horizontal axis shows the number of rows M in measurement matrix Φ, the longitudinal axis shows the value of PSNR in reconstruction image.

In Fig. 18.4, with the improvement of the number of rows of M in measurement matrix Φ, the value of the average PSNR of the reconstructed image is improved with the increase of M. It indicates that the effect of the reconstructed image along with enhanced. The figure shows that comparison with the CS algorithm based on wavelet transform the PSNR of the CS algorithm based on Contourlet transform increases about 1.41–2.49 dB and using Contourlet transform has a better effect on image reconstruction.

Conclusion: Due to Contourlet transform have the multi-directional and anisotropic nature, its image of "sparse" is better than wavelet transform. And the experiments prove that the CS algorithm based on Contourlet transform is better to restore the image information in solving the inverse problem. The experiment realized the CS algorithm based on Contourlet transform by Matlab software platform. Compared with the CS algorithm based on wavelet transform, simulation results demonstrated that the improved CS algorithm based on Contourlet transform improved the quality of recovered image significantly. For the same measurement number, the PSNR of the CS algorithm of Contourlet transform was improved 1.27–2.84 dB. By comparing the experimental data analysis, the proposed algorithm in the chapter has a better effect on image reconstruction.

Acknowledgments This work supported by Tianjin Natural Science Foundation (10JCYBJC00400), Tianjin Younger Natural Science Foundation (12JCQNJC00400) and Tianjin High Education Science & Technology Foundation Planning Project (20100716)

References

1. Candes EJ, Romberg J, Tao T (2006) Robust uncertainty principles: exact signal reconstruction from highly in complete frequency information. IEEE Trans Info Theory 52(2):489–509
2. Do MN, Vetterli M (2005) The contourlet transform: an efficient directional multiresolution image representation. IEEE Trans Image Process 14(12):2091–2106
3. Donoho DL (2006) Compressed sensing. IEEE Trans Info Theory 52(4):1289–1306
4. Cands E (2006) Compressive sampling. In: Proceedings of the international congress of mathematicians, vol 3, Madrid, pp 1433–1452
5. Fang W (2012) Image processing and reconstruction based on compressed sensing. J Optoelectron Laser 23(1):196–202
6. Xiuwei T et al (2010) Image compression algorithm using wavelet-based Contourlet transform. J Data Acquis Process 25(4):437–441
7. Jun MA et al (2011) Design of a compressive sensing theory based single-pixel imaging system. Infrared Technol 33(8):450–452
8. Guang-ming SHI, Dan-hua LIU et al (2009) Advances in theory and application of compressed sensing. Acta Electronica Sinica 37(5):1070–1081
9. Baraniuk RG (2007) Compressive sensing. IEEE Signal Process Mag 24(4):118–121
10. Candès E, Romberg J (2007) Sparsity and incoherence in compressive sampling. Inverse Probl 23(3):969–985
11. Hai-rong YANG et al (2011) The theory of compressed sensing and reconstruction algorithm. Acta Electronica Sinica 39(1):142–148

Chapter 19
Revealing Image Splicing Forgery Using Local Binary Patterns of DCT Coefficients

Yujin Zhang, Chenglin Zhao, Yiming Pi, and Shenghong Li

Abstract The wide use of powerful image processing software has made it easy to tamper images for malicious purposes. Image splicing, which has constituted a menace to integrity and authenticity of images, is a very common and simple trick in image tampering. Therefore, image splicing detection is of great importance in digital forensics. In this chapter, an effective framework for revealing image splicing forgery is proposed. The local binary pattern (LBP) operator is used to model magnitude components of 2-D arrays obtained by applying multi-size block discrete cosine transform (MBDCT) to the test images, all of bins of histograms computed from LBP codes are served as discriminative features for image splicing detection. To avoid the high computational complexity and possible overfitting for support vector machine (SVM) classifier, principal component analysis (PCA) is utilized to reduce the dimensionality of the proposed features. Our experiment results demonstrate the efficiency of the proposed method over the Columbia image splicing detection evaluation dataset.

Keywords Image splicing detection • Local binary pattern • DCT • PCA

Y. Zhang (✉) • S. Li
Department of Electronic Engineering, Shanghai Jiao Tong University, Shanghai 200240, China
e-mail: yjzhang82@sjtu.edu.cn; shli@sjtu.edu.cn

C. Zhao
School of Information and Communication Engineering, Beijing University of Posts and Telecommunications, Beijing 100876, China
e-mail: clzhao@bupt.edu.cn

Y. Pi
School of Electronic Engineering, University of Electronic Science and Technology of China, Chengdu 611731, China
e-mail: ympi@uestc.edu.cn

Q. Liang et al. (eds.), *Communications, Signal Processing, and Systems*, Lecture Notes in Electrical Engineering 202, DOI 10.1007/978-1-4614-5803-6_19,

19.1 Introduction

Image splicing is a very common and simple tampering manner which creates a composite image by cropping and pasting regions from the same or different images without postprocessing. Spliced images could be so eye-deceiving that they are scarcely distinguished from authentic ones even without any postprocessing. In addition, malicious image splicing manipulation may mislead the public and persuade them to believe something that never exists.

Recently, many techniques have been developed to reveal image splicing tampering. Ng et al. in [1] proposed to use third order moment spectra (i.e. bicoherence) based features for splicing detection. It is claimed that bicoherence is sensitive to quadratic phase coupling (QPC) caused by splicing discontinuity. The detection accuracy as high as 72% over the image dataset [2] was achieved. Johnson and Farid in [3] developed a method to determine whether an image has been tampered with the assumption that both the original part and tampered part were taken under the same or approximately similar lighting conditions. In [4], Fu et al. generated features from Hilbert-Huang Transform (HHT) and moments of characteristic function of wavelet sub-bands, a detection accuracy of 80.15% was reported. Chen et al. in [5] utilized 2-D phase congruency and statistical moments of wavelet characteristic function to capture splicing artifacts. The detection accuracy as high as 82.32% over the image dataset [2] was achieved. In [6], the detection performance of two types of statistical features derived from moments of characteristic functions of wavelet subbands and Markov transition probabilities of difference 2-D arrays, which are proposed by Shi et al., outperformed the prior arts in the field of image splicing detection. Their statistical features have achieved detection rates of 86.82% and 88.31% respectively.

The methods mentioned above have achieved very promising detection results. In this chapter, image splicing detection is considered from a different perspective. The LBP operator is used to model magnitude components of 2-D arrays obtained by applying multi-size block discrete cosine transform (MBDCT) to the test images, all of bins of histograms computed from LBP codes can be served as discriminative features for image splicing detection. Principal component analysis

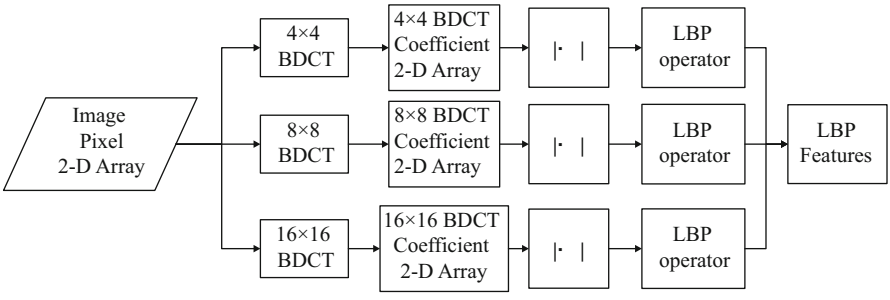

Fig. 19.1 Feature extraction procedure

(PCA) is used to reduce the dimensionality of the proposed features. It is expected that the proposed method can detect the splicing introduced trace effectively.

The rest of this chapter is organized as follows. The proposed method is described in Sect. 19.2. The experimental results are reported in Sect. 19.3. Finally, conclusions are drawn in Sect. 19.4.

19.2 Proposed Method

In this Section, a concrete feature extraction procedure for image splicing tampering detection is proposed, which is shown in Fig. 19.1. The details are as follows.

19.2.1 Preprocessing

From a viewpoint of signal processing, image splicing detection can be considered as a problem of weak signal (i.e. splicing artifacts) detection in the background of strong signal (i.e. image content). To reduce the effects caused by the diversity of image content and enhance the splicing artifacts, it is necessary to preprocess images before feature extraction. The block discrete cosine transform (BDCT) has been commonly used in the popular image and video compression schemes such as JPEG and H.264 owing to its good property of decorrelation and energy compaction. In order to capture the splicing artifacts caused by different possible splicing operations, different test images and different pasted image fragments, we first preprocess the test images by multi-size block discrete cosine transform (MBDCT) which is proved to be effective for image splicing detection [6], and resulting BDCT coefficient 2-D arrays are used for subsequent feature extraction.

The $b \times b$ BDCT of an image can be divided into the following steps:

1. Split the given image into non-overlapping $b \times b$ blocks.
2. Perform 2-D DCT on each $b \times b$ image block independently. The corresponding DCT coefficient 2-D array Y for a $b \times b$ image block X is given as

$$Y = C^T X C \tag{19.1}$$

Where

$$\begin{cases} C(k,l) = \dfrac{1}{\sqrt{b}}, & 0 \le k \le b-1, l = 0 \\ C(k,l) = \sqrt{\dfrac{2}{b}} \cos\left(\dfrac{\pi(2k+1)l}{2b}\right), & 0 \le k \le b-1, 1 \le l \le b-1 \end{cases} \tag{19.2}$$

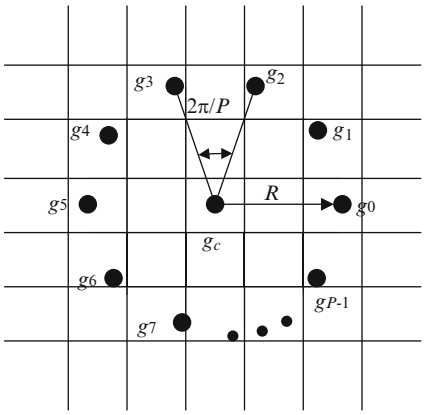

Fig. 19.2 Circularly symmetric P neighbor set with radius R

3. Combine all the $b \times b$ DCT coefficient 2-D arrays of the given image into a BDCT coefficient 2-D array.

Based on the experimental dataset [2], we empirically choose the block size as 4×4, 8×8, and 16×16 to perform BDCT for a compromise between detection performance and computing complexity when preprocessing the test images.

19.2.2 Feature Extraction

19.2.2.1 Brief Review of LBP

LBP [7] is a powerful texture classification method. As shown in Fig. 19.2, given a central pixel g_c, g_p ($p = 0, 1, 2 \ldots P-1$) is the value of its neighbors, P is the total number of involved neighbors, and R is the radius of the neighborhood. Suppose the coordinate of g_c is (x_c, y_c), then the coordinates of g_p are $(x_c + R\cos(2\pi p/P), y_c - R\sin(2\pi p/P))$. The gray values of neighbors which do not fall exactly on pixels can be estimated by bilinear interpolation. For the central pixel g_c, the LBP coding strategy can be formulated as

$$LBP_{P,R} = \sum_{p=0}^{P-1} s(g_p - g_c)2^p \tag{19.3}$$

Where

$$s(x) = \begin{cases} 1, & x \geq 0 \\ 0, & x < 0 \end{cases} \tag{19.4}$$

After the LBP codes of all pixels for a gray image are computed, a histogram is built as a texture descriptor which characterizes important information about spatial structure of image texture.

Furthermore, the U value of an LBP pattern is defined as the number of spatial transitions (bitwise 0/1 changes), it can be formulated as

$$\begin{aligned} U(LBP_{P,R}) = &\left|s(g_{p-1} - g_c) - s(g_0 - g_c)\right| \\ &+ \sum_{p=1}^{P-1} \left|s(g_p - g_c) - s(g_{p-1} - g_c)\right| \end{aligned} \tag{19.5}$$

The uniform LBP patterns refer to the patterns which have U values of at most 2 while the remaining patterns are all classified into non-uniform class. Therefore, the number of bins in a histogram computed from LBP codes can be reduced from 2^P to $P(P-1) + 3$ by means of uniformity mapping, the resulting LBP descriptor is denoted as $LBP^{u2}_{P,R}$. The uniformity mapping can be implemented with a lookup table of 2^P elements. In this chapter, $P = 8$ and $R = 1$ are investigated for image splicing detection. Consequently, the number of bins in a histogram computed from $LBP_{8,1}$ is 256 while that computed from $LBP^{u2}_{8,1}$ is 59.

19.2.2.2 Capturing the Splicing Artifacts Using Local Binary Patterns of DCT Coefficients

From the image splicing procedure, sharp splicing edges could be exposed in a spliced image without any postprocessing, thus the key of image splicing detection is how to capture these splicing artifacts. The splicing manipulation changes the local frequency distribution of the host images. BDCT coefficients can reflect these changes to a certain degree. The essence of the LBP technique is that each element of a given 2-D array is compared with its neighbor elements and then binarized. Hence, LBP coding records the occurrences of various patterns. LBP can be employed to model the magnitude components of the 2-D arrays obtained by applying MBDCT to the test images. It is expect that the LBP operator can reflect the local frequency distribution change of the host images effectively.

In order to catch the artifacts caused by image splicing more sensitively and obtain more discriminative information between authentic images and spliced images, (19.4) can be redefined as

$$s(x) = \begin{cases} 1, & x \geq \sigma \\ 0, & x < \sigma \end{cases} \tag{19.6}$$

Based on the experimental dataset [2], σ is selected as 0.9 in the proposed method. The details are given in Sect. 19.3.2. When computing $LBP_{8,1}$ or $LBP^{u2}_{8,1}$

features, we only use the block size as 4×4, 8×8, and 16×16 to generate the MBDCT coefficient 2-D arrays. Therefore, we have $256 \times 3 = 768$ $LBP_{8,1}$ features and $59 \times 3 = 177$ $LBP^{u2}_{8,1}$ features for each test image in this specific implementation.

19.3 Experiments and Results

The Columbia Image Splicing Detection Evaluation Dataset [2] is used to evaluate the efficiency of the proposed method in our experimental work. There are 933 authentic and 912 spliced images in this dataset. Images in this dataset are all in BMP format with a fixed size of 128×128 pixels. LIBSVM [8] is used as the classifier. The RBF kernel function is selected for classification. In each experimental, 5/6 of the authentic images and 5/6 of the spliced images are randomly picked out to train the SVM classifier, and the remaining 1/6 of the authentic images and 1/6 of the spliced images are used to test the trained SVM classifier. The optimal parameters for the RBF kernel function of SVM classifier are achieved by cross-validation and grid-search procedure. The above procedure is repeated 100 times for eliminating the effect of randomness caused by image selection for training and testing. Experimental results are evaluated by the average true positive rate (TPR), average true negative rate (TNR) and average detection accuracy over 100 times random experiments.

Table 19.1 Detection results of $LBP_{8,1}$ and $LBP^{u2}_{8,1}$ features (standard deviation in parentheses)

	$LBP_{8,1}$	$LBP^{u2}_{8,1}$
Feature size	768	177
TPR	90.52% (2.33%)	88.79%(2.41%)
TNR	89.32% (2.18%)	88.61%(2.55%)
Accuracy	89.93% (1.50%)	88.70%(1.76%)

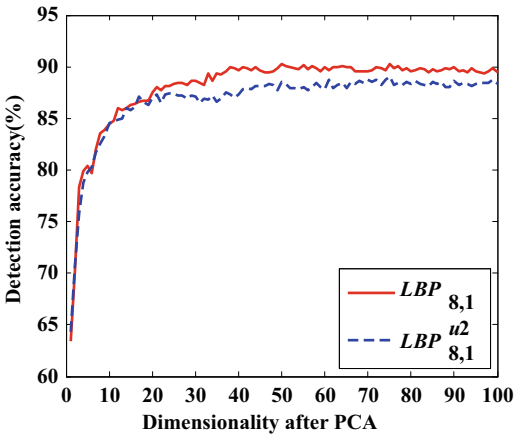

Fig. 19.3 Detection performance of $LBP_{8,1}$ and $LBP^{u2}_{8,1}$ features after PCA dimensionality reduction

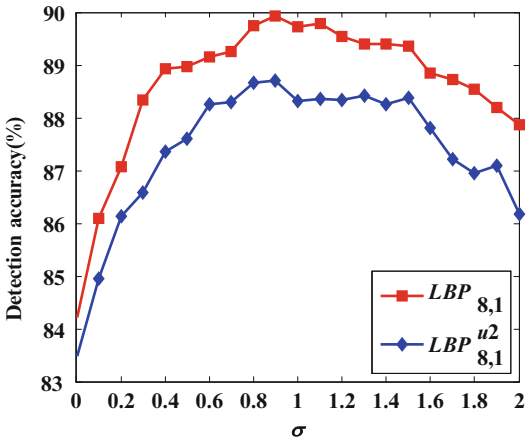

Fig. 19.4 Detection performance of original $LBP_{8,1}$ and $LBP^{u2}_{8,1}$ features with various thresholds of σ

19.3.1 Experimental Results

To evaluate the effectiveness of the proposed method, a series of experiments on the Columbia Image Splicing Detection Evaluation Dataset are carried out. Note that $\sigma = 0.9$ is set in this implementation. Detection results of $LBP_{8,1}$ and $LBP^{u2}_{8,1}$ features are shown in Table 19.1. As can be seen in Table 19.1, $LBP_{8,1}$ features perform better than $LBP^{u2}_{8,1}$ features even though $LBP_{8,1}$ features are of higher dimensionality. To avoid the high computational complexity and possible overfitting for SVM classifier, PCA [9] can be used to reduce the dimensionality of the proposed features. PCA achieves a linear transformation of a high dimensional input vector into a low dimensional one whose components are uncorrelated, and the first few features can be considered as dominant features for classification. Detection performance of $LBP_{8,1}$ and $LBP^{u2}_{8,1}$ features after PCA dimensionality reduction is shown in Fig. 19.3. Note that the first 100 dimensional PCA features are used for classification.

From Fig. 19.3, the observations can be made as follows:

1. For $LBP_{8,1}$ and $LBP^{u2}_{8,1}$ features, the detection accuracy increases dramatically with the increase of dimensionality of dominant features obtained by PCA, and then it fluctuates on comparatively small scales.
2. Compared with Table 19.1, PCA features with dimensionality larger than 40 can perform as well as original $LBP_{8,1}$ and $LBP^{u2}_{8,1}$ features.
3. $LBP_{8,1}$ features always perform better than $LBP^{u2}_{8,1}$ features with dimensionality larger than 30.

19.3.2 Choice of Threshold σ

In order to select a desired threshold σ, we need to find the best detection performance with various thresholds of σ. Too small or too large σ, the LBP operator will not be able to sensitively catch the artifacts caused by image splicing. The resulting LBP features will also offer relatively small discriminative information. Detection performance of original $LBP_{8,1}$ and $LBP^{u2}_{8,1}$ features for the threshold σ set in the range of 0–2 is shown in Fig. 19.4. From Fig. 19.4, it can easily be seen the best detection performance for the proposed features can be reached when $\sigma = 0.9$.

19.4 Conclusion

In this chapter, local binary patterns of DCT coefficients have been investigated for image splicing detection. Specifically, the LBP operator were used to model magnitude components of 2-D arrays obtained by applying MBDCT to the test images, the resulting LBP features were served as discriminative features for image splicing detection. Owing to the high dimensionality of the proposed features, PCA was therefore used for dimensionality reduction. Experimental results have shown that both $LBP_{8,1}$ and $LBP^{u2}_{8,1}$ features perform well for capturing the image splicing artifacts, but the detection performance of the former outperforms that of the latter. Furthermore, PCA reduced the dimensionality of original features greatly without losing discriminative information. The preliminary study has indicated that our proposal to use local binary patterns of DCT coefficients is effective for capturing the image splicing artifacts. Our future work is to make a further study to enhance the detection performance of the proposed method.

Acknowledgments This work is supported by National Science Foundation of China (61071152, 60702043), 973 Program (2010CB731403, 2010CB731406) of China and National "Twelfth Five-Year" Plan for Science & Technology Support (2012BAH38 B04). Credits for the use of the Columbia Image Splicing Detection Evaluation Dataset are given to the DVMM Laboratory of Columbia University. CalPhotos Digital Library and the photographers listed in http://www.ee.columbia.edu/ln/dvmm/downloads/AuthSplicedDataSet/photographers.htm.

References

1. Ng T-T, Chang S-F, Sun Q (2004) Blind detection of photomontage using higher order statistics. In: Proceedings of the IEEE international symposium on circuits and systems, Vancouver, Canada, vol 5, pp V688–V691
2. Ng T-T, Chang S-F (2004) A dataset of authentic and spliced image blocks. ADVENT Technical Report, #203-2004-3, Columbia University
3. Johnson MK, Farid H (2005) Exposing digital forgeries by detecting inconsistencies in lighting. ACM multimedia and security workshop, New York, pp 1–9

4. Fu D, Shi YQ, Su W (2006) Detection of image splicing based on Hilbert-Huang transform and moments of characteristic functions with wavelet decomposition. In: International workshop on digital watermarking, LNCS, Springer, Heidelberg, vol 4283, pp 177–187
5. Chen W, Shi YQ, Su W (2007) Image splicing detection using 2-D phase congruency and statistical moments of characteristic function. Society of photo-optical instrumentation engineers conference series, SPIE, Washington, vol 6505, pp 65050R.1-65050R.8
6. Shi YQ, Chen C, Chen W (2007) A natural image model approach to splicing detection. In: Proceedings of the 9th workshop on multimedia and security, Dallas, Texas, USA, pp 51–62
7. Ojala T, Pietikainen M, Maenpaa T (2002) Multiresolution gray-scale and rotation invariant texture classification with local binary patterns. IEEE Trans Pattern Anal Mach Intell 24 (7):971–987
8. Chang CC, Lin CJ (2001) LIBSVM: a library for support vector machines [EB/OL]. http://www.csie.ntu.edu.tw/cjlin/libsvm
9. Theodoridis S, Koutroumbas K (2009) Pattern recognition. Academic, Burlington

Part VI
Design and Implementation of Signal Processing System

Chapter 20
Sampling Synchronization for OFDM-Based System with Unified Reference Clock

Zhuo Sun

Abstract Due to the constraint of cost and size for mobile wireless communication terminals, many orthogonal frequency division multiplexing (OFDM) based systems required the same crystal driving the sampling and the channel frequency, which lead to the challenge of a more comprehensive sampling clock synchronization scheme needed. In this chapter, we proposed a two-stage scheme of sampling clock synchronization based on theoretical derivation: The preliminary sampling frequency offset(SFO) was jointly acquired with the carrier frequency offset by using the improved preamble-aided algorithm firstly. Secondly, the timing drift resulted from residual SFO and sampling timing error(STE) was derived together with performance analysis. The deviation properties of the estimation were achieved theoretically, which reveals that the variance of timing drift is in inverse proportion to SNR and grows linearly by square of the number of total subcarrier. The results of simulation show the proposed synchronization scheme can introduce preferable tracking and robust synchronizing performance for this kind of OFDM-based system.

Keywords System synchronization • Sampling clock error • Joint estimation • Timing drift

20.1 Introduction

The sampling clock synchronization in Orthogonal frequency division multiplexing (OFDM) system is to mitigate the sampling clock errors due to the mismatch of the crystal oscillators between the transmitter and the receiver [1]. The sampling clock

Z. Sun (✉)
Key Laboratory of Universal Wireless Communications, Ministry of Education, Beijing University of Posts and Telecommunications, Beijing, China
e-mail: Zhuosun@bupt.edu.cn

Q. Liang et al. (eds.), *Communications, Signal Processing, and Systems*, Lecture Notes in Electrical Engineering 202, DOI 10.1007/978-1-4614-5803-6_20,

error can essentially be divided into two parts: sampling clock frequency offset (SFO) and sampling timing error (STE). SFO means the offset of sampling frequency between transmitter and receiver. STE implies the sampling does not align at the central of the samples, which was also named sampling clock phase offset in some literatures [2]. The sampling clock error will cause inter-carrier interference (ICI), and a drift in the symbol timing and further worsen inter-symbol interference (ISI) [1–3]. The effect of SFO on the system performance are analyzing in terms of BER degradation and inter-sample-interference in [3] and [4] respectively.

In many wireless communication systems, such as WiMAX, there are the constraints of low cost and miniaturization for mobile communication device, and the specification requires that the same crystal must be used to drive the sampling and the channel frequency, which is adopted for many personal handheld terminals (e.g. Smart phone) especially. However, the same reference clock property introduce a new challenge for the design of joint carrier and sampling clock synchronization, where the frequency offset have relationship with the sampling frequency offset besides the Doppler shift. It is seen that most research on joint sampling and frequency synchronization [5–7] have only considered the sampling clock frequency synchronization but ignored the sampling timing error. Additional, they view the synchronization of sampling clock frequency all at once whereas neglecting the permanent drift of sampling clock frequency. Most of important, they have not utilize the relationship between the frequency offset and sampling frequency offset due to the same reference clock.

In this chapter, we address on the problem of sampling clock synchronization in OFDM receiver system with the same driving clock source. Firstly, the preliminary sampling clock frequency offset is jointly acquired with carrier frequency offset by taking the benefit of the same crystal for both sampling and channel frequency in Sect. 20.3.1. Secondly, the timing drift resulted from the residual sampling clock frequency offset and sampling timing error is tracked and periodically corrected in Sect. 20.3.2. The simulation results and discussion are given in Sect. 20.4.

20.2 System Model and Design of Training Sequence

- System Model

  The OFDM system model and signal flow are illustrated by Fig. 20.1. It needs to point out the same crystal drives both the sampling and carrier frequency mixing here. As the output of D/A converting, the transmitted OFDM signal during one OFDM symbol duration can be expressed as:

$$s(t) = \sum_{k=0}^{N-1} A_k e^{j2\pi kt/(NT_s)} \tag{20.1}$$

  where A_k denotes the OFDM symbol on the carrier k, N is the number of total carrier. T_s is the sampling interval for OFDM symbol.

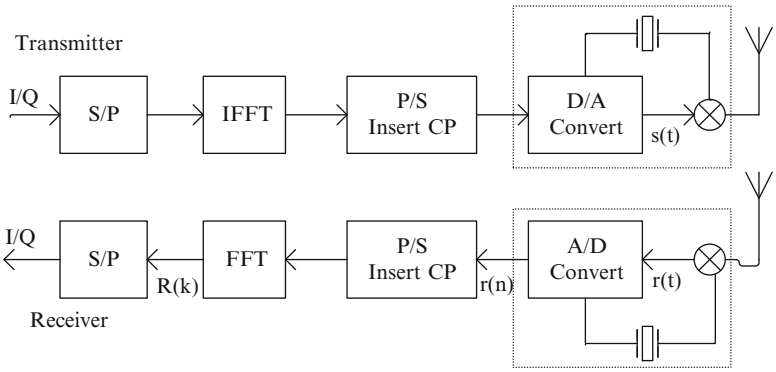

Fig. 20.1 OFDM system model with the unified driving crystal

The *s(t)* successively passes through the procedures: upper converting onto carrier frequency, additive white Gaussian noise channel, down-converting, then can be written as:

$$r(t) = \left[s(t)e^{j2\pi f_c t} + n(t)\right]e^{-j2\pi(f_c+f_c)t} = s(t)e^{-j2\pi f_c t} + n(t)e^{-j2\pi(f_c+f_c)t} \tag{20.2}$$

In (20.2), Δf_c is the carrier frequency offset between receiver and transmitter, which is caused by Doppler shift and mismatch between the clock of receiver and transmitter.

Here we define the A/D sampling interval offset as $\Delta T = T_r - T_s$ (T_r is the sampling interval of A/D converter), and the sampling timing error as Δt, $\Delta t \leq T_s/2$. The sampling clock frequency offset obviously equals to $\Delta f_s = 1/T_r - 1/T_s$. During an OFDM symbol, the sampling time of A/D converter at receiver is $t = nT_r - \Delta t$, $n = 0,1,\ldots N\text{-}1$. The sampled signal can be expressed as:

$$r(n) = r(t)|_{t=nT_r-\Delta t} = \sum_{k=0}^{N-1} A_k e^{j2\pi k(nT_r-\Delta t)/(NT_s)} e^{-j2\pi f_c(nT_r-\Delta t)} + \eta \tag{20.3}$$

and $\eta = n(t)e^{-j2\pi(f_c+f_c)t}|_{t=nT_r-\Delta t}$ is the sample of channel noise.

Due to the same driving crystal for sampling and channel frequency, the relationship between sampling clock frequency offset and the carrier frequency offset can be denote as:

$$f_c/f_s = \triangle f_c/\triangle f_s = \varepsilon_c/(N \cdot \varepsilon_s) \tag{20.4}$$

where f_s equals to $1/T_s$, ε_c is the relative carrier frequency offset and defined as the ratio of Δf_s to subcarrier spacing. ε_s is sampling clock frequency offset normalized by f_s. In (20.4), the effect of Doppler shift on carrier frequency offset has been neglected.

- Design of Training sequence

  The preamble aided estimation is adopted in this chapter. The preamble is the first symbol of transmission frame, of which the subcarriers are modulated using a boosted BPSK modulation with a specific pseudo-noise(PN) code.
  For the structure of preamble sequence in frequency domain, only each third of subcarriers ($M = N/3$) are modulated with pseudo noise sequence, the remainder subcarriers are filled with zero. It can be proved this structure of the preamble in frequency domain means three repletion parts in time domain:

$$C(k) = C(k + M) = C(k + 2M), k = 0, \ldots M - 1 \tag{20.5}$$

  where we assume $M = N/3$ is integer, C(k) is the PN sequence.
  The frame period is defined as L_s in sample at transmitter, it means the preamble symbol will appears for every L_s samples. The measuring of the frame period at receiver is used in the estimation of timing error in the tracking stage.

20.3 Sampling Clock Synchronization

In this section, we will elaborate on how to achieve the accurate estimation of sampling clock frequency offset and the timing drift caused by residual sampling clock frequency offset and sampling timing error. Moreover, we complete the theoretical performance of the sampling clock synchronization scheme by through analyzing the deviation property of estimation result.

20.3.1 Sampling Frequency Offset Estimation

From (20.4), the estimation of sampling frequency offset can be translated into the estimation of carrier frequency offset, and the result of carrier frequency estimation can be used to compensate both the sampling frequency offset and carrier frequency offset.

In the general, the relative carrier frequency offset is divided into fractional part and integer part and estimated separately:

$$\varepsilon_c = \varepsilon_F + \varepsilon_I \tag{20.6}$$

where ε_F represents the fractional part and ε_I is the integer part of carrier frequency offset.

- Fractional Carrier Frequency Offset

Consider the preamble in time domain there are three identical parts, except a phase shift between the adjacent parts caused by the carrier frequency offset. Therefore, estimation of FCFO is based on the idea: if the conjugate of the first part is multiplied by the second part, the effect of channel can be eliminated, and the result is exactly the phase shift. When neglecting the cyclic prefix, the received OFDM symbol in time domain can be expressed as:

$$r(n) = \sum_{k=0}^{N-1} C(k)H(k)e^{j2\pi n(k+\varepsilon_F)/N} \tag{20.7}$$

and $n = 0,1,\ldots N\text{-}1$. $C(k)$ is the preamble sequence in time domain, and the $H(k)$ is the transfer function on the kth subcarrier. Here we use ε_F to represent the overall carrier frequency offset. It will be proved the estimation by the method actually is the fractional frequency offset later.

Let define the $P(M)$ as the correlation function of $r(n)$:

$$\begin{aligned} P(M) &= \sum_{n=0}^{M-1} r^*(n)r(n+M) \\ &= \sum_{n=0}^{M-1}\sum_{u=0}^{N-1} C^*(u)H^*(u)e^{-j2\pi n(u+\varepsilon_F)/N} \cdot \sum_{v=0}^{N-1} C(v)H(v)e^{j2\pi(n+M)(v+\varepsilon_F)/N} \end{aligned} \tag{20.8}$$

By substituting $R_h(0) = \sum_{k=0}^{N-1} H(k)H^*(k) = \sum_{k=0}^{N-1} |H(k)|^2$ and $A = \sum_{k=0}^{M-1} |C(k)|^2$ into (20.8), then we have

$$P(M) = e^{j2\pi\varepsilon_F/3} M \cdot A \cdot R_h(0) \tag{20.9}$$

From (20.9), it can be found frequency offset is equal to:

$$\varepsilon_c = \frac{3}{2}\pi \cdot \angle P(M) \tag{20.10}$$

The estimation range of frequency offset by (20.10) is $(-3\pi/2, 3\pi/2)$, which means the offset beyond the range can not to be calculated using the aforementioned method. Therefore, the fractional carrier frequency offset is mainly achieved here.

The derivation in (20.10) has not considered the channel noise. If the channel noise exists the received signal in (20.7) will be rewritten as:

$$r(n) = \sum_{k=0}^{N-1} C(k)H(k)e^{j2\pi n(k+\varepsilon_F)/N} + w_n \tag{20.11}$$

w_n is the complex additive white Gaussian noise with the zero mean and the variance$\sigma_n{}^2$. Similarly in [8], it shows the maximum-likehood estimation (MLE) of the fractional frequency offset is:

$$\hat{\varepsilon}_F = \tan^{-1}\{\mathrm{Im}(P(M)/\mathrm{Re}(P(M))\} \tag{20.12}$$

When using the method in [8], the variance of ε_F is:

$$D(\hat{\varepsilon}_F) \approx \frac{1}{\pi^2 M \cdot SNR} \tag{20.13}$$

The ratio of signal power to noise power (*SNR*) on an OFDM symbol is defined as $SNR = R_h(0)A/\sigma_n{}^2$ Actually, because the fractional frequency offset is the MLE by (20.12), it states that the Cramer-Rao bounds are almost met by the estimation with high *SNR* in [8]. Here, the phase shift is calculated over all of the subcarriers in (20.8), which usually can satisfy the condition of the high average effective *SNR*.

- Integer carrier frequency offset

The integer carrier frequency offset should be estimated in frequency domain for accurate acquisition. We still achieve the estimation by taking the use of the property of PN sequence and preamble structure.

Firstly, it is known that the PN sequence used for the preamble have the auto-correlation property:

$$R_c(\tau) = \left\{ \begin{array}{r} M, \tau = i \cdot M \\ -1/M, \tau \neq i \cdot M \end{array} \right\}, i = 0, 1 \ldots \tag{20.14}$$

We rewrite the value of the *k*th subcarrier value in received signal in frequency domain as:

$$R(k) = H(k)C(k + \varepsilon_I) + W(k) \tag{20.15}$$

Here $W(k)$ is the FFT conversion of $w(n)$, which can be proved that $W(k)$ is still a Gaussian variable with the zero mean and variance $\sigma_n{}^2$. We use $C(k + \varepsilon_I)$ to denote the signal has shift ε_I subcarriers compared to local preamble sequence.

When shifting the local preamble sequence with i subcarriers, then multiplying with $R(k)$:

$$\begin{aligned} Y(k) &= R(k) \cdot C(k + i) \\ &= H(k)C(k + \varepsilon_I)C(k + i) + W(k)C(k + i) \end{aligned} \tag{20.16}$$

As to the second term in (20.16), since the $C(k + i)$ is a BPSK modulated symbol with value +1 or −1, the product will still hold as the same property of Gaussian

variable *W(k)*. Especially, when the shift number i equals to the existed frequency offset ε_I, the (20.16) will be:

$$\begin{aligned} Y(k)|_{i=\varepsilon_I} &= R(k)C(k+\varepsilon_I) \\ &= H(k)|C(k+\varepsilon_I)|^2 + W(k) = H(k) + W(k) \end{aligned} \tag{20.17}$$

Here we have used the result $|C(k)|^2 = 1$ and eliminated the $C(k)$ element in the result.

Next, the correlation function of *Y(k)* is defined as:

$$R_y(\tau) = \frac{1}{M}\sum_{k=0}^{N-1} Y^*(k)Y(k+\tau) \tag{20.18}$$

Based on (20.18), we define a metric of integer frequency offset estimation as:

$$M(i) = \left|R_y(3)\right|/R_y(0) \tag{20.19}$$

It is not difficult to deduce that the value of $|R_y(3)|$ on the condition of $i = \varepsilon_I$ is more large than that while $i \neq \varepsilon_I$. It can be explained as follows. When $i \neq \varepsilon_I$ the first term of *Y(k)* in (20.17) will be the product of *H(k)* and random +1/ −1, which produces the counteract within the sum of $R_y(3)$. For $R_y(0)$, it actually represents the totoal power of signal and noise, which is used in (20.19) for normalizing the $M(i)$.

Therefore, the estimation of integer carrier frequency offset is to find the value of i when satisfying:

$$\hat{\varepsilon}_I = \arg\max_i \left[M(i)\right] \tag{20.20}$$

The statistical property of *M(i)* can be derived as:

$$M(\hat{\varepsilon}_I) \approx \frac{\sigma_s^2}{\sigma_s^2 + \sigma_n^2} = \frac{1}{1 + 1/SNR} \tag{20.21}$$

It can be deduced that the metric approaches to 1 as SNR increases. The metric value is greater than 0.9 when SNR is above 5 dB, which could be used for verifying the result of (20.20).

- Sampling clock frequency offset

Once the estimation of fractional carrier frequency offset and integer carrier frequency offset are achieved, the sampling clock frequency can be calculated using the linear relationship with the carrier frequency offset as (20.4):

$$\hat{\varepsilon}_s = \frac{f_s(\hat{\varepsilon}_F + \hat{\varepsilon}_I)}{f_c N} \tag{20.22}$$

The method in (20.22) ignores the existence of Doppler shift in the CFO, so the estimation of SFO is not strict. However, we will deal with amend the estimation in tracking stage.

20.3.2 Timing Drift Estimation

Except residual sampling clock error, the fractional symbol timing error that may be ignored also contributes to the timing drift, which can be considered as a uniform adjustable variable. This adjusting variable is derived in frequency domain and then fed back into time domain to adjust digital oscillator, guaranteeing the synchronization stability. Firstly we focus on the estimation of timing drift.

We assume the received signal compensated with the estimation ε_s still has the timing drift denoted by Δn sampling interval(note it may be decimals), that is:

$$R(k) = H(k)C(k)e^{-i2\pi k\triangle n/N} + W(k) \tag{20.23}$$

In order to eliminate *C(k)* in the first term of (20.23), we similarly define:

$$Y(k) = R(k) \cdot C(k) = H(k)e^{-j2\pi k\triangle n/N} + W(k) \tag{20.24}$$

When $\tau = 3$ the correlation of *Y(k)* is:

$$R_y(3) = \frac{1}{M}\sum_{k=0}^{N-1}\Big\{H^*(k)H(k+3)e^{-j6\pi\triangle n/N} + H(k+3)W^*(k)e^{-j2\pi(k+3)\triangle n/N} + H^*(k)W(k+3)e^{j2\pi k\triangle n/N} + W(k+3)W^*(k)\Big\}$$

When neglecting the noise, the (20.25) only reserves the first term:

$$R_y(3) = R_h(3)e^{-j6\pi\triangle n/N} \tag{20.26}$$

if the coherence bandwidth of channel is greater than the range of three subcarriers, the transfer function on the adjacent three subcarriers are viewed relatively, the phase of $R_h(3)$ is approach to 0. Therefore, the timing drift can be estimated as:

$$\widehat{n} = \frac{N}{6\pi} \cdot \angle R_y(3) \tag{20.27}$$

The maximum like-hook estimation Δn of is:

$$\triangle n = \frac{N}{6\pi} \cdot \tan^{-1}\{\mathrm{Im}[\mathrm{R}_y(3)]/\mathrm{Re}[\mathrm{R}_y(3)]\} \tag{20.28}$$

we can get the variance of Δn:

$$D(\triangle n) = \frac{N^2}{(6\pi)^2 SNR} \tag{20.29}$$

The result reveals that the variance of timing drift is in inverse proportion to SNR and grows linearly by square of the number of total subcarrier.

20.4 Simulation and Discussion

The simulation is implemented for evaluate the performance of proposed sampling clock synchronization in AWGN channel and multipath fading channel (ITU V-A channel[9]), the multipath channel have been developed with Doppler spread of 38.9 kHz. The parameters of OFDM transmission system are as follows: frame length 5 ms, sampling clock 22.4 MHz (eight times interpolation), subcarrier spacing of 10.94 kHz with 256 subcarriers. The OFDM subcarriers are modulated by QPSK, Reed-Solomon and circular convolution code are used as the outer and inner forwarding error correction scheme with code rate 1/2.

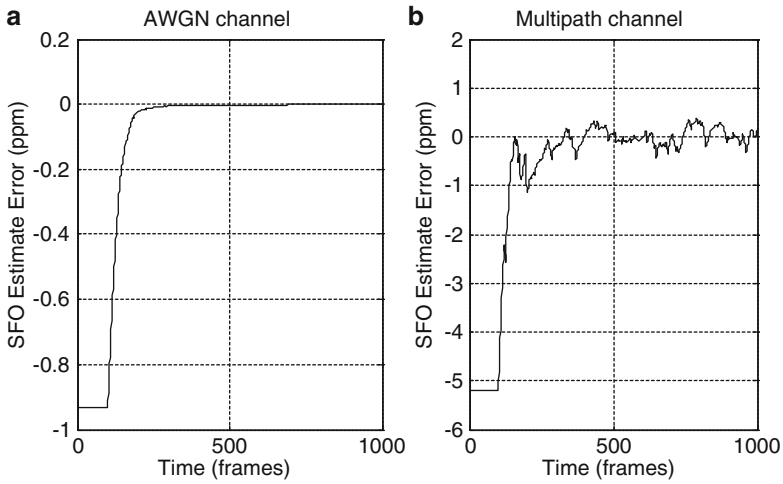

Fig. 20.2 SFO tracking process

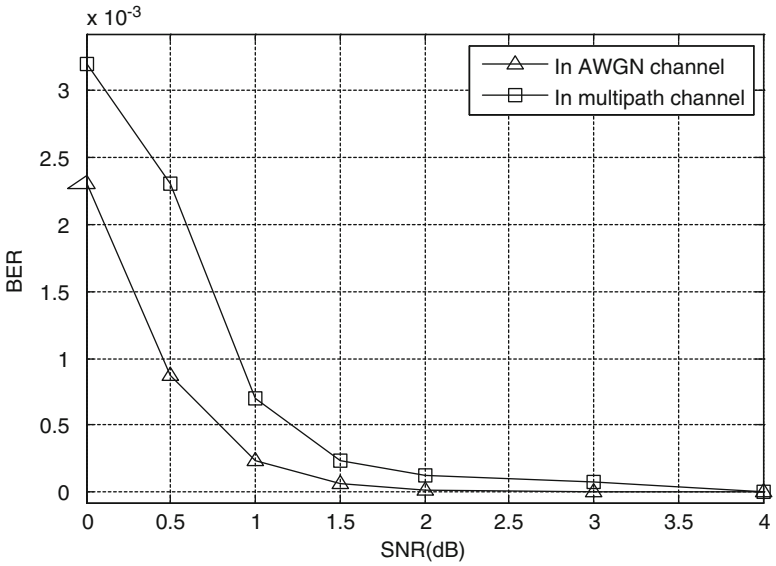

Fig. 20.3 BER performance of proposed synchronization scheme

Figure 20.2a, b depict the tracking process of sampling clock frequency offset in AWGN and multipath fading channel. The simulation is performed at SNR 10 dB and normalized sampling clock frequency offset 73.728 ppm. In the first 100 number of frames, the PLL is initialized using the first group parameters, of which the beta filter value is set to zero for considering that the timing error is mainly caused by the inaccurate of symbol timing at the beginning of synchronization, so sampling clock frequency remain major error. The next two group parameters are used for 100 number of frame sequentially, but during the third 100 frames if the lock metric exceeds a upper threshold 1 it will retreat running with the second group parameters. From Fig. 20.2a, b, it can be seen the sampling clock frequency offset is nearly eliminated after 300 number of frames. Since then the fourth group parameters are bring into use all the time unless the lock metric exceed the threshold 0.1 and go back using the third group parameters.

The BER performance of the proposed synchronization scheme in multipath channel is given in Fig. 20.3. In the simulation, we adopt the method of symbol timing synchronization proposed in [8]. The BER is figured up after the PLL is locked. The simulation result shows that, when using proposed synchronization scheme together with robust QPSK modulation and RS + CC with 1/2 code rate, the BER approach 10^{-6} when SNR $\geq$4 dB. It proved the proposed sampling clock synchronization scheme can achieve preferable performance for the OFDM system with unified driving crystal.

20.5 Conclusion

Regarding the requirement of miniaturization and low cost for wireless personal communication device, on which the same crystal to drive the sampling and channel frequency is equipped generally. The proposed scheme of sampling clock synchronization is perfectly appropriate for this kind of OFDM-based communication system, and it actually be a complete and practical synchronization scheme together with a symbol timing synchronization method for OFDM system.

References

1. Ai Bo, Yang Zhixing, Pan Changyong et al. (2006) On the synchronization techniques for wireless OFDM systems. IEEE Trans Broadcast 52(2):236–244
2. Yang BaoGuo, Letaief KB, Roger S (2000) Timing recovery for OFDM transmission. IEEE J Sel Areas Comm 18(22):2278–2291
3. Pollet T, Spruyt P, Moeneclaey M (1994) The BER performance of OFDM systems using nonsynchronized sampling. In: Proceedings of IEEE Globecom'94, vol 1, San Francisco, Dec 1994, pp 253–257
4. Kim J, Powers EJ, Cho Y (2002) A nonsynchronized sampling scheme. In: Proceedings of the 36th Asilomar conference on signals, systems and computers, vol 2, Pacific Grove, Nov 2002, pp 1900–1904
5. Lee H, Lee J (2011) Joint clock and frequency synchronization for OFDM-based cellular systems. IEEE Signal Process Lett 18(12):757–760
6. Del Castillo-Sanchez E, Lopez-Martinez FJ et al (2009) Joint time, frequency and sampling clock synchronization for OFDM-based systems. In: Wireless communications and networking conference, vol 1, Budapest, Apr 2009, pp 1–6
7. Sliskovic M (2001) Carrier and sampling frequency offset estimation and correction in multicarrier systems. In: Proceedings of IEEE global telecommunications conference, vol 1, San Antonio, Sept 2001, pp 285–289
8. Moose PH (1994) A technique for orthogonal frequency division multiplexing frequency offset correction. IEEE Trans Comm 42(10):2908–2914
9. ITU-R M.1225 (1997) Guidelines for evaluation of radio transmission technologies for IMT-2000. www.itu.int

Chapter 21
A New Low Voltage Low Power Consumption Comparator for Successive Approximation Register ADCs

Shitong Yuan, Hai Huang, and Qiang Li

Abstract A New low-voltage low-power comparator for Successive-Approximation Register Analog-to-Digital Converter (ADC) has been designed. The input is amplified by a differential amplifier with positive feedback structure in the pre-amplifier. The positive feedback latch can reduce the power consumption. Using a constant bias circuit to provide two different bias voltages, an eliminated effect of different process variations on the amplifier is observed. All cells of the dynamic comparator have been simulated in a 0.13um CMOS technology process by Cadence tools. The total size of this dynamic comparator is less than 0.02 mm^2.

Keywords Analog-to-digital converter • Preamplifiers • Latches

21.1 Introduction

In today's world, an increasing number of devices are required for portable battery; a major thrust is given towards low power = applications. This reduction in power can be achieved by moving towards lower supply voltage. However, as we move towards lower supply voltage, the process variations and other non-idealities will greatly affect the overall performance of the device in question. One such application where low power, low supply voltages are required is Analog-to-Digital Converters (ADCs) for mobile and portable devices. In recent years, low voltage and low power are becoming prevailing technologies of ADCs due to a great

S. Yuan (✉) • H. Huang • Q. Li
School of Communication and Information Engineering, University of Electronic Science and Technology of China, Chengdu, China
e-mail: ShitongYuan@gmail.com

Q. Liang et al. (ed.), *Communications, Signal Processing, and Systems*, Lecture Notes in Electrical Engineering 202, DOI 10.1007/978-1-4614-5803-6_21,

demand of portable electronic products. A high-performance comparator with low voltage and low power is indispensable as an important cell of ADCs. In literature one will find that a major emphasis has been made in regard to the high speed, high resolution comparators but very little effort has been made towards the design of low power low supply voltage comparators. The accuracy of such comparators, which is defined by its offset,and speed, along with power consumption which is of keen interest in achieving higher performance of ADCs. In the past, pre-amplifier based comparators have been used for ADC architectures such as flash and pipeline. The main drawback of pre-amplifier = based comparators is the high constant power consumption. To overcome this problem, dynamic comparators are often used that make a comparison once every clock period and require much less power as compared to the pre-amplifier based comparators. The main characteristics of Successive-Approximation Register (SAR) ADCs are power consumption changes with the sampling rate and the small size.

In literature, a few dynamic comparators can be found; e.g. [1] designed a low power comparator with the average power consumption of 584 μW. Another high speed comparator was working at the sampling frequency of 5.78 GHz where its power consumption is 33.2 μW [2]. [2, 3] are concentrated on high speed structures, however, very little emphasis is placed on low power consumption low supply voltage comparator structures which are used to Successive Approximation Register ADCs [3–6]. These experimental supply voltages vary from 1.2 to 1.8 V. The comparator speed decreases with the lower supply voltage, however latch apply positive feedback structure can improve the compare speed. Few authors talk about how to avoid the effect to the performance of preamplifier with the process variations. In some preamplifier structures, the bias voltages are usually necessary. Bias voltages are often provided by the supply voltage, rather than the external circuit. In the same voltage supply, different process angle will result in the transistors' actual width to length ratio change. As a result, bias voltage will change, and the preamplifier can not work properly.

To resolve the problems above, this chapter designed a new comparator with three stages. This chapter first introduces the three modules of the new compare, and then lists the circuit simulation results. At last, the advantages and the disadvantages are given in the conclusion.

21.2 Circuit Architecture

This comparator circuit comprises two modules, the latch and the differential amplifier. Differential signal input can improve the noise resisting ability of the circuit. The preamplifier can improve the accuracy of the comparator and brief structural design reduce the power consumption of the circuit as much as possible. The structure of this circuit is shown in Fig. 21.1.

The overall layout of the circuit is shown in Fig. 21.2.

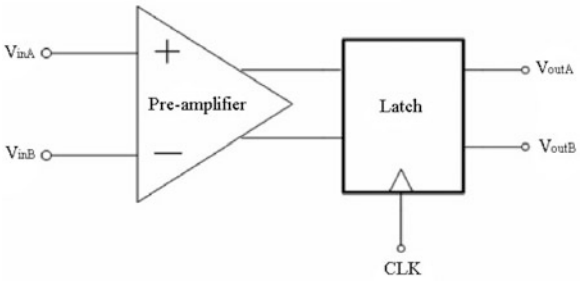

Fig. 21.1 Fully comparator structure

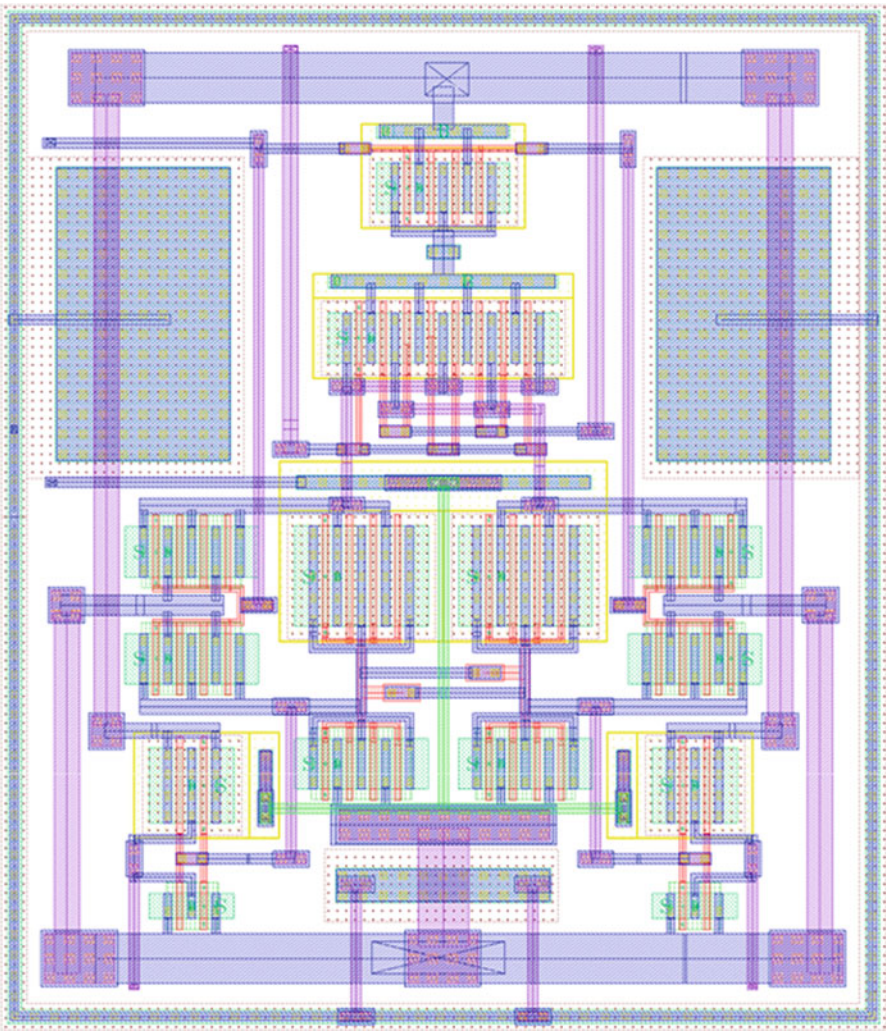

Fig. 21.2 The layout of the circuit

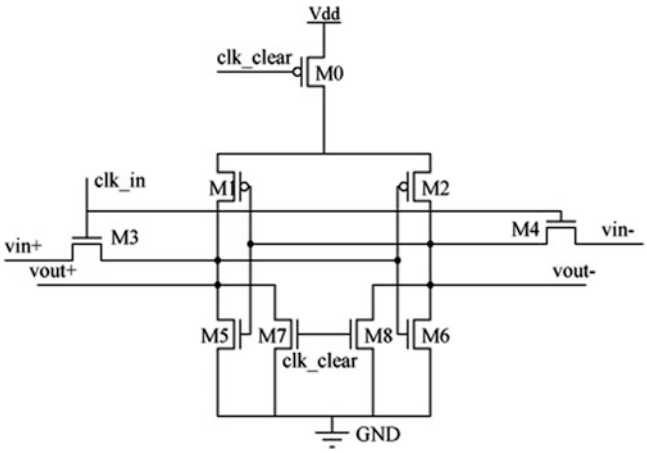

Fig. 21.3 Fully differential typical dynamic comparator

21.2.1 Latch

A traditional fully differential dynamic comparator is shown in Fig. 21.3. The comparator consists of two cross coupled differential pairs with inverter latch at the top. Comparison is made based on the inverter currents, which are related to the inputs, when the clock signal goes high.

There are a few points that are worth noting in regard to the problems present in this structure. The first drawback of this comparator is the comparator's accuracy is not high when the supply voltage is low to 500 mV. That means when the input signal is small, it may give wrong comparison results and the circuit is instable. The second problem is related to the different clock signal inputs. Although the two clock signal inputs are inverted, this structure will still increase the complexity of the circuit.

To overcome the drawbacks of the typical differential pair mentioned above, a new dynamic comparator has been proposed which addresses the above listed problems. This new dynamic latch is shown in Fig. 21.4.

In this new structure, the entire circuit shared the same clock. And the input signal is amplified through a MOS transistor, and then as an input for comparator. Such a structure can improve the accuracy of the comparator.

21.2.2 Pre-amplifier Design

Because we need a low supply voltage, low-power consumption comparator, the pre-amplifier should have a simple structure rather than a harsh requirement on gain. In order to meet the design requirements, a simple structure of amplifier is chosen which shown in Fig. 21.5. Point a and b are the inputs of the bias voltages.

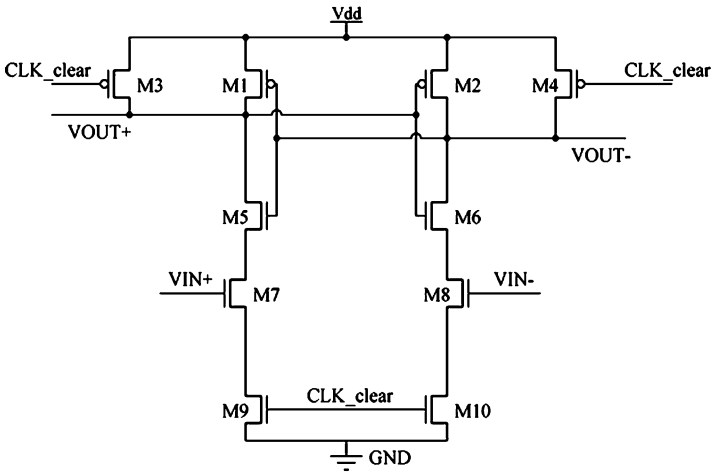

Fig. 21.4 New dynamic comparator

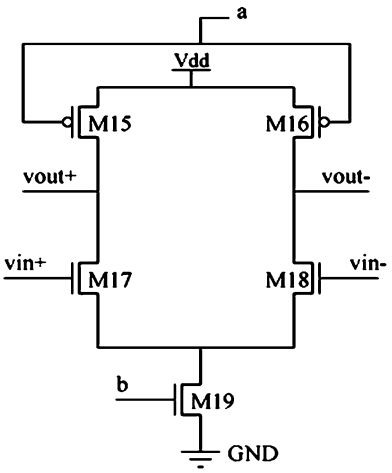

Fig. 21.5 The amplifier circuit

The DC gain and unity gain bandwidth of the amplifier are

$$A_{V0} = \frac{g_{m1}}{r_{o1} + r_{o2}} \tag{21.1}$$

$$\omega_u = \frac{g_{m1}}{C_L} \tag{21.2}$$

The output voltage swing range and slew rate are

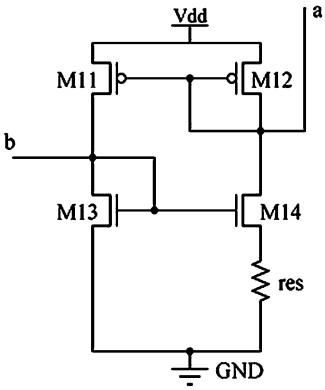

Fig. 21.6 Bias circuit

$$V_{SW} = 2 \cdot (V_{DD} - 3V_{DS,sat}) \tag{21.3}$$

$$SR = \frac{\mathrm{I}_{19}}{C_L} \tag{21.4}$$

21.2.3 Bias Circuit

When the circuit is operating in the actual case, the supply voltage often has small fluctuation. In most circumstances, the fluctuation can be ignored, however the circuit designed in this chapter operates in a very low supply voltage. In the traditional structure, the bias voltage is highly related to the power supply voltage, as a consequence, the amplifier cannot operate normally. To solve this problem, we can expect that the circuit must be biased by itself. A bias circuit which can provide independent current is shown in Fig. 21.6.

In this figure PMOS devices have the same size, so we may safely draw the following equations [7]

$$V_{GS1} = V_{GS2} + I_{D2}R_S \tag{21.5}$$

Ignore the body effect

$$\sqrt{\frac{2I_{out}}{\mu_n C_{ox}(W/L)_N}}\left(1 - \frac{1}{\sqrt{K}}\right) = I_{out}R_S \tag{21.6}$$

Therefore

$$I_{out} = \frac{2}{\mu_n C_{ox}(W/L)_N}\frac{1}{R_S^2}\left(1 - \frac{1}{\sqrt{K}}\right)^2 \tag{21.7}$$

In order to reduce effect to the amplifier performance of the process corners as much as possible, all the PMOS's width are set the same to M0,M1 and all the NMOS's width are set the same to M4.

The preamplifier designed before needs two different bias voltages, in order to simplify the circuit structure as much as possible, the bias is designed to provide two different bias voltages. This makes a very harsh requirement on the size of these transistors.

21.3 Simulation Result

In IBM's cmrf8sf process, tt process angle, the per-amplifier has a good performance. Figure 21.7 shown the output of the amplifier when a very small signal inputs.

And some parameters (Gain, 3 dB bandwidth, Phase-domain, Power consumption, Delay) which amplifier operates in different voltages are shown in Table 21.1. Amplifier can work properly in the case of voltage instability.

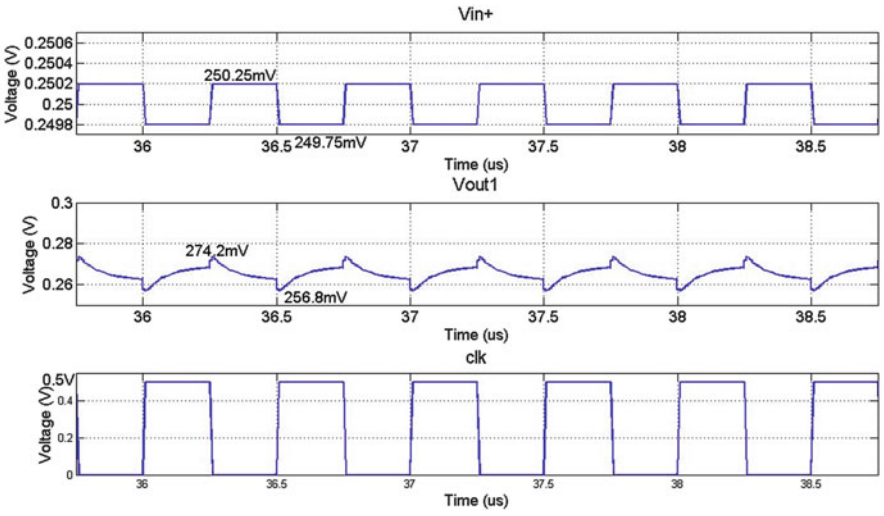

Fig. 21.7 The result of a small signal inputs to amplifier

Table 21.1 The amplifier performance in different supply voltages

Voltage	450 mV	500 mV	550 mV
Gain(dB)	26.20	27.06	27.18
3 dB bandwidth	3.85	3.75	3.98
Phase-domain(°)	75.1	74.5	74.1
PC(μW)	1.138	1.344	1.564
Delay(μs)	0.12	0.10	0.08

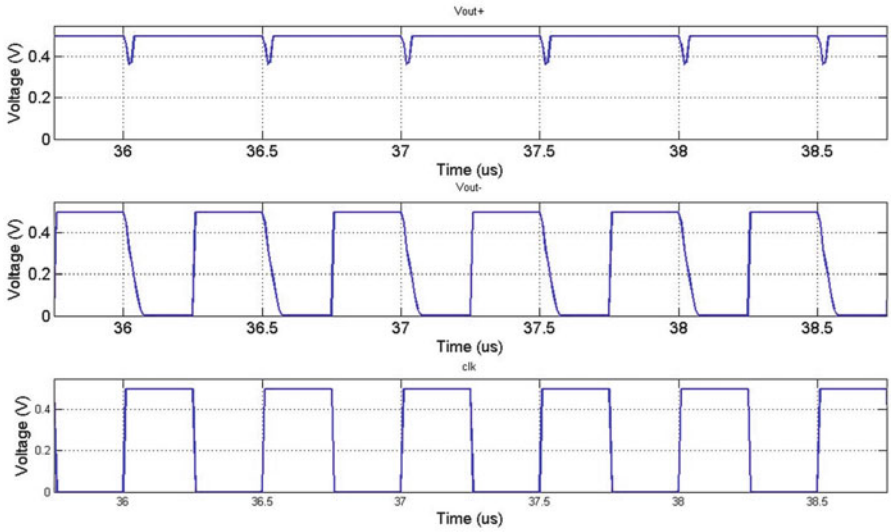

Fig. 21.8 Simulation result of the circuit

When the input differential signal is a square wave with 0.5 mV amplitude, the output signals are shown in Fig 21.8.

21.4 Conclusion

A new low voltage low power consumption comparator was proposed for Successive Approximation Register ADC application. In the new design, when the input signal is very small, the comparator can still be able to generate the result accurately. The advantages of this design are the small layout area and the simple structure. According to the simulation results, this amplifier has a good performance under low voltage and is not sensitive to voltage fluctuations. Two different bias voltages created by one bias circuitreduce the chip area and power consumption. The latch adopts positive feedback structure, greatly improving the compare speed and precision. When power supply voltage is 500 mV and the inputs are 0.5 mV differential signals, the power consumption is about 1.4 μW. At 1MSPS, the power consumption is about 5.6 mW.

References

1. Goll B, Zimmermann H (2007) A clocked, regenerative comparator in 0.12um CMOS with Tunable Sensitivity. In: Proceedings of the IEEE international solid-state circuits conference, p 12

2. Sundstrom T, Alvandpour A (2007) A kick-back reduced comparator for a 4-6-bit 3-GS/S Flash ADC in a 90nm CMOS process. In: Proceedings of the IEEE 14th international conference, p 6
3. Goll B, Zimmermann H (2007) A low-power 4 GHz comparator in 120 nm CMOS technology with a technique to tune resolution. In: Proceedings of the IEEE international solid-state circuits conference, p 12
4. Goll B, Zimmermann H (2009) A 65 nm CMOS comparator with modified Latch to achieve 7 GHz/1.3 mW at 1.2 V and 700 MHz/47uW at 0.6 V. In: Proceedings of the IEEE international solid-state circuits conference, p 2
5. Song Ye, Jie Wu (2009) An ultra-high-speed comparator for ADC in 90 nm CMOS technology IEEE microwave antenna, propagation and EMC technologied for wireless communications, p 12
6. Goll B, Zimmermann H (2009) A comparator with reduced delay time in 65-nm CMOS for supply voltages down to 0.65 V. In: Proceedings of the IEEE transactions on circuits and systems, p 9
7. Behzad Razavi (2001) Design of analog CMOS integrated circuits. The McGraw-Hill

Part VII
Information Theory and Coding

Chapter 22
A Novel High-Resolution Wide-Swath SAR Imaging Algorithm*

Weihua Zuo, Rui Min, and Jin Li

Abstract Based on the theory of compressive sensing, in this chapter a novel high-resolution and wide-swath Scan SAR imaging algorithm is proposed. The proposed algorithm consists in range compression by the traditional matching filter method, range cell migration correction and the cross range compression by compressive sensing technique. The comparison between the traditional range-Doppler algorithm and the proposed method shows that the proposed method is suitable for high resolution wide swath imaging based on Scan SAR.

Keywords Compressive sensing • Synthesis aperture radar • Scan mode • High resolution • Wide swath

22.1 Introduction

Synthetic Aperture Radar (SAR) is a kind of all-weather and all-time imaging radar. In one flight mission, high resolution wide swath (HRWS) images are always expected. High azimuth imaging resolution and wide ground image swath, however, impose contradicting requirements on system design. High azimuth resolution requires wide Doppler band or PRF, while wide swath requires low PRF. Scan mode is a wide swath imaging mode, while the azimuth resolution is bad because of

*This work is supported by the Fundamental Research Funds for the Central Universities under Projects ZYGX2011J020. And it is partly supported by the education department of Hunan Province project 11C0985.

W. Zuo (✉)
University of Electronic Science and Technology of China, Chengdu 611731, China

Huaihua University, Huaihua 418000, China
e-mail: kingso801021@163.com

R. Min • J. Li
University of Electronic Science and Technology of China, Chengdu 611731, China

Q. Liang et al. (eds.), *Communications, Signal Processing, and Systems*, Lecture Notes in Electrical Engineering 202, DOI 10.1007/978-1-4614-5803-6_22,

bursts' modulation. At present the main solutions for HRWS SAR systems focus on the operating mode improvements. Reference [1] proposed the multiple elevation beam (MEB) mode and the multiple azimuth beam mode (MAB). Reference [2] combined the MEB and MAB. The combination of MAB and MEB with other imaging modes such as Scan and TOPS mode were researched in [3, 4]. Although these solutions can get HRWS images, they are at the expense of system complexity and the signal processing difficulty.

Compressive Sensing (CS) is a new signal processing method proposed by Candes and Tao [5, 6] in 2004. Some researchers [7, 8] have involved the CS technique in the SAR systems.

In this chapter, based on the Scan mode, a novel HRWS imaging algorithm is proposed, which will include CS technique in the azimuth compression. Because of the Scan mode, wide ground imaging area can be assured. The deficiency of azimuth resolution in Scan mode will be compensated by the CS technique.

22.2 Compressive Sensing Thoery

The sparsity or compressibility of signals is the prerequisite of applying the CS theory. Consider a finite complex discrete signal $x \in \pounds^{N\times 1}$ as (22.1). $\{\psi_i\} \in \pounds^{N\times 1}$ $(i = 1, 2, \ldots N)$ is a basis of the signal space. If only K of c_i coefficients are nonzero and the other $N - K$ coefficients are zero or very small, x can be called K −sparse when $K = N$.

$$x = \sum_{i=1}^{N} c_i \psi_i = \sum_{i=1}^{N} <x, \psi_i> \psi_i \text{ or } x = \Psi g \text{ C} \tag{22.1}$$

The sparse signal can be measured by a measurement matrix $\Phi \in \pounds^{M\times N}$ and a measurement vector $y \in \pounds^{M\times 1}(M<N)$ is gotten as (22.2). The matrix Θ is called recovery matrix.

$$y = \Phi x = \Phi \Psi \text{C@} \Theta \text{C} \tag{22.2}$$

In order to recover x from y, it is needed to solve the ill-posed equation as (22.2). A sufficient condition for a determined solution of (22.2) is that Θ satisfies the restricted isometry property (RIP). Normally if the elements of the matrix Φ are selected randomly, the RIP can be achieved easily. In this condition, we can choose L_0 norm to solve (22.2), and (22.3). Although (22.3) is a NP-Hard problem, greedy algorithms such as regularized OMP (ROMP) algorithms [9] can be used to obtain the optimal solutions as long as $M \geq K \log(N)$.

$$\arg\min_{\hat{C}} ||\hat{C}||_0 \quad s.t. \quad y = \Theta \hat{C} \tag{22.3}$$

22.3 SAR Azimuth Returns' Reconstruction Based on Compressive Sensing

22.3.1 The Decomposition of Azimuth Returns

A side-looking SAR system is considered here. Suppose that the emitting signal is a chirp signal. When the observed ground areas contain some strong reflectivity targets, the return signals will satisfy the sparsity or compressibility. The returns of the k th point target in the azimuth direction after range compression and RCMC can be expressed as (22.4). $A_k(t)$ is the fast time expressions. t is the fast time. s is the slow time. s_k is the beam center crossing time. T_a is the synthetic aperture time. K_a is the azimuth frequency modulation rate.

$$r_k(s,t) = A_k(t) \cdot rect\left(\frac{s-s_k}{T_a}\right) \exp(-j\pi K_a(s-s_k)^2) \tag{22.4}$$

Suppose $s \in (s_0, s_1)$, the azimuth sampling time period is T_s and the discrete points of s is $s_0 + kT_s(k = 0, 1, \ldots, N_s - 1)$, in which $N_s = \left\lfloor \frac{X_w}{V} \right\rfloor$ and X_w is the azimuth sampled distance. Let:

$$r_0(s,t) = A_k(t) \cdot rect\left(\frac{s-s_0}{T_a}\right) \exp(-j\pi K_a(s-s_0)^2) \tag{22.5}$$

Then the returns can be expressed as (22.6), in which Λ is an index set whose power is K and denotes K point targets in the azimuth direction.

$$r(s,t) = \sum_{k\in\Lambda} r_0(s - kT_s, t) \tag{22.6}$$

The basis vectors Ψ as (22.7) can be used to decompose the azimuth returns.

$$\Psi = (r_0(s), r_0(s-T_s), \ldots, r_0(s-(N_s-1)T_s))\left(\psi_1, \psi_2, \ldots \psi_{N_s}\right) \tag{22.7}$$

Set $M = \left\lfloor \frac{T_a}{T_s} \right\rfloor$. Then we can get a band-like matrix as (22.8).

$$\Psi = \begin{pmatrix} r_0(1) & 0 & \text{L} & 0 \\ \text{M} & r_0(1) & \text{M} & 0 \\ \text{M} & \text{M} & \text{M} & r_0(1) \\ r_0(M) & \text{M} & \text{M} & \text{M} \\ 0 & r_0(M) & \text{M} & \text{M} \\ 0 & 0 & \text{L} & r_0(M) \end{pmatrix}_{(M+N_s-1)\times N_s} \tag{22.8}$$

The azimuth returns can be converted as (22.9) with (22.8). $\text{C}(t)$ is the decomposition coefficients and $n(t)$ is the noise. If the number of targets in the

azimuth direction $K = N_s < M + N_s - 1$, the return is $K -$ sparse in the space spanned by Ψ.

$$r(s,t) = \Psi \mathrm{C}(t) + n(t) \tag{22.9}$$

22.3.2 Azimuth Returns of Scan Mode

Because of the burst mode, the returns in azimuth direction are incomplete. But for CS technique, complete returns in azimuth direction are not necessary. The measurements of the azimuth returns will be selected randomly. For burst mode returns, the selection will be made in all of the bursts randomly, from which we can get a random matrix Φ. The multiplication of the basis matrix Ψ and the random matrix Φ forms the reconstruction matrix Θ.

With the sparsity and the measurement matrix Θ, the CS technique will be available for the reconstruction of the azimuth targets information with incomplete returns in azimuth direction. And high azimuth resolution and wide swath images can be expected.

22.3.3 Measurement Matrix for Scan Mode Returns

In order to get the random matrix Φ, the random measurement of the azimuth returns and the reconstruction matrix Θ, zero rows are firstly inserted between the bursts of the sub-swath to get a complete strip-map like data.

In CS theory, the measurements are selected randomly. For the burst mode, the selection must be made only in the bursts duration randomly, because the other rows are all inserted zeros that cannot represent the real echoes.

From the random selection index we can get a random vector, which will form the random matrix Φ. The same selection of the rows of the zeros-inserted returns will form the random measurement matrix. And the same selection of the rows of the basis matrix Ψ forms the reconstruction matrix Θ. Here only 25 % data are selected.

With the measurement matrix and the reconstruction matrix Θ, the CS technique will be available for the reconstruction of the azimuth targets information with 25 % returns in azimuth direction. And high azimuth resolution and wide swath images can be expected.

22.4 High Resolution Imaging Algorithm of Scan SAR Based on Compressive Sensing

In Fig. 22.1 shows the flow diagram of the processing steps of the proposed high resolution imaging algorithm of the scan SAR based on CS technique.

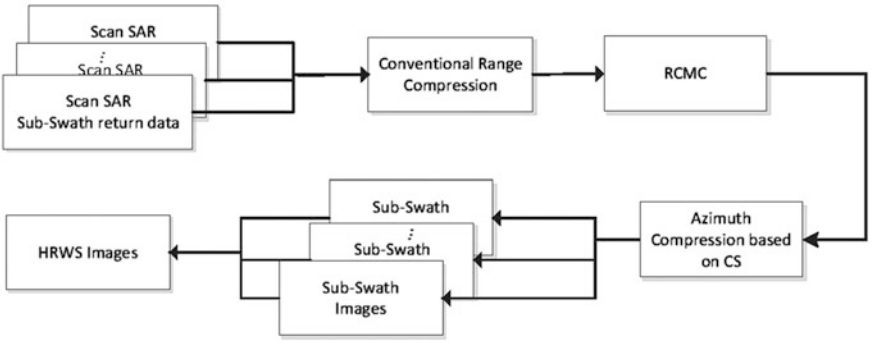

Fig. 22.1 Scan SAR imaging algorithm flow diagram based on CS

The first step of the processing is to insert zero rows between the bursts of the sub-swath echoes to get a complete strip-map mode like data. Then random selection will be made only in the burst rows. The index of the selections will compose the random matrix Φ, which will be used in the azimuth compression based on CS. The random selected data are the measurement matrix, which is the input to the next steps.

The second step is the conventional range compression, which can be completed with the matched filtering method. The third step is the range cell migration correction, which can be finished with interpolation in range Doppler domain.

The forth step is the azimuth compression based on CS. With the random matrix Φ and the measurement matrix gotten in the first step and the basis matrix as (22.8), random selection in which forms the reconstruction matrix Θ, CS technique can be used to reconstruct the azimuth targets information as described in Sects. 22.2 and 22.3.

The final step is the combination of the sub-swath images to get the high resolution and wide swath images.

22.5 Simulation and Analysis

In this section the simulation of Sects. 22.3 and 22.4 will be given out.

The first experiment includes 1-D point targets imaging based on CS and the comparison between it and the matching filtering method. The simulation results are shown in Fig. 22.2.

In Fig. 22.2 (a) shows the reconstruction matrix. (b) is the measurement matrix (Only 25 % data randomly selected from the reconstruction matrix in the bursts). (c) gives the conventional matching filtering result in the form of sinc function with complete data. (d) is the rebuilt result by the CS method with only 25 % data selected randomly. Every peak has no side-lobes, which means the proposed

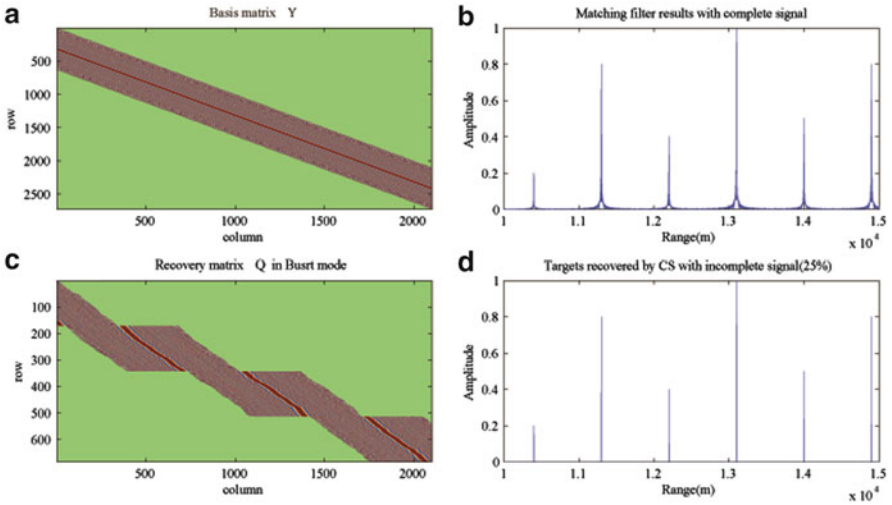

Fig. 22.2 Simulation results of the 1-D points imaging based on (**c**) matching filter (**d**) CS

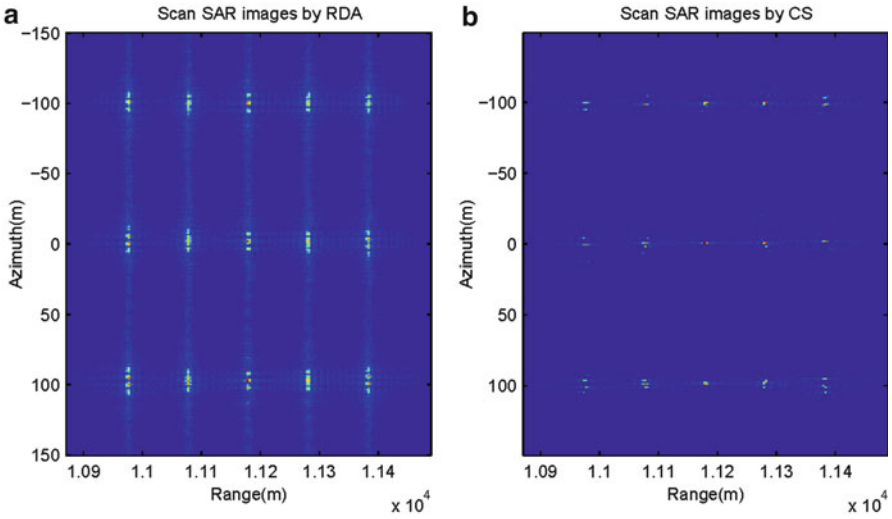

Fig. 22.3 Scan SAR images by (**a**) RDA (**b**) CS technique

method can get ultra-resolution. High azimuth resolution can be expected in Scan mode with the proposed method.

The second experiment is the 2-D Scan SAR data focusing based on CS, shown in Fig. 22.3.

- In (a) and (b), all targets' position are correct. It means the proposed method is feasible.

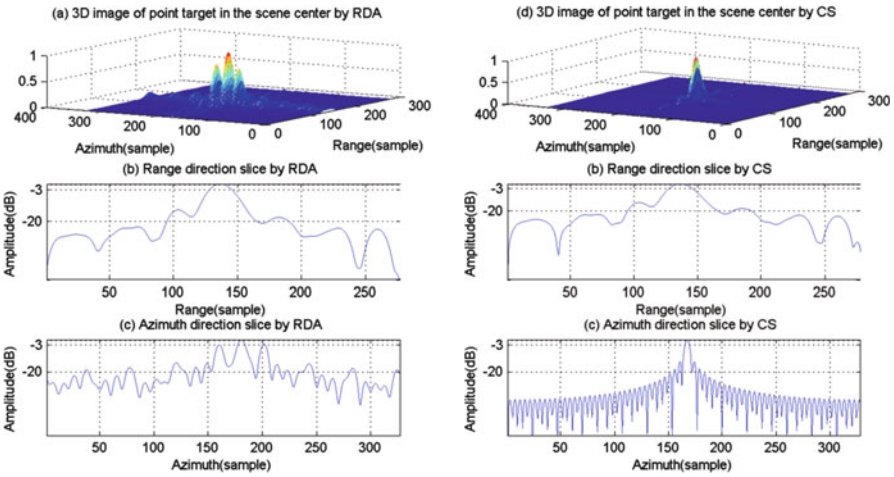

Fig. 22.4 Detail images of the scene-center point target (*Left*) by RDA (*Right*) by CS technique

Table 22.1 Performance parameters

Method	ρ_r(m)	ρ_a(m)	$PSLR_a$(dB)	$PSLR_r$(dB)	$ISLR$(dB)
RDA	4.3808	11.2923	−3	−13.4	−0.4041
CS	4.6385	1.0505	−13.4	−13.4	−1.2449

- In (a), every target's image has three peaks. In contrast to (a), every target's image has only one peak in (b). The tailing phenomenon in azimuth decreases greatly, which means the azimuth resolution is improved.

Figure 22.4 gives the detail images of the point target in the scene center focused by RDA and CS technique respectively. In order to make the images smooth, interpolation operations in frequency domain are employed. The performance parameters calculated from Fig. 22.4 are listed in Table 22.1. The ideal azimuth and range resolution is about 2 and 4 m respectively. From the Table 22.1, we find ρ_r by CS technique (4.6358 m) is a little worse than that by RDA (4.3808 m). But ρ_a by CS technique (1.0505 m) is much better than that that by RDA (11.2923 m). For the RDA, because of the incomplete data and the burst period modulation, the azimuth resolution is much worse than the ideal value (2 m).

For the CS technique, the targets' information is reconstructed by CS exactly. Even Only 25 % of the complete azimuth return data are used, the azimuth resolution is much better than the ideal resolution. These simulation results show that the proposed method can improve the Scan SAR azimuth resolution greatly. Because wide swath can be assured in Scan mode, the proposed method is feasible for HRWS imaging.

22.6 Conclusion

Scan SAR can get wide swath, while the azimuth resolution is worse than the conventional SAR because of incomplete azimuth direction sampling. In this chapter we proposed a method based on the CS technique to rebuild the azimuth data from incomplete random samples from the burst data. The theory analysis and the simulation show that the proposed method is feasible for HRWS Scan SAR system.

Acknowledgments This work is mainly supported by the Fundamental Research Funds for the Central Universities under Projects ZYGX2011J020. And it is partly supported by the education department of Hunan Province project 11C0985.

References

1. Currie A, Brown MA (1992) Wide-swath SAR. IEE Proc Inst Elect Eng F 139(2):122–135
2. Callaghan GD, Longstaff ID (1999) Wide swath spaceborne SAR using a quad element array. IEE Proc Radar Sonar Navig 146(3):159–165
3. Nicolas G, Gebert N, Moreim A (2010) Multichannel azimuth processing in ScanSAR and TOPS mode operation. IEEE Trans Geosci Rem Sens 48(7):2994–3008
4. Xu W, Huang PP, Deng YK (2011) Multi-channel SPCMB-TOPS SAR for high-resolution wide-swath imaging. Prog Electromagn Res 116:533–551
5. Candes E (2006) Compressive sampling. In: Proceedings of the international congress of mathematicians, vol 3, Madrid, pp 1422–1452
6. Candes E, Romberg J, Tao T (2006) Robust uncertainty principles: exact signal reconstruction from highly incomplete frequency information. IEEE Trans Inf Theory 6(2):227–254
7. Patel VM, Easley GR, Jr Healy DM, Chellapa R (2010) Compressed synthetic aperture radar. IEEE Sel Top Signal Process 4(2):244–254
8. Alonso T, Dekker L, Mallorqui J (2010) A novel strategy for radar imaging based on compressive sensing. IEEE Trans Geosci Rem Sens 48(12):4285–4295
9. Needell D (2009) Topics in compressed sensing. University of California, Davis, pp 53–59

Chapter 23
The Robust Sparse PCA for Data Reconstructive via Weighted Elastic Net

Wang Ling and Jihao Yin

Abstract ℓ_2 / ℓ_1-norm is widely used to measure coding residual in principal component analysis (PCA). In this case, it usually assumes that the residual follows Gaussian/Laplacian distribution. However, it may fail to describe the coding errors in practice when there are outliers. Toward this end, this paper proposes a robust sparse PCA (RSPCA) approach to solve the outlier problem, by modeling the sparse coding as a sparsity-constrained weighted regression problem. By using a series of equivalent transformations, we show RSPCA is equivalent to the weighted elastic net (WEN) problem and thus the least angle regression elastic net (LARS-EN) method is used to yield the optimal solution. Simulation results illustrated the effectiveness of this approach.

Keywords Robust statistics • Principal component analysis • Sparse representation • Elastic net

23.1 Introduction

Sparse learning based dimension reduction approaches have drawn many attention of many researchers over world recently since it can reduce not only dimensionality of feature spaces but also the number of explicitly used feature vectors [19, 21]. As we know, principal component analysis (PCA), whose each principal component (PC) can decomposed as a linear combination of all the original features, are widely used in data processing and dimensionality reduction [10, 17]. PCA can be formulated as a regression-type optimization problem, and then we can obtain sparse loadings by imposing least absolute shrinkage and selection operator

W. Ling (✉) • J. Yin
School of Electrical Engineering, University of Electronic Science and Technology of China, Chengdu, Sichuan, China
e-mail: eewangling@uestc.edu.cn; jhyin@uestc.edu.cn

Q. Liang et al. (eds.), *Communications, Signal Processing, and Systems*, Lecture Notes in Electrical Engineering 202, DOI 10.1007/978-1-4614-5803-6_23,

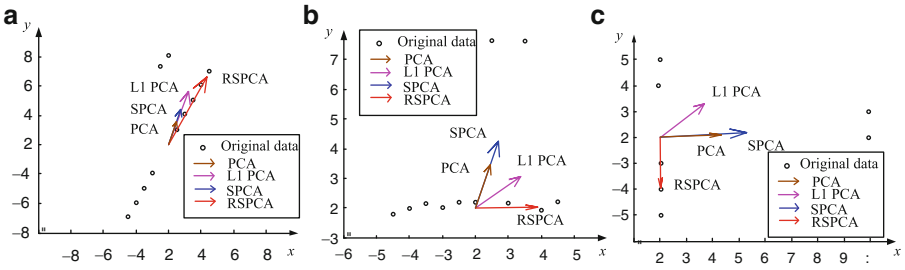

Fig. 23.1 A toy data with outliers: the 'o' denote the original data; the lines with arrow denote the first loading vector yielded by PCA, ℓ_1-PCA, SPCA and RSPCA respectively. (**a**) Original data with outliers and the projection vectors. (**b**) y-outliers and the projection vectors. (**c**) x-outliers and the projection vectors

(LASSO) constraints on the regression coefficients [10, 21]. Moreover, convex optimization is also used to improve interpretation of the standard PCA [5]. Traditionally, when the number of feature dimensions is larger than the number of observation vectors, we have to select all of the feature vectors and thus it cannot reduce their dimensions. It would be of interest to discover sparse principal components (SPCA), i.e., sets of sparse vectors spanning a low-dimensional space that explains most of the variance present in the data.

In this case, SPCA provides a direct way to reduce the number of feature vectors for feature representation and learning [21]. Accordingly, various SPCA approaches have been developed [5, 9, 13, 14, 16], where the residual follows Gaussian/Laplacian distribution. However, there are some outliers in the sample data in practice. In this case, the ℓ_2-norm can't give the right solution, shown in Fig. 23.1. The outliers have a very large influence on ℓ_2-norm because the residual $\mathbf{e}$is squared. Consequently, $y = \|\mathbf{e}\|_2^2$is increased sharply when its value is increasing. Furthermore some strategies using ℓ_1-norm is used to handle this issue in PCA [2, 8, 11, 12, 15]. Indeed, in some cases, the ℓ_1-norm performs better than ℓ_2-norm, shown in Fig. 23.1a, b. Unfortunately, ℓ_1-norm can not model the outlier problem explicitly. From Fig. 23.1b, c, we can see when the outlier lies in x-axis, the ℓ_1-norm fails to obtain the right solution. In this case, robust PCA using ρ function could handle these outliers very well.

There are other robust PCA or SPCA were proposed [1, 6, 7] to solve the outlier problem. Candes et al. also given the solutions on robust PCA [3] by using Augmented Lagrangian Method on low-rank matrix decomposition. Croux et al. used grid algorithm to compute the sparse and robust principal components [4]. Yang et al. induced a robust sparse coding for face recognition [18], where an iteratively re-weighted sparse coding approach was used.

In this paper, we proposed a novel robust SPCA (RSPCA) approach, which is formulated as a weighted elastic net (WEN) approach. The proposed RSPCA approaches are not only to reduce the dimensionality of data matrix but also to make it more robust under noise. Here, we consider SPCA as a regression-type optimization problem. By replacing the data item in the LARS-EN method using specific robust function, the LARS-EN method can be formulated as the

WEN approach, which models the outlier problem explicitly thus improving the robustness of SPCA.

The rest of this paper is organized as follows. Section 23.2presents the problem formulation, and then the algorithm of the robust sparse PCA model is proposed in Sect. 23.3. Section 23.4conducts the experiments, and Sect. 23.5concludes this paper and the future work.

23.2 Problem Formulation

Let's first briefly review regression-type optimization framework of PCA. The PCs of data matrix $\mathbf{X}$ is $\mathbf{P} = \mathbf{X}V_k{}^T$, where $\mathbf{X} = \mathbf{U}\mathbf{D}\mathbf{V}^T$, $\mathbf{V}_k$ is called as loading matrix or projecting matrix. Usually $k \ll p$, and thus dimensionality reduction is achieved. Furthermore, the uncorrelated PCs capture the maximum variability of $\mathbf{X}$, which guarantees minimal information loss. In regression-type optimization frameworks, PCA can be formulated as an LARS-EN problem [21]. The sparse solution of j-th component $P_{\cdot j}$can be solved by

$$\hat{\beta}_{opt} = \arg\min_{\beta_j} \|P_{\cdot j} - \mathbf{X}\beta_j\|_2^2 + \lambda_1\|\beta_j\|_2^2 + \gamma_1\|\beta_j\|_1, \tag{23.1}$$

where both λ_1 and γ_1 are non-negative Lagrange multipliers. Afterwards, we can obtain $\hat{V}_{\cdot j} = \hat{\beta}_{opt}/\|\hat{\beta}_{opt}\|_2$.

Equation (23.1) is a convex combination of the ridge penalty and ℓ_1-norm penalty. The ridge penalty is used to ensure the reconstruction of PCs, while the ℓ_1-norm penalty is used to ensure the sparsity of loadings. Larger $\gamma_1$encourages a sparser $\hat{\beta}$. Given a fixed $\lambda_1$and γ_1, optimizing Eq. (23.1) can efficiently obtain $\hat{\beta}_{opt}$by using the LARS-EN method [20].

Now we discuss sparse PCA with noise. Assume data matrix $\mathbf{X} = \mathbf{S} + \mathbf{N}$, where $\mathbf{S}$is original data matrix, $\mathbf{N}$is noise matrix. The noise-free PCs of $\mathbf{S} = \overline{\mathbf{U}}\,\overline{\mathbf{D}}\,\overline{\mathbf{V}}^T$ are $\overline{\mathbf{P}} = \mathbf{S}\overline{\mathbf{V}}_k$, where $\overline{\mathbf{V}}_k = [\alpha_1, \cdots, \alpha_k]$. Then the j-th principal component $\overline{P}_{\cdot j} = \mathbf{S}\alpha_j = \mathbf{X}\alpha_j - \mathbf{N}\alpha_j$.

Similarly, we can estimate optimal PCs from observation matrix, $P_{\cdot j} = \mathbf{X}\beta_j$, where $\beta_j$is from the loading matrix $\mathbf{V}_k$estimated from $\mathbf{X}$. Suppose the ideal PCs be estimated by $\mathbf{X}\alpha_j$, and the actual PCs be estimated by $\mathbf{X}\beta_j$, then the PCA optimization problem is formulated as

$$\arg_{\alpha_j,\beta_j} \min\|\mathbf{X}\alpha_j - \mathbf{X}\beta_j\|_2^2, \quad \text{s.t.}\ \|\alpha_j\|_2^2 = 1,\ \|\beta_j\|_2^2 = 1. \tag{23.2}$$

In this equation, we can add a sparse constraint, $\|\beta_j\|_1 < \xi_1, \|\alpha_j\|_1 < \xi_2$, where ξ_1, $\xi_2$are small constants.

Now we discuss how to get the sparse loadings of $\mathbf{X}$.

Theorem 1 *For any $\lambda_1 > 0$, $\lambda_2 > 0$, if $\hat{\beta}_j$ is given by*

$$(\hat{\alpha}_j, \hat{\beta}_j) = \arg_{\alpha_j, \beta_j} \min \|\mathbf{X}\alpha_j - \mathbf{X}\beta_j\|_2^2 + \lambda_1 \|\beta_j\|_2^2 + \lambda_2 \|\alpha_j\|_2^2, \tag{23.3}$$

then $\hat{V}_{\cdot j} = \hat{\beta}_j / \|\hat{\beta_j}\|_2$.

Define $\varepsilon_j = \mathbf{X}\alpha_j - \mathbf{X}\beta_j = [e_1, \cdots, e_N]^T$, and assume that e_n, $(n = 1, \cdots, N)$ are independently identically distributed (*i.i.d*) with probability density function (*p.d.f.*) $f(e_n)$, then the likelihood function is $\mathbf{L}(e_1, \cdots, e_N) = \prod_{n=1}^{N} f(e_n)$. We minimize the objective function by using maximum likelihood estimation (MLE)

$$-\ln \mathbf{L} = \sum\nolimits_{n=1}^{N} -\ln f(e_n) = \sum\nolimits_{n=1}^{N} \rho(e_n) = \mathbf{F}(\varepsilon_j), \tag{23.4}$$

where $\rho(e_n) = -\ln f(e_n)$. Approximating $\mathbf{F}(\varepsilon_j)$ by its first order Taylor expansion in the neighborhood of ε_0, we have

$$\mathbf{F}(\varepsilon_j) = \mathbf{F}(\varepsilon_0) + (\varepsilon_j - \varepsilon_0)^T \mathbf{F}'(\varepsilon_0) + \mathbf{R}_1(\varepsilon_j), \tag{23.5}$$

where $\mathbf{R}_1(\varepsilon_j)$ is the high order residual term. In sparse coding, it usually assume that the fidelity term is strictly convex. We approximate the residual term as

$$\mathbf{R}_1(\varepsilon_j) = \frac{1}{2}(\varepsilon_j - \varepsilon_0)^T \mathbf{W}_{(j)} (\varepsilon_j - \varepsilon_0), \tag{23.6}$$

where $\mathbf{W}_{(j)}$is a diagonal matrix for that the elements in $\varepsilon_j$are independent and there is no cross term between $e_n$and e_i, $(n \neq i)$. Since $\mathbf{F}(\varepsilon_j)$ reaches its minimal value at $\varepsilon_j = \mathbf{0}$, we also require that $\tilde{\mathbf{F}}(\epsilon_j)$has its minimal value at $\varepsilon_j = \mathbf{0}$. Letting $\mathbf{F}(\mathbf{0}) = \mathbf{0}$, we have the diagonal elements of $\mathbf{W}_{(j)}$as

$$W_{nn} = \omega(e_{0,n}) = \rho'(e_{0,n}) / e_{0,n}. \tag{23.7}$$

Then $\tilde{\mathbf{F}}(\varepsilon_j)$can be written as

$$\tilde{\mathbf{F}}(\varepsilon_j) = \frac{1}{2} \left| \mathbf{W}_{(j)}^{1/2} \varepsilon_j \right|^2 + b, \tag{23.8}$$

where $b$is a scalar value determined by ε_0.

Since the logistic function has properties similar to the hinge loss function in SVM, we choose it as the weight function

$$\omega(e_n) = \exp(\mu\delta - \mu e_n^2) / (1 + \exp(\mu\delta - \mu e_n^2)). \tag{23.9}$$

For the relationship in Eq. (23.7), we have

$$\rho(e_n) = -\frac{1}{2\mu}\left(\ln(1+\exp(\mu\delta - \mu e_n^2)) - \ln(1+\exp(\mu\delta))\right), \tag{23.10}$$

where μ and δ are positive scalars. μ controls the decreasing rate from 1 to 0, and δ controls the location of demarcation point. when the residual $|e|$ exceeds a threshold, it cannot increase with the residual. In other words, the outlier would be adaptively assigned with low weights to reduce their affects on the regression estimation thus resulting in more robust dimension reduction.

Then the Eq. (23.3) can be approximated by

$$\begin{aligned}(\hat{\alpha}_j, \hat{\beta}_j) = \arg_{\alpha_j,\beta_j} \min \|\mathbf{W}_{(j)}^{1/2}(\mathbf{X}\alpha_j - \mathbf{X}\beta_j)\|_2^2 \\ + \lambda_1\|\beta_j\|_2^2 + \gamma_{1,j}\|\beta_j\|_1 + \lambda_2\|\alpha_j\|_2^2 + \gamma_{2,j}\|\alpha_j\|_1.\end{aligned} \tag{23.11}$$

This is a weighted Elastic Net problem, which can be solved by LARS-EN algorithm.

23.3 The Proposed Robust Sparse PCA

Theorem 2 *For any $\lambda_1 > 0$, $\lambda_2 > 0$, $j = 1,2,\cdots,k$, let*

$$(\hat{\mathbf{A}}, \hat{\mathbf{B}}) = \arg_{\mathbf{A},\mathbf{B}} \min \sum_{j=1}^{k}\left(\|\mathbf{W}_{(j)}^{1/2}(\mathbf{X}\alpha_j - \mathbf{X}\beta_j)\|_2^2 + \lambda_1\|\beta_j\|_2^2 + \lambda_2\|\alpha_j\|_2^2\right), \tag{23.12}$$

where $\mathbf{A} = \overline{\mathbf{V}}_k = [\alpha_1, \cdots, \alpha_k]$, $\mathbf{B} = \mathbf{V}_k = [\beta_1, \cdots, \beta_k]$. *Then* $\hat{\beta}_j \propto V_{\cdot j}$.

Only the first sparse loading is β_1, it is commonly that the first leading sparse loading may not be sufficient for obtain a variable support, and it is desirable to further estimate a few subsequent sparse loadings as well. Several techniques [13] have been explored for reliably deflating the covariance matrix of SPCA. Here we use the low-rank approximations [9] to eliminate the influence of the first sparse loading. Given the first sparse loading β_1, we have

$$\overline{\mathbf{X}} = \mathbf{X} - \mathbf{X}\beta_1\beta_1^T. \tag{23.13}$$

Then the second sparse loading β_2 of $\mathbf{X}$ becomes the leading sparse loading of $\overline{\mathbf{X}}$, and can be estimated again by using RSPCA.

According to the Theorem 2, we propose an iterative approach to minimize the RSPCA. The detail algorithm is summarized in Table 23.1.

Table 23.1 The proposed RSPCA via weighted elastic net algorithm

Input: observation data matrix $\mathbf{X}$
Output: $\hat{V}_i$ loadings of PCs
Initialization: $\mathbf{X} = \mathbf{UDV}^T$, $\alpha_j = V_{\cdot j}$, $\beta_j = \mathbf{0}$, $P_{ite}{}^{(1)}$ = means of every rows of $\mathbf{X}$
start:
for $j = 1, \cdots, k$
$t = 1$
while $\hat{\beta}_j$ is not converges
• Compute residual $\epsilon_j^{(t)} = [e_1, \cdots, e_N]^T = \mathbf{X}^{(j)}\alpha_j - P_{ite}^{(t)}$
• Estimate weights $\omega(e_i{}^{(t)})$ with Eq. (23.9)
• For given fixed α_j, solve the elastic net problem in following equation,

$$\hat{\beta}_j = \arg_\beta \min_j (\alpha_j - \beta_j)^T \mathbf{X}^T \mathbf{W}_{(j)} \mathbf{X}(\alpha_j - \beta_j) + \lambda_1 \|\beta_j\|_2^2 + \gamma_{1,j} \|\beta_j\|_1. \tag{23.14}$$

• For fixed β_j, update $\alpha_j$by the following equation

$$\hat{\alpha_j} = \arg_\alpha \min_j (\alpha_j - \beta_j)^T \mathbf{X}^T \mathbf{W}_{(j)} \mathbf{X}(\alpha_j - \beta_j) + \lambda_2 \|\alpha_j\|_2^2 + \gamma_{2,j} \|\alpha_j\|_1. \tag{23.15}$$

• Update: $\mathbf{X}^{(j+1)} = \mathbf{X}^{(j)} - \mathbf{X}^{(j)} \hat{\beta}_j \hat{\beta}_j^T$, $P_{ite}^{(t)} = \mathbf{X}^{(j)} \hat{\beta}_j$.
• Let $t = t + 1$.
end *while*
end *for*.
Normalization: $\hat{V}_{\cdot j} = \hat{\beta}_j / \|\hat{\beta}_j\|_2, j = 1, \cdots, k$.

23.4 Experimental Results and Analysis

23.4.1 A Toy Problem with Outliers

Consider the following 2-D toy data $\mathbf{X}$

$$\mathbf{X} = \begin{bmatrix} x_i \\ y_i \end{bmatrix} = \begin{bmatrix} -2.5 & -2 & -1.5 & -1 & \mathbf{-0.5} & \mathbf{0} & 0.5 & 1 & 1.5 & 2 & 2.5 \\ -4.93 & -3.96 & -2.94 & -1.98 & \mathbf{5.32} & \mathbf{5.95} & 1.03 & 2.01 & 3.01 & 4.08 & 5.07 \end{bmatrix}$$

where x_i are generated from $-$ 2.5 to 2.5 with similar interval 0. 5, y_i are generated from $-$ 5 to 5 with similar interval 1 and then are added uniform distribution in [0, 0. 1], except the two points $x_i = -0.5$ and $x_i = 0$, the corresponding values of y_i are much more bigger than others, we name this data with outliers. If we discard the outliers, the loading vector or projection vector would be $\beta = [0.45, 0.9]^T$.

For this data, ℓ_2-PCA, ℓ_1-PCA, SPCA and the proposed RSPCA are applied and the loading vectors $\beta_{l_2} = [0.31, 0.95]^T$, $\beta_{l_1} = [0.33, 0.94]^T$, $\beta_{SPCA} = [0.31, 0.95]^T$, $\beta_{RSPCA} = [0.44, 0.89]^T$are obtained respectively, shown as in Fig. 23.2a. The estimation of each data point also are shown in Fig. 23.2d. The average residual errors of ℓ_2-PCA, ℓ_1-PCA, SPCA and the proposed RSPCA $e_i = |x_i - x_i \beta\beta^T|$ are 1.03, 1.02, 1.03 and 0.94 respectively.

Secondly, consider the following 2-D toy data $\mathbf{Y}$

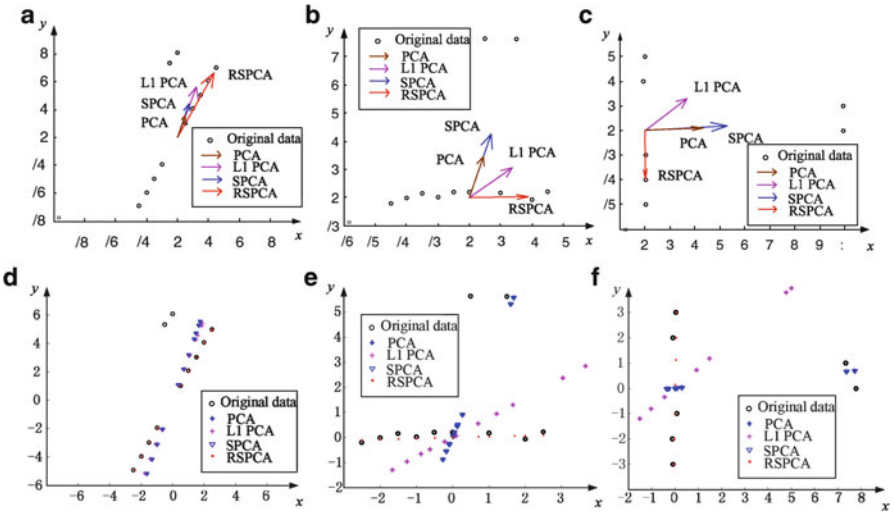

Fig. 23.2 A toy data with outliers: the lines with arrow denote the first loading vector yielded by PCA, ℓ_1-PCA, SPCA and RSPCA respectively; the ' ∘ ' points denote the original data points; the ' ∗ ', ' + ', '▿', '.' denote the estimated data points by the four methods respectively. (**a**) Original data with outliers and the projection vectors. (**b**) y-outliers and the projection vectors. (**c**) x-outliers and the projection vectors. (**d**) Original data with outliers and the estimated data points. (**e**) y-outliers data and the estimated data points. (**f**) x-outliers and the estimated data points

$$\mathbf{Y} = \begin{bmatrix} x_i \\ y_i \end{bmatrix} = \begin{bmatrix} -2.5 & -2 & -1.5 & -1 & -0.5 & 0 & \mathbf{0.5} & 1 & \mathbf{1.5} & 2 & 2.5 \\ 0.06 & 0.14 & 0.22 & 0.24 & -0.15 & -0.18 & \mathbf{5.48} & -0.2 & \mathbf{5.39} & 0.02 & 0.18 \end{bmatrix}$$

where x_i are generated from $-$ 2.5 to 2.5 with similar interval 0.5, and y_i are following uniform distribution on [$-$ 0.25, 0.25]. It is obvious that there are two outliers at $x_i = 0.5$ and $x_i = 1.5$, the corresponding values of $y_i$are much more bigger than others, we name this type data as y-axis outliers. If we discard the outliers, the loading vector or projection vector would be $\beta = [1, 0]^T$.

For this data, ℓ_2-PCA, ℓ_1-PCA, SPCA and the proposed RSPCA are applied and the loading vectors $\beta_{l_2} = [0.28, 0.96]^T$, $\beta_{l_1} = [0.82, 0.56]^T$, $\beta_{SPCA} = [0.28, 0.96]^T$, $\beta_{RSPCA} = [0.\ 99, 0.\ 05]^T$are obtained respectively, shown as in Fig. 23.2b. The estimation of each data point also are shown in Fig. 23.2e. The average residual errors of ℓ_2-PCA, ℓ_1-PCA, SPCA and the proposed RSPCA $e_i = |x_i - x_i\beta\beta^T|$ are 1.69, 0.83, 1.69 and 0.01 respectively.

On the other hand, we also generate a x-axis outliers toy data $\mathbf{Z}$ as following,

$$\mathbf{Z} = \begin{bmatrix} x_i \\ y_i \end{bmatrix} = \begin{bmatrix} -0.01 & -0.09 & -0.04 & \mathbf{7.9} & \mathbf{7.4} & -0.06 & 0.06 \\ -3 & -2 & -1 & \mathbf{0} & \mathbf{1} & 2 & 3 \end{bmatrix}$$

where y_i are generated from -3 to 3 with similar interval 1, and x_i are following uniform distribution on $[-0.1, 0.1]$. It is obvious that there are two outliers at $y_i = 0$ and $y_i = 1$, If we discard the outliers, the loading vector would be $\beta = [0, 1]^T$.

For the data $\mathbf{Y}$, ℓ_2-PCA, ℓ_1-PCA, SPCA and the proposed RSPCA are applied and the loading vectors $\beta_{l_2} = [0.99, 0.08]^T$, $\beta_{l_1} = [0.79, 0.61]^T$, $\beta_{SPCA} = [1, 1]^T$, $\beta_{RSPCA} = [0.01, 0.99]^T$are obtained respectively, shown as in Fig. 23.2c. The estimation of each data point also are shown in Fig. 23.2f. The average residual errors of ℓ_2-PCA, ℓ_1-PCA, SPCA and the proposed RSPCA $e_i = |y_i - y_i\beta\beta^T|$ are 3.46, 2.26, 2.22 and 0.03 respectively.

With those results, we can see that ℓ_2/ℓ_1PCA were much influenced by the outliers while the proposed RSPCA suppressed the effect of the outlier efficiently.

23.4.2 Test on Benchmark Data with Intrinsic Noises and Outliers

In this section, we consider the data proposed by [4, 21], the data set first be created by following hidden factors

$$V_1 \sim N(0, 290),\ V_2 \sim N(0, 300),\ V_3 = -0.3V_1 + 0.925V_2 + \epsilon \tag{23.16}$$

where $\varepsilon \sim (0, 1)$, and V_1, $V_2$and ε are independent; afterwards, ten observed variables be generated as

$$\begin{aligned} x_i &= V_1 + \varepsilon_i,\ i = 1, 2, 3, 4 \\ x_i &= V_2 + \varepsilon_i,\ i = 5, 6, 7, 8 \\ x_i &= V_3 + \varepsilon_i,\ i = 9, 10 \end{aligned} \tag{23.17}$$

where $\varepsilon_i \sim N(0, 1)$, $\varepsilon_i$are independent. The number of observations $n = 500$ and features $p = 10$. The variance of the V_1, V_2, V_3 is 290, 300 and 283.8, respectively. Then the first two principal components correspond to $V_2$and V_1. Ideally, the first PC should recover the V_2 only using $[X_5, X_6, X_7, X_8]^T$, and the second PC should recover the V_1 only using $[X_1, X_2, X_3, X_4]^T$.

We add outliers generated in [4], which follow the distribution of $N(\mu_{out}, \sigma_{out}{}^2\mathbf{I}_{10})$, where $\mu_{out} = [0, -100, 100, 50, 0, 100, -100, 50, 75, -75]^T$ and $\sigma_{out}{}^2 = 20$. These added data are not follow the factor structure described above. The ℓ_2-PCA, SPCA and the proposed RSPCA methods be applied on the benchmark data and with outlier portions 20 % respectively. The simulation results are presented in Table 23.2.

Without the outliers, the results of SPCA and RSPCA are according to the expectations. But in ℓ_2/ℓ_1PCA, because of the high correlation between V_2 and V_3, variables X_9 and X_{10} gain loadings which are even higher than the true

Table 23.2 simulation experiment on benchmark data

	PCA				L1 PCA				SPCA ($\lambda = 1$)				RSPCA ($\lambda = 1$)			
	No outliers		20 % outliers		No outliers		20 % outliers		No outliers		20 % outliers		No outliers		20 % outliers	
	PC1	PC2	PC1	PC2	PC1	PC2	PC1	PC2	PC1	PC2	PC1	PC2	PC1	PC2	PC1	PC2
X_1	0.14	0.47	− 0.14	− 0.47	0.14	0.46	0.26	− 0.38	0	0	0	0	0	0	0	0
X_2	0.11	0.47	0.08	− 0.49	0.10	0.47	0.29	− 0.41	0	0	−0.33	0	0	−0.99	0	−0.88
X_3	0.13	0.47	0.22	− 0.44	0.14	0.46	0.23	− 0.38	0	−1	0	0	0	0	0	0
X_4	0.13	0.47	0.19	− 0.46	0.14	0.47	0.23	− 0.39	0	0	−0.95	0	0	0	0.06	−0.43
X_5	−0.39	0.16	0.39	0.07	−0.39	0.15	0.38	0.21	−1	0	0	0	0	0	0.24	0
X_6	−0.39	0.16	0.47	0.12	−0.39	0.16	0.36	0.24	0	0	0	1	−0.91	0	0.97	0
X_7	−0.39	0.16	0.32	0.05	−0.39	0.15	0.40	0.18	0	0	0	0	0	−0.16	0	0
X_8	−0.39	0.16	0.44	0.11	−0.39	0.15	0.37	0.22	0	0	0	0	0	0	0	0
X_9	−0.40	0.01	0.38	0.23	−0.40	0.02	0.26	0.30	0	0	0	0	0	0	0	0.19
X_{10}	−0.40	0.01	0.26	0.21	−0.40	0.02	0.30	0.31	0	0	0	0	−0.37	0	0	0

variables $[X_5, X_6, X_7, X_8]^T$. When adding outliers, in ℓ_2 / ℓ_1PCA, the loadings not concentred on one variables. The SPCA gets distorted, the first PC and the second PC be exchanged. The proposed RSPCA, however, still deliver sparse and nearly right solutions.

23.5 Conclusion and Future Work

In this paper, we have proposed a weighted RSPCA approach to estimate the data principal components under outlier sampling. By modeling the MLE of residues, the LS problem was formulated as a weighted LARS-EN expression. With an iteratively LARS-EN processing, a better estimated performance was obtained compare with PCA and SPCA methods. In the future work, we will use the proposed approach on object categorization and discuss its convergence.

Acknowledgements This work was supported by "the Fundamental Research Funds for the Central Universities" under award number ZYGX2010J016.

References

1. Aanæs H, Fisker R, Astrom K, Carstensen JM (2002) Robust factorization. IEEE Trans Pattern Anal Mach Intell 24(9):1215–1225
2. Baccini A, Besse P, and Falguerolles de A (1996), An l1-norm pca and a heuristic approach. Ordinal and symbolic data analysis, pp 359–368
3. Candes EJ, Li X, Ma Y, Wright J (2009) Robust principal component analysis? Arxiv preprint ArXiv:0912.3599
4. Croux C, Filzmoser P, Fritz H (2011) Robust sparse principal component analysis. Catholic University of Leuven Department of Decision Science and Information Management Working Paper No. 1113
5. d'Aspremont v, El Ghaoui L, Jordan MI, Lanckriet GRG (2004) A direct formulation for sparse PCA using semidefinite programming. Computer Science Division, University of California
6. De la Torre F, Black MJ (2001) Robust principal component analysis for computer vision. In: IEEE international conference on computer vision (ICCV), vol 1. IEEE, pp 362–369
7. De La Torre F, Black MJ (2003) A framework for robust subspace learning. Int J Comput Vis 54(1):117–142
8. Ding C, Zhou D, He X, Zha H (2006) R 1-pca: rotational invariant l 1-norm principal component analysis for robust subspace factorization. In: Proceedings of the 23rd international conference on machine learning. ACM, New York, pp 281–288
9. Frieze A, Kannan R, Vempala S (2004) Fast monte-carlo algorithms for finding low-rank approximations. J ACM (JACM) 51(6):1025–1041
10. Jolliffe IT (2002) Principal component analysis, vol 2. Wiley Online Library
11. Ke Q, Kanade T (2005) Robust l1 norm factorization in the presence of outliers and missing data by alternative convex programming. In: IEEE computer society conference on computer vision and pattern recognition (CVPR), vol 1. IEEE, pp 739–746

12. Kwak N (2008) Principal component analysis based on l1-norm maximization. IEEE Trans Pattern Anal Mach Intell 30(9):1672–1680
13. Mackey L (2009) Deflation methods for sparse pca. Adv Neural Inf Process Syst 21:1017–1024
14. Moghaddam B, Weiss Y, Avidan S (2006) Spectral bounds for sparse pca: exact and greedy algorithms. Adv Neural Inf Process Syst 18:915
15. Rousseeuw PJ, Leroy AM, Wiley J (1987) Robust regression and outlier detection, vol 3. Wiley Online Library
16. Shen H, Huang JZ (2008) Sparse principal component analysis via regularized low rank matrix approximation. J Multivar Anal 99(6):1015–1034
17. Wold S, Esbensen K, Geladi P (1987) Principal component analysis. Chemom Intell Lab Syst 2(1–3):37–52
18. Yang M, Zhang L, Yang J, Zhang D (2011) Robust sparse coding for face recognition. In: IEEE conference on computer vision and pattern recognition (CVPR). IEEE, pp 625–632
19. Zhou T, Tao D, Wu X (2011) Manifold elastic net: a unified framework for sparse dimension reduction. Data Min Knowl Dis 22(3):340–371
20. Zou H, Hastie T (2003) Regression shrinkage and selection via the elastic net, with applications to microarrays. In: Technical report. Department of Statistics, Stanford University. Available via DIALOG. http://www-stat.stanford.edu/~hastie/pub.htm
21. Zou H, Hastie T, Tibshirani R (2006) Sparse principal component analysis. J Comput Graph Stat 15(2):265–286

Chapter 24
Research on Theory of Almost Perfect Binary-Third-Order Cyclic Autocorrelation Sequences

Yi Zhong, Zheng Zhou, and Ting Jiang

Abstract Because higher-order cumulant (HOC) is insensitive to the adding Gaussian noise and symmetry non-Gaussian noise, a new kind of perfect discrete signal with good periodic correlation function is presented, which is the almost perfect binary-third-order cyclic autocorrelation sequences (APBTOCAS). We present the definitions of APBTOCAS and its transformation properties. Based on these properties, we search out an almost perfect binary-third-order cyclic autocorrelation sequence 667 (octal) within length 26. Then, we theoretically prove that binary-third-order cyclic autocorrelation sequences can effectively suppress colored Gaussian noise. Finally, the simulation shows that almost perfect binary-third-order cyclic autocorrelation sequences have such good periodic correlation that they can they are feasible for engineering applications as synchronization codes and multiuser codes, remedying the defect of the current Pseudo-noise (PN) code used in very low signal-noise-ratio (SNR) environments.

Keywords Perfect signal • Higher-order cumulant • Correlation signal • Information theory

24.1 Introduction

Higher-order statistics (HOS) is a mathematical tool to describe the higher-order statistical properties of the random process, including higher-order cumulants and moments. In fact, it has been shown that estimation methods that exploit the non-Gaussian signals have some inherent advantages over second-order method, such as: (1) the ability to reconstruct the phase of non-minimum phase systems, (2)

Y. Zhong (✉) • Z. Zhou • T. Jiang
Key Laboratory of Universal Wireless Communication, Ministry of Education, Beijing University of Posts and Telecommunications, Beijing 100876, People's Republic of China
e-mail: zhongyim2m@gmail.com; zzhou@bupt.edu.cn; tjiang@bupt.edu.cn

Q. Liang et al. (eds.), *Communications, Signal Processing, and Systems*, Lecture Notes in Electrical Engineering 202, DOI 10.1007/978-1-4614-5803-6_24,

the array aperture is spread in space domain, and (3) the ability to separate non-Gaussian signals form Gaussian additive noise [1]. Based on the above characteristics, higher-order cumulant recently has been becoming a powerful tool for signal processing and system theory, widely used in many diverse fields; e.g., radar [2], sonar [3], telecommunication [4], geophysics [5] and fault diagnosis [6].

The main advantage of using high-order cumulant is that HOC is constantly zero for Gaussian process and even the colored Gaussian process. The current researches define the perfect signal by the inner product of sequence itself and its delay sequence. However, these traditional sequences based on second-order statistics cannot handle colored Gaussian measurement noise automatically, thus affecting the accuracy of their properties in engineering application. Since high-order cumulants are blind to any kind of a Gaussian process, this chapter introduces HOC into the field of perfect binary sequence, which breaks through the limitations of the perfect signal defined by second-order statistics, to fill out the blank of perfect signal in the area of research on Gaussian noise suppression. In this chapter, we proposes a new concept of perfect binary sequence based on higher -order cumulant, which is the perfect binary-third-order cyclic autocorrelation sequence. Detailed analysis proves that the proposed sequences improve the performance of anti-noise for perfect signal significantly, and more perfect signals could be obtained in engineering application with this method.

The rest of this chapter is organized as follows: In Sect. 24.2, we present the definition of almost perfect binary-third-order cyclic autocorrelation sequence. The remainder of this chapter is organized as follows. In Sect. 24.3, we study the properties of the sequences. In Sect. 24.4, we theoretically prove that almost perfect binary-third-order cyclic autocorrelation sequences can effectively suppress Gaussian noise, even if that noise is colored. In Sect. 24.5, we apply the above properties to search out the almost perfect binary-third-order cyclic autocorrelation sequences with short lengths by computer, and the periodic correlation performances of APBTOCAS are analyzed by using of MATLAB tool. In Sect. 24.6, we conclude our work and discuss future research.

24.2 Definition

Definition 1 Suppose a sequence $x(n) = (x_0, x_1, \cdots, x_{N-1})$ with length N, $x(n)$ is defined as the binary sequence, if $x(n) \in \{-1, 1\}$ holds.

Definition 2 The imbalance of sequence $x(n)$ with length N is defined to be:

$$I = \sum_{n=0}^{N-1} x(n) = n_p - n_q \tag{24.1}$$

Where n_p and n_q respectively denote the numbers of 1 and -1 in the binary sequence $x(n)$.

Definition 3 Suppose a sequence $x(n) = (x_0, x_1, \cdots, x_{N-1})$ with length N and its imbalance satisfies $I \in \{-1, 0, 1\}$, $x(n)$ is considered as a zero-mean or a closely approximate zero mean stationary random process, then the third-order cumulant of cyclic autocorrelation binary sequence $x(n)$ is defined as:

$$c_{3x}(\tau_1, \tau_2) = \frac{1}{N} \sum_{n=1}^{N} x(n)x(n+\tau_1)x(n+\tau_2) \tag{24.2}$$

where $0 \le \tau_1 \le N-1$, $0 \le \tau_2 \le N-1$.

Definition 4 Suppose a binary sequence $x(n) = (x_0, x_1, \cdots, x_{N-1})$ with length N and its imbalance satisfies $I \in \{-1, 0, 1\}$, $x(n)$ is defined as the perfect binary-third-order cyclic autocorrelation sequences, if there exists a value $\tau_1 = u$ $(0 \le u \le N-1)$, and satisfies the following equation:

$$c_{3x}(u, \tau_2) = \begin{cases} E & \tau_2 = m \\ 0 & \tau_2 \ne m \end{cases} \tag{24.3}$$

where $0 \le \tau_2 \le N-1$.

Definition 5 Suppose a binary sequence $x(n) = (x_0, x_1, \cdots, x_{N-1})$ with length N and its imbalance satisfies $I \in \{-1, 0, 1\}$, $x(n)$ is defined as the almost perfect binary-third-order cyclic autocorrelation sequences, if there exists a value $\tau_1 = u$ $(0 \le u \le N-1)$, and satisfies the following equation:

$$c_{3x}(u, \tau_2) = \begin{cases} E & \tau_2 = m \\ -E & \tau_2 = n \\ 0 & \tau_2 \ne m, n \end{cases} \tag{24.4}$$

where $0 \le \tau_2 \le N-1$.

Definition 6 The imbalance I of a perfect binary-third-order cyclic autocorrelation sequence with length N is given by

$$I = 0 \tag{24.5}$$

The sequence is defined to be a constant-weight binary perfect binary-third-order cyclic autocorrelation sequence, otherwise defined as a non-constant-weight binary perfect binary-third-order cyclic autocorrelation sequence. On the other hand, we have similar definition to the almost perfect binary-third-order cyclic autocorrelation sequences.

24.3 Transformation Features

It will take a huge amount of time to do an exhaustive computer search for the almost perfect binary-third-order cyclic autocorrelation sequence in length N. According to the definition in Sect. 24.2 and the important properties of higher-order cumulant [18], we can get some features as follows to reduce the search domain significantly.

If sequence $x(n) = (x_0, x_1, \cdots, x_{N-1})$ is an almost perfect binary-third-order cyclic autocorrelation sequence with length N, we can get the following four important properties.

Proposition 1 (Reverse Transformation) *If an almost perfect binary-third-order cyclic autocorrelation sequence $x(n)$ after the transformation: $x_1(n) = -x(n)$, then sequence $x_1(n)$ is an almost perfect binary-third-order cyclic autocorrelation sequence.*

Proof It is easy to verify the propositions mentioned above by using the definition of almost perfect binary-third-order cyclic autocorrelation sequence in (24.4), so we leave out here.

Proposition 2 (Mapping Transformation) *If an almost perfect binary-third-order cyclic autocorrelation sequence $x(n)$ after the transformation: $x_1(n) = x(-n)$, then sequence $x_1(n)$ is an almost perfect binary-third-order cyclic autocorrelation sequence.*

Proof Consider the sequence $x(n) = (x_0, x_1, \cdots, x_{N-1})$ with length N, where $c_{3x}(\tau_1, \tau_2)$ is the third-order cumulant defined in (24.3). We have

$$
\begin{aligned}
c_{3x_1}(\tau_1, \tau_2) &= \frac{1}{N}\sum_{n=0}^{N-1} x_1(n)x_1(n+\tau_1)x_1(n+\tau_2) \\
&= \frac{1}{N}\{x_1(0)x_1(\tau_1)x_1(\tau_2) + \cdots + x_1(N-1)x_1(N-1+\tau_1)x_1(N-1+\tau_2)\} \\
&= \frac{1}{N}\{x(0)x(\tau_1)x(\tau_2) + x(-1)x(-1+\tau_1)x(-1+\tau_2) + \cdots \\
&\quad + x(-N+1)x(-N+1+\tau_1)x(-N+1+\tau_2)\} \\
&= \frac{1}{N}\{x(N)x(\mathrm{N}+\tau_1)x(\mathrm{N}+\tau_2) + x(N-1)x(N-1+\tau_1)x(N-1+\tau_2) \\
&\quad + \ldots + x(1)x(1+\tau_1)x(1+\tau_2)\} \\
&= \frac{1}{N}\{x(0)x(\tau_1)x(\tau_2) + \cdots + x(N-1)x(N-1+\tau_1)x(N-1+\tau_2)\} \\
&= c_{3x}(\tau_1, \tau_2)
\end{aligned}
$$

According to the definition in (24.4), we prove that sequence $x_1(n)$ is an almost perfect binary-third-order cyclic autocorrelation sequence. This completes the proof.

Proposition 3 (Reverse Order Transformation) *If an almost perfect binary-third-order cyclic autocorrelation sequence* $x(n)$ *after the transformation*: $x_1(n) = x(N-n)$, *then sequence* $x_1(n)$ *is an almost perfect binary-third-order cyclic autocorrelation sequence*.

Proof Consider the sequence $x(n) = (x_0, x_1, \cdots, x_{N-1})$ with length N, where $c_{3x}(\tau_1, \tau_2)$ is the third-order cumulant defined in (24.3). We have

$$\begin{aligned} c_{3x_1}(\tau_1, \tau_2) &= \frac{1}{N}\sum_{n=0}^{N-1} x_1(n)x_1(n+\tau_1)x_1(n+\tau_2) \\ &= \frac{1}{N}\sum_{n=0}^{N-1} x(N-n)x(N-n-\tau_1)x(N-n-\tau_2) \\ &= \frac{1}{N}\{x(N)x_1(N-\tau_1)x_1(N-\tau_2) + x_1(N-1)x_1(N-1+\tau_1)x_1(N-1+\tau_2) \\ &\quad + \cdots + x(1)x_1(1-\tau_1)x_1(1-\tau_2)\} \\ &= \frac{1}{N}\{x(0)x(0-\tau_1)x(0-\tau_2) + \cdots + x(N-1)x(N-1-\tau_1)x(N-1-\tau_2)\} \\ &= c_{3x}(\mathrm{N}-\tau_1, N-\tau_2) \end{aligned}$$

According to the definition in (24.4), we prove that sequence $x_1(n)$ is an almost perfect binary-third-order cyclic autocorrelation sequence. This completes the proof.

Proposition 4 (Cyclic Shifting Transformation) *If an almost perfect binary-third-order cyclic autocorrelation sequence* $x(n)$ *after the transformation*: $x_1(n) = x(n+u)$, $u \le N$, *then sequence* $x_1(n)$ *is an almost perfect binary-third-order cyclic autocorrelation sequence*.

Proof Consider the sequence $x_1(n) = (x_0, x_1, \cdots, x_{N-1})$ with length N, where $c_{3x}(\tau_1, \tau_2)$ is the third-order cumulant defined in (24.3). We have

$$\begin{aligned} c_{3x_1}(\tau_1, \tau_2) &= \frac{1}{N}\sum_{n=0}^{N-1} x_1(n)x_1(n+\tau_1)x_1(n+\tau_2) \\ &= \frac{1}{N}\sum_{n=0}^{N-1} x(n+u)x(n+u+\tau_1)x(n+u+\tau_2) \\ &= \frac{1}{N}\sum_{n=u}^{N-1+u} x(n)x(n+\tau_1)x(n+\tau_2) \end{aligned}$$

Since $n+\tau_1 = (n+\tau_1) \bmod N$, $n+\tau_2 = (n+\tau_2) \bmod N$, hence

$$c_{3x_1}(\tau_1, \tau_2) = \frac{1}{N}\sum_{n=u}^{N-1+u} x(n)x(n+\tau_1)x(n+\tau_2) = \hat{c}_{3x}(\tau_1, \tau_2)$$

According to the definition in (24.4), we prove that sequence $x_1(n)$ is an almost perfect binary-third-order cyclic autocorrelation sequence. This completes the proof.

24.4 Proof of Anti-Noise Capability for the Class of Binary-Third-Order Cyclic Autocorrelation Sequence

Theorem 1 *If a sequence $x(n) = (x_0, x_1, \cdots, x_{N-1})$ belongs to the class of binary-third-order sequence, then $x(n)$ can completely suppress the effect of Gaussian noise.*

In order to prove this theorem, we need the following important properties of higher-order cumulants [7].

Proposition 5 *If the random variables $\{x_i\}$ are independent of the random variables $\{y_i\}$, $i = 1, \cdots, k$, where $cum(x_1, \cdots, x_k)$ is defined as the joint kth-order cumulant of the random variables $x_0, x_1, \cdots, x_k$, then*

$$cum(x_1 + y_1, \cdots, x_k + y_k) = cum(x_1, \cdots, x_k) + cum(y_1, \cdots, y_k) \tag{24.6}$$

Proposition 6 *If a subset of the k random variables $\{x_i\}$ is independent of the rest, then*

$$cum(x_1, \cdots, x_k) \equiv 0 \tag{24.7}$$

We are now ready to prove *Theorem 1*.

Proof Suppose the measurement of a binary-third-order sequence $x(n)$ is interfered by independent additive Gaussian noise, and then we have

$$y(n) = x(n) + e(n)$$

Therefore, by *Proposition 9*, we obtain the third-order cumulant of the measurement for sequence $x(n)$

$$c_y(u, \tau_2) = c_x(u, \tau_2) + c_e(u, \tau_2)$$

From *Proposition 10*, the equation:

$$c_e(u, \tau_2) \equiv 0, \; c_e(u, \tau_2) \equiv 0$$

holds.

Thus, the following expression holds:

$$c_y(u, \tau_2) = c_x(u, \tau_2)$$

Therefore, we obtain the third-order cumulant of the measurement for sequence $x(n)$ that can completely suppress the effect of Gaussian noise, even if that noise is colored. This completes the proof.

24.5 Searching Results

We use the proposition 1–4 in Sect. 24.4 to reduce the searching range effectively, since all the almost perfect binary-third-order cyclic autocorrelation sequences seem as only one if they can get from one sequence by using the proposition 1–4.

From the output of the third-order cumulant $c_{3x}(\tau_1, \tau_2)$ of the 667 (octal) sequence, we can find that there are 36 peak values, and we can see below the contour and the mesh plotting for the sequence and it is clear that it has peak points with value $= \pm 8/15 \approx 0.5333$, and any other value will be $= 0$. The results are shown in Figs. 24.1 and 24.2, represented in mesh and contour plot. At the (τ_1, τ_2) pair, in which the circle indicates that there is a positive peak, and the fork indicates that there is a negative peak.

Among the 36 peaks, we choose 8 sets of peaks in Table 24.2. In each set, we can see that there will produce two opposite peaks in the same value with the change of shift count and any other value will be $= 0$, when the another shift count $\tau_1 = 2, 4, 5, 6, 8, 9, 10, 12$, which are the same as the theoretical results. As a result, when we fix one shift count τ_1 in Table 24.1 and move another shift count of the sequence, we can get one set of the peak location (τ_1, τ_2) in Table 24.2 and while the value at any other point will be equal to zero, which indicates that the 667 (octal) almost perfect binary-third-order cyclic autocorrelation sequence has a good periodic correlation performance

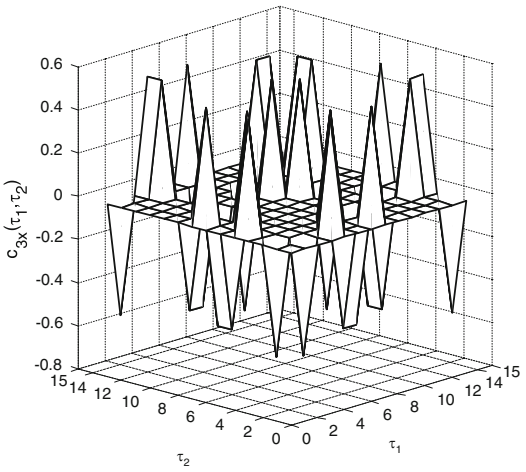

Fig. 24.1 Mesh plot

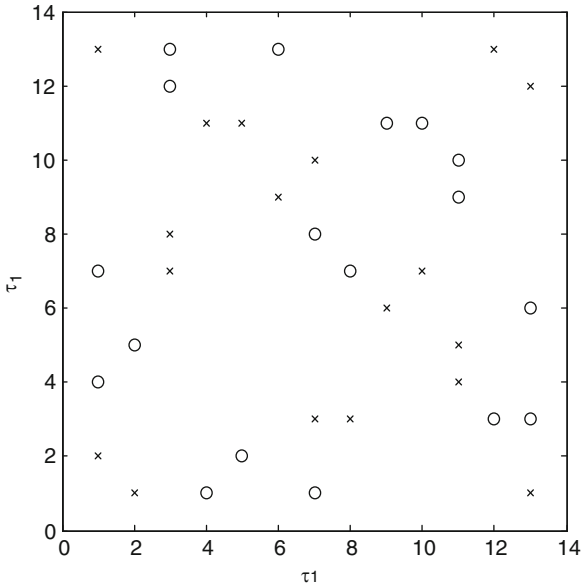

Fig. 24.2 Contour plot

Table 24.1 Some searching results of apbtcos within length 26

Length	Sequence(Octal)	Position of $\tau_1 = u$
14	667	2,4,5,6,8, 9,10,12

Notes: the sequence is denoted as octal in Table 24.2, where "1" means "+ 1" and "0" means "−1".

Table 24.2 Peaks locations for sequence 667(Octal)

Set 1		Set 2		Set 3		Set 4		Set 5		Set 6		Set 7		Set 8	
τ_1	τ_2	τ_1	τ_2	τ_1	τ_2	τ_1	τ_2	τ_1	τ_2	τ_1	τ_2	τ_1	τ_2	τ_1	τ_2
2	1	4	1	5	2	6	9	8	3	9	6	10	7	12	3
2	5	4	11	5	11	6	13	8	7	9	11	10	11	12	13

24.6 Conclusion

A new concept of perfect binary-third-order cyclic autocorrelation sequences is proposed in the chapter. Since the higher-order cumulant is more robust to additive measurement noise than correlation, even if that noise is colored, this article introduces higher-order cumulants into the research of perfect binary sequence, which can enrich the research field of perfect signal theory. According to the theoretical proof, the perfect binary-third-order cyclic autocorrelation sequence can draw itself out of Gaussian noise, thereby boosting their signal-to-noise ratios in engineering application.

Because of the limit of program algorithm and the computer operating speed, only some almost perfect binary-third-order cyclic autocorrelation sequences have been found. Although we have not found the perfect binary-third-order cyclic autocorrelation sequences of the definition in (24.3) at present, the realization of almost perfect binary-third-order cyclic autocorrelation sequences could be further constructed according to the conjecture. On the other hand, the existence of the perfect binary-third-order cyclic autocorrelation sequences also requires further study. Furthermore, the almost perfect binary-third-order cyclic autocorrelation sequences with good cyclic autocorrelation function shown in Table 24.1 can be widely used in the engineering application with a strict requirement on bit error rate.

Acknowledgments This work was supported by Important National Scenes & Technology Specific Projects (2010ZX03006-006), NSFC (61171176), Scientific Research Fund of Zhejiang Provincial Education Department under Grant No. Y201225956 and Natural Science Foundation of Ningbo under Grant No. 2012A610015.

References

1. Feng Liu, Jingqing Lv, Shaoqian Li (2006) Signal direction of arrival estimation based high-order cumulants and a partially calibrated array. In: International conference on communications, circuits and systems proceedings, vol 1. 25–28 June 2006, pp 293–297
2. Anandan VK, Ramachandra R (2001) Spectral analysis of atmospheric radar signal using higher order spectral estimation technique. IEEE Trans Geosci Remote Sens 39(9):1890–1895
3. Trucco A (2001) Experimental results on the detection of embedded objects by a prewhitening filter. Oceanic Eng IEEE J 26(4):783–794
4. Mendel JM (1991) Tutorial on higher-order statistics (spectra) in signal processing and system theory: theoretical results and some applications. Proc IEEE 79(3):278–305
5. Lazear GL (1993) Mixed—phase wavelet estimation using fourth order cumulants. Geophysic 58(7):1042–1051
6. Wu-xing LAI, Tse PW, Gui-cai ZHANG et al (2004) Classification of gear faults using cumulants and the radial basis function network. Mech Syst Signal Process 18(2):381–389
7. Mendel JM (1991) Tutorial on higher-order statistics (spectra) in signal processing and system theory: theoretical results and some applications. Proc IEEE 79(3):278–305

Chapter 25
A Strategy of Network Coding Against Nodes Conspiracy Attack

Rong Du, Chenglin Zhao, Feng Zhao, and Shenghong Li

Abstract In recent years network coding has attracted significant attention in telecommunication. The benefits of network coding to a communication network include the increased throughput as well as secure data transmission. In this chapter, we investigate the advantages of applying network Coding in sensor networks for security purpose. In particular, the problem of constructing a secure unicast system is considered. Unlike previous wiretapping scenarios, where the threat is posed by external wiretappers .we approach the security from an internal angle: all nodes comply with the communication protocols yet are potential eavesdroppers and the eavesdroppers can cooperate with each other to decode the packets sent from the source node. Different from most existing research on network coding that designs the network coding scheme based on a given topology, we will consider the network topology design. We first try to find the transmission topology that is suitable for network coding in unicast system. Based on the topology, we use linear network coding scheme which is weakly secure. We conduct simulations to show that it prevents cooperative eavesdroppers from acquiring any useful information transmitted from source node to sink node.

R. Du (✉) • S. Li
School of Information Security Engineering, Shanghai Jiao Tong University, Shanghai 200240, People's Republic of China
e-mail: durongorc@163.com; shli@sjtu.edu.cn

C. Zhao
School of Information and Communication Engineering, Beijing University of Posts and Telecommunications, Beijing 100876, People's Republic of China
e-mail: clzhao@bupt.edu.cn

F. Zhao
Department of Science and Technology, Guilin University of Electronic Technology, Guilin 541004, China
e-mail: zhaofeng@guet.edu.cn

Q. Liang et al. (eds.), *Communications, Signal Processing, and Systems*, Lecture Notes in Electrical Engineering 202, DOI 10.1007/978-1-4614-5803-6_25,

Keywords Weakly-secure • Network coding • Cooperative eavesdroppers • Conspiracy attack

25.1 Introduction

Network coding [1] is a new message forwarding technique that allows a forwarder to encode multiple input messages together to form an output one. Unlike the traditional approach that always duplicates every forwarding message, network coding is able to maximize the throughput of multicast networks. Li [2] demonstrated that the maximum flow from a source to multiple destinations can be achieved by linear network coding with a finite field size. Because of this nice property, network coding has been widely used not only in wired networks but also in wireless networks.

Network coding systems suffer from various attack, existing studies on secure network coding can be classified into two groups based on attack types. Wiretapping attacks (passive attacks) [3–6] and polluting attacks (active attack) [7–11]. And the focus of this chapter is the passive attacks, such as wiretapping attack, defined by Cai et al. in [4]. In this attack, adversaries are capable to wiretap or eavesdrop on a subset of the links of some network coding system and gain access to information transmitted through the links as the problem is how to prevent information from leaking to adversaries. For secure linear network coding, there are mainly two secure models in previous, namely, Shannon-secure and weakly-secure. The difference is that Shannon-secure ones do not allow any information leakage, while weakly-secure ones do not allow any meaningful information leakages. An an example, given two information symbols x_1 and x_2, in weakly-secure schemes, the adversaries may learn the value of $x_1 + x_2$ but not x_1 or x_2 alone; in Shannon-secure, they cannot learn neither of x_1, x_2 nor the combination $x_1 + x_2$.

In this chapter, secure network coding generally can be implemented in two steps: construct a transmission topology and use secure network coding scheme based on the constructed transmission topology. When there exists two or more nodes can cooperate in the conspiracy attack. We can use another example in Figs. 25.1 and 25.2 to further show how the transmission topology design can affect the number of original messages that can be transmitted under security requirements.

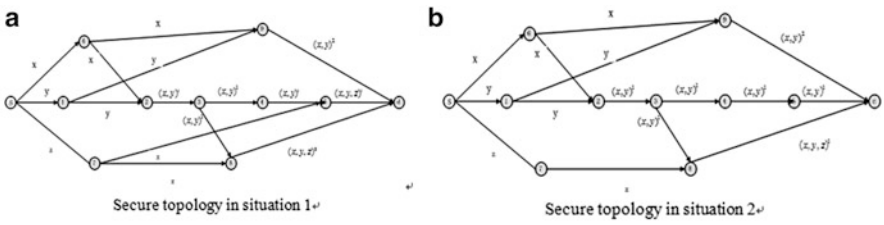

Fig. 25.1 Transmission topologies with transmission rate of 3 in unicast system

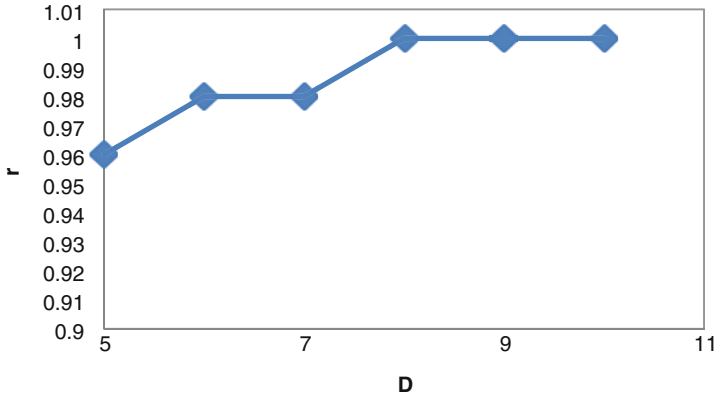

Fig. 25.2 Successful rate r versus D

The rest of chapter is organized as follows. Section 25.2 describes the system model, the threat model and the security goals. In Sect. 25.3, we discuss the problem and present an algorithm for secure network code design. The simulation works are discussed in Sect. 25.4 and the chapter is concluded in Sect. 25.5.

25.2 Problem Statement

25.2.1 System Model

A communication network is represented by a directed acyclic graph $G = \langle V, E \rangle$, where V and E are the node set and the edge set respectively. The capacity of each edge has the same unit capacity, which is 1 date unit per time slot. The single source S generates and sends out a message vector X which consists of n symbols in a finite field F_q .

25.2.2 Threat Model and Security Goals

In conspiracy attack, the malicious nodes are able to gain access to the information transmitted on these nodes. The positions of malicious nodes were known. And they cooperate with each other to decode the packet sent from the source S. precisely, they can wiretap on a collection of $M = \langle M_1, M_2, \cdots M_K \rangle$ where M represents a set of malicious nodes.

In this chapter, our security goal is to prevent the source information from leaking to the adversaries. We focus on designing weakly-secure network coding schemes. And integrated network topology design to maximize the transmission data rate under the condition of satisfying the weakly secure requirements.

25.3 Problem Analysis Proposed Scheme

25.3.1 Security Analysis and Discussion

As directed diffusion construct acyclic network, we can represent the resulted topology as a directed graph $G = \langle V, E \rangle$, where V is the set of nodes and E is the set of edges. The number of different data streams $X = \langle X_1, X_2, \cdots X_{\mathrm{L}} \rangle$ form source node s to sink node d, Intermediate nodes $V = \langle V_1, V_2, \cdots V_{\mathrm{m}} \rangle$. Let $\ln(\mathrm{v_i})$ and Out $(\mathrm{v_i})$ be the set of input and output links of a given node $\mathrm{v_i}$ without loss of generality we assume that each edge $e \in E$ has a unit capacity. The capacity $C_G(s, d)$ of the network G is the maximal possible information rate from node s to d.

Assume $C_G(s, d) = k$, for any intermediate node $\mathrm{v_i}$ in a directed graph G, if the $\mathrm{In}(\mathrm{v_i})$ is less than the capacity of the graph $C_G(s, d)$, then for sufficiently large size q, the generated network code is said to be secure with high probability, because the intermediate node $\mathrm{v_i}$ cannot recover any of the k symbols based on $k - 1$ or fewer linear equations. On the other hand, if $C_G \leq |\ln(\mathrm{v_i})|$, the security is said to be topology dependent, the network is considered secure if and only if $rank(in(v_i)) < C_G$.

By parity of reasoning, if there has a set of malicious nodes $v = \langle v_1, v_2, \cdots v_{\mathrm{n}} \rangle$, to satisfy the weakly secure requirements $\sum_{i=1}^{\mathrm{n}} In(v_{\mathrm{i}}) < C_G$, which means more links should be removed and more network energy will be consumed. But in physical, sometimes $\sum_{i=1}^{m} In(v_{\mathrm{i}})$ is not need to be less than K to satisfy the weakly secure requirements by topology design. As in Fig. 25.1, We can see the integrated network topology design can affect the transmitted under security requirement. And maximize the transmission data rate against the Conspiracy Attack.

Now we suppose a couple of situation as follows:

1. Suppose node 3, 5 and 8 are malicious nodes. $in(3) = 1, in(5) = 2, in(8) = 2$. As we know, if $in(3) + in(5) + in(8) < 3$. The network can achieve weakly secure, which means we should remove three links of input links of node 3, 5 and 8, but in fact that links $\{2 \rightarrow 3, 4 \rightarrow 5, 3 \rightarrow 8\}$ carry the same message of (x, y), and $\{7 \rightarrow 5, 7 \rightarrow 8\}$ carry the same message of z. so the topology is already weakly secure.
2. Suppose node 5and 9 are malicious nodes. $in(5) = 2$, $in(9) = 2$. links $\{1 \rightarrow 9, 6 \rightarrow 9, 4 \rightarrow 5, 7 \rightarrow 5\}$ carried the different messages of y, x, (x, y) and z .to satisfy the secure requirements. We should remove two links of the four. As in Fig. 25.1b, we just removed $\{7 \rightarrow 5\}$ that make the topology weakly secure.

It obviously that sometimes it is no need to remove so much links to achieve weakly-secure, we just remove few links to achieve the same effect.

Let G be a $(m+1) \times (m+1)$ matrix, $G_{i,j}$ denotes message from node i to node j. the last row denotes the output links of source node s and the last column denotes the input links of sink node d. It is interesting to analysis the transmission matrix G to solve the security problem.

$$G = \begin{array}{c} \\ 1 \\ 2 \\ 3 \\ 4 \\ 5 \\ 6 \\ 7 \\ 8 \\ 9 \\ s \end{array} \begin{array}{c} \begin{array}{cccccccccc} 1 & 2 & 3 & 4 & 5 & 6 & 7 & 8 & 9 & d \end{array} \\ \begin{pmatrix} 0 & y & 0 & 0 & 0 & 0 & 0 & 0 & y & 0 \\ 0 & 0 & (x,y)^1 & 0 & 0 & 0 & 0 & 0 & 0 & 0 \\ 0 & 0 & 0 & (x,y)^1 & 0 & 0 & 0 & (x,y)^1 & 0 & 0 \\ 0 & 0 & 0 & 0 & (x,y)^1 & 0 & 0 & 0 & 0 & 0 \\ 0 & 0 & 0 & 0 & 0 & 0 & 0 & 0 & 0 & (x,y,z)^1 \\ 0 & x & 0 & 0 & 0 & 0 & 0 & 0 & x & 0 \\ 0 & 0 & 0 & 0 & z & 0 & 0 & z & 0 & 0 \\ 0 & 0 & 0 & 0 & 0 & 0 & 0 & 0 & 0 & (x,y,z)^2 \\ 0 & 0 & 0 & 0 & 0 & 0 & 0 & 0 & 0 & (x,y)^2 \\ y & 0 & 0 & 0 & 0 & x & z & 0 & 0 & 0 \end{pmatrix} \end{array} \tag{25.1}$$

We define $(x, y, \cdots)^n = a_n x + b_n y \cdots$, and a_n, b_n is a set of coefficients. Consider the situation (1) by the transmission matrix G, node 3, 5and 8 are malicious nodes. We get five polynomial expressions. $G_{2,3} = (x,y)^1, G_{4,5} = (x,y)^1$, $G_{3,8} = (x,y)^1$, $G_{7,5} = z, G_{7,8} = z$. The helpful polynomial expression to decode the source message are $(x,y)^1$ and z. we cannot use these polynomials to get the complete message of the source. In situation (2), we get four polynomial expressions of $G_{1,9} = y, G_{6,9} = x, G_{4,5} = (x,y)^1, G_{7,5} = z$ from G .we can removed $\{7 \rightarrow 5\}$ and rest of them cannot decode the complete message.

In this chapter, we aim to design efficient weakly-secure network coding. Our goals are as follows: (1) Maximum the maxflow of the network which means efficient data transmission. (2) Removed links as little as possible to make the network topology secure.

How to remove the links is the problem that we mainly faced with. We propose two standards.

1. The maxflow should be changed as small as possible after removed the links. in Fig. 25.1. If we remove $\{1 \rightarrow 9, 6 \rightarrow 9\}$, the maxflow of the network changes to 2. Even the sink node d cannot get complete information of source node. And the transmission fail. So after polluted links remove we must make sure the last row and column have enough polynomial to send and decode the whole messages.
2. We remove the links which appear the least number of data flow. For example, we get five different data streams of $(x,y)^1, (x,y)^2, (x,y)^3, (x,y)^4$ and z. In fact we just remove z that we can achieve the secure requirement Instead of remove the three of others.

Need to be mentioned, once a link removed, the matrix G need to be refilled. In reality, when we removed a link from the network.,rest of the network was changed coinstantaneous. In Fig. 25.1a. After $G_{2,3}$ removed, $G_{3,4}$ and $G_{4,5}$ become 0, and the transmission failed. We can obviously see that 3rd column of matrix G only has one nonzero value. If $G_{2,3} = 0$, the elements of the 3rd column all become 0 which means node 3 has no incoming data. So node 3 has no outgoing data which result in the elements of the 3rd row all become 0, then the elements of the 4th column all become 0 and then the elements of the 4th row become 0. Both nodes 5 and 8 just have one incoming data z which lead to transmission fail.

25.3.2 Secure Unicast Routing Algorithm

To sum up, our method can be implemented in five steps:

Step 1: fill the matrix of the network, mark the data stream of each link of G, calculate the maxflow of G.
Step 2: $V' = (v'_1, v'_2 \cdots v'_m)$ is the set of malicious nodes. $E' = (e'_1, e'_2 \cdots e'_n)$ is the set of the incoming edges of V'.we call it polluted edges.
Step 3: remove the same linear correlation of incoming message. E'' is the set of the remaining edges which we called it polluted edges.
Step 4: remove some of the polluted edges with two standards, refilled the matrix G that the remaining polluted edges are less than $C(G)$, and the sink node d can get the complete information from source s.
Step 5: if there is no such a topology that satisfy the condition. Than the message leakage is unavoidable.

25.4 Simulation

Simulations have been conducted for the algorithm with randomly generated instances. The network is defined by these parameters, the number of nodes, N, the probability of malicious nodes in intermediate nodes, p. the largest degree of each D (the largest amount of incoming links)and the successful rate of transmission r. For each combination of parameters, we generate 50 instances.

In Fig. 25.2, we set $N = 50, p = 0.1$ and vary D in range of $[5 - 10]$ to calculate the r. with the increase of D, the performance of r increases. This is because the linear independence messages carried by polluted edges increase with the increase of D, more different messages cause more polluted edges to be remove, but the complicate of the topology increases more, which cause the probability of $C(G)$ no changes and better performance.

In Fig. 25.3, we set $N = 50, D = 7$ and vary p in range of $[0.05 - 0.2]$ to calculate the r. with the increases of p, the performance of r is performed worse. The reason is

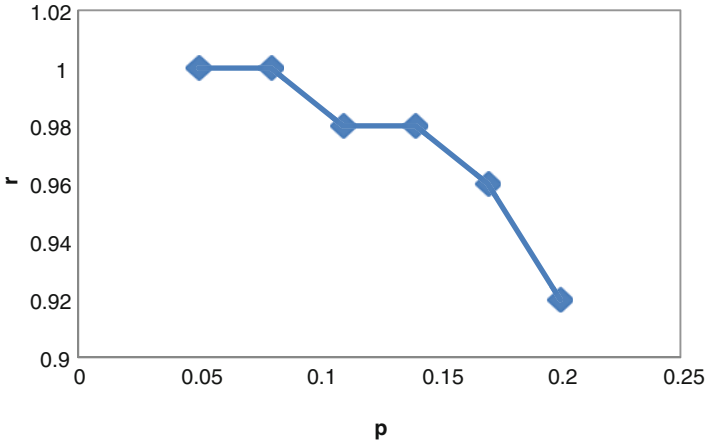

Fig. 25.3 Successful rate r versus p

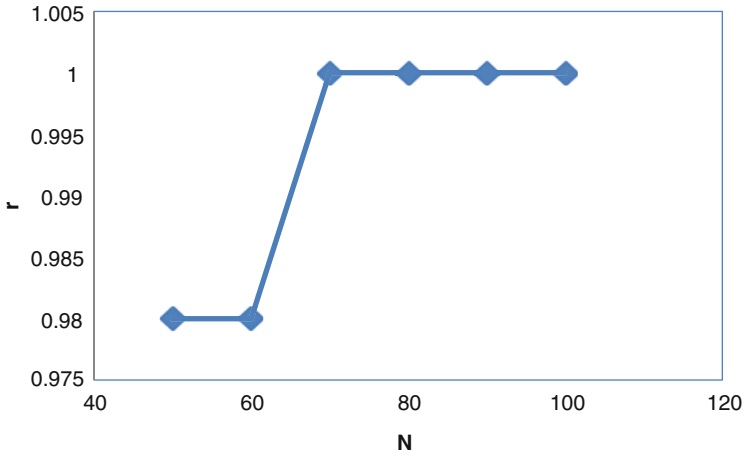

Fig. 25.4 Successful rate r versus N

similar to Fig. 25.2, when p increases, the number of linear dependence messages carried by polluted edges decreases, the probability of $C(G)$ changes, which reduces the probability of successful transmission.

In Fig. 25.4, we set $p = 0.1, D = 7$ and vary N in range of $[50 - 100]$ to calculate the r. similar to Fig. 25.2, with the increases of N, the performance of r is better. This is because with the increase of N, though the polluted edges increases, but the probability of $C(G)$ changes a little, because the complexity of the topology increases more.

25.5 Conclusion

In this chapter, we have investigated the problem of Conspiracy Attack in unicast system. We analyze the sufficient condition to achieve weak secure transmission given a set of wiretap nodes. We then develop secure routing algorithm based on the transmission topology design. Simulations show that the proposed unicast routing algorithm achieves good performance. In the future, we will evaluate our scheme by implementing it on multicast system.

Acknowledgments This work is funded by National Science Foundation of China (61071152, 60702043), 973 Program (2010CB731403, 2010CB731406) of China and National "Twelfth Five-Year" Plan for Science & Technology Support (2012BAH38 B04).

References

1. Ahlswede R, Cai N, Li S-YR, Yeung RW (2000) Network information flow. IEEE Trans Inf Theory 46(4):1204–1216
2. Li S, Yeung R, Cai N (2003) Linear network coding. IEEE Trans Inf Theory 49(2):371–381
3. Lima L, Medard M, Barros J (2007) Random linear network coding: a free cipher. In: Proceedings of IEEE international symposium on information theory (ISIT), Acropolis Congress and Exhibition Center, Nice, France 24th–29th June 2007, pp 546–550
4. Cai N, Yeung R (2002) Secure network coding. In: Proceedings of IEEE international symposium on information theory (ISIT), Palais de Beaulieu Lausanne, Switzerland, June 30–July 5, Chicago downtown Marriott, p 323
5. Feldman J, Malkin T, Stein C, Servedion RA (2004) On the capacity of secure network coding. In: Proceedings of the 42nd annual allerton conference on communication, control, and computing, Allerton House, Monticello, Illinois, USA, September 29–October 1
6. Bhattad K, Narayanan KR (2005) Weakly secure network coding. In: Proceedings of the first workshop on network coding, theory, and applications (Netcod), Riva del Garda
7. Yu Z, Wei Y, Ramkumar B, Guan Y (2008) An efficient signature-based scheme for securing network coding against pollution attacks. In: Proceedings of IEEE INFOCOM 2008, the 27th conference on computer communication, April 13–18, Phoenix, Arizona, USA, pp 1409–1417
8. Ho T, Leong B, koetter R, Medard M, Effros M, Karger D (2004) Byzantine modification detection in multicast networks using randomized network coding. In: Proceedings of IEEE international symposium on information theory (ISIT), Chicago downtown Marriott, Chicago, Illinois, USA, 6.27–7.2, p 144
9. Jaggi S, Langberg M, Katti S, Ho T, Katabi D, Medard M (2007) Resilinet network coding in the presence of byzantine adversaries. In: Proceedings of IEEE INFOCOM 2007, the 26th conference on computer communications, Acropolis Congress and Exhibition Center Nice, France, 24th–29th June, pp 616–624
10. Krohn M, Freedman M, Mazieres D (2004) On-the-fly verification of rateless erasure codes for efficient content distribution. In: Proceedings of IEEE symposium on security and privacy, May 9–12, Claremont Resort in Oakland, California, USA, pp 226–240
11. Gkantsidis C, Rodriguez PR (2006) Cooperative security for network coding file distribution. In: Proceedings of INFOCOM 2006 the 25th IEEE international conference on computer communications, Barcelona, Spain, 23–29, April, pp 1–13

Part VIII
Millimeter Wave Communications

Chapter 26
A New Modulation Diversity Technique of 60 GHz Millimeter-Wave System to Reduce PAPR

Yueteng Liu, Qizhu Song, Junfeng Wang, Bin Li, Xuebin Sun, Chenglin Zhao, and Zheng Zhou

Abstract In this chapter, we investigated a promising physical layer network coding-based two-way relay technique for the emerging 60 GHz millimeter-wave wireless personal area networks (WPANs), in order to address the problem of throughput reduction in relay nodes caused by the blockage of links. Because of the small wavelength at 60 GHz frequency band, links may be seriously blocked by the involved obstacles such as furniture and humans. The key idea of the most common solution to handle blockage proposed by now is to substitute the two line-of-sight (LOS) links for the blocked link. However, this method reduces the throughput of the network by a factor of two, which may hence fail to provide the required Qos guarantees to realistic WPAN applications. Our suggested new approach introduces a two-way relay scheme using physical layer network coding to the 60 GHz millimeter-wave WPANs, which can accomplish information exchange within two time slots instead of four. Simulation results, such as bit error rate and throughput, demonstrate the effectiveness of the proposed two-way relay scheme in 60 GHz WPANs.

Keywords 60GHz Millimeter-wave System • OFDM • Signal space diversity • PAPR

Y. Liu (✉) • B. Li • X. Sun • Z. Zhou
Key Laboratory of Universal Wireless Communication, Ministry of Education, Beijing University of Posts and Telecommunications, Beijing 100876, People's Republic of China
e-mail: liuyueteng@gmail.com

Q. Song • J. Wang
The State Radio Monitoring Center Testing Center, No. A-98 Bei lishi Road, XiCheng District, Beijing 100037, People's Republic of China
e-mail: sagacious@189.cn

C. Zhao
School of Information and Communication Engineering, Beijing University of Posts and Telecommunications, Beijing 100876, China

Q. Liang et al. (eds.), *Communications, Signal Processing, and Systems*, Lecture Notes in Electrical Engineering 202, DOI 10.1007/978-1-4614-5803-6_26,

26.1 Introduction

OFDM has drawn much attention as the alternative modulation scheme of 60 GHz Millimeter-wave short range communication systems [1]. OFDM is a multi-carrier modulation scheme with very high spectral efficiency and the ability of anti-multipath fading. OFDM allocates its transmitted symbols into narrow-band sub-carriers and keeps the orthogonality of its sub-carriers in order that it can avoid ISI (inter-symbol-interference) over a frequency selective fading channel [2]. However a major design challenge for its practice application is that an OFDM signal exhibits a very high peak to average power ratio (PAPR) [3]. The rapid growing need of high data transmissions over fading channels in WPAN(Wireless Personal Area Network) application scenarios has stimulate interest in signal space diversity [4]. Signal space diversity is an uncoded multi-dimensional modulation scheme with an intrinsic diversity order. It can achieve substantial coding gains over fading channels without expanding the bandwidth. This chapter proposes a new modulation scheme combined OFDM with signal space diversity to improve system performance. It can bring down the PAPR of the pure OFDM modulation scheme. Simulations results show that the new modulation scheme can bring down the PAPR.

This chapter is structured as follows: Section and Section introduce the system model and concepts of rotated modulation. In Sects. 26.4 and 26.5 simulation results verify the conclusion of the theory and shows that it can bring down the PAPR, thus making the OFDM more practical.

26.2 System Model

26.2.1 Transceiver Model

Figure 26.1 shows the transmitter end model. Raw bit stream is firstly encoded. We adopt LDPC (Low density check code) as the encode scheme as it is widely used in 60 GHz WPAN systems. After encoding, the bit stream is interleaved. The modulation mode is 16QAM. After modulation, the constellation is rotated for a certain

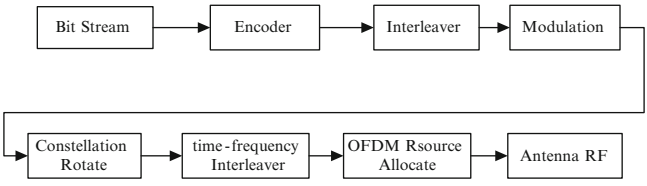

Fig. 26.1 System model in transmitter end

angle in order to bring down PAPR. We decompose constellations into in-phase component and quadrature-component and use time-frequency two-dimensional interweaver to compose new constellations. Then the bit stream is allocated for time and frequency resource before transmitted out antenna. This means that we map the new constellations into some sub-carriers in frequency domain of OFDM and OFDM operation is perform such as adding CP(cyclic prefix) and IFFT(inverse fast Fourier transform). In 60 GHz product applications scenarios, a multi-path fading channel is a typical one, which is a frequency-selective fading channel. In the receive end, reverse operations are performed of transmitter end. First, OFDM demodulation is carried out such as deleting CP, performing FFT (fast Fourier transform). Then the quadrature-component is de-interleaved with the original in-phase component to compose new constellations. Then ML(Maximum-likelihood) demodulation is performed of the rotated constellations to produce encoded bits. LDPC decoder can decode the information bit stream into the raw bit stream. A complete transceiver model is described as above.

26.2.2 Signal Space Diversity

We now study signal space diversity i.e. uncoded multidimensional modulation schemes with an intrinsic diversity order. The diversity order of a multidimensional signal set is the minimum number of distinct components between any two constellation points [5]. That means diversity order is the minimum Hamming distance of any two constellation points. We use modulation diversity or signal space diversity of uncoded multidimensional modulation schemes for short to distinguish from other types of diversity,such as time diversity or frequency diversity etc.. The key point to increase the modulation diversity is to apply a certain rotation to a modulation constellation in order to achieve the maximum number of distinct components. We rotate the constellation in order to bring down PAPR of the new scheme. And also, signal space diversity is more suitable for fading channels. For example, when a 4-psk constellation has rotated a certain angle, if a deep fade hits only one of components of the transmitted signal vector, the rotated constellation" offer more protection against the noise because in-phase component and quadrature component would not collapse together as would happen in constellations without signal space diversity. We add interweaver between encoder and modulator because we assume in-phase and quadrature components of symbols are independent of fading effects.

Uncoded multidimensional modulation scheme does not add any kind of redundancy to the information bit stream. We group the information bits into blocks and map them onto multidimensional constellation points. The coding gain of uncoded multidimensional modulation scheme is obtained without spending additional

power and bandwidth. The cost of uncoded of multidimensional modulation scheme is increasing the complexity of modulation operations and demodulation operation.

Compared to non-rotated signal set, rotated signal set produces significant gains in the fading channel. While used over pure additive white Gaussian noise(AWGN) channel, rotated signal set has the same performance as the non rotated signal set. Rotated signal set has a performance between the extreme cases of Gaussian and Rayleigh fading channel [6]. However, uncoded rotated multidimensional modulation is designed for independent flat fading channels and cannot directly be used for frequency selective fading channels with ISI. So we combine signal space diversity schemes with OFDM. The superiority of the new scheme is that it adopts both of the advantages of signal space diversity and OFDM system. The new scheme can bring down the PAPR of OFDM systems in a distinguished way.

26.2.3 OFDM Module

In a one period OFDM symbol, we can express the continuous time OFDM signal in (26.1), where S_k is the k^{th} subcarrier's QAM value, $g(t)$ is the rectangular window of unit height and N is the subcarrier number.

$$s(t) = \frac{1}{\sqrt{N}} \sum_{k=0}^{N-1} S_k e^{j2\pi kt/T} g(t) \tag{26.1}$$

The sampled OFDM signal can be expressed in (26.2)

$$s_n = \frac{1}{\sqrt{N}} \sum_{k=0}^{N-1} S_k e^{j2\pi kn/N} \tag{26.2}$$

Thus we can get samples $[s_0, s_1, \ldots s_{N-1}]^T$ from input symbols $[S_0, S_1, \ldots S_{N-1}]^T$. The PAPR of OFDM signal s_i is defined as

$$PAPR\{s_i\} = \frac{max_{i \in N} |s_i|^2}{E\left\{ |s_i|^2 \right\}} \tag{26.3}$$

26.3 Concepts of Rotate Modulation

We obtain diversity order by rotating the constellation for a certain angle. Assume the rotated constellation is x and non-rotated constellation is u, we can obtain x by applying the rotation matrix R to u, i.e. $x = Ru$, $u \in Z^n$ where x belongs to the n-dimensional cubic lattice $Z_{n,L}$. As has been illustrated in Sect. 26.2, the diversity order L of a multidimensional signal set is the minimum number of distinct

components between any two constellation points. It is proved that when the diversity order L is large, multidimensional rotated QAM constellation is not insensitive to multi-path fading channels [7]. It is no doubt that we adjust rotation angle to maximize the diversity order L to improve system performance [8]. Here we take an example. The QPSK constellation $x = x_1 + jx_Q$ is obtained by rotate an angle θ_1 to $u = u_I + ju_Q$, we can describe in matrix form as follows:

$$\begin{pmatrix} x_I \\ x_Q \end{pmatrix} = R\begin{pmatrix} x_I \\ x_Q \end{pmatrix} = \begin{pmatrix} cos\theta_1 & sin\theta_1 \\ -sin\theta_1 & cos\theta_1 \end{pmatrix}\begin{pmatrix} u_I \\ u_Q \end{pmatrix} \tag{26.4}$$

We try to consider bringing down PAPR and the diversity order together. Through adjusting θ_1, we can get the best system performance . The fact is that through adjusting θ_1, we can bring down the PAPR of the OFDM system. In this chapter, bringing down the PAPR is the first thing for us to consider. Simulation results that a little sacrifice in BER can pay for the promotion in PAPR and compared to pure OFDM systems, the system performance is better in BER and PAPR.

Before rotating constellations, we add interweavers which destroy the correlation between in-phase component and quadrature component. Interweaver is important in obtaining the modulation diversity to bring down PAPR and obtain code gains. Now we describe the time-frequency interweaver as it is more comprehensive than the one between encoder and modulation. We assume an OFDM symbol has 1,024 sub-carriers. We design a low-complexity and efficient quadrature component interweaver. We assume six quadrature component signals $(q_1, q_2, q_3, q_4, q_5, q_6)$ take up the time-frequency $\{(f1, 1), (f2, 4), (f1, 2), (f2, 5), (f1, 3), (f2, 6)\}$ resource block where (fi, j) means that the component signal occupy the f^{th} subcarrier in frequency domain and j^{th} time slot in time domain. After interleaving, they occupy $\{(f2, 4), (f1, 2), (f2, 5), (f1, 3), (f2, 6), (f1, 1)\}$. That means the interleaving is the right-cyclic-shift result of the original signals. The time interval between in-phase and quadrature component is greater than the coherence time of the fading channel. In other words, the frequency interval between them is greater than the coherence bandwidth of the fading channel.

26.4 Simulation and Analysis

Simulations are carried out to compare the PAPR of pure OFDM systems and the OFDM systems with signal space diversity. The parameter of simulation are showed in Tables 26.1 and 26.2. The OFDM system has 1024 subcarriers and the modulation scheme is 16QAM. The maximum dropper frequency shift of the fading channel is 56 Hz. From Fig. 26.2, we can see that the OFDM with signal space diversity is more superior to the conventional one, while simulation results

Table 26.1 Parameters of simulations

Parameter	Value
Channel model	LOS(AWGN)
Number of subcarriers	1,024
Subcarrier modulater	16-QAM
Channel coding	LDPC(R = 10/16)
LDPC size	336 × 672
Output back-off	4 dB
Synchronization	Ideal
Channel estimation	Ideal

Table 26.2 Parameters of LDPC

Parameter	Value
Column number of inspection matrix	672
Row number of inspection matrix	252
Iteration number	50

Fig. 26.2 Rotate angle is π

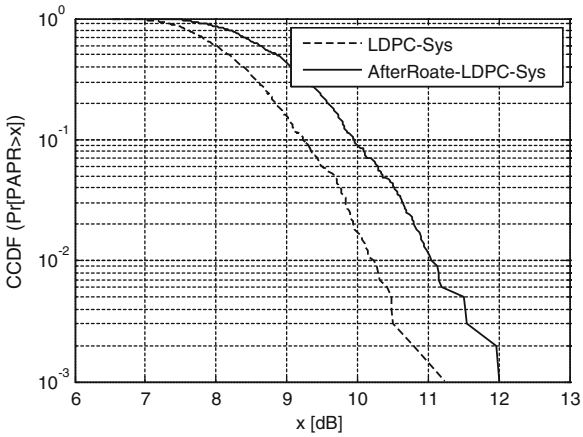

shows that they have almost the same BER (Bit Error Ratio) performance. We use complementary cumulative distribution function to describe the PAPR comparison. In Fig. 26.2, we can see that the PAPR performance of the OFDM scheme with signal space diversity has improve a lot while the BER of both the modulation schemes are 10^{-6} where x axes stands for the power to achieve the BER.

Simulations show that when we adopt four dimensional rotate modulations, the improvement of PAPR varies with different rotate angle. From Fig. 26.3,we point that only when the rotate angle is in times of $\pi/2$, the improvement of PAPR is notable. When the rotate angle is $\pi/2$ or $3\pi/2$, as shown in Figs. 26.4 and 26.5, we can see that the PAPR improves about 1 dB.

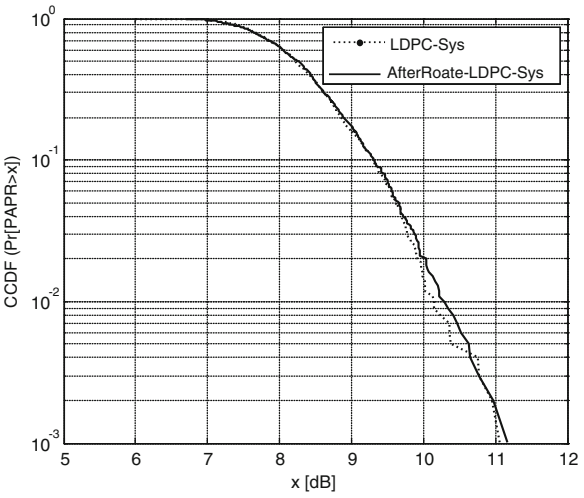

Fig. 26.3 Rotate angle is $\pi/5$

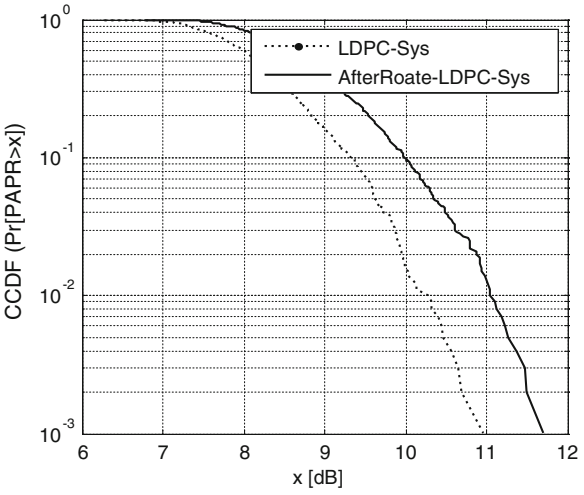

Fig. 26.4 Rotate angle is $\pi/2$

26.5 Conclusion

A new modulation scheme is proposed. The new scheme combines OFDM with signal space diversity to bring down the PAPR the OFDM. The constellation is rotated for a certain angle and that we add time-frequency interweaver to make in-phase and quadrature component independent. We take full advantage of modulation of diversity of rotated QAM modulation to bring down PAPR. Simulation results have turned out this new scheme can bring down the PAPR of the OFDM system. In other words, the new scheme is makes OFDM more practical.

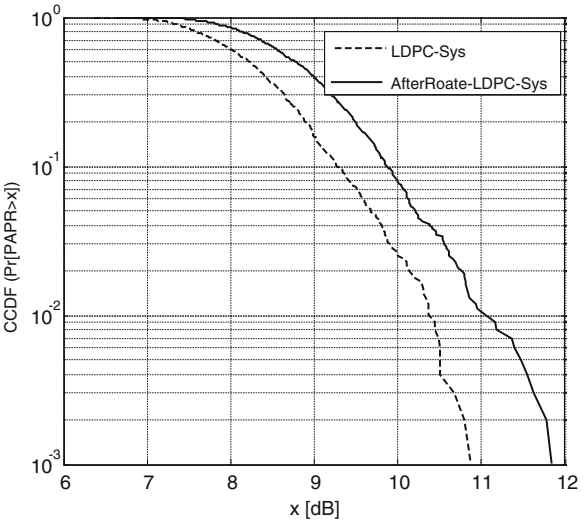

Fig. 26.5 Rotate angle is $3\pi/2$

Acknowledgments Supported by the National Natural Science Foundation of China (Grant No.60902046, 60972079) and the Important National Science & Technology Specific Projects of China (Grant No.2011ZX03005-002, 2012ZX03001022)

References

1. Lily Yang L (2009) 60 GHz: opportunity for gigabit WPAN and WLAN convergence. ACM SIGCOMM Comput Commun Rev 39(1):56–61
2. Doan CH, Emami S, Niknejad AM, Broderson RW (2005) Millimeter-wave CMOS design. IEEE J Sol State Circ 40(1):144–155
3. Zhou X, Caffery J Jr (2002) A new distribution bound and reduction scheme for OFDM PAPR. Wireless Personal Multimedia Communications
4. Zhanji Wu, Tingting Fu, Xu Wang (2009) A novel coding-rotated-modulation OFDM scheme. In: Proceedings of Communications Technology and Applications, 2009. ICCTA '09
5. Boutros J, Viterbo E (1988) Signal space diversity: a power and bandwidth efficient diversity technique for the rayleigh fading channel. IEEE Trans Inf Theory 44(4):1453–1467
6. Tran NH, Nguyen HH (2009) Performance analysis and design criteria of BICM-ID with signal space diversity for keyhole nakagami fading channels. IEEE Trans Inf Theory 55(4):1592–1602
7. Sampei S, Sunaga T (1993) Rayleigh fading compensation for QAM in land mobile radio communications. IEEE Trans Veh Technol 42:137–147
8. Du J, Vucetic B (1993) Trellis coded 16-QAM for fading channels. European Trans Telecom 4 (3):335–341

Chapter 27
Artificial Reflector Based Efficient NLOS Transmissions in 60 GHz Millimeter-Wave Wireless Communication

Peng Zhang, Chenglin Zhao, Bin Li, Yun Liu, and Zhou Li

Abstract 60 GHz millimeter-wave communications have been considered as one of the most promising wireless transmission technology in the future. Compared with the received power in the presence the line-of-sight (LOS) path, it is apparent that the power of non-line-of-sight (NLOS) path may be attenuated seriously, leading to the poor signal to noise ratio. One feasible approach to combat the obstacle transmission in 60 GHz communications is to use a relay device, which is served as the accessing point. In this article, an efficient method is suggested to improve the link quality, by using an artificial reflector under NLOS path so as to avoid significant path loss. This proposed method can be easily implemented in the 60 GHz wireless personal area network, and has a much lower configuration cost compared with the relay node. The theoretic analysis and experimental simulations have demonstrated the effectiveness of the presented method.

Keywords 60GHz • LOS • NLOS • Artificial reflector

P. Zhang (✉) • B. Li
Beijing University of Posts and Telecommunications, Beijing, China
e-mail: yuzhiboyou@bupt.edu.cn; stone_123456@126.com

C. Zhao
School of Information and Communication Engineering, Beijing University of Posts and Telecommunications, Beijing 100876, China
e-mail: clzhao@bupt.edu.cn

Y. Liu • Z. Li
China Academy of Telecommunications Research, Beijing, China
e-mail: liuyun@catr.cn; lizhou@catr.cn

Q. Liang et al. (eds.), *Communications, Signal Processing, and Systems*, Lecture Notes in Electrical Engineering 202, DOI 10.1007/978-1-4614-5803-6_27,

27.1 Introduction

60 GHz millimeter wireless communication system, which seems to be extremely suitable for short-range and high-rate wireless transmissions, has up to 7 gigahertz (GHz) of bandwidth. On the basis of Shannon theorem, the wider the bandwidth, and the greater the channel capacity. Thus, 60 GHz millimeter communications have been considered as one of the most promising wireless communication in the future, which are supposed to provide the high data rate up to Gbps.

Although 60 GHz wireless communications have a lot of advantages, there are also several challenges that are needed to face in practice [1–4], which have made 60 GHz communications difficult to implement deployment. Compared with the lower frequency bands, the 60 GHz channel has 20–40 dB additional free space path loss. Moreover, multipath effects are vastly reduced at 60 GHz making non-line-of-sight (NLOS) communication very difficult.

So far, there have been few results on the channel capacity of 60 GHz communications. However, the research on the channel capacity over indoor LOS and NLOS channels is more meaningful. In order to improve the link quality and the channel capacity, we present a promising artificial reflector approach to conduct obstacle transmission so as to avoid significant path loss under NLOS path. This new method can be easily implemented in the 60 GHz wireless personal area network, and has a much lower configuration cost compared with the relay node. Based on this basis, we also study the channel capacity of 60 GHz systems over indoor LOS and NLOS channels following the Chinese spectrum allocation and give the simulation results.

The rest of this chapter is organized as follows. In Sect. 27.2, background information related to beam-forming is provided. Section 27.3 presents the channel capacity over indoor LOS and NLOS channels. Different path loss in three scenarios (i.e., the LOS path, the NLOS path and NLOS path with an artificial reflector) are given in Sect. 27.4. The Conclusions are drawn in Sect. 27.5.

27.2 Beam-Forming

As a result of the additional path loss and the enlarged transmission bandwidth of 60 GHz systems, the poor link budget become the primary difficulty the 60 GHz technology needs to face. Antenna-array based beam-forming is the critical solution to resolve the limited link budget problem as the recent research chapters on 60 GHz technology denoted. In order to support beam-forming, the adaptive antenna arrays should be fixed at least at one end of the transceiver system and thereby supply reliable communication links in the both scenarios of LOS and NLOS.

If the beam-forming technology is adopted when calculating the path loss under the LOS or NLOS case, the gain of the beam-forming should be considered. For a $T \times R$ (T means number of transmitter antennas and R means number of receiver antennas) system, the theoretical array gain is given by $10 \times \log10(RT)$. From the simulation results in the literature [5], we can draw a conclusion that there is a

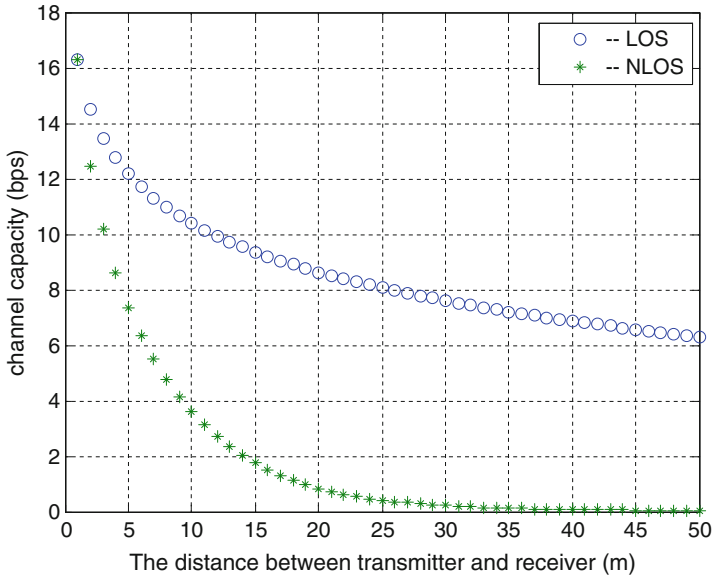

Fig. 27.1 The channel capacity for a 60 GHz wireless system over the LOS and NLOS channel with the change of distance [6]

consistent gap between the beam-forming gain and the theoretical array gain, ranging from approximately 4.5–6.5 dB. In our studies, we can obtain the beam-forming gain with the antenna gain minus 5 dB. The beam-forming gain is 22.9 dB when T and R are both set to 25.

27.3 Channel Capacity of 60 GHz over LOS and NLOS Channels

Before introducing the artificial reflector to the NLOS path, it is necessary to know the channel performance of 60 GHz under the LOS and NLOS case, so as to understand the need for improving the transmission quality of NLOS path. In Sect. 27.3, we mainly research channel capacity of 60 GHz over the LOS and NLOS channels.

It can be seen from Fig. 27.1, there are different variation of channel capacity over the LOS and NLOS channels. Over LOS channel, when the distance from the transmitter to the receiver is 1 m, the channel capacity is 16(bit/s/Hz). When the distance is 50 m, the channel capacity is 6(bit/s/Hz). The larger the distance from the transmitter to the receiver is, the smaller the channel capacity is. But there is only a small capacity decrease compared with the normalized channel capacity over NLOS channel. Over NLOS channel, when the distance from the transmitter to the receiver is 1 m, the channel capacity is 16(bit/s/Hz) too. But when the distance

increases to 15 m, the normalized channel capacity could be down to 1.6(bit/s/Hz). If the distance exceeds 25 m, the channel capacity is nearly 0. It means that it is difficult to implement communication over NLOS channel when the distance exceeds 25 m.

The result reveals that channel capacity decreases rapidly when the distance increases, especially in NLOS channels. Therefore, it is necessary to use some method to reduce the path loss and improve the channel performance under the NLOS channel.

27.4 Path Loss of Different Scenarios

27.4.1 Blockage Problem

Through experiments in conference room and cubicle environments, the conclusion can be drawn that LOS, first-and second-order reflections are the primary propagation mechanisms for 60 GHz indoor wireless system. Therefore, the reflection paths are suitable for the NLOS paths. Because LOS is the shortest path and power loss usually happens when the reflection takes place, the LOS path is the optimal choice. But the LOS path can't be guaranteed all the time. If there are human bodies or moving objects between the transmitter and receiver, the LOS path is blocked. So far, there are two ways to solve the blockage problem. One way is to use multiple antenna arrays, another method is to use a relay device.

Although the two methods are good, they must be used in specific conditions. In addition, no matter the multiple antenna arrays or the relay device is not easy to install in indoor environment, so using an artificial reflector under the NLOS path is proposed. In order to do the comparison of performance of the channel to show the effectiveness of an artificial reflector, we use the following three scenarios.

27.4.2 Scenario One

The LOS path is used for scenario one. There is no obstacle between the transmitter and the receiver. The path loss is given by

$$P_L(d) = 10\log\left(\frac{4\pi d_0}{\lambda}\right)^2 + 10n\log(d/d_0) \tag{27.1}$$

where d is the distance between the transmitter and receiver, d_0 is reference distance (usually 1 m), λ is the wavelength of 60 GHz system, n is the path loss exponent (which is 1.77 over the LOS path [6]).

Table 27.1 Measured attenuation for different obstructions

Type	Material description	Thickness	Attenuation(dB)
A	Double glass	15 mm	4.5
B	Simple glass	5 mm	3.5
C	Wooden closet	2 cm	13.8
D	Metal closet	8 mm	8
E	Whiteboard	1.5 cm	11.6
F	Plywood panels	0.5 cm	6
G	Brick wall	23 cm	48
H	Iron door	8 cm	49

27.4.3 Scenario Two

The NLOS path without an artificial reflector is used for scenario two. In consideration of the additional path loss from the obstructions between the transmitter and receiver, the model which estimates path loss for the NLOS topographies is chosen. This model is given by

$$L(d) = L_{FS}(d_0) + 10n\log_{10}(d) + \sum_i K_{oi}L_i \tag{27.2}$$

where $L(d)$ is path loss at the distance d, $L_{FS}(d_0)$ is path loss at the reference distance which is set to 1 m, n is the path loss exponent which is set as two in the particular model. Furthermore, i means different types of obstructions, K_{oi} represents the number of obstructions which belong to type i, L_i stands for the attenuation of obstruction which is type i.

The measured attenuation factor for different types of obstructions along with a particular material description and thickness can be obtained from Table 27.1 [7].

In scenario two, we decide to use the brick wall of 23 cm as the obstacle between the transmitter and the receiver. In order to lock on the direction of the direct path, it is necessary to use beam-forming in this scenario. As the beam-forming technology is applied, the real path loss should be equal to $L(d)$ minus the beam-forming gain.

27.4.4 Scenario Three

In scenario three, we propose to use an artificial reflector under the NLOS condition and compare it with the result under the condition without a reflector to show the effectiveness of the reflector.

In the view of an NLOS path with a reflector plate, as is expressed in Fig. 27.2

The received power in dBm can be expressed by

$$S_{RX}[dBm] = S_{TX} + G_{RX} + G_{TX} + R_r - L(r_1) - L(r_2) \tag{27.3}$$

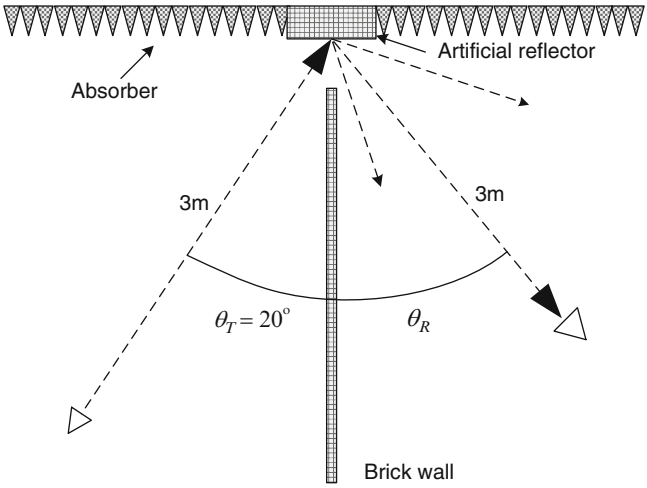

Fig. 27.2 Measurement situation with an artificial reflector

where S_{TX} is the transmitter power in dBm, G_{TX} is the antenna gain for the transmitter, G_{RX} is the antenna gain for the receiver, r_1 is the distance from the transmitter to the reflector and r_2 is the distance from the reflector to receiver. $L(r)$ means the path loss at the separation distance of r, and R_r is called radar cross section in dBm^2, which stands for a reflector gain. For instance, when applying a square flat plate in scenario three, the R_r in dBm^2 can be expressed by [8]

$$R_r = \frac{4\pi A_r^2}{\lambda_e^2} \times \frac{\sin(kb\sin(\theta))}{kb\sin(\theta)} \tag{27.4}$$

$$\lambda_e = \frac{\lambda}{\cos(\beta/2)} \tag{27.5}$$

where A_r means the area of square plate, b means the size of the flat plate side, $k = 2\pi/\lambda_e$, λ means the wavelength of 60 GHz, β is the angle from the transmitter-reflector to receiver-reflector, and θ is the angle between the plate normal and the bisector of the transmitter-reflector and receiver-reflector.

$$L(d) = S_{TX} + G_{TX} + G_{RX} - S_{RX} = L(r_1) + L(r_2) - R_r \tag{27.6}$$

For the purpose of directing the antenna beam-patterns towards the strongest reflection, we propose to apply beam-forming in scenario three. Thus, due to applying the beam-forming technology, the real path loss should be equal to $L(d)$ minus the beam-forming gain.

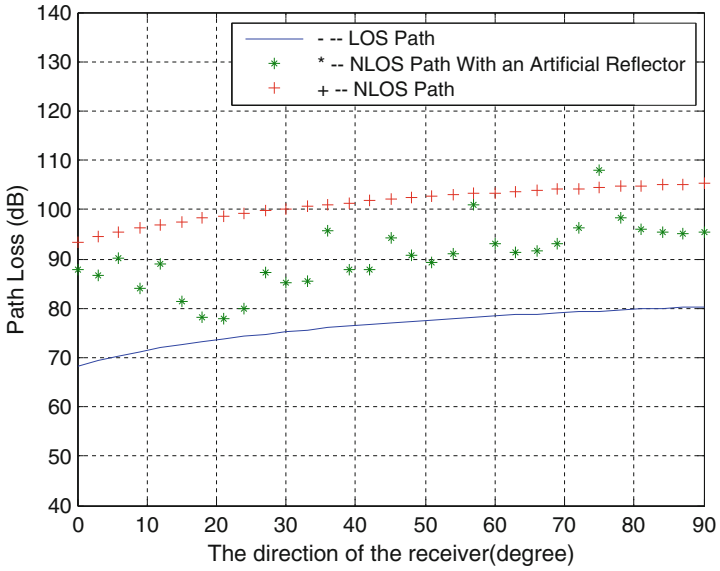

Fig. 27.3 The path loss of three different scenarios (LOS path, NLOS path, NLOS path with an artificial reflector)

27.4.5 Simulation Results

In this section, through the experimental simulations, we will evaluate the performance of the presented approach to combat the NLOS transmission in 60 GHz millimeter-wave communications.

In our simulation platform, the transmitter's direction θ_T is set to 20° [9], and the distances of the transmitter to reflector and reflector to receiver are both set to 3 m. The distance between the transmitter and the receiver can be obtained by using the geometry degree of the receiver's direction θ_R, i.e. the law of cosines. The received power level and the path loss are as a function of θ_R.

It can be drawn from Fig. 27.3, the path loss of the NLOS path with an artificial reflector is obviously less than that of the NLOS path without a reflector. From the averaging perspective, the additional gain of 10 dB can be achieved by resorting to our suggested method compared with the NLOS case. The reflector indeed improves the transmission quality. Besides, the minimum path loss can be achieved when θ_R is equal to 20° under the NLOS path with a reflector. The result is closely related to the transmitter's direction θ_T.

27.5 Conclusion

It is shown that the channel capacity decreases rapidly when the distance increases, especially in NLOS channels of 60 GHz millimeter-wave communications. In order to improve the link quality in NLOS transmissions, we propose to employ an artificial reflector under the NLOS condition to avoid the significant propagation loss in this investigation. The conclusion can be drawn that the path loss of the NLOS path can be improved by 5–20 dB or more via a reflector plate from the simulation result. Except for the performance improvement, it is easy to place the reflector on the surface of the wall or ceiling in a room. In addition, it is more economical compared with the installation of an additional base station. So it is fit to choose an artificial reflector under the NLOS condition, and hence provide a promising solution to 60 GHz millimeter-wave communications.

Acknowledgments This work was supported by National Natural Science Foundation of China (60972079, 6090204661271180) and the BUPT excellent Ph.D. students' foundations (CX201122).

References

1. Giannetti F, Luise M, Reggiannini R (1999) Mobile and personal communication in 60 GHz band: a survey. Wirel Pers Commun 10:207–243
2. Yong SK, Chong C-C (2007) An overview of multigigabit wireless through millimeter wave technology. Wirel Commun Netw 2007(1):50–50
3. Doan C, Emami S, Sobel D, Niknejad A, Brodersen R (2004) Design considerations for 60 GHz CMOS radios. Commun Mag 42(12):132–140
4. Karkkainen M, Varonen M, Kangaslahti P, Halonen K (2005) Integrated amplifier circuits for 60 GHz broadband telecommunication. Analog Integr Circ Signal Process 42(1):37–46
5. Trees HLV (2002) Front matter and Index [A]. Optimum array processing: part IV of detection, estimation, and modulation theory. Wiley, New York
6. Dong Jie, Jing-jing Wang, Hao Zhang, Guo-yu Wang (2010) Channel capacity of 60 GHz wireless communication systems over indoor line-of-sight and non-line-of-sight channels. WiCOM, Chengdu, 23–25 Sept 2010, pp 1–4
7. Moraitis N, Constantinou P (2004) Indoor channel measurements and characterization at 60 GHz for wireless local area network applications. IEEE Trans 12:3180–3189
8. Kell R (1965) On the derivation of bistatic RCS from monostatic measurements. Proc Inst Elect Eng 8:983–988
9. Kajiwara A (1997) Millimeter-wave indoor radio channel with artificial reflector. IEEE Trans Veh Technol 46:486–493

Chapter 28
A Novel Frequency Drift Tracking Algorithm Based on Kalman Filter in 60GHz mm-WaveSystem

Jingya Ma, Chenglin Zhao, Bin Li, Yun Liu, and Zhou Li

Abstract In order to study and solve the frequency drift problem in 60 GHz wireless communication system, a new data auxiliary frequency synchronization and tracking algorithm is proposed in this article, which is on the base of Chu sequence as training pilots, utilizing the time feature of frequency variation to estimate frequency offset by Kalman filter. It not only promotes the OFDM system synchronization performance, but also reduces the length of pilots and extends pilots interval to promote signal transfer efficiency. The simulation results prove its feasibility and validity.

Keywords 60GHz • Synchronization • Kalman • Frequency drift • OFDM

J. Ma (✉)
Beijing University of Posts and Telecommunications, Beijing, China
e-mail: michelle6613@gmail.com;

C. Zhao
School of Information and Communication Engineering, Beijing University of Posts and Telecommunications, Beijing 100876, China
e-mail: clzhao@bupt.edu.cn

B. Li
Key Lab of Universal Wireless Communications, MOE Wireless Network Lab, Beijing University of Posts and Telecommunications, Beijing 100876, P.R.C
e-mail: stone_123456@126.com

Y. Liu • Z. Li
China Academy of Telecommunications Research (CATR), Ministry of Industry and Information Technology Telecommunication Metrology Center (MIIT), Beijing 100088, P.R.C
e-mail: liuyun@catr.cn

Q. Liang et al. (eds.), *Communications, Signal Processing, and Systems*, Lecture Notes in Electrical Engineering 202, DOI 10.1007/978-1-4614-5803-6_28,

28.1 Introduction

With rapid development of wireless multimedia services, the requirement of higher speed data transmission for wireless communication system has been raised. The unlicensed wide spectrum and path loss as high as 15 dB/km of 60 GHz attract more and more attention to develop and standardize the technology in this band. The standardization on 60 GHz band was originally launched by the IEEE802.15 WPANs Millimeter-Wave Alternative PHY Task Group 3c (TG3c)[1], and released in 2009. Then, following TG3c, the IEEE 802.11ad Task Group[2], was established in 2010 and also works on standardizing 60 GHz communications as an appealing spectral reuse candidate for WLAN.

OFDM (Orthogonal Frequency Division Multiplexing, OFDM) is adopted in 60 GHz mm-wave system standards. High-precision time-frequency synchronization is the premise of the normal work of OFDM systems. But in the design of mm-wave RF, the original frequency needs to be multiplied several times to reach the goal of high-frequency in 60 GHz band. When frequency drifts in VCO (Voltage Controlled Oscillator), the frequency offset will be extremely severe that the performance of OFDM system would drop dramatically, such as ICI (Inter Carriers Interference, ICI) and data loss. A lot of attention has been focused on searching the solution to against frequency drift in high frequency spectrum.

In general, frequency offset is estimated by well-designed training sequence of cyclic prefix. In the [3], Van de Beek proposed a maximum likelihood estimation algorithm using the nature of cyclic prefix. In [4], the initial approach to synchronize time and frequency with training sequences is presented that Schmidl and Cox designed two frames to estimate frequency and time. In [5], author described a frequency synchronization and tracking algorithm in high dynamic spread spectrum system receiver with PN code. In [6], Zadoff-Chu sequence was promoted to sync frequency. It is more suitable for integer frequency offset estimation and wider estimation range. The frequency offset estimation range depends on the length of Chu sequence, but frequency drift in high frequency spectrum is so wide that the transmission efficiency of the system is badly damaged. So its not appropriate for 60 GHz wireless system.

In this article a new frequency estimating and tracking algorithm is proposed to against frequency drift problem in 60 GHz system. Considering the time correlation of frequency drift, frequency offset problem is modeled as tracking of floating value by Kalman filter. This new algorithm can achieve precise frequency synchronization with less than half training sequence.

28.2 System Model

28.2.1 OFDM System Model

Base on S-V channel mode, the 60 GHz system channel mode and pulse response are provided in [7] as bellow:

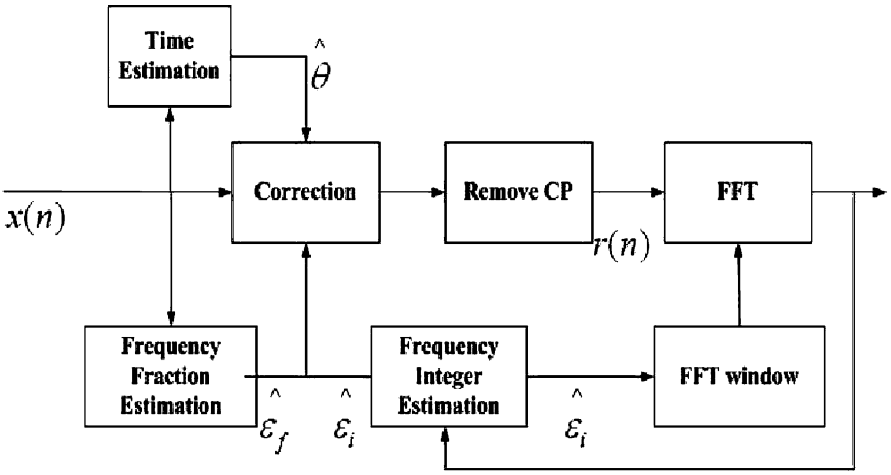

Fig. 28.1 OFDM synchronization process in receiver

$$h(\tau,\phi) = \beta\delta(\tau,\phi) + \sum_{l=0}^{L}\sum_{k=0}^{K_l}\alpha_{k,l}\delta(\tau - T_l - \tau_{k,l})\delta(\phi - \theta_l - \omega_{k,l}) \tag{28.1}$$

where β is the LOSLine of Sightparameter, l is the complex gain of isolated paths; τ_k, lis related delay. The distribution of parameters above is mentioned in [7].

Figure 28.1 illustrates a block diagram of synchronization in receiver. If the signal in receiver is perfectly synchronized, the received discrete signal can be described as

$$r(k) = \sum_{i}\sum_{l=0}^{L-1} h(l)s_i(k - l - iN_T) + w(k) \tag{28.2}$$

where $w(k)$ represents the complex additive white Gaussian noise with power spectral density $\sigma_w{}^2$. The element of $r(k)$, $r_i(k)$, is the ith OFMD symbol. The received data with CP deduced, are transformed by FFT unit as below.

$$R_i(n) = H(n)d_i(n) + W_i(n) \tag{28.3}$$

In real situations, however, oscillator instabilities result in a carrier frequency offset ε between the received and local carrier. The frequency offset produces a shift of the signal in frequency domain and lead to orthogonality loss between subcarriers. In order to understand the impact, the expression of signal with frequency offset is

$$R_i(n) = e^{j\varphi_i}\sum_{p=0}^{N-1} H(p)d_i(p)f_N(\varepsilon + p - n) + W_i(n) \tag{28.4}$$

where $\varphi_i = 2\pi_i \varepsilon N_T/N$, and f_N is impulse response. As to frequency offset ε, there are two situations. One is that ε is integer multiple of the subcarrier spacing, and (28.4) can be expressed as

$$R_i(n) = e^{j\varphi_i} H(|n-\varepsilon|_N) d_i(|n-\varepsilon|_N) + W_i(n) \tag{28.5}$$

in which $n - \varepsilon_N$ is the value of $n - \varepsilon$ reduced to interval $[0,N-1]$. This equation indicates that integer frequency offset only results in a shift of modulated subcarriers by ε positions. Orthogonality among subcarriers is still preserved, but the received symbols appear in wrong position at FFT, which leads to data loss.

In the other case that frequency offset is not integer value, the receiving signal can be expressed as

$$R_i(n) = e^{j\varphi_i} H(n) d_i(n) f_N(\varepsilon) + I_i(n,\varepsilon) + W_i(n) \tag{28.6}$$

in which $I_i(n, \varepsilon)$ is a zero-mean ICI term with power $\sigma_I{}^2(\varepsilon)=E\{I_i(n, \varepsilon)^2\}$.

28.2.2 Frequency Drift Model

The method of producing high frequency in 60 GHz mm-wave wireless communication system is that a fundamental frequency produced by VCO passes to several layers of FDs and PLLs to reach the goal high frequency. Fukasawa [8] describes the frequency drift model. When temperature changes between $-30 \sim 85$ °C, the output frequency drops almost 0.8 GHz, as wide as 150 subcarriers spacing. And output power drops 1.5 dBm. So the frequency drift parameter is -6.7 MHz/°C.

Template loss cannot be avoided in the circuit of the diode chip, which raises its temperature. Considering the time property of circuit heat production, the frequency drift can be modeled as (28.7).

$$f_d(t) = \rho_f \frac{h}{K_* S} \eta P \cdot t + v_k \tag{28.7}$$

where ρ_f is frequency drift parameter, h is thickness of chip, S is surface area, K is crystal thermal conductivity parameter, η is the template loss ratio, P is power, v_k is phase noise.

28.3 Kalman Based Frequency Offset Estimation

28.3.1 Synchronization Method with Chu Sequence

Constant envelope, small PAPR (Peak to Average Power Ratio, PAPR), good autocorrelation feature Chu sequence. So compared with traditional training sequence (like m sequence and Barker code), the peak-to-side lobe ratio of Chu

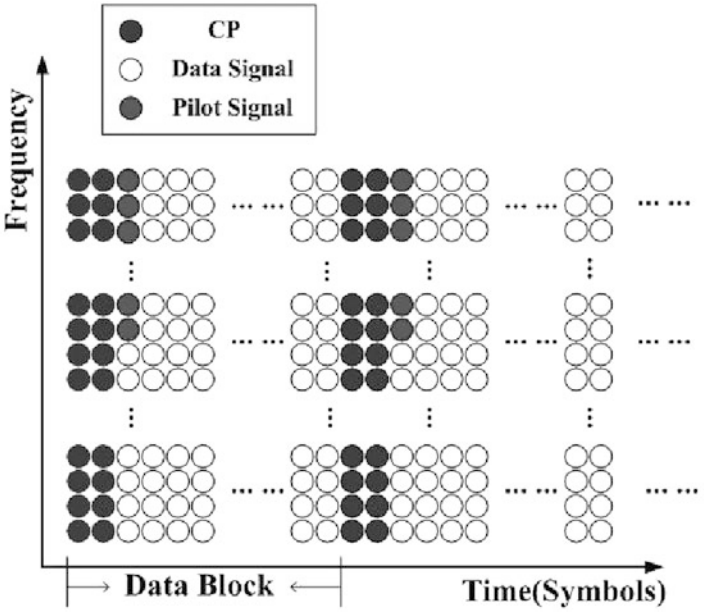

Fig. 28.2 Packet configuration

sequence is much bigger. The autocorrelation impulse function makes it easy to locate frequency offset. The definition of Chu sequence in [9] is

$$C_n^{(r)} = \exp(j\frac{\pi r n^2}{N_p}) \tag{28.8}$$

The correlation between Chu sequences with frequency offset is

$$\begin{aligned} R_{m,\varepsilon} &= \sum_{n=1}^{N_p-1} C_n C^*_{(n+m)} \quad \bmod N_p \exp(-j\frac{2\pi\varepsilon(n+m)}{N_{pilot}}) \\ &= \begin{cases} N_p \exp(-j\frac{2\pi}{N_{pilot}}) \exp\left(-j\frac{\pi(N_p-1)(\varepsilon/p)^2}{N_p}\right) & m = \varepsilon/p \\ 0 & m \neq \varepsilon/p \end{cases} \end{aligned} \tag{28.9}$$

As shown in (28.9), the correlation function only has the value in the offset position, other positions for 0. The frequency offset can be easily located by envelope detection.

$$\varepsilon_i = \arg\max Corr(r) = \arg\max \sum_{m=0}^{L_{chu}-1} local(m) r^*(d+m+N/2) \tag{28.10}$$

Because the frequency drift changes obviously with time, to make sure of frequency synchronization, pilots need to be added in front of every block as

shown in Fig. 28.2. To evaluate the actual transmission efficiency, this article employs the classic frame format, whose duty ratio is

$$\rho_{frame} = \frac{N_{pilot}}{N_{pilot} + N_{data}} \tag{28.11}$$

As shown above, for certain-length frame, with less pilots, more information can be loaded.

28.3.2 Frequency Synchronization with Kalman Filter

The time property of frequency drift is shown in (28.7). Considering priori information, the frequency synchronization performance will enhanced effectively. And the length of pilot required would be significantly reduced.

The frequency offset is set as x_k, and the relevant pilots Chu sequence is the output. So the state equation is

$$x_k = f(x_{k-1}, v_k) = x_{k-1} + \rho_{f*} \frac{h}{K*S} \eta P * \Delta t + v_k \tag{28.12}$$

The phase noise is mutual independent, obeying gaussian distribution as $v_k \sim N(0,\sigma^2_v)$. σ^2_v is $4\pi B_\theta T_s$. B_θ is the band width when power drops 3dB [8]. The observe equation is

$$Z_k = h(x_k, w_k) \tag{28.13}$$

The sequence is $z_k = \{z_{k,1}, z_{k,2}, z_{k,3},, z_{k,N}\}$, and

$$z_{k,n} = c_n \exp\{-j\frac{2\pi n x_k}{N}\} + w_k \tag{28.14}$$

where w_k is AWGN channel noise. In Kalman method, the prediction equation is

$$x_{k|k-1} = f(x_{k-1}, 0) \tag{28.15}$$

$$P_{k|k-1} = F_k P_{k-1} F_k^T + Q_k \tag{28.16}$$

The fixed prediction is

$$x_k = x_{k-1} + K_k[Z_k - h(x_{k-1}, 0)] \tag{28.17}$$

The remaining fraction frequency offset can be estimated described in [3].

$$\varepsilon_f = \frac{1}{\pi} angle\left(\sum_{m=1}^{Ng} r(\hat{d} - m) r^*(\hat{d} + N - m)\right) \tag{28.18}$$

The range of estimation is less than half of the subcarrier spacing, $\varepsilon_f < 0.5$.

28.4 Computer Simulation

The parameters are based on IEEE 802.15.3c standard, with length of a frame is 512, QPSK modulation, channel band width 2.16 GHz, subcarrier spacing 5.15625 MHz. The surface of Gunn VCO is 510 * 400 μm with thickness of 150 μm. The heat power is 2.0 W when working voltage is 3.6 V. And the crystal thermal conductivity parameter is 230 W/m °C.

Figure 28.3 simulated the correlation function of Chu sequence in length of 64. The capture range is the length of the chu sequence, L_{chu}. If the frequency offset is out of capture range, the output of estimated frequency offset is L_{chu}. So although

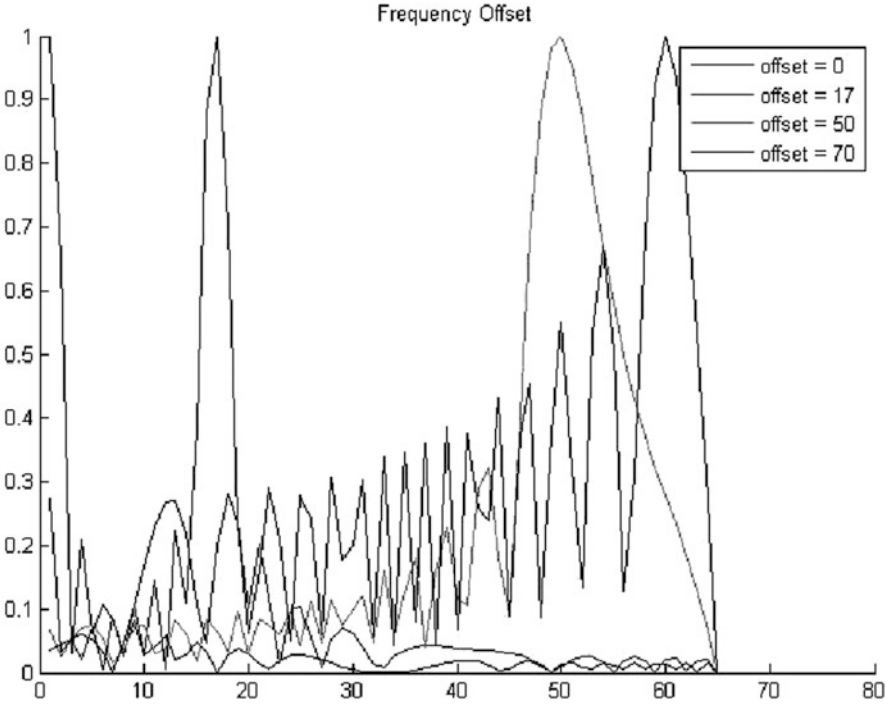

Fig. 28.3 Normalized correlation function of Chu sequence

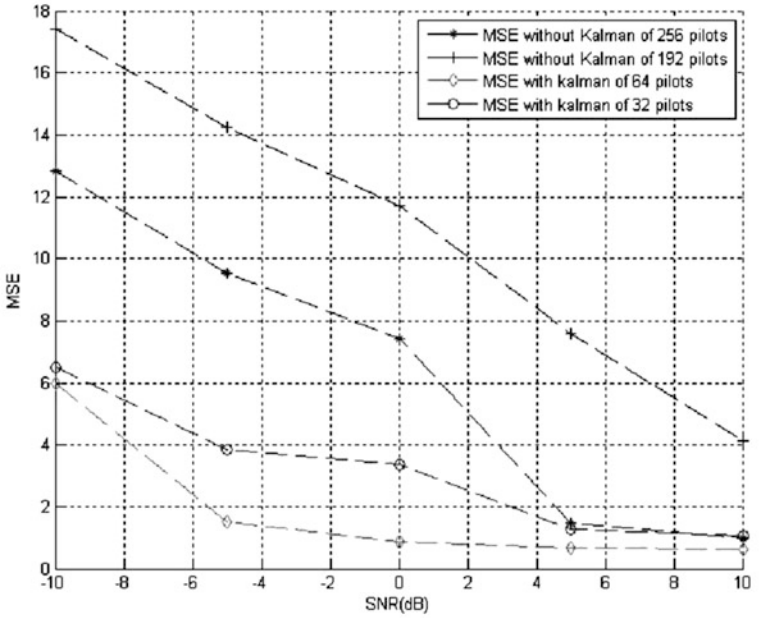

Fig. 28.4 MSE comparison with different SNR in certain

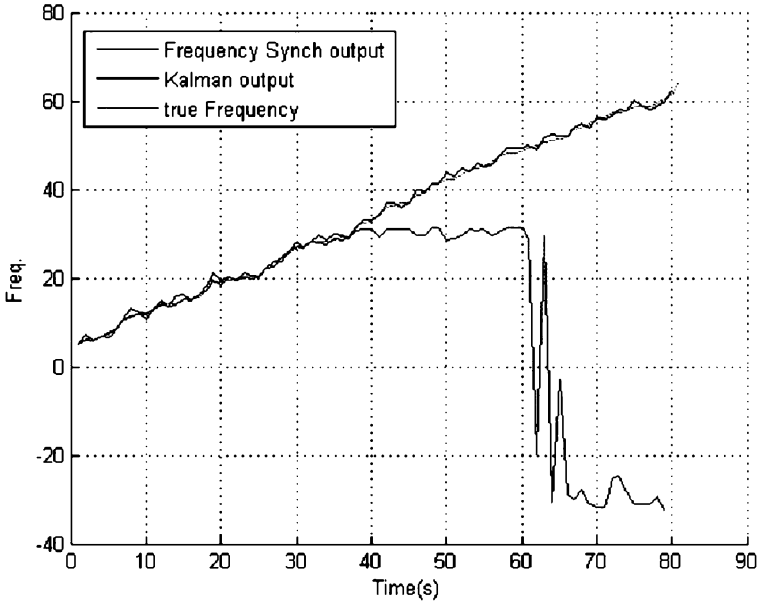

Fig. 28.5 Algorithm stability and robustness comparison in frequency drift

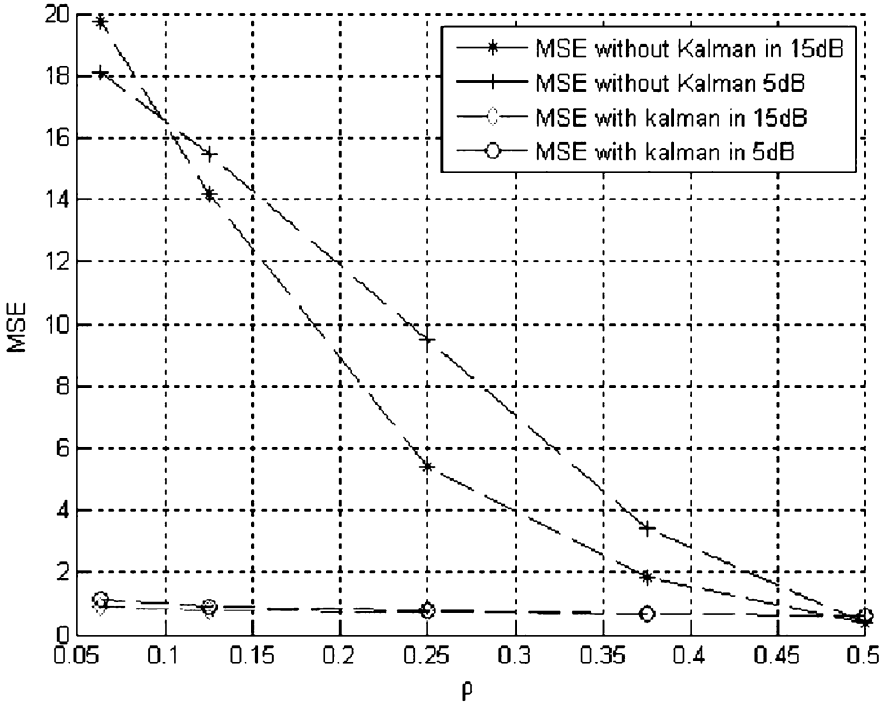

Fig. 28.6 MSE comparison between Chu sequence Syn. Algorithm and new algorithm with Kalman in different duty ratio

Chu sequence can precisely sync frequency, the synchronization range is limited that $f_{max}<L_{chu}$.

Figure 28.4 compares synchronization MSE of traditional Chu sequence algorithm and the new algorithm in different SNR. Even the length is only 1/4 or 1/8 of the original algorithm, the synchronization MSE is smaller.

Figure 28.5 is the frequency tracking pattern of the Chu sequence and the algorithms proposed in this article in time domain. If the value of frequency offset exceeds the threshold which is length of the pilots, the original algorithm cannot achieve frequency synchronization resulting in frequency distortion. But the new proposed algorithm can track the frequency drift very well. The simulation demonstrates better robustness of new algorithm.

Figure 28.6 depicts frequency offset synchronization performance in different duty ratio ρ. It is shown that even using 1/8 length of origin algorithm, the new algorithm can achieve same or even better frequency estimation performance.

28.5 Conclusions

For 60 GHz OFDM mm-wave radio system, this article proposes a new frequency synchronization method that establishes a dynamic frequency variation system on the base of Chu as training sequence. The new algorithm bases on Kalman filter theory utilizing time transfer characteristic to against 60 GHz frequency variation. The computer simulation and analyze prove the effectiveness of the new algorithm. It significantly reduce length of training sequence and achieve the same or better frequency estimation with less pilots, and promote the transfer efficiency at the same time. In all, the algorithm proposed in this article provides a very competitive solution for 60 GHz mm-Wave radio communication, especially easy for system design and implementation.

Acknowledgements This work was supported by National Natural Science Foundation of China (60972079, 60902046) and the BUPT excellent Ph.D. students foundations (CX201122).

References

1. (2009) IEEE Standards 802.15.3c – Part 15.3: wireless medium access control (MAC) and physical layer (PHY) specifications for high rate wireless personal area networks (WPANs) Amendment 2: millimeter-wave-based alternative physical layer extension. IEEE Computer Society, New York
2. (2010) IEEE P802.11ad/D0.1 – Part 11: wireless lan medium access control (MAC) and physical layer (PHY) specifications -Amendment 6: enhancements for very high throughput in the 60GHz band. IEEE 802.11 Committee of the IEEE Computer Society, New York
3. Van de Beek JJ, Sandell M, Borjesson PO (1997) ML estimation of time and frequency offset in OFDM system[J]. Signal Process 45(7):1800–1805
4. Schmidl TM, Cox DC (1997) Robust frequency and timing synchronization for OFDM[J]. Communications 45(12):1613–1621
5. Wei C, Rui-juan Y (2009) A joint time and frequency synchronization method based on PN sequences for OFDM[A]. Computer science and information technology. In: 2nd IEEE international conference[C]. ICCSIT, Beijing, pp 112–116
6. Geetha C (2010) Combined PAPR reduction and frequency offset estimation using precoded Zadoff-Chu OFDM in WLAN system[C]. In: 2010 3rd IEEE ICCSIT, Chengdu, China, vol 3, pp 461–465
7. Wang J, Lan Z, Pyo C et al (2009) Beamforming codebook design and performance evaluation for millimeter-wave WPAN[C]. In: Proceedings of the IEEE vehicular technology conference (VTC 2009 Fall), Anchorage, USA, 20–23 Sept 2009, pp 1–6
8. Fukasawa Y (2007) 76-GHz planar Gunn VCO with low oscillation frequency drift of 1.5MHz/[C]. In: Asia-Pacific microwave conference, Bangkok Thailand, pp 1–4
9. Meng-meng L (2011) A joint timing and frequency synchronization algorithm for OFDM system based on training sequence[J]. J Yanshan Univ 3:257–261

Chapter 29
An Efficient Hybrid Beamforming for Uplink Transmissions of 60GHz Millimeter-Wave Communications

Chenglin Zhao, Wei Zhang, Bin Li, Yun Liu, and Zhou Li

Abstract In this investigation, a promising hybrid beamforming technology for the uplink transmissions of the emerging 60 GHz millimeter-wave system is proposed, in order to effectively compromise the performance and implementation complexity. The beam switching based on the predefined beam codebook, is applied at the transmitter; while a step-wise refinement-based beam switching technology and further improved recursive least squares algorithm are used at the access point receiver. The simulation further validates the effectiveness of this presented hybrid beam forming algorithm, and the results show that our new scheme can significantly enhance the SINR performance of the received signal in access point.

Keywords 60GHz millimeter-wave • Hybrid beamforming • Uplink communication • Improved recursive least squares (RLS)

29.1 Introduction

With the continuous improvement of high-quality data transmission, the demands on wireless communications transmission rate and signal bandwidth keep growing. For the reason of the availability of abundant spectrum resources and the potential

C. Zhao (✉)
School of Information and Communication Engineering, Beijing University of Posts and Telecommunications, Beijing 100876, China
e-mail: clzhao@bupt.edu.cn

W. Zhang • B. Li
Beijing University of Posts and Telecommunications, Beijing, China
e-mail: avyle@163.com; stone_123456@126.com

Y. Liu • Z. Li
China Academy of Telecommunications Research, Ministry of Industry and Information Technology Telecommunication Metrology Center, Beijing, China
e-mail: liuyun@catr.cn; lizhou@catr.cn

Q. Liang et al. (eds.), *Communications, Signal Processing, and Systems*, Lecture Notes in Electrical Engineering 202, DOI 10.1007/978-1-4614-5803-6_29,

providing high-speed data rate, the 60 GHz millimeter-wave communications recently gained more and more attention for the development of short-range high-speed wireless networks [1]. The transmission path loss of 60 GHz millimeter-wave is very serious in practice [2], which may also facilitate short range security communication. Another primary advantage is beamforming, which can be easily implemented on tiny portable devices for millimeters wavelength and commonly adopted to improve the link communication qualification. For example, the lower complicated beam switching based on the fixed codebook has been adopted in IEEE 802.15.3c criteria [3] and IEEE 802.15.ad criteria [4]. However, it is relatively difficult to acquire the best transmission performance when multi-links are communicating, as the high side-lobe gain may introduce noticeable interference. In this paper, we propose an efficient hybrid beamforming in order to compromise between performance and complexity, which can be properly used to convey high rate information over relatively short distances in 60 GHz high data rate systems.

The rest of this paper is organized as follows. In Sect. 29.2, background information related to system model is provided. In Sect. 29.3, hybrid BF technical proposals are explained in detail. Simulation results are given in Sect. 29.4. The Conclusions are drawn in Sect. 29.5.

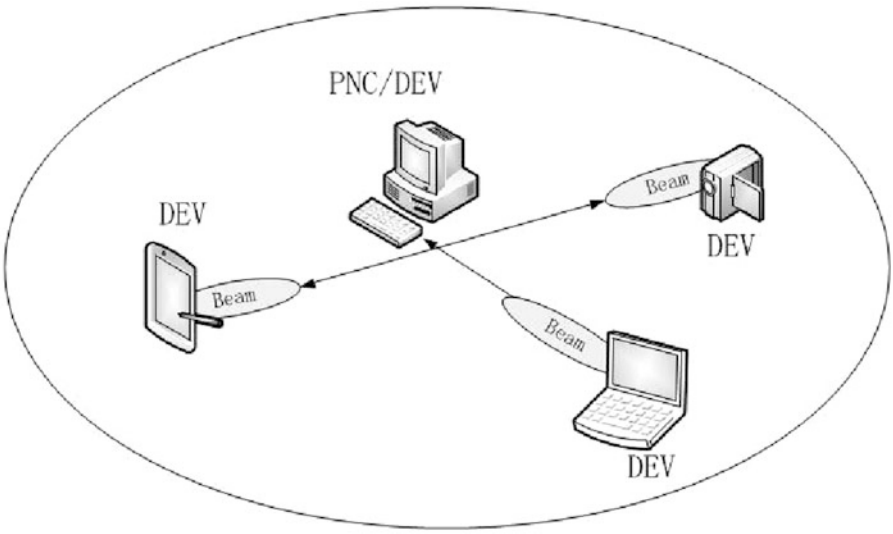

Fig. 29.1 An example of WPAN piconet architecture

29.2 Related Work

29.2.1 Network Topology

The basic network topology in a wireless personal area network (WPAN) is commonly known as a piconet [5] shown in Fig. 29.1. Such a piconet consists of several independent DEVs(Device), one of which is selected as the PNC (Piconet Coordinator) to schedule peer-to-peer communications, provide the basic timing and manage the shared wireless resource. As the PNC or AP (access point) is almost selected near the center in case of block, the accumulated interference in PNC or AP is serious when one DEV is requesting to the PNC and the else DEVs are communicating with others at the same time. This work focuses on how to reduce this interference in uplink communication from DEV to PNC, by presenting a promising hybrid beamforming technology.

29.2.2 Path Loss Model

Depending on typical application scenarios in 60 GHz wireless communications, the common indoor radio propagation path loss model [6, 7] is used as the path loss, which is expressed as follows.

$$\mathrm{PL} = L(d) + \sum_{q=0}^{Q} FAF(q) + \sum_{p=0}^{P} WAF(p) \tag{29.1}$$

where $L(d)$ is the average path loss and d is a transmission path. $FAF(q)$ is the average floor attenuation factor and q is the number of the floors. $WAF(p)$ is the average wall attenuation factor and p is the number of walls.

29.2.3 Beamforming

With the purpose of effectively improving transmission quality and enhancing the system capacity, the beamforming technology is widely used in 60 GHz millimeter-wave communications [3], with a system diagram shown in Fig. 29.2. The number of antennas is M in the transmitter and it is N in the receiver. The transmitted signal from device is multiplied by sending weight vector $w = [w_1, w_2, , w_M]^T$ and then launched into the RF channel; accordingly, the received signal is multiplied by receiving weight vector $c = [c_1, c_2, , c_N]^T$ and then sent to the subsequent signal processing module.

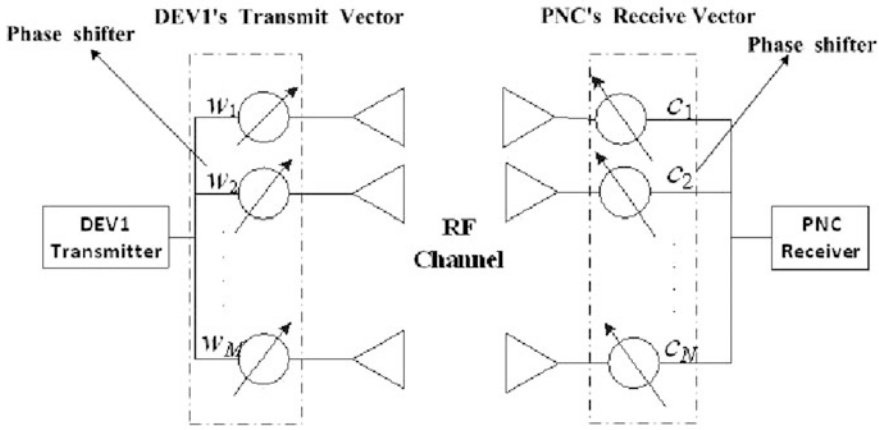

Fig. 29.2 BF system model

29.2.4 Beam Codebook

In IEEE 802.15.3c criteria, a code-book, serving as a prescribed pool of weight vectors, is an $M \times K$ matrix where each column specifies a pattern or direction [3]. The matrix element w_m, k can be expressed as follow:

$$w_m, k = j^{fix\left\{\frac{m \times mod[k + (K/2), K]}{K/4}\right\}} \tag{29.2}$$

where M and K are respectively the total number of antennas elements and beam. m is current antenna number and k is the current beam number. We set K = 2M, in practice, to reduce the gain loss [7]. In order to minimize the power consumption and simplify the phase shifter, the codebooks are designed for a phased antenna array only with 90 ° phase resolution and without amplitude adjustment.

29.3 Hybrid Beamforming

In this section, by taking into account that the interference [8] from multi-links among PNC and several DEVs will seriously degrade the transmission performance in 60 GHz WPAN uplink communication, a promising hybrid beamforming technique is proposed to compromise between performance and complexity. The beam switching, based on a predefined beam codebook, is applied at the transmitter, while the optimum adaptive beam forming is used at the receiver. Meanwhile, an improved hybrid beamforming algorithm is suggested, which is to update the receiving weight vector by using beam searching and then provide the identified

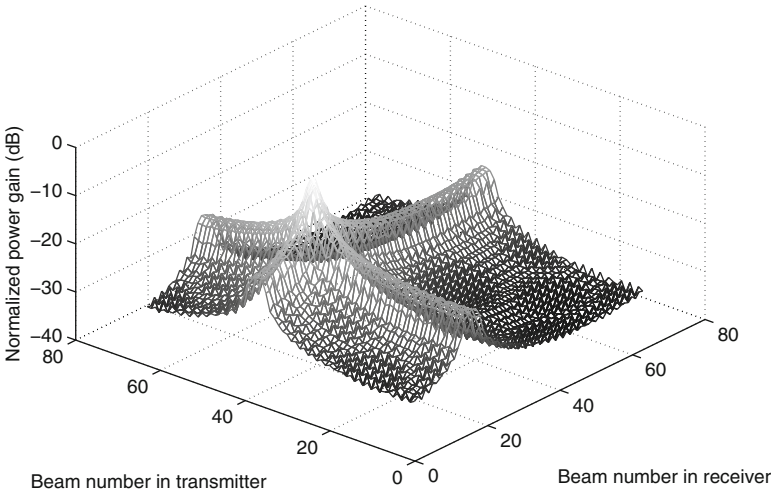

Fig. 29.3 Two-dimensional surface of normalized power gain

initial weight value to the RLS algorithm in order to further increase the iterative performance efficiently. This efficient hybrid beam forming can be used in fast networking WPAN network, which is implemented by two steps, i.e. SWR beam switching based interference estimation and adaptive beamforming.

29.3.1 SWR Beam Switching

Beam switching selects the optimal beam by searching the maximum SNR. To shorten the BF setup time, the beam pattern is divided into three levels [9]: Quasi-omni, Sector and beam. However, with the increase of antenna elements, the complexity of beam searching will also significantly increase. A more efficient beam searching algorithm, step-wise refinement (SWR) [10], is taken. Figure 29.3 shows the two-dimensional surface of normalized power gain where beam number in transmitter and receiver are both 64. The core idea is relying on the dividing and conquering to reduce preamble transmissions and energy consumption. Firstly a wide beam search is used and then the refined beam with higher directional resolution continually is searched, which is making full use of the beam characteristics produced by a different number of array elements, narrowing the search space by gradually increasing the number of antennas, and finally realizing optimum beam searching.

Table 29.1 The description of improved RLS algorithm

Input	Desired signal $\mathbf{d}n$, transmitted signal $\mathbf{u}n$, maximum iteration counter n.
Step 1	Use SWR beam switching to get the optimum weight vector from the codebook $\mathbf{w}_{3c}$
Step 2	Initialize where setting as a small number of normal $\mathbf{w}(0) = \mathbf{w}_{3c}$, $\mathbf{P}(0) = \delta^{-1}\mathbf{I}$
Step 3	Iteration of the loop, where $n = 1, 2, \ldots$ (1) Calculate the estimated error. $\mathbf{e}(i) = \mathbf{d}(i) - \mathbf{w}^H(n)\mathbf{u}(i)$ (2) Calculate the gain vector $\mathbf{k}(n) = \frac{\mathbf{p}(n-1)\mathbf{u}(n)}{\lambda + \mathbf{u}^H(n)\mathbf{p}(n-1)\mathbf{u}(n)}$ (3) Calculate the inverse autocorrelation function of $\mathbf{u}(n)$ $\mathbf{P}(n) = \frac{1}{\lambda}\left[\mathbf{P}(n-1) - \mathbf{k}(n)\mathbf{u}^H(n)\mathbf{P}(n-1)\right]$ (4) Calculate the weight vector.$\mathbf{w}(n) = \mathbf{w}(n-1) + \mathbf{k}(n)\mathbf{e}^H(n)$ (5) Return the value of $\mathbf{w}(n)$ in steady state

29.3.2 RLS Algorithm

As a most important adaptive beamforming technique, the RLS (Recursive Least Squares) algorithm will recursively minimize the cost function that is a weighted linear least squares relating to the input signals [11]. In sharp contrast to the other algorithms, such as the LMS (Least Mean Squares) which aims to reduce the mean square error, the RLS exhibits extremely efficient convergence performance and more favorable stability. In our investigation, the RLS algorithm is exponentially weighted least squares algorithm, taking the sum of exponential weighted squared errors as the cost function.

$$J(n) = \sum_{i=0}^{n} \lambda^{n-i} |\varepsilon(i)|^2 \tag{29.3}$$

where λ $(0 < \lambda < 1)$ is the forgetting factor constant. According to the characteristics of exponential function, the smaller λ is, the smaller contribution to previous samples is and the more sensitive to recent samples the filter is. $\lambda = 1$ means infinite memory and $\lambda = 0$ means completely forgotten. $\varepsilon(i)$ is the posteriori error estimation.

29.3.3 Improved RLS Algorithm

Even though the effectiveness of RLS algorithm, the relatively slow convergence is still adverse to the requirements of fast access and low-power realization in 60 GHz

millimeter-wave devices. In this work, we further design an improved hybrid beamforming algorithm. It firstly uses the SWR beam switching algorithm to get a receiving weight vector, and subsequently provides it as the initial value to the RLS algorithm to increase the iterative performance effectively. As a consequence, this developed fast hybrid beamforming can be used in fast networking WPAN system, and the design is proposed in Table 29.1.

29.4 Simulation Results

In this section, we follow the guidelines of the IEEE 802.15.3c criteria to estimate the performance of the proposed hybrid beamforming technology comprehensively. Assume the simulation indoor scence where length = 10m, width = 10m, and height = 3m. Both the transmitted and received antennas are assumed to be one-dimensional uniform linear array, and the positions of 60 GHz devices are distributed randomly in the room. Taking the first antenna element as the reference and set its coordinate position as the origin. The horizontal direction of antenna array is the x-axis and the vertical direction is the y-axis. Furthermore, set the clockwise direction as the positive angle and counter-clockwise as the negative angle. In our experimental simulation, the number of interference devices N = 10; the antenna elements M = 8 and the beam number K = 16; the transmit power Pt = 10 mW; the average noise power N = 20.4 dBm/Hz; bandwidth B = 1.7 GHz [12].

In order to comprehensively evaluate the performance, the ratio of effective signal to interference and noise (SINR) is selected as the metric to estimate the system performance. Make 100 times simulation respectively and then calculate the statistic average to compare the convergence rate between the RLS algorithm and improved RLS algorithm. Figure 29.4 illustrates the convergence trend of the SINR with the evolution of adaptive iterations of the two hybrid algorithms and 3c criteria. It is

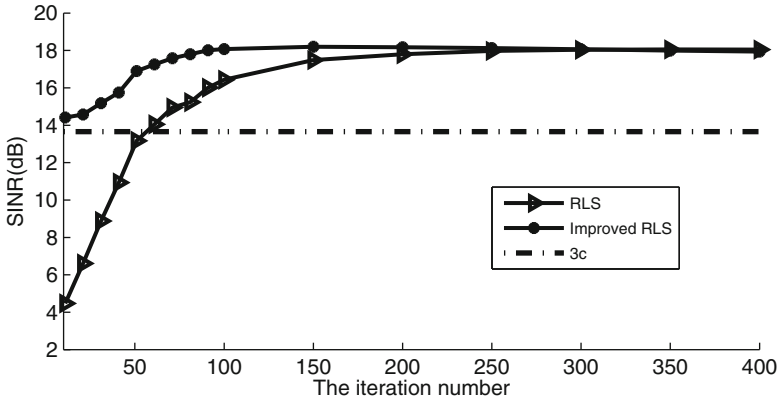

Fig. 29.4 The trend of average SINR

Table 29.2 The mean and CV of SINR

Scheme	Mean dB	CV
IEEE 802.15.3c	13.66	0.9176
RLS(100 times)	16.08	0.7932
RLS(200 times)	17.52	0.6436
RLS(300 times)	18.15	0.6270
Improved RLS(100 times)	18.07	0.6671
Improved RLS(200 times)	18.12	0.6478
Improved RLS(300 times)	18.17	0.6389

clearly seen that the improved RLS algorithm has a faster convergence speed and a lower power consumption, which may remarkably enhance the SINR and improve the performance of 60 GHz uplink communications.

Table 29.2 shows the mean value and the coefficient of variation (CV) of SINR of the IEEE 802.15.3c beam switching and the two proposed hybrid beamforming techniques, respectively in the average and probability distribution. It is observed that the improved RLS algorithm reaches a steady state at near 100 times iterations, while RLS algorithm needs 300 times to approach convergence. From the steady state, we may acquire almost 4.5 dB improvement in mean of SINR between the improved RLS and IEEE 802.15.3c codebook, and simultaneously, the lowest CV value of the hybrid beamforming indicates that the system is relatively robust to realistic applications. Therefore, our suggested hybrid beamforming can significantly enhance the desired signal and also suppress interference signals by optimizing receiving beams, and hence effectively improve the communication anti-jamming ability. This new beamforming scheme, especially the improved RLS algorithm with fast iterative convergence properties, can be properly used in the high-speed 60 GHz millimeter-wave WPANs.

29.5 Conclusions

In this investigation, by fully considering the different requirements between PNC (or access point) and DEV, we propose a promising hybrid beamforming technique for uplink transmissions of the emerging 60 GHz WPANs, which can elegantly compromise the transmission performance and implementation complexity. In the distributed user devices end, the beam switching relying on the predefined beam codebook is applied, while the SWR beam switching technology provides the initial value and adaptive RLS algorithm is further applied at the PNC receiver. The simulation results demonstrate that the new hybrid beamforming can effectively enhance the transmission throughput of 60 GHz uplink and improve the communication anti-jamming performance of 60 GHz WPANs. This new hybrid beamforming, especially the improved RLS algorithm based technique with a fast iterative convergence, can be used in the 60 GHz millimeter-wave WPANs.

Acknowledgements This work was supported by National Natural Science Foundation of China (60972079, 60902046) and the BUPT excellent Ph.D. students foundations (CX201122).

References

1. Yong S-K, Xia P et al (2011) 60GHz technology for Gbps WLAN and WPAN: from theory to practice [M]. Wiley, Hoboken, pp 1–14, 89–115
2. Lin Z, Peng X (2011) Enhanced beamforming for 60GHz OFDM system with co-channel interference mitigation [C]. IEEE international conference on ultra-wideband, ICUWB, Singapore, 14–16 Sept 2011, pp 29–33
3. JPK Gilb(Technical Editor) (2009) IEEE Standards 802.15.3c?–Part 15.3: wireless medium access control (MAC) and physical layer (PHY) specifications for high rate wireless personal area networks (WPANs) Amendment 2: millimeter-wave-based alternative physical layer extension[S]. IEEE Computer Society, New York
4. Cordeiro C (2010) IEEE P802.11ad?/D0.1– Part 11: wireless LAN medium access control (MAC) and physical layer (PHY) specifications -Amendment 6: enhancements for very high throughput in the 60GHz Band[S]. IEEE 802.11 Committee of the IEEE Computer Society, New York
5. Wang J, Lan Z, Pyo C-W et al (2010) A pro-active beam forming protocol for multi-Gbps millimeter-wave WPAN systems. In: Wireless communications and networking conference, WCNC, Sydney, April 2010, pp 1–5
6. TK Sarkar, Ji Z et al (2003) A survey of various propagation models for mobile communication [J]. IEEE Antennas Propag Mag 45(3):51–82
7. Weixia Z, Zhifang C, Bin L et al (2012) N phases based beamforming codebook design scheme for 60 GHz wireless communication[J]. J Beijing Univ Posts Telecommun 35(3):1–5
8. Park M, Gopalakrishnan P (2009) Analysis on spatial reuse and interference in 60-GHz wireless networks[J]. IEEE J Sel Areas Commun 27(8):1443–1452
9. Wang J, Lan Z et al (2009) Beam codebook based beamforming protocol for multi-Gbps millimeter-wave WPAN systems[C]. In: Global telecommunications conference, GLBECOM, Japan, 30 Nov 2009–4 Dec 2009, pp 1–6
10. Wei-xia Z, Guang-long D, Bin L (2012) A novel beam search algorithm for 60GHz millimeter wave communication[J]. J Electron Inf Technol 34(3):682–688
11. Godara LC (1997) Application of antenna arrays to mobile communications. II. Beam-forming and direction-of-arrival considerations [J]. Proc IEEE 85(8):1195–1245
12. Yoon S, Jeon T, Lee W (2009) Hybrid beam-forming and beam-switching for OFDM based wireless personal area networks [J]. IEEE J Sel Areas Commun 27(8):1425–1423

Chapter 30
A Novel Phase Noise Compensation Scheme for 60GHz OFDM System Based on Quantum Genetic Algorithm

Jianfei Zhao, Chenglin Zhao, Bin Li, and Zheng Zhou

Abstract This paper proposes a new phase noise compensation scheme for 60 GHz OFDM system employing optimal blind data detection based on quantum genetic algorithm to alleviate performance degradation due to the phase noise. High data-rate OFDM system in 60-GHz millimeter-wave band have been extensively studied, but the relatively large phase noise in the phase locked loop (PLL) synthesizer severely degrades transmission performance. This proposed scheme employ an optimal (maximum a posteriori) data estimator, utilizing prior statistical knowledge of PHN. In addition, quantum genetic algorithm is used to further reduce the computational complexity. Simulation results under 802.15.3C system show that the proposed scheme mitigates the degradation due to PHN effectively over both AWGN channel and frequency selective fading channel.

Keywords Phase noise compensation • 60 GHz

30.1 Introduction

Wireless personal area network (WPAN) systems in the millimeter-wave band, especially the unlicensed spectrum at the 60 GHz carrier frequency, have been extensively studied in recent years [1]. The 60-GHz WPAN (wireless personal area network) standardization in IEEE 802.15.3C features both orthogonal frequency division multiplexing (OFDM) and single-carrier transmission with frequency

J. Zhao (✉) • B. Li • Z. Zhou
Beijing University of Posts and Telecommunications, Beijing, China
e-mail: congyum1989@126.com

C. Zhao
School of Information and Communication Engineering, Beijing University of Posts and Telecommunications Beijing 100876, China
e-mail: clzhao@bupt.edu.cn

Q. Liang et al. (eds.), *Communications, Signal Processing, and Systems*, Lecture Notes in Electrical Engineering 202, DOI 10.1007/978-1-4614-5803-6_30,

domain equalization (SC-FDE) as its PHY layer modulation scheme. OFDM is robust to multipath propagation, and offers significantly high spectral efficiency. But it's highly sensitive to the phase noise [2]. This is because the phase noise causes signal distortion in OFDM, which can be divided into common phase error (CPE), and inter-carrier interference (ICI). Such a phase noise degrades transmission performance of the higher bit-rate OFDM in the 60-GHz WPAN system. Moreover, due to millimeter-wave hardware limitations, the relatively large phase noise from the phase locked loop (PLL) synthesizer occurs. Therefore, a compensation method for the larger phase noise is necessary because it is much more difficult to make the PLL synthesizer with the sufficiently low-level phase noise.

The CPE compensation method estimates CPE by using pilot subcarriers inserted in OFDM symbol. However, the phase noise suppression compensates only CPE, and it still suffers from ICI due to the time-varying phase noise in the symbol duration [3].

In order to provide an reliable solution to the phase noise problem in the 60-GHz WPAN system, this paper proposes a phase noise compensation scheme [4] based on Quantum Genetic Algorithm by exploiting the prior distribution of phase noise in PLL synthesizer. The rest of this paper is organized as follows. Section 30.2 describes the system model of an OFDM system [5] with phase noise, the model of phase noise [6], as well as the Quantum Genetic Algorithm. Section 30.3 introduce the QGA and describes the proposed phase noise Compensation Scheme. Section 30.4 presents the computer simulation results in terms of packet error rate performance of the proposed receiver. Finally, some concluding remarks are given in Sect. 30.5.

30.2 System Model

30.2.1 60 GHz OFDM System Description

A block diagram of the OFDM system with phase noise is illustrated in Fig. 30.1. Let us begin by considering a simplified baseband OFDM system with symbol length N [7].

At the transmitter, the bits from information sources are mapped into constellation symbols, and then modulated to subcarriers using the IFFT algorithm and then converted to OFDM symbols, i.e.

$$X[n] = \frac{1}{\sqrt{N}} \sum_{k=0}^{N-1} x[k] e^{j\frac{2\pi nk}{N}}, \quad n = 0, 1, \ldots, N-1 \tag{30.1}$$

In order to eliminate the inter-symbol interference due to multipath propagation, a cyclic prefix is added to the IFFT component output. Then the result are converted

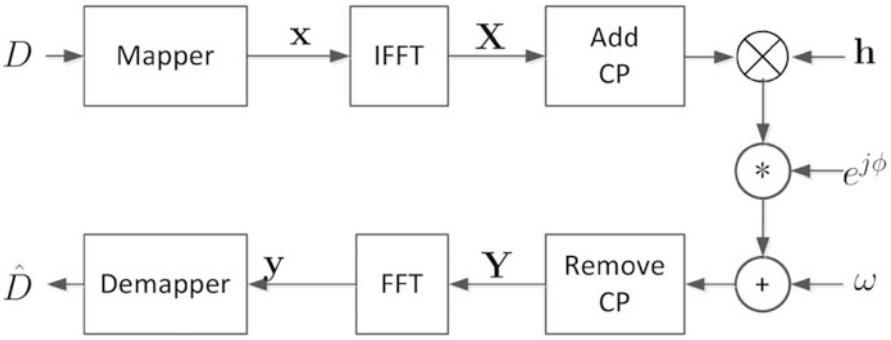

Fig. 30.1 OFDM baseband model with phase noise

into a baseband signal. Let be the impulse response function of the equivalent baseband channel, and be the phase noise caused by PLL synthesizer, the received signal is given by follow equation after the cyclic prefix removed:

$$\begin{aligned} Y[n] &= e^{j\phi[n]}(X[n] \otimes h[n]) + \omega[n] \\ &= e^{j\phi[n]} \sum_{k=0}^{N-1} X[r]h[(n-k)_N] + \omega[n] \end{aligned} \tag{30.2}$$

where $\omega = [\,\omega[0], \omega[1] \ldots \omega[N-1]\,]$ is additive white Gaussian noise.

At the demodulator, a FFT component is employed to recover data on subcarriers. Let

$$\alpha[n] = \frac{1}{N} \sum_{k=0}^{N-1} e^{j\phi[k]} e^{-j\frac{2\pi kn}{N}}, \quad n = 0, 1, \ldots, N-1 \tag{30.3}$$

and

$$H[n] = \frac{1}{N} \sum_{k=0}^{N-1} h[k] e^{-j\frac{2\pi kn}{N}}, \quad n = 0, 1, \ldots, N-1 \tag{30.4}$$

$$\Omega[n] = \frac{1}{N} \sum_{k=0}^{N-1} \omega[k] e^{-j\frac{2\pi kn}{N}}, \quad n = 0, 1, \ldots, N-1 \tag{30.5}$$

then the constellation data on n-th subcarrier can be given by:

$$y[n] = \sum_{r=0}^{N-1} Y[r] e^{-j\frac{2\pi nr}{N}} = \alpha[n] \otimes (H[n]x[n]) + \Omega[n] \tag{30.6}$$

30.2.2 Phase Noise Model

In this paper, we assume the phase noise to be a zero-mean, colored Gaussian process that is wide-sense stationary and has finite power. It varies from symbol to symbol. Then the phase noise samples in one OFDM symbol have a multivariate Gaussian prior distribution: $\phi \sim \mathcal{N}(0, \Phi)$, where Φ is the covariance matrix of phase noise samples.

Power spectrum density (PSD) of the phase noise can be expressed as:

$$PSD(f)_{\mathrm{PHN}} = PSD(0)\frac{1 + (f/f_z)^2}{1 + (f/f_p)^2} \tag{30.7}$$

where $PSD(0)$ is the phase noise level that the loop filter determines in the low frequency, f_z and f_p are the zero and pole frequencies, respectively. According to the definition in IEEE 802.15.3c, $PSD(0) = -90$ dBc/Hz, $f_z = 100$ { MHz}, $f_p = 1$ {MHz}. The autocorrelation function of phase noise $R_\phi(\tau) = \mathbf{E}[\phi(t)\phi(t+\tau)]$ can be obtained from the inverse Fourier transform of PSD.

30.2.3 Quantum Genetic Algorithm

Quantum genetic algorithm (QGA) is a combination of genetic algorithm and quantum computing. The key steps of quantum genetic algorithm include: chromosome coding and decoding, population measurement, population regeneration etc.

The basic component element of chromosome in quantum genetic algorithm is the qubit (short for quantum bit). A qubit is the quantum analogue of the classical bit and it can be represented by a unit vector of a two dimensional Hilbert space ($\alpha, \beta \in \mathbb{R}$) :

$$|\Psi\rangle = \alpha|0\rangle + \beta|1\rangle \tag{30.8}$$

where α and β are probability amplitudes. This is known as quantum parallelism. When we measure this qubit, the probability of outcome $|1\rangle$ is β^2 and the probability of outcome $|0\rangle$ is α^2. Because the absolute squares of the amplitudes equate to probabilities, it follows that and must be constrained by the equation: $|\alpha|^2 + |\beta|^2 = 1$. A chromosome q consisting of N qubits, can be shown as follows:

$$q = \left[\begin{array}{c|c|c|c} \alpha_1 & \alpha_2 & \ldots & \alpha_N \\ \beta_1 & \beta_2 & \ldots & \beta_N \end{array}\right] \tag{30.9}$$

Table 30.1 Angle of rotation

x_i	b_i	$f(x) > f(b)$	$\Delta\theta_i$	$\alpha_i\beta_i > 0$	$\alpha_i\beta_i < 0$	$\alpha_i = 0$	$\beta_i = 0$
0	0	*	0	*	*	*	*
1	1	*	0	*	*	*	*
0	1	×	$\Delta\theta$	+ 1	− 1	0	± 1
0	1	√	$\Delta\theta$	− 1	+ 1	± 1	0
1	0	×	$\Delta\theta$	− 1	+ 1	± 1	0
1	0	√	$\Delta\theta$	+ 1	− 1	0	± 1

where $|\alpha_j|^2 + |\beta_j|^2 = 1$, $j = 1, 2, \ldots, N$. After quantum coding, the chromosome population in QGA can be represented as:

$$Q^g = \{q_1^g, q_2^g, \ldots, q_L^g\} \tag{30.10}$$

where g is evolution time and P is population size, $q_j{}^g$ represent the j-th chromosome in the g-th chromosome population.

The measurement collapse each qubit into one of the two pure states, $|0\rangle$ or $|1\rangle$. Performing measurements on the whole population of Q^g result in a group of classical binary string $P^g = \{ p_1{}^g, p_2{}^g, \ldots, p_L{}^g\}$. Each binary string $p_j{}^g$ consist of L classic information bits.

Updating of population can be realized by employing quantum rotation gate in QGA:

$$\begin{bmatrix} \alpha\prime \\ \beta\prime \end{bmatrix} = \begin{bmatrix} cos\theta & -sin\theta \\ sin\theta & cos\theta \end{bmatrix} \begin{bmatrix} \alpha \\ \beta \end{bmatrix} \tag{30.11}$$

where $\begin{bmatrix} \alpha \\ \beta \end{bmatrix}$ is one of the qubit in chromosome, and $\begin{bmatrix} \alpha' \\ \beta' \end{bmatrix}$ represent the qubit after updated, θ is rotation angle of quantum rotation gate.

The rotation angle θ can be determined through the expression $\theta = s * \Delta\theta$, where s is the direction of rotation, and $\Delta\theta$ is the angular size. As shown in Table 30.1.

The adjustment strategy we use in this paper is as follows: suppose the qubit to be adjusted in current individual is x and the corresponding qubit in optimum solution is b, the fitness value of currently measured individual $f(x)$ will be compared with the optimal fitness value in population $f(b)$. If $f(x) < f(b)$, then adjust the corresponding qubit of the individual to make $\begin{bmatrix} \alpha \\ \beta \end{bmatrix}$ change toward the direction conducive to the emergence of b, and vice versa. The angular size $\Delta\theta$ must be chosen carefully. If $\Delta\theta$ is too big, the algorithm will be easily trapped into local minima and premature convergence. On the contrary, the speed of the algorithm is very slow, even at a standstill.

The working flow of Quantum Genetic Algorithm are as follows:

1. Initial population $Q^g = \{q_1^g, q_2^g, \ldots, q_L^g\}, g = 0$.
2. Measure each chromosome in population G^0, to get a group of state P^0 .
3. Employ fitness evaluation on P^0, then save the optimal solution to B^0.

4. Judge whether the termination condition is satisfied, if yes, terminate the algorithm.
5. Let $g = g + 1$.
6. Measure each chromosome in population Q^{g-1}, to get a group of state P^g
7. Employ fitness evaluation on P^g
8. Update the population with quantum rotation gate, get a new population Q^g.
9. Save the optimal solution in P^g and B^{g-1} to B^g, then turn to 4.

30.3 PHN Compensation Scheme Proposed

Assuming perfect timing synchronization, and the value of phase noise far less than 1, the complex baseband received signal sampled can be written in time domain as:

$$\begin{aligned} Y[n] &= e^{j\phi[n]}(X[n] \otimes h[n]) + \omega[n] \\ &\approx (1 + j\,\phi[n])(X[n] \otimes h[n]) + \omega[n] \end{aligned} \tag{30.12}$$

where $h[n]$ is the impulse response function of the equivalent baseband channel,

Using matrix notation, expression above can be represented as:

$$\mathbf{Y} = (1 + j\,diag(\phi))\mathbf{C}\mathscr{F}\mathbf{x} + \omega \tag{30.13}$$

where

$$\mathbf{C} = \begin{bmatrix} h[0] & h[N-1] & \dots & h[1] \\ h[1] & h[0] & \dots & h[2] \\ \vdots & \vdots & \ddots & \vdots \\ h[N-1] & h[N-2] & \dots & h[0] \end{bmatrix} \tag{30.14}$$

and

$$\mathscr{F} = \begin{bmatrix} 1 & 1 & \dots & 1 \\ 1 & e^{-j\frac{2\pi}{N}} & \dots & e^{-j\frac{2\pi(N-1)}{N}N} \\ \vdots & \vdots & \ddots & \vdots \\ 1 & e^{-j\frac{2\pi(N-1)}{N}N} & \dots & e^{-j\frac{2\pi(N-1)^2}{N}N} \end{bmatrix} \tag{30.15}$$

On account of the fact that both phase noise samples $\boldsymbol{\phi}$ and additive noise $\boldsymbol{\omega}$ subject to multivariate normal distribution, the prior distribution can all be expressed in terms of Gaussian random vectors:

$$\begin{aligned} p(\phi) &= \mathcal{N}(\mathbf{0},\, \Phi) \\ p(\mathbf{Y}\,|\mathbf{x}\,, \phi) &= \mathcal{N}(\mathbf{C}\mathscr{F}\mathbf{x} + j\,diag(\phi)\,\mathbf{C}\mathscr{F}\mathbf{x},\, \sigma^2\mathbf{I}) \end{aligned} \tag{30.16}$$

where σ^2 is the power of additive white Gaussian noise $\boldsymbol{\omega}$.

We can now obtain posterior distribution of $\mathbf{x}$ through the following process: Since $p(\phi)$ and $p(\mathbf{Y} \mid \mathbf{x}, \phi)$ are Gaussian distributed, it can be inferred that the distribution of $p(\mathbf{Y} \mid \mathbf{x})$ is also Gaussian. Suppose the mean of $\mathbf{Y} \mid \mathbf{x}$ to be $\varepsilon(\mathbf{Y} \mid \mathbf{x})$ and the variance to be $\nu(\mathbf{Y} \mid \mathbf{x})$, then we have:

$$\begin{aligned} \epsilon(\mathbf{Y}|\mathbf{x}) &= \varepsilon_{\phi}[\varepsilon_{\mathbf{Y}}(\mathbf{Y}|\mathbf{x}, \phi)] \\ &= \varepsilon_{\phi}[\mathbf{C}\mathscr{F}\mathbf{x} + j\, diag(\phi)\, \mathbf{C}\mathscr{F}\mathbf{x}] \\ &= \mathbf{C}\mathscr{F}\mathbf{x} \end{aligned} \tag{30.17}$$

$$\begin{aligned} v(\mathbf{Y}|\mathbf{x}) &= v_{\phi}[\varepsilon_{\mathbf{Y}}(\mathbf{Y}|\mathbf{x}, \phi)] + \varepsilon_{\phi}[v_{\mathbf{Y}}(\mathbf{Y}|\mathbf{x}, \phi)] \\ &= diag(\mathbf{C}\mathscr{F}\mathbf{x})\, \Phi\, diag(\mathbf{C}\mathscr{F}\mathbf{x})^{H} + \sigma^2\mathbf{I} \end{aligned} \tag{30.18}$$

The optimal posterior estimate of $\mathbf{x}$ is

$$\hat{\mathbf{x}} = arg\ max_{\mathbf{x}}\ p(\mathbf{x}|\mathbf{Y}) \tag{30.19}$$

Allow for the fact that $\mathbf{x}$ follows uniform prior distribution,

$$\begin{aligned} p(\mathbf{x}|\mathbf{Y}) &\propto p(\mathbf{Y}|\mathbf{x})\, p(\mathbf{x}) \\ &\propto ln\, p(\mathbf{Y}|\mathbf{x}) \\ &= ln\, \mathcal{N}[\mathbf{C}\mathscr{F}\mathbf{x}, diag(\mathbf{C}\mathscr{F}\mathbf{x})\, \Phi diag(\mathbf{C}\mathscr{F}\mathbf{x})^{H} + \sigma^2\mathbf{I}] \end{aligned} \tag{30.20}$$

Then the optimal posterior estimate of $\mathbf{x}$ is the one which maximizes the log Clikelihood function shown in above expression. But, testing each symbol hypothesis to find the optimal estimate of $\mathbf{x}$ is complex. So, instead of searching the entire signal space, we employ QGA to estimate $\mathbf{x}$ signal. Each state p_j^g, obtained after measuring the quantum chromosome, represent an estimation of $\mathbf{x}$. By using the logarithm likelihood probability $ln\, p(\mathbf{Y} \mid \mathbf{x})$ as the fitness function, we can finally get an estimation of $\mathbf{x}$ maximum posterior probability $p(\mathbf{x} \mid \mathbf{Y})$.

30.4 Performance Evaluation and Simulation Result

To verify the effectiveness of the proposed PHN cancellation schemes, we present a set of simulations as follows. The parameters of the simulation of 60 GHz OFDM system is depicted in Table 30.2.

As illustrated in Fig. 30.2, we demonstrate the performance of the proposed QGA scheme compared to the conventional scheme. The dotted line indicates the bit-error-rate (BER) of a OFDM receiver free of PHN (the ideal scenario), and the solid line indicates the BER of an OFDM receiver with PHN but without a PHN compensation (the worst case scenario). In between these two curves are the BER

Table 30.2 Parameters of simulation

Parameter	value
Channel model	LOS(AWGN)
Number of subcarriers	512
Subcarrier modulater	64-QAM
Phase noise model	Colored Gaussian noise
Synchronization	Ideal
Channel estimation	Ideal

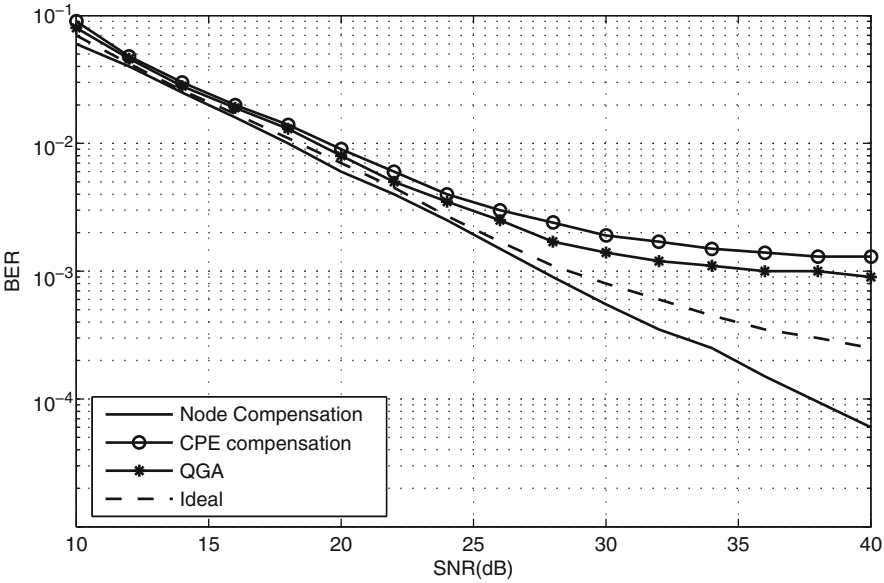

Fig. 30.2 BER performance

performance of receivers implementing the conventional PHN cancellation scheme (triangles) and the proposed PHN compensation schemes (crosses and circles). It is obvious that the scheme we propose perform much better than the conventional one.

30.5 Conclusions

In this paper, we studied the blind cancellation of phase noise distortions at the OFDM receiver frontend. Instead of devising an optimal detection scheme for the phase noise, we focused on the optimal of the clean data sequence x. We derived the posterior distribution $p(\mathbf{x}|\mathbf{Y})$ and simplify the phase noise compensation problem into a search problem in high-dimensional signal space. Finally, a practical search scheme – Quantum Genetic Algorithm is employed to further reduced the complexity.

Acknowledgements This work was supported by National Natural Science Foundation of China (60972079, 60902046) and the BUPT excellent Ph.D. students foundations (CX201122).

References

1. Lily Yang, L (2009) 60GHz: opportunity for Gigabit WPAN and WLAN convergence [J]. ACM SIGCOMM Comput Commun Rev 39(1):56–61
2. Pollet T, Bladel MV, Moeneclaey M (1995) BER sensitivity of OFDM systems to carrier frequency offset and Wiener phase noise[J]. IEEE Trans Commun 43(2):191–193
3. Nikitopoulos K, Polydoros A (2001) Compensation schemes for phase noise and residual frequency offset in OFDM systems[C]. In: IEEE global telecommunication conference, GLOBECOM, San Antonio, vol 1, pp 330–333
4. Shentu J, Panta K, Armstrong J (2003) Effects of phase noise on performance of OFDM systems using an ICI cancellation scheme [J]. IEEE Trans Broadcast 49(2):221–224.
5. Casas RA, Biracree SL, Youtz AE (2002) Time domain phase noise correction for OFDM signals[J]. IEEE Trans Broadcast 48(3):230–236
6. Wu S, Bar-Ness Y (2003) OFDM channel estimation in the presence of frequency offset and phase noise[C]. In: IEEE international conference on communications (ICC), Anchorage, vol 5, pp 3366–3370
7. Suyama S, Suzuki H, Fukawa K, Izumi J (2009) Iterative receiver employing phase noise compensation and channel estimation for millimeter-wave OFDM systems[J]. IEEE J Sel Areas Commun 27(8):1358–1366

Chapter 31
Physical Layer Network Coding Based Two-Way Relay for 60 GHz Millimeter-Wave Wireless Personal Area Networks

Hankun Zhu, Xiao Peng, Xuebin Sun, and Zheng Zhou

Abstract In this chapter, we investigated a promising physical layer network coding-based two-way relay technique for the emerging 60 GHz millimeter-wave wireless personal area networks (WPANs), in order to address the problem of throughput reduction in relay nodes caused by the blockage of links. Because of the small wavelength at 60 GHz frequency band, links may be seriously blocked by the involved obstacles such as furniture and humans. The key idea of the most common solution to handle blockage proposed by now is to substitute the two line-of-sight (LOS) links for the blocked link. However, this method reduces the throughput of the network by a factor of two, which may hence fail to provide the required QoS guarantees to realistic WPAN applications. Our suggested new approach introduces a two-way relay scheme using physical layer network coding to the 60 GHz millimeter-wave WPANs, which can accomplish information exchange within two time slots instead of four. Simulation results, such as bit error rate and throughput, demonstrate the effectiveness of the proposed two-way relay scheme in 60 GHz WPANs.

Keywords 60 GHz WPAN • Physical layer network coding • Two way relay

H. Zhu (✉) • X. Sun • Z. Zhou
Key Laboratory of Universal Wireless Communication, Ministry of Education, Beijing University of Posts and Telecommunications, Beijing 100876, People's Republic of China
e-mail: zhuhankunbupt@yahoo.com.cn; sagacious@189.com; zzhou@bupt.edu.cn

X. Peng
The State Radio Monitoring Center Testing Center, No. A-98 Bei lishi Road, XiCheng District, Beijing 100037, People's Republic of China
e-mail: b0_xer@163.com

Q. Liang et al. (ed.), *Communications, Signal Processing, and Systems*, Lecture Notes in Electrical Engineering 202, DOI 10.1007/978-1-4614-5803-6_31,

31.1 Introduction

In recent years, we are witnessing an explosive growth in the demand for wireless networks. The huge amount of the bandwidth available in the unlicensed 60 GHz band, which is also known as the millimeter-wave band, has aroused a great deal of interest to develop new wireless communication techniques. The large bandwidth around 60 GHz (more than 3 GHz wide) may potentially enable the multi-gigabit wireless communication products and applications worldwide. New applications which could make full use of the increased data rate enabled by 60 GHz WPANs such as cameras, personal computers and uncompressed high definition television (HDTV) may be an emerging market [1, 2].

However, because of the huge difference between 60 GHz millimeter-wave communication and the existing wireless networks such as Wi-Fi and Bluetooth, the future of 60 GHz millimeter-wave WPAN applications largely depends on network system designs. Since the wavelength at 60 GHz frequency band is so small (5 mm), links are seriously blocked by obstacles such as humans and furniture. For example, blockage by a human body will lead to about 20–30 dB loss of the gain. Meanwhile, the movement of humans can cause sudden blockage of 60 GHz networks, which may result in the change of network topology. Maintaining seamless network connectivity as well as providing the QoS needed for applications such as HDTV in such a scenario poses great challenge for channel characteristics which is largely different from that at lower carrier frequencies.

The most common solution to handle blockages proposed by now is to route around obstacles. When the LOS link between the two terminal nodes is available, it operates at a fixed data rate. Otherwise, if the link is blocked we may find an available relay node, which may be usually the access point (AP) of WPANs or WLANs, and route around the obstacle. However, using conventional store-and-forward one-way relay scheme between two terminal nodes will lead to the throughput of the network reduce by a factor of two [3].

In order to maintain the throughput while using relay nodes to deal with blockage problems, in this investigation we introduce the physical layer network coding-based two-way relay scheme to the 60 GHz millimeter-wave WPANs. The principle of physical layer network coding is that the relay node can receive transmitted packets from both terminal nodes, encode the two messages into one packet, and then broadcast the encoded packet to the terminal node. Through these two steps, two time slots are saved to exchange packets between them, so that the overall network throughput can be increased and spectral efficiency is improved.

The rest of chapter is organized as follows. In Sect. 31.2, we discuss the system model including network topology and 60 GHz channel model. In Sect. 31.3, we proposed physical layer network coding-based relay scheme for the 60 GHz millimeter-wave WPANs. Then, in Sect. 31.4, we provide some simulation results and analysis. We also discuss the feasibility of applying two new proposed two-way relay scheme in 60 GHz millimeter-wave WPANs in this section. Finally, we conclude the chapter in Sect. 31.5.

31.2 System Model

There are two terminal nodes in demand of exchanging information in a simple network as shown in Fig. 31.1. However, the LOS link is blocked by an obstacle. A relay node can be introduced to this network to relay the packets transmitted from the terminal nodes.

However, in the classical relay system, as each relay node can only deal with one communication links, for one thing, the relay node may become the hot node when the network is seriously blocked. And for another, when there exists two communication links simultaneously call for relay operations, then we have to configure two relay nodes, which is of great expense to the 60 GHz communication networks. In fact, in each indoor scenario, there usually contains only one relay node, that is the access point. Therefore, it can hardly perform efficient relay with the traditional relay framework.

In data transmission, throughput is the amount of data transmitted successfully from one terminal node to another in a given time period.Mathematical expression of throughput for the network is presented as follows [4]:

$$C = \sum_{i=0}^{N} R_i(1 - P_{bi}) \tag{31.1}$$

where N represents the total number of links in a network, R_i denotes the maximum transmission data rate of $i - th$ link, and P_{bi} denotes bit error rate of each link.

In this article, we model the indoor channel at 60 GHz band using the model proposed by the IEEE802.11.TG3c (Next generation WLAN standard at 60 GHz band), which assumes that the received signals arrive in clusters. The rays within a cluster have independent phases as well as independent Rayleigh amplitudes whose variances decay exponentially with cluster and rays delays [5, 6].

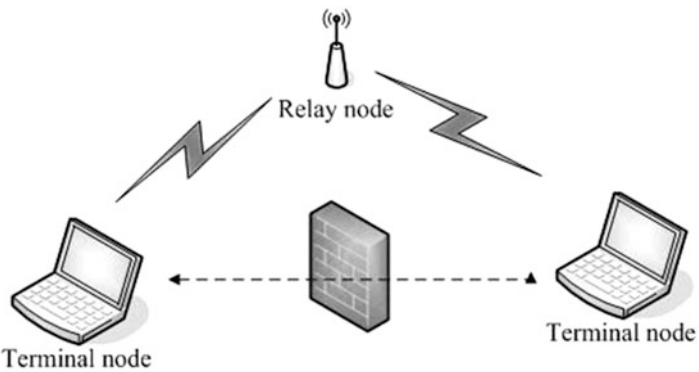

Fig. 31.1 Network topology

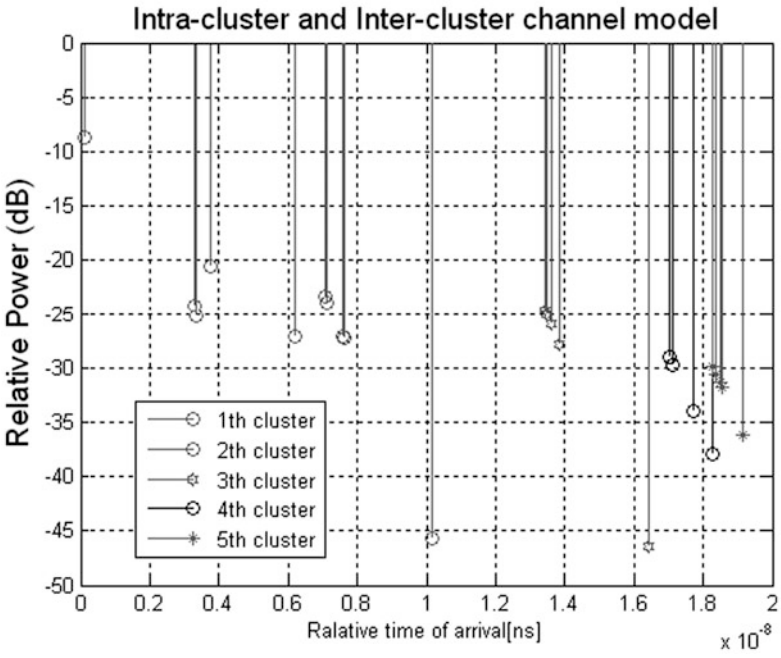

Fig. 31.2 The impulse response for LOS scenarios

The mathematical expression of inter-cluster model listed as follows.

$$h(t) = \sum_{l=0}^{L} \sum_{m=-M_b}^{M_f} \alpha_l \beta_m \sigma(t - T_l - \tau_{lm}) \tag{31.2}$$

$$|\beta_{lm}^2| = \begin{cases} \exp\left(\frac{\tau_{lm}}{\gamma_-}\right) \tau_{lm} < \tau_{l0} \\ \exp\left(\frac{\tau_{lm}}{\gamma_+}\right) \tau_{lm} > \tau_{l0} \end{cases}. \tag{31.3}$$

$$P\left(\tau_{l(m-1)} | \tau_{lm}\right) = \lambda_- \exp\left(-\lambda_- \left(\tau_{lm} - \tau_{l(m-l)}\right)\right), \ m<0 \tag{31.4}$$

$$P\left(\tau_{lm} | \tau_{l(m-1)}\right) = \lambda_+ \exp\left(-\lambda_+ \left(\tau_{lm} - \tau_{l(m-l)}\right)\right), \ m>0 \tag{31.5}$$

where γ_- and γ_+ represent ray decay parameters, λ_- and λ_+ are ray arrival rates which assumed to follow Poisson processes, m and l denote the index of ray and cluster. M_b and M_f represent the total number of rays for each side in the cluster. The phase of each ray is assumed to be an independent uniform random variable. α_l, T_l and L denote the peak power of $l-th$ cluster, the arrival time, and the total number of cluster.

The impulse response for LOS scenarios in the indoor channel at 60 GHz band is shown in Fig. 31.2. According to the figure, the amplitude of first cluster is about

20 dB higher than that of second cluster. Meanwhile the amplitude of the following clusters after the second cluster is even lower than that of the second cluster.

While considering high resolution directional transmission with LOS links, ignoring the clusters whose time of arrival is later than the first cluster is reasonable. In the following analysis, from the engineering point of view, we may using the Additive White Gaussian Noise (AWGN) channel model for indoor channel model at 60 GHz band to simplify our discussion.

31.3 Network Coding-Based Relay Scheme

Considering a three-node liner network, as shown in Fig. 31.3, where two terminal nodes T_1 and T_2 transmitting information to each other with the help of a relay node R.

In conventional store-and-forward relay scheme, T_1 first sends s_1 to the relay node R, and then R relays s_1 to T_2. After that, T_2 sends s_2 in the reverse direction and the same way. It exploits four time slots for the transmission of two packets in opposite directions between T_1 and T_2.

On the other hand, it only takes two time slots in the two- way relay protocol. In the first time slot, T_1 and T_2 simultaneously send packets to the relay node R. Before relaying the packets, information has been encoded into one packet. While in the second time slot, which is also named broadcasting phase, the combined signal is broadcasted to T_1 and T_2. By knowing the information sent by itself, the information transmitted by the other terminal node can be easily decoded. Thus, compared with the conventional store-and-forward relay scheme, by using physical layer network coding, the throughput of the wireless network can be increased by two times [7].

To ensure end-to-end communication, all we need is a special modulation/demodulation mapping scheme, also known as PNC mapping in relay node to encode the information from T_1 and T_2 into one packet at the physical-layer.

Tables 31.1 and 31.2 illustrate the idea of PNC mapping [8], where $s_j \in \{0, 1\}$ is a variable representing the data bit of T_i and $a_j \in \{-1, 1\}$, denotes a variable representing the BPSK modulated bit of s_j such that $a_j = 2s_j - 1$.

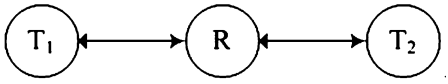

Fig. 31.3 A three-node linear network

Table 31.1 PNC mapping: modulation mapping at T_1,T_2

Modulation mapping at T_1,T_2			
Input		Output	
s_1	s_2	a_1	a_2
1	1	1	1
0	1	−1	1
1	0	1	−1
0	0	−1	−1

Table 31.2 Demodulation and modulation mapping at R

Demodulation mapping at R			
		Output	
		Modulation mapping at R	
Input		Input	Output
s_1	s_2	a_1	a_2
1	1	1	1
0	1	−1	1
1	0	1	−1
0	0	−1	−1

When T_1 receives s_t, it extracts s_2 from s_t using the local information s_1 Similarly, T_2 can also extract s_1 from s_t. Through this two time slot procedure, T_1 and T_2 can get information from the other terminal node by demodulating the received the signal.

31.4 Simulation and Analysis

In this section, we evaluate the performance of the proposed network coding-based relay scheme by experimental simulation. In our simulations, we consider the physical layer network coding-based two-way relay network by using the simplified 60 GHz millimeter-wave channels. As shown in Fig. 31.3, in the three-node liner network, there is only one shared frequency band, and the data rate of a single link is configured to 2Gbps, and the length of a packet is 1,000 bits. Heavy traffic load is also assumed to ensure that T_1 and T_2 always have packets to send. In addition, each result is based on ten times independent simulations. And then, bit error rate (BER) as well as throughput of the network is used to compare different strategies.

Figure 31.4 gives the bit error rate performance in the next three scenarios: (1) direct communication without relay node, (2) conventional store-and-forward one-way relay scheme, and (3) physical layer network coding two-way relay scheme. It is seen that, attributed to the employment of relay node, the end-to-end BER of the two relay schemes is higher than that of the terminal nodes communicating directly. While the BER of two-way relay scheme is not much higher than that of one-way relay scheme, in other word, they are practically comparable.

Throughput of three networks which has been introduced in Sect. 31.2 is displayed in Fig. 31.5. To evaluate the performance of the two relay schemes, we use the throughput of a direct link as the performance indication. Here the throughput in direct link communication is about twice of that in one-way relay network. However the throughput of direct link network is not much higher than that of two-way relay network, moreover, when SNR becomes larger, the gap between the throughputs of the two networks almost diminishes to zero. This is because when transmitting packets in opposite direction, two time slots are spared in direct link communication and two-way relay network, but in one-way relay network it needs four.

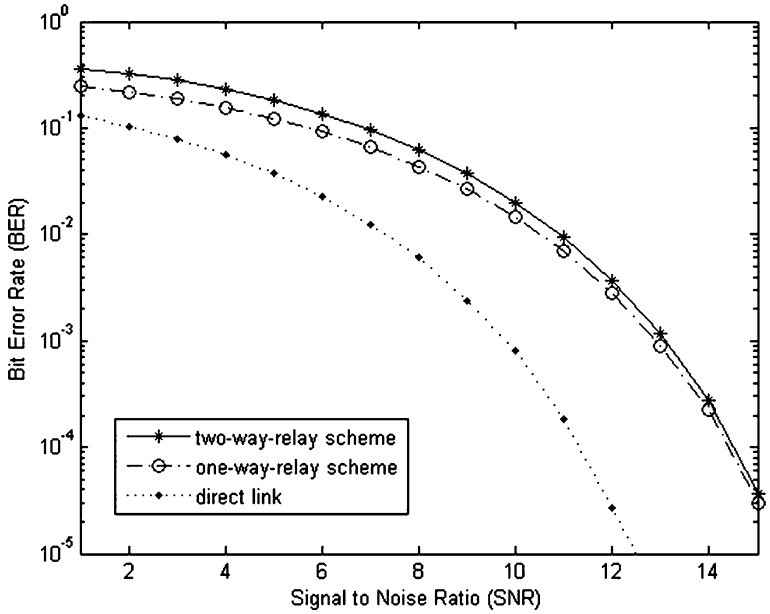

Fig. 31.4 Signal to noise ratio (SNR) versus bit error rate(BER)

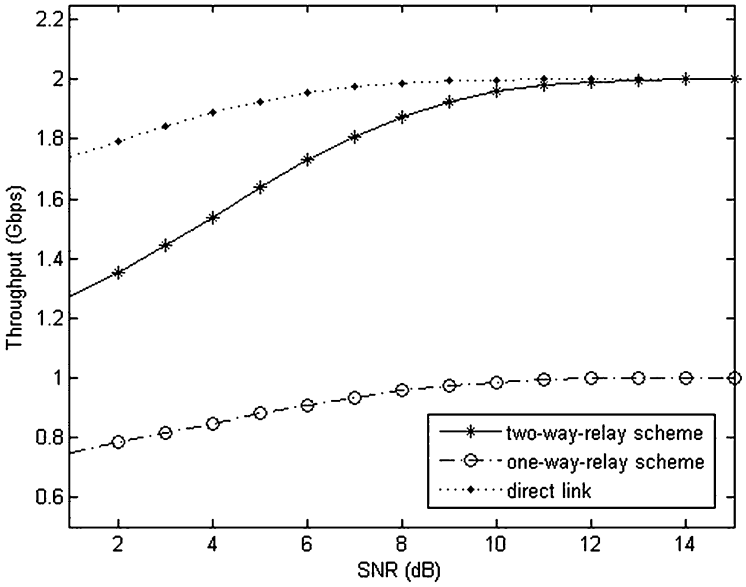

Fig. 31.5 Signal to noise ratio (SNR) versus throughput

Ignoring the slight BER difference, we can draw the conclusion that when we need to use relay nodes to handle blockage problem in 60 GHz millimeter-wave WPANs, we can apply physical layer network coding-based two-way relay networks to achieve larger throughput without worrying about the complex algorithm raising the BER.

31.5 Conclusion

In this investigation, we introduced a promising physical layer network coding-based two-way relay technology to 60 GHz millimeter-wave wireless personal area networks, in order to eliminate the impact of throughput reduction caused by using relay nodes which are used to deal with the blockage of links. The simulation results demonstrate that compared with the conventional store-and forward relay scheme, the application of two-way relay scheme in 60 GHz millimeter-wave WPANs can increase the throughput substantially. Meanwhile the rising of BER is totally acceptable.

As a consequence, the functioning of access point, when it used as the relay node in combating the blockage, can be maximized. Also, by simultaneously providing to relay links, the configuration expense of 60 GHz networks can be reduced to the utmost. With two-way relay networks, routing around the obstacles without reduction of throughput in 60 GHz millimeter-wave WPANs is realizable, which is crucial to maintain seamless network connectivity and providing the QoS needed for applications.

Acknowledgments Supported by the National Natural Science Foundation of China (Grant No.60902046, 60972079) and the Important National Science & Technology Specific Projects of China (Grant No.2011ZX03005-002, 2012ZX03001022).

References

1. Tao Chen, Woesner Hagen, Yabin Ye, Chlamtac Imrich (2005) Wireless Gigabit ethernet extension. 2nd International Conferrnce on Broadband Networks, Broadnets 2005:458–466
2. Yong SK, Chong C-C (2007) An overview of multigigabit wireless through millimeter wave technology: potentials and technical challenges. EURASIP J Wirel Commun Netw 2007 (1):1–10
3. Sumit S, Federico Z, Upamanyu M (2009) Blockage and directivity in 60 GHz wireless personal area networks: from cross-layer model to multihop MAC design. IEEE J Sel Areas Commun 27:1400–1413
4. Ju Minchul, Kim Il-Min (2010) Error performance analysis of BPSK modulation in physical-layer network-coded bidirectional relay networks. IEEE Trans Commun 58:2770–2775
5. Sato Katsuyoshi, Sawada Hirokazu, Shoji Yozo, Kato Shuzo (2007) Channel model for millimeter wave WPAN. IEEE International Symposium on Personal, Indoor and Mobile Radio Communications, PIMRC 1239–1252

6. Sawada H, Nakase H, Kato S (2010) Impulse response model for the cubicle environments at 60 GHz. In: Proceedings of the IEEE 71st vehicular technology conference (VTC 2010-Spring), pp 1–5
7. Zhang S, Liew SC (2010) Applying physical-layer network coding in wireless networks. Eurasip J Wirel Commun Netw 312–320
8. Zhang S, Liew SC (2009) Channel coding and decoding in a relay system operated with physical-layer network coding. IEEE J Sel Areas Commun 27:788–796

Chapter 32
A Novel Scheme of Improving 60 GHz Millimeter-Wave System Performance in the Presence of Nonlinear Power Amplifier

Shaojian Huang, Hongbo Tao, Sha Zhang, Xuebin Sun, and Zheng Zhou

Abstract Two modulation schemes, namely Single-Carrier (SC), Orthogonal Frequency Division Multiplexing (OFDM), are widely recommended in the currently undergoing 60 GHz millimeter-wave standard draft IEEE 802.11ad. Low Density Parity Check (LDPC) code is also adopted in the sense of its much better performance in correcting errors comparing the other FEC codes. However, OFDM system is extremely vulnerable to the nonlinear distortion caused by the 60 GHz power amplifier (PA) nonlinear property as a consequence of its significant peak to average ratio (PAPR). In this article, we utilize a promising companding transform (CT) algorithm which is also combined with predistortion scheme, in order to combat the PA nonlinear distortion. Experimental results demonstrate our proposed scheme exhibits much better performance in resisting PA nonlinear distortion, and the new scheme is also easy to implement in practical design of 60 GHz millimeter-wave systems.

Keywords OFDM • Companding transform • PA nonlinear • predistortion • LUT

S. Huang (✉) • X. Sun • Z. Zhou
Key Laboratory of Universal Wireless Communication, Ministry of Education, Beijing University of Posts and Telecommunications, Beijing 100876, People's Republic of China
e-mail: huangshaojian16@163.com; sunxuebin@gmail.com; zzhou@bupt.edu.cn

H. Tao • S. Zhang
The State Radio Monitoring Center Testing Center, No. A-98 Bei lishi Road, XiCheng District, Beijing 100037, People's Republic of China
e-mail: sagacious@189.cn; 13331013430@189.cn

Q. Liang et al. (eds.), *Communications, Signal Processing, and Systems*, Lecture Notes in Electrical Engineering 202, DOI 10.1007/978-1-4614-5803-6_32,

32.1 Introduction

60 GHz millimeter-wave wireless communication technique is an attractive technology popularized in the most recent years [1]. Though IEEE 802.11n and UWB can reach hundreds of Mbps transfer rate, it is still difficult to meet the demand of the high data rate applications, especially the high-definition video transmission. Fortunately, 60 GHz millimeter-wave is able to provide an ultra-high data rate up to multi-Gbps because of the enormous unlicensed band.

Currently, IEEE 802.11 Task Group ad is developing the standard expected to integrate the wireless local area network (WLAN) and wireless personal area network (WPAN). IEEE 802.11ad is supported by many large companies (such as Intel, IBM, etc.), and the rapid development of millimeter-wave chip and CMOS technology also laid the solid foundation for large-scale commercial process for the 60 GHz products.

In the current draft of IEEE 802.11ad standard [2], single-carrier modulation (SC) and orthogonal frequency division multiplexing (OFDM) are adopted, while OFDM is expected to reach a higher data rate. However, to make OFDM modulation successful in a practical millimeter-wave system, the following two issues must be adequately addressed: (1) OFDM is very sensitive to the phase errors; (2) OFDM signal has high PAPR. Among them, high PAPR would bring serious amplitude distortion and phase distortion after propagated from the nonlinear amplifier, and therefore seriously deteriorate the transmission performance. Although Refs. [3–5] have studied the performance of PA nonlinearity of 60 GHz millimeter-wave systems; they did not offer an effective approach to reduce the impact of the PA nonlinearity. Thus, how to deal with the nonlinear distortion effectively has still remained as one of the major challenges faced in the design of 60 GHz millimeter-wave systems.

In this chapter, we suggest a companding transform (CT) algorithm [6] which is further combined with a predistortion scheme [7], to efficiently alleviate the PA nonlinear distortion. Predistortion scheme is a well-known approach to resist PA distortio; however, the performance of predistortion scheme is not very clear when signal PAPR is significantly high because of its low efficiency. In our new approach, companding transform algorithm is designed to reduce PAPR without modifying the system configuration. As is demonstrated by the experimental simulations, by effectively reducing PAPR and hence enhance the functioning of predistortion, the combination of the two methods would noticeably improve the transmission performance greatly. Therefore, our new technique is of great promise to the practical design of 60 GHz millimeter-wave communication systems.

The rest of this chapter is organized as follows: In Sect. 32.2 the channel model and nonlinear power amplifier model of 60 GHz millimeter-wave communication system is briefly introduced; system model, compading transform algorithm and the predistortion scheme are proposed in Sect. 32.3; Section 32.4 shows the simulation results; Section 32.5 draws the conclusions.

32.2 PA Nonlinear Model

The effects of PA nonlinear include the distortion generated by amplitude modulation-amplitude modulation (AM-AM) conversion and amplitude modulation-phase modulation (AM-PM) conversion. AM-AM model and AM-PM model are expressed as follows [8]

$$G(A) = g\frac{A}{\left(1 + (\mathrm{g}A/A_{sat})^{2s}\right)^{\frac{1}{2s}}} \tag{32.1}$$

$$\Psi(A) = \frac{\alpha A^{q_1}}{(1 + (A/\beta)^{q_2})}. \tag{32.2}$$

where A and $\mathbf{G}(A)$ represent the input and output voltage range in RMS; $g$is the small gain signal, $g = 4.65$; s is the smoothness factor, $s = 0.81$; A_{sat} is the saturation level, A_{sat} =0.58 V. $\Psi(A)$ is the phase in degrees; α, β are 2560, 0.114 respectively, and q_1, $q_2$are 2.4 and 2.3 respectively.

In order to reduce significant nonlinear distortion, an intuitive solution is to use the output power back-off mechanism. Back-off power formula can be described as $R_{backoff} = 10\log_{10}(P_{sat}/P_{out})$,where P_{sat} is the output saturation power, P_{out} is the output power. $R_{backoff}$ is power back-off rate in dB. Obviously, the greater back-off power rate means the smaller the output power, and the smaller the output power means the smaller the nonlinear distortion. On the other hand, lower transmit power will cause the lower signal to noise ratio; this will result in decreasing anti-jamming capability; at the same time, the performance of amplifier device may be greatly deteriorated. Therefore, the power back-off mechanism can only avoid the negative effects of nonlinear distortion in a certain extent, but fail to effectively improve the system performance under the nonlinear device. It is difficult to be adopted widely in the practical design.

32.3 Companding Transform and Predistortion

In order to improve the performance of 60 GHz millimeter-wave system, we propose a novel scheme that uses predistortion combined with companding transform algorithm. The system block diagram is as follow (Fig. 32.1)

In this chapter, we focus on LOS (Line-Of-Sight) channel. Because of the significant principal component of antenna, LOS channel can be approximately regarded as AWGN channel when the beam is aligned. The input signal u, binary bits, which are sent to the LDPC encoder, mapper and IFFT block to be mapped into the symbols with a series of sub-carriers, then processed by companding transform and predistortion block, and finally completed after the PA nonlinear distortion is superimposed. At the receiver, the symbols are converted into bits $\tilde{u}$ after operations in contrast with the transmitter.

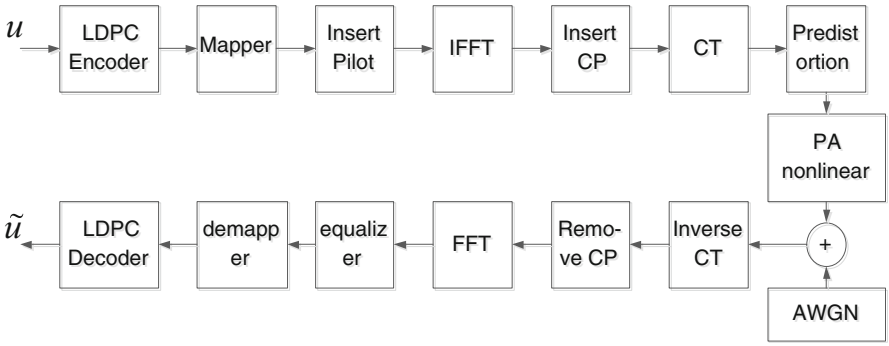

Fig. 32.1 Block diagram of IEEE 802.11ad system

32.3.1 Companding Transform Algorithm

PAPR can be defined as $\max(|x|^2)/E(|x|^2)$, $\max(|x|^2)$ is the peak power of transmit signal, $E(|x|^2)$ is the mean power of signal.

The companding transform algorithm is used to decrease high power and increase low power, so that the signal average power remains the same. Not only it can reduce the PAPR, but also increase the signal anti-jamming capability [6].

Companding transform is expressed as

$$s_{n,k} = \frac{V x_{n,k}}{\ln(1+u)\left|x_{n,k}\right|} \ln\left(1 + \frac{u}{V}\left|x_{n,k}\right|\right) \tag{32.3}$$

where $x_{n,k}$ is k-th sample of n-th OFDM symbol, V is the mean value of $x_{n,k}$, u is the companding rate. At the receiver we can the inverse transform.

32.3.2 Predistortion Model

According to Sect. 32.2, we have known that PA model of 60 GHz millimeter-wave is constant, so we can use an easy way to design the predistorter.

We add a nonlinear element in front of the nonlinear power amplifier, suppose the characteristic function $F(V_{in})$, this nonlinear element which is called predistorter. PA characteristic function is $G(V_d)$, the aim of the $F(V_{in})$ is to make $F(|V_{in}|)\cdot G(|V_d|) = K$.

Predistortion scheme is widely used in PAs [8]. Predistortion can be regarded as a nonlinear compensation that is applied before the signal is presented to a nonlinear PA input.

Figure 32.2 shows a block diagram of the adaptive digital predistorter. The predistorter includes the LUT data, DAC, RF quadrature (I-Q) modulator, PA, quadrature (I-Q) demodulator, ADC, and filters.

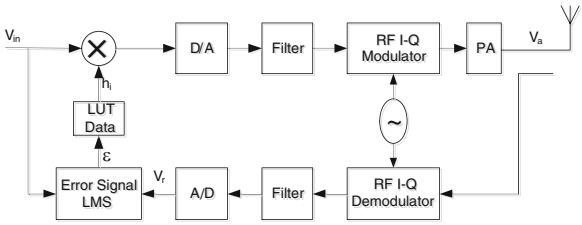

Fig. 32.2 Block diagram of Predistorter With LUT

In the predistorter, before applying to the DAC, the complex digital input signal $V_{in}(n)$ are multiplied by complex coefficients h_i drawn from a lookup table (LUT). The index i corresponds to the amplitude of the input signal $|V_{in}(n)|$, therefore, the value of h_i is chosen depending on the magnitude of the input signal, $|V_{in}|$. The characteristics of predistortion function are stored in the LUT. The LUT is stored with N complex gain values h_i, $i = 0, \ldots, N\text{-}1$. The value of h depends on the magnitude of input $|V_{in}|$. We use least mean square (LMS) to determine the value of the h coefficients.

32.4 Performance Evaluation and Simulation Results

Based on system block diagram in Sect. 32.3, we simulate the 60 GHz physical layer transmissions and also evaluate the performance of our presented scheme. According to the draft of IEEE 802.11ad standard, all parameters of simulation are listed in Table 32.1. The following parts of this section show the simulation results.

32.4.1 PAPR Performance and Distortion

We use companding transform algorithm to reduce PAPR. Figure 32.3 plots the complementary cumulative distribution function (CCDF) of transmit signal, the companding rate is 1, 2, 3 respectively. We can see that bigger companding rate u result in lower PAPR. When u is set as 3, the PAPR is restricted in 6 dB at the ccdf of 10^{-4}, where the original signal is about 6 dB higher. The PAPR performance is significantly improved after implementing the proposed algorithm.

We use companding transform algorithm to reduce PAPR. Figure 32.3 plots the complementary cumulative distribution function (CCDF) of transmit signal, the companding rate is 1, 2, 3 respectively. We can see that bigger companding rate u result in lower PAPR. When u is set as 3, the PAPR is restricted in 6 dB at the ccdf of 10^{-4}, where the original signal is about 6 dB higher. The PAPR performance is significantly improved after implementing the proposed algorithm.

In Fig. 32.4a shows 64-QAM constellation impacts under PA nonlinear, from the figure we can hardly distinguish the specific location of signal in the constellation.

Table 32.1 Parameters of simulations

Parameter	Value
Channel model	LOS(AWGN)
Number of subcarriers	512
Subcarrier modulater	BPSK, QPSK, 16-QAM, 64-QAM
Channel coding	LDPC(R = 1/2)
LDPC size	336 × 672
Output Back-off	4 dB
Synchronization	Ideal
Channel estimation	Ideal

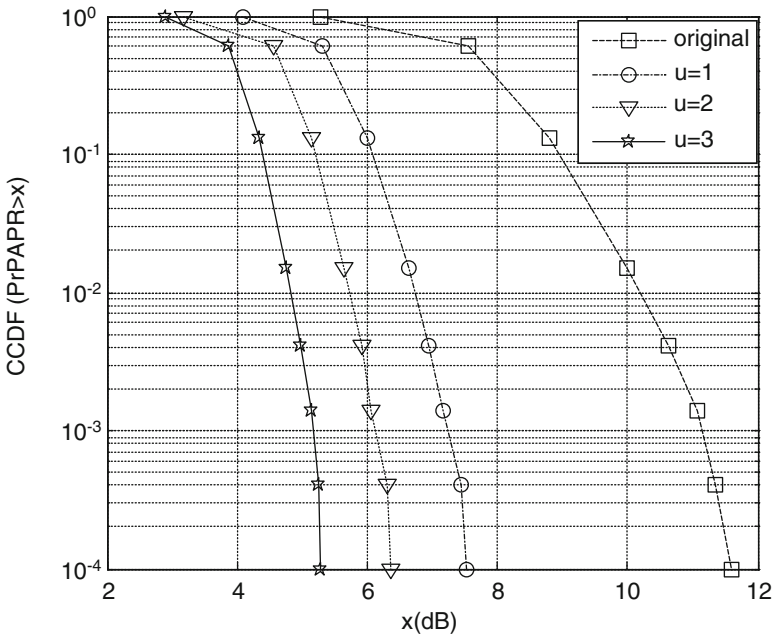

Fig. 32.3 PAPR performance

The result mainly because 64-QAM has small constellations distance, and it is easy to be influenced by PA nonlinear distortion. After implementing predistortion scheme, as Fig. 32.4b depicts, we can clearly distinguish the location of signal, the distortion of PA is noticeably reduced.

32.4.2 System Performance

In the draft of IEEE 802.11ad standard, the OFDM sub-carrier modulations include BPSK, QPSK, 16-QAM, 64-QAM. To evaluate the receiver performance, we use

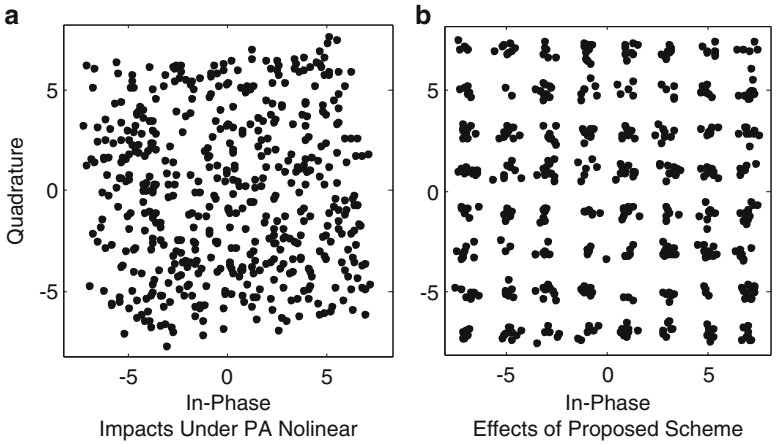

Fig. 32.4 64-QAM constellation

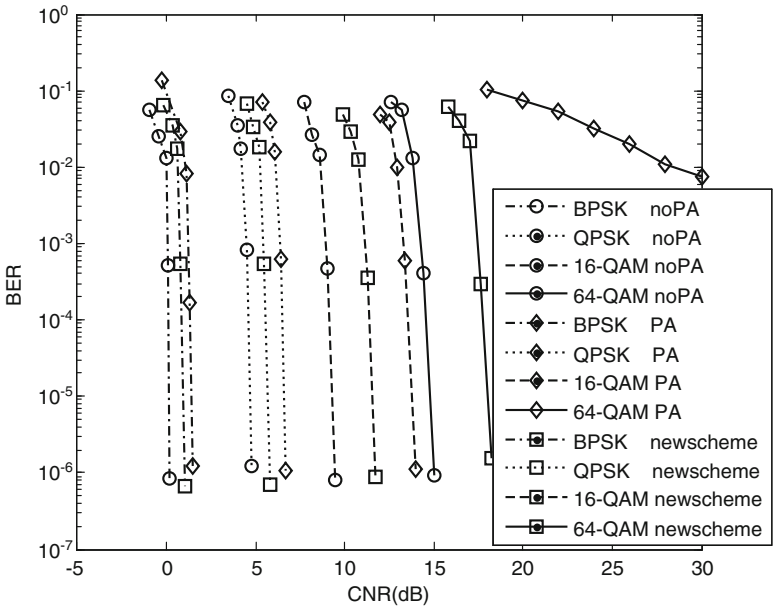

Fig. 32.5 BER versus CNR

CNR (Carrier-to-Noise Rate) versus BER (Bit Error Rate) depicts the system performance.

In Fig. 32.5, bit rate is 1/2 and power back-off is 4 dB. When PA nonlinear distortion is not appended, BPSK, QPSK, 16-QAM and 64-QAM can achieve BER of 10^{-6} at 0, 5, 9.8, 15 dB respectively. Once PA nonlinear distortion is appended,

we can see that PA nonlinear makes a smaller effect on BPSK and QPSK modulation, and the performance loss less than 2 dB at the BER of 10^{-6}. Relatively, the impacts are more significant for QAM modulations. Though 16-QAM can still work well, the performance loss about 5 dB; 64-QAM can hardly achieve a BER of 10^{-3}, because its constellation is closer, thus the signal amplitude and phase is sensitive to nonlinear effects of nonlinear power amplifier.

After applying the companding transform algorithm and predistortion scheme as we presented in previous section. The performance of BPSK and QPSK increase 1 ~ 1.2 dB, 16-QAM increase 2 dB, and more importantly, 64-QAM can achieve BER of 10^{-6} at CNR of 18 dB, so we can use it for transmitting high data rate.

32.5 Conclusion

In this investigation, for the first time we propose a novel scheme, relying on the organic combination of the companding transform algorithm and the predistortion scheme, to efficiently improve the performance of IEEE 802.11ad system. Simulation results verified this presented scheme has much better performance in resisting PA nonlinear distortion comparing others and the scheme is easy to implement in practical 60 GHz millimeter-wave system. The combination of companding transform algorithm and predistortion scheme mentioned in this chapter can not only be applied into the 60 GHz millimeter-wave communication systems, it also can be applied into other OFDM systems.

Acknowledgments Supported by the National Natural Science Foundation of China (Grant No.60902046, 60972079) and the Important National Science & Technology Specific Projects of China (Grant No.2011ZX03005-002, 2012ZX03001022).

References

1. L Lily Yang (2009) 60 GHz: opportunity for Gigabit WPAN and WLAN convergence. ACM SIGCOMM Comput Comm Rev 39(1):56–61
2. IEEE P802.11 Task Group ad (2010) Wireless LAN Medium Access Control (MAC) and Physical Layer (PHY) specifications
3. Changming Zhang, Zhenyu Xiao, Hao Wu, Lieguang Zeng, Depeng Jin (2011) Performance analysis on the OFDM PHY of IEEE 802.11ad Standard. In: Proceedings of the international conference on computational problem-solving (ICCP), Chengdu, 21–23 Oct 2011, pp 708–713
4. Liru Lu, Xin Zhang, Funada R, Chin Sean Sum, Harada H (2011) Selection of modulation and coding schemes of single carrier PHY for 802.11ad Multi-Gigabit mmWave WLAN systems. In: IEEE symposium on computers and communications (ISCC), Kerkyra, June 28–July 1 2011, pp 348–352

5. Xin Zhang, Liru Lu, Funada R, Chin-Sean Sum, Harada H (2010) Physical layer design and performance analysis on multi-Gbps millimeter-wave WLAN system. In: IEEE international conference on communication systems (ICCS), Singapore, 17–19 Nov 2010, pp 92–96
6. Aburakhia SA, Badran EF, Mohamed DAE (2009) Linear companding transform for the reduction of peak-to-average power ratio of OFDM signals. IEEE Trans Broadcast 55:155–160
7. Perahia E, Park M, Stacey R et al (2010) IEEE P802.11 wireless LANs TGad evaluation methodology. IEEE 802.11 TGad Technology Report 09/0296r16, pp 3–5, 9–15
8. Lozhkin AN, Nakamura M (2011) A new digital predistorter linearizer for wide band signals. In: Proceedings of the IEEE 22nd international symposium on personal indoor and mobile radio communications (PIMRC), pp 1376–1380

Part IX
Radar Signal Processing

Chapter 33
An Improved Dynamic Programming Based Track-Before-Detect Approach for Dim Target Detection

Mingming Guo and Xiaobo Deng

Abstract In this chapter, the authors propose an improved dynamic programming (DP) based track-before-detect (TBD) to detect small targets in a high pulse repetition frequency (PRF) radar. Unlike most DP TBD methods in the literature which only use the accumulated energy to decide if a target is present, the proposed algorithm jointly process several low-threshold-crossing data frames, and uses both the accumulated energy and the frequency of being associated to decide if a target is present.

Keywords Dynamic programming • Track-before-detect • High PRF

33.1 Introduction

The detection and tracking of small target is a challenging problem in radar research field. In low signal-noise-ratio (SNR) environment, using the traditional Track-after-Detect (TAD) method to detect small targets is very difficult, because much valuable information is discarded due to the application of a detection threshold. Unlike the TAD methods, TBD methods jointly process several original data frames (or low threshold crossings), accumulate energy, and then declare if a target is present in the accumulated domain. The target track can be retrieved when a target is detected.

M. Guo (✉)
AVIC Radar and Avionics Institute, Wuxi 214063, People's Republic of China
e-mail: guo_greeting@126.com

X. Deng
AVIC Radar and Avionics Institute, Wuxi 214063, People's Republic of China

Tsinghua University, Beijing 100084, People's Republic of China
e-mail: xiaobobo.deng@yahoo.com.cn

Q. Liang et al. (eds.), *Communications, Signal Processing, and Systems*, Lecture Notes in Electrical Engineering 202, DOI 10.1007/978-1-4614-5803-6_33,

The TBD method can efficiently improve the detection and tracking performance of small targets. It attracts much attention of the researchers. Recently, there are mainly three categories of TBD methods, the Hough transform based TBD method [1], the dynamic programming (DP) based TBD method [2, 3], the particle filter (PF) based TBD method [4, 5]. The DP based TBD is not limited by target's trajectory, and it is easy to implement, so it is very promising.

Wallace has studied the application of DP based TBD method in pulse Doppler radars [6], where he utilizes the Doppler information to decide the range cells in former frame.

Buzzi finds the maximum of the observation data matrix in ambiguous Doppler domain, and then processes the range-azimuth data matrix using the TBD method [7]. In this approach, the search area is confirmed by the maximum velocity, so it is inevitably too big.

In addition to the problem above, there are also two problems need to be considered:

1. The problem of high PRF radar. In this condition, we can't consult Buzzi's method, since the observation range is ambiguous, and it is potential to change the ambiguity number in the jointly processed frames. In this thesis, we utilize the known Doppler information and small target's constant-velocity moving to calculate the change of ambiguity number, and then the range cell of target in former frame is confirmed.
2. The problem of realizing the theory in project. This new algorithm keeps examining the detecting spots' correlation times, where, each spot is regarded as a potential target spot, if the correlation time reaches the threshold, export it as a target.

This chapter is organized as follows. Section 33.2 describes the original DP algorithm; the improved algorithm is proposed in Sect. 33.3 and the experiment on simulation data is conducted to demonstrate the detection and tracking performance of this algorithm; finally, conclusion is given in Sect. 33.4.

33.2 The Original DP Algorithm

Dynamic programming is a multi-phases optimizing problem; the problem to be solved is decomposed to several interknitting sub-problems. The sub-problems are the different stages of the whole course. DP is the colligation of classification decision-making and the optimized principle [8]. This method turns one multi-variable complicated problem to several single-variable problems through grading process, which can efficiently predigest the resolving course, and get the optimal solution.

Consider the problem of tracking a point target that moves with constant velocity in the x-y plane. An extended region surrounding the target is monitored by a radar,

consisting of an $L \times L$ grid of square resolution cells of side length Δ, at time k, the matrix of measured intensities recorded by the sensor is $Z_k = \{z_k(i,j)\}, i,j \in [1,L]$, where,

$$Z_k(i,j) = \begin{cases} A_k + w_k(i,j), & \text{target in } (i,j) \\ w_k(i,j), & \text{no target in } (i,j) \end{cases} \tag{33.1}$$

Here, A_k denotes the amplitude which is assumed to be a constant for simplicity, i.e. $A_k = A$. The additive noise $w_k(i,j) \sim N(0, \sigma_w^2)$ is assumed to be IID.

The sensor grid provides the necessary structure to model the target motion by the discrete process

$$X_{k+1} = FX_k, \ k = 1, 2 \cdots K \tag{33.2}$$

$$X_k = \begin{bmatrix} x_k \\ y_k \\ u_k \\ v_k \end{bmatrix} \ F = \begin{bmatrix} 1 & 0 & T & 0 \\ 0 & 1 & 0 & T \\ 0 & 0 & 1 & 0 \\ 0 & 0 & 0 & 1 \end{bmatrix} \tag{33.3}$$

Where, $(x_k, y_k) \in [(1,1),(L,L)]$ is discrete target position, and $(u_k, v_k) \in [(-M/2, -M/2),(M/2,M/2)]$ is the discrete target velocities. T is the time between successive sensor readings, termed frames. For simplicity, we assume that $T = 1$, M is a design parameter, chosen to encompass the velocity range of the target motion.

The TBD estimation objective is: Given the measurement sequence of K frames, determine the trajectories most likely to have the originated from the actual target. The original DP algorithm is applied as follows.

Let X_k be the set of all possible discrete states of the target at time k:

$$X_k = \left\{ [i,r,j,s]^{'} \right\}, \ i,j \in [1,L)], \ r,s \in [-M/2, M/2] \tag{33.4}$$

1. Initialization: For all $x_1 = [i,r,j,s]^{'} \in X_1$,

$$I(x_1) = z_1(i,j) \tag{33.5}$$

$$\Psi_1(x_1) = 0 \tag{33.6}$$

2. Recursion: For $2 \le k \le K$, For all, $x_k = [i,r,j,s]^{'} \in X_k$

$$I(x_k) = \max[I(x_{k-1})|x_{k-1}] + z_k(i,j) \tag{33.7}$$

$$\Psi_k(x_k) = \arg \ \max[I(x_{k-1})] \tag{33.8}$$

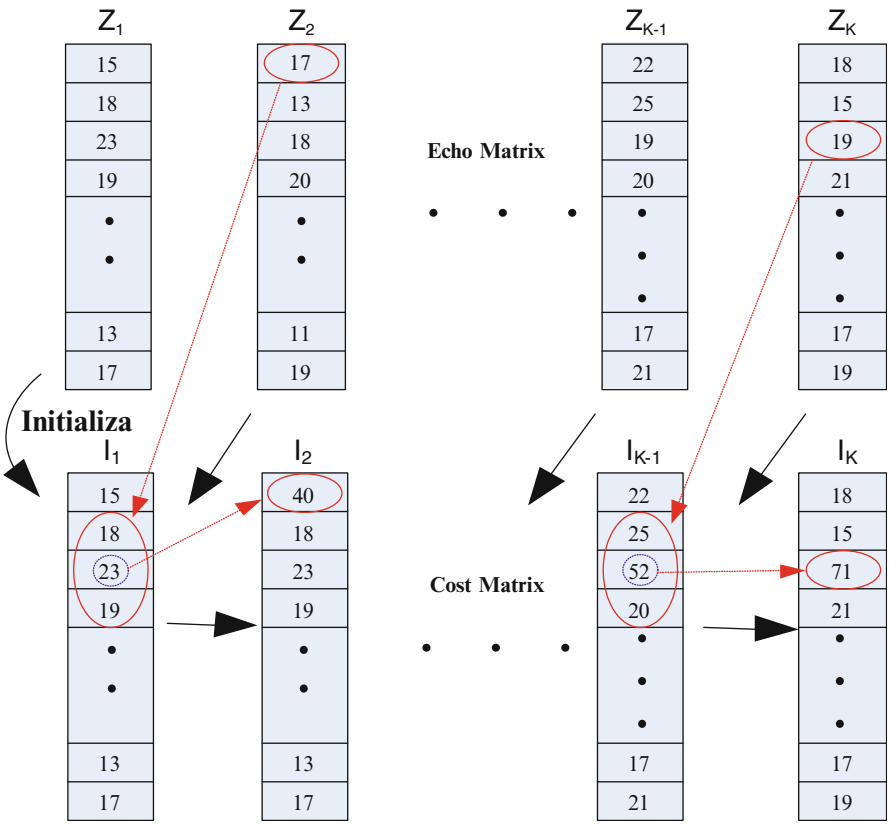

Fig. 33.1 The original DP TBD method

3. Termination: For threshold V_T find,

$$\{\hat{x}_k\} = \{x_k : I(x_k) > V_T\} \tag{33.9}$$

4. Backtracking: For all $\hat{x}_k$, for $k = K - 1, \cdots 1$

$$\hat{x}_k = \Psi_{k+1}(\hat{x}_{k+1}) \tag{33.10}$$

$\{\hat{x}_k\}$ builds up the detected track. The algorithm sketch map and simulation result sketch map are separately given in Figs. 33.1 and 33.2.

For each frame, after CFAR processing, all the points left are saved in an echo matrix which is named as z_i. In z_i, the points appear in row order; in each row, the range cell number is saved in the first column followed by the Doppler cell number, power and correlation time. For simplicity, z_i only shows each point's power in Fig. 33.1.

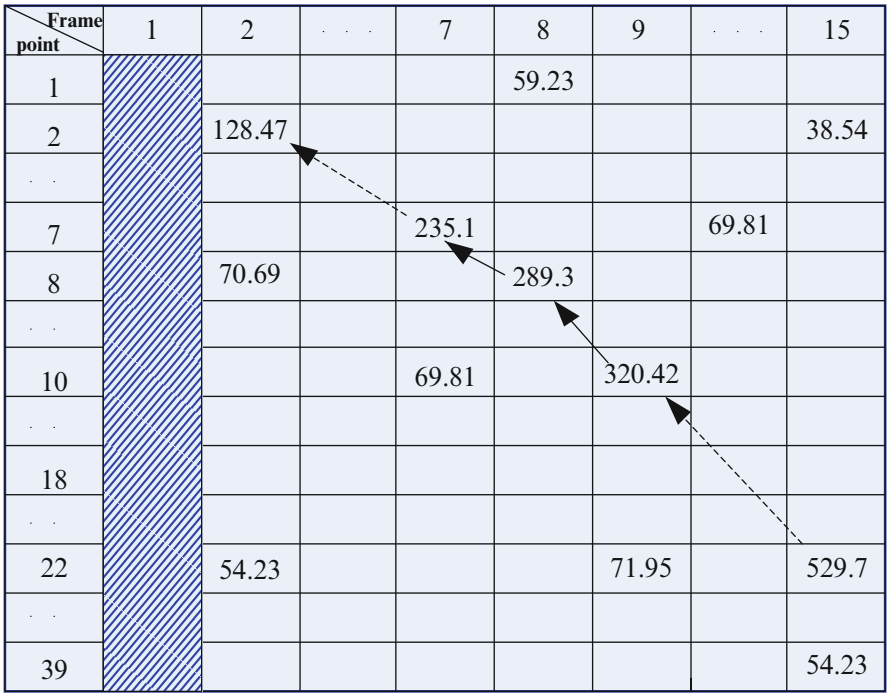

Fig. 33.2 The backtracking process of DP TBD method

In accordance with the principle max power, one track is found, and the process is showed in Fig. 33.2.

33.3 The Improved DPA and Application on Simulation Data

Considering the conditions of high PRF radar and multi-target detecting, an improved DP algorithm is presented in this chapter. The improved DP algorithm is applied as follows.

1. Initialization: For all $x_1 = [i, r, j, s]^{'} \in X_1$,

$$I(x_1) = z_1(i, j) \tag{33.11}$$

$$\Psi_1(x_1) = 0 \tag{33.12}$$

$$C_1(x_1) = 0 \tag{33.13}$$

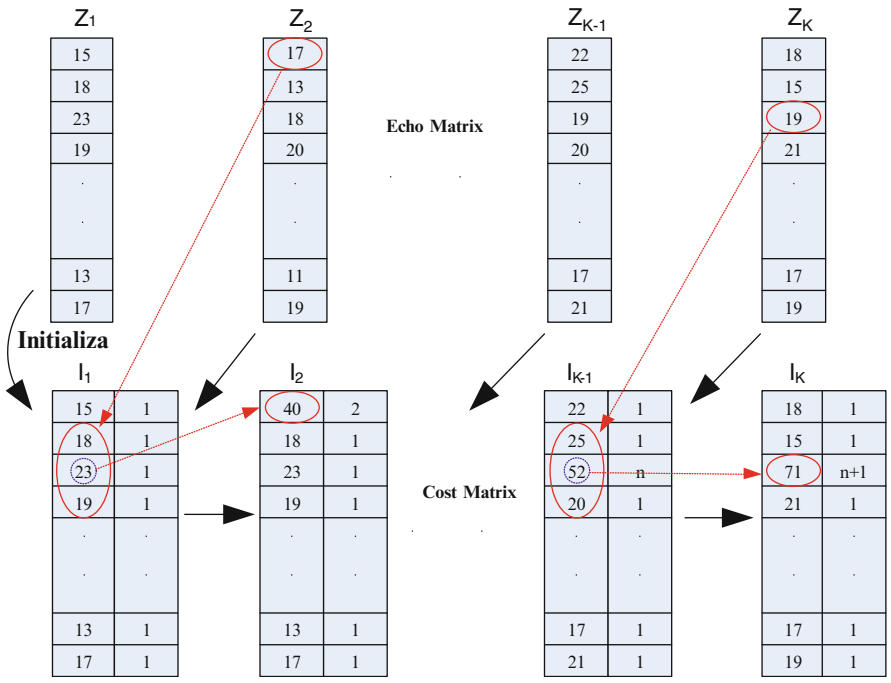

Fig. 33.3 The improved DP TBD method

2. Recursion: For $2 \leq k \leq K$, For all, $x_k = [i, r, j, s]^{'} \in X_k$

$$I(x_k) = \max[I(x_{k-1})|x_{k-1}] + z_k(i,j) \tag{33.14}$$

$$C_k(x_k) = C_{k-1}(x_{k-1}) + 1 \tag{33.15}$$

For every frame, if $C_k(x_k) \geq N$, where N is the threshold of continuing correlation times, record x_k, and save the points having the same root in matrix $D_{ik}(x_k)$. Output the point whose power is the maximum, which will be the target of the ith track. For the point x_k,

$$\Psi_k(\hat{x}_k) = \{x_k : C_k(x_k) > N, I(x_k) = \arg\max[D_{ik}(x_k)]\} \tag{33.16}$$

3. Termination: When $k = K$.
4. Backtracking: For all $\hat{x}_k$, for $k = K-1, \cdots 1$

$$\hat{x}_k = \Psi_{k+1}(\hat{x}_{k+1}) \tag{33.17}$$

The algorithm sketch map and simulation result sketch map are separately given in Figs. 33.3 and 33.4.

frame / point	1		2		. . .		6	
1	70.69	1					69.54	1
2			128.47	2				
. . .								
7							529.7	6
8							531.9	6
9			69.81	1			520.9	6
. . .								
17								
18	54.23	1						
. . .								
22							69.81	1
. . .								
39			54.23	1				

Fig. 33.4 The backtracking process of the improved DP TBD method

The approach to detect and track small targets in sky using this improved DP algorithm is: data pretreatment, track-match point search, track management, dynamic programming, extremum extraction, and target trace estimating. This process is shown in Fig. 33.5, firstly, low the threshold of CFAR detector, get all the supposed track point. Then match all the detected point with the pending tracks, and do short time track, which will produce some pending tracks. Lastly, deal with these pending tracks using DP algorithm, the track which exceeds the threshold will be confirmed as the target track.

Figure 33.5 shows the flowchart of detecting small targets in sky using the proposed DP TBD method.

The proposed method is verified using real data. The result is shown as follows:

Figure 33.6 shows that there are more than hundred false alarm points after CFAR processing, we can't distinguish the target; Fig. 33.7 gives the output of DP algorithm; in order to confirm the targets' track, Fig. 33.8 gives the backtracking result, and the target is detected.

From Figs. 33.6, 33.7, and 33.8, we can say that, system can effectively eliminate the false alarm points; utilizing the improved DP based TBD method, the detecting probability is effectively improved.

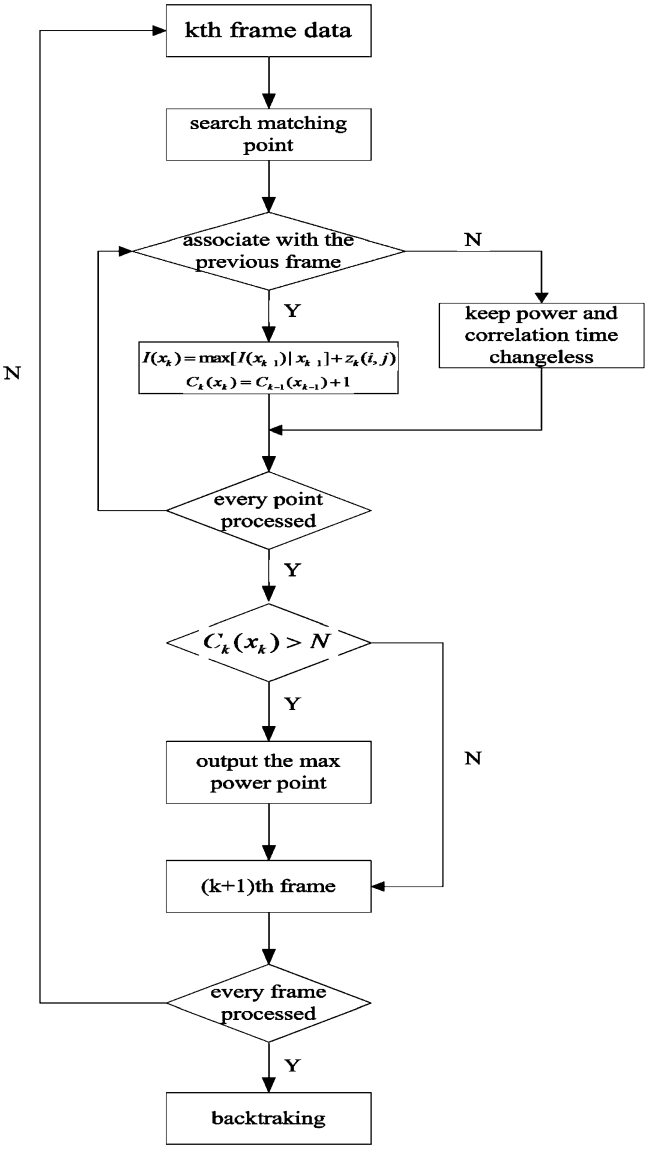

Fig. 33.5 Process simulation data course with DPA

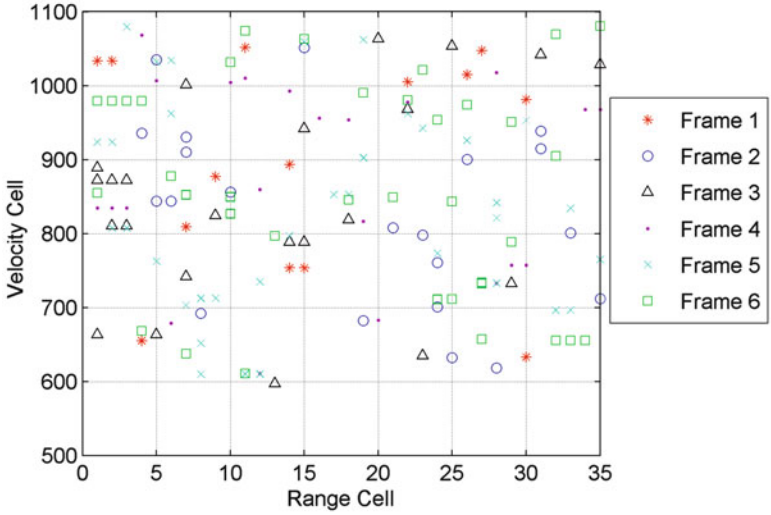

Fig. 33.6 All the points after CFAR

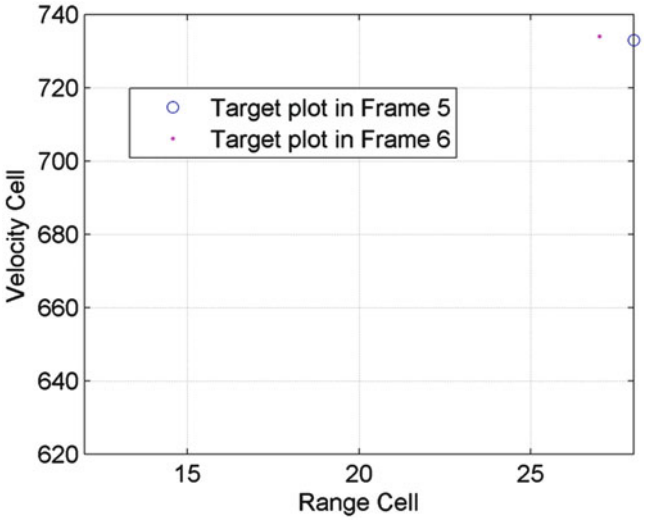

Fig. 33.7 Output of every frame with DPA

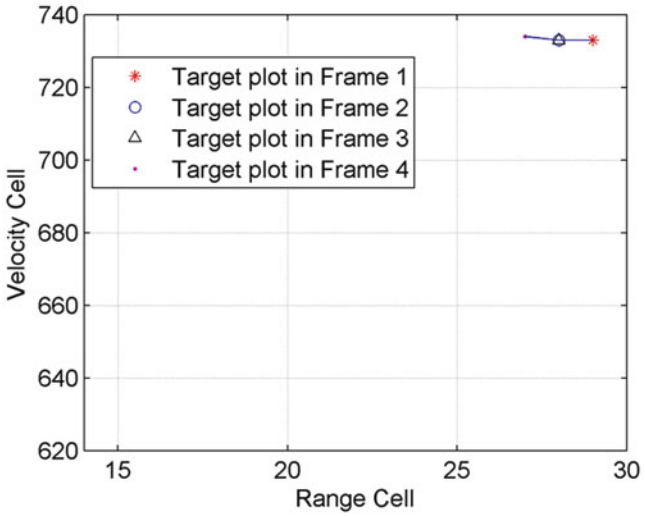

Fig. 33.8 Target tracks

33.4 Conclusion

This chapter presented an improved DP based TBD method. This algorithm is used in high PRF radar; it can give the results instantly. In this chapter, the difference between this improved DP based TBD method and the original DP based TBD method is discussed firstly, then our new method is tested on simulation data, the simulation result proves its efficacy.

References

1. Carlson BD, Evans ED, Wilson SL (1994) Search Radar detection and track with the Hough transform 1 system concept. IEEE Trans Aerosp Electron Syst 30(1):120–108
2. Barniv Y (1985) Dynamic-programming solution for detecting dim moving targets. IEEE Trans Aerosp Electron Syst 21(1):144–156
3. Reed IS, Gagliadi RM, Stotts LB (1990) A recursive moving-target-indication algorithm for optical-image sequences. IEEE Trans Aerosp Electron Syst 26(3):434–440
4. Salmond DJ (2001) A particle filter for track-before-detect. In: Proceedings of the IEEE american control conference, Washington, USA
5. Boers Y, Driessen H, Torstensson J et al (2006) Track-before-detect algorithm for tracking extended targets. IEE ProcRadar Sonar Navigation 153(4):345–351
6. Wallace WR (2002) The use of track-before-detect in pulse-Doppler radar. In: Proceedings of the IEEE international radar conference, Long Beach
7. Buzzi S, Lops M, Venturino L (2005) Track-before-detect procedures for early detection of moving target from airborne radars. IEEE Trans Aerosp Electron Syst 41(3):937–954
8. Leigh AJ, Vikram K (2002) Performance analysis of a dynamic programming track before detect algorithm. IEEE Trans Aerosp Electron Syst 38(1):228–242

Chapter 34
FOD Detection on Airport Runway with Clutter Map CFAR Plane Technique

Jin Erwen, Yan Danqing, Zhang Zhongjin, Zhong Qi, and Yu Xuelian

Abstract Foreign Object Debris (FOD) detection is an importance issue to civil aviation safety. In this chapter, the technique of clutter map CFAR plane detection is discussed in detail and applied to FOD detection on airport runway based on millimeter-wave linear frequency modulated continuous wave (LFMCW) radar. The detection performance of the technique is analyzed, and a simulation experiment is conducted. Simulation result shows the effectiveness of the clutter map CFAR plane detection technique in relatively low signal-to-clutter ratio (SCR) situation.

Keywords Clutter map • FOD detection • CFAR plane detection technique • LFMCW radar

34.1 Introduction

Airport runway foreign object debris (FOD) may cause damages or disasters to aircrafts. The crash of a Concorde jet in France in 2000 is an example of disasters due to FOD. Moreover, a lot of money is spent each year by airlines for repairing the damages caused by FODs to aircrafts. Consequently, some FOD detection systems have been developed and tested on airports recently, such as Tarsier

The National Natural Science foundation of China (No. 61139003) and the Fundamental Research Funds for the Central Universities (No. ZYGX2010J022).

J. Erwen • Y. Danqing (✉) • Z. Zhongjin • Z. Qi
The Second Research Institute of CAAC, Chengdu, China
e-mail: jinerwen@vip.sina.com; yandanqing@gmail.com

Y. Xuelian
School of Electronic Engineering, University of Electronic Science and Technology of China, Chengdu, China
e-mail: iceyu23@126.com

Q. Liang et al. (eds.), *Communications, Signal Processing, and Systems*, Lecture Notes in Electrical Engineering 202, DOI 10.1007/978-1-4614-5803-6_34,

system, FODetect, iFerret, and etc. Most of them are based on millimeter-wave radar and an optical sensor [1, 2]

One of the key problems of FOD detection is how to find small target under relatively strong clutter background. The millimeter-wave linear frequency modulated continuous wave (LFMCW) radar is very suitable to FOD detection since it has excellent properties such as high range resolution, high sensitivity, no range blind area, and etc., which is helpful to detect small target.

The clutter situation on airport runway faced by the FOD detection radar is rather complex. So it is necessary to establish the clutter map and use the constant false alarm rate (CFAR) technique [3, 4] to obtain a satisfactory detection performance, that is, the clutter map CFAR technique. The conventional clutter map CFAR method is often used to detect targets in a temporally stationary and spatially non-homogeneous background, which is also called clutter map CFAR point technique [5]. As an extension of the point technique to spatial processing, the clutter map CFAR plane technique was proposed [6]. And it has been shown that the performance of the plane technique is superior to that of the point technique in a temporally and spatially homogeneous background [5].

In this chapter, the LFMCW radar signal model and the principle of the clutter map CFAR plane technique is described firstly. Then, the detection performance of the technique is derived analytically. Finally, it is applied to airport runway FOD detection based on LFMCW radar, and the simulation result verifies the effectiveness and some good performance of the technique.

34.2 Signal Model

The transmit signal of LFMCW radar in a sweep frequency cycle is:

$$S_t(t) = A_0 \cos[2\pi(f_0 t + \frac{1}{2}\alpha t^2) + \varphi_0], 0 \le t \le T \tag{34.1}$$

where f_0 is the radar initial frequency, $\alpha = B/T$ is frequency modulation rate, B is frequency sweep bandwidth, T is frequency sweep cycle, and φ_0 is initial phase.

Note that the airport runway FOD is static target and thus the main detection task for LFMCW radar is to estimate the distance of FOD targets. Assuming there are one FOD target existed, the time delay of each target is:

$$\tau = \frac{2r}{c} \tag{34.2}$$

where r is the radial distance of target, and $c = 3 \times 10^8 \mathrm{m/s}$ is the speed of light. So the echo signal received can be expressed as:

$$S_r(t) = B \cos\left\{2\pi[f_0(t-\tau) + \frac{1}{2}\alpha(t-\tau)^2] + \varphi\right\}, 0 \le t \le T \tag{34.3}$$

Then, the difference frequency signal after frequency mixing can be obtained as:

$$S_{IF}(t) = A\cos\left\{2\pi[\frac{2r}{c}(f_0 - \frac{\alpha r}{c}) + \frac{2\alpha r}{c}t] + \varphi_0 - \varphi\right\}, 0 \le t \le T \tag{34.4}$$

34.3 Clutter Map CFAR Plane Detection

When radar is working, it stores the clutter echo amplitude coming from its surrounding area by azimuth and distance orderly, so the plane clutter map is established.

Assuming the azimuth dimension is divided into N azimuth units and the distance dimension is divided into M distance units, there are NM azimuth-distance units in the clutter map. Then, a storage which has NM addresses is needed to store the clutter data. Let the detection unit A be the center, the $p \times q$ units be the detection windows, and the others be the background clutter units. The detection windows will not participate in signal processing for preventing the detection signals from getting into the clutter background units area. The way of dividing azimuth-distance units is shown in Fig. 34.1.

The functional block diagram of CFAR plane detection is shown in Fig. 34.2. As can be seen, there are NM registers separately storing each data in the clutter map. Usually, the sliding window processing in the distance is done firstly. According to the requirements of the false alarm rate, the threshold factor can be set as a constant value C.

34.4 The Iteration Technique of Clutter Map

Since the clutter is strongly correlated, only utilizing the average and iteration processing of clutter amplitude of adjacent repeat period to improve the SCR is not obviously effective. However, the interval of different antenna scan is much longer, so the clutter correlation of different scan is very weak, and thus the iteration of clutter map will improve the SCR effectively [6].

The clutter data $C_{n,m}$ of each position-distance unit equals to the mean of all sample data in this position-distance unit. Assuming there is j echo sampling data in one position-distance unit, then

$$C_{n,m} = \frac{1}{j}\sum\nolimits_0^j x_{n,m}(i) \tag{34.5}$$

Let L denote the Lth antenna scanning period, then the clutter data $C_{n,m}(L)$ of different period is time-varying, due to the random characteristics of radar clutter. As a result, the clutter map should be updated along with the antenna scanning.

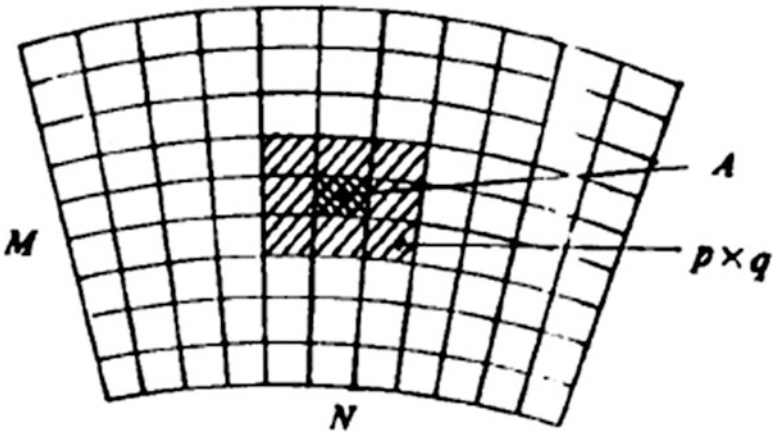

Fig. 34.1 The way of dividing position-distance unit

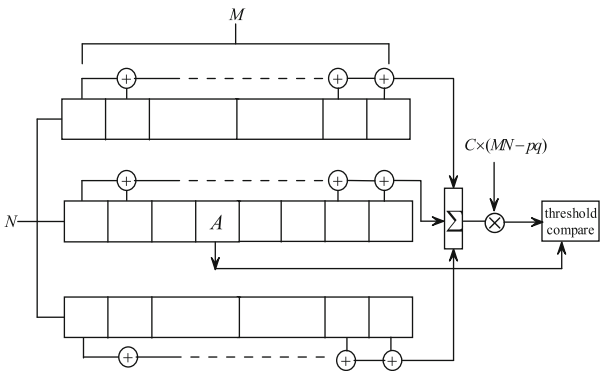

Fig. 34.2 Functional block diagram of plane CFAR detection

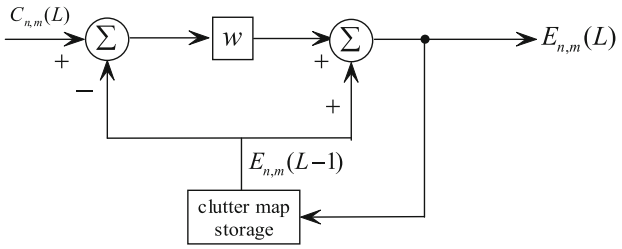

Fig. 34.3 First-order recursive filter

In order to reduce the computational complexity, the data iteration update of clutter map is usually realized by a first-order recursive filter, as shown in Fig. 34.3.

In Fig. 34.3, L and L-1 denote the current and the previous antenna scan cycle, respectively, the output delays than the input by an antenna scan cycle, and the

weighted factor w is a number which greater than 0 and less than 1. The iteration equation can be obtained from Fig. 34.3 as below.

$$E_{n,m}(L) = \omega[C_{n,m}(L) - E_{n,m}(L-1)] + E_{n,m}(L-1) \tag{34.6}$$

34.5 Performance Analysis

Assuming the signal to clutter ratio (SCR_i) before iteration is s^2/σ^2, where s is the target amplitude, and the clutter amplitude obeys Weibull distribution, with the variance σ^2 and mean value μ. According to (34.6), the mean value μ_1 and variance σ_1 of $E_{n,m}(L)$ after iteration could be expressed as:

$$\mu_1 = \omega\mu + (1-\omega)\mu \tag{34.7}$$

$$\sigma_1^2 = \omega^2\sigma^2 + (1-\omega)^2\sigma^2 \tag{34.8}$$

It can be seen that, as the increasing of iteration times, the mean value of iteration data remains unchanged, but the variance reduces continuously. It shows the SCR will be improved after L times iteration, and the improvement factor of SCR I(dB) is:

$$I = 10\lg\frac{SCR_O}{SCR_i} = 10\lg(2-\omega) - 10\lg[\omega + 2(1-\omega)^{2L+1}] \tag{34.9}$$

where SCR_o is the SCR after iteration.

Figure 34.4 shows the relationship between ω and I, if the iteration times are enough, I will be more better. But with the increase of the iterations, the computational complexity of signal processing will greatly increase, so the iterations can't be too great. In addition, it can be seen from Fig. 34.4 that for each value of I, there is a peak value on the curve, so we can choose the value of ω corresponding to the peak value of I to make the SCR greatest.

34.6 FOD Detection Simulation

In the simulation, the detection unit distance is 200 m, $f_0 = 77$ GHz, $B = 800$ MHz, $T = 3$ ms. Assuming the clutter amplitude before iteration obey Weibull distribution, the input $SCR_i = 3$ dB, let false alarm ratio $P_f = 10^{-4}$, so the threshold factor $C = 3.3$, threshold $Th = 6.6$, so we can obtain the detection probability $P_d = 0.36$, it means P_f is smaller, the false dismissal probability is greater, this detection performance could not meet requirement. Figure 34.5 gives the signal and clutter distribution before iteration.

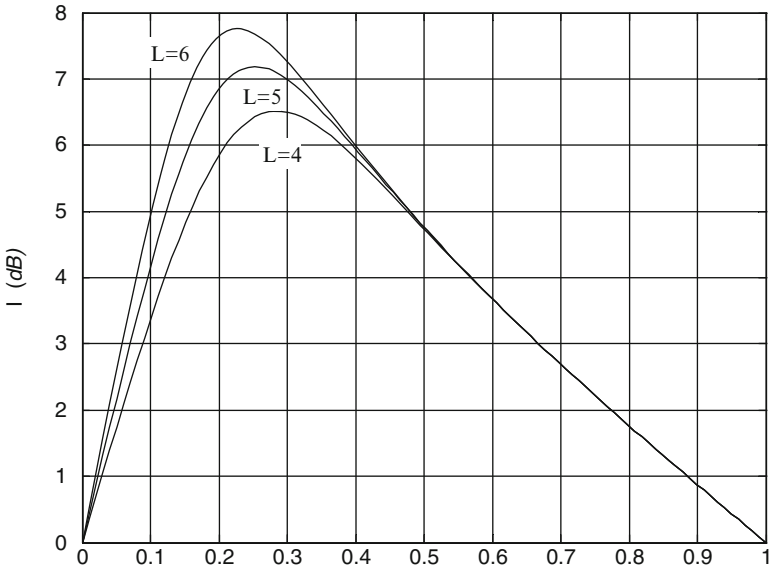

Fig. 34.4 The relationship between ω and *I*

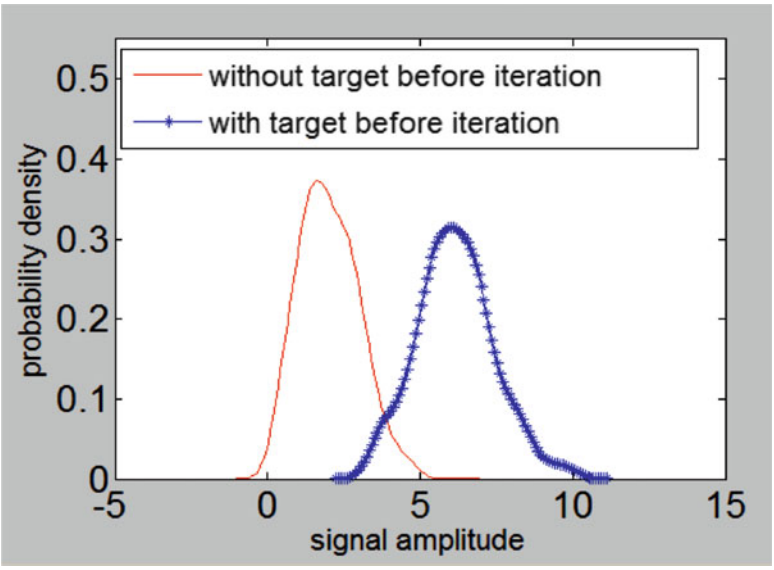

Fig. 34.5 Signal and clutter distribution before iteration

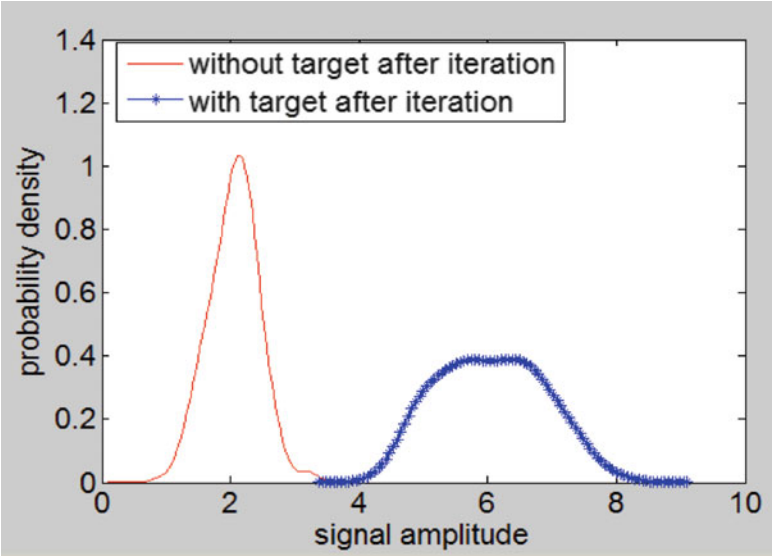

Fig. 34.6 Signal and clutter distribution after iteration

Figure 34.6 shows the signal and clutter distribution after 6 times iteration with $\omega = 0.25$. Obviously, the variance of echo amplitude in both situations without and with target reduces greatly. At this time, let the same false alarm ratio $P_f = 10^{-4}$, then the threshold factor is $C = 1.8$, the threshold is $Th = 3.8$, and the detection probability P_d could reach 0.98. So we may conclude that the system detection performance will be improved effectively after several iterations.

34.7 Conclusion

The basic task of FOD detection is how to find small target under strong clutter background. The clutter map CFAR plane technique is very suitable to the clutter situation which is homogeneous both temporally and spatially. In this chapter, the principle of the clutter map CFAR plane technique is detailed and the detection performance is analyzed at first. Then, the technique is applied to airport runway FOD detection based on millimeter-wave linear frequency modulated continuous wave (LFMCW) radar. It can be seen from the simulation result that the detection probability can be improved effectively by using the clutter map CFAR plane technique in low SCR situation.

Acknowledgments This work is partially supported by the National Natural Science foundation of China (No. 61139003) and the Fundamental Research Funds for the Central Universities (No. ZYGX2010J022).

References

1. Mazouni K, Kohmura A, Futatsumori S, et al (2010) 77GHz FMCW Radar for FODs detection. In: Proceedings of the 7th european radar conference, EuMA, Paris, pp 451–454
2. Essen Helmut, Luedtke Goert, et al (2010) Millmeterwave radar network for foreign object detection. In: Proceedings of the international workshop on cognitive information ElbaIslan, pp 7–10
3. Wu Shun Jun (2008) Radar signal processing and data processing technology. Publishing House of electronics industry p 168
4. He You (2001) The review of radar automatic detection and CFAR processing methods. Syst Eng Electron (11):9–15
5. He You, Liu Yong, Meng Xiang wei (1999) Performance of clutter map CFAR plane technique in homogeneous background. Acta Electronica Sinica 27(3)
6. Shen Fuming AN (1996) approach of CFAR plane detection of radar targets based on integration of clutter image. Syst Eng Electron (7):9–14. K. Elissa, “Title of paper if known, (unpublished)

Chapter 35
An Approach to the Modulation Recognition of MIMO Radar Signals

Xiaojing Wang, Ying Xiong, Bin Tang, and Yunhao Li

Abstract The modulation recognition is of great significance in the electronic reconnaissance. This chapter presents a modulation recognition method for the emerging multiple-input multiple-output (MIMO) radar signals. Signals of interest are classified into three categories based on instantaneous correlation spectrum analysis first. Then none coding MIMO radar signals are discriminated by spectrum analysis, and coding MIMO radar signals are recognized by source number estimation algorithm. Simulation results verify the effectiveness of the method and the overall correct recognition rate is over 90 % when SNR is above 0 dB.

Keywords Modulation recognition • MIMO radar signal • Instantaneous autocorrelation spectrum • Source number estimation

35.1 Introduction

The concept of MIMO radar has drawn considerable attention in recent years [1]. MIMO radar offers quite a lot of advantages, such as more degrees of freedom, higher resolution and sensitivity and better parameter identifiability [2–4]. These advantages mostly result from waveform diversity. Due to the waveform diversity, the intercepted signals are multi-carrier signals. Accordingly, the detection, parameter estimation and modulation recognition are vastly different from single-carrier (SC) signals adopted by conventional radars. As a result, it poses an emerging and powerful challenge in electronic countermeasures.

X. Wang (✉) • Y. Xiong • B. Tang • Y. Li
School of Electronic Engineering, University of Electronic Science and Technology of China, Chengdu 611731, People's Republic of China
e-mail: wangadlinna@yahoo.com.cn

Q. Liang et al. (eds.), *Communications, Signal Processing, and Systems*, Lecture Notes in Electrical Engineering 202, DOI 10.1007/978-1-4614-5803-6_35,

The main topic of this chapter is the modulation recognition of MIMO radar signals based on instantaneous autocorrelation spectrum. Four basic modulation types [5–7] are involved: MP-MIMO (orthogonal monopulse signal in MIMO radar), LFM-MIMO (orthogonal linear frequency modulation signal in MIMO radar), PC-MIMO (orthogonal phase-coded signal in MIMO radar) and FC-MIMO (orthogonal frequency-coded signal in MIMO radar). Besides, MIMO radar signals need to be discriminated from SC signals in conventional radar, such as monopulse (MP) signal, linear frequency modulation (LFM) signal, phase-coded (PC) signal and frequency-coded (FC) signal.

The rest of this chapter is organized as follows. In Sect. 35.2, the basic MIMO radar signal models are given and the recognition method is introduced. Instantaneous autocorrelation spectrum analysis, frequency spectrum analysis and source number estimation algorithm (SNEA) are involved in this section. Simulation results are given in Sect. 35.3 and conclusions are drawn in Sect. 35.4.

35.2 Recognition Method

Assuming that the transmitting arrays are uniform linear arrays, the MIMO radar signal models mentioned above are expressed as follows.

$$s_{MP-MIMO}[n] = \sum_{m=1}^{M} \exp\{j2\pi[f_0 + (m-1)f_p]t + j(m-1)\Delta\varphi\}|_{t=nT_s} \tag{35.1}$$

$$s_{LFM-MIMO}[n] = \sum_{m=1}^{M} \exp\{j2\pi[f_0 + (m-1)f_p + \frac{1}{2}ut]t + j(m-1)\Delta\varphi\}|_{t=nT_s} \tag{35.2}$$

$$s_{PC-MIMO}[n] = \sum_{m=1}^{M}\sum_{i=1}^{I} \exp[j2\pi f_0 t + j\phi_m(i) + j(m-1)\Delta\varphi]g(t-iT_1)|_{t=nT_s} \tag{35.3}$$

$$s_{FC-MIMO}[n] = \sum_{m=1}^{M}\sum_{i=1}^{I} \exp\{j2\pi[f_0 + f_m(i)]t + j(m-1)\Delta\varphi\}g(t - iT_1)|_{t=nT_s} \tag{35.4}$$

where M is the number of MIMO sub-carriers, f_0 is the carrier frequency, $f_p = 1/T$ and $\Delta\varphi$ denote the frequency interval and phase difference between adjacent sub-carriers respectively, u denotes the chirp rate, I is the code length of coding signal, $T_s = 1/f_s$ is the sampling interval and f_s is the sampling rate. $\phi_m(i) \in \{0, \frac{2\pi}{L}, \cdots, (L-1)\cdot\frac{2\pi}{L}\}$ and $f_m(i) \in \{0, \frac{1}{T_1}, \cdots, (N-1)\cdot\frac{1}{T_1}\}$ denote the phase and frequency of subpulse i of the m th component respectively. L is the distinct phase

number in PC-MIMO, T and T_1 represent the pulse and subpulse width respectively, $g(t), 0 \le t \le T_1$ is the envelope function. Particularly, to ensure the orthogonality of components, $\phi_m(i)$ and $f_m(i)$ are obtained by intelligent algorithm, such as genetic algorithm and simulated annealing algorithm.

The rest of this section is divided into three parts. For the sake of convenience, S set is employed: S = {MP-MIMO, LFM-MIMO, PC-MIMO, FC-MIMO and SC signals}. The first part classifies S set signals into three categories: S0 = {SC signals}, none coding MIMO radar signals S1 = {MP-MIMO, LFM-MIMO} and coding MIMO radar signals S2 = {PC-MIMO, FC-MIMO}. S1 and S2 sets signals are recognized in second and third parts respectively.

35.2.1 Instantaneous Autocorrelation Spectrum Analysis

The instantaneous autocorrelation function is define by

$$r[n, \Delta m] = s[n + \Delta m]s^*[n] \tag{35.5}$$

Let $\Delta m = 1$, then the instantaneous autocorrelation of LFM-MIMO signal is

$$r_{LFM-MIMO}[n, 1] = \sum_{m=1}^{M}\sum_{l=1}^{M} \exp[j2\pi\frac{f_0 + f_p(kn + m - 1)}{f_s} + j\pi u\frac{2n+1}{f_s^2} + jk\Delta\varphi] \tag{35.6}$$

Where $k = m - l, |k| \le M - 1$. If $k = 0$, the signal term is get as $\exp\left(j2\pi\frac{f_0}{f_s} + j\pi u\frac{2n+1}{f_s^2}\right)\sum_{m=1}^{M}\exp\left(j2\pi\frac{(m-1)f_p}{f_s}\right)$. If $k \ne 0$, the cross term is obtained as $\exp\left(j2\pi\frac{f_0+kf_pn}{f_s} + j\pi u\frac{2n+1}{f_s^2} + jk\Delta\varphi\right)\sum_{m=|k|+1}^{M}\exp(j2\pi\frac{(m-1)f_p}{f_s})$.

Figure 35.1b shows the instantaneous autocorrelation spectrum of LFM-MIMO signal. The maximum peak results from signal term while other peaks are from cross terms. From the above, the modulus of signal term and cross term are $\left|\frac{\sin(M\pi f_p/f_s)}{\sin(\pi f_p/f_s)}\right|$ and $\left|\frac{\sin[(M-|k|)\pi f_p/f_s]}{\sin(\pi f_p/f_s)}\right|$, respectively. If $|k| = 1$, it is the biggest cross term and appears as the second peak in correlation spectrum.

Thus the ratio of second peak and maximum peak is

$$R_{Amplitute} = \left|\frac{\sin[(M-1)\pi f_p/f_s]}{\sin(M\pi f_p/f_s)}\right| \tag{35.7}$$

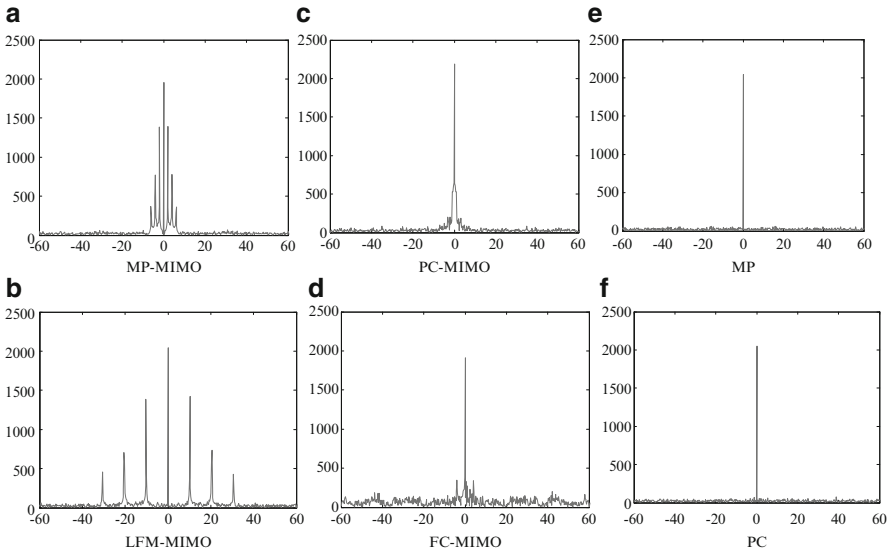

Fig. 35.1 Instantaneous autocorrelation spectrum of S set signals (x-axis denotes frequency, y-axis denotes amplitude. Simulation MIMO radar has four transmitting antennas and SNR = 5 dB)

If $u = 0$, (35.6) is the instantaneous autocorrelation of MP-MIMO. Therefore, MP-MIMO and LFM-MIMO have the same values of $R_{Amplitute}$. Comparing Fig. 35.1a, b, the fact that the values of maximum peak are the same is verified. Given the value ranges of parameters in (35.7), the minimum value of $R_{Amplitute}$ can be obtained.

For PC-MIMO and FC-MIMO, substituting (35.3) and (35.4) into (35.5) respectively, the instantaneous autocorrelation functions are as follows

$$r_{PC-MIMO}[n,1] = \exp\left(j2\pi\frac{f_0}{f_s}\right)\sum_{m=1}^{M}\sum_{l=1}^{M}\exp\{j[\phi_m^{n+1} - \phi_l^n + (m-l)\Delta\varphi]\} \quad (35.8)$$

$$r_{FC-MIMO}[n,1] = \exp\left(j2\pi\frac{f_0}{f_s}\right) \times \sum_{m=1}^{M}\sum_{l=1}^{M}\exp\left[j2\pi\frac{(f_m^{n+1} - f_l^n)n + f_m^{n+1}}{f_s} + j(m-l)\Delta\varphi\right] \quad (35.9)$$

where the superscript of ϕ and f denotes the location of code. The instantaneous autocorrelation spectrums of PC-MIMO and FC-MIMO signals are showed in Fig. 35.1c, d respectively. As can be seen, most of the energy gathers at the zero frequency while some appears at low frequencies, which result from mutations of the codes for PC-MIMO signal and frequency intervals as well as mutations for FC-MIMO signal. As a result, the values of $R_{Amplitute}$ for coding MIMO radar signals

are very small, and are definite less than the value of none coding MIMO signals. The same to the SC signals, which can be seen in Fig. 35.1e, f. Thus taking $R_{Amplitute}$ as feature parameter, S1 signals are discriminated from S0 and S2 set.

Let $\Delta m = 0$, then $r[n,0] = s[n]s^*[n]$. The positive spectrum of $r[n,0]$ is $R_{r[n,0]}[k] = |DFT(r[n,0])|, k = 1,2,\ldots,N_{DFT}/2$, where N_{DFT} is the points of Discrete Fourier transform (DFT). Then we divide it into two segments: the low frequency segment $R1_{r[n,0]}[k], k = 1,2,\ldots,N1$, and the rest part $R2_{r[n,0]}[k]$.

After that, we define the feature parameter R_{mean} as

$$R_{mean} = \frac{Mean(R1_{r[n,0]})}{Mean(R2_{r[n,0]})} \tag{35.10}$$

where $Mean$ is the mean function. Since $r_{SC}[n,0] = 1$ for SC signals, the frequency of $r_{SC}[n,0]$ is zero, which implies that $R1_{r[n,0]}$ and $R2_{r[n,0]}$ are only affected by noise. Thus R_{mean} approximately equals 1 in the additive white Gaussian noise (AWGN) condition. For coding MIMO radar signals, according to (35.3) and (35.4), there are a few mutations in $r[n,0]$. Hence they will lead to some low frequency components, and so the ratio R_{mean} is always greater than 1. This allows us to discriminate SC signals from coding MIMO radar signals.

In summary, setting proper thresholds γ and ς, the S set signals are classified.

$$R_{Amplitute} > \gamma \Rightarrow S_1; R_{Amplitute} < \gamma \Rightarrow \begin{cases} R_{mean} > \varsigma \Rightarrow S_2 \\ R_{mean} < \varsigma \Rightarrow S_0 \end{cases} \tag{35.11}$$

35.2.2 MP-MIMO/LFM-MIMO Selection

For a signal in S1 set, selecting two parts of signal and employing DFT on them, we have $S_a[k] = |DFT(s_a[n])|$ and $S_b[k] = |DFT(s_b[n])|$, where s_a is contained in s_b and the sampling length of s_b is greater than s_a. If the maximum value of S_a is noted by $Max(S_a)$, and the corresponding frequency number is $k_{\max}$, then the value of $S_b[k_{\max}]$ is obtained. We define the following feature parameter

$$\Delta S = Max(S_a) - S_b[k_{\max}] \tag{35.12}$$

The frequency of MP-MIMO signal is not affected by the time while LFM-MIMO signal is modulated along time. That is, for MP-MIMO signal, the energy at a frequency is increasing with the increase of sampling points while the LFM-MIMO is not, for the energy present at the new frequencies. Setting a proper threshold, MP-MIMO signal and LFM-MIMO signal are separated.

35.2.3 PC-MIMO/FC-MOMO Selection

Source number estimation algorithm is employed to recognize the signals in S2 set in this part. For the sake of convenience, only the first code length signal is chosen. We first construct the observation matrix

$$S_{ob} = \begin{bmatrix} s[1] & s[2] & \dots & s[N] \\ s[2] & s[3] & \dots & s[N+1] \\ \vdots & \vdots & \ddots & \vdots \\ s[1+Mr] & s[2+Mr] & \dots & s[N+Mr] \end{bmatrix},$$

and then get its autocorrelation matrix $R = S_{ob}S_{ob}^H/N$.

For PC-MIMO signal, we have $s_m[n+k] = \exp(j2\pi f_0 k)s_m[n]$. To simplify expressions, $T_s = 1$ is employed on the calculation. Let

$$\mathrm{A}_0 = \begin{bmatrix} 1 & 1 & \dots & 1 \\ e^{j2\pi f_0 1} & e^{j2\pi f_0 1} & \dots & e^{j2\pi f_0 1} \\ \vdots & \vdots & \dots & \vdots \\ e^{j2\pi f_0(M_r-1)} & e^{j2\pi f_0(M_r-1)} & \dots & e^{j2\pi f_0(M_r-1)} \end{bmatrix},$$

$$S_0 = \begin{bmatrix} s_1[1] & s_1[2] & \cdots & s_1[N] \\ s_2[1] & s_2[2] & \cdots & s_2[N] \\ \vdots & \vdots & \dots & \vdots \\ s_M[1] & s_M[2] & \cdots & s_M[N] \end{bmatrix} \tag{35.13}$$

As can be seen in (35.13), $S_{ob} = A_0S_0$, $R = A_0S_0S_0^HA_0^H/N$, and $rank(A_0) = 1$, where $rank(*)$ denotes the rank of matrix $*$. According to the nature of rank, it's easy to get that $rank(R) = 1$ for PC-MIMO signal.

For FC-MIMO signal, we have $s_m[n+k] = \exp\{j2\pi[f_0 + f_m(n)]k\}s_m[n]$. Let

$$\mathrm{A}_1 = \begin{bmatrix} 1 & 1 & \dots & 1 \\ e^{j2\pi(f_0+f_1)1} & e^{j2\pi(f_0+f_2)1} & \dots & e^{j2\pi(f_0+f_M)1} \\ \vdots & \vdots & \dots & \vdots \\ e^{j2\pi(f_0+f_1)(M_r-1)} & e^{j2\pi(f_0+f_2)(M_r-1)} & \dots & e^{j2\pi(f_0+f_M)(M_r-1)} \end{bmatrix} \tag{35.14}$$

where $f_1, f_2, \dots, f_M$ denote the first frequency code of each component. To ensure the orthogonality between components, the values of $f_1, f_2, \dots, f_M$ aren't equal. According to (35.14), we have $S_{ob} = A_1S_0$ and $R = A_1S_0S_0^HA_1^H/N$ for FC-MIMO signal, where S_0 has the same structure as (35.13). Substituting (35.4) into S_0, we can obtain that $rank(S_0) = M$. If $M_r > M$, then $rank(A_0) = M$, and so $rank(R) = M$ for FC-MIMO signal.

Here, Akaike Information Criterion [8] is adopted to calculate the rank of autocorrelation matrix. By comparing the rank of autocorrelation matrix with 1, PC-MIMO and FC-MIMO are discriminated.

35.3 Simulation and Analysis

Simulation results are shown in this section, The modulation types in S set, which are given by Ω_1 and Ω_2, are used to test the valid of the proposed approach.

$$\Omega_1 = \left\{ \begin{array}{l} \mathrm{MP}, LFM, \\ \mathrm{MP} - MIMO(4), LFM - MIMO(4), \\ PC - MIMO(4), FC - MIMO(4) \end{array} \right\}$$

$$\Omega_2 = \left\{ \begin{array}{l} \mathrm{PC}, FC, \\ \mathrm{MP} - MIMO(4), LFM - MIMO(8), \\ PC - MIMO(10), FC - MIMO(12) \end{array} \right\}$$

The figure following each MIMO radar signal denotes the number of sub-carriers. Suppose that the received signals are imbedded in complex AWGN and are rectangular pulse shape. Particularly, the experiments are operated on two different simulation conditions, which are showed in Table 35.1. where L is the distinct phase number of PC/PC-MIMO, T_{1PC} and T_{1FC} are the subpulse width of PC/PC-MIMO and FC/FC-MIMO respectively. The simulation results are based on 1,000 Monte Carlo trials for each modulation type and each SNR value. Particularly, we consider SC signals are correctly recognized when the simulation results are S0 set signal but not exact modulation type.

Figure 35.2 represents the final recognition results. As can be seen, the total recognition probability is over 90% when the value of SNR is as low as 0 dB. The results demonstrate that the modulation types are well recognized by suggested method.

This method presents an excellent performance for none coding MIMO radar signals, which is of high recognition rate even if the value of SNR is -5 dB. Comparing (a) with (c), the recognition performance is almost the same, which demonstrates that the sub-carrier number has little influence on the proposed

Table 35.1 Simulation parameters

Simulation parameters	f_0/MHz	f_s/GHz	T/us	$u/THz/s$	L	T_{1PC}/us	T_{1FC}/us
Condition 1	100	0.5	5	2	4	0.25	0.25
Condition 2	100	2	5	4	6	0.05	0.1

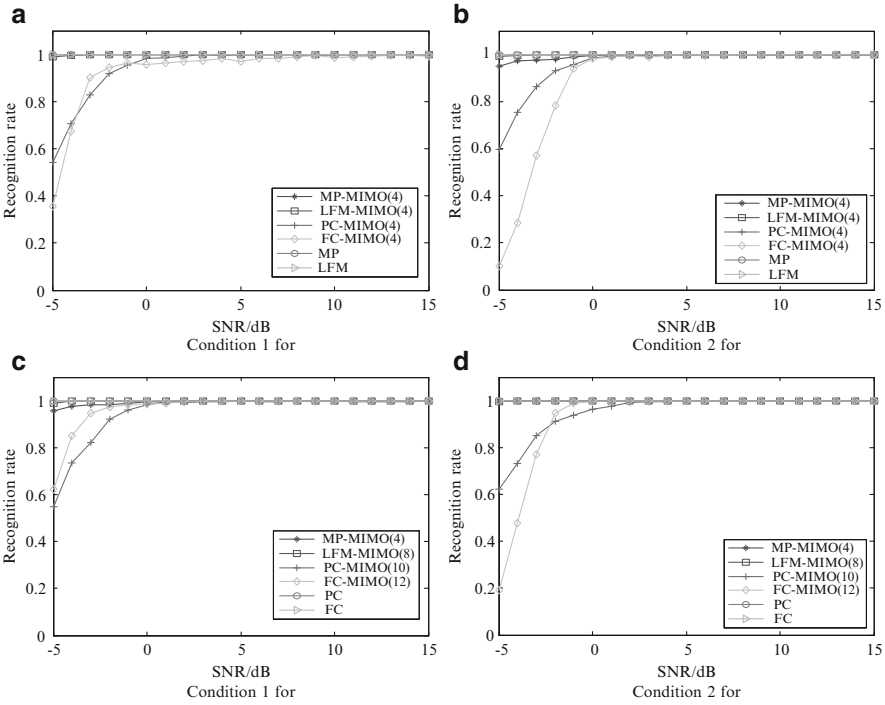

Fig. 35.2 Recognition rate versus SNR. (**a**) Condition 1 for Ω_1. (**b**) Condition 2 for Ω_1. (**c**) Condition 1 for Ω_2. (**d**) Condition 2 for Ω_2

method. This can also be illustrated by comparing (b) with (d). Comparing (b) with (a), the performance of FC-MIMO signal in low SNR slightly decreased, which results from high code rate. The same conclusion can be obtained from Fig. 35.2c, d.

35.4 Conclusion

An approach to recognize the modulation type of MIMO radar signals is presented in this chapter. Three feature parameters are proposed in the recognition method. First, the intercepted signal is classified based on autocorrelation spectrum. Then, taking advantage of the difference in frequency domain, MP-MIMO signal and LFM-MIMO signal are discriminated. At last, SNEA is employed to recognize PC-MIMO signal from FC-MIMO signal. Simulation results verify that the proposed method can extract the features of each modulation type, and effectively recognize the signals in the given set.

References

1. Li J, Stoica P (2008) MIMO radar signal processing. Hoboken, NJ
2. Bliss DW, Forsythe KW (2003) Multiple-input multiple-output (MIMO) radar and imaging: degrees of freedom and resolution. In: Conference record of 37th ACSSC, Asilomar, California, USA
3. Forsythe KW, Bliss DW, Fawcett GS (2004) Multiple-input multiple-output (MIMO) radar: performance issues. In: Conference Record of 38th ACSSC, Asilomar, California, USA
4. Jian L, Stoica P, Xu LZ, Roberts W (2007) On parameter identifiability of MIMO radar. LSP, IEEE 14(12):968–971
5. Liu B, He ZS, Zeng JK, Liu BY (2006) Polyphase orthogonal code design for MIMO radar systems. In: Proceedings of CIE 2006 on Radar, Shanghai, China
6. Liu B, He ZS (2008) Orthogonal discrete frequency-coding waveform design for MIMO radar. Chinese J Electron 25(4):471–476
7. Liu B (2008) Research on generation of orthogonal waveform and signal processing for MIMO radar. Dissertation: University of Electronic Science and Technology (in Chinese)
8. Wax M, Kailath T (1985) Detection of signals by information theoretic criteria. IEEE Trans on ASSP 33(2):387–392

Chapter 36
Experimental Study of Through-Wall Human Detection by UWB Radar with Hilbert Huang Transform

Ashith Kumar, Qilian Liang, Zhuo Li, Baoju Zhang, and Xiaorong Wu

Abstract The detection of human targets hidden by walls or rubble, trapped in buildings is of interest for rescue, surveillance and security operations. In this paper, ultra-wideband (UWB) radar and its detection application are studied. Experiments on target detection of through-wall human being are carried out in two scenarios: through-gypsum-wall, and through-wooden-door, and the UWB radar used in these experiments is PulsOn 220 in monostatic mode. Detection of through-wall human beings with the UWB radar is based on movement detection – respiratory motions and movement of body parts. So Hilbert Huang Transform (HHT) is employed as the detection technique, and the breathing information of human target is contained in the third intrinsic mode function (IMF 3). The experimental results for human target detection behind gypsum wall and wooden door are separately demonstrated.

Keywords Human detection • UWB radar • Hilbert Huang Transform • Intrinsic mode function

36.1 Introduction

UWB radars, which transmit signals across a much wider frequency than conventional radar systems and are usually very difficult to detect, are used for several applications such as subsurface sensing, classification of aircrafts, collision avoidance, as well as target detection. The transmitted signal is significant for its very

A. Kumar (✉) • Q. Liang • Z. Li
Department of Electrical Engineering, University of Texas at Arlington, Arlington, TX, USA
e-mail: ashith.kumar@mavs.uta.edu; liang@uta.edu; zhuo.li@mavs.uta.edu

B. Zhang • X. Wu
College of Physics and Electronic Information, Tianjin Normal University, Tianjin, China
e-mail: wdxyzbj@mail.tjnu.edu.cn; wu.xiaorong@sohu.com

Q. Liang et al. (eds.), *Communications, Signal Processing, and Systems*, Lecture Notes in Electrical Engineering 202, DOI 10.1007/978-1-4614-5803-6_36,

light power spectrum. The most common technique for generating a UWB signal is to transmit pulses with very short durations (less than 1 ns). UWB technology is favored for these applications due to its inherent property of ultra-high resolution and the ability to penetrate most of the non-metallic building materials such as bricks, wood, dry walls, concrete and reinforced concrete.

Detection of human beings with radars is based on movement detection – respiratory motions and movement of body parts. These motions cause changes in frequency, phase, amplitude and periodic differences in time-of-arrival (ToA) of scattered pulses from the target, which are result of periodic movements of the chest area of the target [8].

HHT has been employed for target detection [4, 6], which is a technique to decompose nonlinear and non-stationary signals. The IMFs which contain the micro-Doppler information can be extracted, and specifically, the respiratory infomation of human target is contained in IMF 3.

This paper focuses on the study of UWB radar for target detection, and the experiments on through-wall human being detection using HHT detection method. Due to the effect of dielectric constant of the obstacles, human target are detected through both gypsum wall and wooden door using UWB radar PulsOn 220.

The rest of this paper is organized as follows. Section 36.2 introduces the preliminary knowledge, which are UWB signal and target detection using UWB radar, the hardware equipment used in these experiments-PulsOn 220. The measurement locations are presented in Sect. 36.3, including gypsum wall and wooden door environment. Section 36.4 proposes the detection methods of HHT. Based on the presented experimental environment and target detection method, the experimental results are shown in Sect. ??, followed with the conclusion in Sect. 36.6.

36.2 UWB Radar for Human Detection

36.2.1 Ultra-Wideband (UWB) Signal

The Federal Communication Commission (FCC) defines that any wireless communication technology that produces signals with a bandwidth wider than 500 MHz or a fractional bandwidth greater than 0.2 can be considered as UWB[3], where the fractional bandwidth is defined as:

$$\eta = 2 \times \frac{f_H - f_L}{f_H + f_L} \tag{36.1}$$

where f_L and f_H are the lower bond and upper bond of the spectral frequency of UWB radio.

Two types of UWB technologies are commonly used: impulse radio UWB (IR-UWB) and multiband OFDM UWB (MB-OFDM UWB). In this paper,

IR-UWB technique is employed, which uses short pulses in time domain but occupies a large bandwidth in frequency domain. The most frequently used pulse is Gaussian pulse and its derivatives, i.e., first and second derivatives of Gaussian pulse, which are referred to as *Gaussian Monocycle*.

This approach has a potential to produce signal which has higher immunity to interference effects and improved ToA resolution. Furthermore, according to electromagnetic theory, lower frequencies have better penetrating properties. The combination of larger spectrum and lower frequencies possessed by IR-UWB makes it suitable for ground penetrating radar, foliage penetrating radar and short range radar to detect hidden objects behind walls. This penetration property is also of great importance for indoor geolocation systems[1].

36.2.2 Target Detection Using UWB Radar

The basic principle of target detection by UWB radar is shown in Fig. 36.1. UWB radar generates and transmits short pulse through the transmit antenna TX. When the signal meets target, the part of the electromagnetic energy is reflected from the object and propagates back to receive antenna RX.

36.2.3 UWB Radar PulsON 220 in Monostatic Mode

In this paper, UWB radar PulsON 220 manufactured by Time Domain Corporation was used for through-wall human being detection, as shown in Fig. 36.2. The most commonly used waveforms for UWB signals are Gaussian pulses and their derivatives in time domain which are referred to as Gaussian Monocycle. PulsON 220 generates a series of first order Gaussian monopulse for short pulse transmission, which correspondingly occupies a large bandwidth in frequency domain. Figure 36.3 illustrates the spectrum of UWB pulse in PulsOn 220 with raw data rate of 9.6 MHz and center frequency of 4.3 GHz. It is noteworthy that at 9.6 MHz of data rate, the maximum unambiguous range (distance where a pulse sent/returned and the next pulse sent do not overlap) is approximately 50 ft [7].

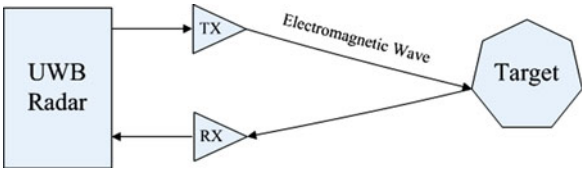

Fig. 36.1 Principle of target detection by UWB rada

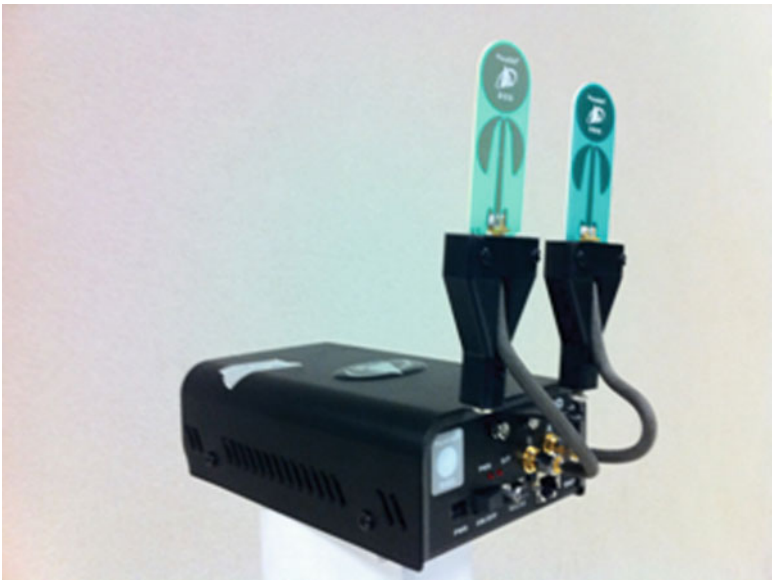

Fig. 36.2 UWB radar PulsON220

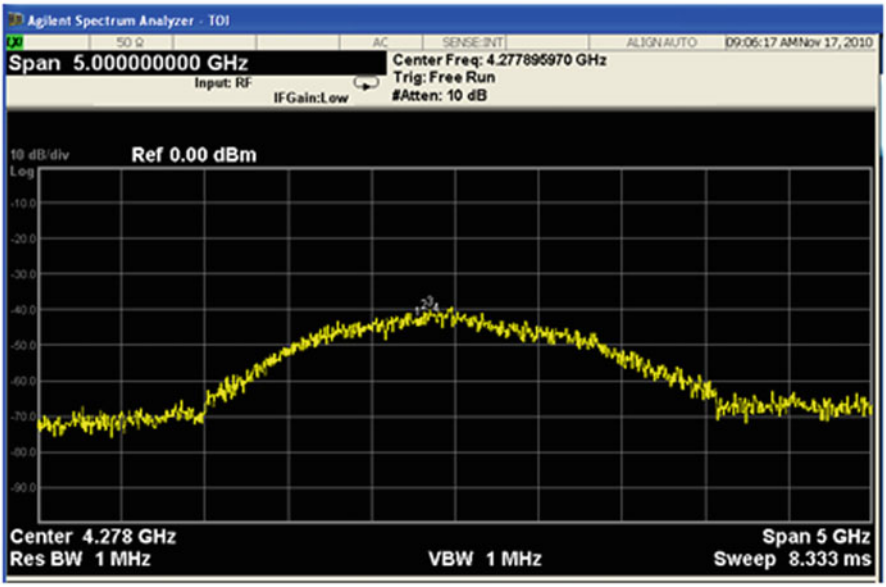

Fig. 36.3 Spectrum of UWB pulse in PulsON220

36.3 Experimental Environment

When radar signals penetrate various obstacles, the attenuation rate is highly related with the qualities of the materials[5], which is mathematically a function of the dielectric constant of the materials. Metal walls are fully reflective and thus detection through such walls is impossible using radar. However, most wall materials in use are wood, concrete, glass, and stone. In this paper, the measurements were taken at two locations at University of Texas at Arlington (UTA), where the obstacles are gypsum wall and wooden door separately.

36.3.1 Gypsum Wall

Figure 36.4 shows the location of the radar and human target on different sides of a $1'1''$ thick Gypsum partition wall. Person is at a distance of 3.5 ft from the radar on the other side of the wall and the height of the antennas from ground is $3'4''$. Other details related to room dimensions and objects in the room can be found in Fig. 36.4.

36.3.2 Wooden Door

Figure 36.5 illustrates the location of the radar and Human target on different sides of a $4''$ wooden door. Person is standing at a distance of 5.5 ft from the radar on the other side of the door and the height of the antennas from ground is $3'4''$. Other details related to room dimensions and objects in the room can be found in Fig. 36.5.

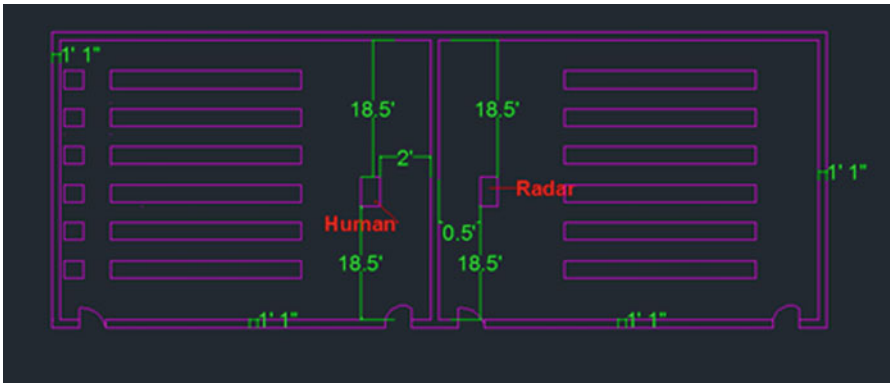

Fig. 36.4 Gypsum wall, location of radar and Human target

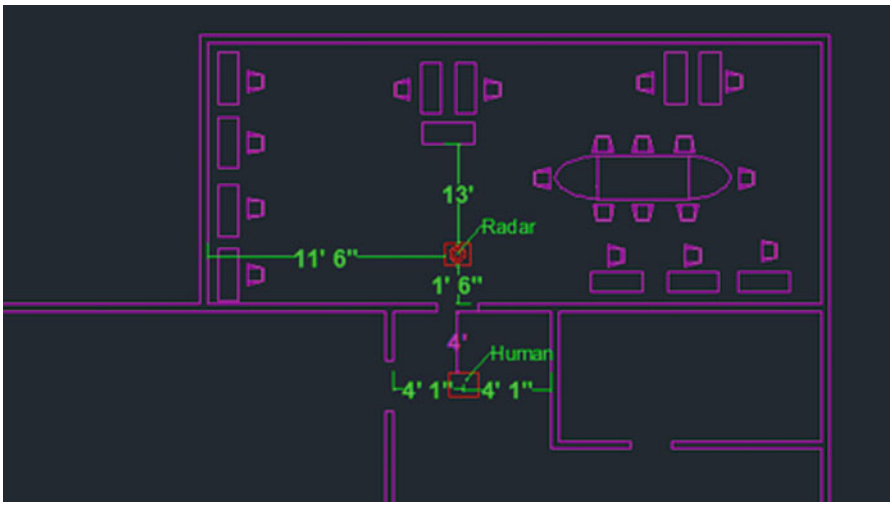

Fig. 36.5 Wooden wall, location of radar and Human target

36.4 Hilbert Huang Transform Detection Method

Breathing signature in radar response is caused by the minor (in comparison to walking) shift of body parts. These changes are extremely small for through-wall detection and certain techniques should be devised to extract these minute variations. Hilbert Huang Transform (HHT) is a technique to decompose nonlinear and non-stationary signals based on the combination of the empirical mode decomposition (EMD) and the Hilbert spectral analysis (HAS) [2, 4, 6]. The EMD identifies intrinsic oscillatory modes by their characteristic time scales in the data empirically. It separates the intrinsic mode functions (IMFs) from the original signal one by one, until the residue is monotonic. The original signal is thus decomposed into a finite and a small number of IMFs, where an IMF is any function with the same number of extrema and zero crossings, with symmetric envelopes. The flowchart of the decomposition process is described in [2]. The IMFs which contain the micro-Doppler information can be extracted and the IMFs which contain clutter and noise are discarded.

36.5 Experimental Results

Experiments are carried out in the two places as mentioned in Sect. 36.3 for human target detection by using UWB radar PulsOn 220. The Doppler signatures of respiration can only be seen in the IMFs, and specifically, IMF 3 contains

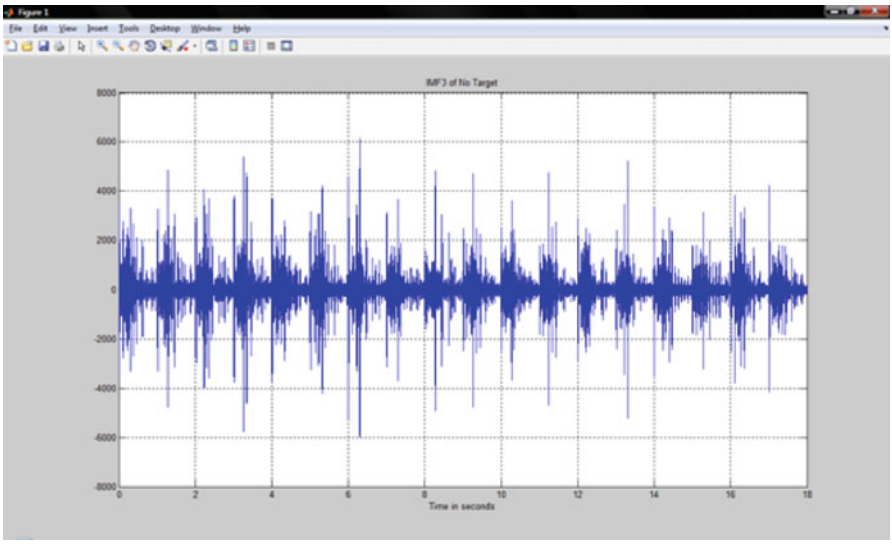

Fig. 36.6 IMF3 without Human target through gypsum wall

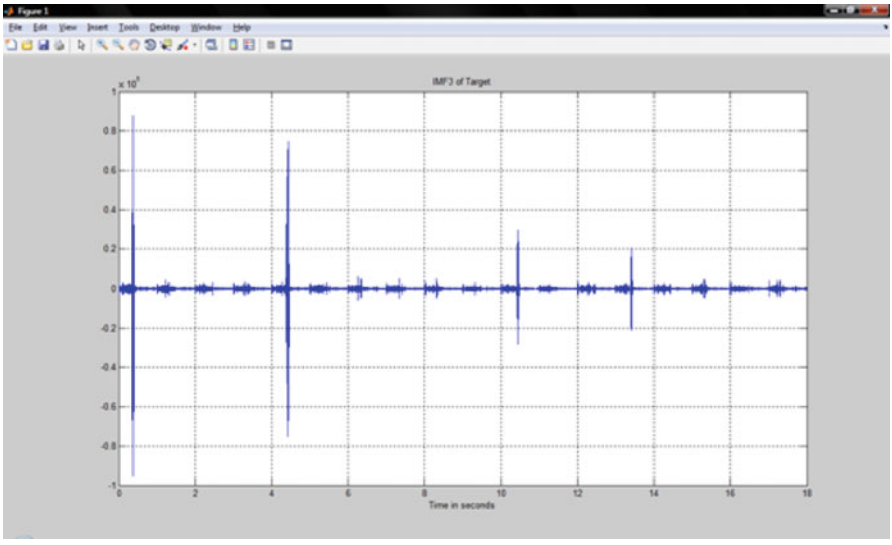

Fig. 36.7 IMF3 with Human target through gypsum wall (Peaks = 4 in 18 s)

the respiration information. Figures 36.6 and 36.7 show the experiment results of IMF 3 without and with human target through gypsum wall separately. For the case of wooden door environment, the experimental results are correspondingly illustrated in Figs. 36.8 and 36.9.

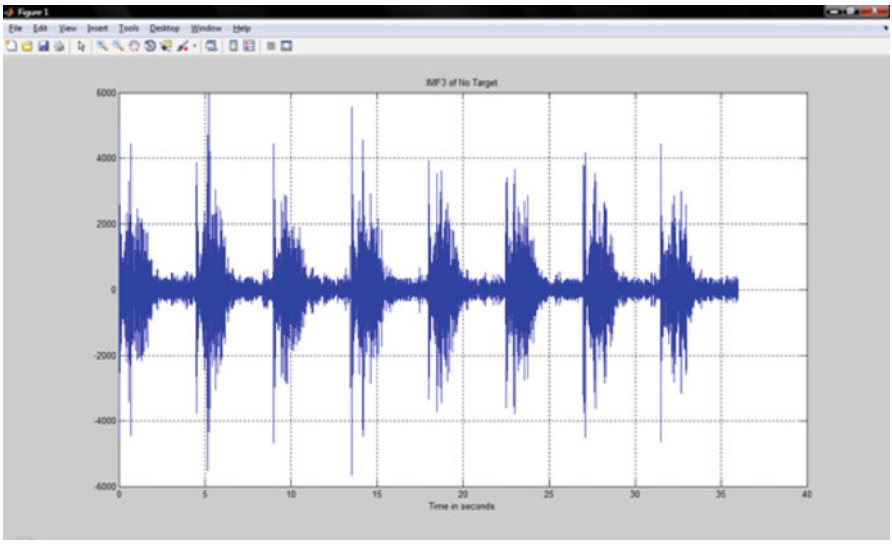

Fig. 36.8 IMF3 without Human target through wooden door

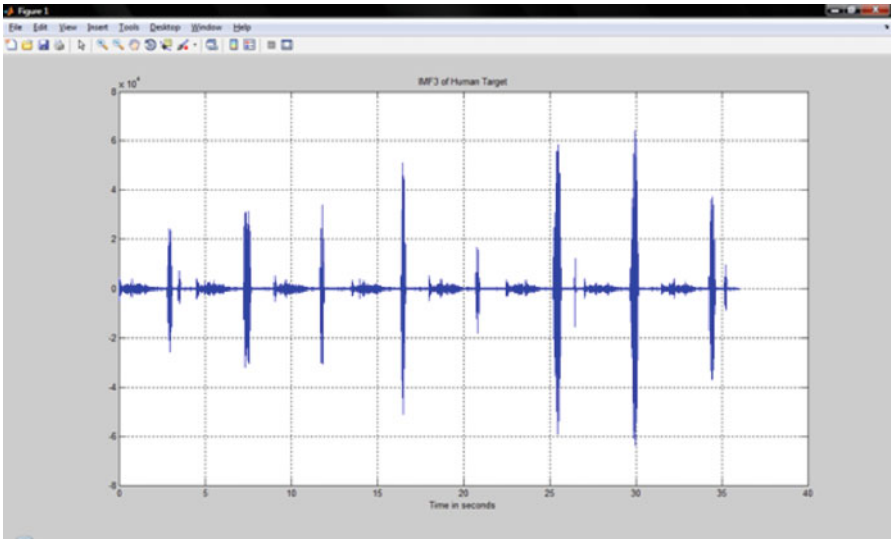

Fig. 36.9 IMF3 with Human target through wooden door (Peaks = 8 in 36 s)

36.6 Conclusion

In this paper, experiments on through-wall human being detection using UWB radar are carried out in two scenarios, which are through-gypsum-wall and through-wooden-door. The equipment used to carry out the experimental work is PulsON

220 UWB radar in monostatic mode. The detection method employed in these experiments is HHT, which is based on extracting Intrinsic Mode functions (IMF) and IMF3 is the signature of breathing Doppler. By employing HHT, the existence of through-wall human target can be clearly detected, but the drawback is that the range information cannot be deduced and is ambiguous.

References

1. Alabacak C (2002) Analysis of ultra wideband (UWB) technology for an indoor geolocation and physiological monitoring system. Master's Thesis, Air Force Institute of Technology
2. Huang NE, Shen Z, Long SR, Wu MC, Shih HH, Zheng Q, Yen NC, Tung CC, Liu HH (1998) The empirical mode decomposition and the Hilbert spectrum for nonlinear and non-stationary time series analysis. In: Proceedings of the royal society Of London series a – mathematical physical and engineering sciences, London, Great Britain, vol 454, March 1998, pp 903–995
3. Huseyin A, Zhining C, Benedetto D (2006) Ultra wideband wireless communication. Wiley, Hoboken, pp 10–11
4. Lai C-P, Ruan Q, Narayanan MR (2007) Hilbert-Huang transform (HHT) processing of through-wall noise radar data for human activity characterization. In: 2007 I.E. workshop on signal processing applications for public security and forensics, Washington D.C., USA, April 2007, pp 1–6, 11–13
5. Miller EL (2003) Why UWB ? A review of Ultra wideband Technology NETEX Project Office, DARPA
6. Narayanan MR (2008) Through-wall radar imaging using UWB noise waveforms. In: 2008 I.E. international conference on acoustics, speech and signal processing, Las Vegas, USA, March–April 2008, pp 5185–5188
7. Time Domain Corporation (2008) Monostatic radar (MSR) analysis tool application note
8. Yarovoy AG, Matuzas J, Levitas B, Ligthart LP (2009) UWB radar for human being detection. IEEE Aerosp Electr Syst Mag 23(5):36–40

Chapter 37
A Novel Pulse Compression Method for Weather Radar

Haijiang Wang, Zhao Shi, JianXin He, and Yiming Pi

Abstract Pulse compression is a classical topic. Because of its function in resolution enhancement, pulse compression technology has been applied in many kinds of radar such as pulse Doppler weather radar. In this chapter, a combination of two sidelobe suppression techniques for pulse compression is proposed. Simulation results show that the combination of the two techniques has better pulse compression effect.

Keywords Pulse compression • Sidelobe suppression • Weather radar

37.1 Introduction

Radar, serving as a kind of method for detecting, has wide-range application areas such as military, aviation, geosciences and so on. Pulse Doppler weather radar is an important device to detect clouds, wind fields, and precipitation so the resolution is very important for the forecasting of weather phenomena. In pulse Doppler radar, high range resolution can be achieved by pulse compression.

The foundation of pulse compression is matched filtering [1]. But for a radar pulse signal, after compression, the narrower pulse mainlobe always accompanied by higher sidelobe. In the multi-target circumstance, the output sidelobe of strong echoes can often submerge the mainlobe of weak ones; so in fact, a high sidelobe will impact the range resolution of weather radar. Therefore, sidelobe suppression

H. Wang (✉) • Z. Shi • J. He
College of Electronic Engineering, Chengdu University of Information technology, Chengdu, China

CMA. Key Laboratory of Atmospheric Sounding, Chengdu, China
e-mail: whj@cuit.edu.cn

Y. Pi
School of Electronic Engineering, University of Electronic Science and Technology of China, Chengdu, China

Q. Liang et al. (eds.), *Communications, Signal Processing, and Systems*, Lecture Notes in Electrical Engineering 202, DOI 10.1007/978-1-4614-5803-6_37,

is an important content of pulse compression technology. A −30 dB sidelobe is necessary in high performance radar systems. In pulse Doppler radar, there is more severe requirements for the sidelobe level.

In this chapter, compression experiments are conducted on a linear frequency modulation (LFM) sample signal extracted from a period of echo of a weather radar. In these experiments, some sidelobe suppression algorithms are used. The algorithms include multiplying window in frequency domain, phase distortion and frequency modification.

In Sect. 37.2, the data is analyzed and compression basing on matched filtering and windowed matched filtering are carried out. In Sect. 37.3, spectrum modification technique and phase predistortion technique are utilized respectively and the effects are analyzed. Then, the two technique are combined in Sect. 37.4. Experiments are conducted on the real weather echo and the effects are compared. Section 37.5 is the conclusion.

37.2 LFM Pulse and Matched Filtering Compression

A period of weather echo of a pulse Doppler radar is shown in Fig. 37.1. The sample rate of the echo is 4.8 MHz. The pulse width is 33.3 us and the spectrum width after linear frequency modulation is 2 MHz.

A section which is a whole LFM pulse signal is intercepted from the echo above. This LFM pulse, shown in Fig. 37.2, can be taken as the sample signal to do pulse compression. Its amplitude spectrum is shown in Fig. 37.3.

To analyze the frequency modulation quality of the pulse in Fig. 37.2, we extract the phase information and unwrap it. The phase before and after unwrapping are shown in Figs. 37.4 and 37.5 respectively.

Quadratic curve fitting is done on the phase, the fitting result is illustrated in Fig. 37.6.

We found that the phase and the fitting curve superpose each other. This indicates the linearity of the frequency is good and the pulse is a suitable LFM sample.

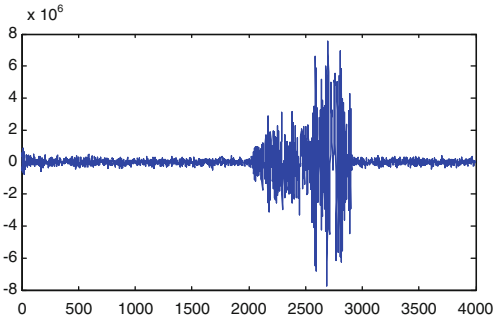

Fig. 37.1 A period of weather echo of a pulse Doppler radar

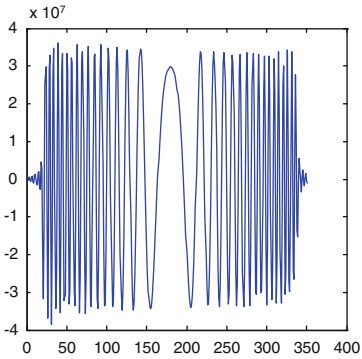

Fig. 37.2 The LFM pulse intercept from the echo

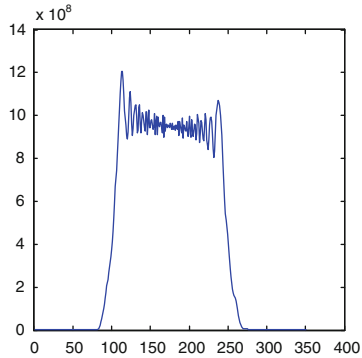

Fig. 37.3 The spectrum of the LFM pulse

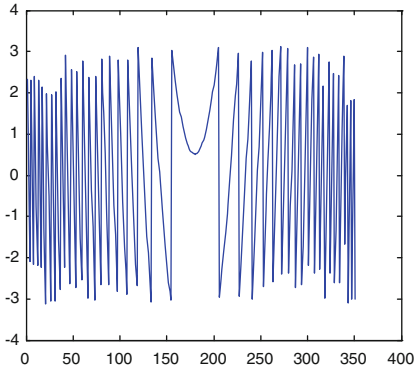

Fig. 37.4 The phase before unwrapping

Matched filtering [1] is carried out on the LFM pulse directly and the compression result is shown in Fig. 37.7

The amplitude of the first sidelobe is −17.4827 dB and the compression ratio is about 83.3.

A sidelobe of −17.4827 dB is not satisfying for most target detecting, because there will be serious range ambition if the sidelobe is too high.

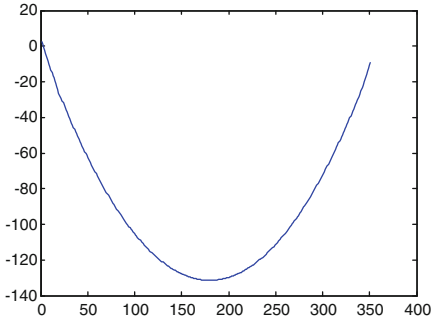

Fig. 37.5 The phase after unwrapping

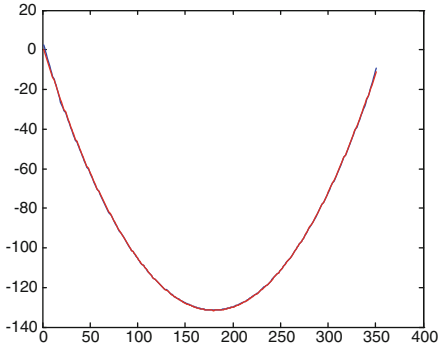

Fig. 37.6 Fitting of the phase

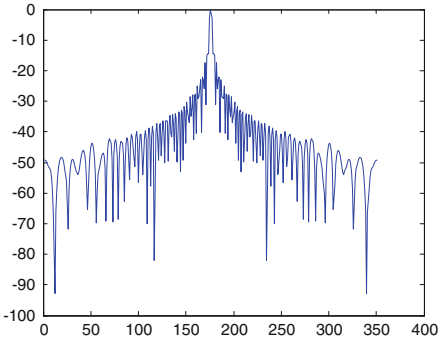

Fig. 37.7 Compression result by matched filtering

During matching filtering, multiplying a window in the frequency domain can suppress the sidelobe to a certain level. But in general, the lower sidelobe is often accompanied by a wider mainlobe after windowed matched filtering.

The general formation of a weighting window can be expressed as [2]:

$$H(f) = K + (1 - K)\cos^n\left(\frac{\pi f}{B}\right) \tag{37.1}$$

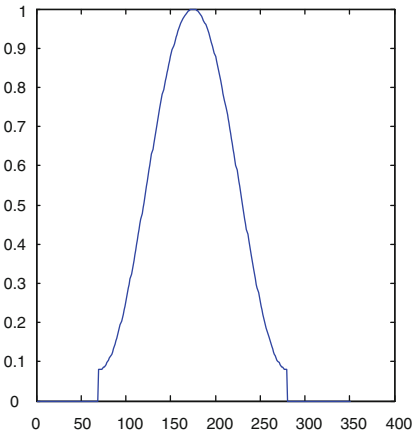

Fig. 37.8 The Hamming window

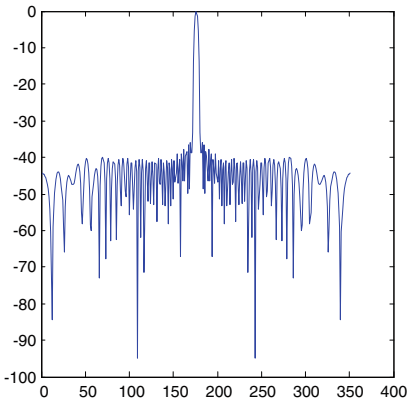

Fig. 37.9 Compression result by Hamming windowed matched filtering

When K = 0.08 and n = 2, the weighting function is a Hamming window; when K = 0.333 and n = 2, the function is a 3:1 taper weighting; when K = 0 and n = 2,3,4 respectively, the function are cosine square, cosine cube, and cosine quartic weighting.

Weighting the LFM pulse in frequency domain with a Hamming window, the window and the compressed pulse after matched filtering are shown in Figs. 37.8 and 37.9.

It can be seen from Fig. 37.9 that the sidelobe is suppressed to the level of −37 dB. From theoretical analysis we can educe that the mainlobe broaden to 1.47 times of the one before windowing.

For Doppler weather radar, to enhance the accuracy of weather target detecting, a lower sidelobe is needed. So, further improvements of pulse compression effects are demanded.

37.3 Sidelobe Suppression by Phase Predistortion and Spectrum Modification

For a LFM signal with little time-band (TB) product, the cubic phase predistortion technique can be used to suppress the sidelobe [3, 4]. The signal with little TB product has large ripples in its spectrum band, so widowing is not satisfying for sidelobe suppression. In this situation, the sidelobe suppression can be achieved by suppressing the ripples in band through phase predistortion. This method is easy to implement with surface acoustic wave (SAW) technique.

Suppose the complex expression of the LMF signal to carry out phase predistortion on is:

$$s(t) = \exp\left[j2\pi\left(f_0 t + \frac{B}{2T}\cdot t^2 + \varphi(t)\right)\right], \quad -T/2 - \Delta T \le t \le T/2 + \Delta T \tag{37.2}$$

where f_0 is the central frequency and B is the bandwidth. And the duration of the pulse is T. Then the additional phase item can be

$$\varphi(t) = \begin{cases} \dfrac{\Delta B}{3\Delta T^2}\cdot(-t - T/2)^3, & -T/2 - \Delta T \le t < -T/2 \\ \dfrac{\Delta B}{3\Delta T^2}\cdot(t - T/2)^3, & T/2 < t \le T/2 + \Delta T \\ 0, & \textit{elsewhere} \end{cases} \tag{37.3}$$

where $\Delta T = 1/B$ and $\Delta B = 0.75B$ [3].

The spectrum of the pulse after phase predistortion is shown in Fig. 37.10 and after multiplying a Hamming window, the predistorted spectrum is illustrated as Fig. 37.11.

After matched filtering, the effect of pulse compression is shown in Fig. 37.12

Figure 37.12 demonstrated that the sidelobes neighboring to the mainlobe are suppressed well (3–4 dB) through matched filtering after phase-predistortion. But in

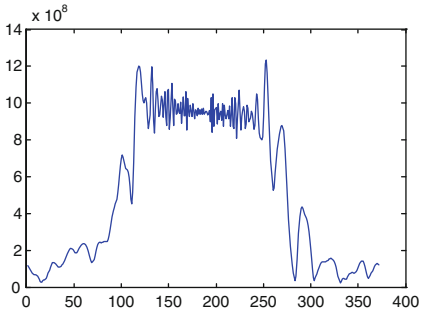

Fig. 37.10 Spectrum after phase predistortion

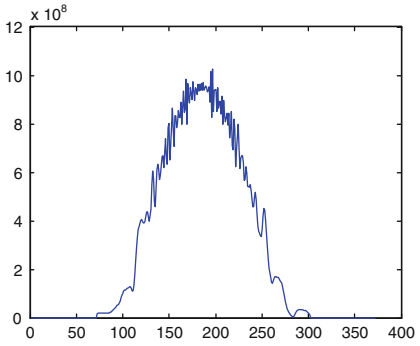

Fig. 37.11 Windowed spectrum after phase predistortion

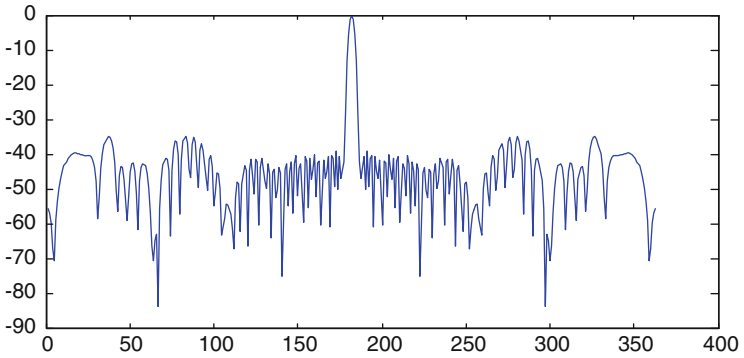

Fig. 37.12 Compression result by windowed matched filtering after phase predistortion

the positions away from the mainlobe, there are some sidelobe hunches and this may bring range ambiguity of two targets far away from each other.

In ideal situation, the output of the matched filter for a LFM signal has rectangular spectrum. After weighting, the rectangular spectrum becomes a certain window. But when the TB product of the LFM signal is small, its ripples in band are large, so the weighting has little effects for ripple suppression in band. In this case, spectrum modification technique can be resorted to make the processed spectrum approaches ideal window function mostly [5, 6] and to enhance the main-to-side lobe ratio.

Spectrum modification can be implemented by modify the transfer function of the matched filter. Suppose the spectrum of the LFM signal is $U(f)$ and the transfer function is $H(f)$, to make the output of the matched filtering to be a rectangular, it is needed that:

$$U(f)H(f) = I(f)I^*(f),\ I(f) = rect(f/B) \tag{37.4}$$

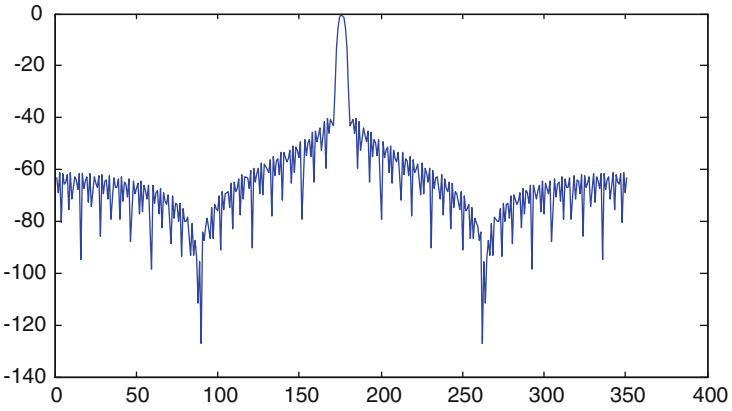

Fig. 37.13 Compression result by windowed matched filtering after spectrum modification

The modified transfer function of the matched filter is:

$$H(f) = U^*(f)[I(f)I^*(f)/|U(f)|^2] \tag{37.5}$$

The pulse compression result after using spectrum modification is shown in Fig. 37.13.

From Fig. 37.13, it can be seen that spectrum modification technique has good suppression effect for the sidelobes neighboring the mainlobe. What is the most important, this technique bring a great advantage that suppress the sidelobes far away from the mainlobe to the level under −62 dB.

It is stressed that both phase predistortion and spectrum modification didn't spread the mainlobe apparently.

37.4 Combination of Phase Predistortion and Spectrum Modification

From the simulation results in Sect. 3, we can find that both phase predistortion and spectrum modification have the ability of sidelobe suppression. But phase predistortion can bring hunches far away from the mainlobe and spectrum modification has good effect of suppression to the sidelobes in the distance. So, we predict that the combination of these two techniques will bring better pulse compression performance. The two techniques are used sequentially as Fig. 37.14. Figure 37.15 is the result of the simulation utilizing two techniques sequentially.

From Fig. 37.15 it can be seen that

- The first sidelobe is suppressed to the level under −45 dB, and the sidelobes attenuate quickly when getting far away from the mainlobe.
- The envelope of the sidelobes is monotonically decreasing.

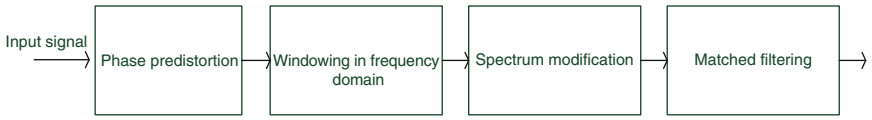

Fig. 37.14 The flow chart of the combined pulse compression technique

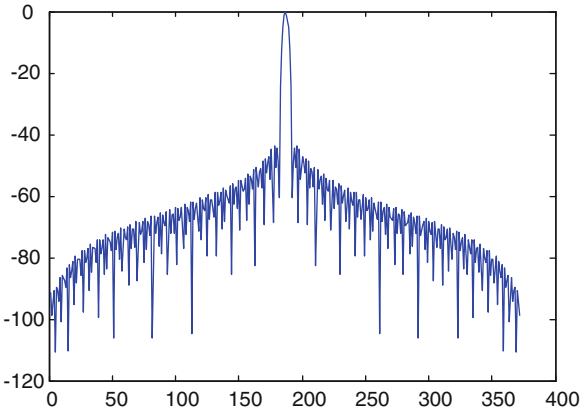

Fig. 37.15 Compression result with sidelobe suppression by combination of phase predistortion and spectrum modification

- The mainlobe doesn't spread apparently comparing with the result only using weighting function.

The whole sky weather echoes before and after pulse compression are shown in Fig. 37.16.

It can be seen from Fig. 37.16 that

- The resolution of weather radar echo is very poor without pulse compression.
- Phase predistortion and spectrum modification can bring comparative resolution enhancement through sidelobe suppression. But spectrum modification technique brings some false target echo in the upper left corner of the reflectivity section.
- The combination of phase predistortion and spectrum modification has the best resolution.

37.5 Conclusion

Sidelobe suppression is an important part in pulse compression. From the simulations and application on weather radar, It can be seen that the combination of phase predistortion and spectrum modification technique has good sidelobe suppression performance. In some applications involving hardware implementation and real-time processing, the SAW device can be used to carry out impulse compression [7, 8].

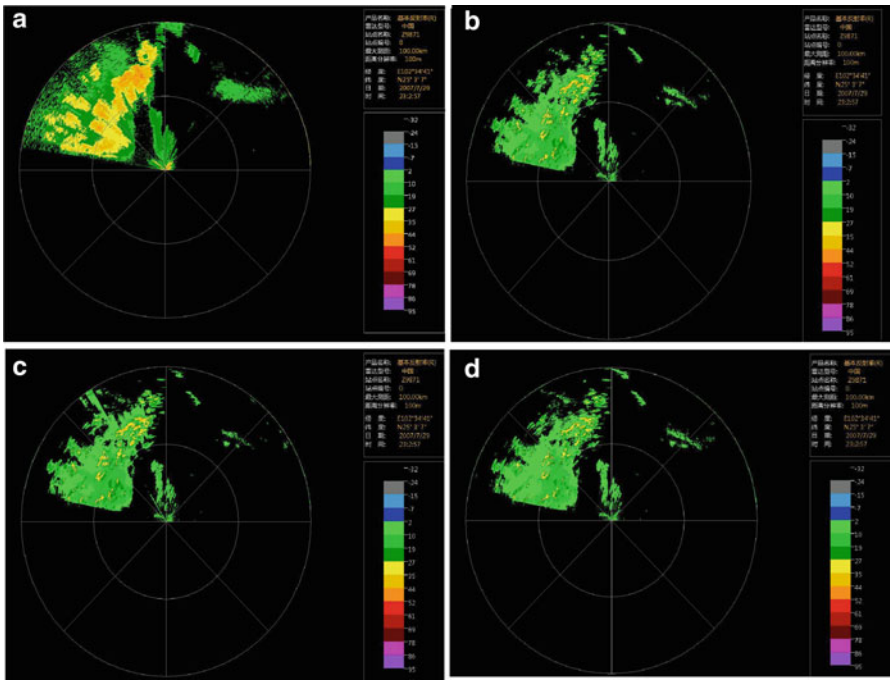

Fig. 37.16 The whole sky weather radar echoes (**a**) Echo with no pulse compression, (**b**) Echo after compression with phase predistortion, (**c**) Echo after compression with spectrum modification, (**d**) Echo after compression with phase predistortion and spectrum modification

References

1. Lin M, Ke Y (1984) Theory of radar signal. National Defense Industry Press, Beijing, pp 87–203
2. Cook CE, Bernfeld M, Paolillo J, Palmier CA (1965) Matched filtering, pulse compression and waveform design. Microwave J, Oct. Nov. Dec. 1964
3. Cook CE, Paolillo J (1964) A pulse compression predistortion function for efficient sidelobe reduction in a high-power radar. Proc IEEE 52:377–389
4. Kowatsch M (1982) Suppression of sidelobes in rectangular linear FM pulse compression radar. Proc IEEE 70(3):308–309
5. Youxin L, Jingcheng X, Fuxin C (1993) A method for reducing range-sidelobes of linear frequency-modulated pulse compression signals. J UEST China 22(4):344–349
6. Yang B, Wu J (2000) A range sidelobe reduction technique based onmodifications to signal spectrum. Syst Eng Electron 22(9):90–93
7. Xianmin Z, Jinlin X, Hongtai W, Qing X (1997) SAW pulse compression systems with lower sidelobes. Microw Conf Proc 2:833–835, APMC '97
8. Arthur JW (1995) Modern SAW-based pulse compression systems for radar applications. I. SAW matched filters. Electron Commun Eng J 7(6):236–246

Chapter 38
A Method of Obstacle Identification Based on UWB and Selected Bispectra

Minglei You and Ting Jiang

Abstract Ultra-wideband (UWB) radar is widely used in the obstacle identification, and the procedure is done by analyzing the echo signals. In this paper, a novel method of target detection is proposed. The perspective of UWB communications is adopted, and this method leads to a potential way to identify obstacles during the normal communications. The selected bispectra algorithm is applied to extract the feature vector, and radial-basis function (RBF) is used to realize the obstacle identification. According to the experiment results, this method is able to identify the existence and the different distances of the obstacles measured in outdoor observed scene, with an average recognition rate of no less than 98%.

Keywords UWB • Obstacle identification • Higher order spectral analysis • Selected bispectra • Ridial-basis function neural network • wireless sensor network

38.1 Introduction

The UWB communication technology has been widely used in short range communications as well as the obstacle identification. Traditionally, a UWB radar is needed in the obstacle identification. The statistics of the received signals and the multipath channel parameters are used by analyzing the echo signals. There has been a lot of applications by using UWB radar, such as security check [1], human activities classifying [2] and concealed obstacles through foliage classifying [3]. However, the parameters in detection and identification have to be from the radar reflected signals. Although there has been a great amount of researches on passive radar, in which model the signal to be analyzed is kind of common wireless

M. You (✉) • T. Jiang
Key Laboratory of Universal Wireless Communication, Ministry of Education, Beijing, University of Posts and Telecommunications, Beijing 100876, P. R. China
e-mail: pomeantylay@gmail.com

Q. Liang et al. (eds.), *Communications, Signal Processing, and Systems*, Lecture Notes in Electrical Engineering 202, DOI 10.1007/978-1-4614-5803-6_38,

signals, such as FM [4], GPS [5], and GSM [6], the UWB radar is so dedicated that the identification and communication are completely two independent processes. The model we adopted is based on the normal wireless network communication, in which the identification and perception will be done simultaneously during the communication procedure.

As we know, the signals are always influenced by the communication channel. Therefore, some channel information is carried on the signal itself. Mostly, we use this information to estimate the channel quality, SNR and so on by analyzing the received signal, but few to detect or identify the obstacle in the channel. There is sufficient information in the signal, such as amplitude, phase, delay. And after training, the changes can be identified by using proper algorithm [7]. Especially when using the bispectra to analyze the signals, amplitude and phase information will be retained. Then many methods like Circularly Integrated Bispectra (CIB) [8], Axially Integrated Bispectra(AIB) [9] and Radially Integrated Bispectra (RIB) [10] have been proposed.

In this paper, we propose a novel obstacle detection and recognition method based on UWB and selected bispectra with RBF neural network as a classifier. By adopting this method, we are able to classify different obstacles data, which is measured in outdoor observed scene, including LOS (line of sight), NLOS (not line of sight) and different distances of the same obstacle. The experiment results show that this method has a very good and robust classification ability, which gives a fine application potential.

The paper is organized as follows. The methodology of the obstacle identification is discussed in Sect. 38.2. This is followed by introducing the selected bispectra algorithm with RBF neural network as a classifier in Sect. 38.3. The experiment results of the method in identifying different obstacles data, which are measured in outdoor observed scene, are presented in the Sect. 38.4 to demonstrate the effectiveness of using this method. Finally conclusions are made in Sect. 38.5.

38.2 Methodology of the Obstacle Identification Based on UWB and Selected Bispectra with RBF Neural Network as a Classifier

38.2.1 The Basic Idea

Our model is based on the normal wireless network, which is shown in Fig. 38.1. The identification and perception will be done during the communication procedure.

When transmitted in the channel, the UWB signal is always been influenced by the obstacles if there is one. The sizes, materials of the obstacle will affect the radiation and scattering of electromagnetic waves, so as a result, there will be some changes in the amplitude and/or phase of the signal. Then if the key different features among the received signals are extracted by training, there will be a possible way to identify different obstacles as well as their conditions.

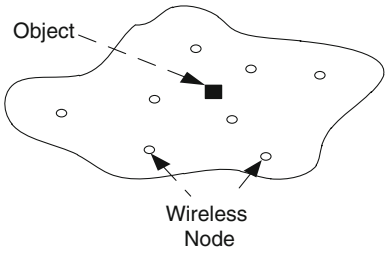

Fig. 38.1 Identification during the communication model

So that if we analyze the received perspective signals by using the Higher Order Spectral Analysis [11] and choose a proper classifier like RBF neural network, the identification can be done during the normal communications, without a traditional UWB radar.

38.2.2 The Feature Extraction Methods Based on Higher Order Spectral Analysis

Although the bispectra have all the advantages of cumulants/polyspectra in feature extraction, their direct use has serious limitations.

We adopt the selected bispectra as the classification feature, in order to avoid the disadvantages [12], such as abandon the little contribution bispectra and a mass of cross-terms of the bispectra. Selected bispectra is first proposed by Zhang in [7], its basic idea is to select only the bispectra at individual bifrequency points with the most discriminant power as feature vectors. Therefore, it avoids the trivial and baneful bispectra or missing some important bispectra.

The bispectra of a deterministic, continuous-time signal x(t) is defined as

$$B(\omega_1, \omega_2) = \int_{-\infty}^{+\infty} \int_{-\infty}^{+\infty} c_{3x}(\tau_1, \tau_2) \mathrm{e}^{-j(\omega_1 \tau_1 + \omega_2 \tau_2)} d\tau_1 d\tau_2 \tag{38.1}$$

where

$$C_{3x}(\tau_1, \tau_2) = \int_{-\infty}^{+\infty} x^*(t) x(t+\tau_1) x(t+\tau_2) = E\{x^*(t) x(t+\tau_1) x(t+\tau_2)\} \tag{38.2}$$

is the triple correlation function of x(t). For simplicity, denote $\omega = (\omega_1, \omega_2)$ and $B(\omega) = B(\omega_1, \omega_2)$. Suppose the training set consists of bispectra samples $\left\{B_k^{(i)}(\omega)\right\}_{k=1,2,\ldots,N_i}$ and $\left\{B_k^{(j)}(\omega)\right\}_{k=1,2,\ldots,N_j}$, where the subscript k stands for bispectra computed from the k th set of observed data, the superscript(i) represents the i th class of the signal, and N_i and N_j are the set number of observed data of the i th and j th class signals, respectively.

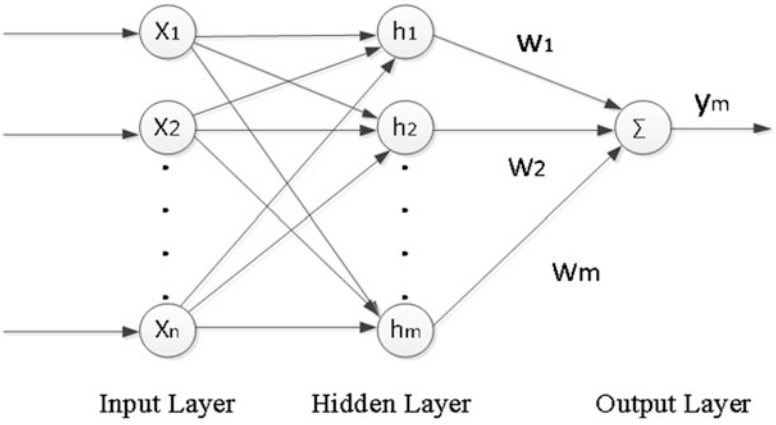

Fig. 38.2 Simplified structure of RBF neutral network

In order to select the powerful bispectra set as the feature parameter set, we choose Fisher's class separability as the discriminant measure function. Therefore, the Fisher class separability measure between the i th and j th classes is defined by

$$m^{(ij)}(\omega) = \frac{\sum_{l=i,j} [mean_k(B_k^{(l)}(\omega)) - mean_l[mean_k(B_k^{(l)}(\omega))]]^2}{\sum_{l=i,j} \mathrm{var}_k(B_k^{(l)}(\omega))}, \; i \neq j \qquad (38.3)$$

where $mean_k(B_k^{(l)}(\omega))$ is the mean(centroid) of all the sample Bispectra at the frequency ω of the l th class; $\mathrm{var}_k(B_k^{(l)}(\omega))$ is the variance of all the sample bispectra at the frequency ω of the l th class; $mean_l[mean_k(B_k^{(l)}(\omega))]$ is the total centroid of all the sample bispectra at the frequency ω over all the classes.

We choose as the feature frequencies set {ω(h),h = 1,. . .,Q} with Q largest separability measures among $m^{(ij)}(\omega)$ for all possible combinations(i, j). The bispectra at these selected frequencies $B(\omega_{1,h}, \omega_{2,h})$ are called the selected bispectra.

38.2.3 The Classify Method of the RBF Neural Network

The RBF(Radial Basis Function) neutral network can be used as universal function approximations. They consist of a network with a single hidden layer and a structure like the Fig. 38.2 shows. There have been a lot of researches that confirm the advantages of the RBF neural networks over the others solutions for classification tasks. RBF networks apply real mapping functions f_m which has the general form

$$f_m(x) = \sum_{i=1}^{M} w_i K[(x_i - c_i)/\sigma_i] \tag{38.4}$$

where the c_i is the centroid and σ_i is the smoothing factor. The outputs are nonlinear, radial symmetrical functions of the distance. Thus, the output is the strongest when x_i is the closest to the value c_i.

The function K is a radial symmetric kernel function computed by M kernel units. Gaussian exponential function is commonly used in RBF networks

$$f(x) = \beta \exp\left(-\sum_i [(x_i - c_i)/\sigma_i]^2\right) \tag{38.5}$$

The centroid c_i, constants β and σ_i have to be chosen accordingly to training data set.

38.3 Algorithm of the Identification

Given training samples $x_k^{(l)}(1),\ldots, x_k^{(l)}(N)$ of the k th observation record of the l th class of signal, where l = 1, …, c and k = 1, …, N_l. The Off-line Training Algorithm [7] is as below:

Step 1) Calculate bispectra

$$B_k^{(l)}(\omega) = B_k^{(l)}(\omega_1, \omega_2) = X(\omega_1)X(\omega_2)X^*(\omega_1 + \omega_2) \tag{38.6}$$

Step 2) Use (3) to compute the Fisher class separability measure $m^{(ij)}(\omega)$ for all class combinations(i, j), and requeue M largest measures such that

$$m^{(ij)}(v_1) \geq m^{(ij)}(v_2) \geq \cdots \geq m^{(ij)}(v_M) \tag{38.7}$$

Step 3) Calculate the normalized Fisher class separability measure

$$\overline{m}^{(ij)}(v_p) = \frac{m^{(ij)}(v_p)}{\sqrt{\sum_{k=1}^{M} [m^{(ij)}(v_k)]^2}}, p = 1, \ldots, M \tag{38.8}$$

Determine the 'effective' number of selected bispectra for between-class(i, j), and denote it by $H^{(ij)}$. The corresponding frequencies

$\left\{\omega^{(ij)}(p), p = 1, \ldots, H^{(ij)}\right\}$ are called the 'effective' frequencies, and the repeated frequency for different combinations(i, j) remains only one.

Step 4) Arrange the obtained effective frequencies $\left\{\omega^{(ij)}(p), p = 1, \ldots, H^{(ij)}\right\}$ into the sequent $\left\{\omega^{(ij)}(q), q = 1, 2, \ldots, Q\right\}, Q = \sum_{(i,j)} H^{(ij)}$. And arrange the corresponding selected bispectra of the k th record in class l into the sequent $\left\{B_k{}^{(ij)}(q), q = 1, 2, \ldots, Q\right\}, Q = \sum_{(i,j)} H^{(ij)}$, k = 1,..., N_l. The template feature vectors are given by $s_j = \left[B_k^{(l)}(1), \ldots, B_k^{(l)}(Q)\right]^T$ and the feature vector of the l th class is $S_l = \{s_i\}_{i=lN+1,lN+2,\ldots,(l+1)N}, l = 1, \ldots, c$.

Step 5) Use the selected (powerful) bispectra to train the RBF neural network as a classifier. Let $H = [h_{ij}]_{(c\times N)\times(c\times N)}$ represent the hidden node output matrix, where

$$h_{ij} = \exp\left(-\frac{\left\|\overrightarrow{s_i} - \overrightarrow{s_j}\right\|^2}{\sigma^2}\right) \tag{38.9}$$

and the variance σ^2 of the Gaussian kernel function is the total variance of all feature vectors $s_i, i = 1, \ldots, 3N$. Hence, the weight matrix of the RBF neural network is given by

$$\overrightarrow{W} = \left(\overrightarrow{H}^H \overrightarrow{H}\right)^{-1} \overrightarrow{H}^H \overrightarrow{O} \tag{38.10}$$

Where $\overrightarrow{O}$ is the $(cN) \times c$ desired output matrix given by

$$\overrightarrow{O} = \begin{bmatrix} \underbrace{\begin{matrix} 1 & \cdots & 1 \\ 0 & \cdots & 0 \\ \vdots & \ddots & \vdots \\ 0 & \cdots & 0 \end{matrix}}_{N} & \underbrace{\begin{matrix} 0 & \cdots & 0 \\ 1 & \cdots & 1 \\ \vdots & \ddots & \vdots \\ 0 & \cdots & 0 \end{matrix}}_{N} & \cdots & \underbrace{\begin{matrix} 0 & \cdots & 0 \\ 0 & \cdots & 0 \\ \vdots & \ddots & \vdots \\ 1 & \cdots & 1 \end{matrix}}_{N} \end{bmatrix}^T \tag{38.11}$$

Once the RBF neural network as classifier is trained, the weight matrix $\overrightarrow{W}$ is stored.

Step 6) Let $\overrightarrow{x} = [s(1), s(2), \ldots, s(N)]^T$ is a feature vector computed from a set of measured data of an unknown target. Then, the RBF neural network's hidden node output vector $\overrightarrow{h} = [h_i]_{(cN)\times 1}$ corresponding to x can be computed as

$$h_i = \exp\left(-\frac{\left\|\overrightarrow{x} - \overrightarrow{s_i}\right\|}{\sigma_i^2}\right) \tag{38.12}$$

where the variance σ_i^2 is the variance of the feature vector $\overrightarrow{s_i}$ determined in the training phase. Then, the output vector of the RBF neural network is given by

$$o = W^T h \tag{38.13}$$

which gives the classification result of the unknown target.

38.4 Experiments and Analysis

The experiment is set in the scene of a noisy grove beside a main road. The obstacle is set to be a human being. The experiment is separated into two groups. The first one is to identify whether the channel is LOS or NLOS, i.e. the existence of the obstacle; the second one is designed to identify the different distances between the receiver and the obstacle, which is shown in Fig. 38.3. The corresponding parameters in the experiments are shown in Table 38.1.

The sample records for each class are 600, of which we use 300 to train and the other 300 to identify. The corresponding results are shown in Figs. 38.4 and 38.5, Tables 38.2 and 38.3.

From Figs. 38.3 and 38.4, we can see that a positive relationship exists between the numbers of features and the recognition rates. When the numbers of features are larger than 70, both the two identification groups achieve a good average

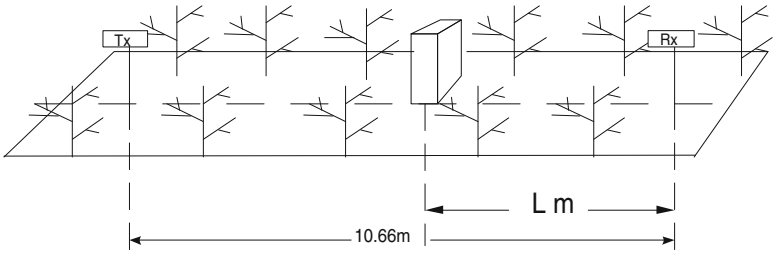

Fig. 38.3 The measured channel model: in a noisy grove beside a main road with few leaves. The obstacle is standing on the straight line between the Transmitter and the Receiver, the distance of which are fixed

Table 38.1 Parameters of the experiments

Class	Sample records	Obstacle to Rx distance: L	LOS/NLOS
D1	600	-(No Obstacle)	LOS
D2	600	3.90 m	NLOS
D3	600	6.40 m	NLOS
D4	600	6.82 m	NLOS

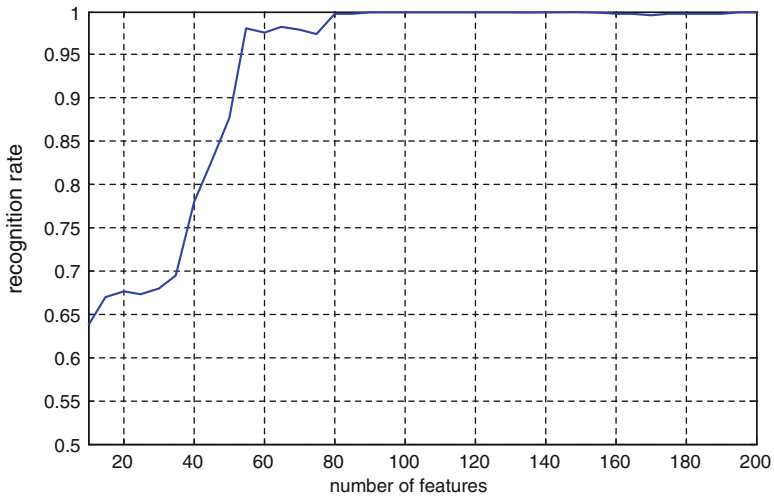

Fig. 38.4 The average recognition rate versus the number of features, when applying the method to identify LOS and NLOS, using D1 and D3

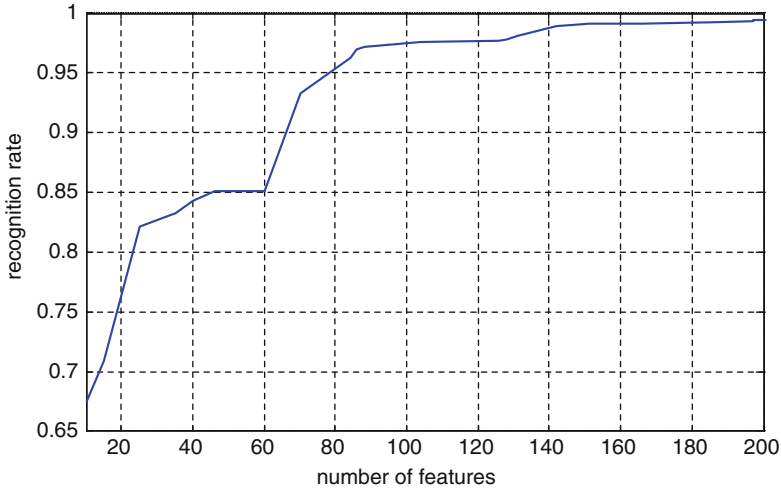

Fig. 38.5 The average recognition rate versus the number of features, when applying the method to identify three different distances in NLOS, using D2, D3 and D4

Table 38.2 Recognition rates of LOS versus NLOS with 150 features

Class	LOS	NLOS
Recognition rate	99.67%	100%

Table 38.3 Recognition rates of different distances with 150 features

Distance	3.90 m	6.40 m	6.82 m
Recognition rate	99.33%	100%	98.00%

recognition rate, which is larger than 90%. And after that point, the recognition rate upgrades very few with the increasing of numbers of features.

From Tables 38.2 and 38.3, we can see that when the number of features is sufficiently large, the average recognition rates for each class are all more than 98%. And this method can distinguish even a very small distance.

38.5 Conclusion

This article proposes a novel method of obstacle identification based on UWB and selected bispectra. Two groups of ultra-wideband out door obstacle identification scenes (LOS versus NLOS and different distances) are measured. The channel features are extracted from the prospective received signal and then the radial-basis function is established. The experiment results demonstrate that the detection and identification method of obstacle based on UWB and selected bispectra is effective for obstacle identification of both existence and the different distances, and this method is sensitive to even a very small distance.

Acknowledgment This work was supported by Important National Scenes & Technology Specific Projects (2010ZX03006-006), NSFC (61171176), Scientific Research Fund of Zhejiang Provincial Education Department under Grant No. Y201225956 and Natural Science Foundation of Ningbo under Grant No. 2012A610015.

References

1. Ariza APG, Thoma RS (2012) Polarimetric ultrawideband MIMO radar for security check points: detecting and classifying suspects carrying wires in Antennas and Propagation (EUCAP). In: Proceedings of the 6th European conference on 2012
2. Bryan JD et al (2012) Application of ultra-wide band radar for classification of human activities. IET Radar Sonar Nav 6(3):172–179
3. Dong WY et al (2011) An improved classification method of concealed obstacles using UWB radar and stereo cameras. In: Proceedings of the Synthetic Aperture Radar (APSAR), 2011 3rd international Asia-Pacific conference on 2011
4. Olsen KE, Baker CJ (2008) FM-based passive bistatic radar as a function of available bandwidth. In: Proceedings of IEEE radar conference 2008 RADAR '08
5. Suberviola I, Mayordomo I, Mendizabal J (2012) Experimental results of air target detection with a GPS forward-scattering radar. IEEE Geosci Remote Sens Lett 9(1):47–51
6. Tan DKP et al (2003) Feasibility analysis of GSM signal for passive radar. In: Proceedings of the 2003 I.E. radar conference 2003

7. Xian-Da Z, Yu S, Zheng B (2001) A new feature vector using selected bispectra for signal classification with application in radar target recognition. IEEE Trans Signal Process 49 (9):1875–1885
8. Xuejun L, Zheng B (1998) Circularly integrated bispectra: novel shift in-variant features for high-resolution radar target recognition. Electron Lett 34(19):1879–1880
9. Tugnait JK (1994) Detection of non-Gaussian signals using integrated poly-spectrum. IEEE Trans Signal Process 42(11):3137–3149
10. Chandran V, Elgar SL (1993) Pattern recognition using invariants de-fined from higher order spectra- one dimensional inputs. IEEE Trans Signal Process 41(1):205
11. Tsatsanis MK, Giannakis GB (1992) Object and texture classification using higher order statistics. IEEE Trans Pattern Anal Mach Intell 14(7):733–750
12. Cai Z, Li J (2007) Study of transmitter individual identification based on bispectra. Tongxin Xuebao/J Commun 28(2):75–79

Chapter 39
Nonlinear Estimation for Ultra-Wideband Radar Based on Bayesian Particle Filtering Detector

Mengwei Sun, Bin Li, Chenglin Zhao, Yun Liu, and Zhou Li

Abstract In order to combat the nonlinearity of the radio component in UWB radar systems, in this paper we present a promising blind estimation algorithm based on the particle filtering (PF). Based on the conception of Bayesian approximation and sequential importance sampling, this appealing Monte-Carlo method can deal with many complicated statistic estimation problems. In sharp contrast to the classical linear equalization problem, nevertheless, in this considered problem the PF based method may become valid due to the nonlinearity and the resulting non-analytic importance function. Thus, a novel PF framework based on the linearization technique is suggested, and we show in particular how to linearize the involved nonlinearity transform. The merit of this method is that it can deal with discrete time dynamic models that are typically nonlinear and non-Gaussian. Experimental simulations demonstrate the superior performance of the presented PF scheme, which may be properly applied to UWB radar systems.

M. Sun (✉)
Key Lab of Universal Wireless Communications, MOE Wireless Network Lab, Beijing University of Posts and Telecommunications, Beijing 100876, China
e-mail: 18810536430@163.com

B. Li
Key Laboratory of Universal Wireless Communications, Ministry of Education, University of Posts and Telecommunications, Beijing 100876, China

C. Zhao
School of Information and Communication Engineering, Beijing University of Posts and Telecommunications, Beijing 100876, China

Y. Liu
China Academy of Telecommunications Research, Ministry of Industry and Information Technology Telecommunication Metrology Center, CATR, MIIT, Beijing 100088, China
e-mail: liuyun@catr.cn

Z. Li
China Academy of Telecommunications Research, Beijing, China
e-mail: lizhou@catr.cn

Q. Liang et al. (eds.), *Communications, Signal Processing, and Systems*, Lecture Notes in Electrical Engineering 202, DOI 10.1007/978-1-4614-5803-6_39,

Keywords UWB radars • Nonlinearity • Particle filtering • Taylor series • Linearization technique

39.1 Introduction

Owing to the enormous bandwidth (typically exceeds 500 MHz) and the resulting excellent time resolution, Ultra-wideband (UWB) impulse or baseband techniques always show great promise to a large number of potential applications. The emerging UWB radar may find significant and even indispensable application in various military and commercial applications, and the most typical senior includes the high resolution radar, the remote medical monitoring, the water pollution sensing and the low-power larger-scale sensor networks. Even through the merit of impulse mechanics, the corresponding extremely high signal Peak to Average Power Ratio (PAPR) may pose great challenges to the design of radio components. Unfortunately, it seems that the nonlinearity of power amplifier is practically inevitable. As a consequence, the signal detection in the presence of nonlinearity distortion has become a major concern in the design of UWB radar systems.

In many realistic applications that can be in general characterized by the state space models, signal detection and the associated adaptive filtering procedures often require the sequential parameter learning and estimations. That is, the output estimation should be prepared in time as the new observation arrives. In this article, relying on a Bayesian approach and Sequential Importance Sampling (SIS) technique, we introduce a novel blind detection algorithm to address the nonlinearity distorti1ons in UWB Radar systems, [1, 2].

Such a SIS method aims to establish a MonteCarlo (MC) representation of the desired probability distribution which may be too complicated to achieve the analytic express, which mainly consists of a group of discrete particles and associated weights. Then, these particles and associated weights will be recursively updated, which can approximate the desired probability distribution. In other words, the discrete particles with their importance weights will provide the Bayesian estimates of input signal sequence. In this investigation, we apply the SIS method to the blind estimation in the presence of nonlinear distortion in UWB radar systems. Firstly, in order to derive the feasible importance function (i.e. the related likehood function) with the complex nonlinear transform, by using the first-order Taylor Expansion we develop a new representative system via local linearization technique. Therefore, the involved importance function can be conveniently obtained. And on this basis, the signal detection with nonlinear distortion is realized by resorting to the PF technique. The experimental simulation are finally conducted, which may essentially demonstrated our suggested method can effectively solve the nonlinear estimation, and hence provide a promising solution to the emerging UWB Radar systems.

This rest of the paper is organized as follows. Section 39.2 provides a model of considered nonlinear radar system. That is, the modulated signals are distorted by a power amplifier. In Sect. 39.3, we briefly review the particle filtering algorithm and provide computational details for implementing the method in blind estimation.

In Sect. 39.4, we propose a novel PF method based on the Taylor Expansion which is to linearize the nonlinear model. Finally, simulations and conclusion are presented in Sect. 39.5.

39.2 Nonlinear System Model

The model of nonlinear UWB radar or communication system considered in this paper has been illustrated by Fig. 39.1. The transmitter source firstly generates the binary symbols bt, and after 16QAM modulation at the transmitting end, the signal sequence xt are fed into the nonlinear power amplifier, and after this process, we may finally get the emission signals whose voltage amplitudes and phases are seriously distorted. For the convenience of analysis, we assume the wireless propagation channel to be single-path with additive white Gaussian noise. However, from our later formulation, it is straightforward to extend to the multi-path propagations. At the receiving end, the observed signals yt are particle-filtered and sampled at a bit rate. The resulting discrete time sequence is demodulated, and we should derive the blind estimations and hence recover the emitted signal.

In practice, the power amplification procedure at the transmitter end will inevitably introduce the nonlinear distortion into the system due to hardware imperfections. As a consequence, the signal constellation in receiver will be sharply distorted, and hence the serious detection error will occur by remarkably degrading the transmission performance. Thus, the nonlinear effect should be carefully considered and many design efforts should be put on this issue.

The effects of PA nonlinear include the distortion generated by amplitude modulation-amplitude modulation (AM-AM) conversion and amplitude modulation-phase modulation (AM-PM) conversion. AM-AM model and AM-PM model are expressed as follows [3]

$$G(A) = g\frac{A}{\left(1+\frac{gA^{2s}}{A_{sat}}\right)^{\frac{1}{2s}}} \tag{39.1}$$

$$\Psi(A) = \frac{\alpha A^{q_1}}{(1+(A/\beta)^{q_2})} \tag{39.2}$$

where A and $G(A)$ represent the input and output voltage range in RMS; g is the small gain signal, $g = 4.65$; s is the smoothness factor, $s = 0.81$; A_{sat} is the

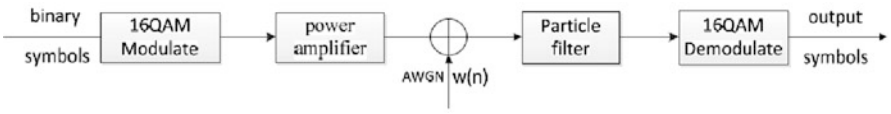

Fig. 39.1 Model of nonlinear communication system

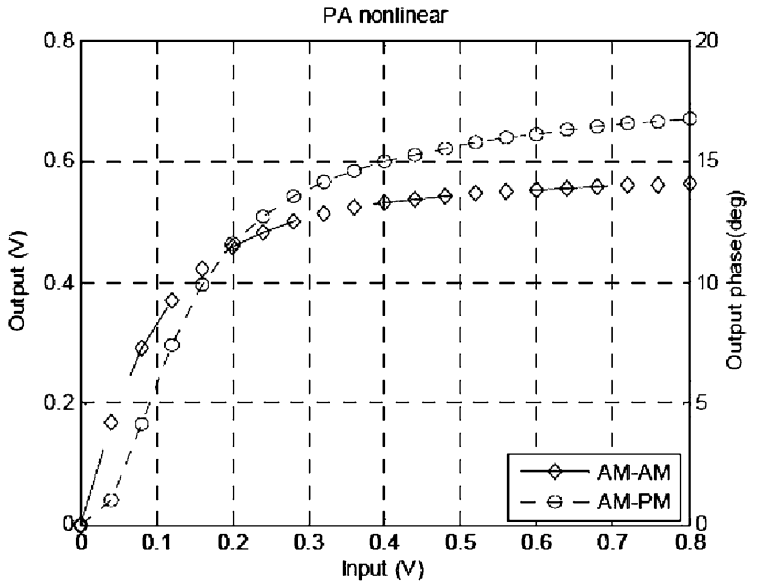

Fig. 39.2 IEEE 802.11ad PA model

saturation level, $A_{sat} = 0.\ 58$ V; $\Psi(A)$ is the phase in degrees; α, β are 2,560, 0.114 respectively, and q_1, q_2 are 2.4 and 2.3 respectively.

Figure 39.2 depicts the curves of AM-AM model and AM-PM model given output saturation voltage of 0.58 V. We can ignore the amplitude distortion and phase distortion when the amplitude of input is less than 0.1 V. But when the input signal amplitude is greater than 0.1 V, the amplifier will work in nonlinear region; this may result in severe nonlinear distortion, and therefore seriously deteriorate the performance of the receiver signal.

In order to alleviate the unflavored effects from the inevitable nonlinear distortion, a simple solution but not efficient approach is to adopt the output power back-off mechanism [3]. Back-off power is usually defined as:

$$R_{backoff} = 10\log_{10}\left(\frac{P_{sat}}{P_{out}}\right) \tag{39.3}$$

Where P_{sat} is the output saturation power, P_{out} is the output power. $R_{backoff}$ is power back-off rate in dB. Obviously, the greater back-off ower rate means the smaller the output power, and the smaller the output power means the smaller the nonlinear distortion. On the other hand, lower transmit power will cause the lower signal to noise ratio, this will result in decreasing anti-jamming capability; at the same time, the performance of amplifier device may be greatly deteriorated. Therefore, the power back-off mechanism can only avoid the negative effects of nonlinear distortion in a certain extent, but fail to effectively improve the system performance under the nonlinear device. It is difficult to be adopted widely in the practical design.

39.3 Blind Estimation and Particle Filtering

39.3.1 System Model

In this investigation, we mainly consider the UWB radar or communication system where the binary symbols b_t are transmitted and modulated to x_t, and then propagated through a linear channel. At the receiving end, the observed signals y_t are matched-filtering and sampled at the bit rate. And correspondingly, the dynamic state-space model can be expressed as followings [4]:

$$\mathbf{x}_t = \mathbf{T}\mathbf{x}_{t-1} + \mathbf{u}_t \tag{39.4}$$

$$\mathbf{y}_t = g\left(\mathbf{x}_t^T\right)\mathbf{h} + v_t \tag{39.5}$$

- Equation 39.4 is usually referred as to the state equation, which essentially describes the evolution process of the hidden state x_t. Correspondingly, T is the $L \times L$ state-transition matrix and the value of T is:

$$\begin{pmatrix} 0 & 1 & 0 & \dots & 0 \\ 0 & 0 & 1 & \dots & 0 \\ \dots & \dots & \dots & \dots & \dots \\ 0 & 0 & 0 & \dots & 1 \\ 0 & 0 & 0 & \dots & 0 \end{pmatrix}$$

- Equation 39.5 is the observation equation, which gives the relationship between the received (or observed) signal y_t and the hidden (or unobserved) state x_t. $u_t = [0, 0, \dots, x_t]$ is a $L \times 1$ vector, the new symbol x_t is a high-order modulated uniform random variable, i.e., $x_t \in A, t = 0, 1, 2, \dots, A = \{\pm 1 \pm i, \pm 3 \pm i, \pm 1 \pm 3i, \pm 3 \pm 3i\}$ and it is independent from the obvious and future symbols. The nonlinear transform $g(.)$ specifies the mapping between the input signal and output signal of the nonlinear power amplifier.
- Our aim is to compute the MAP estimate of state symbols $x_{0:\,T}$ with the unknown channel vector h, int.

In our research of combating the nonlinearity distortion and realizing blind signal detection, we will simulate a scenario of a time-invariant channel with an impulse response of length $L = 3$. It is noteworthy that, although we mainly consider the single-path Gaussian propagation senior in this work, we may still adopt the multi-path model in order to conveniently formulate the dynamic system model in (39.4)–(39.5). That is, this memory model is always necessary when considering the applications of PF to the specific nonlinear estimation problem. And hence, the generalization to the realistic multi-path channel is also practically feasible.

We assumed a Gaussian prior for the channel coefficients, $h \sim N(h_0, C_0)$, where $h_0 = \begin{pmatrix} 0 \\ 0 \\ 1 \end{pmatrix}$ and $C_0 = 10^{-10} \begin{pmatrix} 1 & 0 & 0 \\ 0 & 1 & 0 \\ 0 & 0 & 1 \end{pmatrix}$

And in (39.5), $v_t \sim N(0, \sigma^2)$ is a zero-mean Additive White Gaussian Noise (AWGN) component with variance σ^2 and y_t is the observation at time t. h is a $L \times 1$ vector representing the discrete time channel impulse response which assumed unknown (i.e. , blind).

39.3.2 Blind Estimation Using the SIS Algorithm

Particle filtering is essentially premised on the appealing conception of both Bayesian approximation and sequential importance sampling, such a Monte-Carlo method can deal with many complicated statistic estimation problems. In this section, we mainly focus on the SIS algorithm and the re-sampling approach which can combat the degeneracy of particles.

39.3.2.1 SIS Algorithm

According to the dynamic state-space model in (39.4) and (39.5), the main task of the estimation of state symbols $\{x_{0:T}\}$ can be generally achieved by the optimal MAP algorithm, given the observations $\{y_{0:T}\}$. Assume that $p(x_{0:T}|y_{0:T})$ represents the probability mass function (pmf) of the a posterior distribution of transmitted data sequence, and the MAP estimate of the transmitted symbols is:

$$\hat{\mathbf{x}}_{0:T}^{(MAP)} = \arg_{\mathbf{x}_{0:T}} \max \left\{ p[\mathbf{x}_{0:T}|\mathbf{y}_{0:T}] \right\} \tag{39.6}$$

where $x_{0:T}$ records the trajectory of the transmitted symbols $\{x_t^{(i)}, i = 0, 1, 2, \ldots, N\}$. Since it is in practice generally impossible to directly sample from the posterior distribution $p(x_{0:T} \mid y_{0:T})$ directly, we may alternatively resort to the SIS approach. SIS is the extension of importance sampling (IS). According to the SIS algorithm, we may build the state trajectories and compute the importance weights sequentially. The importance weights can be computed recursively in time as follows (39.7)–(39.8).

$$\mathbf{x}_T^{(i)} \sim \pi\left(\mathbf{x}_T \middle| \mathbf{x}_{0:T-1}^{(i)}, \mathbf{y}_{0:T}\right) \tag{39.7}$$

$$\tilde{w}_t^{(i)} \propto \tilde{w}_{t-1}^{(i)} \frac{p\left(y_t \middle| \mathbf{x}_{0:t}^{(i)}, \mathbf{y}_{0:t-1}\right)}{\pi\left(x_t^{(i)} \middle| \mathbf{x}_{0:t-1}^{(i)}, \mathbf{y}_{0:t}\right)} \tag{39.8}$$

where $\pi(x_{0:\,T} \mid y_{0:\,T})$ represents the trial pmf with the same support as $p(x_{0:\,T} \mid y_{0:\,T})$ but from which it is easier to sample, and is a set of normalized importance weights. The set of particles and normalized weights at time t are discrete random measures, so the formula (39.6) can be written as:

$$\hat{\mathbf{x}}_t^{(MAP)} = \arg_{\mathbf{x}\in\{\mathbf{A}\}} \max \left\{ \sum_{i=1}^{N} \delta\left(\mathbf{x}_t - \mathbf{x}_t^{(i)}\right) w_t^{(i)} \right\} \tag{39.9}$$

where $\sigma = 1$ if $x_t = x_t^{(i)}$ and $\sigma = 0$ otherwise.

39.3.2.2 Re-sampling

As has been illustrated by most investigations and noted from (39.9), the degeneracy of SIS algorithm is usually inevitable, which is referred to the decrease of importance weights over time. Along with a consequence of weight degeneracy, the approximation of a posterior probability may seriously deteriorate and even become useless [5]. An efficient approach to alleviate this difficulty is to conduct a re-sampling procedure in the SIS algorithm. The basic idea of such a method is to eliminate particles with small normalized importance weights while concentrating upon those particles having larger normalized importance weights.

A suitable measure to the serious degeneracy can be estimated from:

$$\mathbf{N}_{eff} = \frac{1}{\sum_{i=1}^{N} \left(w_t^{(i)^2} \right)^2} \leq N \tag{39.10}$$

Thus, in practice, when N_{eff} is below a fixed threshold, the re-sampling procedure is used.

39.4 Taylor Expansion to Linearize the Nonlinear Model

39.4.1 Nonlinear System Model

Because we mainly consider the single-path Gaussian propagation senior in this work, under the nonlinear distortion we may further simplify the observation model (39.5) into (39.11).

$$\mathbf{y_t} = g(x_t) + v_t, \;\; v_t \sim N\left(0, \sigma^2\right) \tag{39.11}$$

where v_t represents addictive complex white Gaussian noise and it can be written as:

$$\mathbf{y_t} \sim N(real(g(x_t)), noise\_var) + i \times N(imag(g(x_t)), noise\_var) \tag{39.12}$$

where the parameter $noise - var = \sigma^2/2$. By performing a Taylor Expansion up to first-order of the observation equation in (39.11), we may further get

$$\mathbf{y_t} = g(x_t) + v_t \simeq \ g(\hat{x}_t) + \frac{\partial\ g(\hat{x}_t)}{\partial \hat{x}_t}|_{x_k=\hat{x}_t}(x_t - \hat{x}_t) + v_t \tag{39.13}$$

where $\hat{a}_t$ represents the hypothetical signal with known value, which can be drawn from the finite alphabet of modulated symbols. We thereby define a new model with a similar evolution equation as (39.11) but with a linear Gaussian observation equation (39.13). This model is not Markov, but it can conveniently calculate the a prior Gaussian importance function $\pi({x_t}^{(i)} \mid {x_{0:\,t-1}}^{(i)}, y_t) \sim N(m_t, \Sigma_t)$ with mean m_t and covariance Σ_t evaluated for each trajectory $i = 1, 2, \ldots N$ by using the following formulas.

$$\Sigma_t = \left[\frac{\partial g\left(\hat{x}_t^{(i)}\right)}{\partial \hat{x}_t^{(i)}}|_{x_t^{(i)}=\hat{x}_t^{(i)}}\right]^{-1} \cdot \sigma^2 \tag{39.14}$$

$$\mathbf{m_t} = \left[\frac{\partial g\left(\hat{x}_t^{(i)}\right)}{\partial \hat{x}_t^{(i)}}|_{x_t^{(i)}=\hat{x}_t^{(i)}}\right]^{-1} \cdot \left(y_t - g\left(\hat{x}_t^{(i)}\right) + \frac{\partial g\left(\hat{x}_t^{(i)}\right)}{\partial \hat{x}_t^{(i)}}|_{x_t^{(i)}=\hat{x}_t^{(i)}} \cdot \hat{x}_t^{(i)}\right) \tag{39.15}$$

Thus, after sampling from the importance function $\pi({x_t}^{(i)} \mid {x_{0:\,t-1}}^{(i)}, y_t)$, we may get the particles at time t, and then send these particles to the power amplifier and get new particles whose voltage amplitude and phase are distortional.

39.4.2 Prior Importance Function

After the process of importance sampling, updating the associated weights of the discrete particles should be carried out, the main idea of weight update over nonlinear channel is same as the method over linear system, so the normalized importance weights can be evaluated from (39.9) and the probability distribution function (pdf) $p(y_t \mid x_{0:\,t}(i), y_{0:\,t-1})$can be expressed for likelihood [6], shown in (39.16):

$$\left(y_t|\mathbf{x}_{0:t}^{(i)}, \mathbf{y}_{0:t-1}\right) = \frac{1}{\sqrt{2\pi(\mathbf{s}^T\mathbf{C}_0\mathbf{s} + \sigma^2)}} \exp\left\{-\frac{\left(y - g\left(x^{(i)}\right)\right)^2}{2(\mathbf{s}^T\mathbf{C}_0\mathbf{s} + \sigma^2)}\right\} \tag{39.16}$$

where C_0 is the initial covariance matrix of channel and s is a $L \times 1$ vector contained by particles at time $t-2, t-1$and t in the same trajectory.

39.5 Computer Simulations and Conclusion

39.5.1 Simulation Setup

In this paper, we focus on a scenario of a time-invariant nonlinear channel with an impulse response of length $L = 3$. We assumed a Gaussian prior for the channel coefficients, $h \sim N(h_0, C_0)$, the value of h_0 and C_0 has given in Sect. 39.3. The configuration of mean and covariance matrix corresponds to an environment with single-path channel. In our experiment, the transmitted signals $\{b_t\}$ were modulated to $\{x_t\}$ using 16QAM scheme, and the a prior distribution of $\{x_t\}$ were assumed known.

At the receiving end, we may simulate the blind signal detection of UWB Radar systems in the presence of nonlinear distortions in the following three steps [7]:

- For $t = 1 : T$
  - Draw N particles from the importance function $\pi(x_t^{(i)} \mid x_{0:\,t-1}^{(i)}, y_t)$, and feed these particles into the nonlinear power amplifier;
  - Compute importance weight of each particle according to (39.8) and (39.16), then normalize the weight;
  - Re-sample in accordance with (39.10);
  - Use the method of MAP estimate to calculate the transmitted symbols.

39.5.2 Numerical Results

Based on the numerical experiment, we studied the detection performance of the proposed PF scheme. In Fig. 39.3, we have plotted the BER curves of six different value of the back-off power (OBO) which is derived from the Monte-Carlo simulation. The BER performance demonstrates that the smaller the output power is, the smaller the nonlinear distortion is produced, and when the output power is small enough, the BER curve of particle filtering become much close to the theoretical AWGN curve with linear PA. The results above can essentially show that the presented method can solve the problem of BER floor which is caused by zero power back-off in the presence of nonlinear distortion, and hence the superiority of this suggested approach in dealing with nonlinear UWB radar systems is rather obvious. It is also easily seen that the particle filter based blind detector, which has been used in linear system, can also be properly applied to the nonlinear channel with the suggested local linearization technique.

39.6 Conclusion

In this article, we have designed a blind estimation method for nonlinear UWB radar systems based on SIS methodology and Bayesian formulation. One of the main features of our proposed blind estimator is that, as a promising solution to

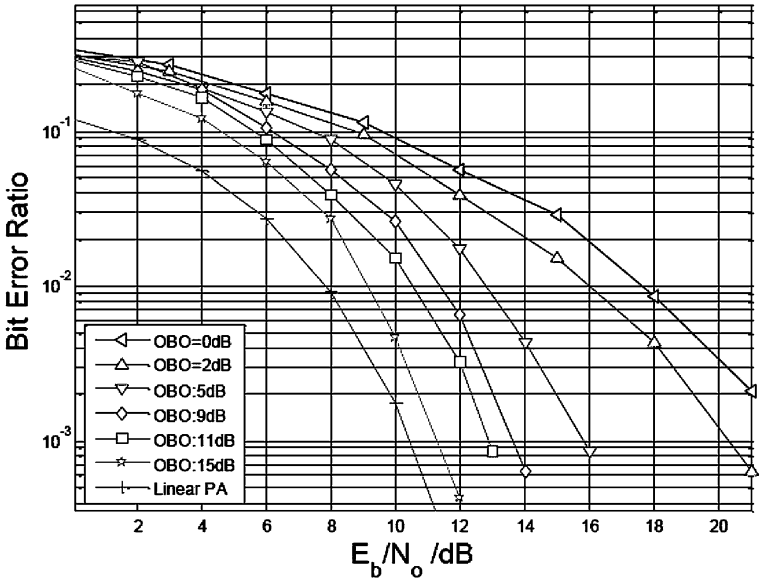

Fig. 39.3 BER curves with different OBO value

address nonlinear estimations, the first order Taylor Expansion is used to approach the involved nonlinear transform, and the weight is then recursively computed for each data trajectory in the particle filtering. The advantage this method is its capability to estimate transmitted symbols sequentially and timely without a training sequence, even in the presence of nonlinear distortions due to hardware imperfections. As is shown by the experimental results, the combination of particle filtering with Taylor Expansion can effectively combat the nonlinearity distortion in the UWB radar systems, which may hence provide a competitive solution to the practical design of UWB radars and other communication systems.

References

1. Liu JS, Chen R (1998) Sequential Monte Carlo methods for dynamic systems. J Am Stat Assoc 93(443):1032–1044
2. Liu JS, Chen R (1995) Blind deconvolution via sequential imputations. J Am Stat Assoc 90(430):566–576
3. Perahia E, Park M, Stacey R, et al (2010) IEEE P802.11 wireless LANs TGad evaluation methodology. IEEE 802.11 TGad Technology Report, pp 9–15, 2010
4. Miguez J, Djuric PM (2004) Blind equalization of frequency-selective channels by sequential importance sampling. IEEE Trans Signal Process 52(10):2738–2748
5. Crisan D, Doucet A (2002) A survey of convergence results on particle filtering. IEEE Trans Signal Process 50:736–746

6. Miguez J, Djuric PM (2002) Blind equalization by sequential importance sampling. Circ Syst IEEE Int Symp 1:I-845-I-848
7. Doucet A, Godsill S, Andrieu C (2000) On sequential Monte Carlo sampling methods for Bayesian filtering. Stat Comput 10(3):197–208

Part X
Communications Theory

Chapter 40
Some Recent Results on the Physical Layer Security of Frequency Hopping Systems

Hao Li, Jian Ren, and Tongtong Li

Abstract This paper considers the physical layer security of frequency hopping (FH) systems. Mainly due to the collision effect among different users, the spectral efficiency of the conventional FH is very low. To overcome this limitation, in this paper, we first propose a general collision-free frequency hopping (CFFH) scheme based on secure spectrum access control; Second, we incorporate the CFFH scheme with OFDMA, and obtain a highly efficient anti-jamming system; Finally, to simplify the secure frequency allocation process in OFDMA based CFFH, we propose an ID based message-driven frequency hopping scheme, which resolves the problem and achieves better jamming resistance with a trade-off in spectral efficiency.

Keywords Frequency hopping systems • Collision-free frequency hopping • Jamming resistance

40.1 Introduction

Mainly due to lack of a protective physical boundary, wireless communications is facing much more serious security challenges than its wirelined counterpart. Recently, physical layer security of wireless systems has attracted more and more attention from the communication research community.

Traditionally, the main function of the physical layer is to ensure that the data stream is transmitted successfully and efficiently from the source to the destination.

H. Li
Department of Mathematics, Chang'an University, Xi'an, Shannxi 710054, China
e-mail: lihaobg@163.com

J. Ren (✉) • T. Li
Department of Electrical and Computer Engineering, Michigan State University, East Lansing, MI 48864-1226, USA
e-mail: renjian@egr.msu.edu; tongli@egr.msu.edu

Q. Liang et al. (eds.), *Communications, Signal Processing, and Systems*, Lecture Notes in Electrical Engineering 202, DOI 10.1007/978-1-4614-5803-6_40,

The research on physical layer design has largely been focus on improving the information capacity and bandwidth efficiency. As a result, the PHY layer of the wireless systems generally does not possess any security features except the spread spectrum systems, including both direct sequence spread spectrum system (known as CDMA) and frequency hopping (FH) spread spectrum.

In this paper, first, we revisit the FH systems and examine the major limitation with the traditional FH systems. Second, we investigate spectrally efficient anti-jamming system design based on FH technique. We propose and compare three FH based secure communication schemes: the general collision-free frequency hopping (CFFH), OFDMA based CFFH, and ID based message-drive FH. These systems can potentially be applied for secure and efficient wireless communications under hostile environment.

40.2 Revisit of the FH System

Traditionally, both CDMA and FH have been used for secure communication under hostile environments. CDMA is especially robust to narrow band jamming by reducing the jamming power through the despreading process. Moreover, CDMA can hide the signal within the noise floor so that the adversary cannot even detect the existence of the signal. On the other hand, FH system is more robust to wideband jamming, since the signal power can be concentrated on a narrower frequency band during each hopping period. As the carrier hops randomly over a wide range of frequencies, it is hard for the adversary to track or jam the active transmission.

The observations above for FH are mainly based on slow frequency hopping (SFH) systems, where hopping period is equal to or larger than the symbol period. In a traditional frequency hopping system, as the transmitter hops in a pseudo-random manner among available frequencies according to a pre-specified algorithm, the receiver has to operates in a strict synchronization with the transmitter and remains tuned to the same center frequency. The strict requirement on synchronization directly influences the complexity, design and performance of the system, and turns out to be a significant challenge in fast hopping system design. For this reason, existing work on FH has mainly been limited to slow hopping systems.

It is interesting to notice that: if we put the strong requirement on frequency acquisition aside and consider the fast frequency hopping (FFH) systems, then we can find that CDMA can be regarded as a special case of FH, for which you happen to "hop" just on (actually fixed to) the same band, and during each hopping period or chip period, you transmit either the chip signal itself or its negative version. In other words, CDMA uses only repeated coding, which is the least efficient channel coding, and CDMA has fixed carrier frequency. On the other hand, FH provides a more general and more flexible framework for anti-interception, anti-jamming system design. For this reason, we choose to work with the FH systems.

Now, what are the major limitations with existing FH systems? In addition to strong requirement on frequency acquisition discussed above, another major

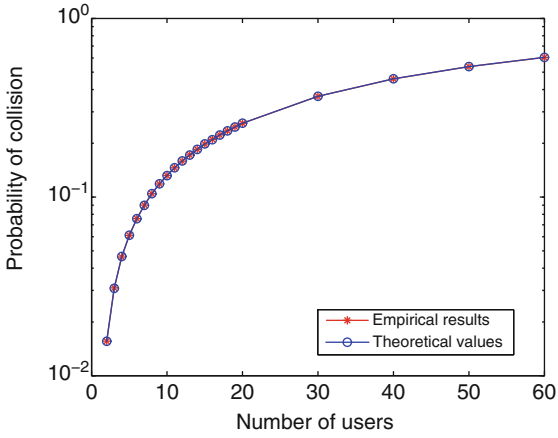

Fig. 40.1 Conventional FH: probability of collision versus the number of users, the total number of channels is $N_c = 64$

limitation with FH is its *low spectral efficiency over large bandwidth* [1, 2]. Typically,FH systems require large bandwidth, which is proportional to the hopping rate and the number of all the available channels. In conventional frequency hopping multiple access, each user hops independently based on its own pseudo-random number sequence, a collision occurs whenever there are two active users over the same frequency band. When there is a collision, it is reasonable to assume that the probability of error is 0.5. As can be seen from Fig. 40.1: *mainly limited by the collision effect, the spectral efficiency of conventional FH systems is very low.*

40.3 Collision Free Frequency Hopping (CFFH) Based on Secure Subcarrier Assignment

In this section, we present the proposed collision-free frequency hopping scheme, for which the major component is an AES (advanced encryption standard) [3] based secure permutation algorithm. The AES-based permutation algorithm is used to securely select the frequency hopping pattern for each user so that: (i) Different users always transmit on non-overlapping sets of subcarriers; (ii) Malicious users cannot determine the frequency hopping pattern and therefore cannot launch follower jamming attacks.

AES is chosen because of its simplicity of design, variable block and key sizes, feasibility in both hardware and software, and resistance against all known attacks. Note that, the secure subcarrier assignment is not limited to any particular cryptographic algorithm, but is highly recommended that only thoroughly analyzed cryptographic algorithms be applied.

We assume there is a total of N_c available subcarriers and there are M users in the system. For $i = 0, 1, \ldots, M-1$, the number of subcarriers assigned to user $i$is denoted as N_u^i. We assume that different users transmit over non-overlapping set of

subcarriers and we have $\sum_{i=0}^{M-1} N_u^i = N_c$. The secure subcarrier assignment algorithm is described in the following subsections.

40.3.1 Secure Permutation Index Generation

A pseudo-random binary sequence is generated using a 32-bit linear feedback shift register (LFSR), which is initialized by a secret sequence chosen by the base station. The LFSR has the following characteristic polynomial:

$$\begin{aligned} &x^{32} + x^{26} + x^{23} + x^{22} + x^{16} + x^{12} + x^{11} \\ &+x^{10} + x^8 + x^7 + x^5 + x^4 + x^2 + x + 1. \end{aligned} \tag{40.1}$$

Use the pseudo-random binary sequence generated by the LFSR as the plaintext. Encrypt the plaintext using the AES algorithm and a secure key. The key size can be 128, 192, or 256. The encrypted plaintext is known as the ciphertext. Assume N_c is a power of 2, pick an integer $L \in [\frac{N_c}{2}, N_c]$. Note that a total of $B_c = \log_2 N_c$ bits are required to represent each subcarrier, let $q = L\log_2 N_c$. Take $q$bits from the ciphertext and put them as a q-bit vector $\mathbf{e} = [e_1, e_2, \ldots, e_q]$.

Partition the ciphertext sequence $\mathbf{e}$into Lgroups, such that each group contains B_c bits. For $k = 1, 2, \ldots, L$, the partition of the ciphertext is as follows

$$\mathbf{p_k} = \left[e_{(k-1)*B_c+1}, e_{(k-1)*B_c+2}, \ldots, e_{(k-1)*B_c+B_c}\right], \tag{40.2}$$

where $\mathbf{p}_\mathrm{k}$ corresponds to the kth B_c-bit vector.

For $k = 1, 2, \ldots, L$, denote P_k as the decimal number corresponding to $\mathbf{p}_\mathrm{k}$, such that

$$\begin{aligned} P_k = {} & e_{(k-1)*B_c+1} \cdot 2^{B_c-1} + e_{(k-1)*B_c+2} \cdot 2^{B_c-2} \\ & + \cdots + e_{(k-1)*B_c+B_c-1} \cdot 2^1 \\ & + e_{(k-1)*B_c+B_c} \cdot 2^0. \end{aligned} \tag{40.3}$$

Finally, we denote $P = [P_1, P_2, \ldots, P_L]$ as the permutation index vector. Here the largest number in P is $N_c - 1$. In the following subsection, we will discuss the secure permutation algorithm.

40.3.2 Secure Permutation Algorithm and Subcarrier Assignment

For $k = 0, 1, 2, \ldots, L$, denote $I_k = [I_k(0), I_k(1), \ldots, I_k(N_c - 1)]$ as the index vector at the kth step. The secure permutation scheme of the index vector is achieved through the following steps:

0. Initially, the index vector is $I_0 = [I_0(0), I_0(1), \ldots, I_0(N_c - 1)]$ and the permutation index is $P = [P_1, P_2, \ldots, P_L]$. We start with $I_0 = [0, 1, \ldots, N_c - 1]$.
1. For $k = 1$, switch $I_0(0)$ and $I_0(P_1)$ in index vector I_0 to obtain I_1. In other words, $I_1 = [I_1(0), I_1(1), \ldots, I_1(N_c - 1)]$, where $I_1(0) = I_0(P_1)$, $I_1(P_1) = I_0(0)$, and $I_1(m) = I_0(m)$ for $m \neq 0, P_1$.
2. Repeat the previous step for $k = 2, 3, \ldots, L$. In general, if we already have $I_{k-1} = [I_{k-1}(0), I_{k-1}(1), \ldots, I_{k-1}(N_c - 1)]$, then we can obtain $I_k = [I_k(0), I_k(1), \ldots, I_k(N_c - 1)]$ through the permutation defined as $I_k(k-1) = I_{k-1}(P_k), I_k(P_k) = I_{k-1}(k-1)$, and $I_k(m) = I_{k-1}(m)$ for $m \neq k - 1, P_k$.
3. After L steps, we obtain the subcarrier frequency vector as $F_L = [f_{I_L(0)}, f_{I_L(1)}, \ldots, f_{I_L(N_c-1)}]$.
4. The subcarrier frequency vector F_L is used to assign subcarriers to the users. Recall, for user $i = 0, 1 \ldots, M - 1$, the total number of subcarriers assigned to the ith user is N_u^i. We assign subcarriers $\{f_{I_L(0)}, f_{I_L(1)}, \ldots, f_{I_L(N_u^0-1)}\}$ to user 0; Assign $\{f_{I_L(N_u^0)}, f_{I_L(N_u^0+1)}, \ldots, f_{I_L(N_u^0+N_u^1-1)}\}$ to user 1, and so on.

Because each frequency index appears in F_L once and only once, the proposed algorithm ensures that: (i) All the users are transmitting on non-overlapping sets of subcarriers; (ii) No subcarrier is left idle. That is, all the subcarriers are active.

The secure permutation index generation is performed at the base station. The base station sends encrypted channel assignment information to each user periodically through the control channels.

The proposed scheme addresses the problem of securely allocating subcarriers in the presence of hostile jamming. This algorithm can be combined with existing resource allocation techniques. First, the number of subcarriers assigned to each user can be determined through power and bandwidth optimization. Then, we use the secure subcarrier assignment algorithm to select the group of subcarriers for each user at each hopping period. In the following, we illustrate the secure subcarrier assignment algorithm though a simple example.

Example. Assume the total number of available subcarriers is $N_c = 8$, to be equally divided among $M = 2$ users; the permutation index vector $P = [4, 7, 4, 0]$, and the initial index vector $I_0 = [0, 1, 2, 3, 4, 5, 6, 7]$, as shown in Fig. 40.2. Note that, the initial index vector I_0 can contain any random permutation of the sequence $\{0, 1, \ldots, N_c - 1\}$, and $L \in [\frac{N_c}{2}, N_c]$. In this example, we choose $L = \frac{N_c}{2}$.

At Step 1, $k = 1$, and $P_k = 4$, thus we switch $I_0(P_k)$ and $I_0(k - 1)$ of the index vector I_0. After the switching, we obtain a new index vector $I_1 = [4, 1, 2, 3, 0, 5, 6, 7]$.

At Step 2, $k = 2$, and $P_k = 7$, thus we switch $I_1(P_k)$ and $I_1(k - 1)$ of the index vector I_1. We obtain the new index vector $I_2 = [4, 7, 2, 3, 0, 5, 6, 1]$. Similarly, $I_3 = [4, 7, 0, 3, 2, 5, 6, 1]$, $I_4 = [3, 7, 0, 4, 2, 5, 6, 1]$. The subcarrier frequency vector is $F_4 = [f_{I_4(0)}, f_{I_4(1)}, \ldots, f_{I_4(N_c-1)}]$. Frequencies $\{f_3, f_7, f_0, f_4\}$ are assigned to user 0 and frequencies $\{f_2, f_5, f_6, f_1\}$ are assigned to user 1.

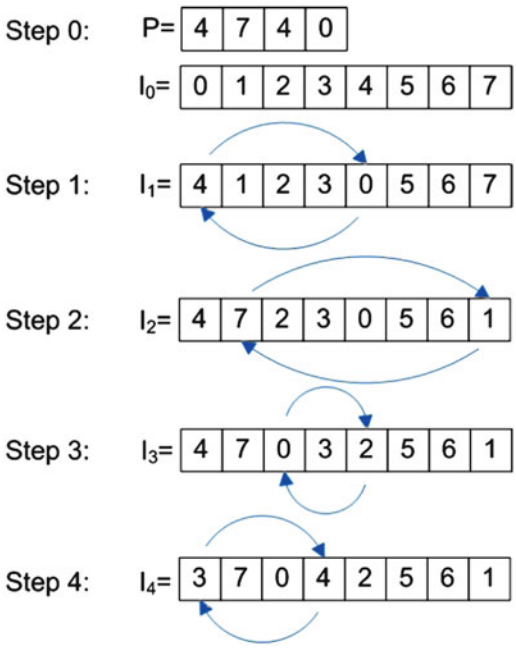

Fig. 40.2 Example of the secure permutation algorithm for $N_c = 8$ subcarriers and $M = 2$ users

40.3.3 OFDMA Based Collision-Free Frequency Hopping

In this section, we incorporate the CFFH scheme with the OFDMA framework, and therefore obtain a highly efficient anti-jamming scheme.

Signal Transmission Consider a system with Musers, utilizing an OFDM system with N_c subcarriers, $\{f_0, \ldots, f_{N_c-1}\}$. At each hopping period, each user is assigned a specific subset of the total available subcarriers. One hopping period may last one or more OFDM symbol periods. Assuming that at the nth symbol, user $i$has been assigned a set of sub-carriers $C_{n,i} = \{f_{n,i_0}, \ldots, f_{n,i_{N_u^i-1}}\}$, that is, user $i$will transmit and only transmit on these subcarriers. Here $N_u{}^i$is the total number of subcarrier assigned to user i. Note that for any n, $C_{n,\,i} \bigcap C_{n,\,j} = \emptyset$, if $i \neq j$. That is, users transmit on non-overlapping subcarriers. In other words, there is no collision between the users. Ideally, for full capacity of the OFDM system, $\bigcup_{i=0}^{M-1} C_{n,i} = \{f_0, \ldots, f_{N_c-1}\}$. For the ith user, if $N_u{}^i > 1$, then the ith users information symbols are first fed into a serial-to-parallel converter. Assuming that at the nth symbol period, user $i$transmits the information symbols $\{u_{n,0}^{(i)}, \ldots, u_{n,N_u^i-1}^{(i)}\}$through the subcarrier set $C_{n,i} = \{f_{n,i_0}, \ldots, f_{n,i_{N_u^i-1}}\}$. User i's transmitted signal at the nth OFDM symbol can then be written as:

$$s_n^{(i)}(t) = \sum_{l=0}^{N_u^i-1} u_{n,l}^{(i)} e^{j2\pi f_{n,i_l} t}. \tag{40.4}$$

Note that each user does not transmit on subcarriers which are not assigned to him/her, by setting the symbols to zeros over these subcarriers. This process ensures collision-free transmission among the users.

At the receiver, the received signal is a superposition of the signals transmitted from all users

$$r(t) = \sum_{i=0}^{M-1} r_n^{(i)}(t) + n(t), \tag{40.5}$$

where $n(t)$ is the additive noise, ${r_n}^{(i)}(t) = {s_n}^{(i)}(t)^* h_i(t)$, with $h_i(t)$ being the channel impulse response corresponding to user i. Note that in OFDM systems, guard intervals are inserted between symbols to eliminate intersymbol interference (ISI), so it is reasonable to study the signals in a symbol-by-symbol manner. We consider an uplink system here, the downlink system can be formulated in a similar manner.

As is well known, the OFDM transmitter and receiver is implemented through IFFT and FFT, respectively. Denote the $N_c \times 1$ symbol vector corresponding to user i's nth OFDM symbol as ${\mathbf{u}_n}^{(i)}$, we have

$$\mathbf{u}_n^{(i)}(l) = \begin{cases} 0, & l \notin \{i_0, \ldots, i_{N_u^i - 1}\} \\ u_{n,l}^{(i)}, & l \in \{i_0, \ldots, i_{N_u^i - 1}\}. \end{cases} \tag{40.6}$$

Let T_s denote the OFDM symbol period. The discrete form of the transmitted signal ${s_n}^{(i)}(t)$ (sampled at $\frac{IT_s}{N_c}$) is ${\mathbf{s}_n}^{(i)} = \mathbf{F}{\mathbf{u}_n}^{(i)}$, where $\mathbf{F}$ is the IFFT matrix defined as

$$\mathbf{F} = \frac{1}{\sqrt{N_c}} \begin{pmatrix} W_{N_c}^{00} & \cdots & W_{N_c}^{0(N_c-1)} \\ \vdots & \ddots & \vdots \\ W_{N_c}^{(N_c-1)0} & \cdots & W_{N_c}^{(N_c-1)(N_c-1)} \end{pmatrix},$$

with $W_{N_c}^{nk} = e^{j2\pi nk/N_c}$. As we only consider one OFDM symbol at a time, for notation simplification, here we omit the insertion of the guard interval (i.e. the cyclic prefix which is used to ensure that there is no ISI between two successive OFDM symbols).

Let $\mathbf{h}_i = [h_i(0), \ldots, h_i(N_c - 1)]$ be the discrete channel impulse response vector, and let $\mathbf{H}_i = \mathbf{F}\mathbf{h}_i$ be the Fourier transform of $\mathbf{h}_i$. Then the received signal corresponding to user $i$is ${\mathbf{r}_n}^{(i)}(l) = {\mathbf{u}_n}^{(i)}(l)\mathbf{H}_i(l)$. The overall received signal is then given by

$$\mathbf{r}_n(l) = \sum_{i=0}^{M-1} \mathbf{r}_n^{(i)}(l) + \mathbf{N}_n(l) \tag{40.7}$$

where $\mathbf{N}_n(l)$ is the Fourier transform of the noise corresponding to the nth OFDM symbol.

Note that due to the collision-free subcarrier assignment, for each l, there is at most one non-zero item in the sum $\sum_{i=0}^{M-1} \mathbf{u}_n^{(i)}(l)\mathbf{H}_i(l)$. As a result, standard channel estimation algorithms and signal detection algorithms for OFDM systems can be implemented. In fact, each user can send pilot symbols on its subcarrier set to perform channel estimation. After channel estimation, user i's information symbols can be estimated from

$$\hat{\mathbf{u}}_n^{(i)}(l) = \frac{\mathbf{r}_n^{(i)}(l)}{\mathbf{H}_i(l)}, \quad l \in \{i_0, \ldots, i_{N_u^i - 1}\}. \tag{40.8}$$

A major challenge for the collision-free frequency hopping techniques discussed above is the secure distribution of the hopping frequency sequences. Can this frequency dispatching process be simplified? In the following section, we try to resolve this using message-driven frequency hopping [4].

40.4 Secure ID Based Message-Driven Frequency Hopping (MDFH)

The idea here is that the message information will used be for hopping frequency selection. In other words, the message information is transmitted through hopping frequency control. For security purpose, the message stream is encrypted before transmission, and a secure ID sequence is inserted during the transmission process.

40.4.1 Transmitter Design

The transmitter structure of ID-based MDFH is illustrated in Fig. 40.3. The encrypted information sequence is transmitted through carrier frequency selction, and each user is assigned a secure ID sequence.

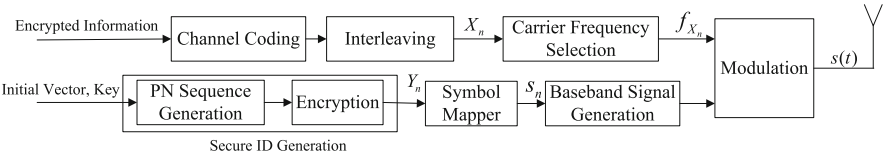

Fig. 40.3 ID-based MDFH: transmitter structure

The secure ID information is generated through a cryptographic algorithm using the shared secret between the transmitter and the receiver, and can be exploited by the receiver to locate the true carrier frequency or the desired channel. On the other hand, protected using advanced encryption techniques, such as AES [3], it is computationally infeasible for malicious users to recover the ID sequence. In other words, *in ID-based MDFH, secure ID signals are introduced to distinguish the true information channel from the disguised channels invoked by jamming interference, and hence ensure robust communications under hostile environment.*

The ID sequence generation process is summarized as follows:

1. Generate a pseudo-random binary sequence using a linear feedback shift register (LFSR), e.g., the one specified by the characteristic polynomial in Eq. (40.1).
2. Take the output of LFSR as the plaintext, group it into blocks of length K_L bits ($K_L = 128$, 192 or 256), and feed it into the AES encrypter of key size K_L. The AES output is then used as our ID sequence.

Recall that $B_c = \log_2 N_c$ and $B_s = \log_2 \Omega$, where N_c is the number of channels, and Ω is the constellation size. We divide the source information into blocks of size B_c and divide the ID sequence into blocks of size B_s. Denote the nth source information block and ID bits block as X_n and Y_n, respectively. Let f_{X_n} be the carrier frequency corresponding to X_n and s_n the symbol corresponding to ID bit-vector Y_n. The transmitted signal can then be represented as

$$\begin{aligned} s(t) &= \sqrt{2} Re\left\{ \sum_{n=-\infty}^{\infty} s_n g(t - nT_h) e^{j2\pi f_{X_n} t} \right\} \\ &= \sqrt{2} Re\left\{ \sum_{n=-\infty}^{\infty} \sum_{i=1}^{N_c} \alpha_{i,n} s_n g(t - nT_h) e^{j2\pi f_i t} \right\}, \end{aligned} \tag{40.9}$$

where T_h is the duration of each hop, $g(t)$ is the pulse shaping function,

$$\alpha_{i,n} = \begin{cases} 1 & \text{if } f_{X_n} = f_i \\ 0 & \text{otherwise.} \end{cases}$$

40.4.2 Receiver Design

The receiver structure for ID based MDFH is shown in Fig. 40.4. The receiver regenerates the secure ID through the shared secret (including the initial vector, the LFSR information and the key).

For each hop, the received signal is first fed into the bandpass filter bank. The output of the filter bank is first demodulated, and then used for carrier bits (i.e., the

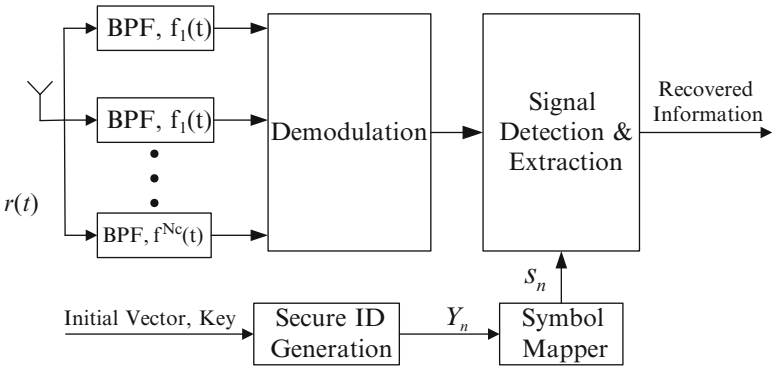

Fig. 40.4 ID-based MDFH: receiver structure

information bits) detection. Let $s(t)$, $J(t)$ and $n(t)$ denote the ID signal, the jamming interference and the noise, respectively. For AWGN channels, the received signal can be represented as

$$r(t) = s(t) + J(t) + n(t). \tag{40.10}$$

We assume that $s(t)$, $J(t)$ and $n(t)$ are independent of each other. If the spectrum of $J(t)$ overlaps with the frequency band of $s(t)$, then the signal is *jammed*; otherwise, the signal is *jamming-free*. If $J(t)$ spreads over multiple channels, we have multi-band jamming; otherwise, we have single band jamming. Note that the true information is embedded in the index of the active carrier over which the ID signal $s(t)$ is transmitted.

For $i = 1, 2, \ldots, N_c$, the output of the ith ideal bandpass filter $f_i(t)$ is $r_i(t) = f_i(t)^* r(t)$. For demodulation, $r_i(t)$ is first shifted back to the baseband, and then passed through a matched filter. At the nth hopping period, for $i = 1, \ldots, N_c$, the sampled matched filter output corresponds to channel $i$can be expressed as

$$r_{i,n} = \alpha_{i,n} s_n + \beta_{i,n} J_{i,n} + n_{i,n}, \tag{40.11}$$

where s_n, $J_{i,n}$ and $n_{i,n}$ correspond to the ID symbol, the jamming interference and the noise, respectively; $\alpha_{i,n}$, $\beta_{i,n} \in \{0, 1\}$ are binary indicators for the presence of ID signal and jamming, respectively. Note that the true information is carried in $\alpha_{i,n}$.

Signal detection and extraction is performed for each hopping period. *For notation simplicity, without loss of generality, we omit the subscript n in* (40.11). That is, for a particular hopping period, (40.11) is reduced to:

$$r_i = \alpha_i s + \beta_i J_i + n_i, \quad \text{for } i = 1, \ldots, N_c. \tag{40.12}$$

Define $\mathbf{r} = (r_1, \ldots, r_{N_c})$, $\alpha = (\alpha_1, \ldots, \alpha_{N_c})$, $\beta = (\beta_1, \ldots, \beta_{N_c})$, $\mathbf{J} = (J_1, \ldots, J_{N_c})$ and $\mathbf{n} = (n_1, \ldots, n_{N_c})$, then (40.12) can be rewritten in vector form as:

$$\mathbf{r} = s\alpha + \beta \cdot \mathbf{J} + \mathbf{n}, \tag{40.13}$$

For single-carrier AJ-MDFH, at each hopping period, one and only one item in α is nonzero. That is, there are N_c possible information vectors: $\alpha_1 = (1, 0, \ldots, 0)$, $\alpha_2 = (0, 1, \ldots, 0), \ldots, \alpha_{N_c} = (0, 0, \ldots, 1)$. If α_k is selected, and the binary expression of $k$is $b_0 b_1 \ldots b_{B_c-1}$, with $B_c = \lceil \log_2 N_c \rfloor$, then the estimated information sequence is $b_0 b_1 \ldots b_{B_c-1}$.

So at each hopping period, the information symbol α, or equivalently, the hopping frequency index k, needs to be estimated based on the received signal and the ID information which is shared between the transmitter and the receiver. We start with the *maximum likelihood* (ML) detector. If the input information vectors are equiprobable, that is, $P(\alpha_i) = \frac{1}{N_c}$ for $i = 1, 2, \ldots, N_c$, then the MAP detector is reduced to the ML detector. For the ML detector, the hopping frequency index $\hat{k}$ can be estimated as:

$$\hat{k} = \arg \max_{1 \le i \le N_c} P\{\mathbf{r} | \alpha_i\}. \tag{40.14}$$

By splitting all the $N_c$channels into non-overlapping groups and let each subcarrier hop over assigned group(s), ID based MDFH can readily be extended to multi-carrier system, which can also be used as a collision-free anti-jamming MDFH scheme to accommodate more users in the multiple access environment. To ensure collision-free multiple access among all users, different users will be assigned to different subcarriers. The number of subcarriers assigned to each user can be different based on the data rate and QoS requirement of the user.

40.5 Simulation Examples

In this section, simulation examples are provided to compare the performances of the proposed CFFH, OFDMA based CFFH and ID based MDFH under partial band jamming over an AWGN channel. The SNR $E_b/N_0 = 10$ dB and the jamming-to-signal ratio (JSR) is defined as the ratio of the jamming power to signal powers per hop. We assume that $\frac{1}{16}$ of the channels are jammed. $N_c = 64$ for CFFH and ID based MDFH; $N_c = 128$ for OFDMA based CFFH due to the overlap between adjacent channels. BPSK modulation is used for both CFFH and OFDMA based CFFH. For MDFH, 32-PSK is used to modulate the ID bits. From Fig. 40.5, it can be observed that MDFH is particularly robust under strong jamming. In this example, the spectral efficiency of OFDMA based CFFH and secure ID based MDFH are 8 and 2 times that of CFFH, respectively.

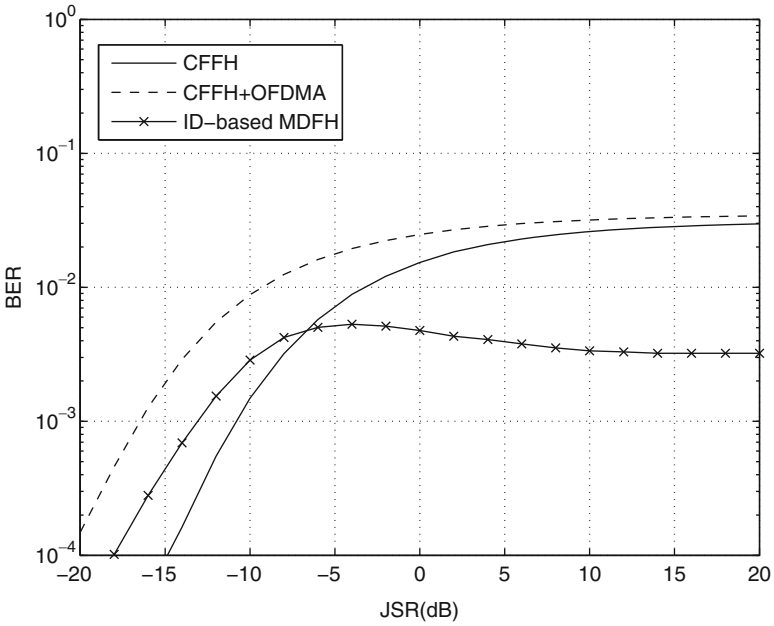

Fig. 40.5 Performance comparison under partial band jamming

40.6 Conclusions

In this paper, we presented three spectrally efficient anti-jamming system design using FH techniques. It is observed that by integrating cryptographic techniques into transceiver design, the PHY security of wireless systems can be improved significantly.

References

1. Glisic S, Nikolic Z, Milosevic N, Pouttu A (2000) Advanced frequency hopping modulation for spread spectrum WLAN. IEEE J Sel Areas Commun 18:16–29
2. Choi K, Cheun K (2004) Maximum throughput of FHSS multiple-access networks using MFSK modulation. IEEE Trans Commun 52:426–434
3. US National Institute of Standards and Technology (2001) Federal information processing standards publication 197-Announcing the ADVANCE ENCRYPTION STANDARD (AES). http://csrc.nist.gov/publications/fips/fips197/fips-197.pdf
4. Zhang L, Ren J, Li T (2009) Jamming mitigation techniques based on message-driven frequency hopping. In: Proceeding of IEEE global telecommunications conference, 2009. GLOBECOM '09, Honolulu

Chapter 41
An Improved Adaptive Filtering Algorithm for Non-Sparse Impulse Response

Songlin Sun, Xiao Xia, Chenglin Zhao, Yanhong Ju, and Yueming Lu

Abstract An algorithm to improve the convergence performance of the improved μ-law PNLMS algorithm (IMPNLMS) for non-sparse impulse responses is proposed in this chapter. In this algorithm, an adaptive parameter μ of the μ-law compression for sparse impulse response is incorporated into the IMPNLMS algorithm. Compared with IMPNLMS algorithm, simulation results demonstrate that the proposed algorithm has better convergence performance.

Keywords Adaptive filtering • IMPNLMS algorithm • Non-sparse impulse response

41.1 Introduction

In some practical applications, the impulse responses are sparse in nature [1, 2], as most of the coefficients take values near zero and only a few have significant values. For instance, in voice transmission over wireless and packet switching networks, the echo path impulse response exhibits an active region and an unknown bulk delay. The unknown bulk delay interval has almost zero energy, making the impulse response sparse [3]. For these systems, classical adaptive algorithms, such as the normalized least-mean-square (NLMS) algorithm, assigning the same step-size to all filter coefficients, converge slowly.

S. Sun (✉) • X. Xia • Y. Ju • Y. Lu
School of Information and Communication Engineering, Key Laboratory of Trustworthy Distributed Computing and Service (BUPT), Ministry of Education, Beijing University of Posts and Telecommunications, Beijing, China
e-mail: slsun@bupt.edu.cn

C. Zhao
School of Information and Communication Engineering, Beijing University of Posts and Telecommunications, Beijing 100876, China

Q. Liang et al. (eds.), *Communications, Signal Processing, and Systems*, Lecture Notes in Electrical Engineering 202, DOI 10.1007/978-1-4614-5803-6_41,

However, the non-sparse impulse responses are exist in most practical applications in real world. In this chapter, we present the improvement of the IMPNLMS algorithm using a variable parameter μ instead of the constant value. Adaptation of μ(n) is done by using the estimate of MSE. The changes of μ(n) are related in a natural way to the changes of MSE. As a consequence, the convergence features of the proposed algorithm are significantly improved.

This is organized as follows. Section 41.2 introduces the related works about NLMS. In Sect. 41.3, the improvement of IMPNLMS algorithm is proposed. In Sect. 41.4, numerical simulations confirm the proposed IMPNLMS performance. Finally, Sect. 41.5 presents conclusions.

41.2 Related Works

Some algorithms exploiting the sparse nature of the impulse response have been proposed. Duttweiler presented a proportionate NLMS (PNLMS) algorithm [4] in the context of echo cancellation. However, its convergence begins to slow dramatically after the initial fast period. Another version of the PNLMS, termed μ-law PNLMS (MPNLMS) algorithm [5], was proposed to solve this problem. Instead of using coefficient magnitude directly, the algorithm used it as the step gain of each coefficient. Such an algorithm provides the fast initial convergence over the whole adaptation process. However, the MPNLMS algorithm is computationally complex. A variable parameter of the μ-law compression makes the AMPNLMS algorithm achieve better convergence performance than MPNLMS algorithm for sparse responses [6]. Recently, individual activation factor PNLMS (IAF-PNLMS) algorithm [7] for high sparse channels was addressed to achieve fast convergence, outperforming the PNLMS algorithm.

All these algorithms, however, are effective only when the impulse response is sparse. Their performance on non-sparse systems is relatively poor. PNLMS++ [8] was proposed to partially solve this problem by alternating the update process each sample period between NLMS and PNLMS algorithms. The improved PNLMS (IPNLMS) algorithm [9] was presented to combine NLMS and PNLMS with an adjustable parameter, and it does not perform worse than NLMS even for dispersive channels. The improved MPNLMS (IMPNLMS) algorithm [10] was proposed to combine NLMS and MPNLMS with an automatic adjustable parameter. If the convergence speed of IMPNLMS algorithm can be further improved, this algorithm will get a good application in time-varying environment.

41.3 The Proposed IMPNLMS Algorithm

For non-sparse response, which also makes the parameter μ time varying instead of constant, we propose that a variable parameter μ is applied to the IMPNLMS algorithm.

Let's recall the adaptive μ in the AMPNLMS algorithm [6]:

$$\zeta(n+1) = \eta\zeta(n) + (1-\eta)e^2(n) \tag{41.1}$$

$$\varepsilon_N(n+1) = \frac{\zeta(n+1)}{v} \tag{41.2}$$

$$\varepsilon_c(n+1) = \sqrt{\frac{\varepsilon_N(n+1)}{N\,\sigma_x^2}} \tag{41.3}$$

$$\mu(n+1) = \frac{1}{\varepsilon_c(n+1)}. \tag{41.4}$$

where $0 \leq \eta \leq 1$ and ν is a constant value relating with the current MSE estimation (obtained by time averaging) to $\varepsilon_N(n+1)$. The term ζ(n + 1) is an estimation of e^2(n + 1). $\varepsilon_N(n+1)$ is the distance to the steady-state MSE that is considered as achievement of convergence when reached by the MSE.

Starting with a large value for $\varepsilon_c(n)$ and slowly decreasing the required ε-neighborhood to be reached by the converged algorithm, the adjustment for this parameter $\varepsilon_c(n)$ can make fast convergence speed at the initial phase with a lower steady-state error in the latter. In doing so, the AMPNLMS algorithm initially behaves like the PNLMS algorithm and then transitions to performing like the NLMS algorithm as time proceeds. Hence, the AMPNLMS algorithm achieves better convergence.

Such adaptive μ(n) is incorporated into the IMPNLMS algorithm [9]. Our proposed IMPNLMS algorithm is as follows:

Gain distribution matrix(N × N)

$$G(n) = diag[\,g_1(n) \quad g_2(n) \quad \ldots \quad g_N(n)\,] \tag{41.5}$$

Individual gain

$$g_i(n) = \frac{1-\alpha(n)}{2N} + \frac{(1+\alpha(n))F(|w_i(n)|)}{2\,\|F(|w(n)|)\|_1 + \varepsilon} \tag{41.6}$$

Logarithmic function

$$F(|w_i(n)|) = ln(1+\mu(n)|w_i(n)|) \tag{41.7}$$

Parameter $\mu(n)$

$$\mu(n) = \frac{1}{\varepsilon_c(n)} \tag{41.8}$$

$$\varepsilon_c(n) = \sqrt{\frac{\zeta(n)}{N\,\sigma_x^2}} \tag{41.9}$$

$$\zeta(n) = \eta\zeta(n-1) + (1-\eta)e^2(n-1) \tag{41.10}$$

Parameter $\alpha(n)$

$$\alpha(n) = 2\xi(n) - 1 \tag{41.11}$$

$$\xi(n) = (1-\lambda)\xi(n-1) + \lambda\,\xi_w(n), \qquad 0<\lambda \le 1 \tag{41.12}$$

$$\xi_w(n) = \frac{N}{N-\sqrt{N}}\left(1 - \frac{||w(n)||_1}{\sqrt{N}||w(n)||_2}\right) \tag{41.13}$$

For a sparse channel with the value of sparseness is close to 1, that is, $\alpha(n) = 1$, the proposed algorithm behaves like AMPNLMS. When the initial MSE is so large that $\mu(n)$ is very small, that is, the proposed algorithm inclines to PNLMS algorithm. As time proceeds, $\mu(n)$ become larger, the algorithm finally performs like NLMS.

For a dispersive channel the value of sparseness is close to -1, that is, $\alpha(n) = -1$, the proposed algorithm is equivalent to NLMS.

Since time-varying $\mu(n)$ are related to the changes of MSE naturally, the parameter $\mu(n)$ is adjusted adaptively. Adaptation of $\mu(n)$ allow our proposed algorithm more flexibility when attempting to minimize the MSE. With this adaptive $\mu(n)$, our proposed algorithm obtains better convergence, besides, it can be used well in time-varying environment where the echo path changes significantly.

41.4 Numerical Simulations

In this section, the simulations of the NLMS, MPNLMS, IMPNLMS and proposed IMPNLMS algorithms are carried out for the various impulse responses, aiming to evaluate the convergence properties of the proposed IMPNLMS algorithm. The common conditions for the simulations are as follows.

Both the unknown system $\boldsymbol{w}^0$ and the adaptive filter w have 100 coefficients, $N = 100$. The disturbance $z(n)$ is a Gaussian signal and the signal-to-noise ratio (SNR) is 40 dB. The constant step size is $\beta = 0.5$ for all algorithms. The initial value of ξ is a large number, such as 0.96. The forgetting factor λ for estimation of channel sparseness is 0.1. In the proposed algorithm, $\eta = 0.99$, and $\nu = 1{,}000$.

To evaluate the algorithm performance, we use the normalized misalignment measure (in dB) given by [1]

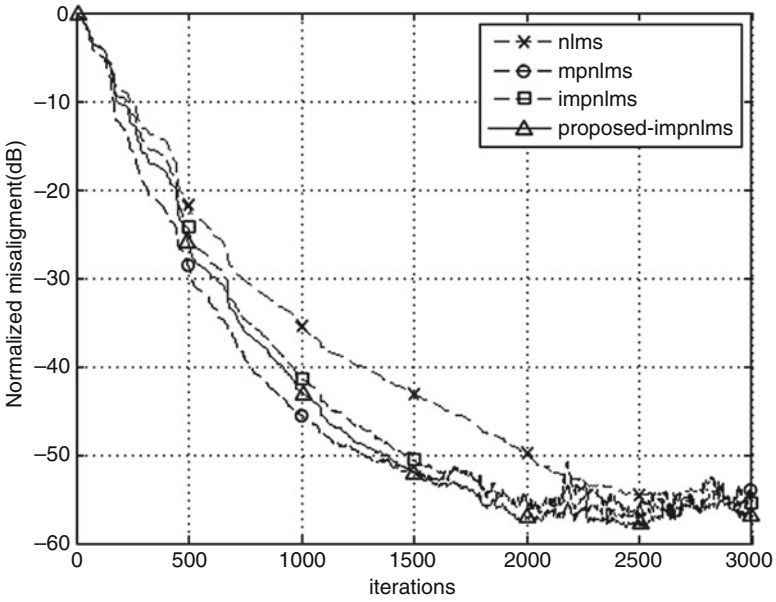

Fig. 41.1 Gaussian input with sparseness degree 0.81

$$k(n) = 10\log_{10}\frac{\left\|w^0 - w(n)\right\|_2^2}{\left\|w^0\right\|_2^2}. \tag{41.14}$$

In Simulation, the input of the simulated system is white Gaussian noise with zero-mean and unit variance. The sparseness degrees of channel are 0.81, 0.61, 0.20, respectively. The figures compare the convergence speed of the related algorithms. From these figures, it can be observed that the proposed algorithm converges faster than the IMPNLMS algorithm. In Fig. 41.3, our proposed algorithm converges as fast as IMPNLMS algorithm. In Fig. 41.1, our proposed algorithm converges almost as fast as MPNLMS algorithm. In Figs. 41.2 and 41.3, our proposed algorithm converges faster than MPNLMS algorithm.

41.5 Conclusion

In this chapter, we have proposed a method to incorporate a variable parameter μ(n) into the IMPNLMS algorithm. With the adaptation of μ, which depends on the MSE estimation, the better performance can be achieved. Simulation results show that the proposed algorithm has faster convergence speed and better tracking ability than the IMPNLMS algorithm.

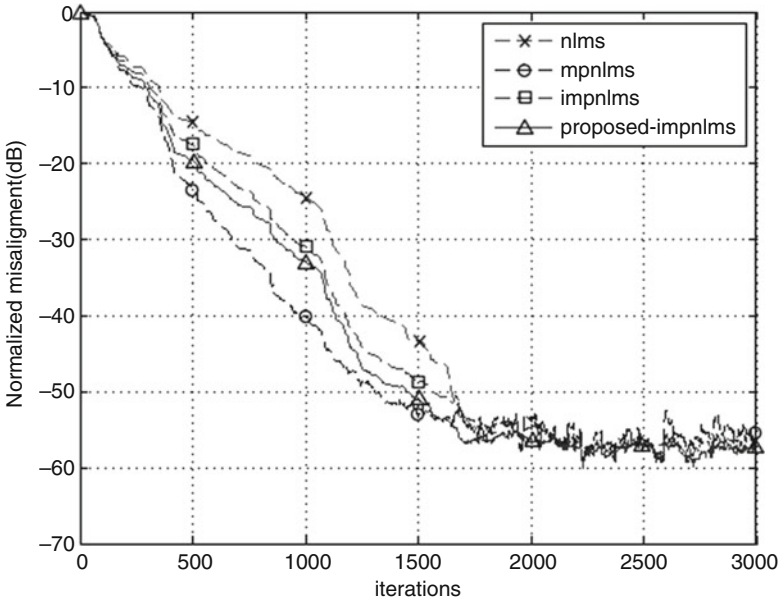

Fig. 41.2 Gaussian input with sparseness degree 0.61

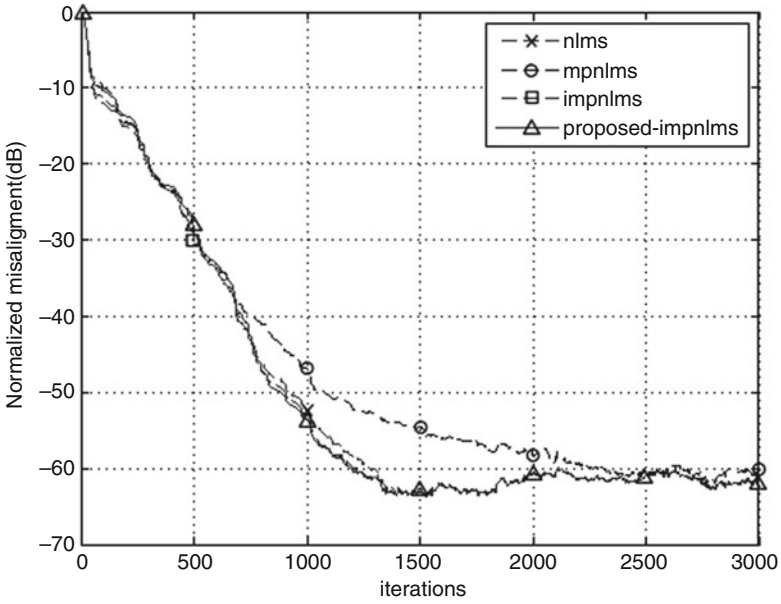

Fig. 41.3 Gaussian input with sparseness degree 0.20

Acknowledgments This work is supported by National High Technology Research and Development Program of China (No. 2011AA01A204), Beijing University of Posts and Telecommunications Research and Innovation Fund for Youths.

References

1. Huang Y, Benesty J, Chen J (2006) Acoustic MIMO signal processing. Springer, New York
2. Martin RK, Sethares WA, Williamson RC, Johnson CR Jr (2002) Exploiting sparsity in adaptive filters. IEEE Trans Signal Process 50(8):1883–1894
3. Krishna VV, Rayala J, Slade B (2002) Algorithmic and implementation aspects of echo cancellation in packet voice networks. In: Proceedings of 36th Asilomar conference signals, systems and computers, vol 2. Milpitas, Nov 2002, pp 1252–1257
4. Duttweiler DL (2000) Proportionate normalized least-mean-squares adaptation in echo cancelers. IEEE Trans Speech Audio Process 8(5):508–518
5. Deng H, Doroslovacki M (2005) Improving convergence of the PNLMS algorithm for sparse impulse response identification. IEEE Signal Process Lett 12(3):181–184
6. Wagner K, Doroslovacki M (2009) Gain allocation in proportionate-type NLMS algorithms for fast decay of output error at all times. In: Proceedings IEEE international conference on Acoustics, speech, and signal processing, Taipei, 19–24 Apr 2009
7. de Souza FC, Tobias OJ, Seara R, Morgan DR (2010) A PNLMS algorithm with individual activation factors. IEEE Trans Signal Process 58(4):2036–2047
8. Gay SL (1998) An efficient, fast converging adaptive filter for network echo cancellation. In: Proceedings of 32nd Asilomar conference on signals and system for computing, Pacific Grove, California, USA, vol 1. pp 394–398
9. Benesty J, Gay SL (2002) An improved PNLMS algorithm. In: Proceedings of IEEE international conference on Acoustic, speech and signal processing, (ICASSP'02), Orlando, May 2002, pp 1881–1884
10. Liu L, Fukumoto M, Saiki S (2008) An improved mu-law proportionate NLMS algorithm. In: Proceedings of IEEE international conference on Acoustic, speech and signal processing (ICASSP'08), Las Vegas, March 2008, pp 3797–3800

Chapter 42
60 GHz Ultra-Band Channel Estimation Based on Cluster-Classification Compressed Sensing

Xuebin Sun, Meng Hou, Hongbo Tao, Sha Zhang, Bin Li, and Chengli Zhao

Abstract In this chapter, we investigated the application of compressed sensing in channel estimation for the emerging 60 GHz millimeter-wave communications. We firstly investigate the regular orthogonal matching pursuit (Regularized OMP) algorithm for 60 GHz systems, and then consider the characteristics of 60 GHz channel, a Cluster-based Classification Compressed Sensing Algorithm is finally proposed on this basis. It may significantly reduce the reconstruction error of the channel estimation. Error ratios of CS-ROMP and algorithm based Cluster-Classification are thoroughly compared and comprehensive analysis is given relying on the experimental simulations. The results show that CS-ROMP algorithms can be properly applied to channel estimation of the 60 GHz system. The developed Cluster-based Classification Compressed Sensing Algorithm shows a superior performance in both the precision of the channel estimation and the complexity of reconstruction.

Keywords 60GHz millimeter-wave • Compressed sensing • Channel estimations • Cluster sparsity • Cluster-sparsity compressive sensing

X. Sun (✉) • M. Hou • B. Li • C. Zhao
Key Laboratory of Universal Wireless Communication, Ministry of Education, Beijing University of Posts and Telecommunications, Beijing 100876, People's Republic of China
e-mail: sunxuebin@bupt.edu.cn

H. Tao • S. Zhang
The State Radio Monitoring Center Testing Center, No. A-98 Bei lishi Road, Beijing 100037, XiCheng District, People's Republic of China

Q. Liang et al. (eds.), *Communications, Signal Processing, and Systems*, Lecture Notes in Electrical Engineering 202, DOI 10.1007/978-1-4614-5803-6_42,

42.1 Introduction

In recent years, we are witnessing an explosive growth in the demand for wireless networks. The huge amount of the bandwidth available in the unlicensed 60 GHz band, which is also known as the millimeter-wave band, has aroused a great deal of interest to develop new wireless communication techniques. The large bandwidth around 60 GHz (more than 3 GHz wide) may potentially enable the multi-gigabit wireless communication products and applications worldwide. New applications which could make full use of the increased data rate enabled by 60 GHz WPANs such as cameras, personal computers and uncompressed high definition television (HDTV) may be an emerging market [1].

Emerging as an extremely powerful technique in signal processing recently, Compressed Sensing (CS) offers the acquisition of signals at rates much lower than previously thought possible. More and more experiments have indicated typically sparse characteristics of radio channel and the sparse characteristics of 60 GHz millimeter-wave channel are more remarkable. Compressed Sensing enable acquire and recover the sparse signal at less than the Nyquist Sampling Rate. When applying Compressed Sensing to channel estimation of 60 GHz communication system, signal reconstruction algorithm has an important influence on precision performance of the original signal recovery. This chapter studies the applications of regularization orthogonal matching pursuit (ROMP) algorithm in 60 GHz channel estimation, and then proposes a compressed sensing algorithm based on the cluster classification of sparse signals. The reconstruction error, iteration times are compared with ROMP algorithms. Based on our experiments, the algorithm exhibits faster convergence.

The remainder of this chapter is organized as follows. In Sect. 42.2, we discuss the system model including compressed sensing theory, 60 GHz channel model and cluster-based classification compressed sensing. In Sect. 42.3, we discuss explicitly the scheme of cluster-based classification compressed sensing algorithm for the 60 GHz millimeter-wave WPANs. Then, in Sect. 42.4, we provide some simulation results and analysis. We also discuss the feasibility of applying cluster-based classification compressed sensing scheme in other fields in this section. Finally, we conclude the chapter in Sect. 42.5.

42.2 System Model

42.2.1 Network Model

The Shannon/Nyquist sampling theorem specifies that to avoid losing information while capturing a signal, one must sample at least two times faster than the signal bandwidth [2]. In many applications, including digital image and video cameras, the Nyquist rate is so high that too many samples result, making compression a necessity prior to storage or transmission. However, increasing the sampling rate

is very expensive. Compressive Sensing (CS) [3] provides a solution to these problems by allowing us to sample signals at a rate significantly lesser than the Nyquist rate. This method employs random linear projections that preserve the structure of signals that are sparse in some basis. An optimization process is then used to reconstruct the required signal. Next, we briefly describe the CS framework proposed in [2].

Assume **f** is a N-point discrete-time sparse signal and Φis a $K \times N$ measurement matrix, then:

$$\mathbf{f} = \sum_{i=1}^{M} \theta_{l_i} \psi_{l_i} = \Psi\Theta \tag{42.1}$$

for $K<<N$, then **f** can be recovered from the received signal, with high probability as long as the measurement matrix Φ is incoherent with the dictionary Ψ.

In (42.1), $\Theta = [\theta_1, \theta_{2,} \ldots, \theta_Z]^{\dagger}$ is a column vector that contains M non-zeros coefficients. The index of the non-zero coefficient defines which element in the dictionary composes the signal and the coefficient value the contribution of that element in defining the signal **f** [2].

The signal **f** can be recovered from the solution of a convex, non-quadratic optimization problem known as Basis Pursuit [4] that yields the sparse vector Θ. Formally, with very high probability, Θ is the unique solution to

$$\min \|\Theta\|_1 \text{ subject to } \mathbf{y} = Vf \tag{42.2}$$

where $\|g\|_1$ denotes the l_1 norm and $V = \Phi\Psi$ is the holographic dictionary, **y** is the received signal. It was shown in [5] that if the random measurement matrix has enough entries taken from a normal distribution and the number of random projection, K, is greater than or equal to $c_1 M \log(\frac{N}{M})$ the probability of exact reconstruction exceeds $(1 - e^{c_2 K})$, where c_1 and c_2 are some constants [6].

42.2.2 60 GHz Channel Model

In this article, we model the indoor channel at 60 GHz band using the model proposed by the IEEE802.11.TG3c (Next generation WLAN standard at 60 GHz band), which assumes that the received signals arrive in clusters. The rays within a cluster have independent phases as well as independent Rayleigh amplitudes whose variances decay exponentially with cluster and rays delays [7].

The impulse response for LOS scenarios in the indoor channel at 60 GHz band is shown in Fig. 42.1. According to the figure, the amplitude of first cluster is about 15 dB higher than that of second cluster. Meanwhile the amplitude of the following clusters after the second cluster is even lower than that of the second cluster. While considering directional, LOS links, ignoring the clusters whose time of arrival is later than the first cluster is acceptable. In the following research, we substitute indoor channel model at 60 GHz band to simplify our discussion.

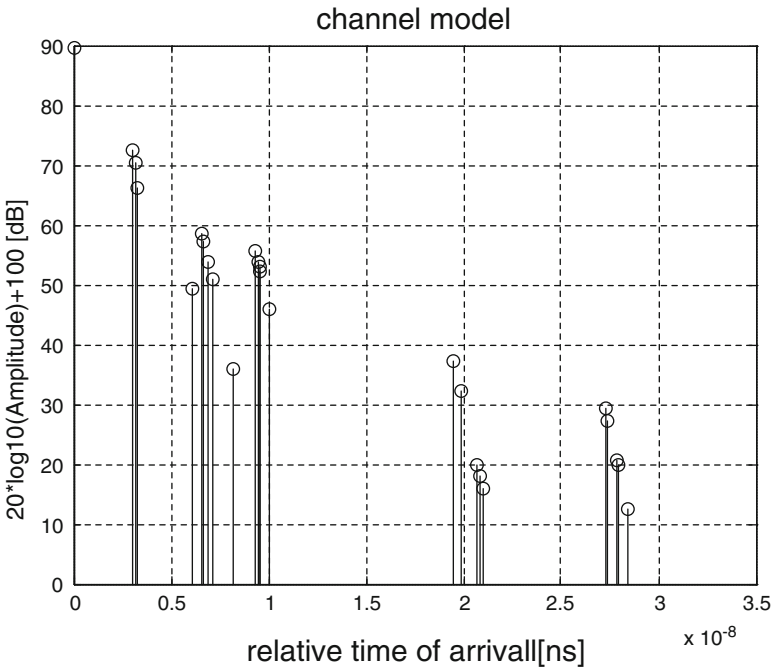

Fig. 42.1 The impulse response for 60 GHz channel

42.2.3 Cluster-Based Classification and Clustered-Sparse Signal

A novel cluster identification algorithm is proposed in [8]. This algorithm can produce reasonable clustering results in more universal propagation environments. Hence, the cluster identification can help us achieve the scheme of cluster-based classification compressed sensing.

Here, we consider the case of sparse vectors x, i.e., x has only a few nonzero entries relative to its arriving time. The standard sparsity model considered in compressed sensing, assumes that x has at most k nonzero elements, which can appear anywhere in the vector. As discussed in [2, 3] there are practical scenarios that involve vectors x with nonzero entries appearing in blocks (or clusters) rather than being arbitrarily spread throughout the vector. There exist plenty of specific examples such as multi-band signals and signals appearing in clusters.

The clustered-sparse signals have nonzero coefficients occurring in clusters and can be represented as follows:

$$\mathbf{y} = \Phi\mathbf{x} \tag{42.3}$$

where $\Phi \in R^{m\times N}$ denotes the measurement matrix, and the precondition is $m<N$. $\mathbf{y}$ represents the received signal. $\mathbf{x}$ denotes the clustered-sparse signal:

$$\mathbf{x} = \left[x_1, \ldots x_d, x_{d+1} \ldots x_{(2d)}, \ldots x_{(N-d+1)}, \ldots x_N\right]^T \tag{42.4}$$

where $N = Md$, $x[l](l = 1, 2, \ldots M)$ is viewed as a sub-block. Clustered-sparse means nonzero coefficients occurring in only few of the sub blocks and K denotes the number. To simplify the problem, we assume that all $x[l]$ are isometric. And similar to (42.4), the measurement matrix is blocked in the following way:

$$\Phi = [\Phi_1 \ldots \Phi_d, \Phi_{d+1} \ldots \Phi_{2d}, \Phi_{N-d+1} \ldots \Phi_N] \tag{42.5}$$

A lot of sparse signals satisfy the form of block-sparse signal in practice, such as multi band signal, DNA array (DNA microarray), radar pulse signal and multiple measurement vector problems. The reconstruction algorithm study of the sparse signal with specific structure is of great significance.

42.3 Cluster-Based Classification Compressed Sensing

The flow of proposed channel estimation algorithm which is based on cluster-classification compressed sensing is shown in Table 42.1. We all know that the goal of channel estimation is to estimate the gain and delay of a group of high energy multipath. Hence we do not need to have perfect reconstructions of pilot symbols. In order to ensure high precision to reconstruct a group of high-energy multi-path gain and delay, classification based cluster identification is proposed. Simulation results show that the algorithm effectively reduces the reconstruction error ratio. The proposed cluster-based classification compressed sensing algorithm is introduced into the existing reconstruction algorithm. Adaptive decision threshold for cluster classification procession is introduced to this chapter. Table 42.2 illustrates the idea of CS-ROMP algorithm.

42.4 Simulation and Analysis

In this section, we evaluate the performance of the proposed cluster-based classification compressed sensing algorithm by simulation. The performance comparison between the proposed scheme and the conventional CS-ROMP is conducted.

Simulations are carried out by MATLAB platform. To verify the reconstruction performance of the algorithm, CS-ROMP are also applied to the 60 GHz channel estimation and then there performances are compared. The 60 GHz indoor line of sight channel impulse response, publicized by the IEEE P8.2.15 wireless personal area networks (WPAS) Working Group, is adopted in this chapter. And h denotes the channel impulse response, which contains N sequences. M of them are nonzero. BPSK modulation is applied and we set the maximum delay spread 100 ns and the sampling rate is M/N. 100 tests are carried out to statistics the reconstruction error of CS- ROMP and the improved algorithm proposed by this chapter. We assume

Table 42.1 Steps of cluster-based classification compressed sensing

Step A	Cluster identification
Step B	Cluster-based classification
Step C	If sparsity of primary cluster is greater than threshold, go to step E, otherwise go to step D
Step D	Extract the primary cluster as the first classification and the rest as the second part
Step E	Extract the primary cluster and the second cluster as the first classification and the rest as the second part
Step F	Reconstruction and signal synthesis

Table 42.2 Regularized orthogonal matching pursuit

Input	Measurement vector $h \in {}^{N}$; sparsity K.
Steps	1. Initialize:Index set $\Lambda = \emptyset$, the residual error $r = h$. Repeat the following steps by K times or until $\|\Lambda\| \geq 2K$.
	2. Select the maximum K nonzero values from measurement matrix $u = \Phi^* r$ and insert into index set J .
	3. Regularized:let all subset $J_0 \subset J$ for all $i, j \in J_0$ satisfy $u(i)\| \leq 2\|u(j)\|$. Then select the index set with a maximum energy asJ_0.
	4. Update:add subset J_0 to index set:$\Lambda \leftarrow \Lambda \cup J_0$,update the residual error $y = \arg\min_{z \in \mathbf{R}^l} \| h - \Phi z\|_2$; $r = h - \Phi y$
	5. If the iteration number is greater than K or the number of indexes is greater than 2 K, stop the iteration, otherwise continue the iteration.
Output	Index set: $\Lambda \subseteq \{1, \ldots d\}$,Reconstruct the signal estimate as $\hat{v} = y$.

that the receiver needs to estimate ten clusters. The reconstruction error is estimated by calculating the BER, which denotes:

$$BER(h) = \left\|\hat{h} - h\right\| / \|h\| \tag{42.6}$$

As is shown in Fig. 42.2, the reconstruction of CS-ROMP and the cluster-based classification compressed sensing reconstruction algorithm for the 60 GHz channel are finished in condition of SNR 20 dB. The vertical axis denotes the original pulse amplitude and the restored ones by CS-ROMP and the improved algorithm. Figs. 42.3 show high sparsity of 60 GHz channel. The reconstructed values by CS-ROMP and the improved algorithm are perfectly in line with the main path, while the reconstruction algorithm improved by this chapter is better in BER performance, that is not only the primary path error is smaller but also the clusters besides has a good compliance. The proposed algorithm is significantly better in reconstruction accuracy than and CS-ROMP algorithms.

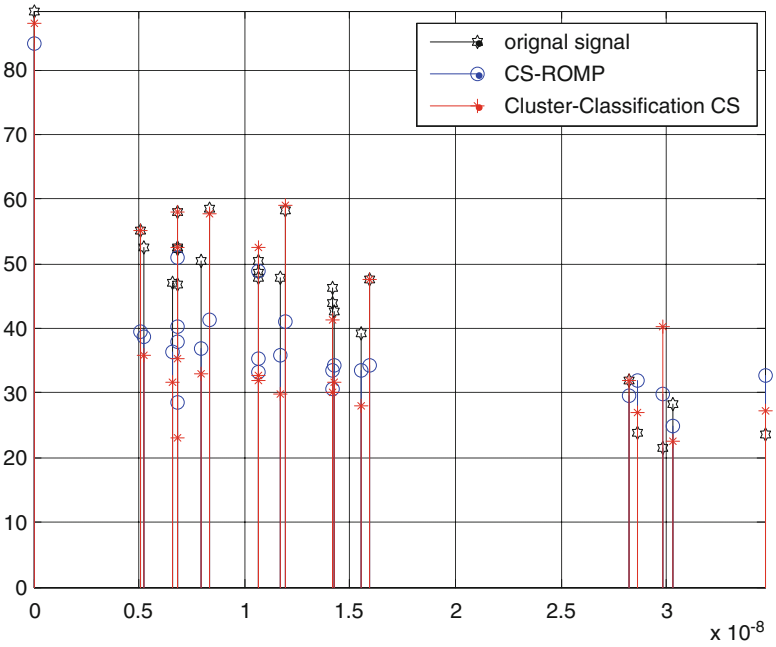

Fig. 42.2 Channel estimation of ROMP and proposed algorithm

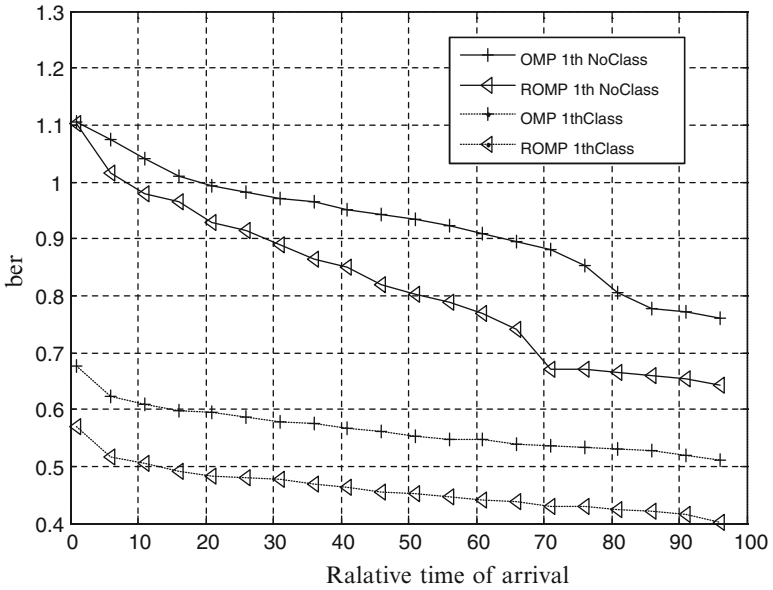

Fig. 42.3 MSE for OMP, ROMP and proposed algorithm

Figure 42.3 shows channel estimation BER performance of CS-ROMP and the cluster-based classification compressed sensing algorithm. The channel is line of sight. In order to make the complexity of the receiver moderate, we constructed the receiver with 25 RAKE values, that is we take the maximum 25 rays as the channel estimation results, then construct RAKE receiver. Each tests runs 100 times and then we calculate the reconstruction error for each algorithm. In the simulation experiments, one training sequence is applied, the training sequence and data symbols are repeated coding, the number of which is ten. Besides the classification threshold is 0.9.

We can draw the conclusion that the BER performance of CS-ROMP is significantly reduced after being introduced the cluster-based classification of compressed sensing algorithm. The first classification of the multi-path has the maximum correlation with channel estimation and thus the channel estimation precision is significantly improved.

Ignoring the slight BER difference, we can draw the conclusion that when we need to use relay nodes to handle blockage problem in 60 GHz millimeter-wave WPANs, we can apply physical layer network coding-based two-way relay networks to achieve larger throughput without worrying about the complex algorithm raising the BER.

As is shown in Fig. 42.3, the reconstruction BER performance of the multipath value which is highly related to channel estimation is compared. The BER of CS-ROMP is 30 % lower after classification based clusters. We can draw the conclusion that the cluster-based classification compressed sensing reduces the reconstruction error by an average of about 30 %. And the cluster-based classification compressed sensing algorithm significantly improves the precision of channel estimation.

42.5 Conclusion

Structural correlation widely exists in natural signals. Motivated by the fact, we propose the cluster-based classification compressed sensing algorithm for 60 GHz channel estimation. CS-OMP and CS-ROMP are also analyzed when applied to 60 GHz channel estimation. In addition there performances are compared with the algorithm proposed in this chapter. The superiority of the cluster-based classification compressed sensing algorithm has been verified by extensive experiments.

Note that current theories and algorithms have shown that recovery performance improves as the number of measurement vectors increases. However, in the presence of structural correlation, the exiting algorithms show less benefits. Our work shows that if cluster-correlation can be properly modeled and incorporated in algorithms, performance improvement is also significant even in severe environments.

Acknowledgments Supported by the National Natural Science Foundation of China (Grant No.60902046, 60972079) and the Important National Science & Technology Specific Projects of China (Grant No.2011ZX03005-002, 2012ZX03001022)

References

1. WIGWAM-Wireless Gigabit with Advanced Multimedia Support. [Online]. Available: http://www.wigwam-project.de/
2. Cotter SF, Rao BD et al (2005) Sparse solutions to linear inverse problems with multiple measurement vectors. IEEE Trans Signal Process 53(7):2477–2488
3. Donoho DL (2006) Compressed sensing. IEEE Trans Inf Theory 52(4):1289–1306
4. Chen J, Huo X (2006) Theoretical results on sparse representations of multiple-measurement vectors. IEEE Trans Signal Process 54(12):4634–4643
5. Hao X, Kukshya V, Rappaport TS (2002) Spatial and temporal characteristics of 60 GHz indoor channels. IEEE J Selected Areas Comm 20(3):620–630
6. Sawada H, Nakase H, Kato S (2010) Impulse response model for the cubicle environments at 60 GHz. In: Proceedings of the Vehicular Technology Conference (VTC 2010-Spring), 2010 I.E. 71st, pp 1–5
7. Zhang P, Hu Zu, Qiu RC, Sadler BM (2009) A compressed sensing based ultra-wideband communication system. IEEE International Conference on Communications (ICC), 2009
8. Li B, Zhou Z, Li D, Zhai S (2011) Efficient cluster identification for measured ultra-wideband channel impulse response in vehicle cabin. Prog Electromagn Res 117:121–147

Chapter 43
The Study About a Novel Beam-Search Strategy in 60 GHz Wireless Communication Environment

Sen Li, Hongbo Tao, and Chenglin Zhao

Abstract 60 GHz Wireless Communication has attracted increasing attention with its distinct advantages such as abundant bandwidth, unlicensed and so on. For overcoming the large path loss of 60 GHz spectrum, devices generally make use of antenna array to get high directivity beam, enhance transmit and receive antenna gain. As a result how to implement fast beam-search is an inevitable challenge for 60 GHz Wireless Communication. Based on IEEE 802.15.3C criteria and channel model(including application environments), this chapter aims to propose a novel beam-search strategy by taking into account the characteristics of 60 GHz Wireless Communication, such as large path loss, strong directional beam and correlation among beam-search of devices. Moreover this strategy was proved by the simulation that it can effectively reduce the range of beam-search, improve efficiency.

Keywords 60GHz • Beam-search • several devices • strategy

43.1 Introduction

With the development of wireless communication technology and multimedia application, the wireless communication application request more and more transmission rate and bandwidth gradually. On the contrary, Wireless spectrum resource

S. Li (✉)
Beijing University of Posts and Telecommunications, Beijing, China
e-mail: lisen0306@bupt.edu.cn

H. Tao
The State Radio monitoring center Testing Center, Beijing, China
e-mail: 45014688@qq.com

C. Zhao
School of Information and Communication Engineering, Beijing University of Posts and Telecommunications, Beijing 100876, China
e-mail: clzhao@bupt.edu.cn

Q. Liang et al. (eds.), *Communications, Signal Processing, and Systems*, Lecture Notes in Electrical Engineering 202, DOI 10.1007/978-1-4614-5803-6_43,

is becoming increasingly scarce. The interest to develop and standardize technologies in 60 GHz band has been generated by amount of relatively unused available bandwidth in this unlicensed band. Among these technologies, the one for short range indoor wireless communications including both Wireless Personal Area Networks (WPAN) and Wireless Local Area Networks (WLAN) is especially concerned

60 GHz band which is known as millimeter-wave band has the common characteristics of millimeter-wave band. Compared with other wireless communication technologies in lower frequencies, the free space propagation loss of millimeter-wave band is higher at same distance. Path loss (PL) at 60 GHz is subject to additional losses due to oxygen absorption and rain attenuation [1, 7]. To compensate for such large PL, high gain directional antennas are essential in order to reach decent range. IEEE 802.15.3C (hereinafter referred to as "3C") as the 60 GHz criteria, introduced and explained the relevant issues of beam-forming and beam-search [3]. This chapter will take the related contents of 3C as the reference object.

3C provided several typical environments of 60 GHz wireless communication [4]. In these environments, there might not be only one pair of communication devices (DEVs), but also other communication DEVs which need communicating to each other. However, 3C did not take correlation of beam-search among several DEVs into consideration, in another words, the beam-search between a certain pair of DEVs does not consider the communication situation of the rest related DEVs. So the beam-search strategy of 3C is blind. For this reason, how to make use of correlation to reduce the price of beam-search among several DEVs is the mainly project to be explored in this chapter.

The rest of this chapter is organized as follows. Section 43.2 describes the path loss model in 60 GHz and the beam-forming content in 3C. In Sect. 43.3, three parts will be presented which are applying scenario, proposing the novel beam-search strategy and estimating the error. After that simulation and analysis is given in Sect. 43.4. Finally, the conclusions are drawn in Sect. 43.5.

43.2 Related Work

43.2.1 Path Loss (PL) Model

The path loss is defined as the ratio of the received signal power to the transmit signal power [5]. It is a reflection of channel characteristics and very important for linking budget analysis. In order to simplify the model, it is proposed to use the mid-band frequency point. Then, the PL as a function of distance, d, is given by

$$PL(d)[dB] = \overline{PL}(d)[dB] + X_\sigma[dB] \tag{43.1}$$

Where $\overline{PL}(d)[dB]$ is the average PL and $X_\sigma[dB]$ is the shadow fading. In line-of-sight (LOS) and non-obstruction scenarios, $X_\sigma[dB]$ can be ignored. $PL(d)[dB]$ can be expressed as

$$PL(d)[dB] = 20\log\left(\frac{4\pi d_0}{\lambda}\right) + 10n\log\left(\frac{d}{d_0}\right) \tag{43.2}$$

Where d_0 and n denote the reference distance and PL exponent, respective. In LOS scenarios, n varies from 1.2 to 2.

The generic mm-wave channel model which takes cluster into account is based on the extension of Saleh-Valenzuela (S-V) model to the angular domain by Spencer [2, 8, 9].

43.2.2 Beam-Forming

3C beam pattern can be divided into the following four:

1. Quasi-omni Pattern
2. Sector
3. Fine Beam
4. High Resolution beams, HRS beams

In 3C, a beam-forming method is adopted based on code-book which serves as a prescribed pool of weight vectors. A code-book is an M × K matrix where each column specifies a pattern or direction [3]. The matrix element $w_{m,k}$ can be expressed as follow:

$$w_{m,k} = j^{fix\left\{\frac{m\times \mathrm{mod}[k+(K/2),K]}{K/4}\right\}} \tag{43.3}$$

where M and K are respectively the total number of antennas elements and beam. m is current antenna number and k is the current beam number. In order to minimize the power consumption and simplify the phase shifter , the codebooks are designed for a phased antenna array only with 90°phase resolution (0°, 90°, 180°, 270°) and without amplitude adjustment [4, 6].

Main response axis (MRA) is the expected physical aimed direction or the biggest gain direction of antenna. It also is the central axis of antenna main lobe. In other word, it is usually the expectation of the maximum signal radiation direction. The MRA set $\{\theta_k\}$ can be reasonable assumed by the arcsin function.

$$\theta_k = \arcsin\left(\frac{2k}{K} - 1\right), k = 0, 1, \ldots K-1 \tag{43.4}$$

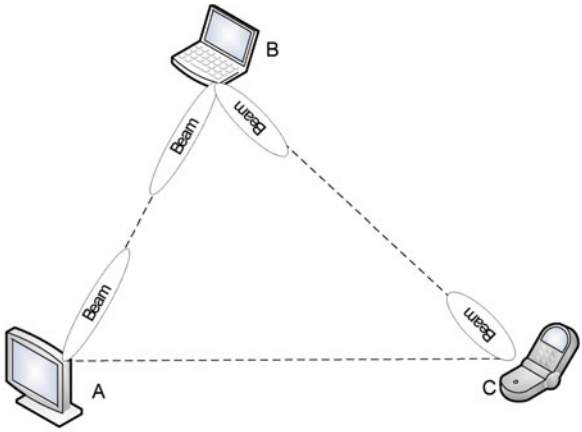

Fig. 43.1 Diagram of the example scenario and devices

43.3 Beam-Search Strategy

At first, we construct application scenario. This chapter assumed that, in the same LOS scenario, there are three 60 GHz communication DEVs (named A, B, C) with random position, any two of them have communication requirements. We make the DVEs A/B/C equipped with one-dimensional liner antenna array of 16 elements, every DEV works in high resolution pattern with 32 beams. We leave the mobility consideration aside and use S-V channel model. Because the PL is only distance-related, we can simplify (43.2) as follow

$$PL{=}N \cdot d^n \tag{43.5}$$

where N is a constant in the same scenario.

Every receive signal power is

$$P_r = P_t + G_t + G_r - PL(dB) \tag{43.6}$$

Where P_r and P_t is respectively receive and transmit power, G_t and G_r is respectively transmit and receive antenna gain. In fact, we can't get the accurate antenna gain because the beam doesn't turn to a certain direction. But we can confirm that the MRA of the optimal beam is not far away from the expected direction. We take the average which was calculated through the gain nearby the MRA as the antenna gain.

With antenna center of A, B, C for vertex, $\triangle$ABC is constructed. The beam-search between A and B, B and C have completed, it means the best communication beams have been confirmed as shown in (Fig. 43.1).

Then, if A, C need to communicate to each other, as it can be seen in 3C, they still have to finish all the steps of beam-search. Actually, because there is reference B, the range of beam-search can be narrowed. The implementation methods of this strategy are designed as follow.

1. Depend on the optimal beam between B and A, C, figure out the MRA of each beam from B (For reducing the complexity, use the result of (43.4) instead of MRA). And estimate ∠B by MRAs.
2. Estimate the PL between A and B according to receive and transmit power, and antenna gain, the same method should be applied to the PL between B and C.
3. Because the PL is only distance-related, we can use the two PLs mentioned above to estimate the distance ratio of A-B and B-C.
4. With the results above, construct a similar triangles of △ABC. Then we can get ∠A and ∠C.
5. By using the MRAs of beams from A and C towards B, and∠A ∠C, estimate the optimal MRAs of communication between A and C. Then, we choose the beams whose MRAs are closest to the estimation results as the optimal beams.

By analysis of estimation above, there are several reasons that would cause the error.

1. For reducing the complexity, we use the result of (43.4) instead of MRA. Actually, the result is only an approximate value of MRA.
2. For S-V channel model, both clusters and rays are stochastic process. Depend on the S-V channel characteristics, receive power can be described as

$$P_r = \lambda \cdot P_{LOS} \tag{43.7}$$

   where λ is the floating coefficient caused by clusters and rays. In the estimation step, we use P_r instead of P_{LOS} to estimate the PL of LOS, and then get the distance ratio. So, λ will cause the distance estimation error.
3. The beam-forming of 3C is based on the predefined beam codebook. The discussion of the beam-search range-reduce strategy depends on the high directivity antenna array and large PL in 60 GHz wireless communication. However to reduce the complexity, the beam-forming is based on codebook. This loses the performance of antenna array. The estimation errors reflect in the following two points:

   (a) When we use MRA to estimate the angle, the connective direction of transmit and receive antenna array is not equal to MRA of the optimal beam. The optimal beam is only the one which can get the highest SNR (signal noise ratio) among those beams generated by codebook. That does not mean the MRA of optimal beam is exactly towards its target.
   (b) Before we calculate the PL, we need know the gain of antenna array. As we mentioned above, the MRA of the optimal beam is not equal to the connective direction of transmit and receive antenna array. The actual gain of antenna is the one of the optimal beam at the antenna connective direction. We assume θ is the angle between two directions, and θ is a uniform distribution random variable which in a certain range. The range depends on the number of beams and elements of antenna array, the optimal beam ID and so on. In this chapter, we choose average nearby the max gain angle instead of actual antenna gain.

4. The PL exponent is uncertain. In LOS scenarios, n varies from 1.2 to 2. The exact value of n could not be found out, so we use the typical value instead of actual value.

It must be pointed out that, although the beam-forming based on codebook can lead to error, the reference parameter of beam-search is an angle range rather than a specific value. This means there is a certain error-tolerance for the strategy.

43.4 Simulation and Analysis

In simulation, the positions of DEVs are randomly generated, and the angles of $\triangle$ABC are random too. Based on the 3C codebook, we generate weight matrixes of DEVs antenna array. DEV B which has figured out the optimal beams used to communicate with DEV A and DEV C is a reference DEV. The aim is using the strategy to estimate the optimal beams of communication between A and C. The actual optimal beams will be compared with the estimate results.

Make 50 times simulations for estimating $\angle$B, the calculated results of estimation value and the actual value are shown in Fig. 43.2.

As it can be seen, the error of using the MRA of optimal beams to estimate $\angle$B is less than 15°. When the ID0 beam is an optimal beam of communication, it will lead to more error. By the basic properties of beam-forming, the more the deflection

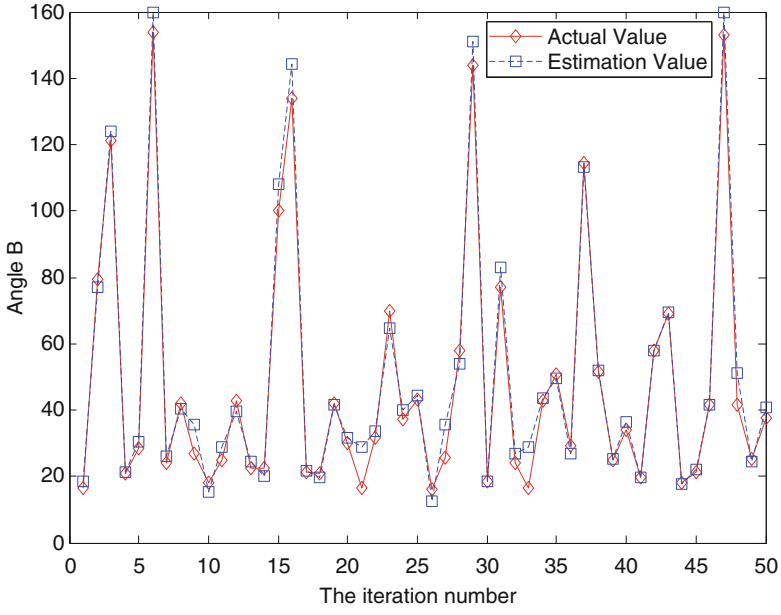

Fig. 43.2 The actual value and the estimation value of $\angle$B

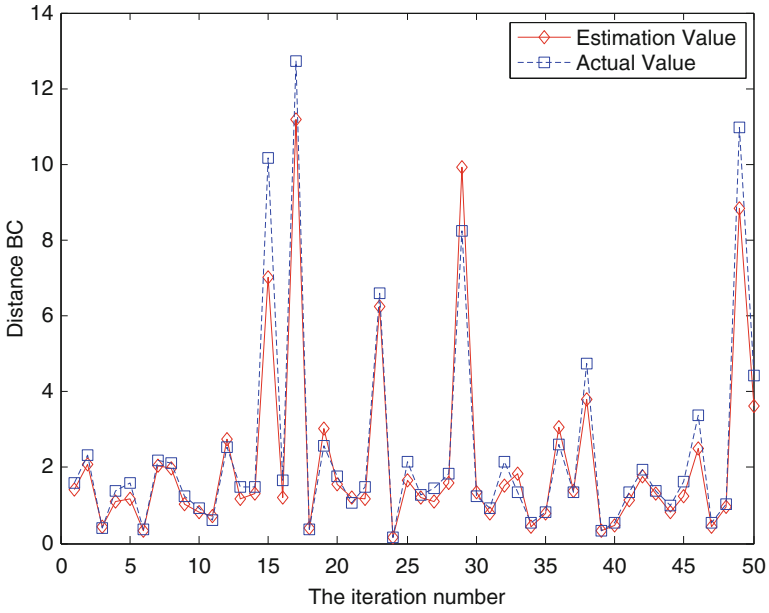

Fig. 43.3 The actual value and the estimation value of BC

of beam is, the wider the HPBW is. The deflection of ID0 beam is the most one among all beams, so its HPBW is the widest too. This causes that the expectation of θ for ID0 beam is the maximum one. In this situation, the estimation error may be bigger than others.

Then, estimate the ratio of AB and BC. We assume that the length of AB is 1, so the ratio converts into the length of BC. According to the actual length of BC, we randomly generate the channel model of AB and BC, use P_r instead of P_{LOS} , take average nearby the max gain angle instead of actual antenna gain. Then, we can estimate the length of BC the result is shown in (Fig. 43.3).

After the preparations, we come to the optimal beam estimation. The DEV A is taken as an example, the estimation follows the steps mentioned above.

Figure 43.4 illustrates that error between estimation beam ID and actual beam ID is a random number. Figure shows us the probability of each error situation. After repeated estimations, we found that the probability that the beam ID error stays in two stabilized at about 90 %.

43.5 Conclusion

In this chapter, the characteristics of 60 GHz communication are used to propose a novel beam-search strategy. This strategy can reduce the range of beam-search effectively. In the situation that all DEVs use the phase antennas array with

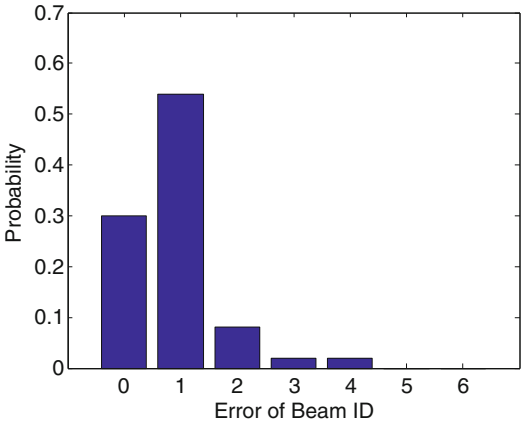

Fig. 43.4 The estimation error of optimal beam

16 elements and 32 beams, this strategy can get an estimation which have over 90 % probability to have an error in two beam IDs. Never the less, this strategy is limited to the two conditions below:

1. The value of $\angle$B can not be too small. Once the value is not big enough, a tiny estimation error of BC will cause the estimation error of $\angle$A and $\angle$C unacceptable. In this chapter, we assumed $\angle$B is bigger than 10°.
2. The strategy depends on the rough position relation among DEVs.

When the conditions are reached, the strategy can get a satisfactory result.

Acknowledgments This work was supported by National Natural Science Foundation of China (60972079, 60902046) and the BUPT excellent Ph.D. students' foundations (CX201122)

References

1. Su-Khiong Yong, Pengfei Xia et al (2011) 60 GHz technology for Gbps WLAN and WPAN: from theory to practice. Wiley, US, 1–14, pp 89–115
2. Sarkar TK, Zhong Ji et al (2003) A survey of various propagation models for mobile communication. IEEE Antenn Propag Mag 45(3):51–82
3. James P. K. Gilb (Technical Editor) (2009) IEEE standards 802.15.3c™–Part 15.3: wireless medium access control (MAC) and Physical layer (PHY) specifications for high rate wireless personal area networks (WPANs) Amendment 2: millimeter-wave-based alternative Physical layer extension. IEEE Computer Society, New York
4. ZouWeixia, Cui Zhifang, Li Bin et al (2012) N phases based beamforming codebook design scheme for 60GHz wireless communication. J Beijing Univ Posts Telecommun 35(3):1–5
5. Siep TM, Gifford IC, Braley RC, Heile RF (2000) Paving the way for personal area network standards: an overview of the IEEE P802.15 working group for wireless personal area networks. Personal Communications, IEEE 7(1):37–43

6. Zhiwei Lin, Xiaoming Peng (2011) Enhanced Beamforming for 60 GHz OFDM system with co-channel interference mitigation. In: IEEE international conference on ultra-wideband, ICUWB, Singapore, 14–16 Sept 2011, pp 29–33
7. Kosugi T, Hirata A, Nagatsuma T, Kado Y (2009) MM-wave long-range wireless systems. IEEE Microw Mag 10(2):68–76
8. Moraitis N, Constantinou P (2004) Indoor channel measurements and characterization at 60GHz for wireless local area network applications. Antennas and Propagation, IEEE Transactions 52(12):3180–3189
9. Dong Jie, Jing-jing Wang, Hao Zhang, Guo-yu Wang (2010) Channel capacity of 60 GHz wireless communication systems over indoor line-of-sight and non-line-of-sight channels. WiCOM, Chengdu, 23–25 Sept 2010, pp 1–4

Part XI
Wireless Networks

Chapter 44
Routing Selection Strategy Based on Link Failure in ZigBee Networks with Changing Mobility

Jiasong Mu, Wei Wang, and Baoju Zhang

Abstract The hierarchical tree routing and Z-AODV routing are both available in ZigBee specification to meet the requirements in different applications. However, the research on principle and method of routing selection is still underway. Moreover, most research on ZigBee routing was examined in a single network condition, and the variation of wireless environment should be more considered. Aiming at lower power consumption, a routing selection strategy based on link failure in the networks with changing mobility is proposed in this chapter. The algorithm utilized the information in network address and neighbor table of ZigBee devices, to recognize the mobility changing of nodes without any extra communication. The simulation results show the algorithm could reduce the average network load in all the conditions have been tested.

Keywords ZigBee • Routing selection • Link failure • Node mobility

44.1 Introduction

One of the primary goals of ZigBee is low power consumption and therefore long-living networks. Current network formation and routing protocols described in the ZigBee specification do not fully address power consumption issues [1]. ZigBee network uses a mixed routing mechanism combined with HRP (hierarchical tree routing) and Z-AODV (ZigBee ad-hoc on demand distance vector) [2]. So far, most researches on ZigBee routing were tested in single network environment [3]. This chapter will focus on routing selection strategy which is adaptive for the changing of node mobility in ZigBee networks, a routing selection strategy based on link

J. Mu (✉) • W. Wang • B. Zhang
Department of physics and electronic information, Tianjin Normal University, Tianjin, China
e-mail: mujiasong@yahoo.com.cn; wangweivip@tju.edu.cn

Q. Liang et al. (eds.), *Communications, Signal Processing, and Systems*, Lecture Notes in Electrical Engineering 202, DOI 10.1007/978-1-4614-5803-6_44,

failure (BLF) is proposed. Network load and power consumption are used to evaluate the performance with OPNET Modeler.

44.2 ZigBee Specification and Routing Methods

44.2.1 Overview of ZigBee

Based on the IEEE 802.15.4 protocol, the ZigBee specification defines the standard of higher layers. Two device types are specified: full function device (FFD) and reduced function device (RFD). An FFD must maintain routing tables; participate in route discovery and etc. Moreover, an FFD has the capability of communicating with any other devices within its transmission range. On the other hand, RFD simply maintains the minimum amount of knowledge to stay on the network. ZigBee network layer (NMK) provides functionality such as dynamic network formation, addressing, routing, and discovering neighbors. The network address is assigned in a hierarchical tree structure. The deployed ZigBee devices automatically construct the network, and then changes such as joining/leaving of devices are automatically reflected in the network configuration [4].

44.2.2 Address Allocation

In ZigBee specification, it is recommended to use Distributed Address Allocation Mechanism (DAAM) for address assignment to form tree structure. The parameter *Cm* represents the largest number of children nodes, *Rm* means the number of children nodes which can be a router and *Lm* decides the most depth in the network. And for the same network, different nodes usually have the constant *Cm* and *Rm*. Every potential parent is provided with a finite sub-block of the address space, which is used to assign network addresses to its children. Given *Cm*, *Lm*, and *Rm*, we can compute the function *Cskip(d)* as the size of the address sub-block distributed by each parent at depth *d* as (44.1).

$$Cskip(d) = \begin{cases} 0, & Rm = 0, \\ 1 + Cm \times (Lm - d - 1), & Rm = 1, \\ \left(1 + Cm - Rm - Cm \times R^{Lm-d-1}\right)/(1 - Rm), & Rm > 1. \end{cases} \quad (44.1)$$

44.2.3 HRP and Its Improvement

Due to the DAAM mentioned above, the network constructs a tree topology. The essential factor which restricts the HPR performance is that the data

transmission is confined in parent–child links. In [5], an enhanced hierarchical tree routing algorithm to expand the optional links was proposed. In ZigBee networks, the number of hops in the hierarchical path between nodes A and B can be determined as (44.2), where $NH(A, B)$ is the number of hops determined by the HRP between nodes A and B,$D(X)$ is the depth of node X, and $FCA(A, B)$ is the first common ancestor node of nodes.

$$NH(A,B) = D(A) + D(B) - 2D \cdot (FCA(A,B)) \tag{44.2}$$

$$RN_{EHRP} = \arg\min_{n} NH(n, Destination) \tag{44.3}$$

44.2.4 Z-AODV and Neighbor Table

In Z-AODV, route requests (RREQ) are broadcasted on-demand when data is to be transmitted to a destination of an unknown path. It can provide efficient paths, while consumes much communication bandwidth and might cause a broadcast storm problem [6]. In addition, the routing table for AODV could be a large memory overhead for low-cost ZigBee devices [7].

Each ZigBee device maintains a neighbor table which has all the neighbor information in 1-hop transmission range. Entries in the table are created when the node joins to an existing network and removed when the neighbor node leaves. Since related information is updated every time a device receives any frame from some neighbor nodes, the information of the neighbor table may be said up-to-date.

44.2.5 Routing Selection in ZigBee

The DiscoverRoute field of the data frame head is defined as the routing approach for data frames. And it can have three values as followed:

- Suppress route discovery (SRD): the device only uses the routing tables that exist already. The network disables the routing discovery, when there is no corresponding address of the destination node, and the network will use HRP.
- Enable route discovery (ERD): if there is not the routing address in the routing table, a routing discovery will be initiated.
- Force route discovery (FRD): the node has to initiate the routing discovery constrainedly no matter whether there is the corresponding routing table or not.

44.3 Routing Selection Strategy Based on Link Failure

44.3.1 Previous Work

The performances of three routing schemes in different network conditions were analyzed in [8],and the conclusion was made that SRD is fit for stable networks and ERD has better performance in unstable ones, while the FRD always had the most network load and power consumption. On that basis, the routing selection strategy will be introduced.

44.3.2 Critical Network Condition

As the average data traffic of sending a data packet in SRD and ERD are denoted by L_{SRD} and L_{ERD}. SRD should be used in the network where $L_{SRD} < L_{ERD}$; when $L_{SRD} > L_{ERD}$, ERD may have better performance. The link failure rate was used to denote the network environment and be demonstrated by link error times in a unit time. P_{rre} is the probability of sending routing requests. We make $P_{rre=} P_{ri} + P_{rm}$, where P_{ri} and P_{rm} are the probabilities of routing invalid and routing entries missing, and P_{rm} could be estimated as $P_{rm} \approx 1-(N_{re}/N)$, where N_{re} is the number of routing entries and N is the total nodes number. As, P_{tes} is the probability of transmission error in SRD, when $P_{tes} = P_{rm}$, it could be considered that despite of limit of routing table, remaining factor that affects the network is node movement. And as the mobility increases, P_{tes} adds quickly, while P_{rm} and P_{rre} hardly change. So, $P_{tes} = P_{rm}$ is used to be the critical condition and threshold in BLF.

44.3.3 Algorithm

The nodes working in BLF have two operating modes named S and E, and SRD and ERD were adopted as routing schemes accordingly. The ratio of routing table capacity and total node number (RN rate) was used to determine critical condition. The algorithm of BLF was shown as following:

```
Algorithm of BLF
const RNRATE = Routing entries/total nodes, UNITTIME = 50;
if currentstate==SMODE
On LinkFailureMessage received do
if currentlink==HRPlink then
if EHRPlink==HRPlink then EHRPlink++;
currentlink = EHRPlink;
else if timerstate==OFF then timerstate==ON;
nodemove++;
```

```
if nodemove > =RNRATE*UNITTIME then timer = 0, timerstate
= ON, currentstate = EMODE;
On timer==UNITTIME received do timer = 0 timerstate = OFF;
if currentstate = EMODE;
On MessageRecieved do
if messagetype==reply && messagedest==localaddress
then neighbortabler.updatereply();
else neighbortable.updatereceiving();
neghbortable.compare();
if M > 2 then nodemove++;
if nodemove > =RNRATE*UNITTIME then timer = 0;
On timer==UNITTIME received do timerstate = OFF, timer
= 0, currentstate = SMODE;
```

Because the origin SRD scheme only relies on the parent–child link, when a certain node broke its link by movement; both its parent and child node would also have link errors examined. This situation may lead to the misjudgment. Nodes of next hop in EHRP were introduced to avoid the faults. If a node finds its parent or child link failed, it will try to send the packet to the node which has the least hierarchical hops. Only when two specified links are found unavailable, the node determines a link failure. When the link failure rate sums to threshold, the device enters into the E mode.

The principle of detecting link failure can not recognize node movement exactly, because the algorithm eliminates the communications to reduce power consumption. The alarm dismissal probability (ADP) is shown in (44.4):

$$P\left(\hat{N}|Y\right) = \frac{P\left(\hat{N}Y\right)}{P(Y)} \leqslant \frac{p^2}{p} = p \tag{44.4}$$

Where, p is the probability of a node moving. For WSN application, p always has low value; the ADP is acceptable with no extra communication.

In ERD scheme, a node could estimate its mobility by the information in neighbor table. A memory block was used for the temporary storage of previous neighbor information, and the comparative analysis of old and new neighbor table were carried out to recognize node movement. Disappearing (DP) of an old neighbor entry and appearance (AP) of new neighbors indicate the node maybe moved; and the reappearance (RP) of an entry indicates the node probably keep stable. For each DP, AP and RP of different nodes, a variable M was made add 1, 1 and -1/n, where n is the numbers of previous neighbors. A node movement is determined when $M > 2$. If node mobility fell down, the node will go back to S mode. The same to it is in S mode; the discriminating of node mobility doesn't cause any extra communication. The ADP of the algorithm is shown as (44.5):

$$P\left(\hat{N}|Y\right) = \frac{P\left(\hat{N}Y\right)}{P(Y)} < \frac{p^n}{p} = p^{n-1} \tag{44.5}$$

The ADP is acceptable when the probability of node moving is not too high, and the more neighbors a node has, the more correct the principle is.

44.4 Simulations

The simulation was implemented in OPNET modeler. Some parameters in the simulation were set as following: simulation duration was 300 s; *Cm, Rm* and *Lm* were set 5, 5 and 4 separately; the data packet size was 100bit; packet interval time followed uniform distribution from 0 to 2 s; the destination nodes were chosen randomly, all the devices are FFDs. And several parameters were changed in order to observe the impact of different conditions on the performance of the algorithm. These parameters, along with their chosen values, are network size (small network of 20 nodes in 100 m*100 m, medium net work of 50 nodes in 150 m*150 m and large network of 100 nodes in 200 m*200 m), ratio of routing table entries and nodes in whole network (RN rate) (10%, 30% and 50%). Node mobility also varied

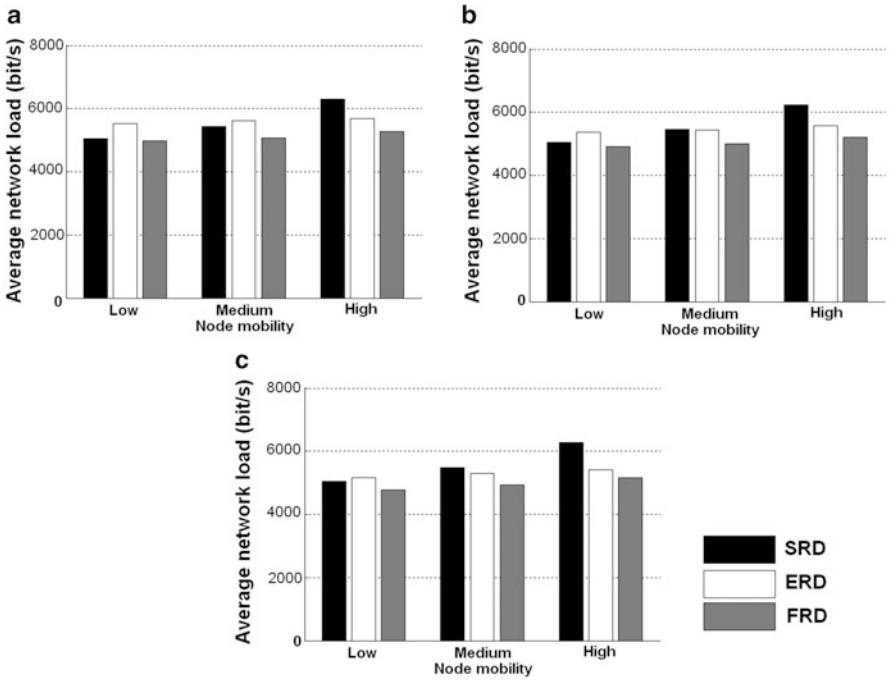

Fig. 44.1 Average network loading in small size network. (**a**) Performance in the network with 10 % RN rate; (**b**) performance in the network with 30 % RN rate; (**c**) performance in the network with 50 % RN rate

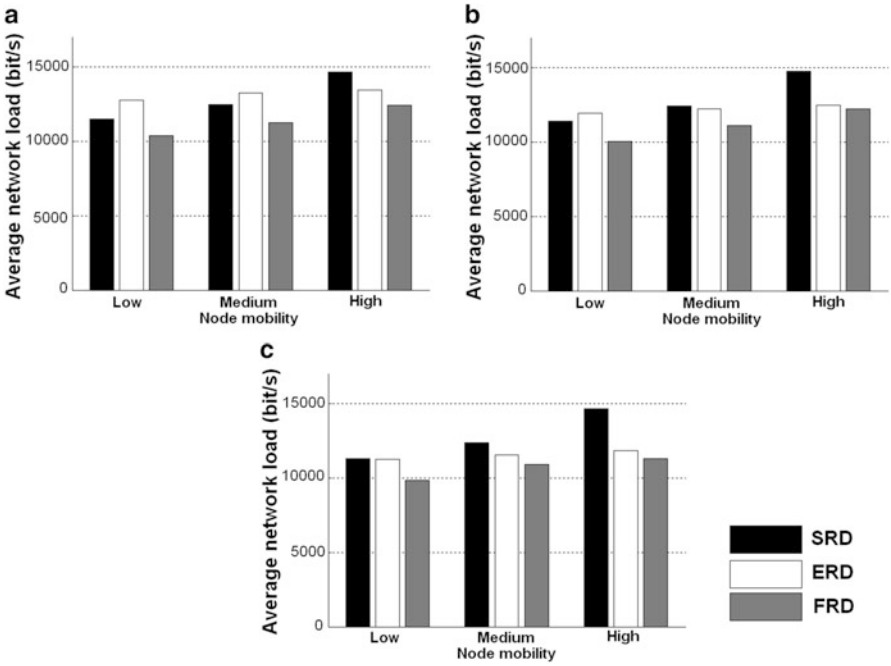

Fig. 44.2 Average network loading in medium size network. (**a**) Performance in the network with 10 % RN rate; (**b**) performance in the network with 30 % RN rate; (**c**) performance in the network with 50 % RN rate

in the simulation by changing the node average static time in ZigBee networks. An average static time followed normal distribution with mean 150, 50 and 20 were called low, medium and high mobility separately in the simulation, and the variance of them were 5. For each combination of aforementioned parameters, the results were averaged across 50 simulations to eliminate the disconnected topologies due to communication range and the orphan problem [9]. The simulation results were shown in Figs. 44.1, 44.2 and 44.3.We compared the average load of the ZigBee networks using SRD, ERD and BLF strategy. It can be seen that BLF can reduce the data in the network to lower the power consumption in all the conditions in the simulations. Network size didn't affect BLF performance much. Although the routing property of SRD declined as the network size and node number added, the optimization level of BLF for ERD was stable. With the rate of routing table entries increased, both the ERD and BLF had better performances. The routing table capacity partly decided the probability of executing routing discovery, thus, to use the devices with more memory space would reduce the network load and power consumption.

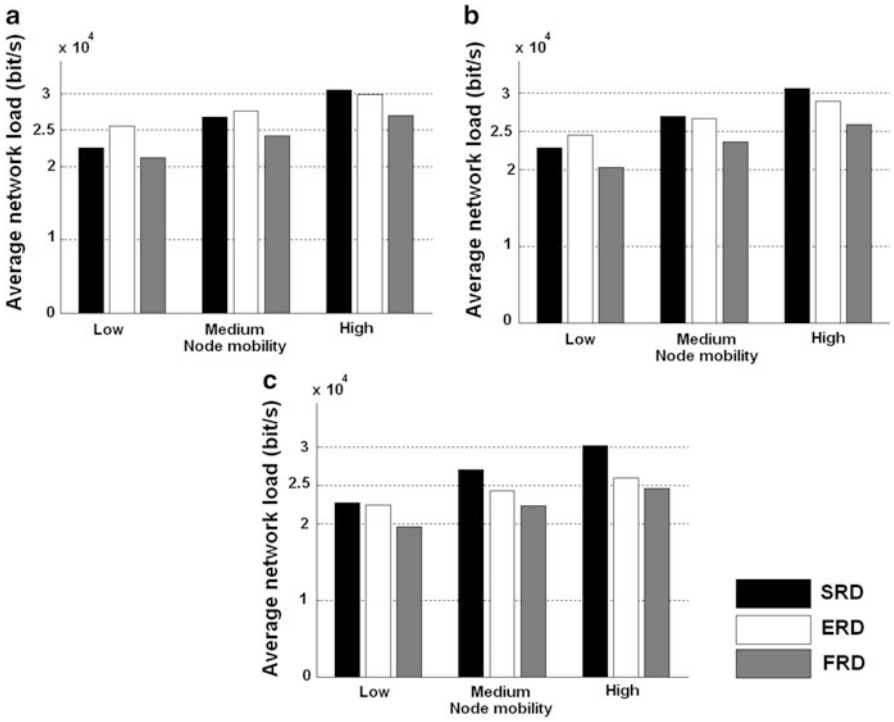

Fig. 44.3 Average network loading in large size network. (**a**) Performance in the network with 10 % RN rate; (**b**) performance in the network with 30 % RN rate; (**c**) performance in the network with 50 % RN rate

44.5 Conclusion

To reduce the network load in ZigBee network with changing node mobility, a routing strategy based on link failure was proposed. The algorithm could identify the node movement without extra communication by examining link errors. Links to nodes with least hierarchical hops and neighbor table information were introduced to achieve BLF. Simulation results showed the strategy might reduce the network load, therefore lessen the power consumption in all the tests. For further work, new routing protocols may be introduced to BLF to make further improvement. And the optimization of determining critical condition according to network parameters and previous effects may be implemented by using machine learning.

Acknowledgments This work is supported in part by High Education Science & Technology Foundation Planning Project of Tianjin (20100716); Tianjin Younger Natural Science Foundation (12JCQNJC00400).

References

1. Metin T, Ibrahim K (2012) PSAR: power-source-aware routing in ZigBee networks. Wireless Netw. doi:10.1007/s11276-012-0424-5
2. Baronti P, Pillai P, Chook VWC, Chessa S, Gotta A, Hu YF (2007) Wireless sensor networks: a survey on the stateof the art and the 802.15.4 and ZigBee standards. Comput Commun 30(7):1655–1695. doi:10.1016/j.comcom.2006.12.020
3. Ran P, Zou SM (2006) ZigBee routing selection strategy based on data services and energy-balanced ZigBee routing. APSCC '06. doi:10.1109/APSCC.2006.116
4. ZigBee standard Organization (2007) ZigBee specification. http://www.zigbee.org/Specifications.aspx
5. Ha JY, Park HS, Choi S, Kwon WH (2007) EHRP: enhanced hierarchical routing protocol for zigbee mesh networks. Commun Lett 11(12):1028–1103. doi:10.1109/LCOMM.2007.071325
6. Ni S, Tsing Y, Chen Y, Sheu J. (2002) The broadcast storm problem in a mobile ad hoc network. Wireless Netw 8(2–3):153–167
7. Sahinoglu Z, Orlik P, Zhang J, Bhargava B (2006) Tree-based data broadcast in IEEE 802.15.4 and ZigBee networks. Mobile Comput 5(11):1561–1574. doi:10.1109/TMC.2006.172
8. Mu JS, Liu KH (2010) A study on the routing selection method in ZigBee networks based on the mobility of the nodes and the scale of the network. Commun Mobile Comput 3:405–409. doi:10.1109/CMC.2010.300
9. Pan MS, Tseng YC (2007) The orphan problem in zigbee-based wireless sensor networks. In: MSWiM '07, pp 95–98. doi:10.1145/1298126.1298144

Chapter 45
Detecting Community Structure of Complex Networks Based on Network Potential

Yuxin Zhao, Chenglin Zhao, Xiuzhen Chen, Shenghong Li, Hao Peng, and Yueguo Zhang

Abstract Community structure is an important topological property of complex networks, which is beneficial to understand the structures and functions of complex networks. In this chapter a new statistical parameter, which we call network potential, is proposed to measure a complex network by introducing the field theories of physics. We then present a detecting algorithm of community structure based on the network potential whose main strategy is partitioning the network by optimizing the value of the network potential. We test our algorithm on both computer-generated networks and real-world networks whose community structure is already known. The experimental results show the algorithm can be effectively utilized for detecting the community structure of complex network.

Keywords Complex network • Community structure • Network potential

45.1 Introduction

Complex network is an abstract presentation of complex systems in real world such as social systems, ecological systems, the Internet and so on [1]. During recent years there has been an explosive growth of interest and activity on the structure and dynamics of complex networks [2]. Many theories of complex network have been applied into life science, social science, computer science and many other fields [3]. Community structure is an important property of complex network, which is widely

Y. Zhao • X. Chen • S. Li (✉) • H. Peng • Y. Zhang
Department of Electronic Engineering, Shanghai Jiao Tong University, 800 Dong Chuan Road, Shanghai 200240, China
e-mail: shli@sjtu.edu.cn

C. Zhao
School of Information and Communication Engineering, Beijing University of Posts and Telecommunications, Beijing 100876, China

Q. Liang et al. (eds.), *Communications, Signal Processing, and Systems*, Lecture Notes in Electrical Engineering 202, DOI 10.1007/978-1-4614-5803-6_45,

defined as the tendency for nodes to divide into clusters with dense connections within clusters and only sparser connections between them [4–6]. It also has much practical significance because it often corresponds to some organized groups in social networks or some functional units with common features such as collections of websites with the same topic.

In recent years, a variety of methods have been developed to detect community structure in complex networks. There are mainly two kinds of community detecting algorithms, one is optimization based methods and the other is heuristic methods. Optimization based methods detect community structures in networks by optimizing the designed objective function. The spectral bisection algorithm [7] utilizes the optimal quadratic form method to minimize the cut function on the basis of eigenvectors of the Laplacian matrix of a graph. Kernighan and Lin proposed K-L algorithm [8], which has the optimization objective of maximizing the difference value of connections within communities and connections between communities. Newman proposed Fast Newman algorithm [9] which optimizes the proposed modularity Q to evaluate the community structure. QCUT algorithm [10] combines spectral graph partitioning and local searching to optimize the modularity Q. From another perspective, heuristic methods are based on some intuitive assumptions which are tough to prove strictly. CPM algorithm [11] is based on the assumption that a community structure is composed of numbers of adjacent k-cliques. FEC algorithm [12] applies Markov random walk model to the signed network and figures out the transition probability matrix to partition the network. Girvan-Newman algorithm [13] has the heuristic assumption that edge betweenness is larger between communities than within communities. Radicchi improved Girvan-Newman algorithm by substitute edge betweenness with link clustering coefficient [14]. Clauset proposed a local community detection algorithm [15] based on local modularity defined by the author. Newman also proposed a community structure detecting algorithm [16], which combines the modularity Q and spectral graph partitioning by substituting the modularity matrix for the Laplacian matrix of networks.

We introduce field theory from physics to complex network in order to measure the network structural compactness, which we call network potential. Then we propose a new community detecting algorithm by the method of optimizing network potential.

The rest of the chapter is organized as follows. In the sequel, we first introduce the potential model of complex networks in detail in Sect. 45.2, and then in Sect. 45.3 we describe the community detecting algorithm based on network potential. The experimental results are reported in Sect. 45.4. Finally, the last Sect. 45.5 summarizes the conclusion.

45.2 Network Potential

In physical science, many mechanical systems are abstracted to the system of particles, which must meet the following two conditions: the system is composed of two or more particles, and there exists interactive force between particles.

Potential energy is the energy of a system of particles derived from the position, which is related with the shortest distance between the particles, according to field theory. It is a significant parameter which is often used to analyze the stability and compactness of systems.

The potential reflects the interaction and co-influence of different particles along with the relative position of them. If this model is applied to the complex network, we can acquire a measurement similar with the potential to analyze the complex network and find some topological property of the network.

In the case of complex network, if we consider the nodes as particles and assume that each node has interaction force for the other nodes, the complex network could be regarded as a system of particles. Thus, field theory could be introduced into complex network in order to describe the topology structure. In a complex network, the shortest path between two nodes could reflect the relative distance between them. Thus complex network would have a sort of energy only due to the relative topological positions of the nodes, which is similar to the potential energy in system of particles. We define this sort of energy as network potential.

Given a complex network $G = (V, E)$, where $V = \{v_1, v_2, \ldots, v_n\}$ is the set of nodes, and E is the set of edges connecting pairs of nodes. Supposing that each node creates a force field at the positions of other nodes, for $\forall u, v \in V$, let $\varphi_u(v)$ be the potential at the position of v produced by u, then $\varphi_u(v)$ must meet all the following conditions:

- $\varphi_u(v)$ is a continuous, smooth, finite and convergent function.
- $\varphi_u(v)$ decreases with the increase of the distance $\|v - u\|$.
- $\varphi_u(v)$ approach to its maximum when the distance $\|v - u\| \to 0$.
- $\varphi_u(v)$ approach to zero when the distance $\|v - u\| \to \infty$.

Considering the simplest case, each node creates a gravitational field at the positions of other nodes. Thus let $\varphi_i(j)$ be the potential at the position of node v_i produced by node v_j, $\varphi_i(j)$ would have a very simple form as follows,

$$\varphi_i(j) = k\frac{1}{d_{ij}} \tag{45.1}$$

where, k is a constant that can only be set as a positive value and d_{ij} is the distance between node v_i and node v_j. The distance between two nodes in a complex network is defined as the number of edges in a shortest path between them, which can be calculated using the procedure in [17]. If there is no path between node v_i and node v_j, the distance between them is considered as $+\infty$.

Obviously we can find that $\varphi_i(j) = \varphi_j(i)$ which accord with field theory in physics. Actually $\varphi_i(j)$ or $\varphi_j(i)$ can be conceived as the potential energy contained by the pair of nodes v_i and v_j.

Thus, the network potential is defined as the summation of the potential contained by each pair of nodes in the network.

$$\varphi(G) = \frac{1}{2}\sum_{i=1}^{n}\sum_{j=1}^{n}\varphi_i(j) = \sum_{i=1}^{n}\sum_{j>i}^{n}\varphi_i(j) = k\sum_{i=1}^{n}\sum_{j>i}^{n}\frac{1}{d_{ij}} \tag{45.2}$$

where n is the total number of nodes in the network G.

Network potential is a new measurement of the complex network which reflects the general closeness between nodes and the compactness of the network topological structure. We can find that the value of the network potential $\varphi(G)$ is between 0 to $kn(n-1)/2$. When $\varphi(G)$ is equal to 0, the network is composed of isolated nodes with no edge connecting them. With the $\varphi(G)$ increases, the network topological structure becomes more compact. When $\varphi(G)$ is equal to $kn(n-1)/2$, the network is totally coupled which means each pair of nodes are connected with an edge.

We also find another important property of network potential about the network topological structure. Let $G_k = G - \{e_k\}$, namely G_k is a subnetwork of G which removes the certain edge e_k from the network G. The difference between G_k and G can be figured out as follows.

$$\Delta\varphi(e_k) = \varphi(G) - \varphi(G_k) \tag{45.3}$$

As G_k is a subnetwork of G, it satisfies $\varphi(G) > \varphi(G_k)$ so that $\Delta\varphi$ has a positive value and the value has relationship with the edge e_k. If there are dense connections around the edge e_k, deleting e_k wouldn't have much influence on the network topological structure and the value of $\Delta\varphi(e_k)$ would be relatively small. On the other hand, if the connections around the edge e_k are sparse, deleting e_k would have much influence on the network topological structure and make the value of $\Delta\varphi(e_k)$ large. Thus by calculating and analyzing $\Delta\varphi(e_k)$, we can distinguish the clusters with dense connections within them and sparse connections between them. In turn, this property of network potential could be utilized to detect the community structure in complex network.

45.3 Community Detecting Algorithm

It has been indicated that there do exits the topological pattern of community structure in many real-world networks [4]. As network potential is an effective measurement of the network and can reflect some features of the network topological structure, we propose the community detecting algorithm based on network potential.

Based on the properties of network potential, the potential difference $\Delta\varphi(e_k)$ is an effective parameter to distinguish the connections within community and between communities. When $\Delta\varphi(e_k)$ is relatively larger, the probability that edge e_k is between communities is higher. On the other side, when $\Delta\varphi(e_k)$ is relatively smaller, the probability that edge e_k is within a community is higher.

The main steps of community detecting algorithm based on network potential are summarized as follows. Here, we adopt the quantitative definition of community [14], which is widely acknowledged in many other community detecting algorithms.

Step 1. Compute the potential difference $\Delta\varphi(e_k)$ for each edge in the network using (45.3).
Step 2. Remove the edge with the largest value of $\Delta\varphi(e_k)$.
Step 3. If the removal does not split the network, return to step 1.
Step 4. If the removal splits the network, test whether the resulting subnetworks fulfill the quantitative definition of community or not. If they do, draw the corresponding part of the dendrogram, where every branch-splitting represents a meaningful division of the network. Then go back to Step 1 and iterate the procedure. If they do not, the whole loop terminates.

45.4 Experimental Results and Discussion

We test our proposed community detecting algorithm with a number of computer-generated networks and real-world networks in order to verify its effectiveness and efficiency. To measure the quality of community detection, we adopt normalized mutual information (NMI) [18] which has become a standard in the community detection literature.

Firstly, we apply our community detecting algorithm to sample networks generated with the method mentioned in [19] and [20]. Here, we take group number $K = 3$, then generate the sample points from the 3-Gaussian mixture distribution with the means

$$\mu 1 = (1.0,\ 4.0)^{\mathrm{T}}, \qquad \mu 2 = (2.0,\ 5.0)^{\mathrm{T}}, \qquad \mu 3 = (0.5,\ 5.5)^{\mathrm{T}}$$

and the covariance matrices

$$\Sigma_1 = \Sigma_2 = \Sigma_3 = \begin{pmatrix} 0.15 & 0 \\ 0 & 0.15 \end{pmatrix}$$

We assign 15 points to each group and set the threshold from 0.3 to 1.2, then apply our proposed algorithm to the generated networks. The result is shown in Fig. 45.1a and we can see that our algorithm works well when threshold < 0.9. Obviously there are more connections between groups and the community structure in the generated network is less prominent along with the increase of the threshold. As the distance between $\mu 1$, $\mu 2$ and $\mu 3$ is around 1.5, when threshold > 0.9, the subnetwork is highly likely to violate the definition of community which results in the decrease of the NMI. So the results just reflect this phenomenon and correspond with the real situation.

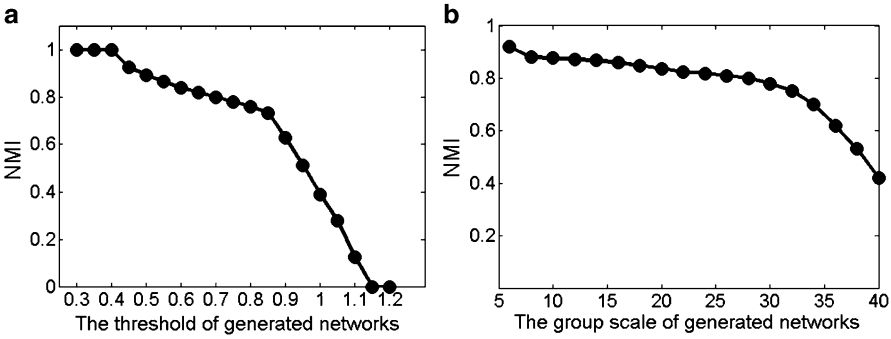

Fig. 45.1 (**a**) NMI of our algorithm in the sample networks with fixed n (n = 45); (**b**) NMI of our algorithm in the sample networks with fixed threshold (threshold = 0.8)

We also set the threshold as 0.8 constantly and assign each group 6–40 points, then apply our algorithm to the generated networks. The result is shown in Fig. 45.1b. When the groups contain more nodes, there are more edges connecting the groups and the community structure is less obvious in the generated networks. Along with the increase of the group scale, the connections between groups become denser so that the whole network is more likely a community rather than composed of three communities. This fact makes our algorithm performance relatively well as the group scale is small and the results correspond with the tendency.

Secondly, we do experiments on three real-world networks with known community structures including karate club network [21], dolphin network [22] and USA college football networks [13], which are commonly employed in the community detection literature.

Figure 45.2a presents the community structure of karate club network using our algorithm. Our algorithm finds two communities, which is in accordance with the real split. Only node 10 is classified by mistake and the NMI is 0.8372. We note that node 10 has one connection to each community so that it is difficult to judge which community it actually belongs to.

Figure 45.2b shows the community structure of dolphin network using our algorithm. Our algorithm finds two communities and the nodes "*PL*", "*SN89*" and "*Oscar*" are classified incorrectly so that so that NMI is 0.7566. But these nodes also have equal connections with each community.

Figure 45.2c presents the community structure of USA college football network using our algorithm. Eleven communities are detected by our algorithm and 11 nodes are classified incorrectly so that so that NMI is 0.8886. Three communities are detected completely correctly, that is, *Big East*, *Big Ten* and *Southeastern*. Six communities, that is, *Atlantic coast*, *Big Twelve*, *Conference USA*, *Mid-American*, *Mountain West* and *Pacific Ten*, are nearly correct with one or two teams assigned to the incorrect community. So the results are in accordance with the real situation and show that our algorithm performs well in USA college football network.

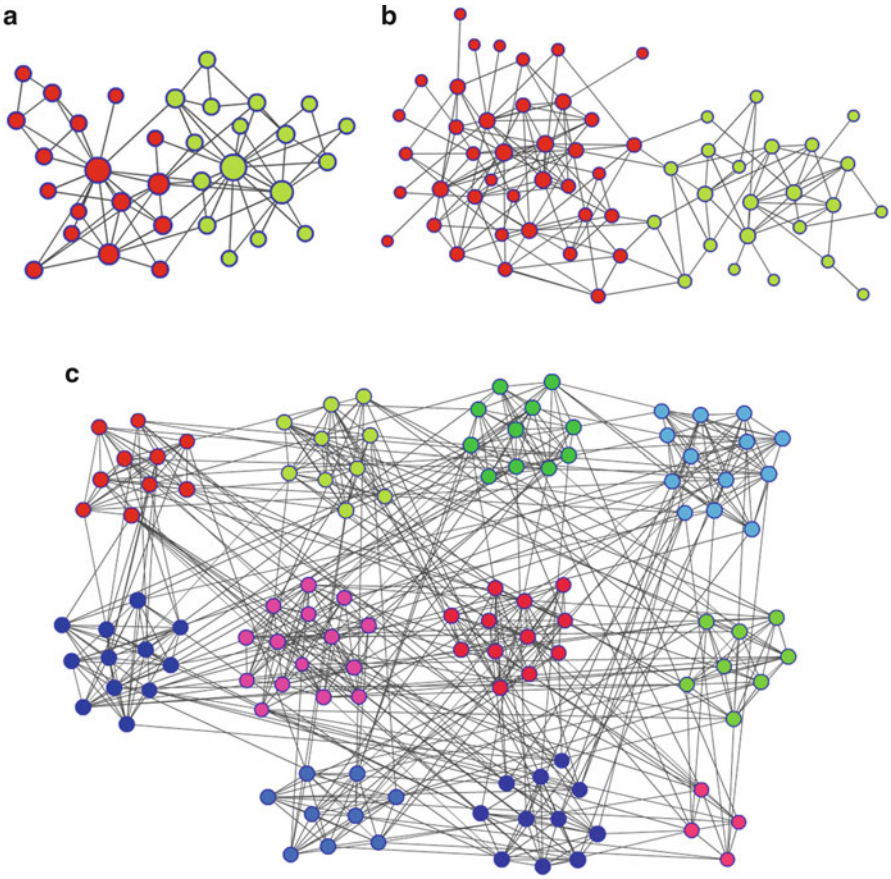

Fig. 45.2 Community structures of karate club network, dolphin networks and USA college football network by our algorithm

We find that most teams classified incorrectly have sparse connections with the teams within the same conference but have dense connections with other conferences so that they are difficult to be classified correctly. For example, all the teams in *Independence* are assigned to other conferences since they have only one connection among them but 45 edges connecting to other conferences. Team *California* belonging to *Pacific Ten* is assigned to *Western Atlantic* because it has no connections with teams in *Pacific Ten* but seven connections with teams in *Western Atlantic*.

45.5 Conclusion

In this chapter, we introduced the notion of potential in physics into the complex network and proposed the definition of network potential, which is a reasonable and effective measurement of the network topological structure. According to the

properties of network potential, we also proposed the community structure detecting algorithm based on the network potential. The algorithm was applied to some artificial networks and we obtain some convincing experimental results. Moreover, the algorithm succeeded in several real-world networks, including karate club network, dolphin network and USA college football network. The results are in accordance with the real situation and demonstrate the effectiveness of our proposed algorithm.

In our future work, we will focus on the how to apply our proposed algorithm to weighted or directed networks. And we also want to find more properties of network potential in the respect of dynamic evolution of complex networks and the evaluation of community structure in networks.

Acknowledgments This work was supported by National Natural Science Foundation of China (61071152), National "Twelfth Five-Year" Plan for Science and Technology Support (2012BAH38B04), and Major State Basic Research Development Program (2010CB731400 and 2010CB731406).

References

1. Strogatz SH (2001) Exploring complex networks. Nature 410:268–276
2. Albert R, Barabási AL (2002) Statistical mechanics of complex networks. Rev Mod Phys 74:47–97
3. Newman MEJ (2003) The structure and function of complex networks. SIAM Rev 45(2):167–256
4. Newman MEJ, Girvan M (2004) Finding and evaluating community structure in networks. Phys Rev E 69:026113
5. Fortunato S (2010) Community detection in graphs. Phys Rep 486:75–174
6. E W, Li TJ, Vanden-Eijnden E (2008) Optimal partition and effective dynamics of complex networks. Proc Natl Acad Sci USA 105:7907–7912
7. Fiedler M (1973) Algebraic connectivity of graphs. Czech Math J 23(98):298–305
8. Kernighan BW, Lin S (1970) An efficient heuristic procedure for partitioning graphs. Bell Syst Tech J 49(2):291–307
9. Newman MEJ (2004) Fast algorithm for detecting community structure in networks. Phys Rev E 69:066133
10. Ruan JH, Zhang WX (2008) Identifying network communities with a high resolution. Phys Rev E 77:016104
11. Palla G, Derényi I, Farkas I, Vicsek T (2005) Uncovering the overlapping community structure of complex networks in nature and society. Nature 435:814–818
12. Yang B, Cheung WK, Liu J (2007) Community mining from signed social networks. IEEE Trans Knowl Data Eng 19:1333–1348
13. Girvan M, Newman MEJ (2002) Community structure in social and biological networks. Proc Natl Acad Sci USA 99(12):7821–7826
14. Radicchi F, Castellano C, Cecconi F, Loreto V, Parisi D (2004) Defining and identifying communities in networks. Proc Natl Acad Sci USA 101(9):2658–2663
15. Clauset A (2005) Finding local community structure in networks. Phys Rev E 72:026132
16. Newman MEJ (2006) Finding community structure in networks using the eigenvectors of matrices. Phys Rev E 74:036104
17. Newman MEJ (2001) Scientific collaboration networks: ii. Shortest paths, weighted networks, and centrality. Phys Rev E 64:016132

18. Danon L, Diaz-Guilera A, Duch J, Arenas A (2005) Comparing community structure identification. J Stat Mech 2005:P09008
19. Penrose M (2003) Random geometric graphs. Oxford University Press, Oxford
20. Liu J, Wang N (2009) Detecting community structure of complex networks by affinity propagation. IEEE Int Conf Intell Comput Intell Syst 4:13–19
21. Zachary WW (1977) An information flow model for conflict and fission in small groups. J Anth Res 33(4):452–473
22. Lusseau D (2003) The emergent properties of a dolphin social network. Proc R Soc Lond B 270(Suppl2):S186–S188

Part XII
Localization and Target Detection

Chapter 46
DOA Estimation Algorithm Based on Compressed-Sensing

Yao Luo and Qun Wan

Abstract A novel kind of method using in the DOA estimate of array signal processing is proposed. This method is based on constructing matrix with random selection of the rows of DFT transformation matrix. Such matrix satisfies the RIP condition (restricted isometry property). Due to the sparsity of space signal, the amount of array sensor is reduced significantly, which results in a lower complexity of the array system. SVD decomposition is used in processing the sampling signal to minimize its dimension and the final performance is much better than traditional algorithms.

Keywords Compressed sensing • DOA estimation • SVD decomposition

46.1 Introduction

Compressed Sensing (CS) is a novel theory which has been widely used in many areas. It shows that sampling rate of one system can be significantly reduced if observed signal satisfy some the sparsity condition [1] and reconstruction of original signal will be exactly the same.

Estimation of direction-of-arrival (DOA) is an important area in array signal processing. Traditional algorithms aiming in solving this problem include multiple classification method (MUSIC) and minimum variance distortionless response (MVDR), etc. But both of them perform unsatisfactory when $SNR < 0$.

In many cases, sources accounted for only a few angular resolution units, which makes the targets' distribution in space sparse and satisfies the requirement of sparsity in CS and makes the reconstruction feasible. In this chaper, we set the array antenna randomly in a direct line, which uses much fewer antennas comparing

Y. Luo (✉) • Q. Wan
School of Electronic Engineering, UESTC, Cheng Du 611731, China
e-mail: Oliver.luo@outlook.com

Q. Liang et al. (eds.), *Communications, Signal Processing, and Systems*, Lecture Notes in Electrical Engineering 202, DOI 10.1007/978-1-4614-5803-6_46,

to the uniform linear array (ULA) and makes the corresponding matrix satisfy RIP condition [2] as well. SVD singular value decomposition is used to reduce dimensions of receiving signal. M-FOCUSS algorithm is used to reconstruct receiving signal and simulation comparing with traditional methods are given.

46.2 The Model of Compressed Sensing

The problems of sparse signal computations appear in many applications. A signal is a sparse one if most values of entries are almost zero, or in some cases equal to zero. For signals that are not sparse enough on some certain basis, transformations that lead to a sparse representation can satisfy the requirement. Consider a vector $x \in R^m$ with $\boldsymbol{m}$ nonzero entries. This vector can be the expression of any kind of signal we interested in such as the array signal. For a standard orthonormal basis $(\psi_i : i = 1, \cdots, m)$ and related coefficients $\theta_i = \langle x, \psi_i \rangle$, the vector is said to be a sparse vector based on the transformation with such basis in the following sense that, for some $0 < \mathrm{p} < 2$ and for some $\mathrm{R} > 0$ [1].

$$\|\theta\|_p \equiv \left(\sum_i |\theta_i| \right)^{1/p} \leq R \tag{46.1}$$

Here we denote the transform matrix $\psi \in R^{m*m}$ and measurement matrix $A \in R^{n*m}$. The observed signal can be expressed as follows:

$$y = A\psi x \in R^{n*1} \tag{46.2}$$

Signal $\mathbf{y}$ has $\boldsymbol{n}$ entries with amount $\boldsymbol{n}$ much lower than $\boldsymbol{m}$. Such property makes the CS theory of great use in applications because decrease of dimensions leads to decrease of sampling rate and amount of sensors directly.

The main aim of CS theory is to reconstruct signal $\boldsymbol{x}$ precisely from observed signal $\boldsymbol{y}$. We use the definition of $\boldsymbol{l0}$ norm introduced in [1]:

$$\|\mathbf{x}\|_0 = \lim_{p \to 0} \|\mathbf{x}\|_p^p = \lim_{p \to 0} \sum_{k=1}^{m} |x_k|^p = \#\{i : x_i \neq 0\} \tag{46.3}$$

The count $\boldsymbol{k}$ of nonzero entries in $\boldsymbol{x}$ can be rewrite as $k = \|\mathbf{x}\|_0$. It is clear that to get original signal $\boldsymbol{x}$ we need to solve an optimization problem denoted as (P0) [1]:

$$(P0) \quad \min_x \|\mathbf{x}\|_0 \ \textit{subject to} \ \mathbf{y} = A\psi\mathbf{x} \tag{46.4}$$

(P0) is a NP-hard problem and can't be solved efficiently using practical tools [1]. Gives a demonstration that with certain conditions, we can solve (P1) instead of (P0) and get the original signal as well. (P1) is described as follow:

$$(P1)\ \min_{x} \|\mathbf{x}\|_1 \ subject\ to\ \ \mathbf{y} = A\psi\mathbf{x} \tag{46.5}$$

(P1) and (P0) describe only the general form with one dimension. In DOA estimation, due to the amount of snapshot observed signal usually has more than one sample, which makes the problem into a MMV problem (Multiple Measurement Vector). The general form of MMV-CS problem is described as follow [3]:

$$\mathrm{AX} = \mathrm{B} \tag{46.6}$$

Where $\mathbf{X} = \left[\mathbf{x}^{(1)}, \mathbf{x}^{(2)}, \cdots, \mathbf{x}^{(L)}\right]$ and $\mathbf{B} = \left[\mathbf{b}^{(1)}, \mathbf{b}^{(2)}, \cdots, \mathbf{b}^{(L)}\right]$.To solve MMV-CS problems, [3] proposed a series of new algorithms including M-OMP, M-BMP, M-ORMP, and M-FOCUSS. To ensure the success of reconstruction, T. Tao and Candes put forwards the RIP condition of matrix $\boldsymbol{A}$ [2]. RIP condition of a certain matrix $\boldsymbol{A}$ tells that for an integer scalar $s \leqslant n$, consider sub-matrices $\mathbf{A}_s$ containing s columns from $\boldsymbol{A}$. Define δ_s as the smallest quantity such that

$$\forall c \in \mathbf{R}^s \quad (1-\delta_s)\|c\|_2^2 \leq \|\mathbf{A}_s c\|_2^2 \leq (1+\delta_s)\|c\|_2^2 \tag{46.7}$$

holds true for any choice of $\boldsymbol{s}$ columns. Then $\boldsymbol{A}$ is said to have an $\boldsymbol{s}$-RIP with a constant δ_s.

46.3 Doa Estimation of Array Signal

All far-field signals receiving from ULA can be described as $s(t) = u(t)e^{j\psi(t)}$ where $u(t)$ is the envelope of receiving signal and $\psi(t)$ is the phase. We put the assumption that ULA has $\boldsymbol{M}$ elements and the distance between each element is d. Denote the first element as the base, a time delay of receiving signal at each element can be observed and expressed as:

$$\tau_m = \frac{md\sin\theta}{c} \tag{46.8}$$

Denote the spatial phase of signal as $\phi = \omega_0\tau = 2\pi d\sin\theta/\lambda$ where λ is the wavelength of signal. Therefore, receiving signal of a certain ULA can be written by the form of vector as the following:

$$x(t) = a(\phi)s(t) \tag{46.9}$$

Where $x(t) = [x_0(t)\ \ x_1(t) \cdot s\ \ x_{M-1}(t)]^T$ and $(\phi) = [\,1 \quad e^{-j\phi} \quad \cdots \quad e^{-j(M-1)\phi}\,]^T$ $a(\phi)$ is called the steering vector and $x(t)$ is simply a combination of $\boldsymbol{K}$ different single tone signals and its discrete Fourier transform is a $\boldsymbol{K}$ sparse vector at which the location of nonzero entries gives the angle of targets.

The fact that DFT of $x(t)$ is a $\boldsymbol{K}$-sparse signal makes application of CS possible. Aiming at reducing amount of array sensors, we use another method to arrange the location of them. We assume that there are $m + d$ elements putting uniformly on a line. Instead of using all the $m + d$ elements, we use only $\boldsymbol{m}$ of them and the selection of $\boldsymbol{m}$ is completely at random. This means that we put $\boldsymbol{m}$ array sensors randomly at $m + d$ locations. This process is mathematically equivalent to select entries randomly in vector $x(t)$. Denote the extraction vector as $y(t)$ and random selection matrix as θ, the connection of $x(t)$ and $y(t)$ can be described as follow:

$$y(t) = \theta x(t) \tag{46.10}$$

Denote the DFT matrix as $\mathbf{F}$ and the frequency- domain expression of $x(t)$ as $s(t)$, (46.10) can be rewritten as follow:

$$y(t) = \theta \cdot \mathbf{F}^{-1} s(t) \tag{46.11}$$

Denote $\theta \cdot \mathbf{F}^{-1}$ as $\mathbf{A}$ and we can define $\mathbf{A}$ as a matrix whose rows are randomly selected from inverse DFT matrix $\mathbf{F}^{-1}$. Such sensor matrix $\mathbf{A}$ satisfies the RIP condition and makes the reconstruction of $y(t)$ from $s(t)$ possible.

In practical applications, we assume that the amount of snapshot is $\boldsymbol{N}$ and targets' movement during each snapshot is less than an angle unit so that the location of nonzero entries won't change between every sample. Besides, we assume the receiving noise obeys Gaussian distribution, $\mathbf{N} \sim (0, \sigma^2\mathbf{I})$. Therefore, the observed signal $y(t)$ becomes a matrix $\mathbf{Y}$ whose dimension is $m \times N$. Accordingly, the dimension of $\mathbf{S}$ turns into $(m + d) \times N$. Thus (46.12) can be rewritten as follow:

$$\mathbf{Y} = \mathbf{A} \cdot \mathbf{S} + \mathbf{N} \tag{46.12}$$

46.4 Doa Based on M-Focuss Algorithm

The observed matrix $\mathbf{Y}$ has $\boldsymbol{m}$ rows and N columns. In the traditional DOA algorithms such as MUSIC, we computed the auto correlative matrix of $\mathbf{Y}$ and use the SVD decomposition to separate signal subspace and noise subspace. By using the property that these two subsets are orthogonal to form peak-searching function and complete DOA estimation. This method requires the signal to be incoherent otherwise the orthogonality of two subsets cannot be satisfied, which may leads to failure of algorithm.

Since equation (46.12) has a standard form of MMV-CS problem, we can simply apply all the algorithms mentioned in Chap. 33 to solve this problem. However, the amount of snapshot, N, is relatively large, which directly leads to the increasing of algorithm complexity and increase the processing time required.

To avoid the problem and deal with coherent signals, a new kind of method is proposed in the following. We use SVD decomposition directly on $\mathbf{Y}$ as $\mathbf{Y} = \mathbf{U}\Lambda\mathbf{V}^H$. Λ is a diagonal matrix where all nonzero entries are singular values of $\mathbf{Y}$ and sized down from the biggest one to the smallest one. We can get target number $\boldsymbol{k}$ by MDL (minimum-description-length) in advance. Therefore, $\boldsymbol{k}$ left singular vectors can be selected and used to span the signal subspace and others to span noise subspace. Notice that we shall not use the orthogonality of these two subspaces so this method can be used to process coherent signal as well.

In most cases, the sum of $\boldsymbol{k^{th}}$ singular values occupied more than 90 % of total sum. Therefore $\mathbf{U}$ can be separated into two parts as: $\mathbf{U} = [\mathbf{U}_S, \mathbf{U}_N]$ where $\mathbf{U}_S$ corresponds to $\boldsymbol{k^{th}}$ biggest singular values and $\mathbf{U}_N$ corresponds to the others. Most features of observed signal can be described using only $\mathbf{U}_S$. Furthermore, denote $\mathbf{Y}_S = \mathbf{YVD}_k$ where $\mathbf{D}_k = [\Lambda_k, \mathbf{0}_{k\times(N-k)}]^H$. Λ_k is the diagonal matrix consists $\boldsymbol{k^{th}}$ biggest singular values. Similarly, denote $\mathbf{S}_S = \mathbf{SVD}_k$ and $\mathbf{N}_S = \mathbf{NVD}_k$. Therefore, the decline dimension express of equation (46.12) can be rewritten as follow:

$$\mathbf{Y}_S = \mathbf{AS}_S + \mathbf{N}_S \tag{46.13}$$

Notice that all the transform mentioned before are some elementary matrix transformations so the row sparsity of $\mathbf{S}_S$ will be the same as $\mathbf{S}$, which means reconstruction from $\mathbf{Y}_S$ and $\mathbf{S}_S$ will have same indices of nonzero entries compares with $\mathbf{S}$. $\mathbf{Y}_S$ has $\boldsymbol{m}$ rows and $\boldsymbol{k}$ columns. Since $m \ll m + d$ in most cases, the computational complexity of equation (46.13) can be significantly reduced.

To solve equation (46.13), traditional CS algorithms find each column one by one since they can only handle one dimensional problem. But such methods cannot guarantee the unite sparsity between each column. In Ref. [3] Cotter and others proposed a class of new algorithms dealing with these multi-measurement vector CS (MMV-CS) problems, among which the M-FOCUSS algorithm has best performance. Therefore we chose M-FOCUSS to solve our problem of (46.13) [5].

To solve equation (46.13), a cost function based noise and sparsity of observed matrix is built as follow:

$$\min_{\mathbf{S}_S} \|\mathbf{S}_S\|_{r0} \quad s.t \quad \|\mathbf{Y}_S - \mathbf{AS}_S\|_F^2 \leq \varepsilon \tag{46.14}$$

Since the optimization of $\|\mathbf{S}_S\|_{r0}$ is a NP-hard problem as well, it is usually replaced by another kind of cost function. Therefore, (46.14) can be rewritten as follow:

$$\min_{\mathbf{S}_S} f_{p,q}(\mathbf{S}_S) \quad s.t \quad \|\mathbf{Y}_S - \mathbf{AS}_S\|_F^2 \leq \varepsilon \tag{46.15}$$

In equation (46.15), $f_{p,q}(\mathbf{S}_S) = \sum_i \|\mathbf{S}_S\|_p^q$ is the function used to replace the ***l0*** norm which measures the row sparsity of $\mathbf{S}_S$ with $p<1$ and $q>1$. In most applications, we use $p = 0.8$ and $q = 2$ thus $f_{p,q}(\mathbf{S}_S) = \sum_i \|\mathbf{S}_S\|_p^q$ becomes the power of source signal. To solve equation (46.15), Lagrange method of multipliers is used with multiplier λ:

$$\min_{\mathbf{S}_S} \sum_i \|\mathbf{S}_S\|_p^q + \lambda \|\mathbf{Y}_S - \mathbf{A}\mathbf{S}_S\|_F^2 \tag{46.16}$$

Here we use λ to balance the influence of calculation accuracy and sparsity of $\mathbf{S}_S$. A bigger λ represents that accuracy is more important than sparsity while a relatively small λ leads to a sparser solution. To determine the exact value of λ, [4] provided a method called *L-curve method*. Here, we simply set λ to 30 in the following simulations. Finally, the peak searching function is given as:

$$P(\theta_i) = \|\mathbf{S}(i,:)\|_2 \; i = 1, 2, 3, \ldots, m \tag{46.17}$$

46.5 Simulations

In our test, we set the distance ***d*** from each array element as $d = \lambda/2$ where λ is the wavelength of signal. The number of snapshot is $N_s = 64$. $L = 32$ array elements are located at a ULA of 64 elements randomly. Therefore it is equal to select half of the ULA randomly. Assume three receiving signals are random noise radar signal which are located at the angle of 0°, 15° and 45°. With $SNR = -2dB$, giving 10 independent tests, the result is shown as follow:

As shown in Fig. 46.1, MUSIC cannot separate these three signals out from noise while MFOCUSS and MVDR detect three signals successfully. Actually,

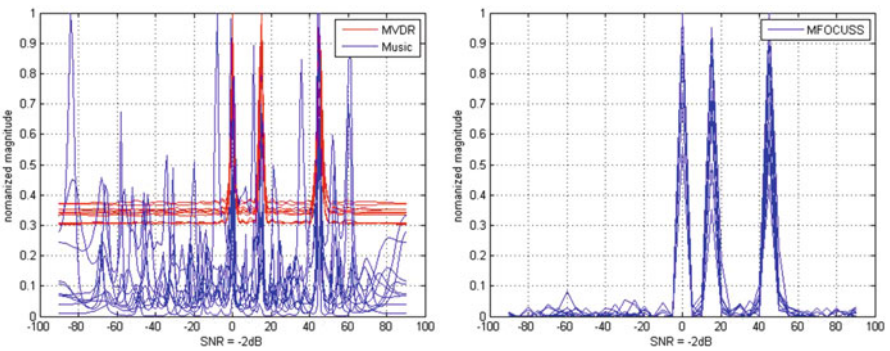

Fig. 46.1 DOA based on MUSIC and MVDR shows a poor performance compared to the result of using MFOCUSS

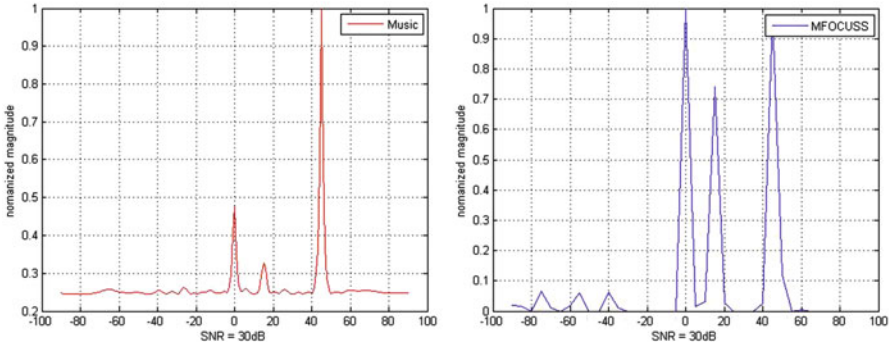

Fig. 46.2 DOA of coherent signal based on MUSIC (*left*) and MFOCUSS (*right*)

traditional methods such as MUSIC reach to a failure once and snapshot is small. But MVDR has higher amplitudes besides angle of signal as well.

Dealing with coherent signal, due to interoperability of subspace mentioned before, MUSIC cannot separate different signals while MFOCUSS does as well. The performances of these two methods are shown as follow:

As is shown in Fig. 46.2, MFOCUSS reaches a peak on every DOA angle while targets at 0° and 15° have a much lower level compare to target at 45° in the traditional method.

46.6 Conclusion

A new kind of algorithm dealing with lower SNR signal is proposed. In this method, CS theory is used to reduce amount of array element into half of original. By selecting location of each element randomly, projection matrix is assured to satisfy the RIP condition. SVD decomposition is used to reduce dimension of receiving signals. MFOCUSS algorithm is introduced to reconstruct receiving signal and a better performance is observed. This method is also effective when dealing with coherent signal while traditional method such as MUSIC has a bad performance.

References

1. Donoho DL (2006) Compressed sensing. IEEE Trans Inf Theory 52(4):1289–1306
2. Candes EJ, Romberg J, Terrence T (2006) Robust uncertainty principles: exact signal reconstruction from highly incomplete frequency information. IEEE Trans Inf Theory 52(2):489–509
3. Cotter SF, Rao BD, Engan K, Delgado K (2005) Sparse solutions for linear inverse problems with multiple measurement vectors. IEEE Trans Signal Process 53(7):2477–2488
4. Rao BD, Engan K, Cotter SF, Palmer J, Kreutz-Delgado K (2003) Subset selection in noise based on diversity measure minimization. IEEE Trans Signal Process 51(3):760–770
5. Gorodnitsky IF, Rao BD (1997) Sparse signal reconstruction from limited data using FOCUSS: a re-weighted norm minimization algorithm. IEEE Trans Signal Process 45(3):600–616

Chapter 47
A Novel Method of Acoustic Source Localization Using Microphone Array

Chunlong Liao, Xiang Xie, Yongtao Jia, and Ming Tu

Abstract The acoustic source localization is widely used in tele-conference system. This article proposed a novel acoustic source localization algorithm for microphone array which is based on delay-and-sum beamforming and GCC-PHAT. The algorithm shows that time delay between microphones on a basis of GCC-PHAT can be estimated and localize the acoustic source in search space by using improved delay-and-sum beamforming algorithm. Experimental results demonstrate that the proposed algorithm is much more robust than TDOA alone as well as SRP-PHTA algorithm when in noise and reverberation environment.

Keywords Microphone array • Acoustic source localization • Delay-and-sum beamforming

47.1 Introduction

In the environment without noise, single microphone of high directivity can easily get localization direction. However, in real environment, the quality of collected signal may be decreased due to ambient noise. In order to solve the problem of limitation of single microphone system, microphone array for speech localization has been studied for years, which can be widely applied in fields like speaker localization [1], speech recognition and hearing aids [2].

C. Liao (✉) • X. Xie • Y. Jia • M. Tu
School of Information and Electronics, Beijing Institute of Technology, Beijing 100081, China
86-010-68915838
e-mail: 278409122@qq.com

Q. Liang et al. (eds.), *Communications, Signal Processing, and Systems*, Lecture Notes in Electrical Engineering 202, DOI 10.1007/978-1-4614-5803-6_47,

Acoustic source localization with microphone array can be roughly divided into three categories [3, 4]:

1. Based on the maximum steerable output power beamforming technology. The acoustic source received by microphone array is filtered, weighted sum, and then directly point to the direction of maximum output power.
2. Directional technology based on high resolution spectral estimation. The method solves the correlation matrix between the microphone signals to set the direction angle, then further set the acoustic source position;
3. Technology based on time difference of arrival (TDOA). Firstly, find the time difference of sound reaching the different microphones, then re-use the time difference to obtain the distance of acoustic source reaching the different position of the microphones, finally determine the location of the acoustic source by searching or using geometric knowledge.

This chapter suggests a fast search strategy for an energy map to locate the acoustic source direction, which is called a combination of TDOA and delay-sum beamforming algorithm. This strategy works because it first locate the quadrant of acoustic source in the coordinate by using GCC-PHAT, then using improved delay-sum beamforming algorithm to scan specific direction in the located quadrant. It is particularly suitable for the case where there is prior knowledge of the spatial domain. The comparison with other localization algorithms shows that the result of ours is significantly better.

47.2 Recent RESearch in Microphone Array Localization

Liu Jianping [5] proposed to use GCC-PHAT (Generalized cross-correlation—phase transform) method for time delay estimation, and thus get the orientation of the acoustic source. This method has small amount of calculation, easy to achieve real-time and higher accuracy, especially more suitable for a small microphone array. But when in reverberation or noise environment, the acoustic source localization algorithm based on GCC performance sharply declines, making it impossible to achieve accurate localization.

In order to eliminate reverberation and noise impacts, N.Zotkin [6] proposed the combined use of delay-sum beamforming and the SRP-PHAT (Steering Response Power-Phase Transform) acoustic source localization algorithm.

Because the SRP-PHAT algorithm (Steering Response Power-Phase Transform) is faced with a huge computational complexity in practical engineering applications, which cannot meet the real-time localization requirement, we try to use generalized cross-correlation phase transform (GCC-PHAT) combined with improved delay-sum beamforming method for acoustic source localization.

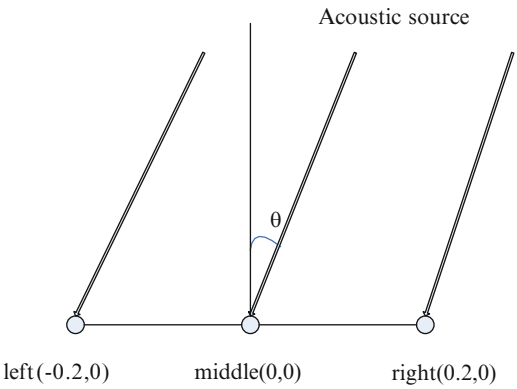

Graph 47.1 Relative position of the microphone array and acoustic source

47.2.1 Improved Delay-Sum Beamforming

Delay-sum beamforming algorithm is traditional array-process algorithms, but sound is different from radar and sonar signal, it has short-term stable characteristics, which cannot be directly applied into this method. Some improvements based on the characteristics of the acoustic source need to be done [7].

Delay-sum beamforming algorithm is suitable to process smooth and far-field signal. First of all, the sound we produce is short-time stationary signal. In order to achieve the algorithm's weak stationary process requirements, endpoint detection need to be done so as to get voice segment, which is assumed as a wide stationary signal. Secondly, the acoustic source signal is divided into the far-field signal and the near-field signal source. When the distance between acoustic source and microphone array is greater than three times the microphone spacing, the acoustic source is considered to be a plane wave. In the actual environment, the microphone space is selected to be 0.2 m, when producing sound signal, the distance of the sound source from the microphone array will be greater than 1 m, so in this system, only the far-field signal microphone array localization is taken into consideration.

The microphone array is put in a linear line like Graph 47.1. Before voice processing, we frame acoustic source signal, endpoint detection need to be done to remove the noise and mute frame. A frame signal of short-term energy defined as:

$$E_k = \sum_{i=kN+1}^{(1+k)N} [x(i)^2]$$

Therefore, before and after the two signals in the short time difference is set to $E_{k+1} - E_k$

Single frame of the noise energy is set as follows: $W_k = \sum_{i=kN+1}^{(1+k)N} [n(i)^2]$

$n(i)$is on behalf of the ambient noise when system initialization starts,

When the sound source is satisfied $\begin{cases} |E_{k+1}-E_k|>D \\ E_k > W_k \end{cases}$

It represents the corresponding voice segment start and end position. In which D is representative of the sound of a priori knowledge of the short-term energy, considering the obtained threshold. Start and end part can be shown as the followings:

When $E_{k+1} - E_k > D$ the sound begins

When $E_k - E_{k+1} > D$ the sound ends

Through differential detection, two frames are brought in to compared with each and at the same time are matched the single frame with the standard value D, in order to get accurate voice segment starting position and end position.

A coordinate system is set for the linear microphone array, the angel that acoustic source from the microphone array's zero coordinates is set to θ as Graph 47.1 shows:

According to the final formula of [8], after derivation, localization based on the delay-sum beamforming algorithm to find the angel θ of the acoustic source is as follows:

$$F(\theta) = \left| \frac{\sin[N\pi d(\sin\theta - \sin\theta_0)/\lambda]}{\sin[\pi d(\sin\theta - \sin\theta_0)/\lambda]} \right|$$

Through this formula, when$\theta = \theta_0$, $F(\theta)$ reaches maximum value, θ_0 is a known angel we need to find by scanning function $F(\theta)$, and θ_0 represents the θ current angel. Because of the characteristics of the sinusoidal signal, if the acoustic source is in the range of 0–180°, the scanning θ process may occur two possible location values.

Because: $\sin\theta = \sin(180 - \theta)$

This situation can also occur within the range of 180–360°. To address this problem, the time difference (TDOA) method is introduced to the acoustic source localization.

47.2.2 Time Difference of Arrival (TDOA)

In order to simplify the model of acoustic source localization, we only consider the case of 0–180°. Within the range of 0–180°, if the acoustic source is produced, it may be in the range of 0–90°, or 90–180°, or 90°, 0°, 180° coordinates.

If the relative position of the microphone array and acoustic source is shown as Graph 47.1:

Left—left microphone;middle—middle microphone;
Right—right microphone;mobile—acoustic source(e.g. speaker);

The time difference of sound reaches the microphone can be modeled, suppose the microphones arranged in a linear array, the m-th microphone and the n-th microphone received signal, respectively as follows [8]:

$$x_m(t) = a_m s(t - t_m) + n_m(t)\ x_n(t) = a_n s(t - t_n) + n_n(t)$$

By using the generalized cross correlation (GCC) method [9], followed by the introduction of the phase transformation (Phase Transform, PHAT) to be weighted, the time difference of the voice signal to reach each microphone time difference can be got: $\tau = t_m - t_n$

As the linear microphone array is used like Graph 47.1 shows, then we assume:

$$\text{if} \quad \begin{cases} t_{left} - t_{right} < 0 \\ t_{left} - t_{middle} < 0 \end{cases}$$

then we know the acoustic source is located in the second quadrant.

By the time difference of acoustic source to each microphone, we can determine the range of the microphone location, and then use the improved delay-sum beamforming method to scan in the fourth quadrant, finally to determine the acoustic source location, which reduces the computation and meet the real-time requirements.

47.3 Implementation of Microphone Array Localization

47.3.1 Microphone Parameters

In this system, we set up a linear microphone array with three microphones (MPA416). Setting microphone spacing to be 0.2 m, so long as the distance of acoustic source from the microphone array is more than 0.6 m, the acoustic source can be considered as far-field range [10].

47.3.2 Localization Algorithm Realization Platform

The acoustic source localization system use virtual instrument of National Instruments as a platform,and use Labview as a software language for algorithmic programming [11, 12]. The system flowchart is like Graph 47.2.

47.3.3 Experiment Result analysis

Clapping experiments is made standing on the vertical distance 1 m from the microphone linear array, with the reference microphone angle is 50°, after the experiment, we get measured angle of 49.5625°,which is very accurate.

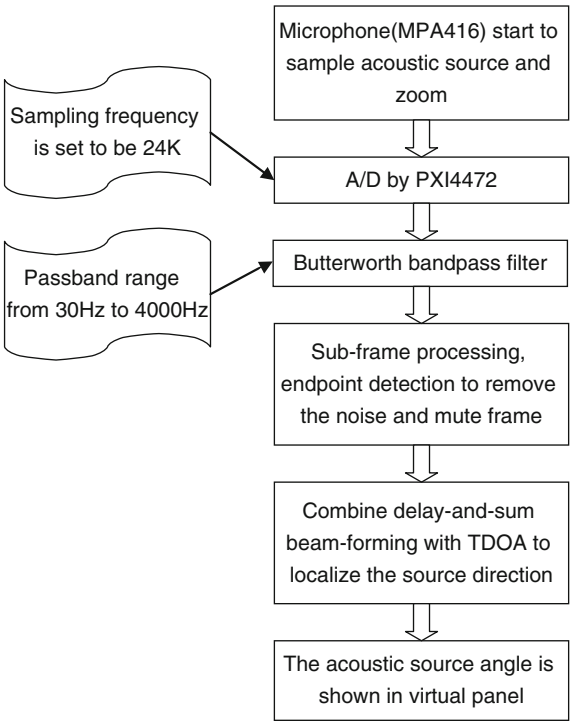

Graph 47.2 System flowchart

Table 47.1 The localization result

	Angle/°	Angle/°	Angle/°	Angle/°
Theoretical value	30	45	60	90
Experimental value	30.4334	46.64	60.9356	91.4703
Theoretical value	120	135	90	73.3
Experimental value	120.514	133.7	92.7189	74.9092

A 4 m × 7 m offfice room is selected to carry out our experiments with the presence of reverberation and echo effects. The Table 47.1 represents for the data measured in different directions.

As the experimental result shows, when the distance of acoustic source from microphone array is 2 m, the average angel error is 0.8181°, lower than the error value of 1.1657° reported in the [5] by using GCC-PHAT algorithm alone, and less than the average error value of 0.9250° reported in the [6] by using the SRP-PHAT-DHBF (controllablethe power response—phase transformation—beamforming)

mode. Therefore, this algorithm can achieve a higher accuracy. Because the entire system deals with the noise in three aspects, Butterworth band-pass filter, endpoint detection and the data preprocessing in the beamforming algorithm, it has a round capability of resistance to ambient noise,

47.4 Conclusion

This chapter studies a indoor acoustic source localization algorithm, which accumulates sum-delay beamforming and time difference of arrival (TDOA) localization algorithm applied to the microphone array, reaching real-time and robust localization. During endpoint detection, combined with the traditional speech endpoint detection, we introduce single frame energy to compare with standard value, making voice segment detection more accurate. The implementation is based on virtual instrument platform. The results show that the angle error is less than used TDOA (Time Difference of Arrival) or the SRP-PHTA-DHBF algorithm alone, and the localization errors are mostly from the microphone directivity and dissemination of media.

Acknowledgements This work is supported by the National Natural Science Foundation of China (Grant No. 11161140319, No. 90920304 and No. 91120015).

Graphs and Charts

The distance between microphones is set by 0.2 m. Acoustic source is 2-m away. Sampling frequency is set by 24 k samples/s

References

1. Jacob B, Yiteng H, Jingdong C (2007) Time delay estimation via minimum entropy. IEEE Signal Proc Lett 14(3):157–169
2. Smith R (1970) Constant beamwidth receiving arrays for broad band sonar systems. Acustica 23:21–26
3. Flanagan JL, Berkeley DA, Elko GW et al (1991) Autodirective microphone systems. Acustical 73:58–71
4. Khalil F, Jullien JP, Gilloire A (1994) Microphone array for sound pickup in teleconference systems. J Audio Eng Soc 42(9):691–700
5. Jianping L (2012) Recognition and localization of car whistles using the microphone array. J Xidian Univ 39(1):163–167
6. Zotkin DN, Duraiswami R (2004) Accelerated speech source localization via a hierarchical search of steered. IEEE Trans Speech Audio Process 12(5):1470–1478

7. Video Conference System [M/OL]. http://www.polycom.com/usa/en/products/video/video/conferencingsystems/videoconferencingsystems.html/
8. Microphone Array Support in Windows Vista [M/OL] (2005) http://www.microsoft.com/whdc/device/audio/MicArrays.mspx/
9. Georgiou PG, Kyriakakis C (2002) An alternative model for sound signals encountered in reverberant environments; Robust maximum likelihood localization and parameter estimation based on a sub-gaussian model. Audio engineering society (AES) 113th convention paper, Los Angeles, CA, 5–8 Oct 2002
10. Potamitis I, Chen H, Tremoulis G (2004) Tracking of multiple moving speakers with multiple microphone arrays. IEEE Trans Speech Audio Process 12(5):520–529
11. Alvarado VM (1990) Talker localization and optimal placement of microphone for a linear microphone array using stochastic region contraction. Ph.D. thesis, Brown University, Providence, Rhode Island, May 1990
12. Dibiase A (2000)A high-accuracy, low-latency technique for talker localization in reverberant environments.,Ph.D. thesis, Brown University, Providence, Rhode Island, May 2000

Chapter 48
GTD-Based Model of Terahertz Radar Scattering Center Distance Estimation Method

Zhengwu Xu, Yuanjie Wu, Jin Li, and Yiming Pi

Abstract A large increase in terahertz radar resolution under large bandwidth condition is particularly important for one-dimensional distance projection method to obtain more extensive information about the target feature. This chapter presents the details of a terahertz radar echo data model in terms of the geometrid theory of diffraction concept. The MUSIC spectral estimation algorithm in the implementation process is discussed. Finally, the MUSIC spectral estimation algorithm from the estimated scattering center projections and at different signal-to-noise ratios is simulated. The results obtained exhibited high precision, and noise immunity was better, which proves the effectiveness of the spectral estimation using MUSIC algorithm.

Keywords Terahertz • MUSIC algorithm • GTD model • Distance from the scattering center

48.1 Introdution

The range resolution cell of a radar is expressed as $c/2B$. The wider the bandwidth is, the smaller is the range resolution cell. Usually, the range resolution cell of a wideband radar is much smaller than the radial size of the target [1, 2]. The terahertz radar techniques of increasing the bandwidth of a signal can significantly obtain more detailed information on the dimension of a target range [3, 4]. The scattering intensity and location of the target attitude angle in scattering centers change significantly. Thus, extracting stable features is difficult, resulting in the difficulty of recognizing the target from the range direction. The type of scattering centers can

Z. Xu (✉) • Y. Wu • J. Li • Y. Pi
School of Electronic Engineering, University of Electronic Science and Technology of China, Chengdu, China
e-mail: zwxu@uestc.edu.cn

Q. Liang et al. (eds.), *Communications, Signal Processing, and Systems*, Lecture Notes in Electrical Engineering 202, DOI 10.1007/978-1-4614-5803-6_48,

remain unchanged at an attitude angle range up to a certain degree of stability, and the range direction can be as robust as the identification features [5, 6]. The problem of solving the geometrid theory of diffraction (GTD) model is the scattering center parameter estimation process of the echo data from the target. Potter et al. presented the approximate maximum likelihood algorithm of the model [7]. Based on the GTD scattering model, which is closer to the physical mechanism of high-frequency electromagnetic scattering, and the more complete GTD-based model of the echo signal, this chapter discusses the GTD of the terahertz spectral estimation methods in radar applications [8–10]. This chapter introduces the GTD model, discusses the MUSIC spectral estimation algorithm, and applies the MUSIC algorithm as an example in estimating the distance projection under different signal-to-noise ratios (SNRs).

48.2 GTD Model

In the optical region, the radar target scattering response is equivalent to some of the radial distribution of scattering centers of the coherent superposition of electromagnetic scattering. The target frequency response can be expressed as the sum of the frequency responses of the scattering centers. Assuming that electromagnetic waves are emitted along the Z-axis, the vector $\vec{r}$ field can be expressed as follows:

$$\vec{E}^{i} = \vec{E}_0 e^{-jk\hat{z}\cdot\vec{r}} \tag{48.1}$$

According to GTD, when the incident wavelength is sufficiently small, the reflected field can be seen as a collection of discrete scattering centers, thus the following expression:

$$\vec{E}^{8}(k,z) \approx \frac{\vec{E}_0}{|z|} e^{jkz} \sum_{m=1}^{M} \phi_{m,k} e^{-j2k\hat{z}\cdot\vec{r}_m} \tag{48.2}$$

where $k = 2\pi/\lambda$ is the wavelength and is the mth scattering center position vector. $\phi_{m,k}$ is determined by the scattering coefficient of the point movement mechanism, independent of frequency. In reality, the far-field backscatter and the scattering center point of the distance are almost constant, i.e. $\left|z - \hat{z}\cdot\vec{r_m}\right| \approx |z|$. For any given pole, the normalized field expression is as follows:

$$E(k) = \sum_{m=1}^{M} A_m \left(j\frac{k}{k_c}\right)^{\alpha_m} e^{-j2kr_m} \tag{48.3}$$

In this model, $\{A_m, r_m, \alpha_m\}_{m=1}^{M}$ represents the first M scattering point, indicating a more complete description of the characteristics of M scattering centers. A_m is the

Table 48.1 Definition of the GTD model scattering center coefficient

Coefficient	Definition
M	The number of scattering
r_m	The range of Mth scattering center relative to the zero phase reference plane
A_m	Mth scattering center of the complex scattering intensity coefficient
α_m	Scattering coefficient of the mth point of the diffraction way; dimensionless

Table 48.2 Values of the different forms of diffraction corresponding to A

Value of a	Form of diffraction
-1	Angle diffraction
$-1/2$	Edge diffraction
0	Point scattering centers; hyperboloid reflector; direct edge reflection
1/2	Single surface reflection
1	Flat reflector, dihedral angle

center of the mth scattering intensity of the complex scattering coefficient, r_m is mth scattering center relative to the zero-phase reference plane distance. The detailed definition of the coefficients are shown in Tables 48.1 and 48.2 shows that α_m is an integer multiple of 1/2, representing the geometric-type mth scattering center.

$\alpha = 1$ is the flat reflector dihedral angle; $\alpha = 1/2$ is the single surface reflection; $\alpha = 0$, as a point of the scattering centers, is the dual surface reflection and direct edge reflection; $\alpha = -1/2$ is the edge diffraction; and $\alpha = -1$ is the diffraction angle.

48.3 Music Algorithm

MUSIC algorithm is a frequency estimation method based on matrix eigenvalue decomposition; it is based on the feature decomposition of a correlation matrix. The feature decomposition of the correlation matrix is mainly used in the estimation of the frequency or power spectrum of sinusoidal signals mixed with white noise [11, 12]. The MUSIC algorithm for the estimation of the scattering center position of terahertz radar is implemented as follows:

1. *Estimation of the covariance matrix according to measurement data*

$$R_p \begin{bmatrix} r_x(0) & r_x(1) & \dots & r_x(p) \\ r_x(1) & r_x(0) & \dots & r_x(p-1) \\ . & . & . & . \\ . & . & . & . \\ r_x(p) & r_x(p-1) & \dots & r_x(0) \end{bmatrix}_{(p+1)*(p+1)} \tag{48.4}$$

where the correlation matrix is made up of $r_x(k)$, where the number is $p + 1$, and $r_x(k)$ is the autocorrelation function of the signal. If the definition of the signal vector is $e_i = [1, \exp(jw_i), \ldots, \exp(jw_i p)]^T, i = 1, 2, \ldots, M$, then

$$R_p = \sum_{i=1}^{M} A_i e_i {e_i}^H + r_w I \tag{48.5}$$

2. *Decomposition of the eigenvalue of the covariance matrix and determination of the the number of scattering centers*
If the signal matrix is defined as

$$S_p = \sum_{i=1}^{M} A_i e_i {e_i}^H \tag{48.6}$$

then the eigen decomposition can be expressed as follows:

$$R_p = \sum_{i=1}^{M} \lambda_i V_i {V_i}^H + \rho_w \sum_{i=1}^{p+1} V_i {V_i}^H = \sum_{i=1}^{M} (\lambda_i + \rho_w) V_i {V_i}^H + \sum_{i=M+1}^{p+1} \rho_M V_i {V_i}^H \tag{48.7}$$

3. *Using the MUSIC algorithm to establish the center of scattering spectrum*
As signal vector e_i and each vector($V_{M+1,\ldots,}V_{P+1}$)of the noise space are orthogonal, they are orthogonal to their linear combination as follows:

$${e_i}^H \left(\sum_{k=m+1}^{p+1} \alpha_k V_k \right) = 0, i = 1, 2, \ldots, M \tag{48.8}$$

Let $e(w) = [1, e^{jw}, \ldots, e^{jwM}]^T$. Then, $e(w_i) = e_i$. From the previous equation, inference can be made that

$$e^H(w) \left[\sum_{k=M+1}^{p+1} \alpha_k V_k {V_k}^H \right] e(w) = \sum_{k=M+1}^{p+1} \alpha_k \left| e^H(w) V_k \right|^2 \tag{48.9}$$

Equation (48.9) is equal to zero when $w = w_i$, thus

$$\hat{p}_x(w) = \frac{1}{\sum_{k=M+1}^{p+1} \alpha_k \left| e^H(w) V_k \right|^2} \tag{48.10}$$

which is infinite when $w = w_i$. However, as V_k is obtained by the decomposition of the correlation matrix and the correlation matrix is obtained by estimation, an error could possibly exist; thus, its value is limited. However, the peak is sharp,

and the frequency corresponding to the peak is equal to the frequency of the sinusoidal signal. The power spectrum estimation of the signal can also be obtained by this method.

By letting $\alpha_k = 1$ in (48.10), where $k = M + 1 \ldots P + 1$, then the MUSIC estimation is obtained as follows:

$$\hat{P}_{MUSIC}(w) = \frac{1}{e^H(w)\left(\sum_{k=M+1}^{p+1} V_k V_k{}^H\right)e(w)} \tag{48.11}$$

48.4 Simulation Results and Analysis of the MUSIC Parameter Estimation Algorithm

First, nine scattering points in outer space are estimated, as shown in Fig. 48.1. Their coordinates are respectively (0,−0.1,0), (0,0.1,0), (0.1,0,0), (−0.1,0,0), (0.2,0, −0.8), (−0.2,0, −0.8), (0,0.2, −0.8), (0, −0.2, −0.8), and (0,0,0.8). The scattering factor is equal to one. The algorithm uses step frequency signal, and the measurement band is 270–280 GHz. The SNRs are 0, 5, 10, and 15 dB. The search range of the projection distance field is from −1 m to –1 m, assuming that the sight pitch angle of the radar is 45° and the azimuth is 10°

When the SNRs are 0, 5, 10, and 15 dB, the results are as shown in Fig. 48.2 when the MUSIC algorithm is used to estimate the five scattering centers. Table 48.3 shows the comparison between the projection distance of the scattering center obtained by the estimation under different SNRs and the true value. From the table, we can infer that the estimated accuracy of the MUSIC algorithm is higher, and it has a better noise immunity.

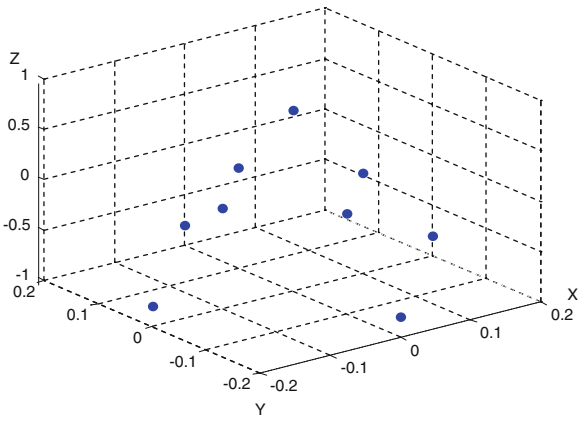

Fig. 48.1 Three-dimensional map of the scattering center

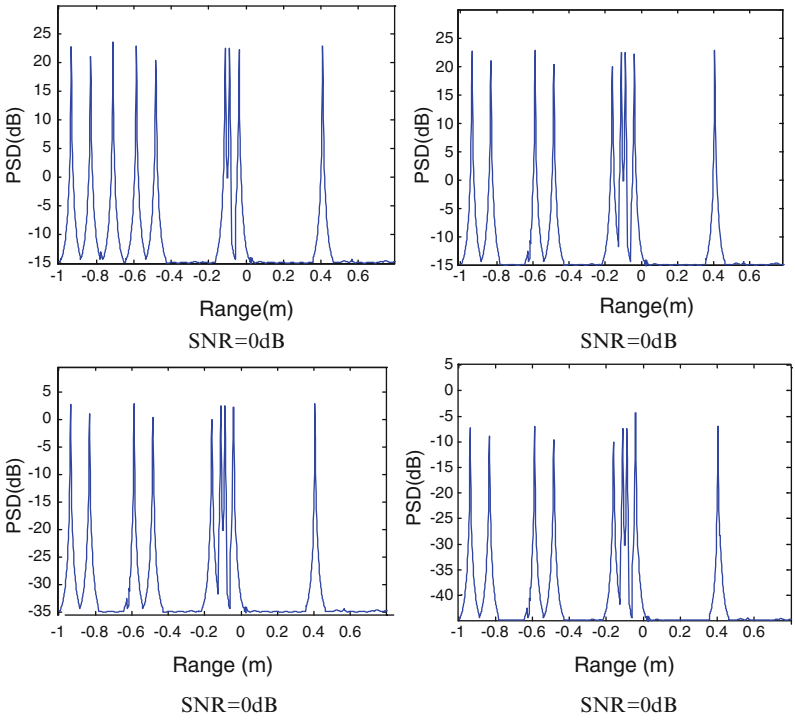

Fig. 48.2 MUSIC spectrogram under different SNRs

Table 48.3 The projection distance between the scattering center obtained by estimation under different SNRs and the real distance

	Real distance(m)	Estimated distance (m)			
SNR(dB)		0	5	10	15
(0,−0.1,0)	−0.0122	−0.0127	−0.0127	−0.0127	−0.0127
(0,0.1,0)	0.0122	0.0127	0.0127	0.0127	0.0127
(0.1,0,0)	0.0696	0.0694	0.0674	0.0654	0.0634
(−0.1,0,0)	−0.0696	−0.0694	−0.0674	−0.0654	−0.0634
(0.2,0,−0.8)	−0.426	−0.4252	−0.4272	−0.4292	−0.4312
(−0.2,0,−0.8)	−0.7048	−0.7048	−0.7028	−0.7028	−0.7008
(0,0.2,−0.8)	−0.541	−0.5406	−0.5425	−0.5425	−0.5445
(0,−0.2,−0.8)	−0.7048	−0.7048	−0.7028	−0.7028	−0.7028
(0,0,0.8)	0.5660	0.5660	0.5660	0.5640	0.5640

48.5 Conclusion

This chapter has described a method using GTD spectrum estimation algorithm to estimate the projection distance of one-dimensional terahertz radar. First, we discussed the GTD model details. Second, the estimation steps of the scattering

center position of the terahertz radar based on the MUSIC algorithm was provided. Finally the MUSIC spectrum estimation algorithm was used in the estimation of the scattering center projection distance, yielding a comparison between the projection distance of the scattering center obtained by estimation under different SNRs and the true value. The simulation results were then analyzed. The proposed algorithm in this study presents an effective new method of improving the resolution of wideband terahertz radar.

Acknowledgments This work is supported by the Fundamental Research Funds for Central Universities under Project ZYGX2009J095.

References

1. Shinnan YD, Leshchenko SP, Oflenko VM (2004) Wideband radar (advantages and problems). Ultrawideband and ultrashort impulse signals. In: 2004 second international workshop, Sevastopol, Ukraine, pp 71–76
2. Wehner DR (1987) High resolution radar. Artech House, Norwood, MA
3. Siegel PH (2002) Terahertz technology. IEEE Trans Microw Theory and Tech 50(3):910–928
4. Chen han (2007) Terahertz technology and its applications. China Sci Technol Inf 20:274–275
5. Wehner DR (1995) High resolution radar, 2nd edn. Artech House, Boston/London
6. Ausherman DA (1984) Development in radar imaging. IEEE Trans AES 20(4):363–397
7. Potter LC (1995) A GTD-based parametric model for radar scattering. IEEE Trans Antennas Propag 43(10):234–245
8. Davies AG, Linfield EH, Pepper M (2004) The terahertz gap: the generation of far-infrared radiation and its applications. Phil. Trans. R. Soc. Lond. A 362, 195–414
9. Cooper KB, Dengler RJ, Llombart N (2009) An approach for sub-second imaging of concealed objects using terahertz (THz) radar. J Infrared Millim Terahertz Waves 30(12):1297–1307
10. Cooper KB, Dengler RJ, Llombart N et al (2010) Fast, high-resolution terahertz radar imaging at 25 meters, terahertz physics, devices, and systems IV: advanced applications in industry and defense. In: Proceedings of SPIE, vol 7671. Orlando
11. Kim K, Seo D, Kim H (2002) Efficient radar target recognition using the MUSIC algorithm and invariant features. IEEE Trans Antennas Propag 50(3):325–337
12. Yoon Y, Amin MG (2008) High-resolution through-the-wall radar imaging using beamspace MUSIC. IEEE Trans Antennas Propag 56(6):1763–1774

Chapter 49
An Kalman Filter-Based Method for BeiDou/GPS Integrated Navigation System

Xu Yang, Qing Xu, and Haijiang Wang

Abstract To improve precision of double-star positioning system (DSPS) in China and overcome the defects due to the shadiness of DSPS in the war, an indirect Kalman filter-based loosely coupled method for tri-star passive BeiDou/Global Positioning System (BeiDou/GPS) integrated navigation system is presented. This chapter uses tri-star passive positioning technique to solve the shadiness of DSPS in the war. An indirect Kalman filter-based method is proposed to combine BeiDou with GPS to fuse into an integrated navigation system to enhance precision of BeiDou when GPS is available. Experimental results demonstrate that the proposed Kalman filter-Based method can effectively reduce the positioning error, and precision of the BeiDou/GPS integrated navigation is better than GPS-only navigation.

Keywords BeiDou • GPS • Kalman filter • Tri-star passive positioning • Integrated navigation

49.1 Introduction

Currently, a sole satellite positioning system cannot meet the increasing demand for high-precision positioning. DSPS using two geostationary satellites providing radio determination satellite service (RDSS) has been established in China since 2000. The third navigation and positioning geostationary satellite was launched in May 2003 which is a backup satellite for DSPS. That is milestone that China owns a regional RDSS system which combines rapid positioning with short message communication. But, unlike GPS and GLONASS, DSPS works in an active mode

X. Yang (✉) • Q. Xu • H. Wang
College of Electronic Engineering, Chengdu University of Information Technology, Chengdu 610225, China
e-mail: joyodsp@163.com; whj@cuit.edu.cn

Q. Liang et al. (eds.), *Communications, Signal Processing, and Systems*, Lecture Notes in Electrical Engineering 202, DOI 10.1007/978-1-4614-5803-6_49,

[1], which means the positioning function is provided by the center station and transferred to users by satellite. The fatal defect of this mode is that the users are easily exposed in the war. Another defect is that the capacity of user is subject to the control center's ability of calculation and communication.

GPS is a satellite-based high-precision positioning system which provides positioning and time information in all weather, anywhere on or near the earth, where there is an unobstructed line of sight to four or more GPS satellites. It is widely applied to a variety of areas such as aerospace, aeronautics, missile guidance etc. However GPS is maintained by the United States government and it is not available for our troops in the war. BeiDou/GPS integration can combine reliability with high-precision.

There have been many literatures over last decades on the improvement of the DSPS performance. Xiaofeng He et al. [2] employ fuzzy inference-based Kalman filtering SINS/RDSS integrated algorithm to improve DSPS performance. Benlei Su et al. [3] use BeiDou/INS integration navigation system to avoid the limitation of the DSPS. Erhu Wei et al. [4] propose the protective system with the integration of GPS and BeiDou navigation system to overcome the security of using GPS-only positioning. Little attention is paid to BeiDou with GPS integration navigation system.

Herein, a new technique for BeiDou/GPS integration based on an indirect Kalman filter is proposed to overcome defects of the easily exposed in the war and the limited capacity of users of the DSPS. Above all, this method can improve precision of navigation system. The experiential results demonstrate that precision of this integrated navigation system is better than GPS-only navigation or BeiDou-only navigation.

49.2 Principle of Tri-Star Passive Positioning

In July 2007, the first receiver of BeiDou positioning system has been made successfully [5] which overcome the limited capacity of users, the easily exposed, and the low precision of positioning etc.

As the principle of positioning of GPS, the technique of BeiDou positioning system is based on measurement of pseudo-range [6]. Together with the backup satellite of DSPS, there are three satellites to form tri-star positioning system. When all of the three satellites are available, a receiver of BeiDou positioning system can reckon the location (x_i, y_i, z_i) in the Earth Centered Earth Fixed (ECEF) frame of satellite i in terms of ephemeris data received from signals of BeiDou positioning system transmitted. By means of measuring time difference between instant of time arrived at receiver and instant of time transmitted from satellites, it can calculate the range $\rho_i$from the receiver to satellite i, the formula of range is given by

$$\rho_i = \sqrt{(x - x_i)^2 + (y - y_i)^2 + (z - z_i)^2} + c\Delta t, i = 1, 2, 3 \tag{49.1}$$

where (x, y, z) is the location of receiver of BeiDou positioning system in the ECEF frame, $c = 3 \times 10^8 m/s$ and Δt is time difference. Because the time of users is asynchronous with the time of BeiDou, it needs the fourth equation to solve more accurate time difference. By using an elevation device, it can obtain the height h of the receiver of BeiDou. At the same time, the earth is ellipsis on the xoz plane. The firth equation is given by

$$\frac{x^2}{(a+h)^2} + \frac{z^2}{(b+h)^2} = 1, \tag{49.2}$$

where a and $b$is the long and short axle of earth respectively. Therefore we obtain the location (x, y, z) of receiver of BeiDou and the time difference by combining (49.1) with (49.2).

49.3 System Design

Kalman filter has been widely used for optimal estimation. The block diagram of the integrated BeiDou/GPS navigation system is illustrated in Fig. 49.1. Figuer 49.1 shows that the integrated navigation system consists of a BeiDou receiver, an elevation device, a GPS receiver, the computer of tri-star passive BeiDou solution, and a Kalman filter. The scheme of the integrated BeiDou/GPS navigation system uses an indirect Kalman filter-based loosely coupled technique to improve the precision of BeiDou-only navigation. Where (x_b, y_b, z_b) is position error of a BeiDou receiver, h is an elevation error, and $\left(x_g, y_g, z_g\right)$ is position error of a GPS receiver. In this system, (x_b, y_b, z_b) and h are inputs to the computer of tri-star passive algorithm, the output of computer of tri-star passive algorithm and $\left(x_g, y_g, z_g\right)$ are inputs to Kalman filter. Then, the output of Kalman filter input to BeiDou to correct position error.

49.3.1 Error Model of BeiDou and GPS

According to practical experience, the model of tracking filter of BeiDou with GPS is based on the Langevin equation [7]

$$\frac{d}{dt}v(t) = \underbrace{-\frac{1}{\tau_{vel}}}_{F(t)} v(t) + \omega(t), \tag{49.3}$$

where $v(t)$ is a velocity component, τ_{vel} is a correlate time constant, and $\omega(t)$ is a zero-mean white-noise process in continuous time. A position error model of BeiDou or GPS in terms of (49.3) is given by

$$\frac{d}{dt}\begin{bmatrix}\delta_{pGNSSN}\\ \delta_{pGNSSE}\\ \delta_{pGNSSD}\end{bmatrix} = \underbrace{\begin{bmatrix}\frac{-1}{\tau_{hor}} & 0 & 0\\ 0 & \frac{-1}{\tau_{hor}} & 0\\ 0 & 0 & \frac{-1}{\tau_{vert}}\end{bmatrix}}_{F(t)}\begin{bmatrix}\delta_{pGNSSN}\\ \delta_{pGNSSE}\\ \delta_{pGNSSD}\end{bmatrix} + \begin{bmatrix}\omega_{hor}(t)\\ \omega_{hor}(t)\\ \omega_{vert}(t)\end{bmatrix}, \tag{49.4}$$

where τ_{hor} and τ_{vert} is a horizontal correlate time constant and a vertical correlate time constant of BeiDou or GPS respectively, δ_{pGNSSN}, δ_{pGNSSE}, δ_{pGNSSD} is a north position error component, a east position error component, and a down position error component of BeiDou or GPS respectively, $\omega_{hor}(t)$, $\omega_{vert}(t)$ is a horizontal, a vertical zero-mean white-noise process in continuous time of BeiDou or GPS respectively.

Let $\left(\delta_{pGNSSN}, \delta_{pGNSSE}, \delta_{pGNSSD}\right)^T$ and $\left(\omega_{hor}(t), \omega_{hor}(t), \omega_{vert}(t)\right)^T$ be δ and ω respectively. $\delta_0(t)$ is assumed to be δ_0 and the solution to (49.4) is given by

$$\delta(t) = \Phi(t, t_0)\delta(t_0) + \int_{t_0}^{t} \Phi(t, \tau)\omega(\tau)d\tau, \tag{49.5}$$

where $\Phi(t, t_0)$ is a 3-order matrix of state transition and the solution of equation given by

$$\left\{\dot{\Phi}(t, t_0) = F(t)\Phi(t, t_0)\Phi(t_0, t_0) = I_n, \right. \tag{49.6}$$

where the solution of (49.6) is given by

$$\Phi(t, t_0) = e^{\int_{t_0}^{t} F(t)dt}. \tag{49.7}$$

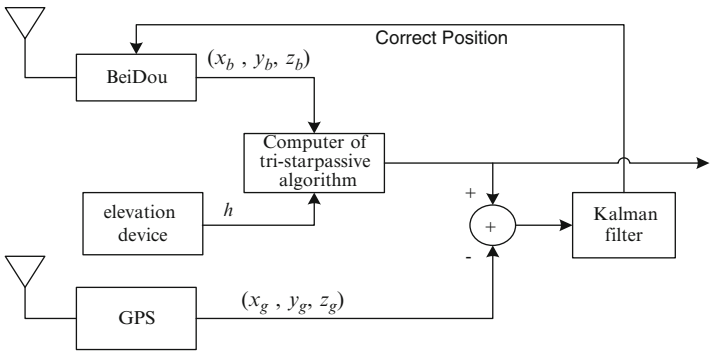

Fig. 49.1 Block diagram of an indirect Kalman filtering-based loosely-coupled BeiDou/GPS integrated navigation system

49.3.2 Vehicle Dynamic Model for GNSS Receiver

In Kalman filter, dynamic models are completely specified by two matrix parameters:

1. The dynamic coefficient matrix F(or equivalent state transition matrix Φ)
2. The dynamic disturbance covariance matrix$Q$

In this chapter, we use a model called DAMP3 [7].This type of filter is designed for vehicles with limited but nonzero position variation such as land vehicle. The model parameters are given by

$$\underbrace{\begin{bmatrix} -1/\tau_{pos} & 1 & 0 \\ 0 & -1/\tau_{vel} & 1 \\ 0 & 0 & -1/\tau_{acc} \end{bmatrix}}_{F} \text{ and } \underbrace{\begin{bmatrix} 0 & 0 & 0 \\ 0 & 0 & 0 \\ 0 & 0 & \sigma_{jerk}^2 \Delta t^2 \end{bmatrix}}_{Q}$$

Because Kalman filter is based on discrete state, so we need to discretize continuous state. When do equally spaced sampling on continuous state and the sampling interval $\Delta t = t_{k+1} - t_k (k = 0, 1, 2, \cdots)$ is very small, $F(t)$ is seen as a constant, i.e.,

$$F(t) \approx F(t_k)\, t_k \leq t \leq t_{k+1}. \tag{49.8}$$

therefore $\Phi(t_{k+1}, t_k) = e^{\Delta t F(t_k)}$. The discrete state equation is given by

$$\delta(k) = \Phi(k, k-1)\delta(k-1) + w(k-1), \tag{49.9}$$

where $w(k-1)$ is a zero-mean white-noise process in discrete time. The discrete observation equation is given by

$$Y(k) = C_k \delta(k) + v(k), \tag{49.10}$$

where $v(k)$ and C_k is a zero-mean white-noise process in discrete time and a coefficient matrix of the observation equation.

49.3.3 Kalman Fiter

In this chapter, the six measurements include three position outputs from the GPS receiver and three position outputs from the BeiDou receiver. By combining (49.9) with (49.10), we can obtain a set of equations [8] given by

$$\begin{cases} \hat{\delta}(k) = \Phi(k,k-1)\hat{\delta}_{k-1} + H_k(Y_k - C_k\Phi(k,k-1)\hat{\delta}_{k-1}) \\ H_k = P'_k C_k{}^T (C_k P'_k C_k{}^T + R_k)^{-1} \\ P'_k = \Phi(k,k-1)P_{k-1}(\Phi(k,k-1))^T + Q_{k-1} \\ P_k = (I - H_k C_k)P'_k, \end{cases} \tag{49.11}$$

where the coefficient matrix C_k of observation equation is given by

$$C_k = \begin{bmatrix} 1 & 0 & 0 & 0 & 0 & 0 & 0 & 0 & 0 & 1 & 0 & 0 & 0 & 0 & 0 \\ 0 & 0 & 0 & 1 & 0 & 0 & 0 & 0 & 0 & 0 & 1 & 0 & 0 & 0 & 0 \\ 0 & 0 & 0 & 0 & 0 & 0 & 1 & 0 & 0 & 0 & 0 & 1 & 0 & 0 & 0 \\ 1 & 0 & 0 & 0 & 0 & 0 & 0 & 0 & 0 & 0 & 0 & 0 & 1 & 0 & 0 \\ 0 & 0 & 0 & 1 & 0 & 0 & 0 & 0 & 0 & 0 & 0 & 0 & 0 & 1 & 0 \\ 0 & 0 & 0 & 0 & 0 & 0 & 1 & 0 & 0 & 0 & 0 & 0 & 0 & 0 & 1 \end{bmatrix}. \tag{49.12}$$

49.4 Experimental Results

When BeiDou receiver and GPS receiver work normally, the state space of Kalman filter consists of 3 position components from tri-star passive BeiDou receiver, 3 position components from GPS receiver, and 9 state variables of dynamic vehicle i.e., position, velocity, and accelerate component in the horizontal level, the vertical level and the down direction. The simulation parameters of integrated navigation system are given by Tables 49.1 and 49.2. The interval of Kalman filter is 1 s, the length of simulation time is 2 h, and R is 0.1 m.

As shown in Figs. 49.2 and 49.3, the results of simulation demonstrate that an indirect Kalman filter-based loosely coupled BeiDou/GPS integration navigation system can improve the positioning accuracy greatly in contrast to GPS-only or BeiDou-only in the horizontal level and the vertical level.

Table 49.1 Parameters for simulation of GPS and BeiDou

Navigation system	Correlate time/s		Position errors/m	
—	—	North	East	Down
BeiDou	39	20.1024	15.1103	2.2930
GPS	39	10.0715	9.1029	1.5347

Table 49.2 Parameters for simulation of DAMP3

Components	North	East	Down
Position(m)	212.934	70.9768	3.5361
Velocity(m/s)	22.3017	14.8678	0.3724
Accelerate(m/s/s)	2.335	3.1134	0.0377
Accelerate correlate time(s)	13.4097	7.6696	9.6786

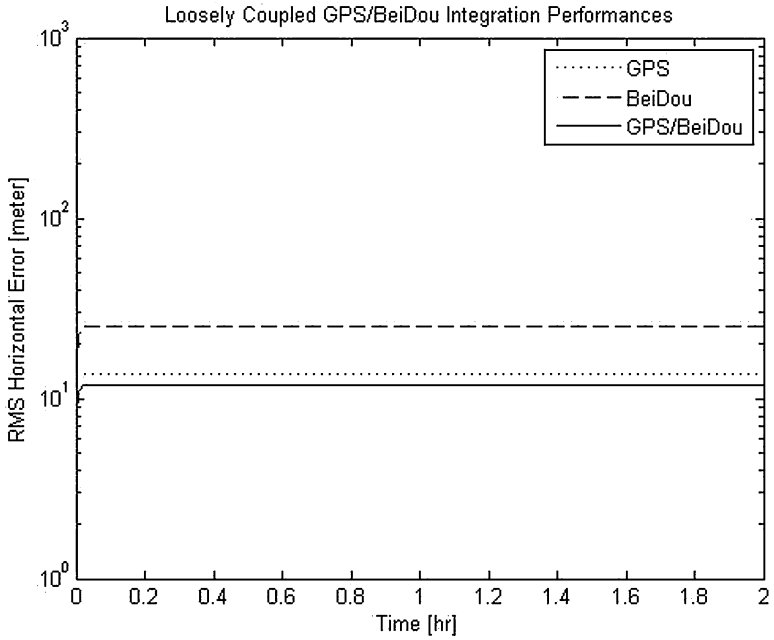

Fig. 49.2 Curve: performance of indirect Kalman filtering-based loosely coupled BeiDou/GPS integrated navigation system on horizontal level

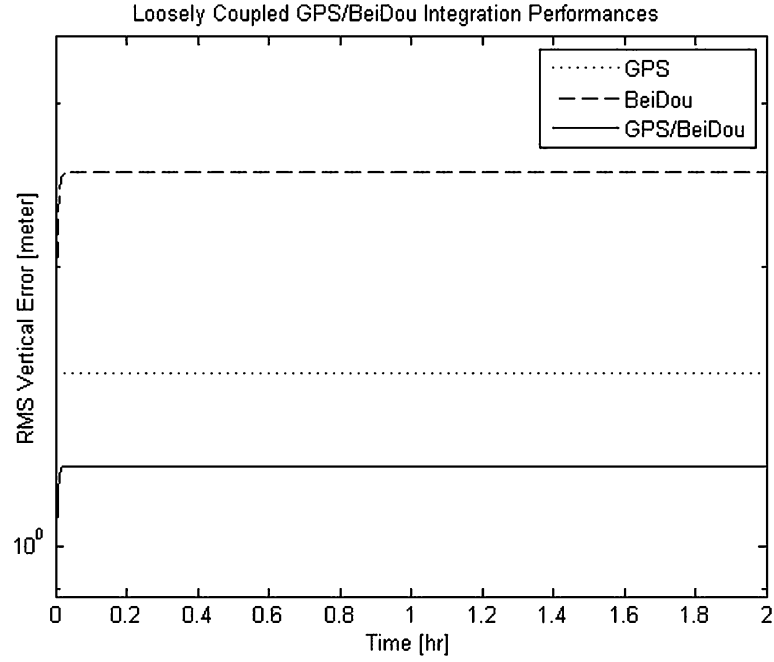

Fig. 49.3 Curve: performance of indirect Kalman filtering-based loosely coupled BeiDou/GPS integrated navigation system on vertical level

49.5 Discussions and Conclusions

An indirect Kalman filter-based loosely coupled BeiDou/GPS integrated navigation system is presented here not only to improve accuracy of positioning of DSPS but also to overcome the fatal defects of shadiness of DSPS in the war. The experimental results verify that the proposed algorithm is effective and feasible. Although the precision of DSPS is less than GPS, it provides our country with a way to explore BeiDou-II in future. In addition, these contributions can be applied not only to land vehicles, but also to the fields of ships and airplanes by necessary modifications.

References

1. Kimura K, Morikawa E, Kozono S, Obara N, Wakana H (1996) Communication and radio determination system using two geostationary satellites. II. Analysis of positioning accuracy. Aerospace Electron Syst IEEE Trans 32:314–325. doi:10.1109/7.481271
2. He X, Xiaoping H, Wenqi W et al (2009) Intelligent SINS/RDSS integrated algorithms for land vehicle navigation. Aerospace Electron Syst Mag IEEE 24:4–11. doi:10.1109/MAES.2009.4811083
3. Benlei S, Qing X, Yao Z (2008) The study on low cost passive-BD/INS integration navigation system. Microelectron Comput 25:169–171
4. Wei E, Zhang X, An Z, Feng X (2008) On the design of the protective system with the integration of GPS and Beidou navigation systems. Bull Surv Mapp 7:4–6
5. Xiaodong W, Siliang W, Li J (2009) Application of Kalman filter in BeiDou passive position. Microcomput Inf 25:247–249
6. Liu Y (2006) Passive location technique with three BeiDou geostationary satellites. Radio Eng China 36:36–39
7. Grewal MS, Weill LR, Andrews AP (2007) Global positioning systems, inertial navigation, and integration. Wiley-Interscience, Hoboken
8. Grewal MS, Andrews AP (2008) Kalman filtering: theory and practice using MATLAB. Wiley-IEEE Press, Hoboken

Chapter 50
A 2-Dimensional Correlation Interferometer Algorithm Based on Dimension Separation

Xin Zhang, Ting Cheng, and Zishu He

Abstract A 2-dimensional correlation interferometer algorithm based on dimension separation is proposed and can be widely applicable to arbitrary geometry arrays. The approach simplifies the original 2-dimensional angle searching by dividing it into two 1-dimensional searching corresponding to azimuth angle and elevation angle, thus reduces the computational complexity. Meanwhile it ensures the direction finding precision of correlation interferometer. Simulation results indicate the effectiveness of the method, which highly improves the speed of the broadband direction finding system.

Keywords Dimension separation • Correlation interferometer • 2-dimensional direction finding

50.1 Introduction

The information contained in the phase of the signal received by the elements of an array is commonly used to determine the incoming angles of an incident wave [1]. Such a configuration is usually called direction finding system known as the interferometer. In the existing direction finding systems, interferometer has the advantages of high direction finding precision, simple algorithm and high speed, and is widely applied in military and civil fields. In military field, it not only can be applied to tracking and locating targets [2] for radar signal processing [3], but also plays an important role in carrying out pertinent electronic jamming and military

Project supported by the National Natural Science Foundation of China (Grant No.61101171)

X. Zhang (✉)
School of Electronic Engineering, University of Electronic Science and Technology of China, Chengdu, Sichuan 611731, People's Republic of China
e-mail: christiana61@126.com

Q. Liang et al. (eds.), *Communications, Signal Processing, and Systems*, Lecture Notes in Electrical Engineering 202, DOI 10.1007/978-1-4614-5803-6_50,

attack. And in civil field, it can be applied in traffic control, life rescue, management of radio spectrum etc.

Phase interferometer calculates the direction-of-arrival signal with measured space phase differences between receiving elements [4]. Correlation interferometer is a direction finding system that utilizes the information residing in the measured phase vector consisting of phase differences between various elements of array and then compare it with the assumed phase vectors in sample database [5]. The issues such as ambiguities and the mutual coupling [6] between antennas are reduced to a lower level by virtue of the correlation computation process. However, phase difference vectors in sample database are different according to variable signal frequency, azimuth angle and elevation angle [7], which lead to large computational complexity of correlation calculation that may not satisfy the requirement of real-time broadband direction finding system [8]. To solve the problem mentioned above, this chapter proposes a 2-dimensional correlation interferometer algorithm based on dimension separation. In the proposed algorithm, two different similarity functions are respectively chosen to searching for azimuth angle and elevation angle. Experimental results are shown to certify the effectiveness of the algorithm.

50.2 Phase Difference Model

Consider an M-element uniformly spaced circular array with radius R, as depicted in Fig. 50.1.

Assume the signal discussed here as a far-field narrowband model. The incident plane wave arrives at the array with directions (φ,θ), where φ is the azimuth angle and θ is the elevation angle [9]. Let the reference point be the origin of the array. In the case of circular array, the phase difference between element m and the reference point is

$$\phi_m = \frac{2\pi R}{\lambda} \sin\theta \cos\left(\varphi - \frac{2\pi}{M} m\right) \tag{50.1}$$

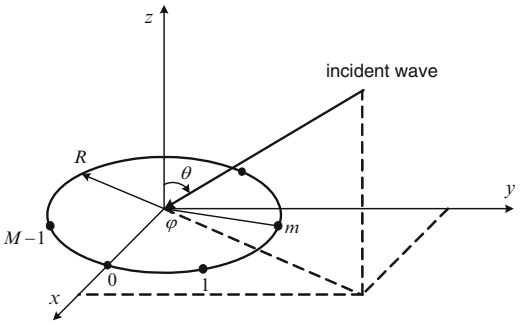

Fig. 50.1 Signal model

where λ is the wavelength of the carrier wave. Therefore we can obtain the phase difference between arbitrary element m and element n ($\neq m$) of the array

$$\phi_{m,\mathrm{n}} = \phi_n - \phi_m = \frac{4\pi R}{\lambda} \sin\left(\frac{\pi(n-m)}{M}\right) \sin\theta \sin\left(\varphi - \frac{\pi(n+m)}{M}\right)$$

The angles of incident signal contained in the expression above can be determined by finding the solution to more than one equation similar to (50.3) when several phase differences are available.

50.3 Correlation Interferometer Algorithm Based on Dimension Separation

Correlation interferometer algorithm is an algorithm based on the comparison of measured phase difference vector and phase difference vectors in sample database. Here, let $\Phi(i)$ denotes the assumed vector of phase differences, the quantity of which is calculated across the elements of a specified baseline in the antenna array. Commonly the continuous space of directions is divided into many discrete angle samples with a constant separation such as 1°. Define $\Phi^{'}$ as the measured phase difference vector of an incident signal arriving. Therefore, the process of direction finding can be written as:

$$\arg\max_{(\varphi,\theta)} \left\{ f\left[\Phi^{'} - \Phi(i)\right], i = 1,2,\cdots,P \times Q \right\} \tag{50.3}$$

Here, P and Q is respectively the number of sample point in azimuth angles and elevation angles, and $f(\cdot)$ is a similarity function used for comparison.

Considering two incident signals with incident angles (φ,θ_1) and (φ,θ_2), which means the two incident signals share the same azimuth angle but different elevation angles. Then we determine the direction estimate by means of finding the value of incident angle that maximize the similarity between the assumed and measured phase difference vectors. If correlation coefficient $f_1(\cdot)$ is adopted as the similarity function between measured phase difference vector $\Phi^{'}$ and sample vector $\Phi(i)$, we can obtain:

$$f_1^{(\varphi,\theta_1)}(i) = \frac{\Phi(i)\Phi_{(\varphi,\theta_1)}^{'\mathrm{T}}}{\sqrt{\Phi_{(\varphi,\theta_1)}^{'}\Phi_{(\varphi,\theta_1)}^{'\mathrm{T}}}\sqrt{\Phi(i)\Phi^{\mathrm{T}}(i)}} \tag{50.4}$$

$$f_1^{(\varphi,\theta_2)}(i) = \frac{\Phi(i)\Phi'^{\mathrm{T}}_{(\varphi,\theta_2)}}{\sqrt{\Phi'_{(\varphi,\theta_2)}\Phi'^{\mathrm{T}}_{(\varphi,\theta_2)}}\sqrt{\Phi(i)\Phi^{\mathrm{T}}(i)}} \tag{50.5}$$

Here, $\Phi'_{(\varphi,\theta_l)}$ is the phase difference vector of incident angle (φ,θ_l) (θ_l is an arbitrary elevation angle), and $\Phi'^{\mathrm{T}}_{(\varphi,\theta_l)}$ is the transposed matrix of $\Phi'_{(\varphi,\theta_l)}$. The following equation can be derived from (50.2):

$$\Phi'_{(\varphi,\theta_2)} = \frac{\sin\theta_2}{\sin\theta_1}\Phi'_{(\varphi,\theta_1)} \tag{50.6}$$

By substitution of (50.6) into (50.5), then we get

$$f_1^{(\varphi,\theta_2)}(i) = \frac{\frac{\sin\theta_2}{\sin\theta_1}\Phi(i)\Phi'^{\mathrm{T}}_{(\varphi,\theta_1)}}{\sqrt{\left[\frac{\sin\theta_2}{\sin\theta_1}\right]^2\Phi'_{(\varphi,\theta_1)}\Phi'^{\mathrm{T}}_{(\varphi,\theta_1)}}\sqrt{\Phi(i)\Phi^{\mathrm{T}}(i)}} \tag{50.7}$$

Since the range of elevation angle is $(0°,90°]$, $\frac{\sin\theta_2}{\sin\theta_1}>0$. Therefore

$$f_1^{(\varphi,\theta_1)}(i) = f_1^{(\varphi,\theta_2)}(i) \tag{50.8}$$

which means the correlation coefficients of two incident directions (φ,θ_1) and (φ,θ_2) between measured phase difference vector and sample vector are the same, and it only depends on azimuth angle. The relationship also indicates that the correlation coefficients between the measured phase difference vector and the samples corresponding to the same azimuth angle are the same. Since correlation coefficient is only relevant to azimuth angle but irrelevant to elevation angle, in 2-dimensional direction finding system, we can fix the elevation angle and search for the azimuth angle which corresponds to the sample that maximizes the correlation coefficient as the estimated azimuth angle. Once we get the estimated azimuth angle, we can calculate the similarity between measured phase difference vector and samples which share the same azimuth angle with estimated value. And this time, the similarity function $f_2(\cdot)$ must be sensitive to elevation angle. Therefore the similarity function utilized for searching for elevation angle is defined as:

$$f_2(i) = \sum_{k=1}^{K}\cos\left(\Phi'_{\mathrm{k}} - \Phi_{\mathrm{k}}(\mathrm{i})\right) \tag{50.9}$$

where, Φ'_{k} is the k th dimension value of measured phase difference vector Φ' and $\Phi_k(i)$ is the kth dimension value of a certain phase difference vector in sample database.

Based on above illustration, the 2-dimensional correlation interferometer algorithm based on dimension separation can be obtained. The steps are shown as follows:

Step1: Choose a fixed elevation angle, and choose all of the phase difference vectors corresponding to the same elevation angle but different azimuth angles in sample database;
Step2: Compute the similarity between measured phase difference vector and all of the chosen phase difference vectors in Step1 according to function $f_1(\cdot)$;
Step3: Choose the azimuth angle corresponding to the phase difference vector which has the maximum correlation value as estimated azimuth angle and denote it as φ_0;
Step4: Choose all of the phase difference vectors which share the same azimuth angle estimated in Step3 but different elevation angles;
Step5: Compute the similarity between measured phase difference vector and all of the chosen phase difference vectors in Step4 according to function $f_2(\cdot)$;
Step6: Choose the elevation angle corresponding to the phase difference vector which has the maximum correlation value as estimated elevation angle and denote it as θ_0.

Let azimuth angle in sample database be divided into P discrete angle samples with a constant separation $\Delta\varphi$, and Q discrete angle samples with a constant separation $\Delta\theta$ for elevation angle, the quantity of 2-dimensional searching in conventional correlation interferometer algorithm is $P \times Q$ times. However, in dimension split algorithm the quantity of 2-dimensional searching is reduced to $P + Q$ times, which accelerates the algorithm greatly.

50.4 Conditions for Correlation Interferometer Algorithm Based on Dimension Separation

The following part is to discuss the conditions for dimension separation, which is the conditions for unambiguous situation in essence. According to (50.2), ambiguity occurs when the absolute value of phase difference $\phi_{m,\mathrm{n}}$ exceeds π since the phase detector can only output a value that varies from $-\pi$ to π. Meanwhile, because of the effects that the noise brings, the range of the radius-to-wavelength ratio which is available in dimension separation is limited.

In a practical situation with additive noise, it will be much more complicated to analyze the conditions of ambiguous. In this environment, (50.2) can be written as follows:

$$\phi_{m,\mathrm{n}}(i) = \phi_{m,\mathrm{n}} + \delta_{m,\mathrm{n}}(i) = \frac{4\pi R}{\lambda} \sin\left(\frac{\pi(n-m)}{M}\right) \sin\theta \sin\left(\varphi - \frac{\pi(n+m)}{M}\right) + \delta_{m,\mathrm{n}}(i) \tag{50.10}$$

Here, $\delta_{m,\mathrm{n}}(i) = \delta_m(i) - \delta_n(i)$ is the real Gaussian stationary random process with zero mean and variance of $2\sigma_\delta^2$. For incident angles $\varphi \in [0°,360°)$,$\theta \in [\theta_\mathrm{L},\theta_\mathrm{H}]$, we can define

$$u_{m,\mathrm{n}} = \frac{4\pi R}{\lambda} \sin\left(\frac{\pi(n-m)}{M}\right) \sin\theta_\mathrm{H} \tag{50.11}$$

When ambiguous probability is $1-\alpha$ at least, the condition can be given as

$$1 - \alpha \leqslant \int_{-\pi}^{\pi} p_{\phi_{m,\mathrm{n}}}(z)dz \tag{50.12}$$

Here, $p_{\phi_{m,\mathrm{n}}}(z)$ is the probability density function of $\phi_{m,\mathrm{n}}(i) = u_{mn} + \delta_{mn}(i)$, which is

$$p_{\phi_{m,\mathrm{n}}}(z) = \frac{1}{\sqrt{2\pi\sigma_{mn}^2}} \exp\left(-\frac{(2-u_{mn})^2}{2\sigma_{mn}^2}\right) \tag{50.13}$$

By substitution of (50.13) into (50.12), we can get

$$\begin{aligned} 1 - \alpha \leqslant \frac{1}{\sqrt{2\pi\sigma_{mn}^2}} \exp\left(-\frac{(2-u_{mn})^2}{2\sigma_{mn}^2}\right) &= \int_{-(\pi+u_{mn})}^{(\pi-u_{mn})} \frac{1}{\sqrt{2\pi}} \exp\left(-\frac{z^2}{2}\right)dz \\ &= \Phi((\pi-u_{mn})/\sigma_{mn}) - \Phi(-(\pi+u_{mn})/\sigma_{mn}) \end{aligned}$$

Here, $\Phi(x)$ is defined as

$$\Phi(x) = \int_{-\infty}^{x} \frac{1}{\sqrt{2\pi}} \exp\left(-\frac{z^2}{2}\right)dz \tag{50.15}$$

In high signal-to-noise ratio situation, we have $\sigma_{mn}^2 \ll \pi^2$. Thus

$$\Phi(-(\pi+u_{mn})/\sigma_{mn}) \approx 0 \tag{50.16}$$

And (50.14) can be approximately equivalent to

$$1 - \alpha \leqslant \Phi((\pi-u_{mn})/\sigma_{mn}) \tag{50.17}$$

which is

$$\Phi^{-1}(1-\alpha) \leqslant (\pi-u_{mn})/\sigma_{mn} \tag{50.18}$$

Thus (50.17) can be rewritten as

$$\pi - \sigma_{mn} \cdot \Phi^{-1}(1-\alpha) \geqslant u_{mn} \tag{50.19}$$

namely

$$\frac{4\pi R}{\lambda}\sin\left(\frac{\pi(m-n)}{M}\right)\sin\theta_{\mathrm{H}} \leqslant \pi - \sigma_{mn}\cdot\Phi^{-1}(1-\alpha) \tag{50.20}$$

Simplify the function formula above and we can obtain

$$\frac{R}{\lambda} \leqslant \frac{\pi - \sigma_{mn}\cdot\Phi^{-1}(1-\alpha)}{4\pi\sin\left(\frac{\pi(m-n)}{M}\right)\sin\theta_{\mathrm{H}}} \tag{50.21}$$

50.5 Experimental Results

Consider a 7-elements UCA with a radius $R = 1\mathrm{m}$. Incidental wave arrived at the array with azimuth angle of 103° and elevation angle of 5°, and the central frequency is 120MHz. Seven short baselines are chosen and correlation coefficient is chosen as similarity function. Figure 50.2 shows the similarity surface results from similarity function of correlation coefficient. It can be seen from the figure that the correlation coefficient values of angles which share the same azimuth angle but different elevation angles are the same.

The simulation below is carried out to compare the precision of direction finding of 2-dimensional correlation interferometer algorithm and 2-dimensional correlation interferometer algorithm based on dimension separation. Direction finding range of azimuth angle is [0°,359°] with dispersion 1°, while direction finding range of elevation angle is [0°,90°] with dispersion 1°. The similarity function for correlation interferometer is chosen as (50.9). The simulation result of correlation interferometer algorithm is obtained after 1,000 Monte Carlo experiments by giving the RMSE of direction estimate as a function of signal-to-noise ratio. Figures 50.3 and 50.4 is respectively shows the RMSE of azimuth angle and elevation angle.

From the two figures shown above, we can see that 2-dimensional correlation interferometer algorithm based on dimension separation maintains azimuth angle precision and elevation angle precision.

In the CPU platform of Pentium E5700 with main frequency 3.00 GHz, we choose C language as programming language to compare the time of direction finding by means of correlation interferometer algorithm and correlation interferometer algorithm based on dimension separation. The results are illustrated in Table 50.1.

From Table 50.1, it is obviously that the speed of correlation interferometer algorithm based on dimension separation is almost 40 times of correlation interferometer algorithm, therefore, proves the rapidity of correlation interferometer algorithm based on dimension separation.

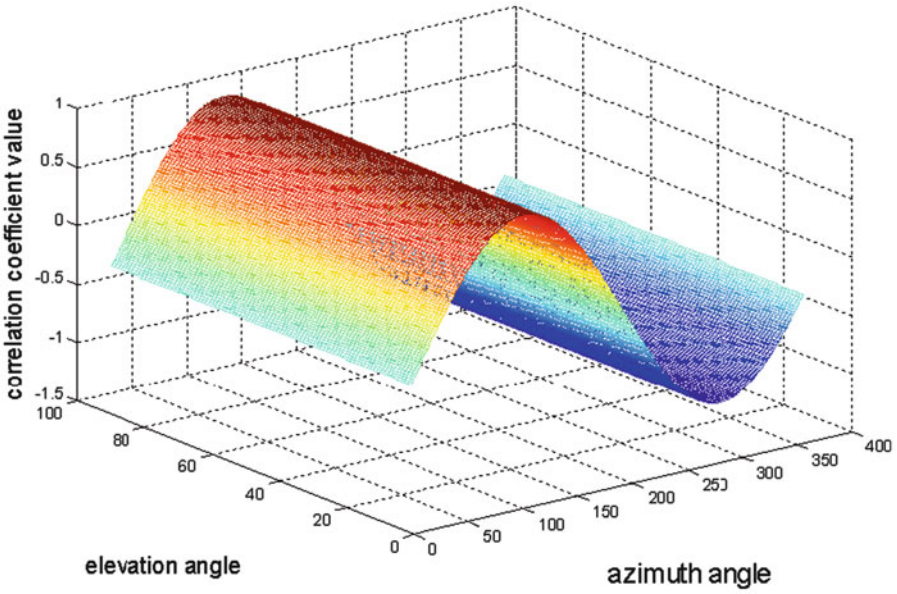

Fig. 50.2 Distances between assumed phase differences and actual values

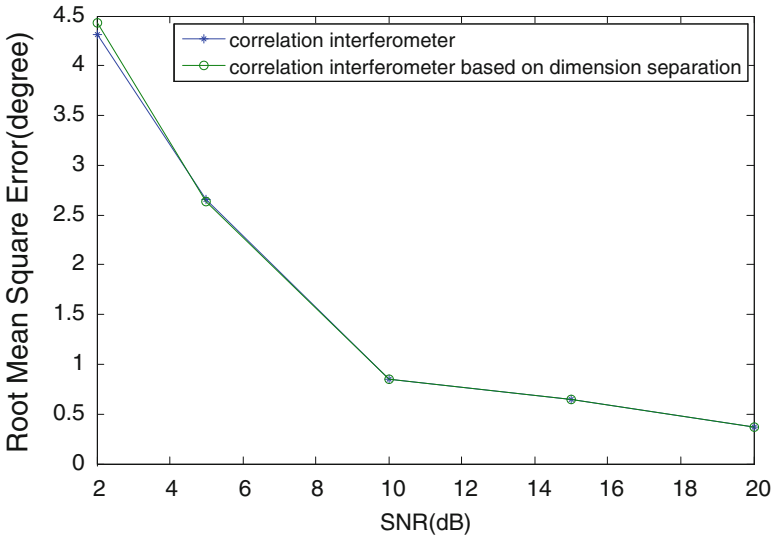

Fig. 50.3 Azimuth angle

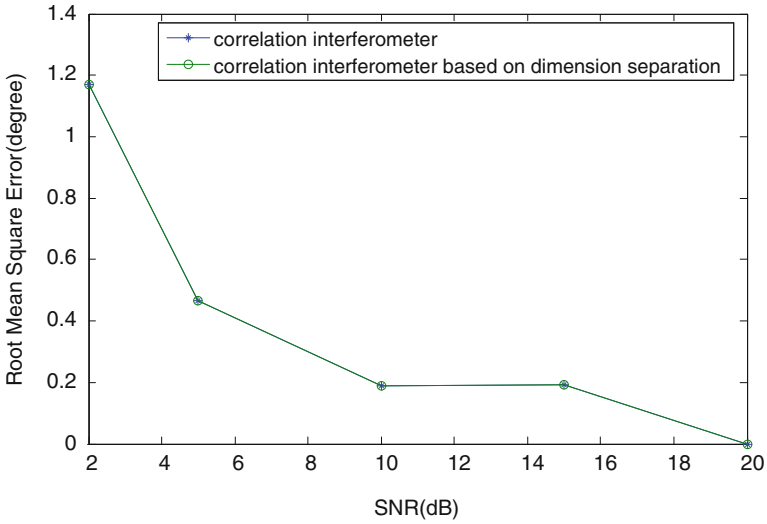

Fig. 50.4 Elevation angle

Table 50.1 The Comparison of Correlation Interferometer and Correlation interferometer based on dimension separation

Algorithm	Correlation interferometer	Correlation interferometer based on dimension separation
Time(ms)	4.904367	0.120739

50.6 Conclusion

Two-dimensional correlation interferometer algorithm based on dimension separation proposed in this chapter that provides intensive ability to resolve the long-time direction finding in conventional correlation interferometer. The proposed approach utilizes the principle that the same azimuth angle has the same correlation coefficient value in different elevation angles to simplify the original 2-dimensional angle searching by dividing it into two 1-dimensional searching corresponding to azimuth angle and elevation angle, and reduce the computational complexity. Meanwhile, the conditions for dimension separation are discussed. Computer simulation of direction finding algorithm based on the correlation interferometer is given to prove that correlation interferometer algorithm based on dimension separation has superior performance and at the same time maintains high direction finding precision.

References

1. Davies N (1983) Cicular arrays. In: The handbook of antenna design, vol 2, chapter 12. Peregrinus, London
2. Bensson O, Vincent F, Stoica P, Gershman AB (2000) Approximate maximum likelihood estimator for array processing in multiplicative noise environments. IEEE Transon SP 48 (9):2506–2518
3. Ghogho M, Swami A, Durrani TS (2001) Frequency estimation in the presence of Doppler spread: performance analysis. IEEE Trans SP 49(4):777–789
4. Pujo GL, Sintes C, Lurton X (2005) High-resolution interferometry for multibeam echosounders. Oceans Europe 1:345–349
5. Struckman K (2006) Correlation interferometer geolocation. In: Antennas and propagation society international symposium, IEEE, pp 1141–1144
6. Henault S, Antar YMM, Rajan S, Inkol R, Wang S (2008) Impact of mutual coupling on wideband adcock direction finders. In: Canadian conference on electrical and computer engineering, CCECE 2008, pp 001327–001332
7. Bo Xiong (2006) DOA estimation based on phase-difference. In: 8th international conferece on signal processing, vol 1
8. Dev C-S, Lab EW, Kim D-Y (2006) The fast correlative interferometer direction finding using I/Q Demodulator. In: Communications, APCC' 06, Asia-Pacific Conference, pp 1–5
9. Shar R (2008) Simulation of polarizer impact on circular interferometer performance. In: 11th IEEE international conference on computational science and engineering workshop, CSEWORKSHOPS' 08, pp 334–339
10. Yilong Niu, Jincai Sun, Yi Wang (2009) 2-D direction finding based on signal phase matching principle using an acoustic vector-sensor. In: 4th IEEE conference on industrial electronics and applications, ICIEA 2009, pp 3872–3875

Chapter 51
Improved Positioning Algorithm Using the Linear Constraints of Scatterer in Two Base Stations

Fei Zhou and Xin-Yue Fan

Abstract How to restraint non-line-of-sight(NLOS) error is an interesting field. Traditional way to restraint NLOS mainly includes: NLOS identify and NLOS reconstruction. In high multipath environment, these ways can not get good performance. The way proposed by this chapter mainly utilizes the linear constraints of scatterer in two base stations to improve traditional way. Simulation results shows improved positioning algorithm can suit for complicate multipath environment and get good positioning precision.

Keywords NLOS • Multipath • Reconstruction • Scatterer

51.1 Introduction

Positioning Algorithm Using scatterer information is a developing idea to restraint NLOS error in recent years. These are mainly divided into two kinds, one way is utilizing different scatterer model to get some statistic information, e.g. Probability density function (pdf) of time-of-arrival (TOA) or angel-of-arrival (AOA). Then some algorithms was used to reconstruct parameters that relate to positioning [1, 2]. Another way does not need scatterers model and statistic information. It mainly utilizes geometry layout relation among base station, scatterer and mobile station (MS) to design positioning model. And uncertain NLOS is transformed to fixed factor. Influence of NLOS error would be weakened. So positioning error mainly influenced by measurement parameters. It can improve positioning precision very much without doubt [3–5].

F. Zhou (✉) • X.-Y. Fan
School of Communication and Information Engineering, Chongqing University Posts and Telecommunication, ChongQing 400065, China
e-mail: zhoufei@cqupt.edu.cn

Q. Liang et al. (eds.), *Communications, Signal Processing, and Systems*, Lecture Notes in Electrical Engineering 202, DOI 10.1007/978-1-4614-5803-6_51,

In this chapter, we mainly consider the kind of algorithm, If MS and several scatterer are in the same line, their Doppler frequency shift of signal is the same. So three cases are exits: (1) One scatterer and MS are in the same line; (2) Two scatterers and MS are in the same line; (3) Three or more scatterers and MS are in the same line.

The third case is studied in literature [6]. However, the second case is more generally than the first case. So how to implement positioning in second cases is more valuable. Aimed to high performance of line constraint positioning and inappeasable precondition, this chapter proposed an improved positioning algorithm using the linear constraint in two base stations.

This chapter is organized as follows, in Sect. 51.2, multipath signal match is presented and analyzed. In Sect. 51.3, based on signal match results, TOA reconstruction is implemented to positioning estimation. In Sect. 51.4, a common positioning algorithm is introduced. Lastly, the conclusion and simulation are drawn in Sect. 51.5

51.2 Pairing of Multi-path Signal about Different Base Station

Figure 51.1 gives brief frame of the improved algorithm, the whole algorithm includes three steps.

1. Multipath Signal Match: Base station receives multipath signal and measures its Doppler frequency shift. Signal that reflected from scatterers to base station are matched and selected to acquire two scatterers that in the same line with MS.
2. TOA Reconstruction: After multipath signal match and scatterer selection, scatterer can be positioned based on its AOA that measured by two base stations. Base on serious research proposed by this chapter, distances between MS and two scatterers can be computed. Lastly, combined to linear constraint of two scatterers, TOA reconstruction can be implemented.
3. Positioning estimation using TOA: Two scatterers are regard as virtual base station. Added that two real base stations, four TOA can be gotten. So some mature algorithms can be used to compute positioning of mobile station.

Mentioned previously, multipath components that reflected from the same scatterer to different base stations and from different scatterer that the same line with MS to the same base station is all equivalent. So the key of multipath signal match is how to distinguish the same Doppler frequency multipath signals that received from the same base station and how to pair multipath signal that reflected from the same scatterers to different base station correctly. In Fig. 51.2, positioning parameter (xsi,ysi) of ith scatterer is derived by (51.1)

$$\begin{aligned} x_{Si} &= \frac{x_2 - x_1 \tan\beta_{2i} \tan\beta_{1i} + (y_1 - y_2)\tan\beta_{2i}}{1 - \tan\beta_{1i}} \\ y_{Si} &= (x_{Si} - x_1)\tan\beta_{1i} + y_1 \end{aligned} \tag{51.1}$$

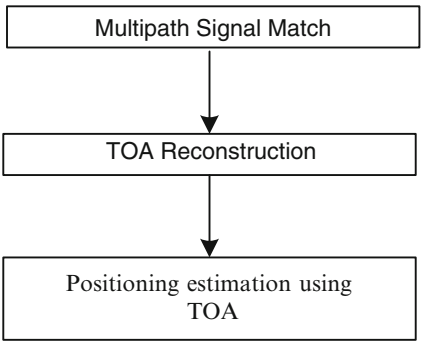

Fig. 51.1 Positioning algorithm frame

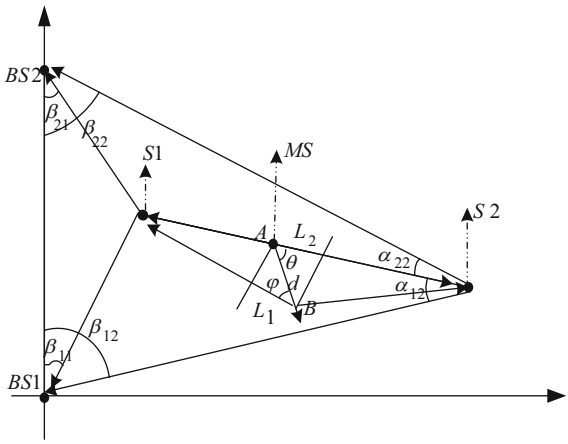

Fig. 51.2 Layout of mobile terminal

Where,(x_1,y_1) and (x_2,y_2) are positioning parameter of two base stations. β_{ji} is DOA of *i*th Scatterer that measured by *j*th base station. And the linear distance between *i*th base station and *j*th base station is derived by (51.2)

$$L_{ji} = \sqrt{\left(x_{Si} - x_j\right)^2 + \left(y_{Si} - y_j\right)^2} \tag{51.2}$$

If measurement error is zero, (51.3) is logical.

$$L_i = l_{1i} - L_{1i} = l_{2i} - L_{2i} \tag{51.3}$$

Where, (51.4) is the measurement error.

$$EN = \left[\left(l_{2i} - L_{2i}\right) - \left(l_{1i} - L_{1i}\right)\right]^2 \tag{51.4}$$

When EN is close to minimum, two sets of data is matching. So four sets of data from two base stations, $(l_{11}, \beta_{11})$and (l_{21}, β_{21})、(l_{11}, β_{11}) and (l_{22}, β_{22})、$(l_{12}, \beta_{12})$and

(l_{21}, β_{21})、$(l_{12}, \beta_{12})$and (l_{22}, β_{22}), are grouped four pair.Their EN can be computed by (51.4). The set of data that its EN is minimum must be reflected by the same scatterer and measured by two base stations separately, in others word, the set is correct pair. So the others set of data measured by the same two base stations is the others correct pair.

51.3 TOA Reconstruction

If multipath signal that different base stations is success to pair, their positioning parameter of Scatterers S_i and S_j, (x_{Si}, y_{Si}) and $\left(x_{Sj}, y_{Sj}\right)$,can by computed by (51.1). And distance between two Scatterers can by derived by (51.5)

$$L_S = \sqrt{\left(x_{Si} - x_{Sj}\right)^2 + \left(y_{Si} - y_{Sj}\right)^2} \tag{51.5}$$

So their line relation among S_i, S_j and MS can be determined by L_i, L_j, L_S.

If $L_j > L_S$ and $L_j > L_i$, S_i is located between S_j and MS.
If $L_i > L_S$ and $L_i > L_j$, S_j is located between S_i and MS
If $L_S > L_i$ and $L_S > L_j$, MS is located between S_j and S_i,

In case (1), S_i、S_j and $BS1$ can form a triangle, So (51.6) can be derived.

$$\cos\alpha_{1j} = \frac{L_S^2 + L_{1j}^2 - L_{1i}^2}{2L_S L_{1j}} \tag{51.6}$$

And In another triangle formed by S_j、MS and $BS1$, the line distance L_{line1} between MS and $BS1$, can be derived by (51.7), So TOA of $BS1$ is success to reconstruct .

$$L_{line1} = \sqrt{r_j^2 + L_{1j}^2 - 2r_j L_{1j}\cos\alpha_{1j}} \tag{51.7}$$

Similarly, the distance,L_{line2}, between MS and $BS2$,also can be derived by (51.8)

$$L_{line2} = \sqrt{r_j^2 + L_{2j}^2 - \frac{\left(L_S^2 + L_{2j}^2 - L_{2i}^2\right)r_j}{L_S}} \tag{51.8}$$

In case (2), according to triangle relations among S_j,S_i and $BSi(i = 1,2)$, L_{line1} and L_{line2} also can be acquired by (51.9). In others word, TOA reconstruction also can implemented.

$$L_{line1} = \sqrt{r_i^2 + L_{1i}^2 - \frac{\left(L_S^2 + L_{1i}^2 - L_{1j}^2\right) r_i}{L_S}}$$
$$L_{line2} = \sqrt{r_i^2 + L_{2i}^2 - \frac{\left(L_S^2 + L_{2i}^2 - L_{2j}^2\right) r_i}{L_S}} \tag{51.9}$$

Similarly, in case 3, The resolution of case (1) and (2) is still in effect.

51.4 Positioning Parameter of Mobile Computation

In Fig. 51.2, S_i,S_j can be consider as virtual base station. r_i and r_j are TOA about Line-of-Sight(LOS) from MS to two scatterers (Si,Sj). And TOA about LOS of $BS1$ and $BS2$ can be reconstruct effectively. So four TOA from different BS to MS can be used to compute positioning parameter about MS. Here, Least-Square algorithm is preferred and useful algorithm.

$$\left(x_j - x_1\right)x + \left(y_j - y_1\right)y = \frac{1}{2}\left[x_j^2 + y_j^2 - \left(x_1^2 + y_1^2\right) + r_1^2 - r_j^2\right] \tag{51.10}$$

Where, $r_j^2 = \left(x_j - x\right)^2 + \left(y_j - y\right)^2$; So (51.10) can be derived and represented by vector matrix form, (51.11):

$$AX = B \tag{51.11}$$

$$\text{Where,} X = \begin{bmatrix} x \\ y \end{bmatrix} A = \begin{bmatrix} x_2 - x_1 & y_2 - y_1 \\ x_{Si} - x_2 & y_{Si} - y_2 \\ x_{Sj} - x_{Si} & y_{Sj} - y_{Si} \end{bmatrix}$$

$$B = \begin{bmatrix} \frac{1}{2}\left[x_2^2 + y_2^2 - \left(x_1^2 + y_1^2\right) + L_{line1}^2 - L_{line2}^2\right] \\ \frac{1}{2}\left[x_{Si}^2 + y_{Si}^2 - \left(x_2^2 + y_2^2\right) + L_{line2}^2 - r_i^2\right] \\ \frac{1}{2}\left[x_{Sj}^2 + y_{Sj}^2 - \left(x_{Si}^2 + y_{Si}^2\right) + r_i^2 - r_j^2\right] \end{bmatrix}$$

Lastly, positioning of MS can be computed by (51.12)

$$X = \left(A^T A\right)^{-1} A^T B \tag{51.12}$$

51.5 Simualtion and Analysis

A macrocellular district is assumed, *BS*1 is located in the original point of Cartesian coordinate system, *BS*2 is located in (0,2000)m, and Base Station is stationary. Other parameters of simulation refer to the following table (Table 51.1).

Figure 51.3 shows MSE of different TOA and AOA measurement errors in Disk of scatterers (DOS) model that its radius is 500 m. It concludes that AOA error influences positioning precision greater than the TOA error. So when AOA error is enough small, the influence of TOA error is a littler obvious. But if AOA error is enough large, positioning error mainly is influenced by AOA error.

Figure 51.4 shows RMSE comparison of different radius of model. Its model is DOS, its standard error of TOA measurement error is 1.5 m, and its standard error of AOA measurement error is 0.005 rad. It concluded that performance of improved algorithm that proposed by this chapter is better than traditional algorithm. The performance of traditional algorithm degrades obviously when radius of model turn large. But improved positioning algorithm using the linear constraints of scatterers in two base stations has better performance. Its positioning error is briefly stable.

Table 51.1 Simulation parameters

Coordinate of MS	(800,800)
Velocity about X axis of MS	10 m/s
Velocity about Y axis of MS	10 m/s
Simulation number	2,000
Multipath number	2

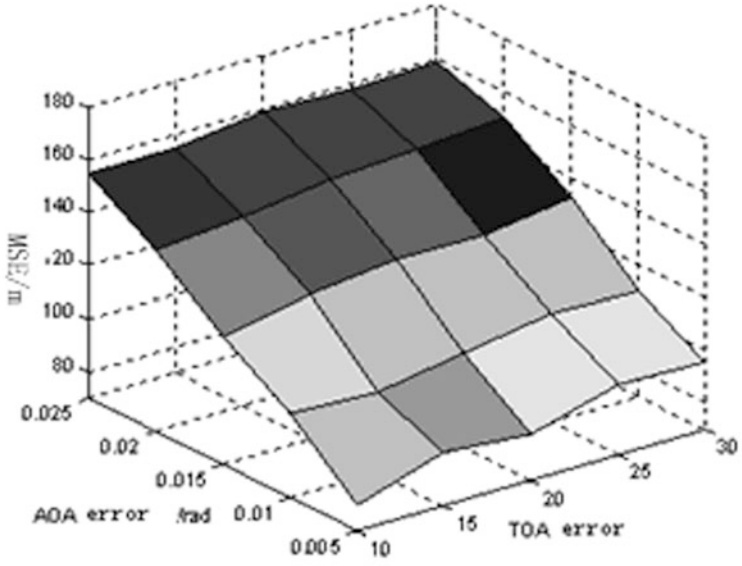

Fig. 51.3 MSE of different error about AOA and TOA

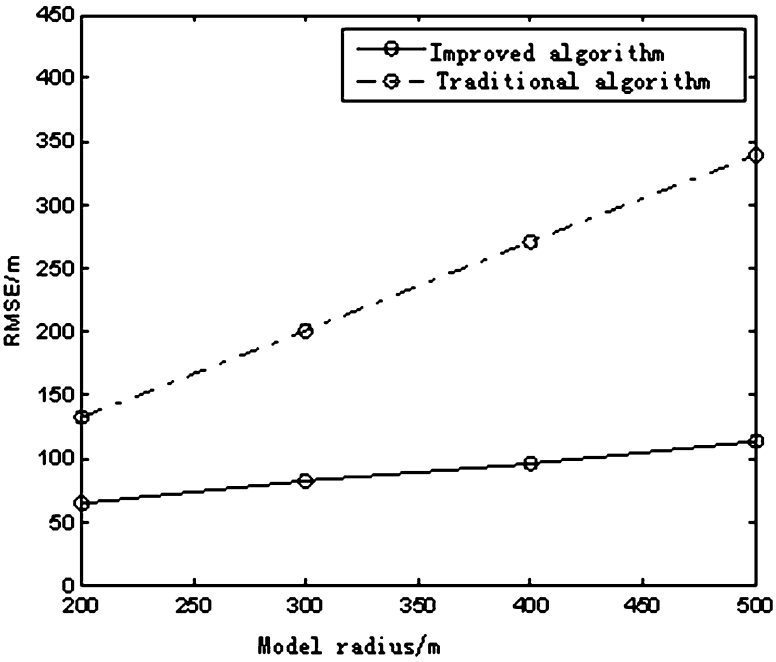

Fig. 51.4 RMSE of different radius of model

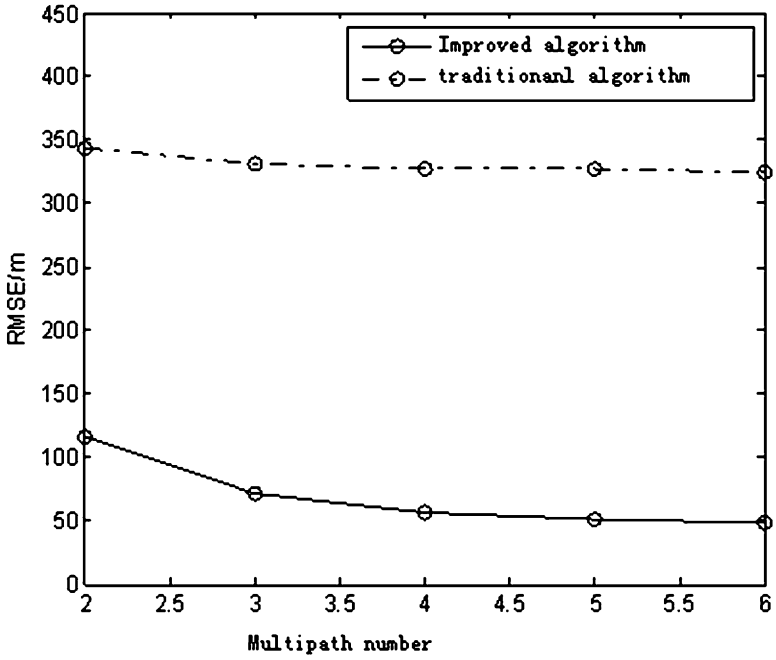

Fig 51.5 Positioning error of different multipath number in DOS Model

Figure 51.5 gives comparison of positioning error of different multipath number in DOS model. It concluded that when multipath number is more, RMSE of positioning is smaller.

Lastly, from the above comparisons, improved algorithms have the better performance than traditional algorithm. So it is necessary to continue research further.

References

1. Thomas NJ, Cruickshark DGM, Laurenson DI (2001) Calculation of mobile location using scatter information. Electron Lett 37(19):1193–1194
2. Wan Q, Yang WL, Peng YN (2004) Closed-form solution to mobile location using linear constraint on scatterer. Electron Lett 40:883–884
3. Yang TianChi, Jin Liang (2011) Single station location method in NLOS environment: the circle fitting algorithm. Sci China Inform Sci 54(2): 381–385
4. Yang TianChi, Yu ChaoQun, Wang TianPeng, Jin Liang (2011) A single observer location method under the scatter signals position disturbance situation: the constraint total least square method. Sci China Inform Sci 54(1): 146–152
5. Miao H, Yu K, Juntti M (2007) Positioning for NLOS Propagation: algorithm derivation and Cramer-rao bounds. IEEE Trans Veh Technol 56(5):2568–2580
6. Sauoradeep Venkatraman, James Caffery JR (2002) A statistical approach to non-line-of-sight BS identification. In: Proceedings of the IEEE Wireless Personal Multimedia Communications (WPMC) conference, Honolulu, Hawaii, pp 296–300

Chapter 52
Parameter Estimation of Target with Micro-Motion Based on Terahertz Radar

Jian Tu, Zhengwu Xu, and Jin Li

Abstract General model is established for the echo signal of a target with micro-motion. Then time-frequency analysis and Hough transform are utilized for motion parameter estimation and radar signature extraction in terahertz band, and the estimation of reflection coefficients of scatterers is completed through NLS and CLEAN algorithm. The simulation result shows that this method of Hough transform has the advantages of high precision and strong anti-noise. The model of echo signal and method of parameter estimation are useful for radar target detection and identification.

Keywords Micro-Doppler • Time-frequency analysis • Feature extraction • Hough transform • Parameter estimation

52.1 Introduction

Mechanical vibration or rotation of structures in a target may induce frequency modulation on returned signals and generate sidebands about the center frequency of the target's Doppler frequency [1]. The modulation due to vibrations and rotations is called micro-Doppler phenomenon. Micro-Doppler phenomenon is very common in nature, such as the human heartbeat, vibration or spin of missile warheads, etc.... while in terahertz band micro-Doppler phenomenon is particularly significant.

In this chapter, considering the micro-motion of target in the terahertz band, the echo model is established [2], time-frequency transformation and Hough transform are applied to extract the micro characteristic parameters [3–6], and the estimation

J. Tu (✉) • Z. Xu • J. Li
School of Electronic Engineering, University of Electronic Science and Technology of China, Chengdu, China
e-mail: tu_jian9527@126.com

Q. Liang et al. (eds.), *Communications, Signal Processing, and Systems*, Lecture Notes in Electrical Engineering 202, DOI 10.1007/978-1-4614-5803-6_52,

of reflection coefficient of scatterers is completed through nonlinear least squares and the CLEAN algorithm [2, 7]. These are very helpful for radar target detection and identification [8].

52.2 Target Echo Modeling

We assume a target of multiple scatterers containing macro- and micro-motion to do a compound movement on the radar radial direction. Its movement rule is a higher order polynomial of time t or the infinite series of$t$. Weierstras quantitative shows that arbitrary radial rule of motion may be a finite polynomial of t approximation

$$R_1(t) \approx \sum_{j=0}^{n} a_j t^j \tag{52.1}$$

where n is the number of finite polynomial, micro objectives of the target can be approximated as vibration or rotation movement, its rule of motion is

$$R_2(t) = A\sin(Bt + \varphi) \tag{52.2}$$

where A is the vibration amplitude, B is the frequency of vibration, $\varphi$is the initial rotation angle.

Then the echo of target can be expressed as

$$S(t) = \sum_{i=1}^{k} \sigma_i \exp\left[-\frac{j4\pi f_0}{c}\left(R_0 + \sum_{j=0}^{n} a_j t^j + A_i \sin(B_i t + \varphi_i)\right)\right] \tag{52.3}$$

where σ_i is the scattering coefficient of the i^{th} scatterer, $R_0$is the initial distance between radar and target,f_0 is the radar carrier frequency, $c$denotes the speed of light. Here only first-order and second-order translational motion are considered.

When the translational motion of target is secondary motion, that is $\sum_{j=0}^{n} a_j t^j = v_0 t + at^2$, then the rule of target's motion can be approximated as

$$R(t) = R_0 + v_0 t + at^2 + A\sin(Bt + \varphi) \tag{52.4}$$

and the phase of the baseband signal is

$$\Phi(t) = \frac{4\pi}{\lambda} \cdot R(t) = \frac{4\pi}{\lambda} \cdot \left[R_0 + v_0 t + at^2 + A\sin(Bt + \varphi)\right] \tag{52.5}$$

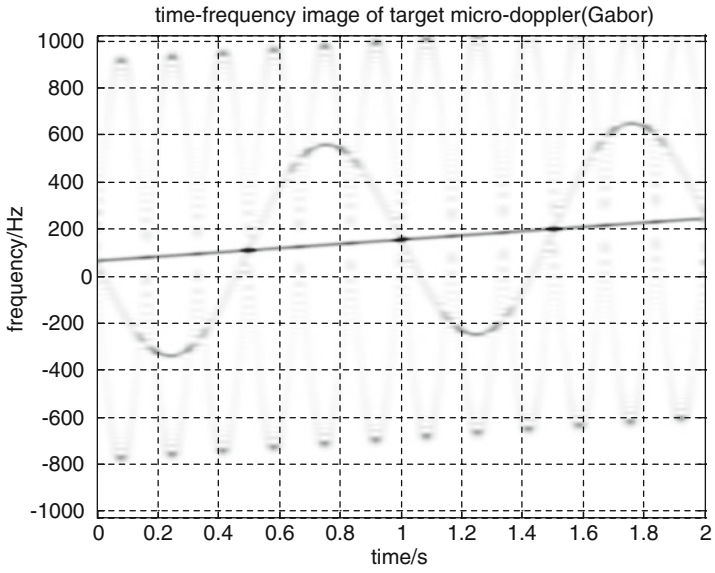

Fig. 52.1 The time-frequency image of target echo

where λ denotes radar wavelength, the instantaneous frequency of the signal can be expressed as

$$f_d = \frac{1}{2\pi} \cdot \frac{d\Phi(t)}{dt} = \frac{2}{\lambda}(v_0 + 2at + AB\cos(Bt + \varphi)) \tag{52.6}$$

Time-frequency transform with respect to the echo of target, one can get its time-frequency graph. Figure 52.1 is obtained in the simulation conditions as follows: radar carrier frequency $f_0 = 340\text{GHz}$, sampling frequency $f_s = 4096\text{Hz}$, sampling points$N = 512$, and observation time$t = 2s$.

52.3 Parameter Estimation

52.3.1 Micro-feature Extraction

We assume the set of parameters to be estimated is $\theta = (v_0, a, A, B, \varphi)$, as the straight line in Fig. 52.1 is only related to parameters(v_0, a), we can divide it into a two-dimensional matrix and three-dimensional matrix to estimate respectively, which can greatly reduce the calculation.

Straight line detection can be realized by Hough Transform which is based on duality of point-line that the collinear points of the image space corresponds to the

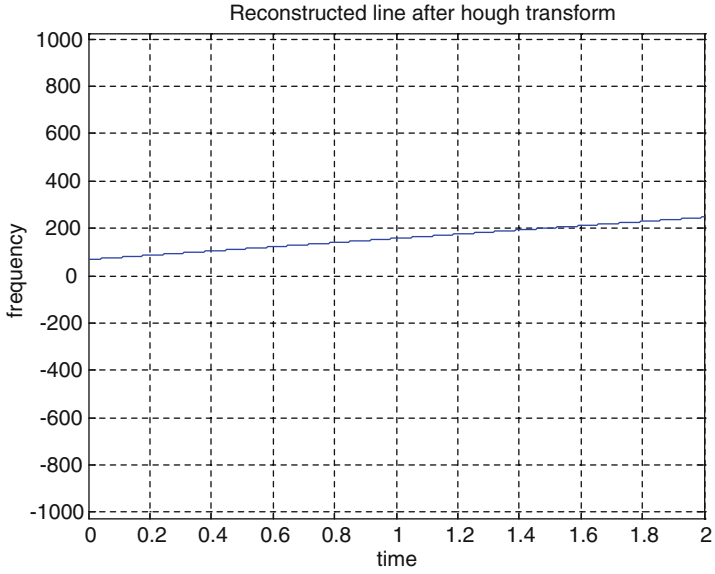

Fig. 52.2 The reconstructed line after Hough transform

lines' intersection in the parameter space. And this method weakens impact from noise and interrupt of line.

The parametric equation of a line can be expressed as

$$c = -mx + y \tag{52.7}$$

where m is the slope of the line, c is the intercept, and the above equation can be used as a straight line equation in the parameter space of c-m, which the slope of the line is x, and intercept is y.

The line detected is shown in Fig. 52.2, and the linear parameters estimated are $m = 90.6, c = 68.2$, respectively. Taking $m = 4a/\lambda$ and $c = 2v_0/\lambda$ into consideration we have $\widehat{v}_0 = 0.030, \widehat{a} = 0.020$.

Estimate the parameters of the curve after estimating the line parameters. As the amplitude, vibration frequency, initial phase of the curve in the figure only depends on parameters A, B, φ. Compensate the phase to correct the curve in the figure to a sinusoidal curve

$$\begin{aligned} S'(t) &= S(t) \cdot \exp\left[\frac{j4\pi f_0}{c}(\widehat{v}_0 t + \widehat{a}t^2)\right] \\ &\approx \sum_{i=1}^{k} \sigma_i \exp\left[-\frac{j4\pi f_0}{c}(R_0 + A_i \sin(B_i t + \varphi_i))\right] \end{aligned} \tag{52.8}$$

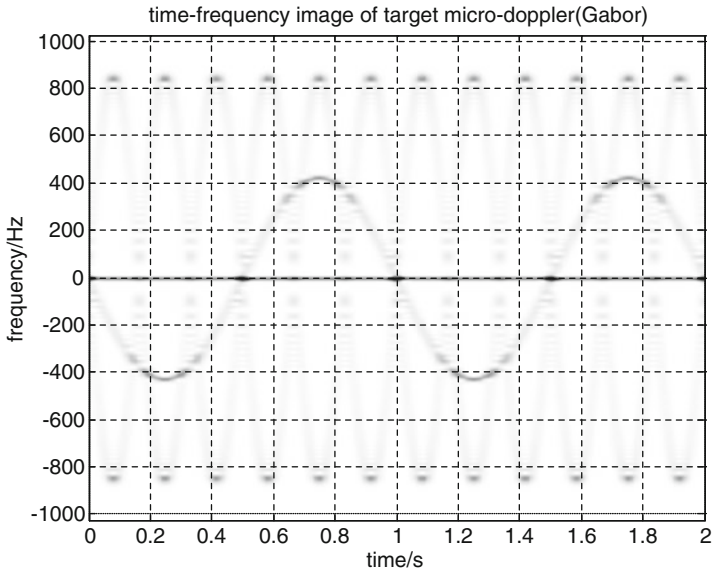

Fig. 52.3 The time-frequency image of target echo

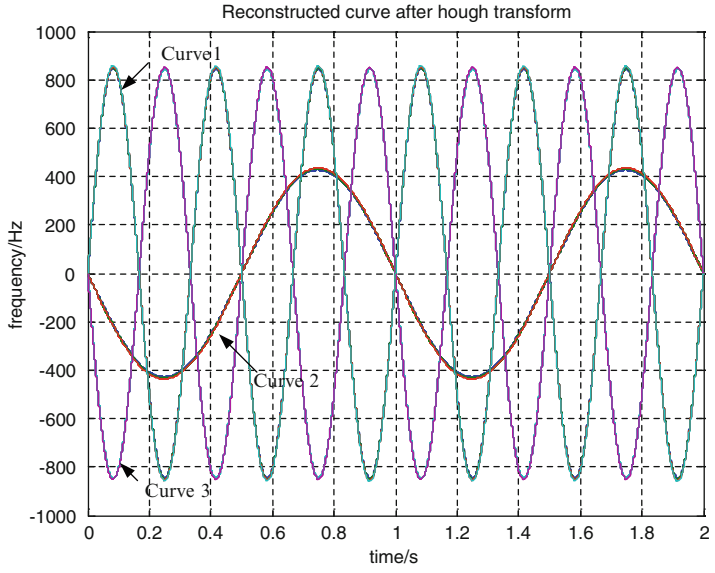

Fig. 52.4 The reconstructed line after Hough transform

Now time-frequency transformation of the echo signal is carried out in the same simulation condition as Fig. 52.1, as shown in Fig. 52.3.

There are a few methods for micro-Doppler feature extraction such as peak detection, the first-order conditional moment method and sinusoidal curve Hough transform detection method, that are all based on time-frequency analysis methods. Here sinusoidal curve Hough transform detection method is chosen (Fig. 52.4).

Micro-Doppler frequency of rotation, vibration target can be written as$f = \rho \sin(\omega t + \theta)$, where $\rho$is the amplitude, $\omega$is the angular frequency, andθdenotes the initial phase. A simple transformation is utilized to the expression

$$\rho = \frac{f}{\sin(\omega t + \theta)} \tag{52.9}$$

Assume that the time-frequency image of the signal is$I$, the steps to parameterize the sinusoidal curves are given as follows:

Step 1 Set the range of ρ, ω, θ, and establish a discrete parameter space.
Step 2 Establish a three-dimensional accumulator array$A(\rho, \omega, \theta)$, and initialize all elements of $A(\rho, \omega, \theta)$ to zero.
Step 3 Set the appropriate threshold, if the amplitude of pixel on$I$exceeds the threshold, add 1 to the corresponding accumulator$A(\rho, \omega, \theta)$.
Step 4 Find the local peak to determine the values of parameters (ρ, ω, θ) of all the sinusoidal curves.

It can be detected that the parameters of curve 1 are $\rho_1 = 854.3$,$\omega_1 = 6\pi$,$\theta_1 = 2\pi$.$\rho_2 = 854.3$,$\omega_2 = 6\pi$, $\theta_2 = \pi$of curve 2. $\rho_3 = 427.2$,$\omega_3 = 2\pi$, $\theta_3 = \pi$ of curve 3.

From (52.6) we know that

$$f = \frac{2}{\lambda} \cdot AB\cos(Bt + \varphi) = \rho \sin(\omega t + \theta) = \rho \cos(\omega t + \theta - \frac{\pi}{2}) \tag{52.10}$$

It can be calculated:

$\widehat{A}_1 = \widehat{A}_2 = 0.020$, $\widehat{A}_3 = 0.030$, $\widehat{B}_1 = \widehat{B}_2 = 6\pi$, $\widehat{B}_3 = 2\pi$, $\widehat{\varphi}_1 = 3\pi/2$, $\widehat{\varphi}_2 = \widehat{\varphi}_3 = \pi/2$.

Compared with the estimation method based on order-one time conditional moment method and W-V peak detection method, sinusoidal Hough transform detection method has the advantages of high precision and strong anti-noise. Consider the simulated condition as follows: the distance between target and radar is 2,000 m, the radar carrier frequency is 340 GHz, there are two scatterers in the target, the radius of gyration of each scatterer are both 0.02 m, and their angular velocity are 6π rad/s and 2π rad/s, respectively, the initial angle of rotation for each are –π/2 and π/2, the observation time is 1 s and SNR = −6 dB.

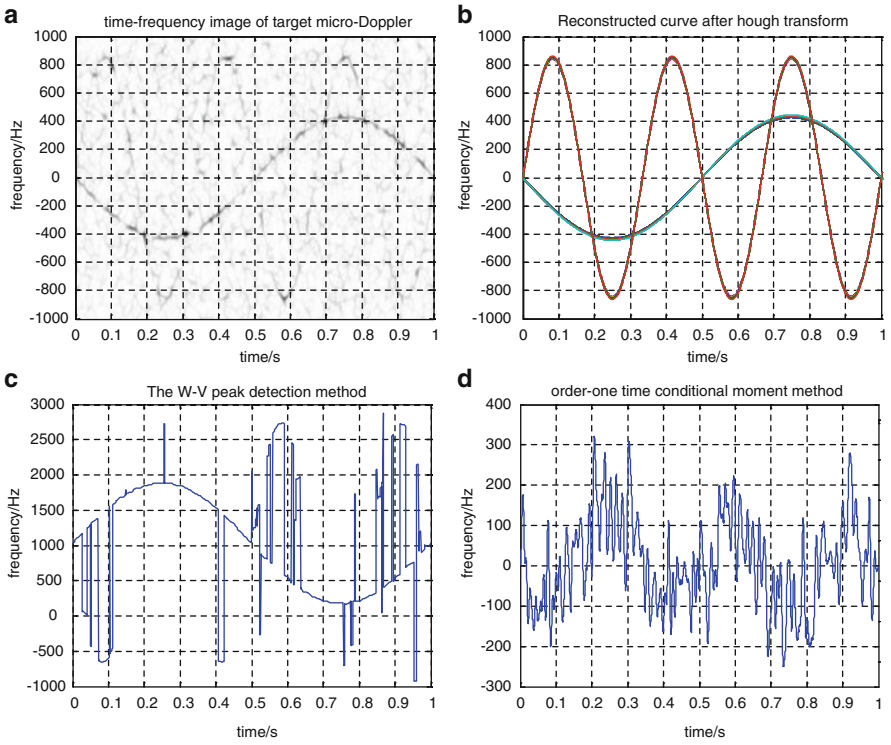

Fig. 52.5 Comparison of three methods of parameters estimation while SNR $= -6$ dB

The simulation results of the sinusoidal Hough transform detection; W-V peak detection method and order-one time conditional moment method are as shown in As seen in Fig. 52.5, for micro-Doppler spectrum estimation of multiple scatterers with noise, order-one time conditional moment method has been completely ineffective, and peak detection, while sinusoidal Hough transform detection method still maintains a high estimation accuracy.

52.3.2 Scattering Coefficient Estimating Based on Non-linear Least Squares (NLS)

In cases when the parameters of scatterers have been estimated, the NLS algorithm may be applied to the data with previously estimated scattering coefficient responses removed via the CLEAN algorithm. The echo of target is

Table 52.1 The estimated parameters of all scatterers

	$\widehat{v}_0$	$\widehat{a}$	$\widehat{A}$	$\widehat{B}$	$\widehat{\varphi}$	$\widehat{\sigma}$
Scatterer 1	0.03	0.020	0	0	0	1.0481
Scatterer 2	0.03	0.020	0.020	6π	$3\pi/2$	0.8154
Scatterer 3	0.03	0.020	0.020	6π	$\pi/2$	0.8959
Scatterer 4	0.03	0.020	0.030	2π	$\pi/2$	1.0452

$$S(t) = \sum_{i=1}^{k} \sigma_i \exp\left[-\frac{j4\pi f_0}{c}\left(R_0 + v_0 t + at^2 + A_i \sin(B_i t + \varphi_i)\right)\right] \tag{52.11}$$

then the i^{th} iteration of NLS may be expressed as

$$\begin{aligned} \min_{\widehat{\sigma}} I(\widehat{\sigma}) &= \arg\min_{\widehat{\sigma}} \left\| S_{i-1}(t) - \widehat{\sigma} S_i(t;\theta) \right\| \\ &= \arg\min_{\widehat{\sigma}} \sum \left| S(t) - \widehat{\sigma} S_i(t;\theta) \right|^2 \end{aligned} \tag{52.12}$$

where

$$S_i(t) = S_{i-1}(t) - S_i(t-\theta) \tag{52.13}$$

Such that $S_{i-1}(t)$ is the residual echo with the echo of $(i-1)^{th}$ scatterer estimated and removed. For $i = 1, S_0(t) = S(t)$, and $S_i(t,\theta)$ denotes the radar echo of i^{th} scatterer.

Following the CLEAN approach, after estimating each scatterer's reflection coefficient, the current scatterer is subtracted from the frame via (52.13) and (52.12) is re-initialized with the location of the next strongest peak. This procedure is performed until the reflection coefficient of all the scatterers has been estimated.

Establish the detection model of target after extracting all the parameters

$$S(t) = \sum_{i=1}^{4} \widehat{\sigma}_i \exp\left[-\frac{4\pi f_0}{c}\left(R_0 + \widehat{v}_0 t + \widehat{a}t^2 + \widehat{A}_i \sin(\widehat{B}_i t + \widehat{\varphi}_i)\right)\right] \tag{52.14}$$

all the parameters in the equation are given in the table below (Table 52.1).

If the translational motion of target is first-order, use the above method can estimate the parameters and establish the detection model of target.

52.4 Conclusion

This chapter establishes a novel echo model of target with micro-motion to analyze the characteristics of micro motion and investigates methods for motion parameter estimation and micro-Doppler signature extraction form target. Estimation of micro

motion parameters is completed through time-frequency transformation of the echoed signal and Hough transformation in terahertz band, and NLS and the CLEAN algorithm is utilized to estimate the scattering coefficients of each scatterer. This simulation result proves that linear Hough transform detection method and sinusoidal Hough transform detection method have high precision and good anti-noise performance which can accurately extract the micro-parameters. By adopting this estimate method, exact parameters are obtained for given signals. Thus greatly precise the following steps of target detection and identification.

References

1. Chen VC, Li FY, Ho SS (2006) Micro-Doppler effect in radar phenomenon, model and simulation study. IEEE Trans AES 42(1):2–21
2. Fogle ORE (2011) Micro-range-micro-doppler feature extraction and association. In: Proceedings of the IEEE radar conference, Dayton, OH, USA, pp 167–171
3. Jin Li, Yiming Pi (2010) Research on terahertz radar target detection algorithm based on the extraction of micro motion feature. J Electron Meas Instrum 24(9):803–807
4. Chen VC, Ling H (2002) Time-frequency transform for radar imaging and signal analysis. Artech House, Boston
5. Boashash B (2003) Time-frequency signal analysis and processing. Elsevier, Amsterdam
6. Shengzhi Du (2012) High accuracy Hough transform based on butterfly symmetry. Electron Lett 48(4):199–201
7. Qi Wang, Mengdao Xing (2008) High-resolution three-dimensional radar imaging for rapidly spinning targets. Geoscience and Remote Sensing. IEEE Trans 46(1):22–30
8. Lei JJ, Lu C (2005) Target classification based on micro-Doppler signature. In: Proceedings of international conference on radar, Washington, USA, May 2005, pp 895–899

Part XIII
Biological Signal Processing

Chapter 53
Terahertz Radar Signal for Heart and Breath Rate Detection Based on Time-Frequency Analysis

Yuanjie Wu, Zhengwu Xu, and Jin Li

Abstract The method of human heartbeat and breath detection in terahertz band is studied in this chapter which uses frequency information extraction with twice T-F (time-frequency) analysis towards echo signal. Firstly, the echo model of human target is built and accurate speed information, containing the micro features of human target ,is got by the combination of WVD (Wigner-Ville distribution) T-F analysis and centroid curve. Then, frequency of heartbeat and breath is extracted accurately by the second T-F analysis. According to the comparative analysis, SPWVD (smoothed pseudo Wigner-Ville distribution) based on the windowed WVD can effectively reduce the disturbance of cross-terms which can favor the detection of heartbeat and breath.

Keywords Terahertz • Heartbeat • Breath • Centroid • SPWVD

53.1 Introdution

Terahertz radar has a very narrow radar beam and huge bandwidth of signal which can be used to precise target imaging [1]. Compared to other band, features of micro Doppler are more obvious [2]. Terahertz signal can penetrate certain material clothes and be reflected back by the skin. Therefore, a Doppler modulation on the radar echo is generated by even the short-term micro movement when human target is in the radar beam [3]. Relative to the movement of human body, breath and heartbeat which are generated by the movement of lungs and heart are micro motions [4].

Y. Wu (✉) • Z. Xu • J. Li
School of Electronic Engineering, University of Electronic Science and Technology of China, Chengdu, China
e-mail: baozi433@gmail.com

Q. Liang et al. (eds.), *Communications, Signal Processing, and Systems*, Lecture Notes in Electrical Engineering 202, DOI 10.1007/978-1-4614-5803-6_53,

Currently, the methods of heart and breath rate detection are divided into contact and non-contact ways [5]. The former one has a lot of detection methods in the clinic, such as: ECG (electrocardiogram), respiration belt. However, these detection methods mainly rely on sensors, electrodes and some other devices attached to the body. As the condition restricts its scope of application, those methods are not suitable for security check and battlefield environment. Micro pulse radar [5] and microwave technology [6] are the non-contact ways which all use the echo signal to detect objects. But these techniques are limited for distance, frequency detection accuracy and capability of weak signal detection in the complex environments such as avalanches, earthquakes and debris flow.

53.2 Target Modeling

For Terahertz continuous wave radar, assuming that the transmitter and receiver are located at the same location away from the radar, the signal transmitted at time t can be defined as

$$S_T(t) = e^{j2\pi f_c t} \tag{53.1}$$

Here, f_c is the frequency of the transmitted signal. In fact, f_c is 240 GHz. The signal received at time t is

$$S_R(t) = e^{j2\pi f_c (t - \frac{2R(t)}{c})} \tag{53.2}$$

c is the speed of light , the delay of radar echo is $2R(t)/c$. This assumption is known as the start-stop approximation. For the speed of light is much larger than the speed of the subject's body, the assumption is of high precision.

Once the radar signal bounces off the target, its energy is collected at the receiver. The signal is then demodulated by local oscillator. The modulated received signal is

$$S_{MR}(t) = S_R(t) \cdot e^{-j2\pi f_c t} = e^{-j2\pi(2\lambda^{-1}R(t))} \tag{53.3}$$

Here, $\lambda = c/f_c$ is the wavelength of radar wave.

There are also some harmonic components besides the main frequencies refer to some ECG data. The periodic motion of breath can be seen as a sinusoidal model. To simplify the analysis, assuming that the human body is stationary which is to say the speed of target is zero, the human target model can be established as

$$R(t) = R_0 + r_1 \sin(2\pi f_1 t) + r_2 \delta(f_2 t - \tau) \tag{53.4}$$

Table 53.1 Model parameters table

Carrier frequency	f_c	240 GHz
Fixed distance	R_0	10 m
Breathing displacement	r_1	5.5 mm
Heartbeat displacement	r_2	0.9 mm
Breath rate	f_1	0.25 Hz
Heart rate	f_2	1.2 Hz
Heartbeat radius	r	0.25 m
Heart rate shift	τ	0

Here, R_0 is the overall fixed distance from the person to the radar, r_1, r_2 is the displacement of breathing and heartbeat, f_1, f_2 is the frequency of breathing and heartbeat, τ is some heart rate shift ,and δ is defined as

$$\delta(t) = \frac{1}{1-2a}\left(\left|t - \frac{1}{2} - \lfloor t \rfloor\right| - a + \left|\left|t - \frac{1}{2} - \lfloor t \rfloor\right| - a\right| \right) \tag{53.5}$$

For $a = 1/2 - r \cdot f_2$, where r is their heartbeat radius.

The following parameters are set to simulation

In accordance with the parameters in Table 53.1, the simulation models are as follows

The signal is simulated from 0 to 6 s and the data consistent with the parameters in the figure and table (Fig. 53.1).

53.3 Detection Algorithms

53.3.1 Principle

For the continuous wave after demodulation, the Doppler frequency is

$$f_D = \frac{d}{dt}\left(2\lambda^{-1}R(t)\right) = \frac{2\dot{R(t)}}{\lambda} \tag{53.6}$$

Here, λ is the wavelength of signal. Thus, the Doppler shift in the received radar signal is proportional to the target's velocity $\dot{R(t)}$ which means that if only we can accurately measure the instantaneous frequency of our data at any given time, the velocity of the subject's body can be determined. When the target is stationary, the speed signals are due to breath and heartbeat completely. Twice T-F analysis are attempted to detect heartbeat and breathing frequency. In order to get real-time diagram of the signal where frequency changes over time, we apply the first T-F

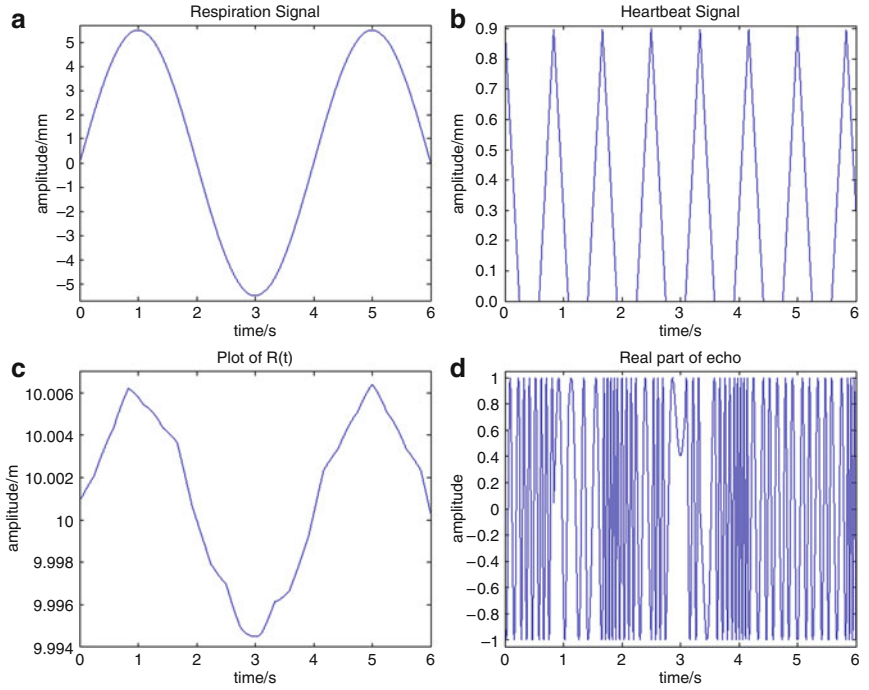

Fig. 53.1 Simulated data. (**a**) the model of breath, (**b**) the model of heartbeat, (**c**) the plot of $R(t)$, (**d**) the real part of simulated data

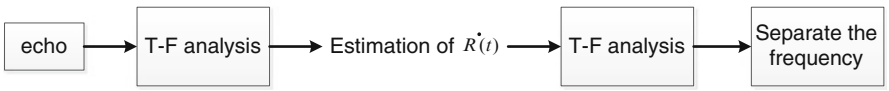

Fig. 53.2 Follow chart

analysis which is the estimation of $\dot{R}(t)$. Then further T-F analysis is used to extract the main frequency of $\dot{R}(t)$.

Initial algorithm processes (Fig. 53.2):

Throughout the analysis, the steps of different T-F analysis methods are not same which means select appropriate T-F analysis methods can effectively reduce the computation. As we can't get the estimated $\dot{R}(t)$ through a simple T-F analysis, the ridgeline and centroid curve extraction method are used to approximate $\dot{R}(t)$, and the approximation results will directly affect the subsequent frequency extraction.

The effect of T-F analysis depends largely on the T-F distribution function. An ideal time-frequency distribution not only has a high resolution in the T-F domain but also should accurately reflect the instantaneous frequency of the signal. Commonly used time-frequency distributions are short-time Fourier transform (STFT) [7] and WVD [8, 9]. T-F resolution of STFT is related to the length of the window, and the time resolution is high while the window is small, and vice versa. When the signal included multiple components, it is difficult to select a window function to meet several different requirements. That is the reason that the application of STFT has been restricted.

53.3.2 Time-Frequency Method

WVD: When the instantaneous autocorrelation of signal is computed, we do the Fourier analysis. Compared to STFT, the result is energetic representation of signal which avoids the windowed resolution. PWVD and SPWVD are the windowed forms of WVD. They reduce the cross-term interference which is at the expense of frequency resolution.

If the T-F analysis is WVD, there is no need to compute the spectrogram, because the WVD itself is the energetic representation of T-F analysis. After the first T-F analysis, the signal $\dot{R}(t)$ is estimated. There are two ways to approximate signal $\dot{R}(t)$ to extract the breath and heart rates:

1. *Ridgeline*

$$ridgeline(t) = \arg\max_{f \in R} W_z(t,f) \tag{53.7}$$

   For any given time t, we find the particular f where the value of $W_z(t,f)$ is maximized. We make these dominant frequencies as a function of t and get a curve known as the ridgeline [10].

2. *Centroid*

$$centroid(t) = \frac{\int_{-\infty}^{\infty} x(f) W_z(t,f)}{\int_{-\infty}^{\infty} W_z(t,f)} \tag{53.8}$$

   We get the weighted average of $W_z(t,f)$ for each time t, the set of points of (t,f) can be used to get the centroid [10] of $W_z(t,f)$.

$x(f)$ is the weighting function of frequency, and the value is f for the sake of simplicity.

If the frequencies resolution is very high, the two curves are similar. However, if the resolution is low, the ridgeline may be discontinuous. The reason is that signals

Table 53.2 Parameters of simulation

Carrier frequency	f_c	240 GHz
Time	t	32 s
Sampling rate 1	f_3	512 Hz
Sampling rate 2	f_4	8 Hz
Window 1	h = hamming	The length of h=127
Window 2	g = hamming	The length of g=127
Frequency points	N	512

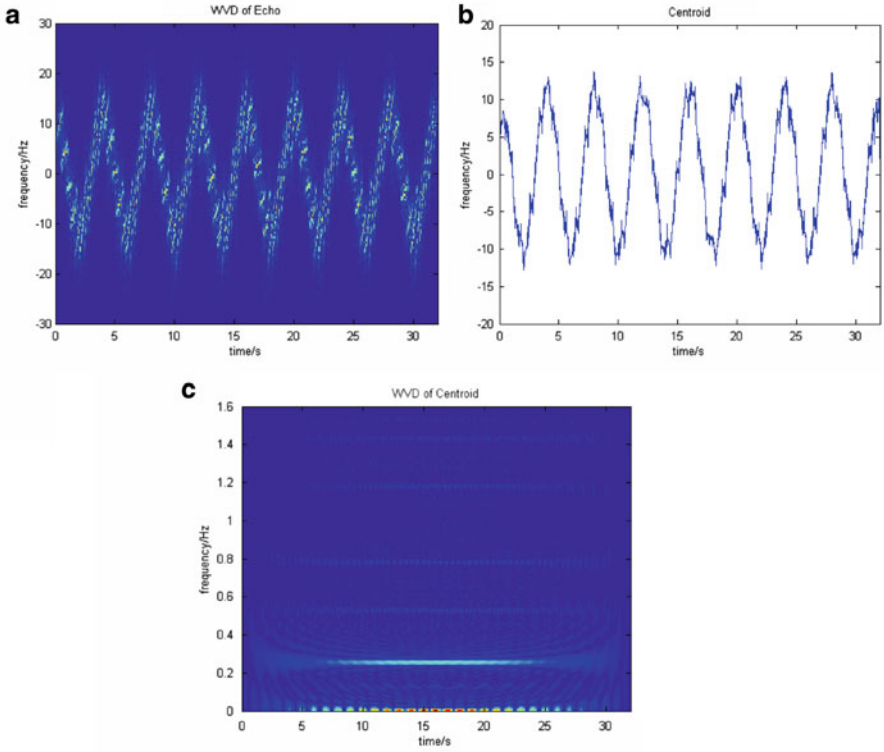

Fig. 53.3 WVD is used for T-F analysis. (**a**) WVD anaylsis of echo, (**b**) centroid curve of (**a**), (**c**) the WVD analysis of centroid

contain multiple frequency components when one frequency peak rises above another. In particular, any discontinuities will manifest themselves as noise which could possibly submerge the relatively weak heartbeat component. So centroid curve is used to approximate $\dot{R}(t)$.

Second T-F analysis is processed directly on the centroids, and different frequency components can be separated.

The following parameters are set for simulation (Table 53.2):

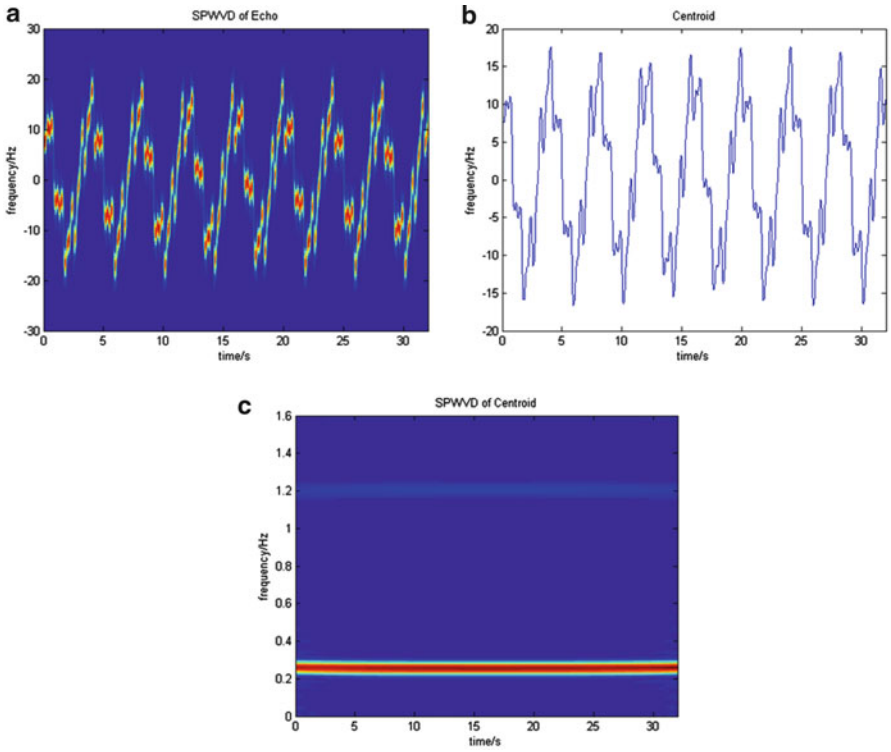

Fig. 53.4 SPWVD is used for T-F analysis. (**a**) SPWVD anaylsis of echo, (**b**) centroid curve of (**a**), (**c**) the SPWVD analysis of centroid

The energy distribution of WVD analysis is very smooth which can be seen from Fig. 53.3a. When signals contain multiple frequency components, the WVD of signal is not just the sum of every component's WVD, auto-term is the main frequency performance which is 0.25 and 1.2 Hz. The other frequencies present in the Fig. 53.3c are cross-term which would affect the extraction of frequencies. The time-frequency resolution is very high which we can get it from Fig. 53.3c. The WVD solve the problem of T-F resolution but the problem of cross-term is still a trouble.

In order to reduce the interference of cross-term, SPWVD is used to analyze the echo of human target which is a windowed form of WVD, and cross-term interference can be reduced effectively at the expense of T-F resolution.

The simulations are as follows

As can be seen from the Fig. 53.4, there are hardly cross-term interference comparing to WVD which is at the expense of T-F resolution and frequency energy is broadening within a certain range. The energy of main frequencies is located at

0.25 and 1.2 Hz which represent the frequencies of heartbeat and breath and it can be easily extracted. If the type and length of window is controlled well, the T-F resolution and reduction of cross-term will both be fine.

53.4 Conclusion

For detection of human heart and breath rate, combining the extraction method of centroid curve and SPWVD T-F analysis can effectively estimate the Doppler information of human target. SPWVD is windowed form of WVD which is able to analyze weak signals and reduce cross-term interference. Similarly, there is still a problem to be solved that is how to analyze weak signals more effectively in the low SNR environment.

Acknowledgements This work is supported by the Fundamental Research Funds for the Central Universities under Project ZYGX2011J020.

References

1. Siegel PH (2002) Terahertz technology. IEEE Trans Microw Theory Tech 50:910–928
2. Wiltse JC (1984) History of millimeter and submillimeter waves. IEEE Trans Microw Theory Tech MTT-32:1118–1127
3. Michahelles F, Matter P, Schmidt A, Schiele B (2003) Applying wearable sensors to avalanche rescue: first experiences with a NovelAvalanche Beacon. Comput Graph 27:839–847
4. Michahelles F, Wicki R Schiele B (2004) Less contact: heart-rate detection without even touching the user. In: Proceedings of the eighth international symposium on wearable computers, Arlington
5. Siegel PH (2004) Terahertz technology in biology and medicine. IEEE Trans Microw Theory Tech 52(10):2438–2447
6. Greneker EF (1997) Radar sensing of heartbeat and respiration at a distance. Radar 97:150–154
7. Allen JB, Rabiner LR (1977) A unified approach to short-time Fourier transform analysis and synthesis. Proc IEEE 65(11):1558–1564
8. Hlawatsch F, Krattcnthaler W (1992) Bilinear signal synthesis. IEEE Trans Signal Process 40 (2):352–363
9. Hlawatsch F, Boudreaux-Bartcls GF (1992) Linear and quadratic time-frequency signal representations. IEEE Signal Process Mag 9(2):21–67
10. Peltonen V, Tuomi J, Klapure A, Huopaniemi J, Sorsa T (2002) Computational auditory scene recognition. In: Proceedings of the IEEE international conference on acoustics, speech, and signal processing, vol 2. pp 1941–1944

Chapter 54
Throat Polyps Detection Based on Patient Voices

Zhen Zhong, Zhangliang Chen, Qilian Liang, and Shuifang Xiao

Abstract In this paper, we present a new approach for throat polyps detection based on patient's vowel voices using fuzzy classifiers. Based on human voice samples and Hidden Markov Model, we show that transformed voice samples (linearly combined samples) follow Gussian distribution, further we demonstrate that a type-2 fuzzy membership function (MF), i.e., a Gaussian MF with uncertain mean, is most appropriate to model the transformed voices samples. We also apply Short-Time-Fourier-Transform (STFT) and Singular-Value-Decomposition (SVD) to the vowel voice samples, and observe that the power decay rate could be used as an identifier in throat polyps detection. Two fuzzy classifiers and a Bayesian classifier are designed for throat polyps detection based on human vowel voices /a:/ and /i:/ only, and the fuzzy classifiers are compared against the Bayesian classifier. Simulation results show that an interval type-2 fuzzy classifier performs the best of the three classifiers.

Keywords Polyps detection • Fuzzy logic systems • Bayesian classifier • Interval type-2 fuzzy classifier • Fuzzy membership functions

Z. Zhong (✉)
Dept of ENT and Neck Surgery, Peking University First Hospital, Beijing 100034, China
e-mail: zhong_zhen@sina.com

Z. Chen
College of Precision Instrument and Opto-Electronics Engineering, Tianjin University, Tianjin 300072, China
e-mail: tjuczl@126.com

Q. Liang
Dept of Electrical Engineering, University of Texas at Arlington, Arlington, TX 76019, USA
e-mail: liang@uta.edu

S. Xiao
Dept of ENT and Neck Surgery, Peking University First Hospital, Beijing 100034, China
e-mail: xiao_ent@yahoo.com.cn

Q. Liang et al. (eds.), *Communications, Signal Processing, and Systems*, Lecture Notes in Electrical Engineering 202, DOI 10.1007/978-1-4614-5803-6_54,

54.1 Introduction

The throat polyps detection is a field which demands more investigation. Traditionally, the methods of diagnosis are indirect laryngoscope, video-laryngoscope, and stroboscope light [1]. However, most of these methods need special instrument, and mainly depend on the experience of the pathologists. It would be desirable if throat polyps could be detected based on the patient vowel voices only. Traditional pattern recognition techniques such as Bayesian classifier, known as the optimal classifier, could be used if the voice samples follow certaain distribution, and this belongs to model-based statistical processing. In human's voices, the voice amplitude is highly bursty, and we believe that no statistical model can really demonstrate the uncertain nature of the voice. Fuzzy logic systems (FLS) are model free. Their membership functions are not based on statistical distributions. In this paper, we, therefore, apply fuzzy techniques to polyps patient diagnosis.

In Sect. 54.2, we model voice samples using interval type-2 Gaussian membership function. In Sect. 54.3, we apply STFT and SVD to voice samples. In Sect. 54.4, a Bayesian classifier is proposed. Performances of the three classifiers are evaluated in Sect. 54.5. Conclusions are presented in Sect. 54.6.

54.2 Modeling Voice Samples Using Hidden Markov Model and GaussianPrimary MF with Uncertain Mean

In [3], autoregressive Hidden Markov Model (HMM) was used to represent voice samples x_i, which means we could have

$$x_k = -\sum_{i=1}^{p} b_i x_{k-i} + n_k \tag{54.1}$$

where n_k is Gaussian noise, and b_i $(i = 1, 2, \cdots, p)$ are the autoregression coefficients where p is autoregressive order. So

$$x_k - \sum_{i=1}^{p} c_i x_{k-i} = n_k \tag{54.2}$$

where $c_i = -b_i$. Which means the difference between samples (or their linear combinations) follows Gaussian distribution.

Based on the voice data we have collected, we observed that the vowel /a:/ samples (x_k) don't follow Gaussian distribution, as illustrated in Fig. 54.1a, but when we choose $p = 5$, $c_1 = c_2 = c_3 = c_4 = 0$, $c_5 = 1$, i.e.,

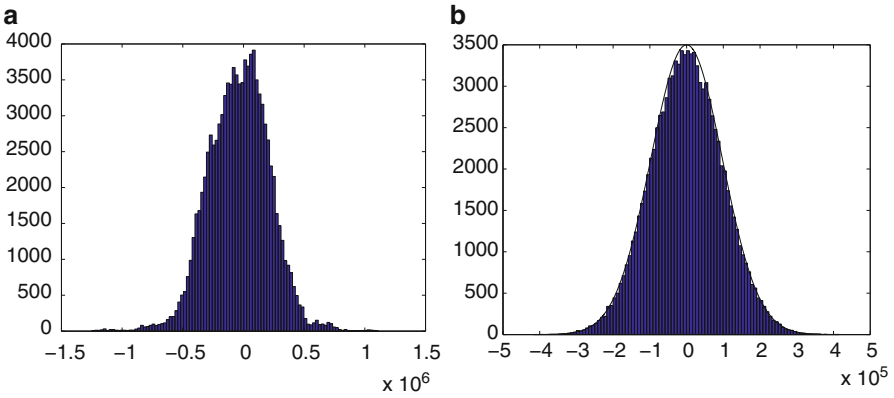

Fig. 54.1 (a) The histogram of 100,000 voice /a:/ samples x_k; (b) the histogram of transformed voice samples $x_k - x_k$-5 and its matching to a Gaussian distribution

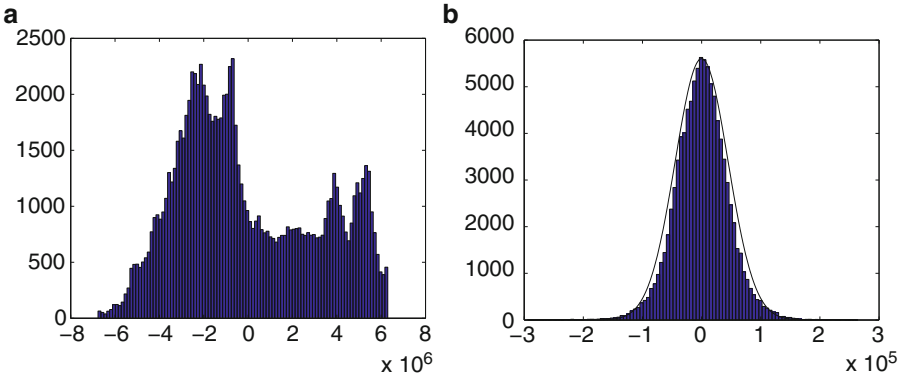

Fig. 54.2 (a) The histogram of 100,000 voice /a:/ samples x_k; (b) the histogram of transformed voice samples $x_k - x_k$-1 and its matching to a Gaussian distribution

$$x_k - x_{k-5} = n_k^a \tag{54.3}$$

the new sequences follow Gaussian distribution, as illustrated in Fig. 54.1b. Similarly, we observed that the vowel /i:/ samples (x_k) don't follow Gaussian distribution, as illustrated in Fig. 54.2a, but if we choose $c_1 = 1$ $p = 1$, i.e.,

$$x_k - x_{k-1} = n_k^i \tag{54.4}$$

follows Gaussian distribution, as illustrated in Fig. 54.2.

We, therefore, tried to model the the new transformed voice sequences $n_k{}^a$ and $n_k{}^i$, to see if a Gaussian MF can match its nature. For $n_k{}^a$ and $n_k{}^i$ from each subject (human) for 100,000 samples, we equally separate it into ten segments, and computed the mean m_i and std σ_i of the ith segment, $i = 1, 2, \cdots, 10$. We also computed the mean m and std σ of the entire sequence (100,000 samples). To see which value – m_i or σ_i – varies more, we normalized the mean and std of each segment using m_i □ m, and σ_i □ σ, and we then computed the std of their normalized values, σ_m and σ_{std}. We observed that $\sigma_m \gg \sigma_{std}$. We conclude, therefore, that if the transformed voice samples of each segment (short range) of the voice samples are Gaussian distributed, then the transformed voice samples in an entire video trAff0054ic (long range) is more appropriately modeled as a Gaussian with uncertain mean. This justifies the use of the Gaussian MFs with uncertain means to model the transformed voice samples.

54.3 Identifying Polyps Patient Voice Using Short-Time Fourier Transform andSingular-Value Decomposition

STFT uses a slide window to determine the sinusoidal frequency and phase content of a signal as it changes over time. The STFT of the voices is a matrix, how to extract its information for throat polyps detection? We use singular-value decomposition (SVD). The SVD is an important factorization of a rectangular real or complex matrix, with many applications in signal processing and statistics. Applications which employ the SVD include computing the pseudoinverse, least squares fitting of data, matrix approximation, and determining the rank, range and null space of a matrix. Given P □ $C^{N \times M}$ (assuming $N > M$), and $rank(P) = r \leq M$. Determine a numerical estimate r' of the rank of the data sets matrix P by calculating the singular value decomposition

$$P = U[\Sigma 000]V^T, (54.5)$$

where, U is an $N \times N$ matrix of orthonormalized eigenvectors of PP^T, V is an $M \times M$ matrix of orthonormalized eigenvectors of P^TP, and Σ is the diagonal matrix $\Sigma = diag(\sigma_1, \sigma_2, \ldots, \sigma_r)$, where σ_i denotes the i^{th} singular value of P, and $\sigma_1 \geq \sigma_2 \geq \cdots \geq \sigma_r > 0$. Using SVD, the STFT of voices could be diagonalized, and the diagonal values in Σ could be used to represent the speaker voice power decay in the frequency domain. Generally the σ_1 is much higher than σ_2, and the decay from σ_1 to σ_2 somehow represent how a person could handle his voice freely. For illustration purpose, we plot the singular values (σ_i) $(i = 1, 2, \cdots, 10)$ in Fig. 54.4 for the two patients whose spectrogram were plotted in Fig. 54.3. Observe Fig. 54.4, the voice power decay rate, i.e., $Pd = \sigma_1 - \sigma_2$, is higher for a normal person than that of a patient with throat polyps, which means that a normal person could handle his/her voices more freely (with higher power changes from one

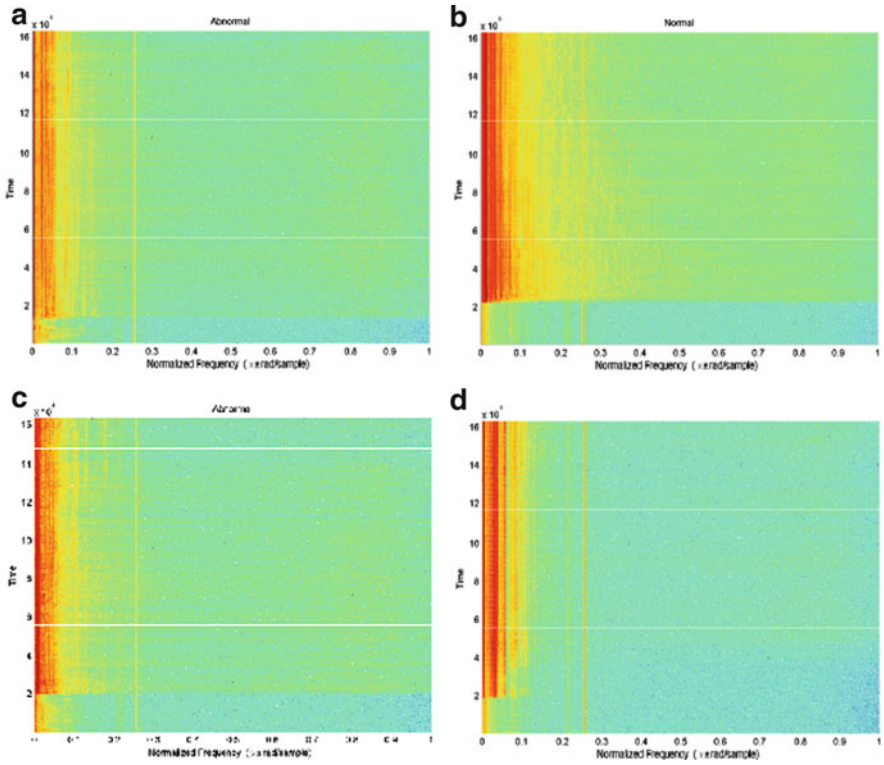

Fig. 54.3 The ten largest singular values of STFT of two patients in Fig. 54.4

frequency to another frequency). So voice power decay rate could be used as an identifier on throat polyps detection. In this paper, we will use the vowel /a:/ and /i:/ power decay rate in fuzzy classifiers for throat polyps detection.

54.4 Bayesian Classifier for Throat Polyps Detection

Bayesian decision theory [2] provides the optimal solution to the general decision-making problem. We assume that each patient has equal probability to have throat polyps, i.e., H_1: *Polyps*, and H_2: *Normal*, so $p(H_1) = p(H_2) = 0.5$. If each transformed vowel voice samples (/a:/ and /i:/) of patient j follows Gaussian distribution, $\mathrm{X_j} \stackrel{\Delta}{=} [x_j^a\ x_j^i]^{\mathrm{T}}$ stands for the samples from patient j for vowel /a:/ and /i:/, then

$$p(\mathbf{x}_j|v_j) = \frac{1}{(2\pi)|\Sigma_\mathbf{j}|^{1/2}} \exp[-\frac{1}{2}(\mathbf{x}_j - \mathbf{m}_j)^T \Sigma_\mathbf{j}^{-1}(\mathbf{x}_j - \mathbf{m}_j)] \tag{54.6}$$

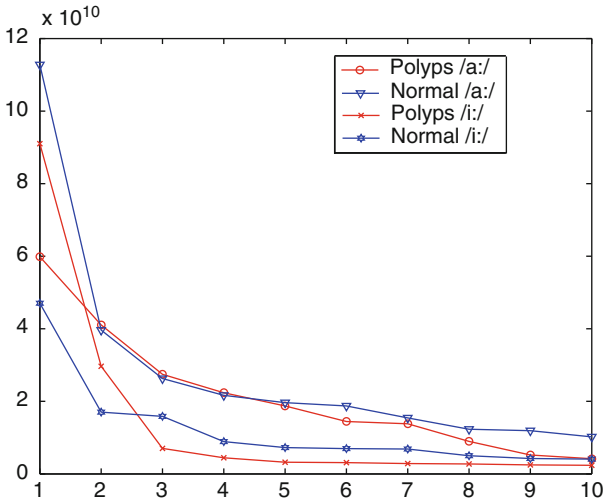

Fig. 54.4 Spectrogram using a Short-Time Fourier Transform (STFT). Window size of STFT is 2,048, and overlap between two neighbor window is 1,024. (a) Is from a throat polyps patient speaking vowel /a:/; (b) is from a normal person speaking vowel /a:/; (c) is from the throat polyps patient speaking vowel /i:/; (d) is from the normal person speaking vowel /i:/

where $\mathrm{m_j} \triangleq [m_{\mathrm{j}}^{\mathrm{a}}\ m_{\mathrm{j}}^{\mathrm{i}}]^{\mathrm{T}}$ and $\mathbf{\Sigma_j} = diag\{\sigma_j^{a2}, \sigma_j^{i2}\}$ are the mean vector (2×1) and covariance matrix (2×2) of $\mathbf{x}_j$. In this case,

$$p(\mathbf{x}|H_1) = \sum_{i=1}^{10} p(\mathbf{x}|v_i)p(v_i) \tag{54.7}$$

$$p(\mathbf{x}|H_2) = \sum_{i=11}^{20} p(\mathbf{x}|v_i)p(v_i) \tag{54.8}$$

Based on Bayes decision theory, since $p(H_1) = p(H_2) = 0.5$, we obtain the decision rule:

$$\text{Claim throat polyps if} p(\mathbf{x}|H_1) > p(\mathbf{x}|H_2) \tag{54.9}$$

$$\text{No throat polyps if} p(\mathbf{x}|H_1) < p(\mathbf{x}|H_2) \tag{54.10}$$

$$Not sure if p(\mathbf{x}|H_1) = p(\mathbf{x}|H_2) \tag{54.11}$$

This Bayesian polyps detector will be used in Sect. 54.5.

54.5 Simulations

We extract the general features and behavior of /a:/ and /i:/ voices for 20 patients, of which 10 have throat polyps and 10 have no throat polyps, and determine one discriminant rule for each patient in the domain of interest. In choosing the antecedents of the fuzzy classifier, we make full use of the statistical knowledge (mean and std) obtained from the patient voices. We used 100,000 samples in vowel /a:/ and /i:/ respectively to establish a discriminant rule for each patient. All-in-all, we obtained 20 rules, one per patient.

To evaluate the performance of the two fuzzy detectors, we used another group of 20 patients (testing group), which has no overlap with the first group of 20 patients whose vowel samples were used for fuzzy rules. By this means, it would help to demonstrate that our classifiers are robust. We also collected 100,000 voice samples for /a:/ and /i:/ respectively for each patient in the testing group. To demonstrate that our classifiers are able to detect throat polyps using a small number of samples, we made our detection based on every 5,000 samples, with 20 independent detections ($20 \times 5,000$) for each patient. During testing, we obtain the mean $\mathbf{m}^{\mathrm{t}} = [m_a{}^t, m_i{}^t]$ for each 5,000 /a:/ and /i:/ samples.

54.5.1 Design of three Throat Polyps Detectors

54.5.1.1 Design of Type-1 Fuzzy Polyps Detector

For a type-1 fuzzy classifier, the lth rule, R^l, is ($l = 1, \cdots, 10$):

R^l: IF the transformed /a:/ voice is $\mathrm{F}_1{}^l$ and the transformed /i:/ voice is $\mathrm{F}_2{}^l$ and /a:/ power decay rate is $\mathrm{F}_3{}^l$ and /i:/ power decay rate is $\mathrm{F}_4{}^l$ THEN this patient has throat polypus (+ 1) [or throat normal (− 1)].

The antecedents $\mathrm{F}_k{}^l$ ($k = 1, 2, 3, 4$) are described by a type-1 Gaussian MF whose mean, $m_p{}^l$, and std, $\sigma_p{}^l$, are determined by known patient voice samples. More specifically, $m_1{}^l$ and $\sigma_1{}^l$ are the mean and std of voice /a:/ samples in the 100,000 samples of patient l in the first group; $m_2{}^l$ and $\sigma_2{}^l$ are the mean and std of /i:/ samples in the 100,000 samples of patient l in the first group. To determine $m_3{}^l$, $\sigma_3{}^l$, $m_4{}^l$, and $\sigma_4{}^l$, we partition the voice samples into ten segments for /a:/ and /i:/ respectively, and obtain the STFT of each segment. Then apply SVD to the STFT matrix to obtain the power decay rate for each segments. The mean and std of the ten power decay rates are $m_3{}^l$ ($m_4{}^l$) and $\sigma_3{}^l$ ($\sigma_4{}^l$). The consequent corresponds to $y^l = +1$ (polypus) or $y^l = -1$ (normal) in the fuzzy detector.

For a *type-1 fuzzy detector*, its input, $\mathbf{m}^{\mathrm{t}} = [m_a{}^t, m_i{}^t, Pd_a, Pd_i]$, is obtained from 5,000 vowel samples from patient in the testing group. Pd_a and Pd_i are the power decay rate for /a:/ and /i:/.

54.5.1.2 Design of Type-2 Fuzzy Polyps Detector

For type-2 fuzzy classifiers, the lth rule, R^l, is ($l = 1, \cdots, 10$):

R^l: IF the transformed /a:/ voice is $\tilde{F}_1^l$ and the transformed /i:/ voice is $\tilde{F}_2^l$ and /a:/ power decay rate is $F_3{}^l$ and /i:/ power decay rate is $F_4{}^l$ THEN this patient has throat polypus (+ 1) [or throat normal (− 1)].

The antecedents $\tilde{F}_k^l$ ($k = 1, 2, 3$) are described by a type-2 MF, i.e., a Gaussian MF with uncertain mean, whose mean $m_k{}^l \in [m_{k1}{}^l, m_{k2}{}^l]$ and std $\sigma_k{}^l$ are determined by the voice samples of patients in the first group. $F_3{}^l$ and $F_4{}^l$ are same as those in type-1 fuzzy detector.

More specifically, $\sigma_k{}^l$ ($k = 1, 2$) are determined using the same method as described in Sect. 54.5.1.1, and $m_{k1}{}^l$ and $m_{k2}{}^l$ are determined as follows. We divided the 100,000 frames of the lth known patient into 10 equal-length (10,000 samples) segments, and computed the mean $m_1{}^{lj}$ of /a:/ samples in the jth segment ($j = 1, \cdots, 5$). Let

$$m_{11}^l = \min_{j=1,\cdots,10} m_1^{lj}$$

$$m_{12}^l = \max_{j=1,\cdots,10} m_1^{lj}$$

so $[m_{11}{}^l, m_{12}{}^l]$ is the range of uncertain mean of /a:/ voice samples of the lth known patient. We obtained the ranges of uncertain mean of /i:/ samples ($[m_{21}{}^l, m_{22}{}^l]$) in a similar manner.

For a *type-2 fuzzy detector*, its input, $\mathbf{m}^t = [m_a{}^t, m_i{}^t, Pd_a, Pd_i]]$, is obtained from 5,000 vowel samples from patient in the testing group.

54.5.1.3 Design of Bayesian Classifier

Observe from (54.6), that the Bayesian classifier needs $\mathbf{m}_i = [m_i{}^a, m_i{}^i]^T$ and $\Sigma_\mathbf{i} = diag\{\sigma_i{}^{a2}, \sigma_i{}^{i2}\}$. In our design, $m_i{}^a$ and $\sigma_i{}^a$ are the mean and std of vowel /a:/ in the 100,000 samples of patient i in the first group; similarly, $m_i{}^i$ and $\sigma_i{}^i$ are the mean and std of vowel /i:/ in the 100,000 samples of patient i in the first group; and, its input $\mathrm{x} \stackrel{\Delta}{=} \mathrm{m}^t$, where $\mathbf{m}^t$ is obtained from the mean value of 5,000 voice samples from a patient in the testing group.

54.5.2 Performance Analysis

We computed the average probability of miss detection ($p_r(\varepsilon)$) for each fuzzy detector as well as for the Bayesian detector in $20 \times 20 = 400$ independent classifications (20 patients each with 20 5,000-sample segments), and please be

aware that the voices of the first group patients were used to design the fuzzy rules, and the testing group of patients have no overlap with the first group. Simulations show that $p_r(\varepsilon) = 25\ \%$ for Bayesian classifier, $p_r(\varepsilon) = 18\ \%$ for type-1 fuzzy classifier, and $p_r(\varepsilon) = 14\ \%$ for type-2 fuzzy classifier.

54.6 Conclusions

Based on human voice samples and Hidden Markov Model, we showed that transformed voice samples (linearly combined samples) follow Gussian distribution, further we demonstrated that a type-2 fuzzy MF, i.e., a Gaussian MF with uncertain mean, is most appropriate to model the transformed voices samples. We also applied STFT and SVD to the vowel voice samples, and observe that the voice power decay rate could be used as an identifier in throat polyps detection. Two fuzzy classifiers and a Bayesian classifier were designed for throat polyps detection based on human vowel voices /a:/ and /i:/ only, and the fuzzy classifiers are compared against the Bayesian classifier. Simulation results showed that an interval type-2 fuzzy classifier performs the best of the three classifiers.

References

1. de Oliveira Rosa M, Pereira JC, Grellet M (2000) Adaptive estimation of residue signal for voice pathology diagnosis. IEEE Trans Biomed Eng 47(1):96–104
2. Duda RO, Hart PE (1973) Pattern classification and scene analysis. Wiley, New York
3. Rabiner LR (1989) A tutorial on hidden Markov models and selected applications in speech recognition. Proc. IEEE 77(2):257286

Index

Q. Liang et al. (eds.), *Communications, Signal Processing, and Systems*, Lecture Notes in Electrical Engineering 202, DOI 10.1007/978-1-4614-5803-6,